Characterization of Minerals, Metals, and Materials 2018

Edited by

Bowen Li
Jian Li
Shadia Ikhmayies
Mingming Zhang
Yunus Eren Kalay
John S. Carpenter
Jiann-Yang Hwang
Sergio Neves Monteiro
Donato Firrao
Andrew Brown
Chenguang Bai
Zhiwei Peng
Juan P. Escobedo-Diaz
Ramasis Goswami
Jeongguk Kim

TMS

Springer

The Minerals, Metals & Materials Series

Bowen Li · Jian Li · Shadia Ikhmayies
Mingming Zhang · Yunus Eren Kalay
John S. Carpenter · Jiann-Yang Hwang
Sergio Neves Monteiro · Donato Firrao
Andrew Brown · Chenguang Bai
Zhiwei Peng · Juan P. Escobedo-Diaz
Ramasis Goswami · Jeongguk Kim
Editors

Characterization of Minerals, Metals, and Materials 2018

TMS

Springer

Editors

See next page

ISSN 2367-1181 ISSN 2367-1696 (electronic)
The Minerals, Metals & Materials Series
ISBN 978-3-319-72483-6 ISBN 978-3-319-72484-3 (eBook)
https://doi.org/10.1007/978-3-319-72484-3

Library of Congress Control Number: 2017960930

Printed on acid-free paper

This Springer imprint is published by Springer Nature
The registered company is Springer International Publishing AG
The registered company address is: Gewerbestrasse 11, 6330 Cham, Switzerland

Editors
Bowen Li
Michigan Technological University
Houghton, MI
USA

Jian Li
CanmetMATERIALS
Hamilton, ON
Canada

Shadia Ikhmayies
Al-Isra University
Amman
Jordan

Mingming Zhang
ArcelorMittal Global R&D
East Chicago, IN
USA

Yunus Eren Kalay
Middle East Technical University
Ankara
Turkey

John S. Carpenter
Los Alamos National Laboratory
Los Alamos, NM
USA

Jiann-Yang Hwang
Michigan Technological University
Houghton, MI
USA

Sergio Neves Monteiro
Military Institute of Engineering
Rio de Janeiro
Brazil

Donato Firrao
Politecnico di Torino
Turin
Italy

Andrew Brown
UNSW Canberra
Campbell, ACT
Australia

Chenguang Bai
Chongqing University
Chongqing
China

Zhiwei Peng
Central South University
Changsha
China

Juan P. Escobedo-Diaz
UNSW Canberra
Campbell, ACT
Australia

Ramasis Goswami
Naval Research Laboratory
Washington, DC
USA

Jeongguk Kim
Korea Railroad Research Institute
Uiwang
South Korea

Preface

The interrelationships among composition, structure, property, process, and performance of a material are fundamental for materials research, development, manufacturing, and application. Materials characterization is the key to reveal these relationships throughout the entire circulation process of materials, from raw materials selection, through various process stages, final products, and applications, up to materials recycling and reuse. Characterization provides accurate and realistic information for the in-depth understanding of a material, such as how the material fails, how to improve the performance, how to simulate a material, and what is the lifetime of the material.

The symposium Characterization of Minerals, Metals, and Materials is sponsored by the Materials Characterization Committee of The Minerals, Metals & Materials Society (TMS) and focuses on the advancements of characterization of the minerals, metals, and materials from the bulk down to the nanoscale and the applications of characterization results on the processing of these materials. The subjects of the symposium include extraction and processing of various minerals, process–structure–property relationship of metal alloys, glasses and ceramics, polymers, composites, and carbon used as functional and structural materials. All characterization methods and techniques and their applications are covered in this symposium. The methodology and instrumentation for materials characterization are emphasized.

The symposium on which this volume is based is one of the largest—and also one of the broadest in terms of scientific coverage—held during the TMS Annual Meeting, which attracts materials scientists, mineralogists, metallurgists, mechanical engineers, chemists, physicists, microscopists, and instrumental experts from academia and industry across the world. In the TMS 2018 Annual Meeting held in Phoenix, AZ, USA, the symposium received 175 abstract submissions; of these 121 were accepted for oral presentation in 14 technical sessions, and 54 will be presented as posters.

This proceedings volume includes 76 manuscripts of original research. The peer-reviewed manuscripts were invited or contributed by the researchers from the fields of materials science, engineering, metallurgy, physics, chemistry,

manufacturing, and applications. The authors of the papers represent diversity from more than 20 countries in the North America, South America, Asia, Europe, Australia, and Africa. Although the papers were divided into 14 sections based on the technical sessions of the symposium, the topics of this volume cover a wide range of materials characterization from composition, structure, process, property, performance, and their interrelations in the materials from bulk-scale down to microscale and nanoscale. The material sequence and related processes were widely covered and include minerals, metals and alloys, ceramics, polymers and composites, semiconductors, optical, electronic, magnetic, environmental materials, and concrete. Among these papers, metallic materials and various composite materials take the major portion of the proceedings.

This book is a valuable reference for academic and industry readers from advanced undergraduates to experienced professionals who wish to learn about all types of characterization methods, their development, and applications in general, specifically in minerals, metals, and materials. It also provides up-to-date achievements on many types of materials for the scientists and engineers engaged in research, development, and production. The readers will enjoy the diversity of topics in this book with novel approaches and contributions on materials, micro- and nanostructures, performance, and relationships in practical uses.

The editors of this book are very grateful to the authors for their contribution of the manuscripts and willingness to share their new findings with the materials community. The editors would also like to express appreciation to TMS for giving this symposium the opportunity to publish a stand-alone volume. We also thank the Materials Characterization Committee and Extraction and Processing Division for sponsoring this symposium. The editors also thank the publisher, Springer, for their production of this book. Finally, we acknowledge the efforts by the past chairs and members of the Materials Characterization Committee, who continuously built this great symposium and who attracted talented and creative people and research groups from around the world to the committee and symposium.

Bowen Li

Contents

Part XIII Poster Session

About the Editors

Bowen Li is a Research Professor in the Department of Materials Science and Engineering and Institute of Materials Processing at Michigan Technological University. His research interests include materials characterization and analysis, metals extraction, ceramic process, antimicrobial additives and surface treatment, porous materials, applied mineralogy, and solid waste reuse. He has published more than 110 technical papers in peer-reviewed journals and conference proceedings, authored/coauthored 3 books, editor/coedited 7 books, hold 15 patents, and delivered more than 30 invited technical talks.

He received a Ph.D. in Mineralogy and Petrology from China University of Geosciences Beijing in 1998, and a Ph.D. in Materials Science and Engineering from Michigan Technological University in 2008. He has been an active member of The Minerals, Metals & Materials Society (TMS), Society for Mining, Metallurgy, and Exploration (SME), and China Ceramic Society. At TMS, he is the current Chair of the Materials Characterization Committee and member of the Powder Materials Committee and Biomaterials Committee, and former Extraction and Processing Division Award Committee member, *JOM* Subject Advisor, and Key Reader of *Metallurgical and Materials Transactions A*. He is the organizer/co-organizer of a number of international symposia and sessions. He also served as the editorial board

member of the *Journal of Minerals and Materials Characterization and Engineering, SciFed Journal of Metallurgical Science,* and *FUTO Journal Series.*

Jian Li is a senior research scientist at Canmet MATERIALS in Natural Resources Canada. He obtained his B.Sc. in Mechanical Engineering from Beijing Polytechnic University, M.Sc. in Metallurgical Engineering from Technical University of Nova Scotia (TUNS), and Ph.D. in Materials and Metallurgical Engineering from Queen's University, Kingston, Ontario, Canada. He has broad experience in materials processing and characterization including alloys deformation, recrystallization, and micro-texture development. He has extensive experience in focused ion beam (FIB) microscope techniques. He is also an expert in various aspects of SEM-EDS and EPMA techniques. He holds a patent, authored three book chapters, and published more than 120 papers in scientific journals and conference proceedings.

Shadia J. Ikhmayies received a B.Sc. from the physics department in the University of Jordan in 1983, an M.Sc. in molecular physics from the same university in 1987, and a Ph.D. in producing CdS/CdTe thin film solar cells from the same university in 2002. Now she works at Al Isra University in Jordan as an associate professor. Her research is focused on producing and characterizing semiconductor thin films and thin film CdS/CdTe solar cells. She also works in characterizing quartz in Jordan for the extraction of silicon for solar cells and characterizing different materials by computation. She published 44 research papers in international scientific journals, three chapters in books, and 73 research papers in conference proceedings. She is the author of two books for Springer *Silicon for Solar Cell Applications*, and *Performance Optimization of CdS/CdTe Solar Cells*, which are in production, the editor-in-chief of the book *Advances in Silicon Solar Cells* for Springer, and the e-book series *Material Science: Current and Future Developments* for Bentham Science Publishers, where these two books are in production.

She is a member of The Minerals, Metals & Materials Society (TMS) and the World Renewable Energy Network (WREN). She is a member of the International Organizing Committee and the International Scientific Committee in the European Conference on Renewable Energy Systems (ECRES2015-ECRES2017). She is a member of the editorial board of the *International Journal of Materials and Chemistry* for Scientific & Academic Publishing, the editor-in-chief of a book for the Research Signpost. She was a technical advisor/subject editor for *JOM*. She is a guest editor for two topical collections published in the *Journal of Electronic Materials*: European Conference on Renewable Energy Systems (2015 and 2016). She is a reviewer for 24 international journals and she is Chair of the TMS Materials Characterization Committee (2016–2017).

Mingming Zhang is currently a lead research engineer at ArcelorMittal Global R&D in East Chicago, Indiana. His main responsibilities include raw material characterization and process efficiency improvement in mineral processing and ironmaking areas. He also leads a technical relationship and research consortium with university and independent laboratory members and manages pilot pot-grate sintering test facility at ArcelorMittal Global R&D East Chicago.

He has over 15 years of research experience in the field of mineral processing, metallurgical and materials engineering. He obtained his Ph.D. in Metallurgical Engineering from The University of Alabama and his master's degree in Mineral Processing from General Research Institute for Non-ferrous Metals in China. Prior to joining ArcelorMittal, he worked with Nucor Steel Tuscaloosa, Alabama where he was metallurgical engineer leading the development of models for simulating slab solidification and secondary cooling process.

He has conducted a number of research projects involving mineral beneficiation, thermodynamics and kinetics of metallurgical reactions, electrochemical processing of light metals, energy efficient, and environmental cleaner technologies. He has published over 50 peer-reviewed research papers and is the recipient of

several U.S. patents. He also serves as editor and reviewer for a number of prestigious journals including *Metallurgical & Materials Transactions A* and *B*, *JOM*, *Journal of Phase Equilibria and Diffusion*, and *Mineral Processing and Extractive Metallurgy Review*.

Dr. Zhang has made more than 20 research presentations at national and international conferences including more than 10 keynote presentations. He is the recipient of 2015 TMS Young Leaders Professional Development Award. He has been invited by a number of international professional associations to serve as conference organizer and technical committee member. These associations include The Minerals, Metals & Materials Society (TMS) and the Association for Iron & Steel Technology (AIST).

Yunus Eren Kalay is an Associate Professor of Metallurgical and Materials Engineering and Assistant to the President at METU Ankara, Turkey. He received his Ph.D. with Research Excellence award from Iowa State University in 2009. His Ph.D. topic was related to the metallic glass formation in Al-based metallic alloy systems. Following his Ph.D., he pursued his postdoctoral research at Ames National Laboratory, where he practiced Atom Probe Tomography. In 2011, he joined the Department of Metallurgical and Materials Engineering (METE) of Middle East Technical University (METU) as an Assistant Professor and in 2014 he was promoted to Associate Professor. His research interests span microstructural evolution in metallic alloys, rapid solidification of metallic alloys, nanostructured and amorphous alloys, lead-free solders, electronic packaging, and advanced characterization techniques such as scanning and transmission electron microscopy, electron and X-ray spectroscopy, application of synchrotron X-ray scattering in materials research. He was awarded the METU Prof. Dr. Mustafa Parlar Foundation Research Incentive Award, which is a prestigious award that recognizes young scientists in Turkey with exceptional achievements and research productivity. He is also an

active member of Materials Characterization Committee and Phase Transformations Committee of TMS, and served on the organizing committees of three international and one national congress including IMMC, MS&T, and TMS. He has also been involved in many synergistic activities such as being founder editor of Turkey's first undergraduate research journal, *MATTER* (http://matter.mete.metu.edu.tr/) and organizing the Materials Science Camps for K-12 students.

John S. Carpenter is a scientist within the manufacturing and metallurgy division at Los Alamos National Laboratory. He received his Ph.D. in Materials Science and Engineering from The Ohio State University in 2010 after performing his undergraduate studies at Virginia Tech.

His research focus is on enabling advanced manufacturing concepts through experiments employing novel processing techniques, advanced characterization, and small-scale mechanical testing. Currently, he is working on projects related to the qualification of additively manufactured components and using high energy X-rays to study phase transformations during solidification in MIG cladding. Throughout his career, he has utilized many characterization techniques including neutron scattering, X-ray synchrotron, XCT, PED, TEM, EBSD, and SEM.

He has more than 55 journal publications, 1 book chapter, and 25 invited technical talks to his credit.

With regard to TMS service, he currently serves as the Extraction & Processing Division (EPD) representative on the Program Committee, the Structural Materials Division representative on the Content Development and Dissemination Committee, chair of the Advanced Characterization, Testing, and Simulation Committee, and the EPD liaison on the Additive Manufacturing Bridge Committee. He is a participating member of the Mechanical Behavior of Materials Committee and has served as chair of the Characterization Committee in the past. John serves as a Key Reader for *Metallurgical and Materials Transactions A* and has coedited special sections in *JOM* related to neutron diffraction, coherent X-ray

diffraction imaging methods, and modeling in additive manufacturing. He is the 2012 recipient of the EPD Young Leaders Professional Development Award.

Jiann-Yang (Jim) Hwang is a Professor in the Department of Materials Science and Engineering at Michigan Technological University. He is also the Chief Energy and Environment Advisor at the Wuhan Iron and Steel Group Company, a Fortune Global 500 company. He has been the editor-in-chief of the *Journal of Minerals and Materials Characterization and Engineering* since 2002. He has founded several enterprises in areas including water desalination and treatment equipment, microwave steel production, chemicals, flyash processing, antimicrobial materials, and plating wastes treatment. Several universities have honored him as a Guest Professor, including the Central South University, University of Science and Technology Beijing, Chongqing University, Kunming University of Science and Technology, Hebei United University, etc.

He received his B.S. from National Cheng Kung University 1974, M.S. in 1980 and Ph.D. in 1982, both from Purdue University. He joined Michigan Technological University in 1984 and has served as its Director of the Institute of Materials Processing from 1992 to 2011 and the Chair of Mining Engineering Department in 1995. He has been a TMS member since 1985. His research interests include the characterization and processing of materials and their applications. He has been actively involved in the areas of separation technologies, pyrometallurgy, microwaves, hydrogen storages, ceramics, recycling, water treatment, environmental protection, biomaterials, and energy and fuels. He has more than 28 patents and has published more than 200 papers. He has chaired the Materials Characterization Committee and the Pyrometallurgy Committee in TMS and has organized several symposiums. He is the recipient of TMS Technology Award and the Michigan Tech Bhata Rath Research Award.

Sergio Neves Monteiro graduated as metallurgical engineer (1966) at the Federal University of Rio de Janeiro (UFRJ). He received his M.Sc. (1967) and Ph. D. (1972) from the University of Florida, followed by a course 1975 in Energy at the Brazilian War College and Post-doctorate (1976) at the University of Stuttgart. He joined (1968) the Metallurgy Department as full professor of the postgraduation program in engineering (COPPE) of the UFRJ; was elected head of department (1978), coordinator of COPPE (1982) and Under-Rector for Research (1983); and invited as Under-Secretary of Science for the State of Rio de Janeiro (1985) and Under-Secretary of College Education for the Federal Government (1989). He retired in 1993 from the UFRJ and joined the State University of North Rio de Janeiro (UENF), from where he retired in 2012. He is now Professor at the Military Institute of Engineering (IME), Rio de Janeiro, and has published over 1200 articles in journals and conference proceedings and has been honored with several awards including the ASM Fellowship. He is top researcher (1A) of the Brazilian Council for Scientific and Technological Development (CNPq) and Top Scientist of State of Rio de Janeiro (FAPERJ); President of the Superior Council of the State of Rio de Janeiro Research Foundation, FAPERJ; (2012) and currently coordinator of the Engineering Area of this foundation. He is also president of the Brazilian Association for Metallurgy, Materials and Mining—ABM (2017–2019), a consultant for the main Brazilian R&D agencies, and a member of the Editorial Board of five international journals as well as Associate Editor of the *Journal of Materials Research and Technology*.

Donato Firrao received his Laurea in Chemical Engineering at the Politecnico di Torino, Turin, Italy, in 1968 and his M.Sc. in metallurgical engineering at The Ohio State University (OSU) on a Fulbright Scholarship in 1970. He began teaching in 1968 as an assistant professor of ferrous extractive metallurgy and a lecturer of chemistry at the Politecnico di Torino since 1971. In 1983 he became associate professor of Technology of metallic materials, gaining full professorship in the subject 3 years later. He also stayed as visiting fellow from 1978 to 1979 at the OSU Materials Science and Engineering Department, where he was named Distinguished Alumnus in 2003. He has authored more than 230 papers, primarily in the fields of physical and mechanical metallurgy and surface heat treatments. He is a member of Associazione Italiana di Metallurgia (AIM), ASTM International, ESIS, TMS, and the Turin Academy of Sciences, Fellow of ASM International (2011) and member of FAS. A founding partner of the Italian Group on Fracture (IGF) he was its secretary since its establishment in 1982, and the President between 1988 and 1994. He was cochair of the ESIS Technical Committee I (Elasto-Plastic Fracture Mechanics) from 1987 to 1996 and was named ESIS Fellow in 2016. He was President of the Federation of European Materials Societies (FEMS) from 2000 to 2001. Since 1993, he has been the president of the board of trustees of the Collegio Universitario di Torino (a private nonprofit university student housing foundation). He served as Dean of the First College of Engineering at the Politecnico di Torino from 2005 to 2012 and retired in November 2015. He is an expert in failure analysis and has acted as technical advisor to the judge in national and international trials (such as the Ustica aircraft crash, the Mattei affair, and the Sgrena/Calipari cases).

Andrew D. Brown is a Research Associate in the School of Engineering and Information Technology (SEIT) at the University of New South Wales (UNSW) Canberra, Australia. He received his B.S. in Mechanical Engineering from N.C. State University in 2009 and Ph.D. in Mechanical Engineering from Arizona State University in 2015. He has previously held research positions at the Nanoscale Tribology Lab at N.C. State and the Multiscale Materials Characterization and Multiphysics Modelling Lab at Arizona State.

His primary research interests encompass the dynamic behavior of materials under high pressures and strain rates. The focus of past research has been on investigating the microstructural weak links in shock-loaded metals. Current and future research interests include the dynamic response and fracture mechanisms in metals and metallic alloys, metallic and polymeric foam structures, novel metallic additive manufactured structures, bulk metallic glasses, and synthetic tissue materials.

He has been a member of TMS since 2011 and has served as a panel chair and poster contest judge for the Characterization of Minerals, Metals and Materials symposium since 2016 and currently serves as the symposium's Awards Committee representative.

Chenguang Bai is a Professor in the Department of Metallurgical Engineering, School of Materials Science and Engineering at Chongqing University, China. He received his B.S. in 1982, M.S. in 1987, and Ph.D. in 2003 from Chongqing University. He also furthered his study in Department of Metallurgy and Materials, University of Toronto as a visiting scholar between October 1995 to January 1997. He has been actively involved in the teaching and scientific research works in ferrous metallurgy, especially in the field of comprehensive utilization of vanadium–titanium magnetite resources. He has more than 20 patents, published more than 200 research articles, about 60 of which were in the international metallurgical periodicals. He also is Vice Chairman of Chongqing Society for Metals, and was a Member of Advisory

Committee of Experts, Department of Engineering and Materials Science, NSFC. He was the Vice President from 2009 to 2011, and the Vice Chairman of University Council of Chongqing University from 2011 to 2016.

Zhiwei Peng is an Associate Professor in the School of Minerals Processing and Bioengineering at Central South University. He received his B.E. and M.S. degrees from Central South University in 2005 and 2008, respectively, and his Ph.D. in Materials Science and Engineering from Michigan Technological University in 2012. His research interests include heat transfer in microwave heating, dielectric characterization of materials, nonthermal microwave effects, extractive metallurgy, computational electromagnetics, microwave absorbing materials, and biomaterials.

He has published 102 papers, including 71 peer-reviewed articles in multiple journals such as *International Materials Reviews*, *Metallurgical and Materials Transactions A*, *Metallurgical and Materials Transactions B*, *JOM*, *Journal of Cleaner Production*, *Journal of Power Sources*, *Fuel Processing Technology*, *Energy & Fuels*, *IEEE Transactions on Magnetics*, *IEEE Transactions on Instrumentation and Measurement*, *Ceramics International*, and *Annals of Medicine*. He has served as a key reviewer for a number of journals and been on the editorial board of the *Journal of Minerals and Materials Characterization and Engineering* since 2012. He received a TMS Travel Grant Award for the 141st TMS Annual Meeting & Exhibition, the Doctoral Finishing Fellowship and Dean's Award for Outstanding Scholarship of Michigan Technological University in 2012 and the Bhakta Rath Research Award of Michigan Technological University in 2013.

He is an active member of The Minerals, Metals & Materials Society (TMS). He has co-organized 7 TMS symposia (Characterization of Minerals, Metals and Materials in 2013, 2014, 2015, 2016, 2017 and 2018, and the 9th International Symposium on High Temperature Metallurgical Processing in 2018) and cochaired 14 TMS symposia sessions since 2012. He is

a member of the Pyrometallurgy and Materials Characterization committees, the chair of the Continuing Education Sub-Committee of the Materials Characterization Committee, a *JOM* advisor for the Pyrometallurgy Committee, and a winner of the TMS EPD Young Leaders Professional Development Award in 2014.

Juan P. Escobedo-Diaz is a Senior Lecturer in the School of Engineering and Information Technology (SEIT) at UNSW Canberra. He obtained his doctoral degree in Mechanical Engineering from Washington State University. Prior to taking up this academic appointment, he held research positions at the Institute for Shock Physics and Los Alamos National Laboratory.

His main research interests center on the dynamic behavior of materials under extreme conditions, in particular high pressure and high strain rate. His focus has been on investigating the effects of microstructural features on the dynamic fracture behavior of metals and metallic alloys. He has published primarily in the fields of Shock Physics and Materials Science.

He has been a member of The Minerals, Metals & Materials Society (TMS) since 2011. During this time he has co-organized more than 5 symposia at the Annual Meetings including the symposium on Characterization of Minerals, Metals and Materials since 2014. He was awarded a 2014 SMD Young Leaders Award.

Ramasis Goswami is a scientist with the Multi-functional Materials Branch of the Materials Science and Technology Division at Naval Research Laboratory, Washington, DC, USA. He obtained his bachelor degree in Metallurgical Engineering from Bengal Engineering College, Shibpur, India. He then earned his master's and Ph.D. degrees in Materials Engineering from Indian Institute of Science, Bangalore. He is a recipient of the Alexander von Humboldt fellowship. His current areas of research include the study of dislocation structures ahead of the crack tip, the microstructure and property relationship in metals, alloys and in multilayered thin films, and the

study of interfaces and defects in semiconducting thin films. He has published over 90 peer-reviewed articles in scientific literature.

Jeongguk Kim received his Ph.D. in Materials Science and Engineering, at the University of Tennessee, Knoxville, in 2002. The title of his Ph.D. thesis was "Nondestructive Evaluation (NDE) and Mechanical Behavior of Continuous Fiber Reinforced Ceramic Matrix Composites (CFCCs)." Currently, he is a director at the Future Transportation Systems Research Division, Korea Railroad Research Institute (KRRI), Korea. He is also a professor in the Railway Systems Engineering Department, the KRRI campus, at the University of Science and Technology, Korea.

His research interests include testing and certification of railroad components and systems, failure and safety analyses of railroad materials and systems based on fracture mechanics and several different types of NDE techniques including ultrasonic testing, acoustic emission, infrared thermography, magnetic particle testing, etc., and mechanical behavior of advanced railway materials.

His recent research efforts include development of future transportation systems such as rail–canal system based on multi-axle bogies, an innovative train–ferry system, and the smart container lift. He also enlarged his research on the development of effective maintenance technologies for high-speed train systems.

He has been a member of TMS since 1996, and he has been a regular contributor at TMS meetings as an author and session chair at the Characterization of Minerals, Metals and Materials sessions since 2005.

Part I
Characterization Methods

On FIB Milling Parameters

Jian Li and Pei Liu

Abstract In recent years, focused ion beam (FIB) has become a powerful microscopy tool. Creating large FIB cross sections are often required to characterize important microstructure features e.g. the depth and morphology of pitting corrosion and stress corrosion cracking in natural gas pipeline steels. Large FIB sectioning often takes long time that not only occupy valuable FIB microscope time, but also consume often expensive consumables that include gallium ion source, aperture and deposition gas etc. The new plasma FIB developed by FEI can speed up milling process by using much larger beam current. However, for most of the laboratories that is limited by conventional Ga ion FIB, the milling speed is limited by the relatively small beam current. In this paper, FIB milling rate are studied against milling parameters that include beam dwell time and pixel overlap. By optimizing the milling parameters, milling rate can increase significantly.

Keywords FIB · Milling rate · Sputter yield

Introduction

Soon after the development of liquid metal ion source (LMIS) in the 1960's, focused ion beam (FIB) system was invented. Small probe size of a few nanometers are available for high-resolution ion beam imaging, and high beam current density are now available with modern FIB columns for high speed ion beam milling [1]. In the early days, FIB microscopes were mostly used for IC device modification [2], failure analysis [3], and lithographic mask modification [4]. In the past decade, with increased resolution, FIB microscopy has been widely used as an effective materials science research instrument [5–7]. Examples includes FIB sectioning and imaging to reveal subsurface corrosion and stress corrosion cracking of pipeline steels, crack

J. Li (✉) · P. Liu
CanmetMATERIALS, Natural Resources Canada,
183 Longwood Road South, Hamilton, ON L8P 0A5, Canada
e-mail: jian.li@canada.ca

B. Li et al. (eds.), *Characterization of Minerals, Metals, and Materials 2018*, The Minerals, Metals & Materials Series,
https://doi.org/10.1007/978-3-319-72484-3_1

tip morphology and crack propagation mechanism studies, and production of stress-free site-specific TEM specimens [8].

Whether to prepare FIB sectioning for imaging or TEM foil extraction, milling large areas are either required or preferred. This involves removing large volume of substrate materials. In order to obtain sufficient information, we frequently need to create large FIB trenches that involve removing $\sim$400,000 μm^3 around the area of interest. For convention FIB with LMIS, this is quite a large under take. Not only it occupies valuable FIB instrument time, but also consumes a large "chunk" of expensive Ga ion source (considering typical sputter yield of 4 when milling crystalline Si). Unlike semiconductors micro devices, engineering materials are often heavy. More ion dose is required in FIB milling. Increasing milling rate is of great interest in FIB microscopy work.

Bischoff [9] summarized earlier work on FIB milling using Co, Ga, Ge, Nd and Au ions sources under acceleration voltages of 35–70 kV. He concluded major factors that could affect FIB milling rate include: acceleration voltage, density of target materials, beam dwell time, beam incident angle and specimen temperature. Using the model proposed by Sigmund [10], the calculated sputter yield of Si target increase from about 4.3 to 5.2 when the accelerating voltage of Ga ion beam increase from 35 to 70 kV. This increase in sputter yield is quite modest. Considering the adverse effect of higher acceleration voltage that include significant ion beam damage to target materials (amorphization), most commercial FIBs nowadays are designed with lower accelerating voltage of 30 kV (as opposed to 50 kV for earlier generation of Micrion FIBs). When milling crystalline materials, relative incident direction between the primary ion beam and lattice my cause significant decrease in sputter yield due to the channeling of ions along crystal axes. Sigmund [10] reported nearly 10 folds sputter yield increase when beam incident angle (θ) increase from 0^0 to 75^0. He suggested sputter yield increase is the function of $1/\cos^n\theta$ where $n \sim 2$. This explains why the milling rate increase significantly during final stage of FIB thinning of TEM specimen (compared to the milling of the bulk). Using a 35 kV Co^+ ion beam, Sigmund [10] found little difference in sputter yield when pixel dwell time change from 1 μs up to 200 μs at room temperature. However when target temperature was set at 430 °C, longer dwell time doubled the sputter yield. He attributed this increase to dynamic annealing of substrate materials when milled under short dwell time. Dynamically recrystallized target area increased chances of primary ion beam channeling that reduced sputter rate.

The ion-specimen interaction physics and these valuable research data provided FIB manufacture valuable information not only to design efficient ion column but also establish efficient milling routines for modern FIB instrument. The available milling (and deposition) routines should have been optimized to provide users with high milling rate while minimizing ion beam damage to target materials (which is extremely important in final stage of TEM specimen preparation). In most organizations, FIB microscopy time are valuable not only to save microscopy time (and reduce consumable cost), but also increase microscopy work turnaround time for clients. Improving milling rate is of great interest. In this study, based on

manufacture's default milling routine, we performed a series of milling experiments by varying beam dwell time and pixel overlap on crystalline Si and aluminum we managed to improve the milling rate significantly.

Materials and Methods

Experiments were carried out using a FEI Helios NanoLab650 FIB. The ion beam column with a Ga ion source can provide imaging resolution up to 4.5 nm, and the SEM column has a resolution of 0.8 nm. Milling experiment was performed on both single crystal Si wafer and commercial aluminum alloy under 30 kV beam acceleration and 2.5 nA current. Ga ion dose was kept constant at 10 nC/μm^2. Size of the milling boxes were set at 8 × 20 μm. Experiments were carried out at combination of various dwell time and pixel overlap. Depths of milled trenches were recorded and compared.

Results and Discussion

Dwell Time

Default milling routine for milling Si include dwell time of 1.0 μs and beam overlap of 50%. The study include changing the dwell time from 0.5 μs up to 100 μs while keeping the beam overlap constant at 50%. Milling rates (R) are also calculated based on Eq. 1. Where "d" is depth of ion milling into the target, "q" primary ion charge, and "D" is the primary ion dose [10].

$$R = \frac{\mathrm{d}}{qD} \tag{1}$$

Sputter yield (Y_s) is the escaped ions or neutrals from the target surface due to physical knock-on process caused by energetic incident Ga ions. Sputter yield can be calculated by volume loss method using a simplified equation below [10], where "d" is milling depth, "N" is atomic density of the target, and "D" is the primary ion dose.

$$Y_s = \frac{d\mathrm{N}}{D} \tag{2}$$

Milling depths, calculated milling rate and sputter yield as a result of various beam dwell times are shown in Table 1. The result show the Dwell time alone (at 50% beam overlap) has little effect in milling rate.

Table 1 Effect of beam Dwell Time on FIB milling rate of Si single crystal

Dwell (μs)	Depth (μm)	R (μm^3/nC)	Ys
0.5	2.7	0.14	4.33
1	2.7	0.14	4.33
5	2.8	0.14	4.49
10	2.8	0.14	4.49
20	3	0.15	4.81
50	3	0.15	4.81
100	3.1	0.16	4.97

The sputter yield in this study correlate well with early work by Musil et al. [11] where they use 35 keV Co beam to sputter GaAs target. When dwell time changes from 1 to 100 μs the sputter yield kept nearly constant at about 2.5 at room temperature. Sigmund [10] also reported similar sputter yield when irradiating Si with 70 keV Co and Ge ion source. The higher sputter yield in this experiment is attributed to the improved column design in modern FIB systems. Milling rates and sputter yields in Table 1 indicate the beam dwell time alone has little impact on milling rate for Si target.

Beam Overlap

Efficient FIB milling involves using energetic primary beam (Ga ions) to efficiently amorphize the top surface layer in the milled area. This reduces ion channeling into crystalline lattice, thus improves sputter yield. Ion beam diameter varies with column design. Hence when working with FIB made by different vendors (e.g. Hitachi, JEOL, Zeiss and FEI), beam diameter can be quite different even with the same beam current. When setting up FIB for milling action, beam overlap control is often made available to FIB operators. The default value are often set at 50%. For example, with 2.5 nA beam current, the beam diameter is estimated to be about 130 nm in FEI's Helios NanoLab ion column. Thus with 50% overlap, the pitch spacing is about 65 nm. In this study, we kept beam dwell time constant at 1.0 μs and change the overlap from 50% to 80% and 90%. The resulted milling rate and sputter yield, shown in Table 2, only marginally improved.

Table 2 Effect of Beam Overlap on FIB milling rate of Si single crystal

Overlap (%)	Depth (μm)	R (μm^3/nC)	Y_s
50	2.64	0.13	4.23
80	3.07	0.15	4.92
90	3.83	0.19	6.14

Both Dwell Time and Beam Overlap

Experiments in the previous sections have shown with the default beam overlap of 50%, beam dwell time has little effect on milling rate. Similarly, at short beam dwell time (1 μs), increasing beam overlap only marginally improved milling rate. In this experiment, we investigated the effect of various combination of beam dwell time and pixel overlap on milling rate. Prior to FIB milling, a strip of Pt was deposited onto a single crystal Si wafer. Milling was carried out using 30 keV beam at 2.5 nA beam current. The milled trenches are shown in Fig. 1.

It appears that when both dwell time and pixel overlap are increased to 100 μs and 90% respectively, the milling rate increased dramatically. Further increase in dwell time did not yield increased milling rate.

As shown in Tables 1 and 2, the milling rate was not affected when dwell time and pixel overlap was changed separately (while keeping the others at default value). In both cases, the milling rate and sputter yield agrees well with that reported in literature [10, 11]. At high dwell time and pixel overlap, milling rate more than tripled. To the author's knowledge, such high sputter yield was not reported previously. Figure 2 summarized milling rate from literature and from current study.

One of the factors that affect FIB milling rate is the effectiveness of amorphize the local target surface in the previous FIB milling pass. When ion channeling along certain crystallographic orientation happens milling rate reduces. In extreme cases, low melting phase can form on certain crystallographic plane when line up with incident Ga ion beam. This significantly hinders milling [12, 13]. At shorter dwell time and lower overlap value, the primary Ga ion beam may not provide enough ion dose to amorphize the top surface of the milled area. The subsequent ion beam milling pass to the same area still encounters crystalline surface. With higher dwell time and increased overlap, the target crystal lattice can be significantly disturbed in one milling pass and be removed easily in the subsequent ion beam pass. This can

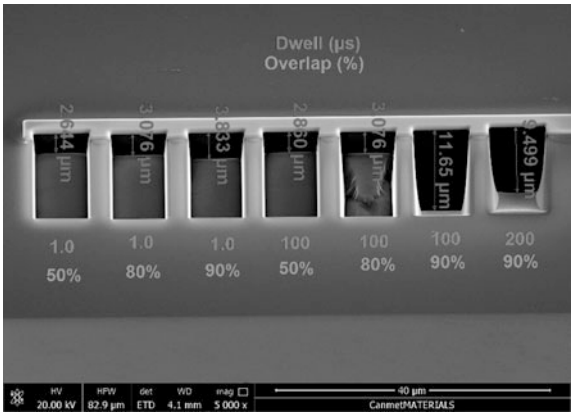

Fig. 1 Secondary electron image showing FIB milling depth on Si wafer

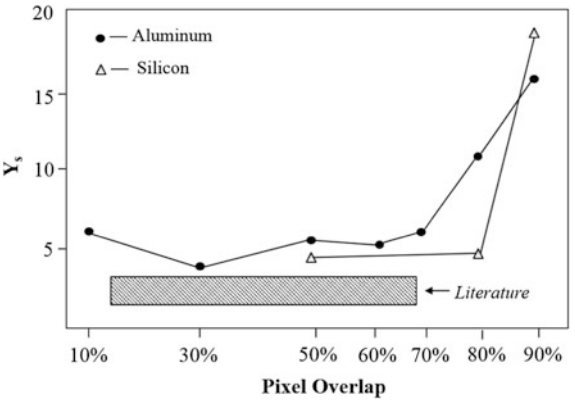

Fig. 2 Sputter yields of Si reported in literature and current study. The shaded region of sputter yields data are extracted from [9–11]

greatly enhance sputter rate. Repeated experiment in both Si and aluminum alloy yield similar results. Experiments in other materials that include steel, Ni and ceramics are underway, and will be reported elsewhere.

Summary

One of the advantages of FIB systems is the availability of digital control of Ga ion beam that include beam dwell time, beam retrace time after each line scan, and pixel pitch that translate to beam overlap during milling. FIB operators should take full advantage of available beam controls. In developing these advanced and expensive FIB columns, each vendor carried out in-depth research that nearly perfected their milling and deposition routines. However, as shown in this study, by varying dwell time and pixel overlap, the milling rate can increase dramatically. This not only saves precious FIB operation time, but shortens turnaround time for microstructure analyses.

References

1. Li J, Liu P (2015) Specimen temperature rise considerations during FIB milling. The Microscope 63(1):3–10
2. Tao T, Wilkonson W, Mengailis J (1991) Focused ion beam induced deposition of platinum for repair processes. J Vac Sci Tech B 9:162–165
3. Bernius MT, Morrison GH (1987) Mass analyzed secondary ion microscopy. Rev. Scio Instrum. 58:1789–1804
4. Prewett PD, Heard PJ (1987) J Phys D Appl Phys 20:1207
5. Phanuef MW (1999) Applications of focused ion beam microscopy to materials science specimens. Micron 30: 277–288

6. Li J (2006) focused ion beam microscope, much more than an ion milling machine. J Metal 58(3):27–31
7. Li J (2008) Advances in materials engineering using state-of-the-art microstructural characterization tools. In Olivante LV (ed) New Material Science Research. Nova Science Publishers Inc., Nova Science Publisher, ISBN-13: 978-1-60021-654-1
8. Li J et al (2006) Microscopy study of intergranular stress corrosion cracking of X-52 line pipe steel. Corrosion 62(4):316–322
9. Bischoff L, Teichert J (1998) Focused ion beam sputtering of silicon and related materials, internal report FZR-217, Institute of Ion Bean Physics and Materials Research
10. Sigmund P (1969) Theory of sputtering. I. Sputtering yield of amorphous and polycrystalline targets. Phys Rev 184:383
11. Musil CR et al (1996) Dose-rate effects in GaAs investigated by discrete pulsed implantation using a focused ion beam. J Appl Phys 80:3727–3733
12. Phaneuf MW et al (2003) Apparatus and method for reducing differential sputter rates. US patent #6,641,705
13. Casey JD Jr et al (2002) Advanced sub 0.13 μm Cu devices—failure analysis and circuit edit with improved fib chemical processes and beam characteristics. In: Conference proceedings from the international symposium for testing and failure analysis, pp 553–557

Part II
Characterization of Ceramics

Preparation and Characteristics of Steel Slag Ceramics from Converter Slag

Mingsheng He, Bowen Li, Wangzhi Zhou, Huasheng Chen, Meng Liu and Long Zou

Abstract Steel slag is an inevitable by-product from a steelmaking furnace such as a converter, an open-hearth furnace or an electric arc furnace. The yield of steel slag increases with the sharp rise of steel production. Utilizing the slag effectively and comprehensively is one of the important tasks to promote the development of iron and steel industry in China in a sustainable and efficient way. In this study, hot-poured steel slag from a converter was used to prepare ceramics by mixing with fly ash, microsilica, and quartz. After heating at 1100–1200 °C, the ceramics were well sintered. XRD revealed that multiple crystalline phases coexisted in the glass-ceramics, and the main crystalline phases were diopside and anorthite. SEM observation indicated that there was a plate-columnar composite structure in the ceramics. Reaction mechanisms were discussed.

Keywords Steel slag · Fly ash · Diopside · Anorthite · Ceramic

Introduction

Steel slag, one of the most common industrial solid wastes, is an alkaline byproduct generated from steelmaking process [1]. Generally, it is produced by a converter or an Electric Arc Furnace during steel refinery. Converter steelmaking is the most important process in China and the output of steel slag is 80–120 million tons a year by 100–150 kg per ton of steel production [2–4]. Steel slag took up large quantities of land resources, and caused water and air pollution. The recycling of steel slag can not only protect the environment, but also make use of natural

M. He (✉) · W. Zhou · H. Chen · M. Liu · L. Zou
Wuhan Iron and Steel Co., Ltd., Wuhan 430080, China
e-mail: hms03@mails.thu.edu.cn

B. Li
Department of Materials Science and Engineering,
Michigan Technological University, 1400 Townsend Dr,
Houghton, MI 49931, USA

B. Li et al. (eds.), *Characterization of Minerals, Metals, and Materials 2018*, The Minerals, Metals & Materials Series,
https://doi.org/10.1007/978-3-319-72484-3_2

resources effectively and promote utilization ratio of resources. In past decades, many efforts have been made to consume the slag as a secondary mineral resource. The applications included the use of slag as aggregates, fertilizer, glasses, coatings, and cementitious mixtures, etc.

The chemical compositions of steel slag mainly are oxides of calcium, iron, silicon, magnesium, and aluminum. However, steel slag with free CaO and MgO, and γ-$2CaO{\cdot}SiO_2$ has a liability to raise expansion and disintegration [5–7]. It is a great challenge for many steel mills to recycling steel slag effectively in large industrial scale because of its high alkalinity and poor chemical stability.

Diopside is the calcium-rich and magnesium-rich mineral phase. The formula of a pure diopside is $CaMgSi_2O_6$. It forms complete solid solution series with hedenbergite ($FeCaSi_2O_6$) and augite. According to CaO-MgO-SiO_2 trinary phase diagram, diopside can be synthesized by adding SiO_2 in steel slag with appropriate amounts. Anorthite is the calcium-rich and end member of the plagioclase feldspar solid solution series. The formula of a pure anorthite is $CaAl_2Si_2O_8$. According to CaO-SiO_2-Al_2O_3 trinary phase diagram, anorthite can be synthesized by adding Al_2O_3 and SiO_2 in steel slag with appropriate amounts [8, 9]. Since diopside and anorthite ceramic has many advantages for manufacturing and applications, such as appropriate strength, low electricity conductivity, low sintering temperature, and broad raw materials supply, and low cost, it has greatly attracted research attentions for synthesis with various minerals [1, 10–12]. Natural mineral with high SiO_2 and Al_2O_3 cannot be used in large scale because of cost. Fly ash and microsilica are cheaper raw materials for synthesis of diopside and anorthite ceramics. This study was to prepare diopside and anorthite composite ceramics by using converter slag.

Materials and Methods

The raw materials used in this study included converter slag, fly ash, microsilica, and quartz. Steel slag was taken from Wuhan Iron & Steel Co., Ltd. (WISCO). The slag was produced by the WISCO Metallic Resources Ltd. The original slag was hot-poured with water, naturally cooled down to ambient temperature, then crushed into granules. After evenly mixing, the granules were dried and ground into −325 mesh powder by a Raymond mill. Fly ash was taken from Wugang Power Plant. Microsilica and quartz were commercial concentrate products with −325 mesh of particle size.

Diopside and anorthite composite ceramic was prepared by mixing converter slag with fly ash, microsilica and quartz in certain ratios in a blender, and then placed the mixed powder in a ball-making machine, spraying water while rotating the powder sample to form green ceramic balls with diameters between 0.5 and 2.0 mm. The green ceramic balls were transferred in a box furnace, heated to designed temperature, maintained the temperature for 2 h, then naturally cooled to room temperature for characterization.

All the raw materials were analyzed by titration to determine the chemical compositions. Particle size and distributions were analyzed by a laser particle size analyzer with aqueous dispersing medium. The crystalline phases of the ceramics samples were identified using X-ray diffraction (XRD, SHIMADZU XRD-7000, copper target, continuous, scanning range 5°–80º, scan rate 3.0°/min). The microstructure of the samples was observed by scanning electron microscopy (SEM, Quanta 400, acceleration voltage 20 kV) after coating with carbon.

Results and Discussions

Characteristics of Converter Slag

Table 1 shows the main chemical compositions of steelmaking slag, fly ash, microsilica, and quartz determined by titration analysis.

The steel slag showed a feature with high content of CaO, and low concentrations of SiO_2, Al_2O_3 and MnO. By XRD analysis, the major crystalline phase of the steel slag is calcium ferrite ($2CaO{\cdot}Fe_2O_3$), calcium hydroxide ($Ca(OH)_2$), wustite (FeO), larnite ($2CaO{\cdot}SiO_2$), quartz (SiO_2) (Fig. 1). To synthesize diopside and anorthite composite ceramics, appropriate amounts of silica and alumina were necessary to be added into the chemical system to obtain stable phase.

Fly ash is a major supplier for Al_2O_3 and SiO_2, and microsilica and quartz for SiO_2 to the composite ceramics. Meanwhile fly ash and microsilica also play a role of the ceramic preparation for the inert steel slag. Especially, microsilica, an amorphous polymorph of SiO_2, which is an ultrafine powder collected as a by-product of the silicon and ferrosilicon alloy production and consists of spherical particles with an average particle diameter of 150 nm, has excellent reactivity. According to the trinary phase diagram of CaO-MgO-SiO_2, the ideal composition ranges of the three oxides for synthesizing diopside are CaO 20–45%, MgO 10–30%, and SiO_2 50–75% by weight. According to the trinary phase diagram of CaO-Al_2O_3-SiO_2, the ideal composition ranges of the three oxides for synthesizing anorthite are CaO 15–40%, Al_2O_3 20–45%, and SiO_2 40–65% by weight. In this study, the ratio of steel slag/fly ash/microsilica/quartz was controlled

Table 1 Main chemical compositions of the raw materials (wt.%)

	SiO_2	Al_2O_3	CaO	MgO	TFe_2O_3	MnO	TiO_2	P_2O_5	K_2O	Na_2O	LOI
Steel slag	10.86	1.35	44.20	8.80	16.60	2.04	0.58	1.29	ND	ND	8.01
Fly ash	43.68	27.13	3.95	0.65	5.83	ND	ND	ND	1.08	0.18	12.14
Microsilica	96.20	0.13	0.20	0.424	ND	ND	ND	ND	ND	ND	1.26
Quartz	85.72	<0.01	0.051	0.015	0.50	ND	ND	ND	ND	ND	0.20

ND not detectable

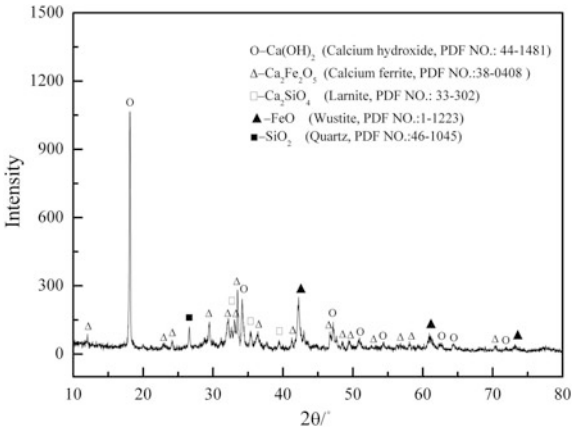

Fig. 1 XRD pattern of steel slag

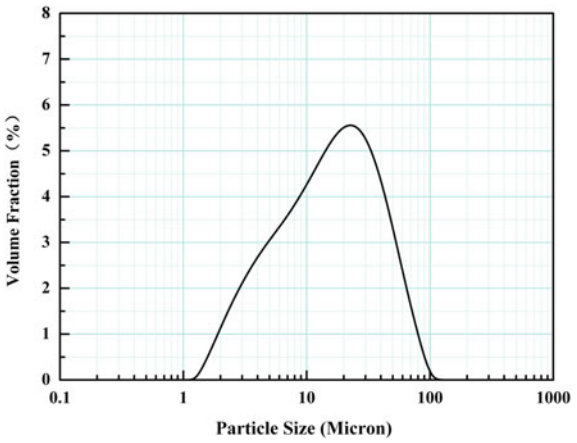

Fig. 2 Particle size distribution of steel slag powder

at 50.0/35.0/10.0/5.0, which is fell at the central area of diopside and anorthite phase on CaO-MgO-SiO_2 and CaO-Al_2O_3-SiO_2 phase diagram, respectively.

The steel slag powder has an average volume size of 22.5 micron and maximum particle size of 110 micron (Fig. 2). The distribution curve has only one peak at 24 micron in size with a volume fraction of 5.5%.

Under SEM, the steel slag particles shows irregular shapes with sharp edges and tips (Fig. 3). The particle feature corresponds with the results from laser analyzer.

Characteristics of Composite Ceramics

The green ceramic balls were fired at 1100, 1130, 1150, and 1200 °C for 2 h, respectively, and then naturally cooled down to room temperature for testing.

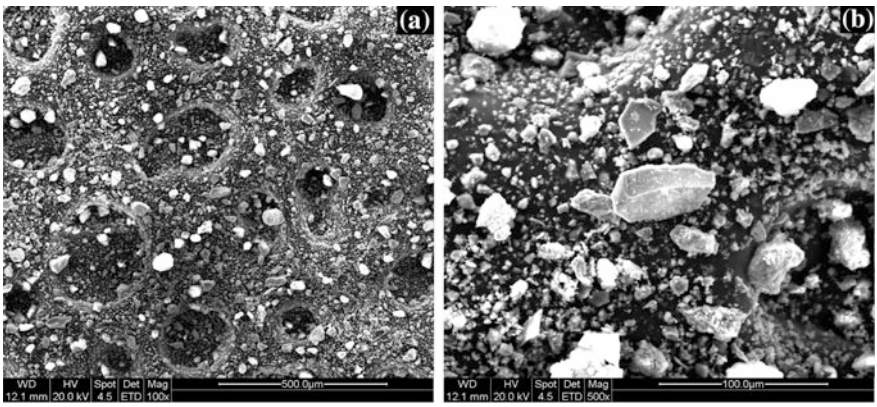

Fig. 3 SEM images of steel slag powder

Heated the samples to 1100 °C, the particles in green balls were partially ceramically bonded, though the mechanical strength was still low. However, when the balls were heated to 1130 °C, the ceramic balls obtained sufficient strength. On the cross-section of ceramic ball, SEM images indicated that the ceramic was well-sintered (Fig. 4a–c). When the balls were heated to 1150 °C, the original green balls were liquidized, and liquid phase became the major component of the ceramic, which indicated an over-burned state Fig. 4d–f. Figure 4b, c shows a fully crystalline structure of the ceramic, which revealed that a re-crystalline process happened during the cooling procedure of ceramic. The recrystallized grains showed plate-like, columnar-like, or irregular shapes, and randomly orientations. The interlock structure of the crystal grains provided mechanical strength of the ceramic body [1]. When the balls were heated to 1200 °C, the green balls were completely melted.

The XRD patterns of the sintered ceramic were showed in Fig. 5. At 1130 °C, the major mineral components of the ceramic are diopside and anorthite, the minor phase is augite and hematite. Elevated the temperature to 1150 °C, the intensities of diopside and anorthite increase, while the characteristic peaks of calcium hydroxide, calcium ferrite, larnite, wustite, and quartz have disappeared. This indicated that the calcium oxide, calcium silicates, and calcium ferrite, larnite in the raw materials have been completely reacted with the mixtures of fly ash, microsilica, and quartz. Fly ash was used as a reaction substance supplying silica and alumina for diopside and anorthite. The experiments showed that fly ash and microsilica with high reactivity with inert steel slag and small particles can lower the sintering temperature evidently, and increase the bulk density.

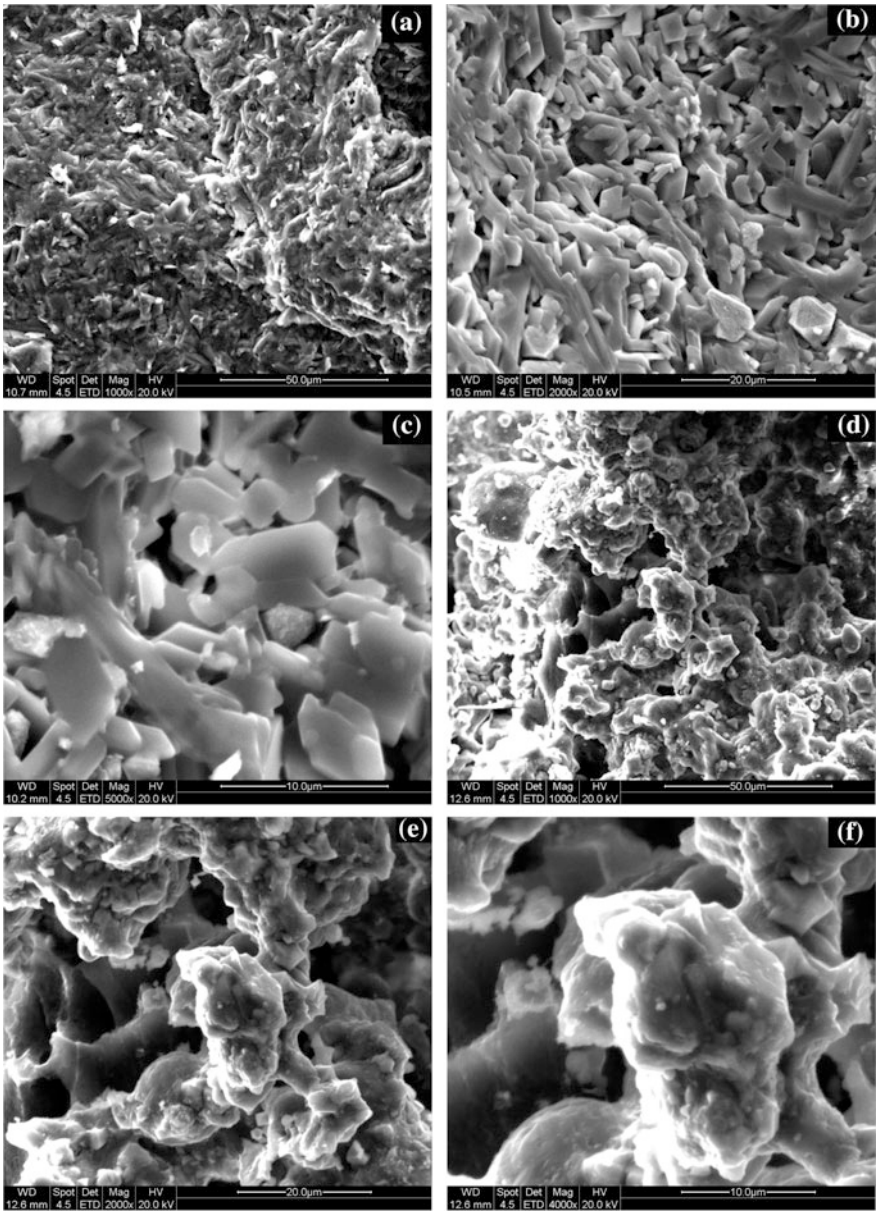

Fig. 4 SEM images of samples sintered at 1130 °C **a–c** and 1150 °C **d–f**

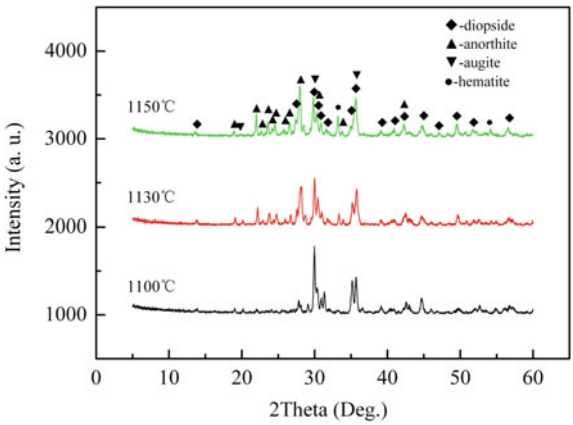

Fig. 5 XRD pattern of samples sintered at different temperature

Conclusions

In conclusion, this paper describes the possibility of manufacturing diopside and anorthite composite ceramics from converter slag with high CaO and silicate based industrial solid wastes such as fly ash, microsilica, and so on. By means of sintering, a ceramic with plate-columnar composite structure was prepared with converter slag, fly ash, microsilica, and quartz. The ceramic products can be well sintered by heating at lower temperature of 1130 °C, but completely melted at 1200 °C. The major mineral phases were diopside and anorthite when sintered at 1150 °C, while calcium hydroxide, calcium ferrite, larnite, wustite, and quartz disappeared. The interlock structure of the plate-columnar crystal grains provided high mechanical strength for the diopside and anorthite composite ceramics.

References

1. Li BW, He MS, Hwang JY et al (2017) Characteristics of anorthite-pyroxene ceramics made from hot-poured steelmaking slag. JOM 69(2):173–177
2. Zhao LH et al (2015) Synthesis of steel slag ceramics: chemical composition and crystalline phases of raw materials. Int J Miner Metall Mater 22(3):325–333
3. Han Y et al (2013) Porous anorthite ceramics with ultra-low thermal conductivity. J Eur Ceram Soc 33(13–14):2573–2578
4. Kobayashi Y, Kato E (1994) Low-temperature fabrication of anorthite ceramics. J Am Ceram Soc 77(3):833–834
5. Harada G, Yen T, Tomari M (1978) Process for treating molten steel slag with red mud from aluminum industry. US Patent, 4,179,279, 30 Jan 1978
6. Harada M, Tomari M (1990) Method of modifying steel slag. US Patent 5,019,160, 15 Mar 1990
7. Zhao LH, Li Y, Zhou YY et al (2014) Preparation of novel ceramics with high CaO content from steel slag. Mater Design 64:608–613

8. Gu Y, Wang Z, Xia C (2007) Applications of $CaO-Al_2O_3-SiO_2$ system phase diagram in ceramic coating. Mechanics 34(7):33–35
9. Mao H, Hillert M, Selleby M et al (2006) Thermodyanimic assessment of $CaO-Al_2O_3-SiO_2$ system. J Am Ceram Soc 89(1):298–308
10. Das B, Prakash S, Reddy PSR et al (2007) An overview of utilization of slag and sludge from steel industries. Res Conserv Recycl 50:40–57
11. He F, Fang Y, Xie JL et al (2012) Fabrication and characterization of glass-ceramics materials developed from steel slag waste. Mater Design 42:198–203
12. Zhang K, Liu JW, Liu WC et al (2011) Preparation of glass-ceramics from molten steel slag using liquid-liquid mixing method. Chemosphere 85:689–692

In-Situ XRD Investigation of Bauxite Dehydroxylation

Hong Peng and James Vaughan

Abstract Thermal activation of bauxite has been proposed to enable bauxite dissolution at a reduced digestion temperature and also to reduce the organic content in the liquor. Research has been carried out on phase transformation of its main hydroxide components (gibbsite, boehmite and kaolinite) during calcination. However, there is limited information available on phase bauxite phase transformation during thermal activation. In this study, two bauxite ore samples were heated from 25 to 700 °C at a rate of 50 °C/min while monitoring the phase transformation using Rigaku in situ XRD. Different phase transformation pathways for gibbsite in the bauxite compared with pure gibbsite was observed. Boehmite and kaolinite in bauxite behaved similarly to their pure phases. The temperature of phase transformation depends to some extent on the bauxite sample. Samples were also characterised by scanning electron microscopy (SEM) to reveal changes in the microstructure.

Keywords Bauxite · Thermal activation · In situ XRD · Boehmite
Kaolinite · Gibbsite

Introduction

Bauxite ore, a mineral composite consisting of gibbsite, boehmite, kaolinite, hematite, anatase and quartz, is the feed material for producing alumina using the Bayer process. Of the minerals, gibbsite ($Al(OH)_3$), boehmite (γ-AlO(OH)) and kaolinite ($Al_2[Si_2O_5](OH)_4$) are the main hydroxides. The properties of bauxite vary widely, in alumina grade, mineralogy, caustic consumption and impurity content. The optimum design and operational productivity of a Bayer refinery is

H. Peng (✉) · J. Vaughan
School of Chemical Engineering, The University of Queensland,
Brisbane, Australia
e-mail: h.peng2@uq.edu.au

B. Li et al. (eds.), *Characterization of Minerals, Metals, and Materials 2018*, The Minerals, Metals & Materials Series,
https://doi.org/10.1007/978-3-319-72484-3_3

tailored to process a specific bauxite feed types, for example low digestion temperatures (~150 °C) for gibbsitic bauxite while higher temperatures (~250 °C) are required for boehmitic [1–3].

Heat treating the bauxite prior to the Bayer process is known as thermal activation [4]. Thermal activation can convert crystalline boehmite to amorphous phases enabling low temperature digestion of what was originally a high temperature digestion bauxite [5, 6]. By altering the reactivity of bauxite in this way, thermal activation can address a number of important issues. The process involves partial thermal dehydration of the bauxite under conditions that are controlled such that digestibility is enhanced and extractable forms of carbon are eliminated. As indicated by Hollit et al. [7, 8], the key to the process is control of temperature and time, to avoid thermal deactivation of dehydrated gibbsite under the influence of water vapour at temperatures that are sufficiently high to decompose boehmite.

The heat treatment of gibbsite has been studied, as it is the basis of the conversion of gibbsite to alumina. Particle size is a factor and there are two general pathways. For coarser sizes (>50 μm), gibbsite gradually transforms to boehmite, then to the less crystalline intermediate phases (alpha-alumina or gamma-alumina) [9–12]. For finer particles, the gibbsite directly decomposes to the intermediate phases. The phase transformation temperature is between 300 and 400 °C. Kaolinite is the main component of the kaolin group of clay minerals and also a common impurity in both ferrous and non-ferrous ores [3, 13]. In the Bayer digestion process, kaolinite dissolves into the highly alkaline solution, then re-precipitate as insoluble sodium aluminate silicate known as the desilication product (DSP). Pure kaolinite has been used as a feed for the synthesis zeolites where it is thermally activated to metakaolin. This study has broad appeal as it is relevant to multiple industrial technologies [14–17].

While detailed studies of the phase transformations of gibbsite and kaolinite exist, research on thermal activation of bauxite using in situ X-ray diffraction (XRD) is limited [18–20]. In situ XRD reveals phase transformations continuously during sample heating and the ability to precisely control the heating rate and holding times. In this study, the technique was applied to three pure phases (gibbsite, boehmite and kaolinite) and two bauxite samples for temperatures ranging from 25 to 700 °C.

Materials and Methods

Materials and Reagents

AR Grade kaolinite, boehmite and gibbsite (99.4%) were sourced from Sigma-Aldrich. The bauxite samples (A and B) were provided by Rio Tinto. The chemical composition of the bauxite samples was determined by XRF analysis.

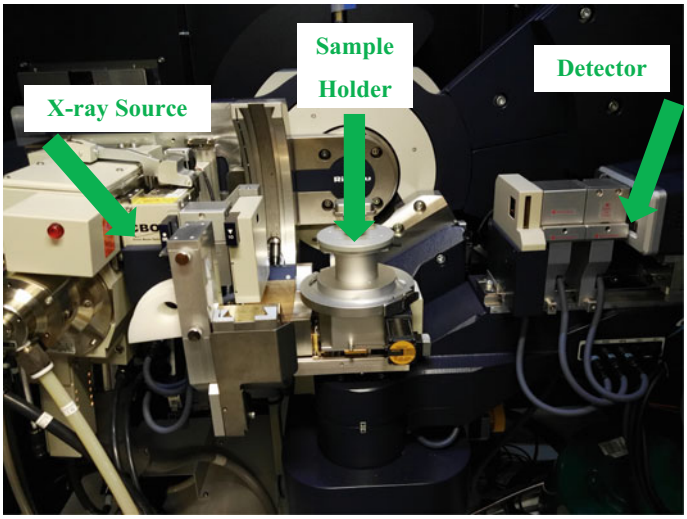

Fig. 1 In-situ powder XRD (Rigaku) experimental apparatus

In-Situ XRD Procedure

Rigaku Smartlab was used to perform the in situ XRD test (Fig. 1). The pulverized solid power was held in a corundum container. The loaded container was placed on top of sampler holder and sealed by the dome. The heating rate was set to 50 °C/minute. The holding time for each scan at each temperature was 10 min. The X-ray scan time was approximately 15 min to scan the 2θ angle range of 5°–60°. The light source is Cu Kα (λ = 1.5406 Å) at 40 kV with a scanning speed of 0.05° per second. The 2014 PDF database from BRUKER was used for peak identification .

SEM

The solid powder samples were disbursed on carbon tape and then carbon coated. The coated samples were imaged by scanning electron microscopy (SEM, HITACHI SU3500). The operating conditions were ambient temperature with an accelerating voltage of 5 kV and spot size of 30. The samples were focused on the higher resolution scale with a working distance of 7–8 mm and images were taken at magnifications of ×2000 or ×5000 with a slow scan rate of 160 s.

Results and Discussion

In Situ Heating for Dehydroxylation of Pure Phases

The microstructures of three pure phases (gibbsite, boehmite and kaolinite) were characterised by SEM, shown in Fig. 2. Particles of gibbsite samples were fine (average size < 10 μm) with hexagonal crystals while the boehmite particles were also fine (average size < 4 μm) exhibiting cuboid and rhomboid shaped crystals. The kaolinite (average size < 6 μm) layered structure is apparent from the images with no distinct shape.

The XRD patterns for gibbsite and heat treated gibbsite presented in Fig. 3 show that gibbsite is stable below 200 °C. At 300 °C, gibbsite is partially transformed into boehmite. This is consistent with previous research for fine sized gibbsite [9, 10, 12]. At this temperature, the intensity of the main crystal planes (G(002), G (110) and G(200)) decreased while other crystal planes with 2Θ value larger than 25° disappeared. At 400 °C, only boehmite peaks are present in the XRD pattern. At higher temperatures of 600 and 700 °C, the peaks for boehmite also disappear. This phase transformation pathway is summarized by Eqs. 1 and 2.

$$\mathrm{Al(OH)_3[gibbsite]} \rightarrow \gamma\mathrm{AlO(OH)[boehmite]} + \mathrm{H_2O}\uparrow \quad (1)$$

$$2\gamma\mathrm{AlO(OH)[boehmite]} \rightarrow \mathrm{Al_2O_3[amorphous]} + \mathrm{H_2O}\uparrow \quad (2)$$

The boehmite phase is stable with increasing heating temperature up to 500 °C as shown in Fig. 4. At 600 °C, the intensity of the main crystal planes [B(020), B(120) and B(031)] decreased while other crystal planes with 2Θ value larger than 45° disappeared. At 700 °C there were no detectable peaks for boehmite due to Eq. 2. By comparing Figs. 2 and 3, it can be seen that the pure boehmite phase is more stable than the boehmite transformed from gibbsite. The amorphous transition temperature is higher for the pure boehmite as a starting material compared to the boehmite transformed from gibbsite.

Kaolinite is stable below 500 °C, shown in Fig. 5. At 600 °C, the intensity of the peaks between 35° and 45° are significantly reduced. At 650 °C, all peaks for kaolinite disappeared and only the minor phase anatase remained. The amorphous

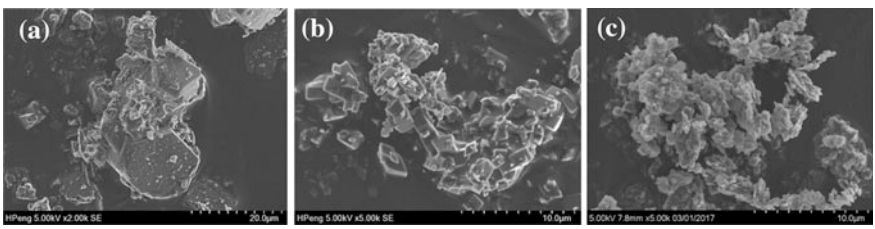

Fig. 2 SEM images of **a** gibbsite **b** boehmite and **c** kaolinite

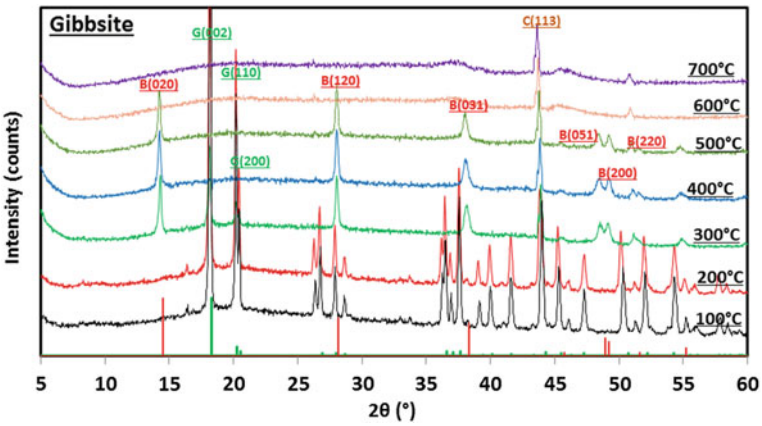

Fig. 3 In-situ XRD patterns of heat treated gibbsite as a function of temperature (*green columns* (*G*) gibbsite; *red columns* (*B*) boehmite; (*C*) corundum)

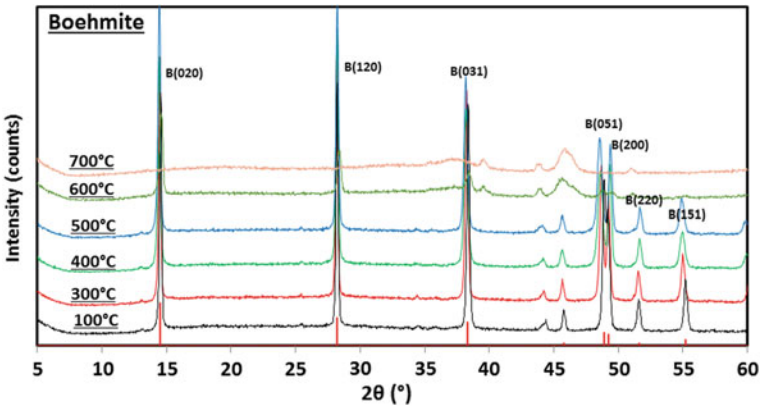

Fig. 4 In-situ XRD patterns of heat treated boehmite as a function of temperature

phase is known as metakaolin, as indicated by Eq. 3. A similar phase transformation route has been reported previously [14, 15, 21–23].

$$Al_2[Si_2O_5](OH)_4[\text{kaolinite}] \rightarrow Al_2O_3 \cdot 2SiO_2[\text{metakaolin}] + 2H_2O \uparrow \qquad (3)$$

In-Situ Heating for Dehydroxylation of Bauxite Samples

The composition of two bauxite samples based on XRF analysis is shown in Table 1. Gibbsite is the main aluminum-bearing phase in both samples. Bauxite A

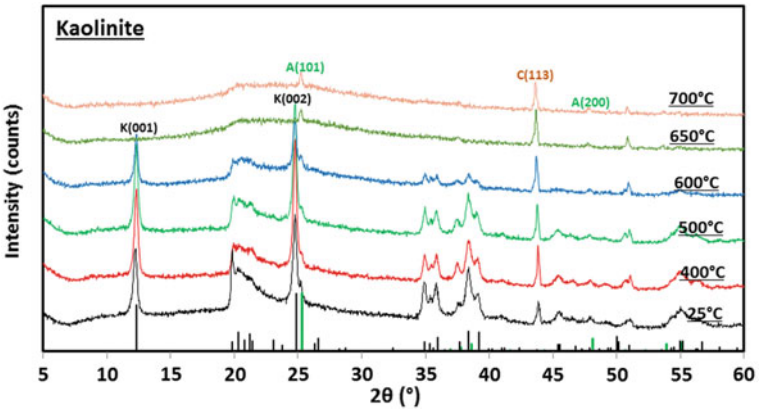

Fig. 5 In-situ XRD patterns of heat treated kaolinite as a function of temperature (*green column* (*A*) anatase phase; *black column* (*K*) kaolinite phase; (*C*) corundum phase)

has higher SiO_2 content but a lower quartz:kaolinite ratio according to the dissolution tests. Bauxite B has a higher Al_2O_3 content and lower Fe_2O_3. As shown in Figs. 6 and 7, even though the compositions are significantly different, they exhibit a similar in situ XRD trend for the three main phases when heated.

From the XRD pattern of Bauxite A at 100 °C, the main phases are kaolinite, gibbsite, hematite and anatase. Both boehmite and quartz are undetectable. With increasing temperatures, the gibbsite phase disappears at 300 °C but did not transform to boehmite as was seen with the pure gibbsite sample. For kaolinite, the peaks were not detectable above 600 °C which is a lower metakaolin transformation temperature than for the pure kaolinite. For both anatase and hematite, there were no significant changes.

Bauxite B contained both gibbsite and boehmite but no detectable kaolinite. There was also both hematite and anatase which maintained their crystal structures throughout the heating range. Interestingly, the gibbsite phases still existed at 300 °C although with lower intensity peaks. The boehmite phase disappeared at 600 °C which is lower than boehmite in the pure state, consistent with Bauxite A. Table 2 summarizes the transition temperature range for the three hydroxide phases (gibbsite, boehmite and kaolinite) for both the pure samples and as components of the bauxites. This implies that the thermal activation process could be of benefit for the bauxites high in boehmite as the newly formed amorphous phases would be suitable to a low temperature Bayer digestion stage.

Table 1 Chemical composition and loss on ignition of bauxite A and B samples (wt.%)

Sample	Al_2O_3	SiO_2	Fe_2O_3	TiO_2	MgO	P_2O_5	Quartz	LOI
Bauxite A	39.3	14.2	24.7	1.9	0.03	0.05	0.3	19.4
Bauxite B	53.2	6.5	13.0	2.6	0.03	0.06	1.5	24.1

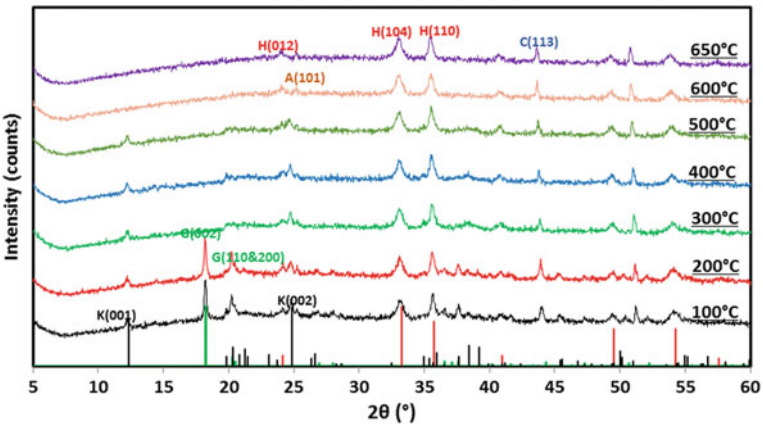

Fig. 6 In-situ XRD patterns of heat treated bauxite A with increasing temperature (*black column* kaolinite; *red column* hematite; *green column* gibbsite; *brown* anatase; *blue* Corundum)

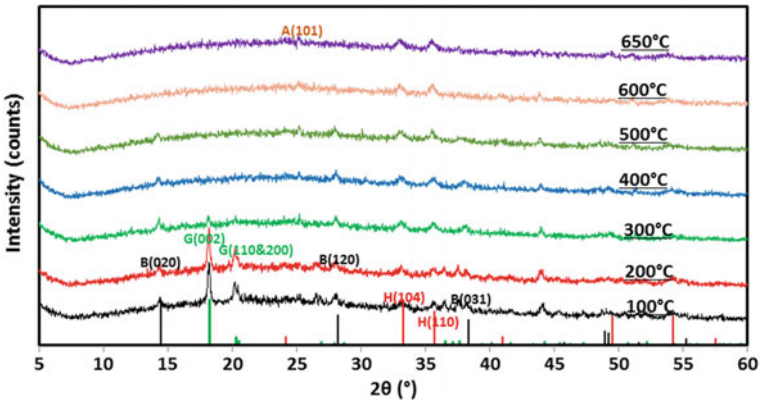

Fig. 7 In-situ XRD patterns of heat treated bauxite B with increasing temperature (*black column* boehmite; *red column* hematite; *green column* gibbsite; *brown* anatase; *blue* corundum)

Table 2 Transition temperature ranges for various phases (°C)

Phases	Pure phases	Bauxite A	Bauxite B
Gibbsite	200–300	200–300	300–400
Boehmite	600–700	–	500–600
Kaolinite	600–650	500–600	–

To explore the heat treatment effect on the microstructure, both Bauxites A and B were characterised by SEM before and after in situ XRD tests as shown in Fig. 8. Due to water evaporating during the loss of hydroxides in the crystals, the surface of heated samples appeared roughened in comparison with the original samples.

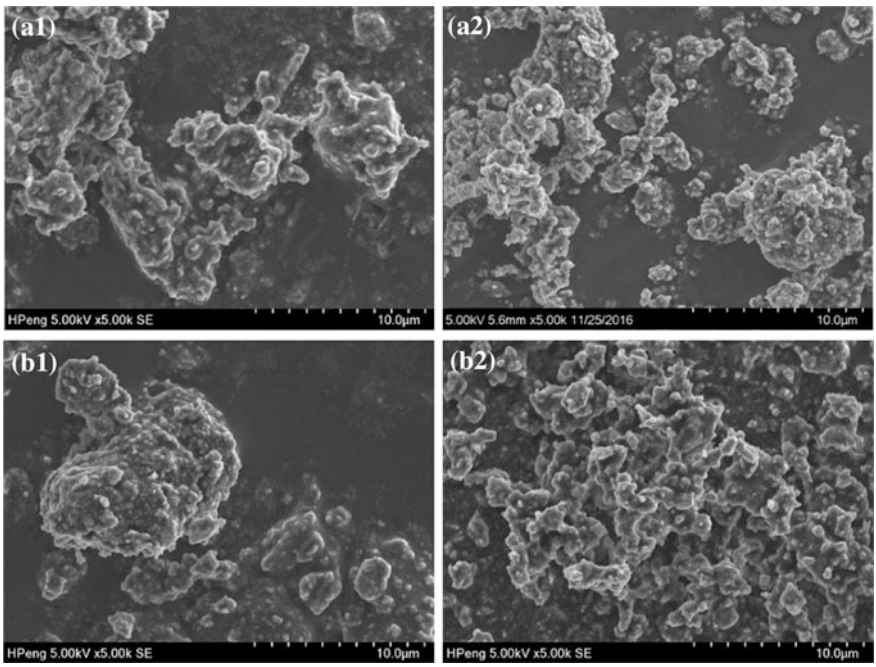

Fig. 8 SEM images of bauxites sample **a1** sample without heating and **a2** after heating at 650 °C; bauxite sample **b1** original sample without heating and **b2** heating at 650 °C

Conclusions

In situ XRD revealed differences in the phase transformation pathway and transition temperatures for three main hydroxides (gibbsite, boehmite and kaolinite) when the pure minerals were compared to the minerals as a component of bauxite during the dehydroxylation process. In bauxite ores, gibbsite transformed to an amorphous phase at temperatures above 300 °C while both kaolinite and boehmite phases required a temperature above 600 °C for complete dehydroxylation. These findings would gain the understanding on how to conduct thermal activation of different types of bauxites.

Acknowledgements The authors gratefully acknowledge the financial support from the Advance Queensland Research Fellowship supported by Rio Tinto and Queensland Government (Grant ID 2015003035). We acknowledge the facilities, and the scientific and technical assistance, of the Australian Microscopy & Microanalysis Research Facility at the Centre for Microscopy and Microanalysis, The University of Queensland. We thank Warren Staker (Rio Tinto) for helpful discussions and support for this project.

References

1. Wenzhong C et al (2015) Research of the mineral fouling composition and removal method in bauxite digestion process. Light metals, p 55–58
2. Heng-qin Z et al (2001) Review of current situation on bauxite resources and production technology of alumina in China. Conserv Util Miner Res 5:38–42
3. Smith P (2009) The processing of high silica bauxites—review of existing and potential processes. Hydrometallurgy 98(1):162–176
4. Munn J et al (1992) In-situ studies of the hydrothermal synthesis of zeolites using synchrotron energy-dispersive X-ray diffraction. Phase Trans A Multinatl J 39(1–4):129–134
5. Kenyon N, Weller M (2003) The effect of calcium on phase formation in the sodium aluminium silicate carbonate system and the structure of $NaCaSiO_3OH$. Microporous Mesoporous Mater 59(2):185–194
6. Hermeler G, Buhl J-C, Hoffmann W (1991) The influence of carbonate on the synthesis of an intermediate phase between sodalite and cancrinite. Catal Today 8(4):415–426
7. Hollit MJ et al. (2001) Process for removing reactive silica from a bayer process feedstock. U.S. Patent 6,309,615. Comalco Aluminum Limited
8. Hollitt M, Kisler J, Raahauge B (2002) The comalco bauxite activation process. In: Proceedings of 6th international alumina quality workshop pp 115–122
9. Wang H et al (2006) Kinetic modelling of gibbsite dehydration/amorphization in the temperature range 823–923 K. J Phys Chem Solids 67(12):2567–2582
10. Gan BK, Madsen IC, Hockridge JG (2009) In situ X-ray diffraction of the transformation of gibbsite to α-alumina through calcination: effect of particle size and heating rate. J Appl Crystallogr 42(4):697–705
11. Zhu B, Fang B, Li X (2010) *Dehydration reactions and kinetic parameters of gibbsite*. Ceram Int 36(8):2493–2498
12. Xu B, Smith P, De Silva L (2013) The Bayer digestion behaviour of transition aluminas formed from roasted gibbsite. Int J Miner Process 122:22–28
13. Misra C, Misra C (1986) Industrial alumina chemicals, vol 17. American Chemical Society Washington, DC
14. Brindley G, Nakahira M (1959) The kaolinite-mullite reaction series: II, Metakaolin. J Am Ceram Soc 42(7):314–318
15. Frost RL, Vassallo AM (1996) The dehydroxylation of the kaolinite clay minerals using infrared emission spectroscopy. Clays Clay Miner 44(5):635–651
16. Sperinck S et al (2011) Dehydroxylation of kaolinite to metakaolin—a molecular dynamics study. J Mater Chem 21(7):2118–2125
17. Cheng H et al (2012) The thermal behaviour of kaolinite intercalation complexes-A review. Thermochim Acta 545:1–13
18. Norby P (2006) In-situ XRD as a tool to understanding zeolite crystallization. Curr Opin Colloid Interface Sci 11(2):118–125
19. Webster NA et al (2010) An investigation of goethite-seeded Al (OH) 3 precipitation using in situ X-ray diffraction and Rietveld-based quantitative phase analysis. J Appl Crystallogr 43(3):466–472
20. Majuste D et al (2013) Applications of in situ synchrotron XRD in hydrometallurgy: literature review and investigation of chalcopyrite dissolution. Hydrometallurgy 131:54–66
21. Johnson HB, Kessler F (1969) Kaolinite dehydroxylation kinetics. J Am Ceram Soc 52(4): 199–203
22. Ilić BR, Mitrović AA, Miličić LR (2010) Thermal treatment of kaolin clay to obtain metakaolin. Hemijska industrija 64(4):351–356
23. Wang H et al (2011) Characterization and thermal behavior of kaolin. J Therm Anal Calorim 105(1):157–160

The Investigation of Humics as a Binder for $LiFePO_4$ Cathode in Lithium Ion Battery

Guihong Han, Shuzhen Yang, Jiongtian Liu and Yanfang Huang

Abstract Binder, as a necessary functional material of electrode in lithium ion battery, has a vital influence on the electrochemical performance. The humics, coupled with polyacrylamide (PAM) and sodium carboxymethyl cellulose (CMC), were used as a water-soluble binder for $LiFePO_4$ (LFP) cathode using in lithium ion battery. The techniques of cyclic voltammetry (CV) and galvanostatic charge-discharge were conducted to evaluate the performance of humics binder in LFP electrode. The reversible specific capacity of LFP (HA + PAM + CMC) electrode can reach to 142 mAh g^{-1} after 50th cycling (100 mAh g^{-1}) on conditions of raw materials with 1 wt% PAM addition, humics and CMC with a mass ratio of 3:1 in binder, and the raw materials mixed in an interval order. Humics has the potential to be used as a novel, eco-friendly and high-efficient binder for lithium-ion battery.

Keywords Humics · Binder · Lithium ion battery · Cathode · $LiFePO_4$

Introduction

Lithium ion battery is one of most the essential parts in our daily life, which is widely used in mobile communication devices, portable electronic devices and the like [1]. Binder, as a necessary functional material of electrode in lithium ion battery, has a vital influence on the electrochemical performance. The most common binder used in the lithium ion battery is polyvinylidene fluoride (PVDF), which is expensive, difficult to recycle [2]. PVDF binder usually requires the use of volatile organic compounds, such as environmentally-harmful and toxic N-methyl-2-pyrrolidone (NMP), for their decentralizing [2]. In addition, the above-mentioned binder may react with the active materials and results into safety

G. Han (✉) · S. Yang · J. Liu · Y. Huang
School of Chemical Engineering and Energy, Zhengzhou University, Zhengzhou 450001, People's Republic of China
e-mail: guihong_han@126.com

B. Li et al. (eds.), *Characterization of Minerals, Metals, and Materials 2018*, The Minerals, Metals & Materials Series,
https://doi.org/10.1007/978-3-319-72484-3_4

issues [3]. The development of eco-friendly binders with quality of high effectiveness is of great significance for lithium ion battery.

Recently, a few of literatures have reported the novel water-soluble binder for $LiFePO_4$ (LFP) using in lithium ion battery. Zhong et al. [4] have reported that the carboxymethyl chitosan/conducting polymer can be used as a water-soluble composite binder for $LiFePO_4$ cathode using in the lithium ion battery. Experimental results indicated that the poly(3,4-ethylenedioxythiophene): poly(styrenesulfonate)/carboxymethyl chitosan (PEDOT: PSS/CCTS) favored the formation of continuous and homogenous conducting bridges throughout the electrode [4]. He et al. [5] have used the cyanoethylated carboxymethyl chitoan (CN–CCTS) as the binder for cathode $LiFePO_4$ and it displayed better resistance to the organic electrolyte solvents than that with sodium carboxymethyl cellulose (CMC) and PVDF. Qiu et al. [6] have reported the carboxymethyl cellulose derivative (CMC–Li) as the binder for $LiFePO_4$ electrode. The CMC–Li can provide an effective electronically conductive network and a stable interface structure for the cathode. Compared with the PVDF, these water-soluble binders are environmentally friendly and perform excellent electrochemical performance. However, the application of these binders may be limited by their complicated preparation process, so it is still full of challenge to develop a new kind of economic binder for lithium ion battery.

poly(3, 4-ethylenedioxythiophene): poly(styrenesulfonate)/carboxymethyl chitosan

Humics, with many polar groups, can be adsorbed on the surface of metals, minerals and materials [7, 8]. However, few researches have been conducted on humics as the binder for $LiFePO_4$ cathode until now. In this paper, the humics were reported as a novel and green binder for lithium ion battery. To enhance the processability of electrode, the CMC and the polyacrylamide (PAM) were taken as an assisted binder coupled with humics. In addition, the ratio of humics to CMC was investigated to get the optimum electrochemical performance. It was found that with the humics as the main binder, the electrochemical performance can be much improved with some reasonable regulation.

Experimental

Materials

Sodium carboxymethyl cellulose [AR, CMC, 0.2 − 0.5 P s (1wt.% water solution)] and polyacrylamide (AR, PAM) (M_r > 5,000,000) were both purchased from Tianjin Kemiou Reagent Co., Ltd., China. $LiFePO_4$ (LIB-LFPO-S21) was purchased from the Shenzhen Kejing zhida Technology Co., Ltd., China. The humics used was purchased from Tianjin Zhiyuan Reagent Co., Ltd., China. The original humics was further purified by repeat precipitation and redissolution with 0.1 M

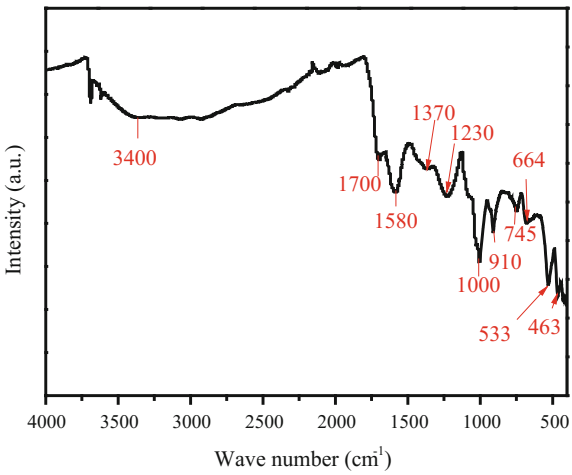

Fig. 1 The FTIR spectrum of humics used in this work

HCl and 0.1 M NaOH respectively, then the humics was heated to 135 °C and kept for 1 h in air to remove the adsorption water before using. The FTIR spectrum of humics was characterized by iS50-Nicolet and is shown as Fig. 1.

The broad peak around 3400 cm^{-1} is ascribed to the O–H stretching vibration from adsorption water. The peaks at 1700 and 1580 cm^{-1} are due to the C=O stretching vibration from carboxyl group and aromatic conjugate double bond absorption peak. The peaks at 1370 cm^{-1} is attributable to the C–OH vibration of –COOH, or the C–O vibration from the aryl ethers and phenols. The peaks at 1230 cm^{-1} is attributed to the aliphatic OH-groups. The peaks at 1000 cm^{-1} can be ascribed to the Si–O groups of silicate. The peaks below 1000 cm^{-1} are mostly due to some inorganic minerals, such as aluminum dioxide etc.

Battery Preparation

CR 2032 coin-type cells were assembled with metallic lithium anodes for electrochemical measurements. The positive electrodes were fabricated by spreading a viscous slurry consisting of $LiFePO_4$, acetylene black, and binder (humics, CMC and PAM), with a mass ratio of 8:1:1, dispersed in deionized water on an aluminum foil with a doctor blade, followed by drying at 135 °C for 12 h under vacuum overnight. Electrodes were punched into discs with diameter of 8 mm, and the active material loading on every electrode was about 3–5 mg. Electrolyte was obtained from CAPCHEM Co. (Item No.: LBC305-01), which was 1 M $LiPF_6$ in 1:1:1 ethylene carbonate/ethyl methyl carbonate/dimethyl carbonate. The cells were assembled in an Ar-filled glove box with O_2 and H_2O lower than 0.1 ppm. The pure lithium foil was used as reference electrode and Celgard 2500 was used as membrane.

Electrochemical Test

The galvanostatic charge/discharge tests were measured in the potential range of 2.5–4.2 V versus Li/Li^+ at the current density 100 mA g^{-1} with LAND-CT2001A battery-testing system. The cyclic voltammograms (CVs) and electrochemical impedance spectroscopy (EIS) measurements were carried out on Autolab PGSTAT204 (Holland) electrochemical working station. The CV was performed between 2.5 and 4.2 V at a scanning rate of 0.1 mV s^{-1}. EIS measurements were obtained by applying the AC amplitude of 5 mV in the frequency range 10^{-2}–10^5 Hz. All the tests were conducted at the room temperature.

Results and Discussion

The Effect of PAM Addition

Humics (HA) is a macromolecular compound with complex components. The cohesiveness may not as high as some linear polymers. To improve the processability and stability of electrode during cycling process, the PAM was added as an assistant reagent for the dispersion of LFP. In the process of slurry preparation, the humics/CMC, acetylene black, $LiFePO_4$ and the PAM were added in stirring water in order with an interval of 30 min. The CVs of $LiFePO_4$ electrode with humics as an addictive binder are shown in Fig. 2.

For the LFP electrode with PAM as an additive binder (1 wt% in all raw materials) (Fig. 2a), the anodic peak at 3.54 V corresponds to the oxidation of Fe^{2+} to Fe^{3+}, while the cathodic one appearing at 3.31 V is associated with the reduction of Fe^{3+} to Fe^{2+} [9]. The potential interval between the cathodic and anodic peaks is 0.23 V, much lower than 0.31 V for LFP without PAM as an additive binder (Fig. 2b). The narrow peak separation means a low polarization of the electrodes, indicating the easy

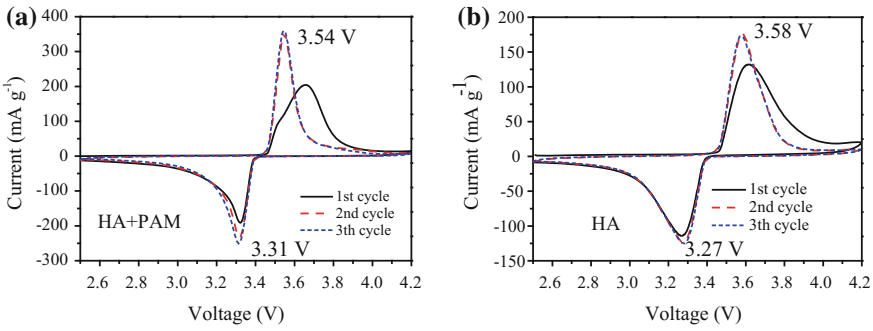

Fig. 2 The cyclic voltammograms of $LiFePO_4$ electrode using humics as binder **a** with PAM as an additive, **b** without PAM additive, scan rate: 0.1 mV/s

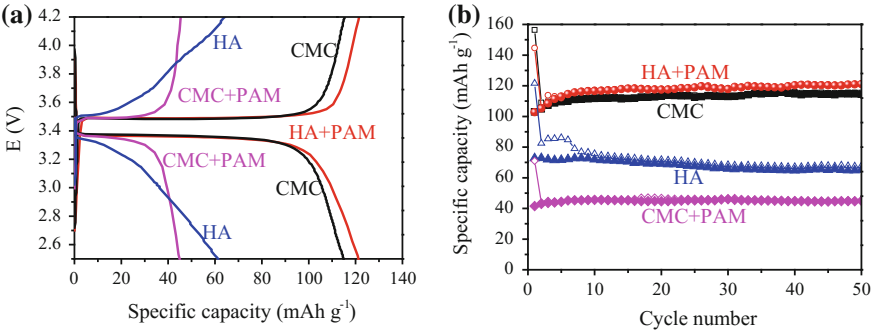

Fig. 3 The effect of PAM addictive: **a** the charge and discharge curves of four electrodes of 50th cycling and **b** the cycle performance of four electrodes with the binders of humics and CMC

electrochemical reverse reaction of Fe^{3+} to Fe^{2+} during the Li^+ insertion-desertion process [10]. Besides, the redox peak profile of LFP (HA + PAM) electrode is sharper and more symmetric than the other one, indicating that the redox kinetics is improved due to the enhanced conductivity [11–13]. Moreover, both the anodic and cathodic peak currents (Ip) of LFP (HA + PAM) electrode are higher than LFP (HA) electrode. Therefore, it could be deduced qualitatively that LFP (HA + PAM) displayed larger Li^+ diffusion coefficient (D_{Li}) during the charge and discharge processes according to Randles–Sevcik formula [12].

Figure 3a, b describe the charge and discharge curves and cycle performances of LFP electrodes with humics, humics-PAM, CMC, CMC-PAM as binder respectively. It can be seen that the charge-discharge plateaus of LFP (HA + PAM) electrode is similar with the LFP (CMC) electrode. PAM addition can obviously lengthen the charge and discharge plateaus of LFP (HA) electrode, but the influence of PAM for LFP (CMC) is opposite. From Fig. 3b, it can be seen that the LFP (HA + PAM) electrode has the highest specific capacity. The LFP (CMC + PAM) has the worst cycle performance among four electrodes.

The Mass Ratio Optimization of CMC to Humics

Based on the humics-PAM binder, the CMC was investigated as an auxiliary binder combined with them. The binders with the mass ratio of CMC to humics from 2:1 to 1:5 were mainly studied. In the process of slurry preparation, the CMC, humics, acetylene black, $LiFePO_4$ and the PAM were added in the stirring water in order with an interval of 30 min. The cyclic voltammograms of $LiFePO_4$ electrodes with the mass ratio of CMC to humics 1:3 and 1:5 are shown in Fig. 4. It can be seen that the redox reaction can be enhanced by increasing the content of humics in binder. The narrow peak separation (3.54–3.33 V) means a lower polarization of the 1:5 electrode.

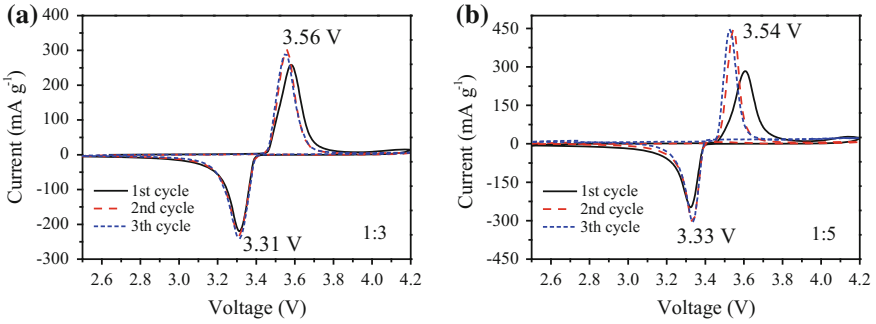

Fig. 4 The cyclic voltammograms of $LiFePO_4$ electrodes with the binders of the mass ratio of CMC to humics of **a** 1:3 and **b** 1:5

Figure 5a, b show the charge and discharge curves and cycle performances of electrodes with the binders of different ratio of humics to CMC. As shown in Fig. 5a, the discharge plateau is decreased with the increase of the ratio of humics, which reveals the irreversibility of batteries is increasing from the ratio of 2:1 to 1:5. However, the specific capacity is increased with the increase of the mass content of humics. The cycle performances in Fig. 5b demonstrate the consistent phenomenon that specific capacity of battery is increased with the increase the content of humics. However, the coulombic efficiency of the 1:5 electrode is decreased seriously with the increase of cycle number; Table 1 shows the coulombic efficiency of batteries of 50th cycling. It indicates that the batteries are reversible during 50 times cycling except for the one with the mass ratio of 1:5, of which the coulombic efficiency is 92.95% of 50th cycling. This may be caused by the interaction of some inorganic impurities in humics and the CMC which weakens the cohesion of LFP and binders and further makes the materials split away off electrode.

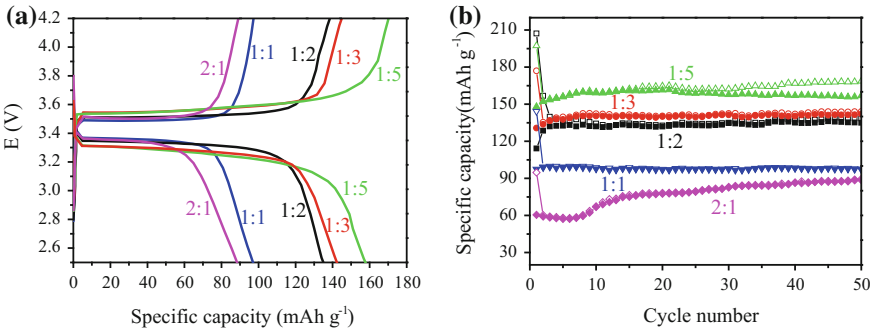

Fig. 5 The effect of mass ratio of CMC to humics: **a** the charge and discharge curves of four electrodes of 50th cyling and **b** the cycle performance of four electrodes with the binders of humics and CMC in different mass ratio

Table 1 The coulombic efficiency of batteries with different binders

Mass ratio of CMC to humics	2:1	1:1	1:2	1:3	1:5
Coulombic efficiency (%)	98.77	99.59	97.47	98.61	92.95

The Way of Materials Mixing

The way materials are mixed has big influence on homogeneous mixing of raw materials and then affects the cohesive action between active particles and current collector. The process of binders, active materials, and conducting materials mixed in one step in this section and the results were compared with those reported in section of 3.2. Figure 6 shows the cyclic voltammograms of $LiFePO_4$ electrode with the mass ratio of CMC to humics of 1:5; it can be seen that the peak currents are lower and the potential interval is bigger than that in Fig. 4b. This may be due to the heterogenous dispersion of raw materials.

Figure 7a, b show the charge and discharge curves and cycle performance of electrodes with the raw materials mixed in one step. It can be seen that specific capacity is influenced seriously when the mass ratio of CMC to humics is more than 1:1. However, when the mass content of humics is lower or equal to CMC, the electrochemical performance is similar to that of the electrodes in the section of 3.2. It proves that the mixing way of raw materials has big influence on particles dispersion and further greatly affects the electrochemical performance of battery.

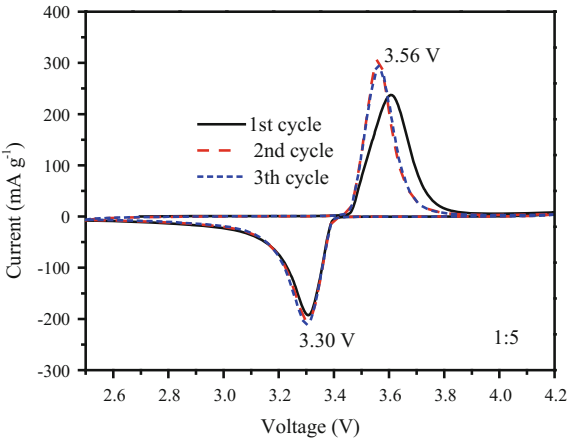

Fig. 6 The cyclic voltammograms of $LiFePO_4$ electrode, with mass ratio of CMC to humics of 1:5

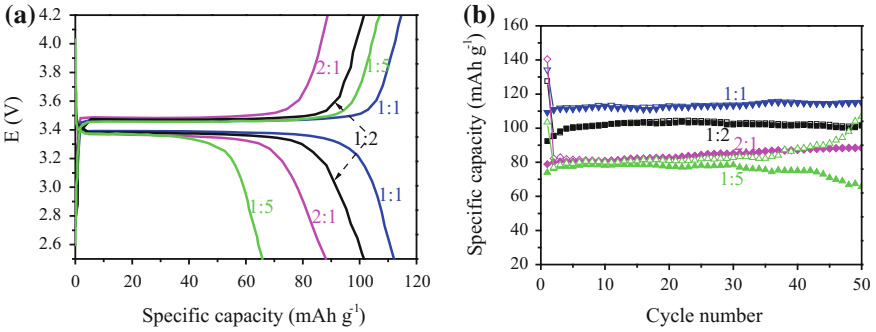

Fig. 7 One step mixing way: **a** the charge and discharge curves of four electrodes of 50th cycling and **b** the cycle performance of four electrodes, with mass ratio of CMC to humics from 2:1 to 1:5

Conclusions

The humics were used as the water-soluble binder in lithium ion battery. With the assistance of PAM and CMC, the electrochemical performance of lithium ion battery can be improved greatly. The way raw materials are mixed is an important factor for the quality of electrode and can greatly affect the electrochemical performance. When the mass ratio of CMC to humics is 1:3 and raw materials are mixed in order of CMC, humics, acetylene black, $LiFePO_4$ and PAM, with the time interval of 30 min, the reversible specific capacity can reach to 142 mAh g^{-1} after 50th cycling. Humics are promising to be a novel, eco-friendly and high-efficient binder used in lithium ion battery.

Acknowledgements The authors acknowledge the financial supports of the financial support from the National Science Fund of China (No. 51404213, No. 51404214, No. 51674225 and No. 51774252), Educational Commission of Henan Province of China (No. 17A450001, No. 18HASTIT011 and No. 18A450001) and the Development Fund for Outstanding Young Teachers of Zhengzhou University (No. 1421324065).

References

1. Zhang WM, Hu JS, Guo YG, Zheng SF, Zhong LS, Song WG, Wan LJ (2008) Tin–nanoparticles encapsulated in elastic hollow carbon spheres for high-performance anode material in lithium–ion batteries. Adv Mater 20(6):1160–1165
2. Courtemanche RJM, Pinter T, Hof F (2011) Just add tetrazole: 5-(2-Pyrrolo) tetrazoles are simple, highly potent anion recognition elements. Chem Commun 47(47):12688–12690
3. Guerfi A, Kaneko M, Petitclerc M, Mori M, Zaghib K (2007) $LiFePO_4$ water-soluble binder electrode for Li-ion batteries. J Power Sources 163(2):1047–1052
4. Zhong H, He A, Lu J, Sun M, He J, Zhang L (2016) Carboxymethyl chitosan/conducting polymer as water-soluble composite binder for $LiFePO_4$ cathode in lithium ion batteries. J Power Sources 336:107–114. https://doi.org/10.1016/j.jpowsour.2016.10.041

5. He J, Wang J, Zhong H, Ding J, Zhang L (2015) Cyanoethylated carboxymethyl chitosan as water soluble binder with enhanced adhesion capability and electrochemical performances for LiFePO4 cathode. Electrochim Acta 182:900–907. https://doi.org/10.1016/j.electacta.2015.10.006
6. Qiu L, Shao Z, Wang D, Wang F, Wang W, Wang J (2014) Novel polymer Li-ion binder carboxymethyl cellulose derivative enhanced electrochemical performance for Li-ion batteries. Carbohydr Polym 112:532–538. https://doi.org/10.1016/j.carbpol.2014.06.034
7. Huang Y, Han G, Liu J, Wang W (2016) A facile disposal of Bayer red mud based on selective flocculation desliming with organic humics. J Hazard Mater 301:46–55. https://doi.org/10.1016/j.jhazmat.2015.08.035
8. Zhang Y, Zhou Y, Liu B, Li G, Jiang T (2014) Roasting characteristics of specularite pellets with modified humic acid based (MHA) binder under different oxygen atmospheres. Powder Technol 261:279–287. https://doi.org/10.1016/j.powtec.2014.04.053
9. Liu T, Zhao L, Wang D, Zhu J, Wang B, Guo C (2014) Carbon-coated single-crystalline $LiFePO_4$ nanocomposites for high-power Li-ion batteries: the impact of minimization of the precursor particle size. RSC Adv 4(20):10067–10075
10. Zhang Q, Huang SZ, Jin J, Liu J, Li Y, Wang HE, Chen LH, Wang BJ, Su BL (2016) Engineering 3D bicontinuous hierarchically macro-mesoporous $LiFePO_4$/C nanocomposite for lithium storage with high rate capability and long cycle stability. Sci Rep 6:25942. https://doi.org/10.1038/srep25942
11. Wang B, Liu T, Liu A, Liu G, Wang L, Gao T, Wang D, Zhao XS (2016) A hierarchical porous C@ $LiFePO_4$/Carbon nanotubes microsphere composite for high-rate lithium-ion batteries: combined experimental and theoretical study. Adv Energy Mater. https://doi.org/10.1002/aenm.201600426
12. Zhao Y, Peng L, Liu B, Yu G (2014) Single-crystalline $LiFePO_4$ nanosheets for high-rate Li-ion batteries. Nano Lett 14(5):2849–2853
13. Nien YH, Carey JR, Chen JS (2009) Physical and electrochemical properties of $LiFePO_4$/C composite cathode prepared from various polymer-containing precursors. J Power Sources 193(2):822–827

Evaluation of Brazilian Bentonite Modified by Acid Attack in Biofuel Production

C. G. Bastos Andrade, S. M. Toffoli and F. R. Valenzuela Diaz

Abstract The climate change observed in the last decades, the increase of global warming, the melting of the polar ice caps, and the sea level rise have in common the non-sustainable development as causative agent. Different nations have mobilized joint efforts with the objectives of minimizing the impact of greenhouse gas (GHG) emissions, investing in the research and the development of new technologies in recycling, in biomaterials, environmentally friendly processes, and new fuel alternatives. This paper evaluates the efficiency of a Brazilian bentonite modified by acid attack, in the purification step of a waste oil to be used for biofuel production, that is, diesel from waste cooking oil (WCO). The following characterization tests were performed: XRD, CEC, XRF, SEM/EDS, specific surface area (BET), stereomicrography, kinematic viscosity, and spectrophotometry at 440 nm. The modified bentonite exhibited good purification capacity for WCO when compared to a commercial product.

Keywords Biofuel · Modified bentonite · Nanotechnology · Recycling
Waste cooking oil

Introduction

Despite the existence of public policies for environmental preservation in many countries, a large amount of pollutants emission into the atmosphere still persists, and the use of fossil fuels is considered to be the principal source for the greenhouse gas emissions. Different countries have adopted the parameters, and policies defined by the United Nations (UN) to reduce GHG emissions, to environment recovery, and for the development of new products, and environmentally friendly processes. In the last decade, an enormous increase in new technologies for recycling, bio-

C. G. Bastos Andrade (✉) · S. M. Toffoli · F. R. Valenzuela Diaz
Department of Metallurgical and Materials Engineering,
EPUSP Polytechnic School—University of Sao Paulo, Sao Paulo, Brazil
e-mail: gianesic@usp.br

B. Li et al. (eds.), *Characterization of Minerals, Metals, and Materials 2018*, The Minerals, Metals & Materials Series,
https://doi.org/10.1007/978-3-319-72484-3_5

materials, and renewable energy alternatives, among which is the biofuels research, was observed [1–9]. Biodiesel, considered a "green" oil, can be obtained using different processes, and different raw materials, such as vegetal oil or animal fat (natural or wastes), algae, and genetically modified oil seed crops. The most efficient and simple preparation method is the transesterification process, which uses a short chain alcohol (ethanol or methanol) in the presence of a catalyst (enzyme, alkali, or acid). In biodiesel production, close to 80% of the total cost is represented by the refined vegetable oils that are produced in fields competing for food production, an issue that can be solved with the use of waste cooking oil (WCO) as the raw material [10–19]. Biodiesel must comply with the parameters set out in the standards EN14214 (Europe), ASTM D6751 (USA), and ANP 14/2012 (Brazil). Their specifications relate to acid value, thermal stability, density, viscosity, water content, free and total glycerol, content of mono-, di-, and triglycerides, among others, in order to guarantee a fuel quality to preserve the diesel engines [20–23].

The industrial use of bentonites is vast, but they are mostly used as drilling fluids, mineral binders, foundry molds, and adsorbents. To many industrial uses, the bentonites must be cleaned of mineral impurities. The acid attack is a common method that provides a good cleaning of such impurities, and also promotes an increase of the acid sites and also an increase in the porosity, which are excellent properties for catalysis uses. The Brazilian bentonite from Cubati, State of Paraiba, is a polycationic bentonite. It presents a low iron content, light color, and is categorized as a non-swelling bentonite [24–30]. This paper discusses the evaluation of a modified bentonite used to the purification process of waste cooking oil, aiming at the biodiesel production.

Experimental

Materials

The clay sample was supplied by ARGILAB (Applied Clays Laboratory) clays collection. It is a bentonite from Brazilian northern region, modified by acid attack using Dr. Bastos Andrade's and Dr. Valenzuela-Diaz's (from University of São Paulo), MAT methodology (patent pending). The waste cooking oil sample was the soybean oil.

Methods

Initially, the modified clay sample was sieved in #200 mesh. Afterwards, it was dried at 60 °C for 24 h. The waste cooking oil (WCO) sample was filtered at 40 °C, then purified using the same amount of commercial activated clay and modified clay by MAT process. The purification of the WCO was performed by a simplified bleaching test: the clay samples were added to 20 mL of filtered oils in a glass vessel, homogenized by stirring, and then treated at 90 °C for 48 h. After being

cooled to 22 °C, the samples were centrifuged at 3000 rpm for 30 minutes. The specific surface area was measured by the N_2-BET method, using a Micromeritics ASAP 2020 analyzer. The semi-quantitative chemical composition of the modified clay sample was measured by X-ray fluorescence (XRF), using TBL rock standards as a parameter, and a Panalytical Axios Advanced equipment. Images and energy dispersive X-ray spectra (EDS) were obtained using a scanning electron microscope (SEM) Philips XL30—EDAX INSPECT 50. The mineral content was obtained using a Panalytical diffractometer, model X'Pert Pro MPD, with Cu-Kα radiation, scan from 5° to 90° 2Θ at 40 kV, and 40 mA. The oil absorbance capacity, before and after purification, was obtained using a spectrophotometer FEMTO 700 Plus, at 440 nm. The bleaching efficiency was calculated as the percentage of the absorbance decrease with reference to the unpurified filtered oil. The oils kinematic viscosities were determined by measuring the time that 10 mL of oil, at 22 °C, flowed down a plastic funnel with a 1 mm aperture.

Results and Discussion

Figures 1 and 2 presents the EDS spectra of the bentonite sample treated with purified water and submitted to MAT process, where it is possible to observe the major peaks related to the presence of Si, Al, and O, in accordance to which is expected for a montmorillonite [31]. The presence of gold in both spectra is due to the required thin coating of the sample surface, necessary to perform the analysis of non-conductive materials.

The semi-quantitative chemical analysis by EDS and XRF of the bentonite submitted to treatment are presented in Tables 1 and 2. In the sample treated with water it is possible to observe the presence of SiO_2 and Al_2O_3 corresponding to around 67% of all oxides present, and about 75% at the sample submitted to MAT

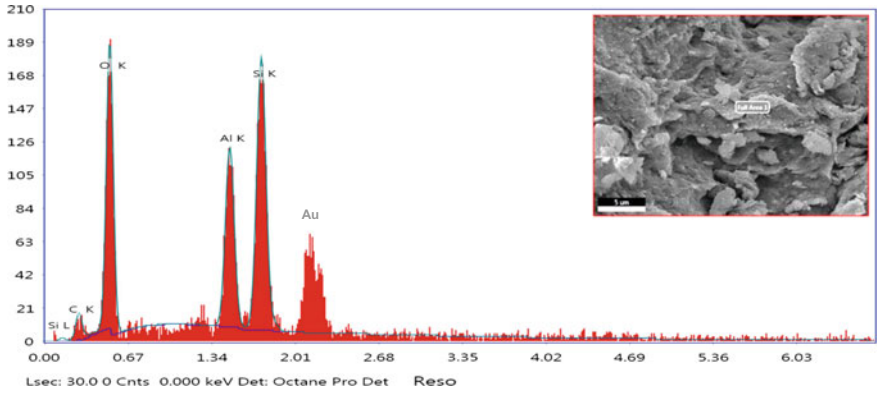

Fig. 1 EDS spectrum of bentonite sample treated with H_2O

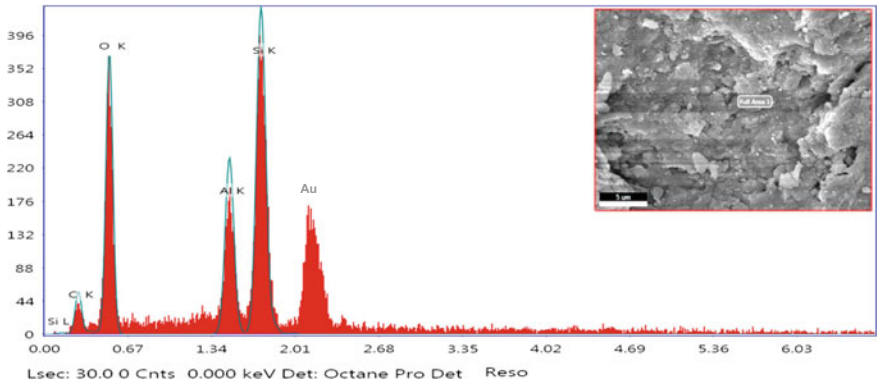

Fig. 2 EDS spectrum of bentonite sample modified by MAT

Table 1 EDS results of bentonite treated with H_2O and submitted to MAT process (in weight percentage)

Element	Weight%		Atomic%	
	H_2O	MAT	H_2O	MAT
Si	31.9	33.5	21.9	22.4
Al	17.5	15.1	12.5	10.5
O	38.1	34.6	45.9	40.7
C	12.3	16.7	19.7	26.2

Table 2 XRF results of bentonite submitted to treatment (in weight percentage)

Treatment	SiO_2	Al_2O_3	Fe_2O_3	MnO	MgO	CaO	Na_2O	K_2O	TiO_2	P_2O_5	LOI
H_2O	45.1	22.0	3.86	<0.10	1.77	4.03	0.17	0.38	0.94	<0.10	21.9
MAT	52.3	22.0	3.01	<0.10	0.78	0.11	<0.10	0.40	1.10	<0.10	20.4

process, with a reduced presence of iron. In same samples, it was observed equal values to Al_2O_3, with a reduction in Fe_2O_3 in the sample modified by MAT with a corresponding increase in SiO_2. According to the literature, bentonites without any treatment present around 75% of these metallic oxides [32, 33].

Table 3 presents the basal distance $d_{(001)}$, the smectitic peak intensity, the specific surface area (BET) results, and the cation exchange capacity (CEC) values. According to the literature, the $d_{(001)}$ values of calcic montmorillonite with two water molecules are in the range of 14.2 to 15.5 Å, present CEC values from 40 to 70 meq/100 g, and specific surface area with values from 50 to 80 m^2/g [28, 34, 35]. The characteristic peak of the bentonite modified by MAT presented basically the same position and slightly less intensity than the ones for the material treated

Table 3 $d_{(001)}$ smectitic peaks, CEC, and BET values of the modified bentonite samples

Treatment	Smectitic peak $d_{(001)}$ (Å)	Smectitic peak intensity (counts)	CEC (meq/100 g)	BET (m^2/g)
H_2O	15.28	144	55	67
MAT	15.16	104	52	207

with purified water, what could indicate the preservation of the crystalline structure. The CEC results of the bentonite sample treated with purified water and modified by MAT process, indicate a non-significant destruction of the crystalline clay mineral structure, with a reduction of 5% in the value for the clay treated by MAT process. On the other hand, the specific surface area measured for the bentonite sample treated with water was 67 m^2/g, and for the bentonite modified by MAT, 207 m^2/g, indicating an intense increase of more than 300%. This high value indicates a great potential for the MAT treated clay to be used as a bleaching clay [30, 36].

The stereomicrocopy images of bentonite samples modified by MAT process and treated with purified water are shown in Figs. 3, and 4, where it is possible to observe the presence of impurity particles on the clay sample treated with purified water, whereas no impurity particles were identified in the MAT process clay sample.

The SEM images of the bentonite samples modified by MAT process and treated with purified water are shown in Figs. 5, 6, 7 and 8. It is possible to observe in Figs. 5 and 6 the crystal dispersion presenting agglomerates with irregular forms, and apparently within similar particle size distribution ranges. In Figs. 7 and 8 it is possible to observe the lamellar structure of the clays, and no apparent damage of the smectite crystal structures after the MAT process.

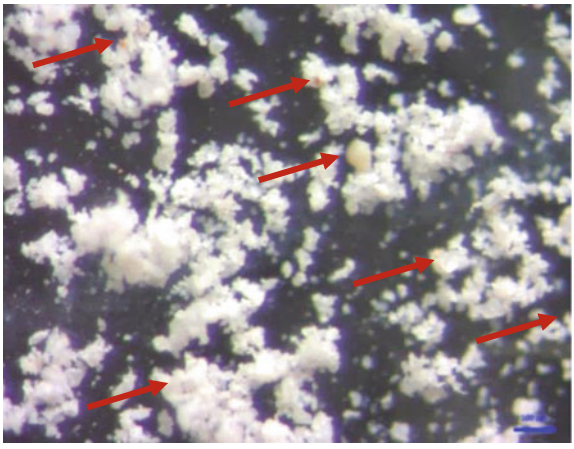

Fig. 3 Stereomicrography of sample treated with water

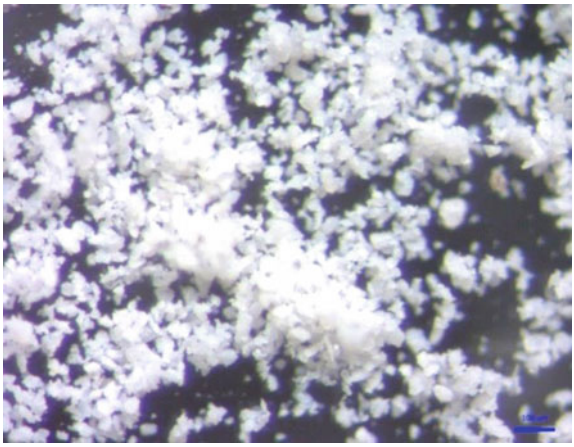

Fig. 4 Stereomicrography of bentonite modified by MAT

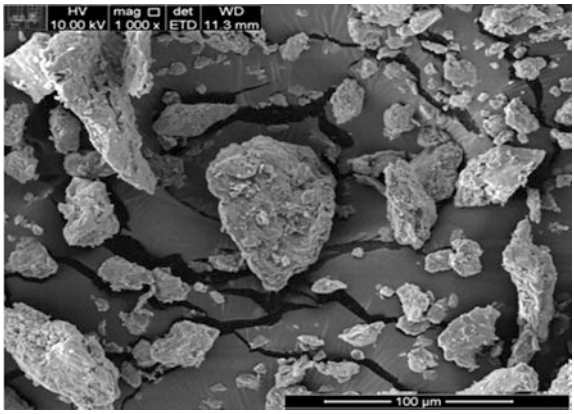

Fig. 5 SEM image of sample treated with water (crystals dispersion)

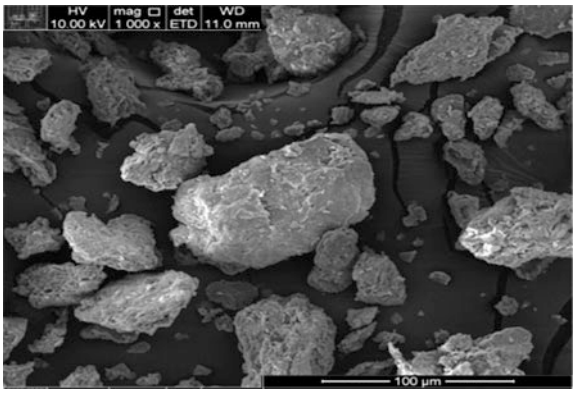

Fig. 6 SEM image of sample bentonite modified by MAT (crystals dispersion)

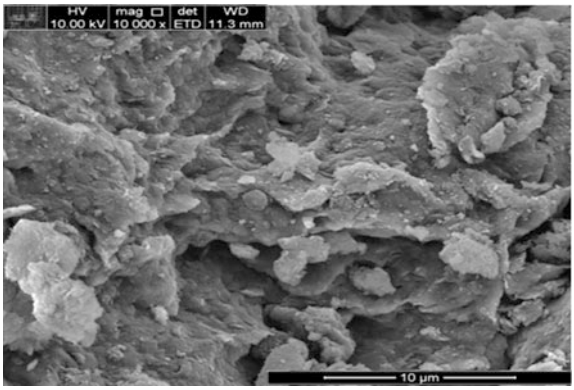

Fig. 7 SEM image of sample treated with water (crystal detail)

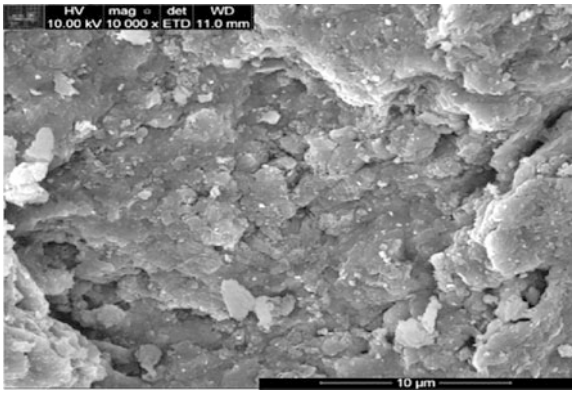

Fig. 8 SEM image of sample bentonite modified by MAT (crystal detail)

Table 4 Bleaching efficiency, and kinematic viscosity results of WCO filtered, and purified

WCO samples	Efficiency (%)	Kinematic viscosity (in sec)
Filtered Soybean	–	121
T I purified with commercial clay (0.75 g)	16.0	121
T II purified with commercial clay (1.50 g)	9.0	120
BC 1 purified with MAT clay (0.75 g)	17.0	121
BC 2 purified with MAT clay (1.50 g)	14.0	121

Table 4 presents the bleaching efficiency, and the kinematic viscosity results, of a commercial bentonite sample, and the results obtained when the MAT modified clay was employed. The as-received soy bean oil used in the purification steps was first paper filtered, at 40 ºC, to remove the particles of food residues. The efficiency and viscosity values obtained for the modified clay were similar to those obtained with the commercial activated clay: for WCO purified with 0.75 g of commercial and MAT clays, it is possible to observe the same bleaching efficiency. Doubling the quantity of activated clay resulted in a dramatic decrease in efficiency, most likely because the centrifugation wasn't capable to separate all the clay from the oil.

purified with MAT clay (1.50 g) BC 2 | purified with commercial clay (1.50 g) T II | Filtered Soybean | purified with commercial clay (0.75 g) T I | purified with MAT clay (0.75 g) BC 1

Fig. 9 Soybean oil samples filtered, and purified

However, in this case, a smaller reduction in the bleaching efficiency was observed for the clay modified by MAT process, with 14%, against 9% for the commercial activated clay.

In Fig. 9 it is possible to observe the bleaching of waste cooking oil purified with the commercial activated clay (T I and T II), and also purified with the MAT modified clay (BC 1 and BC 2). As it may be observed, a minimum difference in color between purified oils samples was obtained, except for the color of sample BC 2, which presented slightly less brightness, what could be caused by the residual presence of clay particles.

Conclusions

The characteristic interplanar distance $d_{(001)}$ and intensity of the smectite peaks of bentonite modified by MAT process presented similar results to the ones obtained for the clay sample treated only with purified water, which is an indication of a minimum destruction of the crystalline clay mineral structure, what is corroborated by the observation of the scanning electron microscopy images and CEC values. The MAT process also promoted an intense increase in BET specific surface area, and a good impurities purification, which can be observed in the stereomicrograph images, and with the reduction in the contents of the metallic oxides (except for SiO_2, Al_2O_3, and maybe Fe_2O_3, which are the oxides that form the crystalline structure of the clay mineral), according to both XRF and EDS analyses. The waste cooking oil exhibited excellent bleaching when the MAT clay was used as purifying agent with MAT clay (0.75 g), and the viscosity of the samples yielded the same result. For higher amount of the clay the possible cause for the bleaching efficiency decrease could be explained by the presence of residual amounts of clay. In conclusion, it is possible to say that the MAT modified bentonite may be considered a “green” alternative to be used in the purification step of the WCO aiming at biodiesel production, first because it would allow the use of a waste, reducing the amount of discarded WCO, and also because of the use of the more environment-friendly MAT process (details to be published elsewhere).

Acknowledgements This work was supported by the São Paulo State Research Foundation—FAPESP, and by the CNPq—National Council for Scientific and Technological Development, of the Brazilian Government.

References

1. Hill K (2000) Fats and oils as oleochemical raw materials. Pure Appl Chem 72(7):1255–1264
2. WRI (2004) The greenhouse gas protocol: a corporate accounting and reporting standard, Revised edn. World Resources Institute and World Business Council for Sustainable Development, USA
3. Hocevar L (2005) Biocombustível de óleos e gorduras residuais—a realidade do sonho. In: II Congresso Brasileiro de Plantas Oleaginosas. Óleos, Gorduras e Biodiesel, Varginha, MG, pp 953–957
4. Pahl G (2005) Biodiesel: growing a new energy economy. Chelsea Green Publishing Company, Vermont
5. European Commission (EC) (2009) Renewable energy directive 2009/28/EC. Report of the European Parliament and of the council of 23 April 2009 on the promotion of the use of energy from renewable sources and amending and subsequently repealing Directives 2001/77/EC and 2003/30/EC. OJL 140:16–62
6. Atabani AE et al (2012) A comprehensive review on biodiesel as an alternative energy resource and its characteristics. Renew Sustain Energy Rev 16:2070–2093
7. Pachauri RK, Meyer LA (eds) (2014) IPCC climate change 2014: Synthesis report. Contribution of working groups I, II and III to the Fifth assessment report of the intergovernmental panel on climate change. Geneva, Switzerland
8. Tabatabaei M et al (2015) Renewable energy and alternative fuel technologies. Biomed Res Int 2015:245935
9. Environmental Protection Agency (EPA) (2016) Renewable fuel standard program: standards for 2017 and biomass based diesel volume for 2018, Final rule. USA, Federal register 81(238)
10. Neto PRC et al (2000) Produção de Biocombustível alternativo ao óleo diesel através da transesterificação de óleo de soja usado em frituras. Quim Nova 23(4):531–537
11. Fernando S et al (2007) Effect of incompletely converted soybean oil on biodiesel quality. Energy 32(5):844–851
12. Geris R et al (2007) Biodiesel de soja - reação de transesterificação para aulas práticas de química orgânica. Quim Nova 30(5):1369–1373
13. Kucek KT et al (2007) Ethanolysis of refined soybean oil assisted by sodium and potassium hydroxides. J Am Oil Chem Soc 84(4):385–392
14. Lam MK et al (2009) Malaysian palm oil: surviving the food versus fuel dispute for a sustainable future. Renew Sustain Energy Rev 13:1456–1464
15. Morais S et al (2010) Simulation and life cycle assessment of process design alternatives for biodiesel production from waste vegetable oils. J Clean Prod 18:1251–1259
16. Araujo CDM et al (2013) Biodiesel production from used cooking oil: a review. Renew Sustain Energy Rev 27:445–452
17. Gudeetal VG (2013) Biodiesel production from low cost and renewable feedstock Central European. J Eng 3(4):595–605
18. Kiakalaieh AT et al (2013) A review on novel processes of biodiesel production from waste cooking oil. Appl Energy 104:683–710
19. Yaakob Z et al (2014) A review on the oxidation stability of biodiesel. Renew Sustain Energy Rev 35:136–153
20. Encinar JM et al (2005) Biodiesel from used frying oil: Variables affecting the yields and characteristics of the biodiesel. Ind Eng Chem Res 44:5491–5499
21. Knothe G et al (eds) (2005) The biodiesel handbook. AOCS Press, Illinois

22. Rutz D, Janssen R (2006) Overview and recommendations on biofuel standards for transport in the EU. Project: BiofuelMarketplace (EIE/05/022/SI2.420009), contribution to WP 3.2 and WP 5.5, WIP Renewable Energies, München, Germany
23. USDA Foreign Agricultural Service (2016) Brazil—biofuels annual report, GAIN-Global Agricultural Information Network, Rep.no. BR16009, USA
24. Ferreira HS et al (2008) Análise da influência do tratamento de purificação no comportamento de inchamento de argilas organofílicas em meios não aquosos. Cerâmica 54:77–85
25. Amorim LV et al (2005) Fluidos de perfuração à base de água. Parte I: efeitos de aditivações poliméricas nas propriedades reológicas. Cerâmica 51(318):128–138
26. Vaccari A (1999) Clays and catalysis: a promising future. Appl Clay Sci 14(4):161–198
27. Grim RE (1978) Bentonites. Elsevier, Amsterdam
28. Grim RE, Güven N (1978) Bentonites—geology, mineralogy. Properties and Uses, Elsevier, Amsterdam
29. Abreu SF (1973) Recursos minerais do Brasil, vol 1, 2ª edn. Edgard Blücher, Sao Paulo
30. Valenzuela-Diaz FR, Souza-Santos P (2001) Studies on the acid activation of Brazilian smetctitic clays. Quim Nova 24(3):345–353
31. Souza-Santos P (1992) Ciência e Tecnologia de Argilas vol 1, 2ª edn. Edgar Blücher, Sao Paulo
32. Souza-Santos P (1992) Ciência e Tecnologia de Argilas, Aplicações vol 2, 2ª edn. Edgar Blücher, Sao Paulo
33. Valenzuela-Diaz RF et al (1992) A Importância das argilas industriais brasileiras. Química Industrial 42:33–37
34. Souza-Santos P (1975) Ciência e Tecnologia de Argilas Aplicada às Argilas Brasileiras e Aplicações, vols 1–2. Edgar Blücher, Sao Paulo
35. Murray HH (2007) Applied clay mineralogy: occurrences, processing and applications of kaolins, bentonites, palygorskitesepiolite, and common clays, develop. In: Clay Science, vol 2. Elsevier, Amsterdam
36. Bastos-Andrade CG (2016) Brazilian bentonites submitted to mild acid attacks aiming industrial use. Ph.D. thesis, University of Sao Paulo

Part III
Characterization of Non-ferrous Metals

Synthesis and Characterization on Nickel Orthosilicate Anode of Lithium-Ion Battery

Guihong Han, Duo Zhang and Yanfang Huang

Abstract Ni_2SiO_4 was prepared by chemical precipitation process as a novel anode material for lithium-ion batteries. The structure and morphology of further annealed Ni_2SiO_4 samples were characterized by XRD and SEM analysis. The electrochemical performance including cyclic voltammetric curves (CV), electrochemical impedance spectra (EIS), charge/discharge curves and cycling performances were also determined. The results demonstrated that the crystal structure of the samples is orthorhombic having space group Pmn21. The morphological structure of materials exhibited cubic particles with sizes in the range of 50–80 nm. The first cycle charge capacity of the pure Ni_2SiO_4 particles reached to 753 mAh g^{-1} with the coulombic efficiency of 63.8%. The charge capacity remained 305 mAh g^{-1} at a current density of 100 mA g^{-1} even after 50 cycles, which is nearly 208% higher than those of the Ni_2SiO_4 with SiO_2 impurity. Ni_2SiO_4 can be a promising alternative anode material.

Keywords Lithium ion battery · Anode materials · Transition metal silicates

Introduction

Lithium-ion batteries (LIBs) have light weight, high specific capacity, and long life to meet the different demands for large scale applications such as high energy-storage devices for portable electronics and electric vehicles. The performances of LIBs largely depend on the electrodes and electrolyte. Research on LIB anode materials has developed from the Li metal and the Li alloy to carbon materials, metal oxides, Sn- or Si-based anode materials, etc. [1–3]. However, the relatively poor high-rate cycling and safety performance of the traditional anode materials make it hard to meet the constantly increasing demands of lithium ion

G. Han (✉) · D. Zhang · Y. Huang
School of Chemical Engineering and Energy, Zhengzhou University, Zhengzhou 450001, People's Republic of China
e-mail: guihong_han@126.com

B. Li et al. (eds.), *Characterization of Minerals, Metals, and Materials 2018*, The Minerals, Metals & Materials Series,
https://doi.org/10.1007/978-3-319-72484-3_6

batteries with high energy density. Therefore, great attention has been gradually attracted by the transition metal oxides, nitrides, fluorides, or phosphides [4–6].

Transition metal silicates, which have always been studied in mineralogy and geophysics because of their high abundance [7, 8], are rarely considered as a possible candidate for novel anode materials. The formation of lithium silicate has so far been proven to be irreversible by studies on the SiO/SiO_2 materials [9–11]. Nevertheless, reversible conversion of the transition metal silicates was reported for the first time by Franziska Mueller in 2014. Co_2SiO_4, resulting in reversible initial lithium silicate formation, revealed a promising high rate capability and an excellent cyclic performance, providing a reversible specific capacity exceeding 650 mAh g^{-1} [12, 13]. Moreover, synthesis of nickel orthosilicate (Ni_2SiO_4, NSO) was always believed to carry out on pretty high temperature and pressure with nickel oxide impurities, both theoretically and experimentally [14–17]. Olivine-supported nickel silicate catalyst was prepared by thermal impregnation for catalyzing tar removal during biomass gasification [18]. To the best of our knowledge, the application of NSO in LIBS electrodes has not been reported by now.

In this paper, a method for the synthesis of NSO is illustrated. In our work, the precursor was obtained by the chemical precipitation reaction of sodium silicate (Na_2SiO_3•$9H_2O$) and nickel nitrate ($Ni(NO_3)_2$•$6H_2O$), followed by calcination at 900 °C in air for 4 h. Their excellent electrochemical performance was tested as a lithium ion anode material battery. For example, the reversible specific capacity can reach 753 mAh g^{-1}, and the cycling stability is promising.

Experiments

Synthesis of Ni_2SiO_4

First, 25 mL 1 M sodium silicate solution was added dropwise to 1 M nickel nitrate solution of equivalent volume with magnetic stirring. The light green powder obtained was collected by centrifugation after reaction at 90 °C for 5 h, washed several times with deionized water and ethanol, followed by drying at 80 °C for 12 h. The precursors were calcined in air at 900 °C for 4 h with a heating rate of 5 °C min^{-1} to obtain a dark green powder.

Physical Characterization

The crystal structure and phase purity of NSO were examined by X-ray diffraction and scattering analysis (Cu–K_α radiation with λ = 1.5406 Å) operating at 40 kV and 30 mA at room temperature. The X-ray patterns were recorded in the 2θ range

10°–40° with a scan rate of 0.02° s^{-1}. The particles morphology was observed by field-emission scanning electron microscopy (FE-SEM; TSM-7500F) at 5.0 kV.

Electrochemical Cell Assemble and Measurements

The working electrode (WE) was prepared from slurry of the active material (NSO), conductive agent (acetylene black) and binder (poly vinyledene difluoride: PVDF) in a weight ratio of 75:15:10. The slurry was pasted with some drops of N-Methyl pyrrolidone (NMP). Copper disk substrate (1 cm^2 area) was coated with the obtained slurry to form the WE with a wet film thickness of 120 µm. The WE was dried in vacuum oven at 100 °C. The active material mass loading of the electrodes ranged between 3.3 and 4.0 mg cm^{-2}. Lithium foil metal (Sigma Aldrich) acted as counter and reference electrode, while polypropylene micromembrane served as a separator. The electrolyte was 1 M $LiPF_6$ dissolved in mixture of 1:1 DEC and EC. The electrodes were assembled into coin-like cells (CR2025) in an Ar-filled glove box with oxygen and water vapor pressure less than 0.1 ppm.

Cyclic voltammetry (0.05–3.00 V, 0.1 mV s^{-1}) was performed using an electrochemical workstation (PGSTAT302 N). Meanwhile, impedance measurements were carried out setting the frequency range to 10^5 and 10^{-2} Hz and applying amplitude of 10 mV. Furthermore, galvanostatic cycling was achieved utilizing a LAND-2001A at current rate of 100 mA g^{-1} in a voltage window of 0.005–3.0 V versus Li/Li^+. All of the electrochemical tests were performed at room temperature.

Results and Discussion

The XRD patterns of the annealed samples are presented in Fig. 1. The main phases in pattern 1a were identified to orthorhombic Ni_2SiO_4 (JCPDS card no. 15-0388) with Pbnm space group and tetragonal SiO_2 (JCPDS no. 39-1425) with P41212 space group. Peak located at 22° was attributed to the SiO_2 impurity. However, all the peaks are well indexed to Ni_2SiO_4 phase without additional reflections of impurities in XRD spectrum 1b. Thus, sample 1b can be considered as a single-phase material within the XRD detection limits.

Morphology feature of the annealed material was investigated (Fig. 2) by the Scanning Electron Microscope (SEM) and the average size of the NSO cubic particles demonstrated in Fig. 2 is found to be about 50–80 nm.

Cyclic voltammetry and galvanostatic charge/discharge tests were undertaken to investigate the oxidation–reduction reactions of Ni^{3+}/Ni^{2+}. Figure 3a shows the first three cyclic voltammograms (CVs) of the pure Ni_2SiO_4-based electrode scanned between 0.05 and 3.0 V at a scan speed of 0.1 mV s^{-1}. The strong and obvious reduction current peak located at (A) about 0.7 V can be detected only in the first cathodic sweep and is generally considered to be resulted from an initial lithium ion

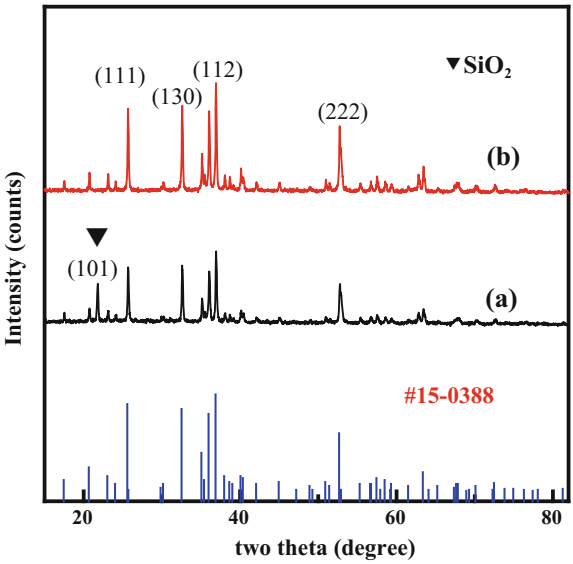

Fig. 1 XRD patterns of samples (**a** Ni_2SiO_4 with impurity SiO_2, **b** pure Ni_2SiO_4)

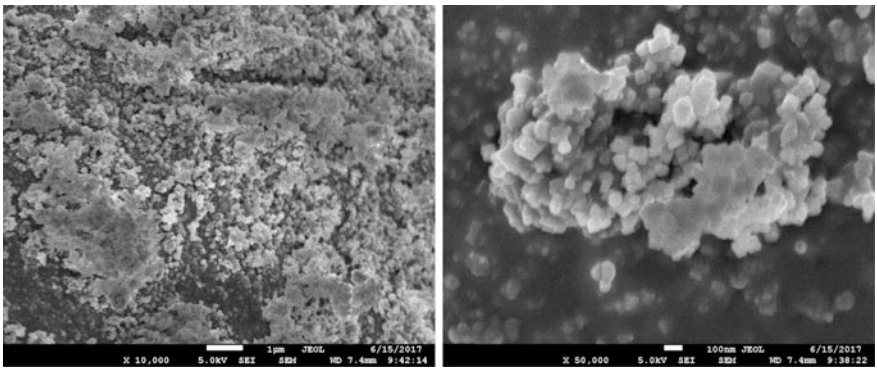

Fig. 2 SEM photograph of pure Ni_2SiO_4 samples

insertion into the crystal and the subsequent reduction of the transition metal(s). The different profile in the following two cathodic sweeps, showing a new reduction current peak appearing at (B) about 1.7 V, are assigned to the lithium ion insertion mechanism after the initial lithiation, which results in structural reorganization. The main anodic peak (C) at about 2.5 V, however, can be characteristic for the re-oxidation of nickel metal. The area under the oxidation peak (C) is about approximately equal to that for the corresponding reduction peak (B), indicating that the electrochemical reactions appeared highly reversible.

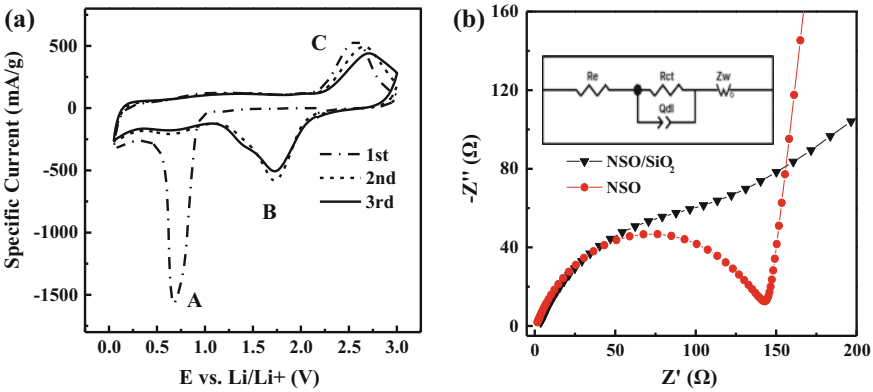

Fig. 3 A typical cyclic voltammogram **a** of annealed pure Ni_2SiO_4 material and fitted EIS **b** of Ni_2SiO_4 with impurity SiO_2 and Ni_2SiO_4 cells

Figure 3b illustrated the electrochemical impedance spectra (EIS) of the cells. The impedance data were fitted by Z View software using equivalent circuit model (in the inset). All of the curves were composed of a semicircle in the high-to-medium frequency region followed by a straight line in the low-frequency region. An intercept on the real axis Z′ at high frequency represents the bulk or solution resistance (Re). The diameter of the semicircle is approximately equal to the charge transfer impedance (Rct) between the active material on the electrode and electrolyte. The sloping line is associated with the diffusion of Li ions inside the bulk of pure NSO, which is called Warburg diffusion (Zw). It is observed that NSO with SiO_2 impurity cells have high Rct (198.7 Ω) in comparison with the pure NSO-based cells (129 Ω).

Figure 4a illustrates the first charge and discharge profiles of NSO with SiO_2 impurity cell and pure NSO-based cell during defined cycling voltage intervals, measured at room temperature. The initial discharge capacity and coulombic efficiency of the pure NSO sample are 753.4 mA h g^{-1} and 63.8%. This result is slightly better than those of NSO with SiO_2 impurity cell, which are 708.5 and 23.2%. The large initial irreversible capacity mainly originates from the structural change and the existence of the SiO_2 impurity.

The specific discharge cyclic performances of the different cells are shown in Fig. 4b. The discharge capacities of both cells all decrease gradually as the cycle number increases. The intrinsic capacity fading can be mainly ascribed to a structural transformation. It is clearly observed that the discharge capacity of the pure NSO—based cell decreased to 305.5 mA h g^{-1}, after 50 cycles, which is nearly 208% higher than those of the Ni_2SiO_4 with SiO_2 impurity. The poor electrochemical performance of the former can be resulted from the presence of SiO_2 impurity.

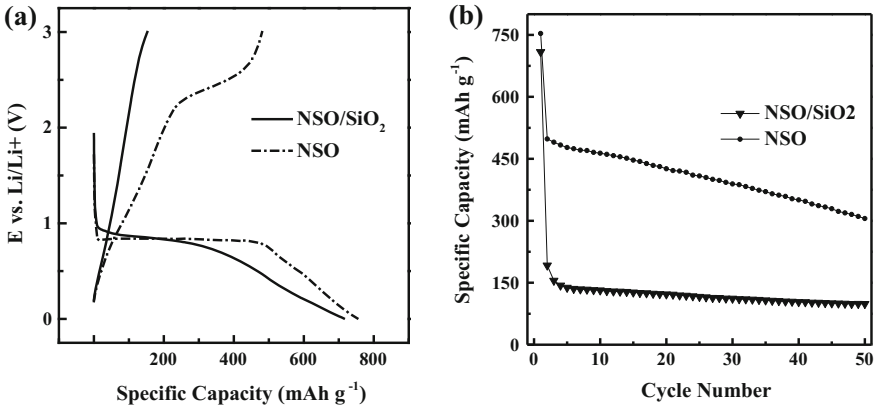

Fig. 4 The initial charge/discharge curves **a** and specific discharge cycling performances **b** of Ni_2SiO_4 with impurity SiO_2 and Ni_2SiO_4 at a current density of 100 mA g^{-1} between 0.05 and 3.0 V

Conclusions

In summary, a nanosized NSO material has been prepared using chemical precipitation process. XRD and SEM measurements revealed that the as-synthesized cubic particles have good crystallinity with orthorhombic structure with space group Pbnm and a uniformly distributed nanosize of ca. 50–80 nm. It is observed that the cell prepared from pure NSO has lower real Rct (charge transfer resistance: 129.1 Ω) in comparison with the other cell (198.6 Ω). The charge-discharge experiments demonstrate that the NSO/SiO_2 cell exhibits good galvanostatic performance with initial discharge capacity of 708.5 mA h g^{-1} at a current rate of 100 mA g^{-1} at room temperature. Furthermore, it was found that removal of impurity SiO_2 resulted in improvement in electrochemical performance over 50 cycles. Therefore, NS electrode materials should be ideal candidates for cathode of Li ion battery technology.

Acknowledgements The authors acknowledge the financial supports of the National Science Fund of China (No.51404213, No. 51404214, No. 51674225 and No. 51774252), Educational Commission of Henan Province of China (No. 17A450001, No. 18HASTIT011 and No. 18A450001) and the Development Fund for Outstanding Young Teachers of Zhengzhou University (No.1421324065).

References

1. Tarascon J, Armand M (2001) Issues and challenges facing rechargeable lithium batteries. Nature 414(6861):359–367
2. Sun Y, Zhao L, Pan H (2013) Direct atomic-scale confirmation of three-phase storage mechanism in $Li_4Ti_5O_{12}$ anodes for room-temperature sodium-ion batteries. Nat Commun 4:1870. https://doi.org/10.1038/ncomms2878

3. Aricò AS, Bruce P, Scrosati B (2005) Nanostructured materials for advanced energy conversion and storage devices. Nat Mater 4(5):366–377
4. Zhang X, Qian Y, Zhu Y et al (2014) Synthesis of Mn_2O_3 nanomaterials with controllable porosity and thickness for enhanced lithium-ion batteries performance. Nanoscale 6(3):1725–1731
5. Kiener J, Tosheva L, Parmentier J (2017) Carbide, nitride and sulfide transition metal-based macrospheres. J Eur Ceram Soc 37(3):1127–1130
6. Antipov EV, Khasanova NR, Fedotov SS (2015) Perspectives on Li and transition metal fluoride phosphates as cathode materials for a new generation of Li-ion batteries. IUCrJ 2(Pt 1):85–94
7. Mysen B (2007) Partitioning of calcium, magnesium, and transition metals between olivine and melt governed by the structure of the silicate melt at ambient pressure. Am Miner 92(5–6):844–862
8. Tang Q, Dieckmann R (2012) Orientation, oxygen activity and temperature dependencies of the diffusion of cobalt in cobalt orthosilicate, Co_2SiO_4. Solid State Ionics 212(24):66–76
9. Yang X, Wen Z, Xu X et al (2007) Nanosized silicon-based composite derived by in situ mechanochemical reduction for lithium ion batteries. J Power Sources 164(2):880–884
10. Guo B, Shu J, Wang Z et al (2008) Electrochemical reduction of nano-SiO in hard carbon as anode material for lithium ion batteries. Electrochem Commun 10(12):1876–1878
11. Hwa Y, Park CM, Sohn HJ (2013) Modified SiO as a high performance anode for Li-ion batteries. J Power Sources 222(2):129–134
12. Mueller F, Bresser D, Minderjahn N et al (2014) Cobalt orthosilicate as a new electrode material for secondary lithium-ion batteries. Dalton Trans 43(40):15013–15021
13. Guo P, Wang C (2015) Synthesis and lithium storage performance of Co_2SiO_4 nanoparticles. Rsc Adv 5(86):70661–70667
14. Syun-iti A, Hideyuki F, Takashi K (1965) The olivine-spinel transition in Fe_2SiO_4 and Ni_2SiO_4. J Geophys Research Atmo 70(8):1969–1977
15. Datta RK, Roy R (1967) Synthesis of cubic nickel orthosilicate. J Am Ceram Soc 50(12):684
16. Róg G, Kozłowska-Róg A (2002) Determination of the activities of cobalt and nickel orthosilicates in xCo2SiO4 + (1 − x) Ni_2SiO_4 using a solid-state galvanic cell method. J Chem Thermodyn 34(8):1151–1156
17. Cruz RA, Romero SA, Vargas RM et al (2005) Thermodynamic analysis of the SiO_2–NiO–FeO system. J Non-Cryst Solids 351(16–17):1359–1365
18. Liu Z, Li Q, Yang T et al (2013) Dissolution behavior of nickel silicate in ammonia-ammonium sulfate aqueous solution. J Cent South Univ 44(7):2669–2674

Eletrochemical Behavior and Corrosion Properties of Ti–6Al–4V Alloy Made by Selective Laser Melting for Immersion in Artificial Seawater at Different Temperature

Yifei Zhang, Jianzhong Li and Wenhao Zhang

Abstract Eletrochemical behavior and corrosion properties of a Ti–6Al–4V alloy fabricated by selective laser melting in artificial seawater at temperature ranges from 20 to 40 °C were investigated using electrochemical techniques, including potentiodynamic polarization, electrochemical impedance spectroscopy (EIS), and Mott-Schottky measurement, etc. Equivalent circuits were simulated to investigate alloy surface and analytic effects of temperature on interface of alloy and solution. The results showed that corrosion potential increased with temperature rise, and the EIS presented a single capacitive resistance characteristics. When the temperature reached 35 °C or above, passive current increased, while the passivation phenomenon was not obvious and corresponding radiating arc radius reduced, indicating that the resistance decreased, conductivity of surface passivation film improved, and corrosion performance improved. According to the Mott-Schottky curves, alloys exhibited n-type semiconductor characteristics. With increasing temperature, conductivity of passivation film enhanced, and alloy corrosion resistance decreased. At 40 °C, alloy possessed the worst corrosion resistance.

Keywords Titanium alloy · Selective laser melting · Polarrization EIS · Passive film

Introduction

Ti–6Al–4V (TC4) alloy fabricated by selective laser melting (SLM) is a moderate strength titanium alloy with a microstructure of $\alpha + \beta$ two-phase. It has been widely researched and used as an ideal marine engineering material after a long period of sea condition test for its numerous advantages, i.e., high strength, small specific

Y. Zhang · J. Li (✉) · W. Zhang
School of Metallurgy, Northeastern University, Shenyang City 110819, China
e-mail: lijz@smm.neu.edu.cn

B. Li et al. (eds.), *Characterization of Minerals, Metals, and Materials 2018*, The Minerals, Metals & Materials Series,
https://doi.org/10.1007/978-3-319-72484-3_7

gravity, non-magnetic, shock-resistant and small expansion coefficient [1]. However, because of its poor corrosion resistance and wear resistance, the surface of components are easy to be scratched and seized, so the working conditions of titanium alloys in the sea water are more stringent than the terrestrial environment, resulting in the greatly shortened service life [2, 3]. Therefore, improving the corrosion resistance of titanium alloy in seawater and enhancing the thermal stability of marine engineering equipment have become an urgent problem to be solved in the structural engineering field.

At present, most of the researches in corrosion wear of titanium alloys are concentrated on the comparison of simulated body fluids, acidic media, specific atmosphere, simulated seawater and different media [4]. Among them, studies on corrosion of body fluids are the most. Bai et al. [5] studied the electrochemical corrosion behavior of Ti-6Al–4V prepared by electron beam melting in phosphate buffered saline and found that EBM-produced Ti-6Al–4V possessed slightly better corrosion resistance than the wrought one. Zhao et al. [6] compared two types of Ti–6Al–4V alloy scaffold fabricated by electron beam melting and selective laser melting for implantation in vivo and pointed out that the corrosion resistance of a SLM specimen was the best under the low electric potential and EBM specimen was the best under the high electric potential. Krząkała et al. [7] analyzed the bioactivity investigations of human bone marrow stromal cells in simulated body fluid and figured out that the application of plasma electrolytic oxidation process can increase the bioactivity and corrosion resistance of a Ti–6Al–4V alloy. Sarraf et al. [8] proposed that the corrosion, bioactivity and wear resistance of Ti–6Al–4V plates in simulated body fluids after nanotubular surface modification was higher than that of without treatment.

Generally, the corrosion behaviors of titanium alloys in simulated seawater environment are performed in a certain concentration of NaCl solution, and many investigations on this have been carried out [9]. Al-Fozan and Malik [10] evaluated the corrosion behavior of different alloys in seawater environment and put forward that seawater had chemical aggressive and the constructional materials working in the seawater were subjected to various degree of corrosion depending on the inherent properties of the materials. Al-Muhanna and Habibb [11] observed that seasonal changes of the seawater affected the formation of the marine biological films on the tested material surface, controlling the corrosion behavior of the titanium alloys. Similar researches have been presented by Wang [12]. Moreover, Pang [13] reported that at high temperature of 200 °C with CO_2, titanium alloys of Grades 2, 5 and 7 in near anaerobic seawater had certain resistance to stress cracking and pitting corrosion, but prone to generate crevice corrosion.

However, the results showed that with 3.5% NaCl solution for the corrosion test the deviation was large. Satisfactory results can be obtained using the artificial seawater instead of natural seawater [14]. In this paper, artificial seawater was chosen to simulate the marine environment, and electrochemical testing was conducted to investigate the effects of seawater temperature on corrosion properties of Ti–6Al–4V alloy produced by selective laser melting, so as to provide theoretical

basis for the inhibition of moisture absorption and deliquescence of metal surface and improve the corrosion resistance of working parts in marine engineering.

Experimental Methods

Spherical powder of the Ti–6Al–4V alloys produced by selective laser melting (SLM) techniques were obtained from Shanghai Research Institute of Materials. Size range of the powder is 20–30 um, and the apparent density is 2.5 g/cm^3. SLM process was performed with standard parameters using EOSINT M270 type of the equipment manufactured by EOS corporation of Germany. The 3D CAD models of titanium alloys were designed by a computer, then the components were fabricated layer by layer by the SLM technique according to the direction of the hierarchical structures given by the CAD models. All of the specimens were produced along the same horizontal direction. The chemical composition of the Ti–6Al–4V alloy is listed in Table 1.

Before electrochemical experiment, all the specimens were ground by silicon carbide papers to 1200 mesh and cleaned for 5 min in an ultrasonic washer filled with ethyl alcohol, then rinsed with distilled water and dried. Eletrochemical behavior of Ti–6Al–4V alloys were analyzed in the simulated seawater at a temperature range from 20 to 40 °C, and the test temperature was controlled by a water bath thermostatically. Chemical composition of the artificial seawater is shown in Table 2. All the electrochemical tests were conducted using a PARSTAT 2273 style (American Princeton Company) electrochemical workstation.

The potentiodynamic polarization was performed in an electrolytic cell with a three-electrode configuration. A standard calomel electrode (SCE) was chosen as a reference and a graphite electrode worked as a counter electrode. The Ti–6Al–4V alloy specimen was used as a working electrode with an exposed area of approximate to 1 cm^2. Before measurement, the open circuit potential remained stabling for 120 min. Then the potentiodynamic polarization was measured from −1.0 to 1.5 V (vs. SCE) at a scan rate of 5 mV/s. Electrochemical impedance spectroscopy (EIS) experiments were conducted from 10^{-2} to 10^5 Hz with an amplitude of 10 mV. Mott-Schottky curves were performed in the range of −2 to 2 V with an amplitude of 5 mV/s and a frequency of 962 Hz. The corresponding impedance

Table 1 Chemical composition of Ti–6Al–4V alloy

Element	N	C	Fe	H	Al	V	O	Ti
wt/%	0.05	0.01	0.3	0.015	6.2	4.5	0.2	88.725

Table 2 Chemical composition of artificial seawater (g/L)

Reagent	NaCl	KCl	$CaCl_2$	$MgCl_2$	$MgSO_4$	$NaHCO_3$
g/L	26.73	0.72	1.15	2.26	3.25	0.20

spectra data were analyzed using ZSimpWin 3.10 software (EG&G,USA) and equivalent circuit models were simulated to evaluate the characteristics of alloys surface. Meanwhile, the semiconductor properties of the oxide film formed on the alloy surface were evaluated.

Results and Discussion

Open Circuit Potential Test

The open circuit potential (OCP) of Ti–6Al–4V alloy specimens in artificial seawater at different temperatures were shown in Fig. 1. It was observed that in the artificial seawater of 25 °C, the fluctuation of open circuit potential of the titanium alloy was the smallest and the thermal stability was the best. When the temperature rose to 35 and 40 °C, the open circuit potential of Ti–6Al–4V alloy was much larger than that at other temperatures, and at the condition of 40 °C the curve was very unstable. The thermodynamic stability of open circuit potential in lower temperature range of 20 and 25 °C were better than that at of the temperature above 30 °C. At the temperature of 40 °C, the thermodynamic stability of the open circuit potential of Ti–6Al–4V alloys was the worst, showing a vigorous fluctuation over the time. The reason may be that the chloride concentration in the seawater is high, the increase of temperature may contribute to the destruction of the oxide film by the chloride ions on the surface of Ti–6Al–4V alloys, leading to a decrease in the stability of open circuit potential curve.

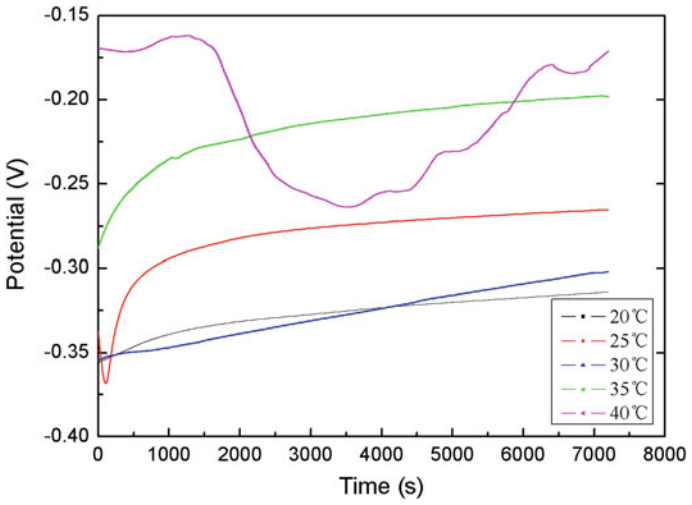

Fig. 1 Open circuit potential as function of time of Ti–6Al–4V alloys in artificial seawater

Polarisation Curves

The polarization curves of titanium alloy samples in corrosive medium of artificial seawater under different experimental temperatures were tested. The results are demonstrated in Fig. 2, and the corresponding values achieved from the polarisation curves are listed in Table 3: the corrosion potential is expressed by Ecorr, and the corrosion current density extracted by extrapolating Tafel slopes at the corrosion potential is denoted by Icorr.

It can be seen from the figure that in the solution temperatures of 20 and 25 °C, the alloy specimens showed an obvious passivation process(0–0.5 v) in which the current density of specimens changed little with the increase of voltage. When the temperature increased to 30 °C, the passivation region of specimen obviously reduced, when the temperature reached 35 °C or above, the passive current density increased and the passivation phenomenon was not evident, indicating when the

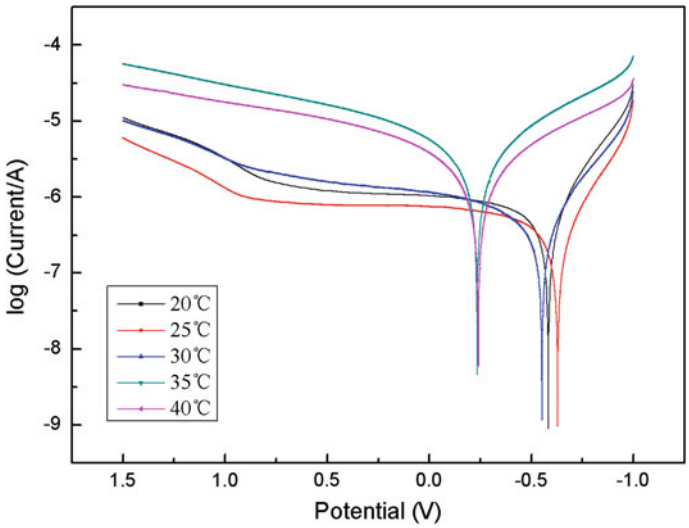

Fig. 2 Polarization curves of Ti–6Al–4V alloys in artificial seawater at different temperature

Table 3 Electrochemical parameters of Ti–6Al–4V alloys in artificial seawater

Sample no.	Temperature (°C)	Parameters	
		Icorr (uA/cm^2)	Ecorr (V)
1	20	0.312	−0.583
2	25	0.187	−0.628
3	30	0.266	−0.552
4	35	1.133	−0.234
5	40	0.747	−0.240

temperature was above 35 °C, the corrosion resistance of Ti–6Al–4V alloys decreased significantly. Corrosion potential is an important index to reflect the corrosion tendency of metals [15]. Corrosion potential of samples was smaller in the range of 20–30 °C than the others at the temperature of 35 °C or 40 °C, manifesting that the corrosion tendency of Ti–6Al–4V alloys was much larger at low temperature (20–30 °C). Moreover, the current density of specimens at the temperature of 35 and 40 °C were significantly increased, indicating that the sample's corrosion rate was faster at high temperature (35–40 °C).

On the whole, although the corrosion tendency at low temperature is larger, the sample has a relatively wide passivation region which hinders the corrosion process of the sample effectively. Meanwhile, compared with Ti–6Al–4V alloys at low temperature, the corrosion rate of sample at high temperature is greatly improved and the reactivity of overall surface is enhanced. So the corrosion resistance of Ti–6Al–4V alloy at low temperature is better.

Electrochemical Impedance Spectroscopy

In order to analyze alloys surface and better evaluate the influence of seawater temperature on interface/solution, electrochemical impedance spectroscopy (EIS) measurements were conducted at open circuit potential (OCP). The Nyquist curves and Bode-phase plots versus temperature were shown in Fig. 3.

From the Nyquist plot it can be seen that all specimens immersed in the artificial seawater exhibit a single capacitive arc. When the temperature was below 30 °C, the capacitive arc radius was bigger, which leads to a better corrosion resistance, when the temperature was increased to 35 °C or above, the capacitive arc radius significantly reduced, indicating that the increase in temperature caused the decrease of charge transfer resistance on the sample surface, resulting in the

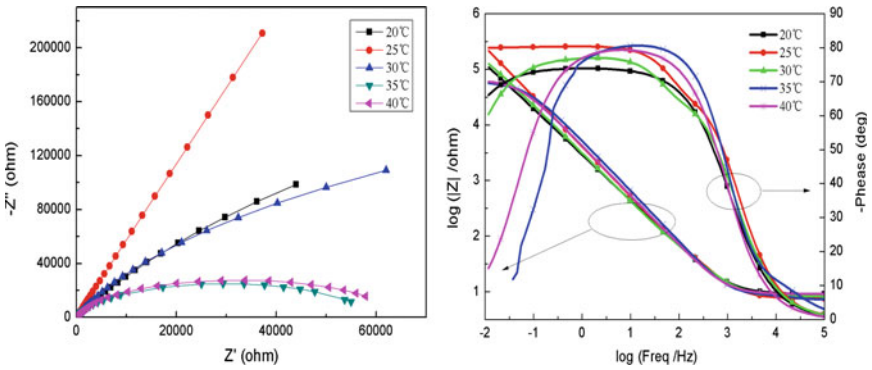

(a) Nyquist plots of Ti-6Al-4V alloys (b) Bode plots of Ti-6Al-4V alloys

Fig. 3 Impedance diagrams of Ti–6Al–4V alloys at different seawater temperature

deterioration of corrosion resistance. Resistance in high-frequency corresponds to the solution resistance, the modulus diagram in the high frequency region has a horizontal shape indicating that the impedance is dominated by the resistance of the corrosive medium [16]. On the phase-frequency characteristic curves, two processes were separated in the frequency range of 10^{-2}–10^{5} Hz, i.e., one in the low-frequency region, and the second in the high-frequency process. Moreover, when the temperature to 35 °C or 40 °C, the negative phase angle of the curve significantly reduced in the low frequency. This suggests the signal of the low frequency is derived from the contribution of the charge transfer resistance, and the change of the charge transfer resistance affects the density of the passivation film on the alloy surface [17]. Therefore, it can be considered that the reduction of corrosion resistance is related to pore size and compactness of the passivation film under the condition of above 35 °C.

The wide range XPS spectrum of Ti–6Al–4V alloy is presented in Fig. 4a. Many elements (Ti, Al, V, C, O, N, Na, K, Fe, etc.) were listed there. After immersion into the artificial seawater, a thin layer composed mainly of titanium, aluminum and vanadium oxides was formed on the surface of titanium alloys. Two peaks of titanium at binding energies of 458.10 eV ($Ti2p_{3/2}$) and 463.70 eV ($Ti2p_{1/2}$) can be seen in Fig. 4b. The detailed analysis of titanium peaks manifested the presence of TiO_2 (458.11 eV) and small amount of TiO/Ti_2O_3 (456.08 eV). Similar results were obtained for aluminum, and the peaks at 74.30 eV ($Al2p_{3/2}$) and 74.71 eV ($Al2p_{1/2}$) indicated the generation of Al_2O_3 (Fig. 4c). The oxygen peaks appeared at the binding energies of 530.30 eV (O1 s). After peaking treatment, the oxygen was found to be existed in the following compounds: titanium, aluminium, vanadium

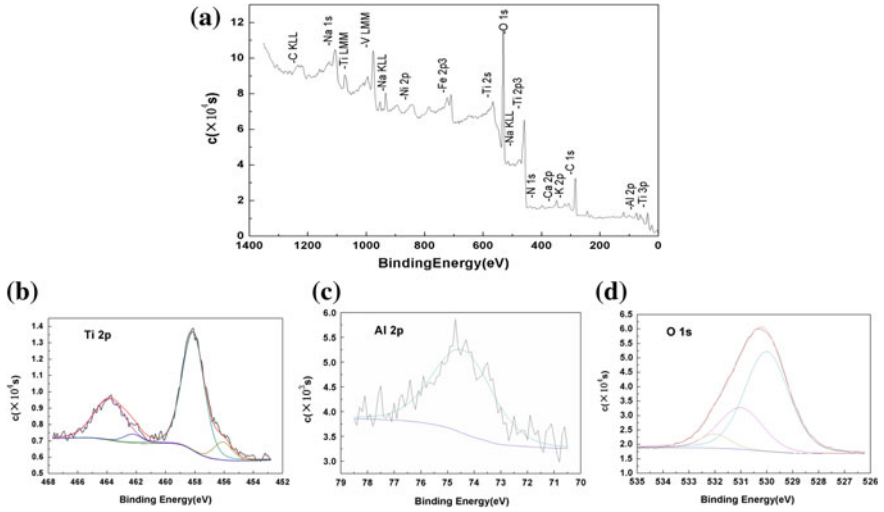

Fig. 4 Representative XPS spectra of oxide films on Ti–6Al–4V alloys after immersion in artificial seawater

oxide (peak at 530.00 eV), OH^- groups (531.01 eV), and adsorbed water (532.02 eV) (Fig. 4d).

The equivalent circuit obtained by fitting with the AC impedance spectroscopy data according to the experiment results is shown in Fig. 5. Where R_L is the solution resistance, the circuit assumes that the passive film formed on the alloy surface are consisted of an oxide layer capacitance (Q_C) and a resistance (R_C), Qd and Rt are the double layer capacitance and the charge transfer resistance, respectively. The specific fitting values of the AC impedance data are illustrated in Table 4.

The data error between obtained and simulated values was evaluated by chi-squared (χ^2) and the error value below 10^{-3} implied a small error and a good fitting [18]. The corrosion rate of Ti–6Al–4V alloys at low temperature is small, the pores or micro-defects on the surface of oxide film are less, contributing to a smaller Rc value; With the temperature increasing, the corrosion rate increased and the electrolyte solution continually immersed into the oxide film along the pores or micro-cracks, which could enhance the reactivity and resistance of Rc effectually. In addition. The Rt value at 35 and 40 °C reduced by an order of magnitude than the other conditions, manifesting that the passivation film compactness of Ti–6Al–4V alloys reduced at high temperature, which in turn would result in a decrease in corrosion resistance.

Mott-Schottky Measurements

The oxide film on titanium alloy surface exhibits the characteristics of a semiconductor. To describe the relationship between the differential capacitance of the semiconductor space charge layer and the semiconductor surface for the noumenal potential, the Mott-Schottky curves of titanium alloy samples in artificial seawater were measured [19]. The temperature of electrolytes varied within 20–40 °C, and the corresponding results are illustrated in Fig. 5.

For n-type semiconductors:

$$\frac{1}{C_{sc}^2} = \frac{2}{\varepsilon \varepsilon_0 e N_D}\left(U - U_{fb} - \frac{kT}{e}\right)$$

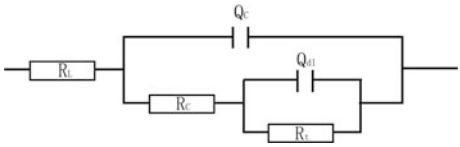

Fig. 5 Equivalent electrical circuits used to adjust EIS results

Table 4 Impedance parameters of Ti–6Al–4V alloys at different seawater temperature

Sample no.	Temperature (°C)	Chi-squared (χ^2)	Parameters				
			R_L (Ω cm^2)	Q_C (Ω cm^2)	R_C (Ω cm^2)	Q_d (Ω cm^2)	R_t (Ω cm^2)
1	20	$2.19e^{-3}$	9.091	7.504×10^{-5}	219.3	1.016×10^{-7}	5.24×10^{6}
2	25	$1.57e^{-3}$	7.534	4.217×10^{-5}	277.2	5.123×10^{-6}	4.387×10^{6}
3	30	$8.83e^{-4}$	8.252	6.038×10^{-5}	216.7	5.48×10^{-6}	4.316×10^{5}
4	35	$2.93e^{-3}$	7.16	2.779×10^{-5}	462.1	9.528×10^{-6}	5.976×10^{5}
5	40	$2.68\ e^{-3}$	9.144	4.531×10^{-5}	482.5	5.251×10^{-6}	5.823×10^{4}

For P-type semiconductors:

$$\frac{1}{C_{sc}^2} = \frac{2}{\varepsilon\,\varepsilon_0 e N_A}\left(U - U_{fb} - \frac{kT}{e}\right)$$

where C_{sc} is the capacitance of the space charge layer, ε is the dielectric constant of the semiconductor, ε_o is the vacuum dielectric constant (8.85×10^{-12} F m), e is the electron charge (1.602×10^{-19} C), N_D, N_A is the concentration of the donor and the receptor, U is the applied potential, U_{fb} is the flat band potential, k is the Boltzmann constant, and T is the absolute temperature. According to the calculation, the relationship between the C_{sc}^{-2} and the applied potential U can be obtained through the potential-capacitance test, the N_D, N_A can be got in the light of the slope, and the flat band potential can be acquired by the intercept.

As can be seen from Fig. 6, the slope of the M-S curves obtained in the simulated seawater is positive, indicating that the samples are the n-type semiconductors in the artificial seawater. The conductivity is achieved through carrying electrons by the defects [20]. Figure 7 also shows the carrier density N_D, it is observed that as solution temperatures rise, carrier density increases, which would promotes the conductivity of passivation film and is adverse to the corrosion resistance of Ti–6Al–4V alloys. In fact, pitting corrosion of titanium often appeared in the concentrated chloride under the high temperature. The occurrence of pitting corrosion resulted in a decrease in the passivation film density and a reduction in corrosion resistance.

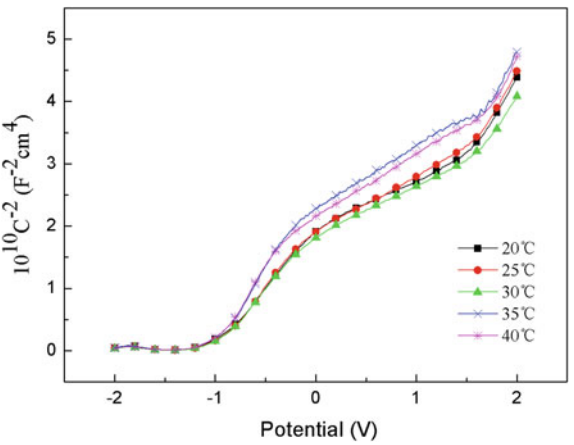

Fig. 6 Mott-Schottky curves of Ti–6Al–4V alloys

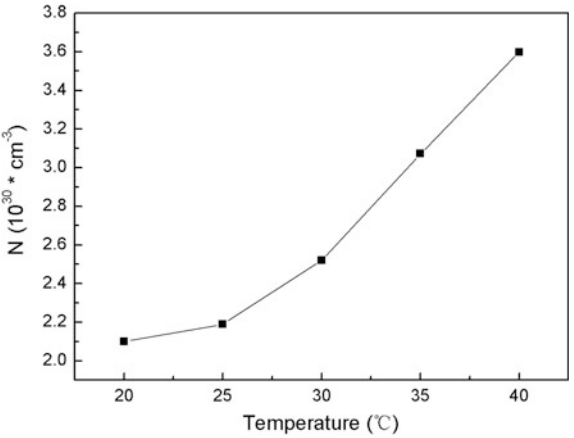

Fig. 7 Carrier density of Ti–6Al–4V alloys

Conclusions

1. During 120 min testing, the open circuit potential of Ti–6Al–4V alloy fluctuated along with time increasing. Thermal stability at high temperatures was better than that at the low temperatures. The OCP curve showed a significant fluctuation at 40 °C, indicating the worst thermodynamic stability.
2. At low temperature the Ti–6Al–4V alloy exhibited an obvious passivation process. When the temperature reached 35 °C or above, the passivation phenomenon was not evident. The corrosion resistance reduced and the corrosion speed increased. Reduction of corrosion resistance is believed to be attributed to the increase of seawater temperature.
3. Electrochemical impedance spectroscopy of Ti–6Al–4V alloy in artificial seawater present a single capacitive arc, and the corrosion resistance was better at 30 °C. When the temperature increased to 35 °C or above, the negative phase angle at low frequency region reduced and the corrosion resistance became weak.
4. Ti–6Al–4V alloy fabricated by selective laser melting shows characteristics of N-type semiconductors in artificial seawater. With temperature increasing, the carrier density improved, leading to an increase in passivation film conductivity and a decrease in corrosion resistance. At 40 °C, the corrosion resistance of Ti–6Al–4V alloy was the worst.

Acknowledgements The authors gratefully acknowledge the support of the National Natural Science Foundation of China (51374053) and the Iron and Steel Joint Research Found of National Natural Science Foundation and China Baowu Steel Group Corporation Limited (U1760118).

References

1. Huang ZH, Qu HL, Deng C (2011) Development and application of aerial titanium and its alloys. Mater Rev 25(1):102–107
2. Attar H, Prashanth KG, Zhang LC (2015) Effect of powder particle shape on the properties of in situ Ti-TiB composite materials produced by selective laser melting. J Mater Sci Technol 31(10):1001–1005
3. Cvijović-Alagić I, Cvijović Z, Bajat J (2016) Electrochemical behaviour of Ti–6Al–4V alloy with different microstructures in a simulated bio-environment. Mater Corros 67(10):1075–1087
4. Kasperovich G, Hausmann J (2015) Improvement of fatigue resistance and ductility of TiAl6V4 processed by selective laser melting. J Mater Process Tech 220:202–214
5. Bai Y, Gai X, Li SJ (2017) Improved corrosion behaviour of electron beam melted Ti–6Al–4V alloy in phosphate buffered saline. Corros Sci 123:289–296
6. Zhao BJ, Wang H, Qiao N (2017) Corrosion resistance characteristics of a Ti–6Al–4V alloy scaffold that is fabricated by electron beam melting and selective laser melting for implantation in vivo. Mater Sci Eng C 70:832–841
7. Krząkała A, Służalska K, Dercz G (2013) Characterisation of bioactive films on Ti–6Al–4V alloy. Electrochim Acta 104:425–438
8. Sarraf M, Razak BA, Nasiritabrizi B (2017) Nanomechanical properties, wear resistance and in-vitro characterization of Ta_2O_5 nanotubes coating on biomedical grade Ti–6Al–4V. J Mech Behav Biomed 66:159–171
9. Mochizuki H, Yokota M, Hattori S (2007) Effects of materials and solution temperatures on cavitation erosion of pure titanium and titanium alloy in seawater. Wear 262:522–528
10. Al-Fozan SA, Malik AU (2008) Effect of seawater level on corrosion behavior of different alloys. Desalination 228(1–3):61–67
11. Al-Muhanna K, Habibb K (2010) Corrosion behavior of different alloys exposed to continuous flowing seawater by electrochemical impedance spectroscopy (EIS). Desalination 250(1):404–407
12. Wang HR, Li WY, Ma L (2007) Corrosion behavior of cold sprayed titanium protective coating on 1Cr13 substrate in seawater. Surf Coat Tech. 201(9–11):5203–5206
13. Pang JJ, Blackwood DJ (2016) Corrosion of titanium alloys in high temperature near anaerobic seawater. Corros Sci 105:17–24
14. Pina VG, Amigó V, Munoz AI (2016) Microstructural, electrochemical and tribo-electrochemical characterisation of titanium-copper biomedical alloys. Corros Sci 109:115–125
15. Ye XX, Wang LS, Tse ZT (2015) Effects of high-energy electro-pulsing treatment on microstructure, mechanical properties and corrosion behavior of Ti–6Al–4V alloy. Mater Sci Eng C 49:851–860
16. Laboulaisa JN, Mata AA, Borrás VA (2017) Electrochemical characterization and passivation behaviour of new beta-titanium alloys (Ti35Nb10Ta-xFe). Electrochim Acta 227:410–418
17. Wu SL, Liu XM, Yeung KWK (2013) Surface nano-architectures and their effects on the mechanical properties and corrosion behavior of Ti-based orthopedic implants. Surf Coat Tech 233:13–26
18. Liu M, Cheng XQ, Li XG (2017) Effect of carbonation on the electrochemical behavior of corrosion resistance low alloy steel rebars in cement extract solution. Constr Build Mater 130:193–201
19. BenSalah M, Sabot R, Triki E (2014) Passivity of Sanicro28 (UNS N-08028) stainless steel in polluted phosphoric acid at different temperatures studied by electrochemical impedance spectroscopy and Mott-Schottky analysis. Corros Sci 86:61–70
20. Fattah-alhosseini A, Vafaeian S (2015) Comparison of electrochemical behavior between coarse-grained and fine-grained AISI 430 ferritic stainless steel by Mott-Schottky analysis and EIS measurements. J Alloy Compd 639:301–307

Part IV
Microstructure and Performance of Materials

Correlation of Microstructure to Mechanical Properties in Two Grades of Alumina

Tomoko Sano, Ian Buterbaugh, Timothy Walter, James Catalano, Brendan Koch, Calvin Lo and James Hogan

Abstract In this research, two grades of alumina, one at nominally 85% composition and the other at 99.5% were characterized. Microstructural and phase characterization was conducted using Scanning Electron Microscopy, Energy Dispersive Spectroscopy, X-ray Diffraction, and micro-computed X-ray tomography. It was determined that the Knoop hardness values were influenced by the porosity in the 85% composition. Quasi-static compressive tests and high strain rate compression experiments were conducted to determine the influence of the microstructure to the compressive properties. It was observed that the overall compressive strengths increased with strain rate. Although the Knoop hardness values were much lower in the 85% alumina due to the porosity, the compressive strength at both quasi-static and dynamic strain rates were not significantly lower than those of the 99.5% composition.

Keywords Alumina · Microstructure · Compressive strength

Introduction

Due to its versatility, polycrystalline alumina (Al_2O_3) ceramics are used in many commercial applications that require materials with good wear resistance, dielectric strength, and thermal conductivity. In addition, its strength and hardness properties

T. Sano (✉) · T. Walter · J. Catalano
US Army Research Laboratory, 4600 Deer Creek Loop, RDRL-WMM-B
Aberdeen Proving Ground, MD 21005, USA
e-mail: tomoko.sano.civ@mail.mil

I. Buterbaugh
Department of Materials Science and Engineering, University of Arizona,
1235 E. James E. Rogers Way, Tucson, AZ 85721, USA

B. Koch · C. Lo · J. Hogan
Department of Mechanical Engineering, The University of Alberta,
Edmonton, AB T6G 2R3, Canada

B. Li et al. (eds.), *Characterization of Minerals, Metals, and Materials 2018*, The Minerals, Metals & Materials Series,
https://doi.org/10.1007/978-3-319-72484-3_8

have made it a desirable material for structural and armor applications. At the Army as well as at other institutions, the microstructure [1], mechanical properties [2–4], shock wave loading on alumina tiles [5, 6] and projectile penetration behavior [7–10] into alumina targets have been studied for many years. The grade of alumina often studied in these projects [3–8, 10] was the Coorstek AD995 grade material, which has a nominal composition of 99.5% alumina. Microstructural effects were broadly mentioned but were not specifically studied. Hence the idea to study two compositions of alumina in an attempt to discern the effects of microstructure on the properties and of the quasi-static and dynamic compressive strength was pursued. The CoorsTek AD995 was chosen as one of the composition, and the other was the AD85, the nominally 85% alumina composition.

Experimental Methods

To prepare the AD85 and AD995 samples for characterization, samples were mechanically polished using the Allied HighTech MetPrep 4™ PH-6 polisher, starting with the 600 grit silicon carbide and progressing down to the 0.25 micron diamond surface. Microstructural characterization of both compositions, AD995 and AD85, were conducted using the FEI Nova NanoSEM 600 scanning electron microscope (SEM). Secondary electron micrographs were used to determine the grain size using the linear intercept method [11]. Energy dispersive spectroscopy (EDS) elemental analyses and texture analysis using the electron backscattered diffraction (EBSD) were conducted with the Pegasus XM4 analysis system from EDAX Inc. attached to the SEM. X-ray diffraction (XRD) for phase analysis was conducted with the PANalytical X'Pert Pro x-ray, from a 2θ of 20°–120°. For 3-dimentional microstructural and defect analysis, micro computed tomography (micro-CT) with the Zeiss Xradia 520 Versa x-ray microscope was utilized. Knoop hardness testing was performed on a Wilson Tukon testing machine with a load of 2 kg according to the ASTM standard C1326 [12]. Knoop indents falling on surface flaws, such as a pore, were rejected. Low strain rate compression testing was done in a quasi-static MTS 810 testing machine at 10^{-3} s^{-1}, while higher rate testing, at strain rates between 500 and 900 s^{-1}, was done in a Split-Hopkinson pressure bar system.

Results

A representative micrograph of the AD85 alumina sample is shown in Fig. 1a and of AD995 in Fig. 1b. The brighter colored areas around the grains in AD85 is the liquid phase, indicating that this alumina was liquid phase sintered. The dark areas were determined to be porosity for both compositions. AD85 has significant porosity and a more elongated grain morphology compared to AD995. From 4

SEM micrographs of each composition, the average grain size was measured to be 2.95 μm for the AD85 and 7.75 μm for the AD995. These grain sizes differ from Coorstek's reported grain size of 6 μm for both compositions [13]. In addition, as can be deduced from Fig. 1b, the AD995 appears to have a bimodal grain size distribution, or population of abnormal grain size in the microstructure. Hence the average grain size is not an adequate indicator of the grain size distribution for AD995.

To identify the secondary phase present in the AD85 material, EDS analysis was conducted. The AD85 EDS results indicated the presence of Mg, and Si, in addition to Al and O. The EDS results of AD995 did not show the presence of Mg, but did show Si peaks. The XRD results shown in Fig. 2a confirmed the presence of Mg and Si in AD85, identifying the secondary phase as Mg_2SiO_4. It is likely that MgO and SiO_2 reacted during the process to form the Mg_2SiO_4 phase. However the XRD results of AD995 shown in Fig. 2b only identified Al_2O_3, and did not identify any silicate phases.

Knoop hardness for AD85 and AD995 were reported by CoorsTek but at the 1 kg load. They were 9.4 and 14.1 GPa, respectively [13]. The 2 kg load (19.6 N) was chosen for this study since a ceramic hardness evaluation work by Swab [14] established that at 2 kg, the hardness curves would be in the load-independent plateau region. At the 2 kg load, the hardness of AD85 was 6.4 GPa with a standard deviation of 0.3 GPa. For AD995, the hardness was 9.6 GPa with a standard deviation of 1.8 GPa. The low hardness value of AD85 can be attributed to the numerous pores in the sample. However for AD995, the minimal amount of pores cannot explain the much lower hardness values compared to the manufacturer reported value. Jones et al. [7] determined their AD995 sample to have a Knoop hardness value of 13.2 GPa with a standard deviation of 1.3 GPa, a value much closer to that reported by CoorsTek. Unfortunately Jones et al. did not include a micrograph of their material in their paper for microstructural comparison to the

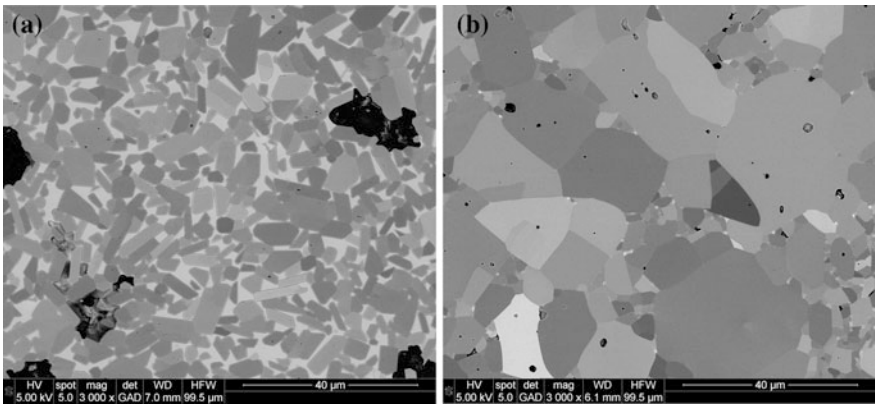

Fig. 1 Representative SEM micrographs of **a** AD85 and **b** AD995

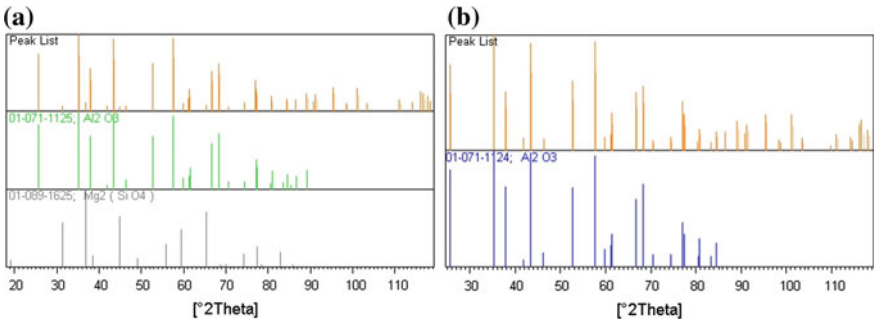

Fig. 2 XRD peaks identified as Al_2O_3 and Mg_2SiO_4 for **a** AD85 and only Al_2O_3 for **b** AD995

current AD995. It is possible that in the current study, some of the Knoop indents were falling on the abnormal grains, lowering the hardness values.

Micro-CT scans were conducted on both AD85 and AD995. As expected from the SEM micrographs, only small pores were observed throughout the AD995 sample volume. However in the AD85, large pores were found throughout the volume of the sample. The micro-CT scans at a resolution of 2 μm/pixel were analyzed to determine the volume fraction of pores. The pores were segmented from the scans using grayscale intensity based thresholding. The binary images of the segmented inclusions were then combined to form a 3D reconstruction, as shown in Fig. 3a, from which sizes of the pores were characterized. The volume distribution of the pores was produced and is shown in Fig. 3b.

Under quasi-static conditions AD85 demonstrated a compressive strength of 1970 ± 100 MPa and AD995 a strength of 2360 ± 180 MPa, both in line with manufacturer's reported values. Under dynamic conditions both see a rise in strength, with AD85 having an average strength of 3180 ± 110 MPa and AD995 a strength of 3880 ± 670 MPa. Eliminating the potential outlier in AD995 from

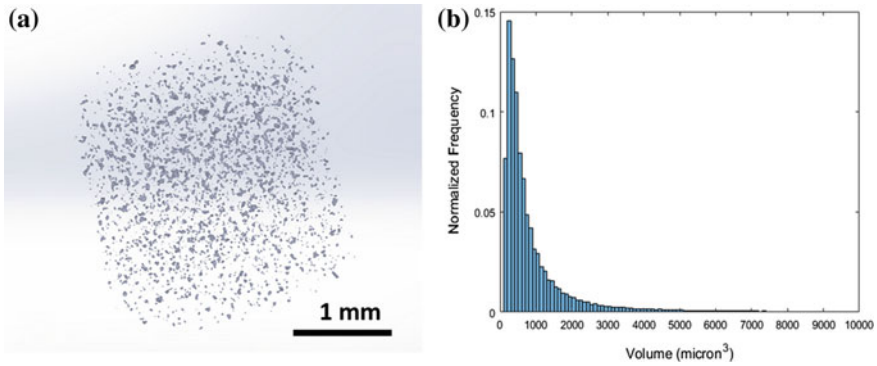

Fig. 3 **a** 3D representation of alumina pores in AD85 reconstructed using micro-CT scans and **b** Volume histogram of the pores characterized using the 3D reconstruction

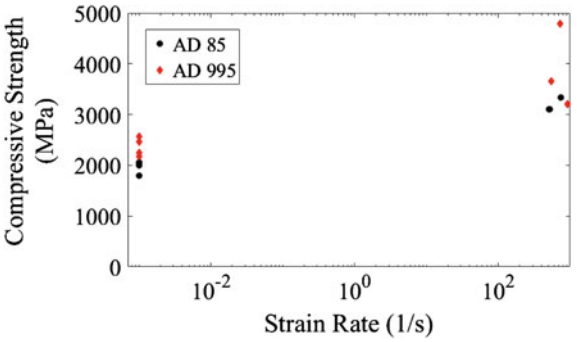

Fig. 4 Compressive strength versus strain rate for AD85 (circles) and AD995 (diamonds)

consideration gives an average strength of 3430 ± 230 MPa. These results plotted in Fig. 4, show that strength increases with strain rate for these materials, although only 2 strain rates were tested. While AD85 has lower strength under both quasi-static and dynamic conditions, over the range tested it also demonstrates a greater proportional increase in strength in comparison to AD995.

Discussions

The two alumina microstructures were drastically different. This is attributed to not only the compositional purity of the alumina samples, but the processing and sintering aids added. Goswami et al. [1] have shown the influence of oxide additions and their amounts on the morphology of alumina grains. It is safe to deduce that in the current AD85 material, the elongated grain shapes and the porosity is due to the liquid phase sintering process. In the case of AD995, the microstructure showed the presence of abnormal grains. This can be explained with the Si (in the form of silica) addition in the microstructure found by EDS analysis. Dillon et al. [15–17] have investigated the role of additives such as silica on grain boundaries and grain growth of alumina. They determined that additives, such as silica cause complexion transitions to occur, inducing abnormal grain growth for some grains, depending on the grain boundary energy of those grains.

The Knoop hardness and the quasi-static and dynamic compressive strength is correlated to the different microstructures. The porosity played a large role in the lower hardness values measured on the AD85 sample. However, although the compressive strength were lower than those of AD995, the porosity found throughout the sample of AD85 did not appear to significantly influence the strength. The preliminary results show that the compressive strength increased with strain rate for both compositions. More research is necessary to understand the role of the homogeneously distributed pores on the quasi-static and high strain rate compressive strengths, and additional compression testing is required to definitively link the increase in the compressive strengths to the strain rate.

Conclusions

Two compositions, nominally 85 and 99.5%, of alumina were characterized. The AD85 sample showed a liquid phased sintered microstructure, consisting of a Mg_2SiO_4 secondary phase surrounding elongated alumina grains. The AD995 sample showed evidence of abnormal grain growth, most likely due to the silica sintering additives causing complexion transitions. There were distinct differences in the Knoop hardness values. The lower hardness of the AD85 material was attributed to the porosity. The compressive strengths were measured and determined to increase with increasing strain rate. The AD85 alumina had lower but not significantly lower compressive strengths compared to those of AD995. More experiments are necessary to deduce the influence of the porosity and microstructural differences on the quasi-static and dynamic compressive strengths of alumina.

References

1. Goswami AP, Sukumar R, Mitra MK, Das GC (2001) Impurity-dependent morphology and grain growth in liquid-phase-sintered alumina. J Am Ceram Soc 84(7):1620–1626. https://doi.org/10.1111/j.1151-2916.2001.tb00886.x
2. Ighodaro OL, Okoli OI (2008) Fracture toughness enhancement for alumina systems: a review. Int J Appl Ceram Technol 5(3):313–323. https://doi.org/10.1111/j.1744-7402.2008.02224.x
3. Wereszczak AA, Swab JJ, Kraft RH (2005) Effects of machining on the uniaxial and equibiaxial flexure strength of CAP3 AD-995 Al_2O_3. Army Research Laboratory Technical Report No. 3617
4. Calomino A, Brewer D, Ghosn L (1994) Fracture behavior of ceramics under displacement controlled loading. Army Research Laboratory Memorandum Report No. 15
5. Dandekar DP, McCauley JW, Green WH, Bourne NK (2006) Global mechanical response and its relation to deformation and failure modes at various length scales under shock impact in alumina AD995 Armor Ceramic. In: 25th army science conference, Orlando, FL 27–30 Nov 2006
6. Bourne NK, Millett JCF (2001) Preliminary shock wave studies in alumina and tungsten carbide. United State Army Report No. 20020429 048
7. Jones TL, Swab J, Meredith CS, Becker B (2016) The first static and dynamic analysis of 3-d printed sintered ceramics for body armor. Army Research Laboratory Technical Report No. 7768
8. Brennan RE, Sands JM, Green WH, Yu JH (2009) Nondestructive damage characterization of alumina ceramics. Army Research Laboratory Technical Report No. 4895
9. Grace FI, Rupert NL (1997) Analysis of long rods impacting ceramic targets at high velocity. Army Research Laboratory Technical Report No. 1493
10. Anderson CE Jr, Walker JD, Lankford J (1995) Investigation of the ballistic response of brittle materials. U.S. Army Research Office Report No. ARO 29788.13-ms
11. ASTM E112–13 (2016) Standard test methods for determining average grain size, ASTM International, West Conshohocken, PA. www.astm.org
12. ASTM C1326 (2013) Standard test method for Knoop indentation hardness of advanced ceramics. ASTM International, West Conshohocken, PA. www.astm.org

13. CoorsTek Inc. (2016) Advanced alumina brochure. https://www.coorstek.com/media/1715/advanced-alumina-brochure.pdf
14. Swab JJ (2004) Recommendations for determining the hardness of Armor Ceramics. Int J Appl Ceram Tech 1:219–225. https://doi.org/10.1111/j.1744-7402.2004.tb00173.x
15. Dillon SJ, Harmer MP (2008) Demystifying the role of sintering additives with "complexion". J Euro Ceram Soc 28:1485–1493. https://doi.org/10.1016/j.jeurceramsoc.2007.12.018
16. Dillon SJ, Harmer MP, Rohrer GS (2010) The relative energies of normally and abnormally growing grain boundaries in alumina displaying different complexions. J Am Ceram Soc 93:1796–1802. https://doi.org/10.1111/j.1551-2916.2010.03642.x
17. Dillon SJ, Miller H, Harmer MP, Rohrer GS (2010) Grain boundary plane distributions in aluminas evolving by normal and abnormal grain growth and displaying different complexions. Int J Mater Res 101(1):50–56. https://doi.org/10.3139/146.110253

Part V
Characterization and Uses of Metallurgical Slags

Preparation and Characterization of $NaNO_3$/BFS Composite Phase Change Materials

Jicheng Liu, Yuanbo Zhang, Zijian Su, Bingbing Liu, Manman Lu, Tao Jiang and Guanghui Li

Abstract Blast furnace slag (BFS), one kind of typical solid waste in the steel industry, was used as structural materials to synthesize $NaNO_3$/BFS composite phase change materials (C-PCMs) by mixing and sintering method. $NaNO_3$ in the composites functioned as phase change materials (PCMs) and BFS as structural skeleton to maintain a stable external form. In this study, the prepared C-PCMs could remain in the solid state without salt leakage even if operating temperature exceeded the melting temperature of $NaNO_3$. The composition and structure of BFS and the prepared composites were characterized by XRD, FTIR, SEM and TG-DSC analyses. The results showed that $NaNO_3$ was well incorporated in the pores of BFS. The melting temperature and latent heat of the final composites were 300.5 °C and 65.53 J/g, respectively. The product also had good thermal storage performance and durability even after 100 thermal cycles. The energy density of the product was calculated as high as 468.03 J/g for an temperature range of 50–400 °C.

Keywords Blast furnace slag · Composite phase change materials
Thermal energy storage · $NaNO_3$

Introduction

Blast furnace slag (BFS) is one of the main by-products discharged from the steel industry. During the production of pig iron, 200–300 kg of BFS is generated per ton of pig iron. The output of BFS is more than 200 million tons in 2015 in China according to the World mineral production report by the British geological survey [1]. The negative impact on the environment caused by BFS and other metallurgical slags becomes more and more severe, thus how to utilize or reuse them is a significant issue [2]. In the past few decades, many attempts have been made to

J. Liu · Y. Zhang (✉) · Z. Su · B. Liu · M. Lu · T. Jiang · G. Li
School of Minerals Processing and Bioengineering,
Central South University, Changsha 410083, Hunan, China
e-mail: zybcsu@126.com

B. Li et al. (eds.), *Characterization of Minerals, Metals, and Materials 2018*, The Minerals, Metals & Materials Series,
https://doi.org/10.1007/978-3-319-72484-3_9

apply BFS into the construction materials such as portland cement [3], ceramic wall tiling [4], cold bonded artificial aggregate used in self-compacting concrete, etc. [5].

Phase change materials (PCMs) are materials that undergo the solid-liquid phase transformation, more commonly known as the melting-solidification cycle at a temperature within the operating range of a selected thermal application [6]. PCMs are widely used in thermal energy storage fields. Due to low thermal conductivity and poor thermal stability, the PCMs are usually used in conjunction with porous materials to fabricate composite phase change materials (C-PCMs) [7]. Some porous materials such as expanded perlite, vermiculite and SiC ceramic honeycomb were used to prepare C-PCMs [8, 9]. However, these materials usually need to be pretreated and it will consume much extra energy.

Previous study showed that the BFS had a porous structure and high adsorption capability. Therefore, the BFS might have potential to act as structural materials for high temperature C-PCMs. In this study, the $NaNO_3$/BFS was prepared as a novel kind of C-PCMs by mixed and sintering method. The products were characterized using TG-DSC, XRD, FTIR, SEM, etc. All the results indicate that BFS can be utilized as a good structural material in thermal energy storage fields.

Experimental

Materials

$NaNO_3$ with 99.9 wt.% purity were purchased from Beijing Chemical Reagents Company. The BFS used in this study was supplied by a steel company in Hunan, China. The chemical constituents of the BFS include CaO (35.18 wt.%), SiO_2 (30.28 wt.%), Al_2O_3 (14.17 wt.%) and MgO (13.21 wt.%). Figure 1 shows the XRD pattern of the BFS, indicating that the BFS is amorphous and the main phases

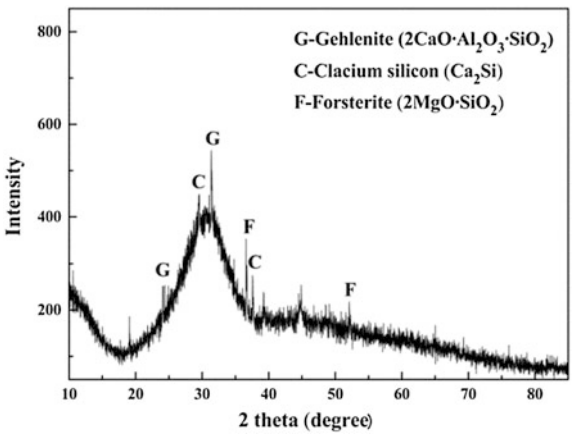

Fig. 1 XRD pattern of the BFS

are gehlenite ($2CaO{\cdot}Al_2O_3{\cdot}SiO_2$), calcium silicon ($Ca_2Si$) and forsterite ($2MgO{\cdot}SiO_2$).

The TG-DSC curves of the BFS are given in Fig. 2. The TG curve showed that the mass of the BFS was almost unchanged as the temperature rose from 0–1000 °C. The DSC curve indicated that there was no chemical reaction occurred when temperature was lower than 800 °C. However, an obvious exothermic peak was found at 800–950 °C, which might be caused by the crystallization reaction of the glass phase [10].

The as-received BFS samples had large grain size. Hence, the BFS was ground to 100 wt.% less than 74 μm. Then, two samples of raw BFS (Sample#1) and the ground BFS (Sample#2) were characterized. The SEM image shown in Fig. 3 is the ground BFS sample with a large number of irregular pores below 1 micron. Figure 4 shows the adsorption-desorption isotherm of BFS sample before and after ground. The results show that the total pore volume increased from 0.008 to 0.025 cm^3/g and the BET surface changed from 3.90 to 10.60 m^2/g.

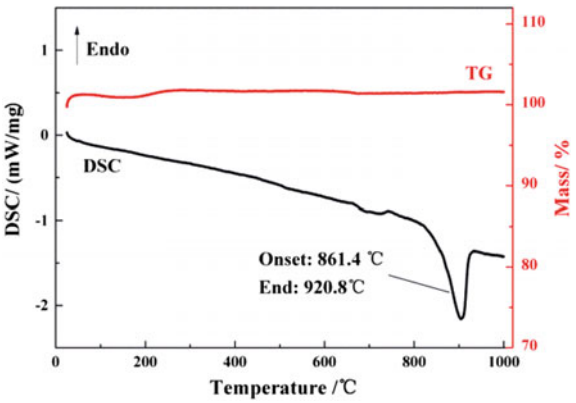

Fig. 2 TG-DSC curves of the BFS

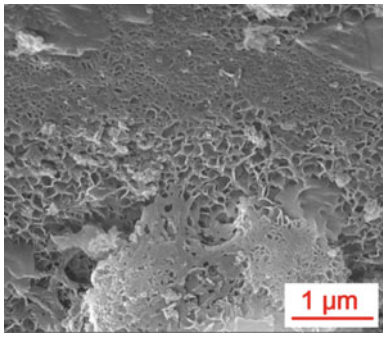

Fig. 3 SEM image of the BFS

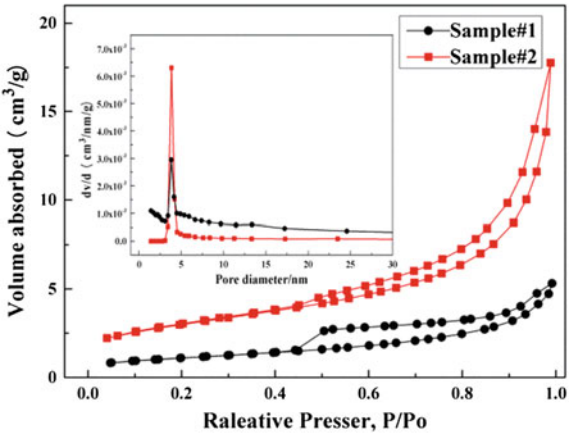

Fig. 4 N_2 adsorption-desorption isotherms of BFS (the inset is the pore size distribution)

Method and Characterization

In this study, the C-PCMs were prepared by mixing and sintering process. The typical PCMs $NaNO_3$ with operating temperature around 300 °C was employed as thermal storage medium. The main experimental procedure included ball-milling, mixing, briquetting and roasting. The BFS was first ground to 100 wt.% less than 0.074 mm, and then mixed with $NaNO_3$ at a certain mass ratio. Then, the mixture was pressed into cylindrical green briquettes with a diameter of 10 mm and height of 6 mm at 20 MPa pressure for 3 min. After that, the green briquettes were dried at 100 °C for 12 h and roasted for 2 h in a muffle furnace. The roasting temperature for $NaNO_3$/BFS C-PCMs was fixed at 350 °C.

The thermal reliability of the $NaNO_3$/BFS C-PCMs was tested by 100 thermal cycles. Thermal cycle test was operated in a muffle furnace and the prepared C-PCMs was maintained at a temperature of 350 °C for 2 h during each thermal cycle. The morphological structure of the prepared C-PCMs was observed by scanning electron microscopy (SEM) and thermal properties were measured by differential scanning calorimeter (DSC). The heat transfer properties were investigated by a laser thermal conductivity meter.

Chemical constituents of the BFS were measured by X-ray Fluorescence (XRF, EDX6000B). Phase compositions of the raw BFS and the prepared C-PCMs were tested by X-ray diffraction (XRD, Rigaku D/max-2500). N_2 adsorption isotherms were obtained at 77.3 K with the aid of a conventional volumetric apparatus (Autosorb-1-MP). The equivalent surface area was obtained from the linear BET plots (S_{BET}), and the pore size distribution of samples was calculated by BJH method. The morphology and structure of the prepared C-PCMs were observed using a scanning electron microscope (SEM, JEOL JSM-6490LV). The latent heat and the phase-transition temperature of the PCMs and the prepared C-PCMs were characterized by differential scanning calorimeter (DSC, NETZSCH STA 449F3) in an Ar atmosphere at a heating rate of 5 °C/min.

Results and Discussion

Preparation of the $NaNO_3$/BFS C-PCMs

The roasting process plays an important role in various properties of C-PCMs during the preparation, especially in the microstructure. Reasonable and correct formulation of roasting system is in favor of the C-PCMs with ideal structure and expected performance. The Fig. 5 exhibited the thermal stability of $NaNO_3$ under 1000 °C. The results indicate that $NaNO_3$ will undergo a decomposition reaction when the temperature is higher than 500 °C and the chemical reaction formula was displayed as Eq. (1):

$$NaNO_3 \rightarrow NaNO_2 + 1/2O_2 \quad (1)$$

According to the DSC curve of $NaNO_3$, it had three endothermic peak in the process of heating up to 1000 °C. The first endothermic peak in the temperature range of 225–290 °C was caused by solid-solid transformation, therefore, the heating rate must be slow as 5 °C/min and maintain 30 min at 290 °C. The second endothermic peak in the temperature range of 300–325 °C was due to solid-liquid transformation, hence the heating rate should increase to 10 °C/min to avoid the loss of $NaNO_3$ due to the evaporation or decomposition. The specific roasting schedule was showed in Fig. 6.

Morphological Structure

During the preparation process, it was found that the C-PCMs with more than 60 wt.% $NaNO_3$ were deformed significantly and the leakage of $NaNO_3$ was serious.

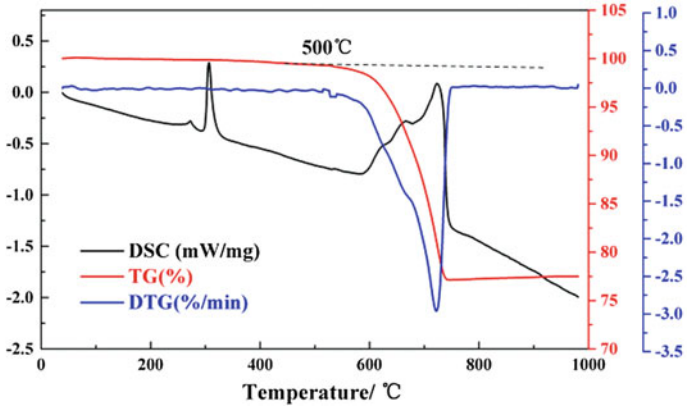

Fig. 5 Thermal stability of $NaNO_3$ under 1000 °C

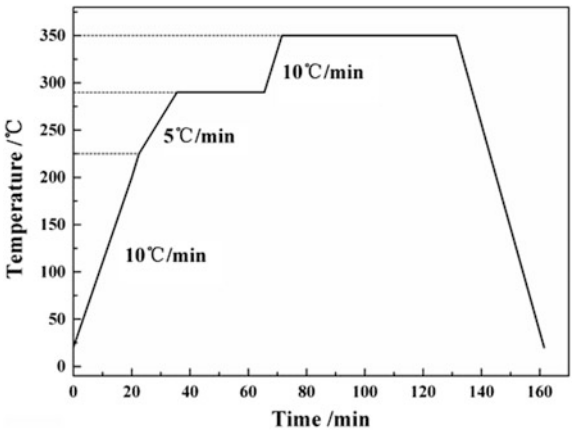

Fig. 6 Roasting schedule of the $NaNO_3$/BFS C-PCMs

Samples with 45 and 60 wt.% $NaNO_3$ were deformed slightly and presented a small amount of $NaNO_3$ leakage. When the content of $NaNO_3$ was lower than 40 wt.%, the prepared C-PCMs had perfect appearance without deformation nor $NaNO_3$ leakage. So, the suitable proportion of $NaNO_3$ and BFS was very important to guarantee a good performance of the C-PCMs. In this study, the addition of $NaNO_3$ was fixed at 40 wt.% in the subsequent studies.

The macroscopic shape of the $NaNO_3$/BFS C-PCMs had no significant change and there was no leakage of $NaNO_3$ after 100 thermal cycles according to Fig. 7a. Figure 7b showed that on the surface of the BFS there existed a large number of irregular nano-scale pores, which could provide plenty of sites for absorbing $NaNO_3$. The molten $NaNO_3$ entered into the pores of BFS and covered almost the entire surface of BFS (Fig. 7c). Compared to the coarse surface of BFS, the $NaNO_3$/BFS C-PCMs had a relatively smooth superficies with even distribution of $NaNO_3$. It showed that $NaNO_3$ was successfully embedded in the pores of BFS. After 100 thermal cycles, no obvious change emerged on the surface of $NaNO_3$/BFS C-PCMs (Fig. 7d). Besides, the surface became smoother and the $NaNO_3$ distributed more uniform after 100 thermal cycles. All these results proved that the $NaNO_3$/BFS C-PCMs were competent to remain in the solid state without salt leakage during the phase-transition.

Thermal Properties

The melting-freezing DSC curves of pure $NaNO_3$ and 40 wt.% $NaNO_3$/BFS C-PCMs are shown in Fig. 8. The melting and freezing temperatures were measured to be 303.6 and 301.1 °C for the pure $NaNO_3$, while the values were 300.5 and 300.4 °C for the $NaNO_3$/BFS C-PCMs, respectively. The melting and freezing latent heat was measured to be 180.23 and 177.96 J/g for the pure $NaNO_3$,

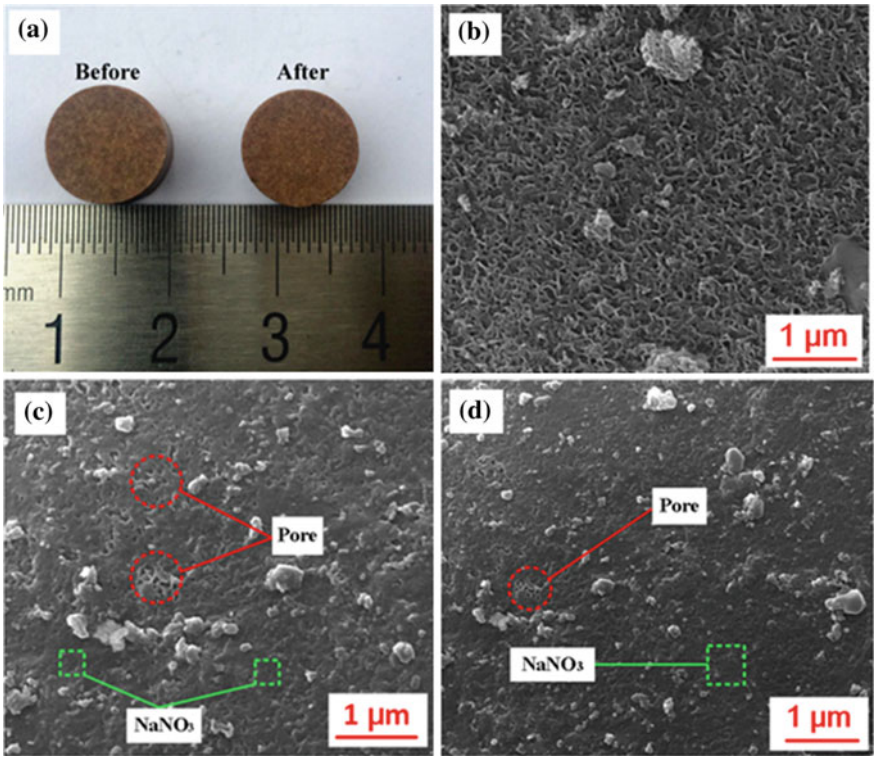

Fig. 7 Images of $NaNO_3$/BFS C-PCMs: **a** macrographs of the $NaNO_3$/BFS C-PCMs before and after 100 thermal cycles **b** SEM image of the BFS used in the preparation process **c** SEM image of the $NaNO_3$/BFS C-PCMs **d** SEM image of the $NaNO_3$/BFS C-PCMs after 100 thermal cycles

and 65.53 and 64.55 J/g for the prepared C-PCMs, respectively. The phase-transition latent heat of the $NaNO_3$/BFS C-PCMs were very close to the theoretical value (with 40 wt.% of $NaNO_3$, 180.23 J/g × 40% = 72.09 J/g). Meanwhile, the results also revealed that the supercooling of the $NaNO_3$/BFS C-PCMs was only 0.1 °C compared to 2.5 °C of pure $NaNO_3$. The low super-cooling was favorable to the stability of the C-PCMs.

The C-PCMs must be stable in terms of thermal performance even over a large number of melting and freezing cycles. Therefore, there should be no or less change in its thermal properties after long-term working period. In this study, 100 thermal cycling test was carried out to determine the change in thermal properties of $NaNO_3$/BFS C-PCMs. Figure 8 displays the melting-freezing DSC curves of the $NaNO_3$/BFS C-PCMs before and after 100 thermal cycles. The results showed that the melting and freezing temperature were 302.1 and 301.7 °C, and the melting and freezing latent heat were 63.30 and 62.97 J/g for the prepared C-PCMs after 100 thermal cycles. After 100 thermal cycles, the melting temperature was increased by 1.6 °C and the freezing temperature increased by 1.3 °C. The increase of the

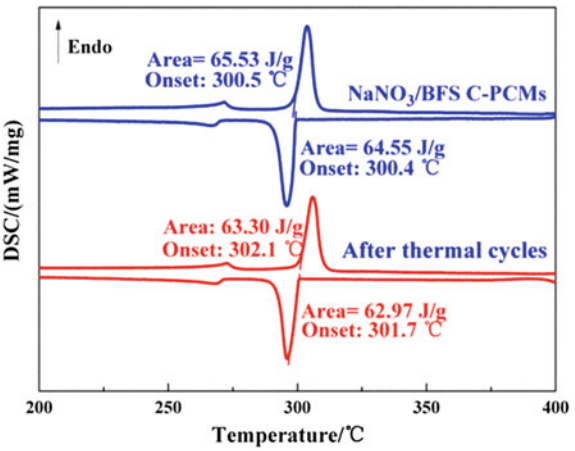

Fig. 8 Melting-freezing DSC curves of $NaNO_3$/BFS C-PCMs before and after 100 thermal cycles

melting and freezing temperature was mainly due to a more uniform distribution of $NaNO_3$ in the prepared C-PCMs. Meanwhile, the super-cooling changed into 0.4 °C after thermal cycles, which was still much smaller than pure $NaNO_3$. The phase-transition enthalpies of the C-PCMs after thermal cycling had no significant change. The results revealed that the $NaNO_3$/BFS C-PCMs had a good thermal reliability with regard to the changes in its phase change temperatures and latent heats.

Energy Density

Energy density of the $NaNO_3$/BFS composite material relies on not only the latent heat of $NaNO_3$, but also the sensible heat of BFS and $NaNO_3$. It can be calculated by using the following Eq. (2) for a temperature range between T_0 and Ts:

$$Q = \int_{T_0}^{T_S} C_{SS}dT + \delta\left(\int_{T_0}^{T_{sf}} C_{lS}dT + \nabla H_{lf} + \int_{T_{ll}}^{T_S} C_{ll}dT - \int_{T_0}^{T_S} C_{SS}dT\right) \quad (2)$$

where Q is the general energy density of the materials in a unit mass, C_{ss}, C_{ls} and C_{ll} is respectively denoted as the specific heat capacities of the structural material, the PCMs in solid phase, and the PCMs in a liquid phase. At the same time, T_o, T_s and T_{sf} represents the original temperature, the upper limit temperature and the melting temperature of the PCMs, respectively. And the δ means the percentage of PCM in the composite materials. Figure 9 was the measured heat capacity curve of the composite materials containing 40 wt.% $NaNO_3$. The results indicated that it had two endothermic peaks at 265–298 °C and 299–314 °C, respectively. Curve-fitting

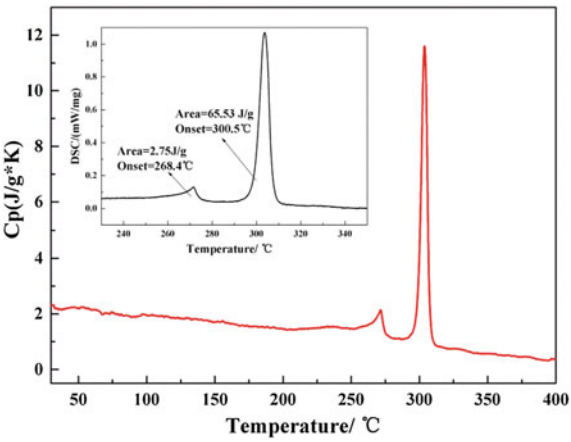

Fig. 9 Heat capacity of the prepared C-PCMs containing 40 wt.% of $NaNO_3$ (the inset is its DSC curve)

of the measured heat capacity data over the two temperature ranges of 50–268 °C and 315–400 °C gives the following two polynomial expressions corresponding to the two temperature ranges:

$$C_{p1} = 2 \times 10^{-5}T^2 - 0.009T + 2.634 \left(R^2 = 0.9415\right) \quad (3)$$

$$C_{p2} = 2 \times 10^{-5}T^2 - 0.0222T + 5.4799 \left(R^2 = 0.9736\right) \quad (4)$$

where T is temperature. Using the heat capacity data discussed above, the energy density of the C-PCMs was calculated to be as high as 468.03 J/g with the $NaNO_3$ content of 40 wt.%. The results indicated that the prepared C-PCMs had a good energy storage density and it rendered this C-PCMs a very promising materials for thermal energy storage.

Conclusions

The study presented a novel route for utilizing BFS to prepare C-PCMs for thermal energy storage, and the following conclusions were obtained:

1. BFS possesses abundant porous structure and excellent thermostability, which can meet the requirements of structural materials for PCMs. A pre-grinding process is beneficial to enlarge the total pore volume for absorpting the PCMs.
2. The $NaNO_3$/BFS C-PCMs even remained good thermal reliability after 100 thermal cycles. The melting point and latent heat of the $NaNO_3$/BFS were 300.5 °C and 65.53 J/g, respectively. The super-cooling of the product was only 0.1 °C, and it remained in the solid state without $NaNO_3$ leakage at a

temperature of 350 °C even after 100 thermal cycles. The prepared C-PCMs with the optimal formulation has an energy density exceeding 468 J/g for an temperature range of 50–400 °C.

Acknowledgements The authors would like to express their heartful thanks to National Natural Science Foundation of China (No. 51574283), the Natural Science Foundation of Hunan Province, China (No. 2016 JJ2143) and Fundamental Research Funds for the Central Universities of Central South University (No. 2017zzts578).

References

1. Brown TJ, Idoine NE, Raycraft ER, Shaw RA, Deady EA, Hobbs SF, Bide T (2017) World mineral production 2011-2015. British Geological Survey, Keyworth, Nottingham
2. Shen JG, Guo CY, Chen M, Yu JK, Jian MF (2006) Utilization of metallurgical slag as resource materials in China. Dev Chem Eng Miner Process 14:487–493
3. Escalante JI, Gómez LY, Johal KK, Mendoza G, Mancha H (2001) Reactivity of blast-furnace slag in Portland Cement blends hydrated under different conditions. Cem Concr Res 31:1403–1409
4. Ozturk ZB, Gultekin EE (2015) Preparation of ceramic wall tiling derived from blast furnace slag. Ceram Int 41:12020–12026
5. Gesoğlu M, Güneyisi E, Mahmood SF, Öz HÖ, Mermerdaş K (2012) Recycling ground granulated blast furnace slag as cold bonded artificial aggregate partially used in self-compacting concrete. J Hazard Mater 235–236:352–358
6. Su W, Darkwa J, Kokogiannakis G (2015) Review of solid–liquid phase change materials and their encapsulation technologies. Renew Sustain Energy Rev 48:373–391
7. Zhang P, Xiao X, Ma ZW (2016) A review of the composite phase change materials: fabrication, characterization, mathematical modeling and application to performance enhancement. Appl Therm Eng 165:472–510
8. Li R, Zhu J, Zhou W, Cheng X, Li Y (2016) Thermal properties of sodium nitrate-expanded vermiculite form-stable composite phase change materials. Mater Des 104:190–196
9. Li Y, Guo B, Huang G et al (2015) Characterization and thermal performance of nitrate mixture/SiC ceramic honeycomb composite phase change materials for thermal energy storage. Appl Therm Eng 81:193–197
10. Liu H, Lu H, Chen D, Wang H, Xu H (2009) Preparation and properties of glass–ceramics derived from blast-furnace slag by a ceramic-sintering process. Ceram Int 35:3181–3184

Characteristics of WISCO Steelmaking Slags

Bowen Li, Mingsheng He and Canhua Li

Abstract Steelmaking slag is a by-product in considerable volume and a valuable material for various applications. In general, steelmaking slag is an alkaline compound of CaO, Fe_2O_3, and SiO_2. However, its characteristics varies depending on the feedstocks, steelmaking process and cooling method of the slag. To utilize this by-product effectively, this study investigated the characteristics of steelmaking slags taken from Wuhan Iron & Steel Co. Ltd. The results showed that the slags mainly consist of the oxides of calcium, iron, and silicon, with low contents of magnesia, alumina, and manganese oxide with a feature of high alkalinity and lime saturation factor. The major mineral phases include belite, calcium ferrite, calcium hydroxide, wustite, quartz, and small amount of elite. Thermogravimetric analysis indicated the weight loss from ambient temperature to 800 °C is 8% in total. Melting test showed the glass transition temperature is between 1300 and 1350 °C, flow temperature is about 1400 °C. The slag samples investigated in this study can be considered as a typical glass-ceramic composite.

Keywords Steelmaking slag · Glass-ceramic · Characteristics

Introduction

Steelmaking slag is a by-product from primary steelmaking processes which include Basic Oxygen Furnace (BOF) and Electric Arc Furnace (EAF) [1]. BOF slag (Converter slag) is generated during the refinery process to remove carbon, phosphorous, sulfur, and other components from the pig iron and to convert the molten pig iron into steel by blowing oxygen. EAF slag is generated when iron

B. Li (✉)
Department of Materials Science and Engineering, Michigan Technological University, 1400 Townsend Dr, Houghton, MI 49931, USA
e-mail: boli@mtu.edu

M. He · C. Li
Wuhan Iron & Steel Co. Ltd, 28 Metallurgical Av, Wuhan 430080, Hubei, China

B. Li et al. (eds.), *Characterization of Minerals, Metals, and Materials 2018*, The Minerals, Metals & Materials Series,
https://doi.org/10.1007/978-3-319-72484-3_10

scrap is melted and refined in an electric arc furnace. In general, the steelmaking slags is cooled down to ambient temperature by cooling with water spraying in a cooling yard, prior to further application process.

Steelmaking slags has a considerable volume in production as 10–13% of steel production [2, 3]. It was estimated that the global steelmaking slag produced in 2016 reached 160–240 million tons [4]. Steelmaking slag has been used as raw materials for road construction, aggregates, fertilizer, soil amendment, cementitious additive in concrete, limestone substitute for cement clinker manufacture and BOF process, sandblasting sand, and ceramics, etc. [5–10].

Steelmaking slag mainly is an alkaline compound of CaO, Fe_2O_3, and SiO_2. However, its characteristics and chemical and physical performance vary depending on the feedstocks and process of steelmaking and cooling method of the slag. Its large quantity also makes it challenging for recycling the material in various industrial applications [1, 11, 12].

To effectively utilize the by-product, this study investigated the characteristics of steelmaking slags from Wuhan Iron & Steel Co. Ltd.

Materials and Methods

The steelmaking slag used for this study was taken from the 3rd cooling yard of Wuhan Iron & Steel Co. Group Metallurgical Slag Division. The initial BOF slag was hot-poured with water spraying while it was cooled down to ambient temperature. Then the slag chunks were crushed into gravels and granules, and the metallic iron was removed with a magnetic separator, then the slag was transferred to stock yard and stored for further use. Figure 1 shows the slag stock piles next to the cooling yard.

For further investigation, the slag granules were mixed completely, and then ground into −325 mesh powder by a Raymond mill. The chemical composition of the slag powder sample was determined by titration method while carbon and sulfur content were determined by a carbon/sulfur analyzer. The particle size distribution of the slag powder samples were measured by a laser particle size analyzer (Malvern Mastersizer 2000) with aqueous dispersing medium. The mineral component of the slags was determined by X-ray diffraction (XRD, SHIMADZU XRD-7000, copper target, continuous, scanning range 10–80º, scan rate 3.0°/min.).

Fig. 1 Slag stock piles of Wuhan Iron & Steel Co. Group

Scanning electron microscopy (SEM, Quanta 400, acceleration voltage 20 kV) associated with EDS was also employed for morphological and microstructural study and microanalysis of the slags. The refractoriness of the slag was determined by Pyrometric Cone Equivalent (Segar Cone) test. The thermal melting behavior of the slag was monitored by a high temperature optical microscope (melting point tester). The thermal gravimetric analysis (TGA) was implemented with a Thermogravimetric Analyzer.

Characteristics of BOF Slag

Chemical Composition

Table 1 shows the chemical composition of the slag samples. It indicates that the slag contains high content of calcium oxide as 42.36–44.20%, but low content of silica, alumina and magnesia. Carbon and sulfur content are lower than the detection limits.

Alkinity coefficient (AE) and Lime saturation factor (LSF) have been widely used to quantitatively assess raw materials for formulations of porcelains and cement clinkers. They can be determined by following equations [13].

$$AE = \left(\frac{C}{56.1} + \frac{M}{40.3}\right) / \left(\frac{S}{60.1} + \frac{A}{101.9}\right) \tag{1}$$

and

$$LSF = \frac{C}{2.8S + 1.2A + 0.65F} X100\% \tag{2}$$

here, C, M, S, A, and F represent the mass percentages of CaO, MgO, SiO_2, Al_2O_3, and Fe_2O_3 in the materials, respectively.

By calculation, the AE for sample 1 and 2 are 5.20 and 4.99, and LSF for sample 1 and 2 are 103.23 and 107.85%, respectively. This indicated the slag samples are highly alkaline and calcium oxide is sufficient to form alite with free CaO if it is used for producing cement clinker.

According to statistic results of chemical analysis of the BOF slags from the plant in 2013 and 2009, the concentrations of the major chemicals were fluctuant but the average content were not changed significantly in the past six years (Fig. 2; Table 2).

Table 2 shows the fluctuating ranges of the major oxides of the steel slags. The data were obtained from the analyses of 900 inline samples for 2013, and 420 for 2009, respectively. Generally, CaO content varied mainly between 42.25 and 49.26%, while its maximum content reached 63.39% and minimum content was

Table 1 Chemical compositions of the slag powder samples (wt%)

Sample	SiO_2	Al_2O_3	CaO	MgO	TFe_2O_3	MnO	TiO_2	P_2O_5	K_2O	Na_2O	C	S	LOI
1	10.86	1.35	44.20	8.80	16.60	2.04	0.58	1.29	ND	ND	ND	ND	8.01
2	10.93	1.38	42.36	8.83	16.51	2.04	0.57	1.27	ND	ND	ND	ND	8.64

ND-not detectable

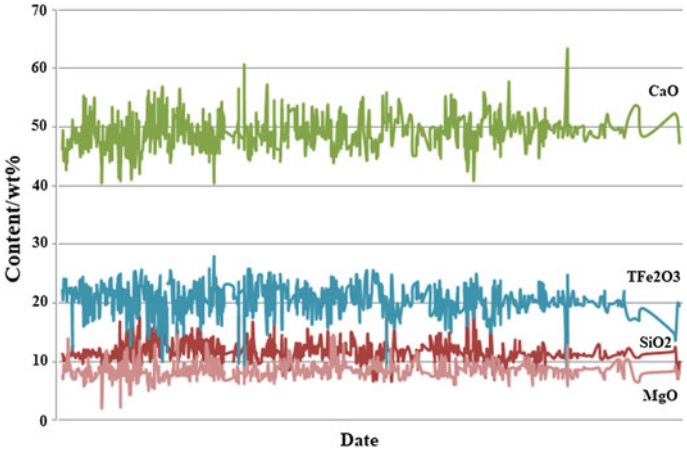

Fig. 2 Fluctuation of major compositions of steel slag in 2013

Table 2 Statistics of chemical compositions of hot-poured slags in 2013 and 2009(wt%)

	Oxide	SiO_2	CaO	MnO	TFe_2O_3	P_2O_5	Al_2O_3	MgO
2013	Maximum	32.77	63.39	9.37	29.2	3.43	19.93	14.53
	Minimum	6.68	10.48	1.14	3.84	0.01	0.37	2.03
	Average	12.06	49.26	2.29	20.13	1.86	0.77	8.37
2009	Maximum	20.19	54.71	5.37	26.92	2.15	34.62	9.65
	Minimum	3.97	20.73	0.86	11.73	0.33	0.47	5.88
	Average	13.73	42.25	1.86	18.16	1.38	1.787	7.51

dropped to 20.73%. The fluctuating ranges of other major contents were: SiO_2 12–14%, TFe_2O_3 17–23%, and MgO 7–9%.

The calculated AE and LSF based on the average contents of 2013 and 2009 analyses are 5.19 and 103.10% for 2013, and 3.82 and 80.64% for 2009, respectively. The slags produced in 2009 have lower alkalinity.

Thermal gravimetric analysis was carried out while elevating temperature from room temperature through 1100 °C (Fig. 3). The average temperature increment was 5.6 °C/min. The results showed that when increasing the heat temperature from room temperature to 800 °C, the total loss of the slag reached 8%. Continuously increased the temperature from 800 to 1100 °C, the slag had no more mass loss. These results indicated that the slag contains 6.5% of volatized contents such as carbon, sulfur, hydroxides of magnesium and calcium, etc., except 1.34% of free water.

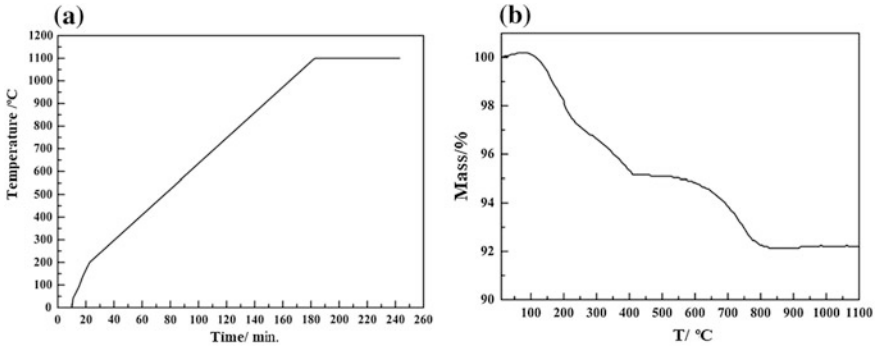

Fig. 3 Thermal gravimetric analysis of slag samples, **a** temperature curve; **b** thermal gravimetric curve

Particle Size and Morphology of the Slag

The particle size distribution of the BOF slag sample is in volumetric percentage and it presents a bimodal feature with one peak at 20–50 mm and the other one at 10 mm[5]. The median size of the powder is about 30 mm, while the maximum particle size is about 100 mm.

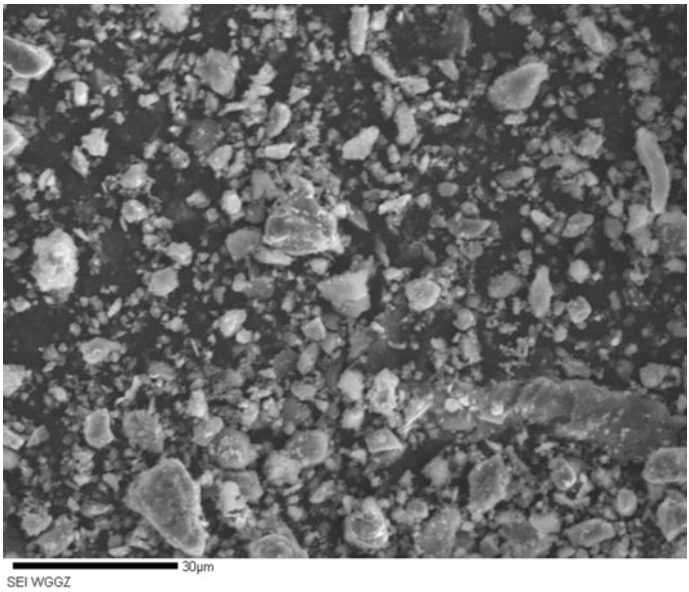

Fig. 4 SEM image of slag powder

SEM imaging showed that the slag particles are in irregular shapes with sharp edges and tips (Fig. 4). A few of micro-pores can be seen on the cross sections. The particle feature is corresponded to the results from laser analyzer.

Mineral Components

The major mineral components in the slag powder is calcium ferrite ($2CaO{\cdot}Fe_2O_3$), calcium hydroxide ($Ca(OH)_2$), wustite (FeO), belite ($2CaO{\cdot}SiO_2$), quartz (SiO_2), while containing less alite ($3CaO{\cdot}SiO_2$), which has been described in an previous publication [5]. The existing of calcium hydroxide indicated that free calcium oxide was formed during the cooling process of slag. This characteristics is in corresponding to the chemical composition of high calcium oxide. It is also indicated that this slag is not appropriate to be directly utilized as an additive of cement or concrete, but would be usable to other sintered materials such as porcelain.

Thermal Properties

The tested refractoriness of the slag powder is 1320 °C by Segar cone method.

The melting behavior of the slag powder samples was measured by monitoring the dimensional change of a cylinder sample under a high temperature melting point microscope. The slag powder sample was mixed with distilled water to form a $\phi 2 \times 2$ mm cylinder, then placed onto a sample stage made of alumina, then put in a tubular furnace and to be heated to desired temperature (temperature control at ±0.3 °C). By heating the sample in the furnace, the slag sample showed a soften temperature at 1327 °C, semi-spherical temperature at 1368 ºC, and flow temperature at 1399 °C. Figure 5 shows the shape change of the cylinder sample along with raising temperature. The softening temperature measured is same to the refractoriness temperature measured by Segar Cone method. Figure 6 shows the molten slag sample after solidification.

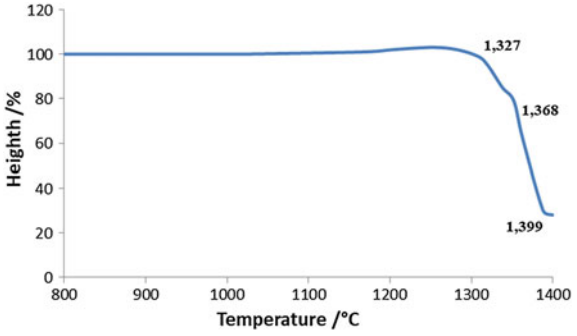

Fig. 5 Melting curve of slag powder

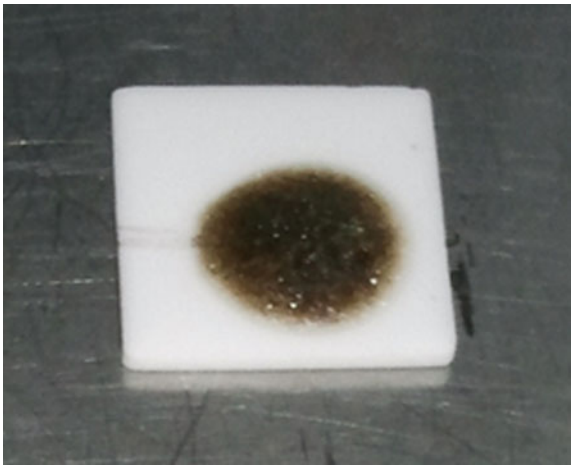

Fig. 6 Melted slag sample

Conclusions

The characteristics of steelmaking slags from Wuhan Iron & Steel Co. Ltd. was investigated. The results showed that the slags mainly consist of the oxides of calcium, iron, and silicon, with low contents of magnesia, alumina, and manganese oxide, with a feature of high alkalinity and lime saturation factor. The major mineral phases include belite, calcium ferrite, calcium hydroxide, wustite, quartz, while containing less alite. Thermogravimetry analysis indicated the weight loss from ambient temperature to 800 °C is 8% in total. Melting test showed the glass transition temperature is between 1300 and 1350 °C, flow temperature is about 1400 °C. The slags are a typical glass-ceramic composite.

References

1. Horii K (2013) Processing and reusing technologies for steelmaking slag. Nippon SteelTech Rep 104:123–129
2. Hao B, Pu L, Xian BA, Li HZ, Qi T, Shu LZ (2010) Analysis on the microstructure characteristics of steel-slag based ceramics. Adv Mater Res 150–151:133–138
3. Siddiqui AR (2014) Iron and steel slag: an alternative source of raw materials for porcelain ceramics. Global NEST J 16:587–596
4. U.S. Geological Survey (2017) Iron and steel slag. Mineral commodity summaries, pp 88–89
5. Li B, He M, Hwang JH, Gan W (2017) Characteristics of anorthite-pyroxene ceramics made from hot-poured steelmaking slag. JOM 69(2):173–177
6. Kimio ITO (2015) Steelmaking slag for fertilizer usage. Nippon Steel Sumitomo Metal Tech Rep 109:130–136
7. Gutierrez J, Hong CO, Lee BH, Kim PJ (2010) Effect of steel-making slag as a soil amendment on arsenic uptake by radish (*Raphanus sativa L.*) in an upland soil. Biol Fertil Soils 46(6):617–623

8. Faleschini F, Brunelli K, Zanini MA, Dabalà M, Pellegrino C (2016) Electric Arc Furnace Slag as Coarse Recycled Aggregate for Concrete Production. J Sustain Metall 2(1):44–50
9. Zhao LH (2015) Synthesis of steel slag ceramics: chemical composition and crystalline phases of raw materials. Int J Miner Metall Mater 3:325–333
10. Murphy JM, Meadowcroft TR, Barr PV (1997) Enhancement of the cementitious properties of steelmaking slag. Can Metall Q 36(5):315–331
11. Tiwari MK, Bajpai S, Dewangan UK (2016) Steel slag utilization—overview in Indian perspective. Int J Adv Res 4(8):2232–2246
12. Koranne SS, Valunjkar SS (2016) Utilisation of steel slag in roads of Marathwada Region. Int Journal of Eng Res 5(1):161–163
13. Sorrentino F (2008) Lime saturation factor: new insight. Cem Lime Concr 2:82–88

Effects of Civil Construction Waste on Properties of Lining Mortars

A. R. G. Azevedo, J. Alexandre, G. C. Xavier, B. C. Mendes, S. N. Monteiro and N. C. Aguiar

Abstract Brazilian civil construction generates a huge amount of waste in different stages of construction, mainly due to the work methodology used in construction sites. The objective of this work is to study the inclusion of the residual of the civil construction in the sand mass in 0, 10 and 20%, with mortars used to cover masonry. For this study, the beneficiation of the material in crusher was obtained so that it obtained granulometry similar to sand and the most recurrent technological tests in mortars for this purpose, as the mechanical resistance (compression and flexion), water absorption and determination of the coefficient of Capillarity beyond the index of consistency, according to Brazilian norms, that define parameters of execution the technological tests. The results showed that the mortars after the incorporation presented value within the norm except the consistency and capillarity to the 20% that presented problems of fluidity and durability, hindering its use.

Keywords Civil construction waste · Sustainable · Mortar

A. R. G. Azevedo (✉) · J. Alexandre · G. C. Xavier · N. C. Aguiar
LECIV—Civil Engineering Laboratory; Av. Alberto Lamego, 2000,
UENF—State University of the Northern Rio de Janeiro,
Campos dos Goytacazes, Rio de Janeiro 28013-602, Brazil
e-mail: afonso.garcez91@gmail.com

A. R. G. Azevedo
IFF—Federal Institute Fluminese, DIRINF—Directorate of Infrastructure
Rectory; St. Cel. Valter Kramer, 357—Parque Vera Cruz,
Campos dos Goytacazes, Rio de Janeiro 28080-565, Brazil

B. C. Mendes
Federal University of Viçosa, UFV. Av. Peter Henry Rolfs,
s/n—Campus Universty, Viçosa, Minas Gerais 36570-000, Brazil

S. N. Monteiro
Department of Materials Science, IME—Military Institute of Engineering,
Square General Tibúrcio, 80, Rio de Janeiro 22290-270, Brazil

B. Li et al. (eds.), *Characterization of Minerals, Metals, and Materials 2018*, The Minerals, Metals & Materials Series,
https://doi.org/10.1007/978-3-319-72484-3_11

Introduction

Civil construction in Brazil has experienced a significant advance in the last decades, driven by the growth of urban infrastructure works and major events that occurred without parents, such as World Cup and Olympic Games that generated large construction sites throughout the country. In addition to major housing construction projects, it is also making great strides due to government programs aimed at reducing the country's housing deficit. According to data from the Brazilian Institute of Geography and Statistics (IBGE), a civil construction presented until the year 2014 to constant and solid growth resulting from the actions of growth [1]. Between the year 2015, the sector lived with large losses from misguided public policies and a series of layoffs from Brazil, which is what is the number of works.

Even though there is a reduction in the number of works in quantity and quantity, and even more important, and it is an important tool for generating employment and income, it is estimated that there are no more than 3 million employees in Brazil, returning to year numbers of 2009 there is thus a significant participation in the economically active population [2].

The civil construction sector, besides having an important economic meaning, still plays an important role in the sustainability of a country due to the large generation of industrial waste, in the production of its inputs or even in the construction stages. It is estimated that about 30% of the material of a work is wasted at different stages of which in addition to occasions in costs increases means a major environmental problem [3].

The whole world on the problem of construction waste, and a production of this material is quite variable as observed in Table 1.

In Brazil, a National Solid Waste Policy was established by law, which defined rules for the packaging, transportation and final destination of construction waste, called RCC, which should be disposed of in an appropriate place as landfills. This disposal in landfills generates excessive costs as companies that end up passing them on to end users [4].

Therefore, the main objective of this work is to evaluate the feasibility of using construction waste in mortars for the manufacture of building linings making replacement in the sand. Three levels of substitution (0, 10 and 20%) were defined in the sand mass by the RCC (construction waste), whereas mortars were submitted to tests for consistency index, mechanical resistance, water absorption and capillary coefficient determination.

Table 1 Per capita generation of construction waste in several countries [2]

Country	Waste generation (Kg $pop^{-1}/year^{-1}$)
Sweden	136–680
Holland	820–1300
U.S.A.	463–584
Italy	600–690
Japan	785
Brazil	400–760

Materials and Method

The waste was collected at three different construction sites located in the city of Campos dos Goytacazes, RJ, Brazil, where care was taken to remove material resulting from the masonry execution process (there is a great variety of materials that could harm the usability of the materials). This material is based on remnants of ceramic brick pieces and mortars left over from the process of laying the blocks.

After the material was collected, it was taken to the Construction Materials Laboratory of the State University of Norte Fluminense where it was identified and processed by grinding until its homogenization and visual similarity to sand. After the beneficiation the three materials type they were mixed in proportional way to have representativeness in the mixture. This method of beneficiation and mixing is recommended for the use of civil construction waste (RCC).

The mortar that will be produced is the cement and lime base that will be used the commercial materials used in the works of the region, which consists of Type III Portland cement (CPIII) and hydrated lime type II (CHII). The sand is natural and comes from the bed of the Paraiba do Sul river.

After the process of selection and separation of the materials, the test was carried out to determine the amount of water required in each of the evaluated traces, for which the trait was adopted with proportions of 1:1:6 (cement, lime and sand respectively) where The proportion of RCC replacement occurred in the sand mass at different levels (0, 10 and 20%). The test of determination of the consistency index is standardized in Brazil [5] and fixes parameters with the spreading of the mass in a specific mass to obtain the amount of water. The water/binder ratio remained fixed at 0.6.

With the amount of water, the specimens were molded, which according to Brazilian standards must be prismatic ($4 \times 4 \times 16$ cm) and a cure time must be observed for the mechanical strength test. Is necessary for the hydration reactions of the cement to occur and the mortar to gain strength in the setting process. Three rupture ages, 7, 14 and 28 days were adopted due to the stability of cementitious composites after 28 days [6]. The measured resistance was three-point flexion and simple compression in a press with computerized actuators and load cell compatible with the speed required by the Brazilian standard [7].

The essential water absorption determination test evaluates the level of internal pores that effect other properties as incorporated air content besides directly affecting the mechanical strength of due to the stress state of the hardened mass. This test is standardized as well as the determination of the capillary coefficient which, other than porosity, measures the internal communication of the pores which causes water to penetrate by soaking the mortar which will directly affect durability properties, very important for the desired application for liners under construction civil [8].

Results and Discussion

With the test of determination of the consistency index, where the amount of water used in each trace is found, as seen in Fig. 1.

As shown in Fig. 1, the amount of water required to maintain the consistency of the trace increases in comparison to the reference value (without additions). This increase is due to the difficulty of filling the pores and excessive moisture variation in the residue due to its diversity of composition, thus requiring more water to maintain its workability and enable its use in civil construction. Figure 2 shows the results of the three-point flexural strength and Fig. 3 shows the mechanical strength of single compression, at all three cure ages (time after molding of the specimens) [9].

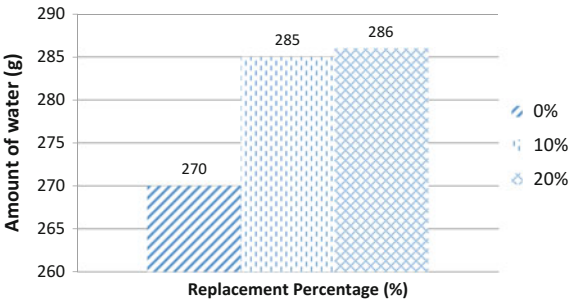

Fig. 1 Quantity of water (g) as a function of the substitution content of sand building waste

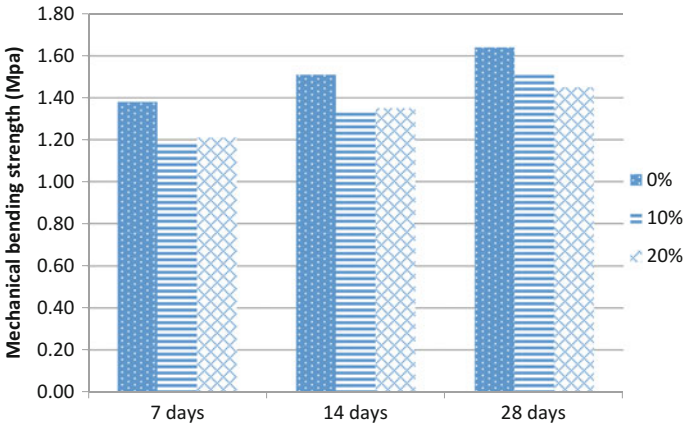

Fig. 2 Bending resistance at three points due to different curing times

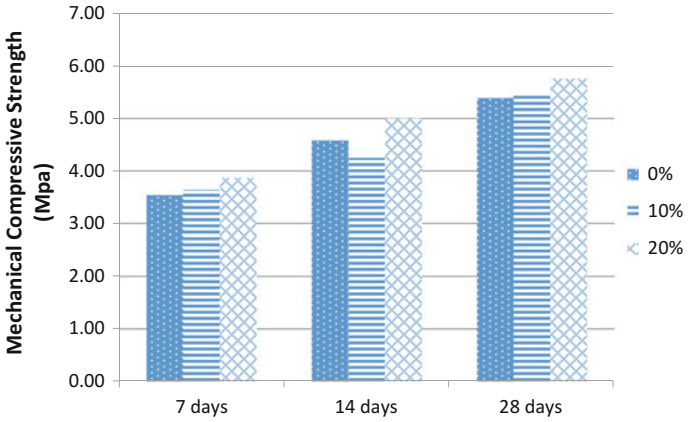

Fig. 3 Comparison of compression resistance due to different curing times

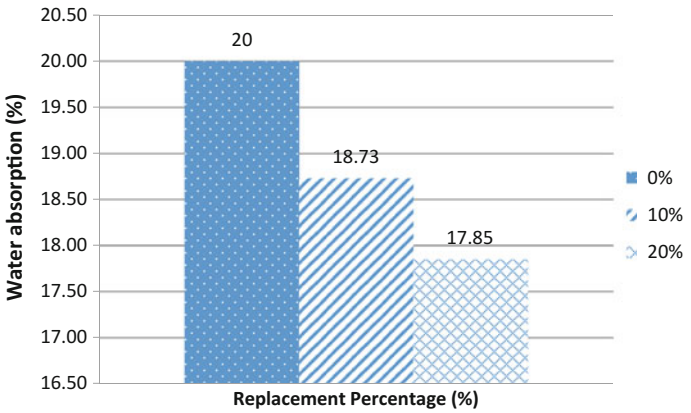

Fig. 4 Water absorption in mortars at different levels of incorporation

According to Fig. 2 the flexural strength of mortars with additions is lower than the reference material, this is due to the internal consolidation state and specific characteristics of cement matrixes. The results of simple compression strength, shown in Fig. 3, show an increase in this resistance due to its curing time, due to the hydration reactions of the cement that gains strength in the hardened state and the consolidation of the mortar. In both tests it is verified that mortars meet the Brazilian normative requirements for the use of mortars to coat walls and ceilings in civil construction. Figure 4 shows the water absorption of mortars and their different traces [10].

According to Fig. 4 it is observed that the water absorption decreases as a function of the level of incorporation, this reduction is due to the fact that the

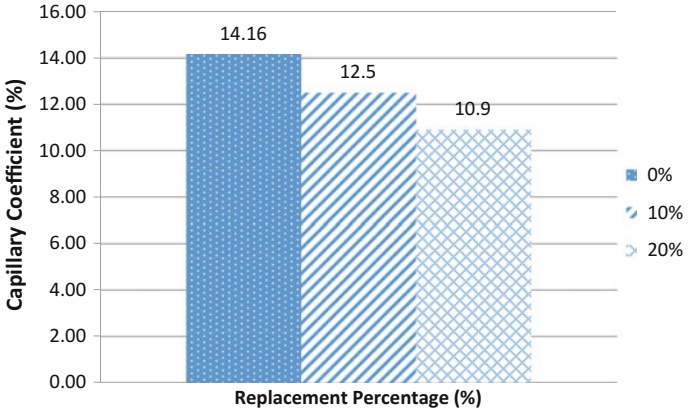

Fig. 5 Determination of the capillary coefficient at different levels of incorporation

existing pores were filled by the reaction of the different materials that constitute the residues of the civil construction with the reducing its absorption capacity [11]. This reduction can contribute to the durability of the composites and should be analyzed in other complementary tests, such as the determination of the capillary coefficient, shown in Fig. 5.

The capillary coefficient (Fig. 5), which is the saturated mass difference after 90 and 10 min of exposure, showed a reduction as a function of the level of the material incorporated (residue), which means that the pores, which also decreased in quantity, have no internal communication, thus reducing Its permeability of the material in the hardened state. This is extremely beneficial to mortars that are exposed, such as in facades of buildings [12].

Conclusions

With the results found it can be concluded that:

- The incorporation of construction waste into mortars to coat walls and ceilings brings economic and technological benefits to mortar, given the savings generated by avoiding disposal of this material.
- Granulometry tests in the bibliography of this material indicate that its replacement, in whole or in part, by the mortar sand may be feasible.
- The technological results in the fresh state, such as the determination of the consistency index, show that up to 10% incorporation are satisfactory. The incorporation of 20% presented fluidity problems that directly affect the workability, which is due to the interaction of the residue within the cement matrix.

- Technological results in the hardened state, such as mechanical strength, show that the mortar presents values close to those indicated in the Brazilian literature for use in buildings, both internal and external.
- Parameters such as water absorption and determination of capillary coefficient are extremely important for the durability of the composite and with the results found they are sufficient results to indicate that the degradation over the shelf life of the material is adequate, but values of 20% are in a transition zone of materials that may be hazardous due to the location of exposure.
- Mortars with traces of incorporation of 10% has potential for use as sealing liner boards in buildings because present mechanical properties and durability compatible, still acoustic tests and external permeability to final product.

Acknowledgements The authors thank the Brazilian agencies: CNPq, CAPES and FAPERJ for the support provided to this investigation.

References

1. James LH, Asce PEM, Nazli Y, Shawna AVS, Wilson WW (2010) Compaction characteristics of municipal solid waste. J Geotech Geoenviron Eng 136(8):1095–1110
2. Staley BF, Barlaz MA (2009) Composition of municipal solid waste in the U.S. and implications for carbon sequestration and methane yield. J Environ Eng 135(10):901–909
3. Flavio LM, Kai LB, Vanderley MJ (2011) The influence of moisture on the deformability of cement–polymer adhesive mortar. Constr Build Mater 150(4):2948–2954
4. Guerrini A, Carvalho P, Romano G, Marques RC, Leardini C (2017) Assessing efficiency drivers in municipal solid waste collection services through a non-parametric method. J Clean Prod 123(10):431–441
5. Brazilian Association of Technical Norms (2016) NBR 13276—Mortars applied on walls and ceiling—determination of the consistence index. (In Portuguese)
6. Povoas YVJVM, Cincotto MA (1997) Standardization Mortars tights. In: Brazilian symposium on technology from Mortars, Salvador, p 501–512. (In Portuguese)
7. Brazilian Association of Technical Norms (1997) NBR 7215—Portland Cement—determination of compressive strength. Rio de Janeiro. (In Portuguese)
8. Brazilian Association of Technical Norms (2009) NBR 7211—aggregates for concrete—specification. Rio de Janeiro. (In Portuguese)
9. Vladimir GH, Graça V, Paulo BL (2011) Influence of aggregates grading and water/cement ratio in workability and hardened properties of mortars. Constr Build Mater 156(3): 2980–2987
10. Jun C, Liang Z (2015) Experimental study of effects of water—cement ratio and curing time on nonlinear resonance of concrete. Mater Struct 169(12):423–433
11. Bravo M, Brito J, Pontes J, Evangelista L (2015) Mechanical performance of concrete made with aggregates from construction and demolition waste recycling plants. J Clean Prod 99: 59–74
12. Azevedo ARG, Alexandre J, Zanelato EB, Marvila MT (2017) Influence of incorporation of glass waste on the rheological properties of adhesive mortar. Constr Build Mater 148(8): 359–368

Pilot Trial of Direct Modification of Molten Blast Furnace Slag and Production of High Acidity Coefficient Slag Wool Fibers

Jun Li, Lingling Zhang, Guizhou Zhao and Daqiang Cang

Abstract Pilot trial of direct modification of molten blast furnace slag and production of high acidity coefficient slag wool fibers were investigated nearby a blast furnace. Molten blast furnace slag discharged from blast furnace and then directly flow into specialized modification furnace and quartz was simultaneously added into the molten slag as modification agent. The modified molten slag was electric heated to 1500–1550 °C and then the melt was produced into slag wool fibers through high-speed centrifugation method. Melt with acidity coefficient of 1.2, 1.4, 1.6 and 1.8 were investigated and fibers with corresponding acidity coefficient were produced. Slag wool fibers with shot content of 5.5, 5.8, 6.2, 6.8% and average diameter of 4.5, 4.9, 5.6, 6.4 μm for four samples were successfully produced, respectively. Total energy consumption and production costs decreased by 50–70% compared to traditional cupola furnace method. This method provides an energy-saving and emission-reduction technology for the direct utilization of molten blast furnace slag.

Keywords Blast furnace slag · Modification · Slag wool fibers
High acidity coefficient

J. Li · G. Zhao · D. Cang
School of Metallurgy and Ecological Engineering, University of Science and Technology Beijing, Beijing 100083, China
e-mail: zhaowow2008@outlook.com

J. Li · G. Zhao · D. Cang
State Key Laboratory of Advanced Metallurgy, University of Science and Technology Beijing, Beijing 100083, China

L. Zhang (✉)
School of Energy and Environmental Engineering, University of Science and Technology Beijing, Beijing 100083, China

B. Li et al. (eds.), *Characterization of Minerals, Metals, and Materials 2018*, The Minerals, Metals & Materials Series,
https://doi.org/10.1007/978-3-319-72484-3_12

Introduction

Iron and steel industry is one of the most energy-intensive industries and accounts for approximately 4–5% of total world energy consumption [1]. Blast furnace slag (BFS) is produced in iron making process and 300–450 kg BFS were discharged for per ton of liquid pig iron. Normally, BFS is discharged at 1450–1550 °C and the total energy carried by molten BFS is about 1770 MJ/t [2, 3]. One effective solution for energy saving and emission reduction is to recover waste heat from molten BFS in iron making and process.

BFS are mainly processed with water granulation to produce glassy granules and then intensively used in cement production as a substitute [4]. However, water granulation process wastes the high-grade waste heat of molten BFS and consumes massive water and could also cause serious air pollution. Hence, an alternative method for processing molten BFS should be proposed to replace water granulation process.

BFS is rich in CaO, SiO_2, Al_2O_3, MgO and its chemical composition is similar to that of mineral wool. As a subgroup of mineral wool using mainly metallurgical slag as raw materials, slag wool is wide applied in civil engineering and industry due to its excellent thermo-acoustic insulation and fire resistance properties [5]. Traditionally, the melting of the raw materials is carried out in copula furnace and coke is the main energy source for melting raw materials [6, 7]. Approximately 350–800 kg/t standard coal is consumed and environmental pollution is also caused by the high temperature flue gas and dust [8–10].

The combination of heat recovery and utilization of molten BFS with the production of slag wool fibers were investigated. Pilot trial of direct modification of molten blast furnace slag and preparation of high acidity coefficient slag wool fibers were carried out nearby a blast furnace. The modification process, production of slag wool fibers and the properties of the fibers were investigated.

Materials and Methods

Materials

Raw materials used in this pilot trial were molten BFS and quartz. Molten BFS directly flowed into the modification furnace though the slag runner and a flow diversion baffle was used to control the BFS flow. The main chemical composition of BFS and quartz as detected by X-ray fluorescence (XRF-1800, SHIMADZU, Japan) were shown in Table 1. It can be seen that BFS mainly consists of CaO, SiO_2, MgO and Al_2O_3. Quartz was homogeneously added into the molten BFS as modification agent to adjust the acidity coefficient M_k [mass ratio of $\omega(SiO_2 + Al_2O_3)/\omega(CaO + MgO)$].

Table 1 Main chemical composition of BFS and quartz (mass ratio, %)

	SiO_2	Al_2O_3	CaO	MgO	Fe_2O_3	TiO_2	K_2O
BFS	30.86	13.85	34.96	9.68	0.45	0.66	0.35
Quartz	94.77	2.26	0.52	0.33	0.65	–	–

Pilot Trial

The production of mineral wool products involves melting of raw materials and subsequent spinning of the melt into fibers. Traditionally, raw materials were melted by coke combustion in cupola furnace and the thermal efficiency is only approximately 50% [8]. In the pilot trial, molten BFS directly flowed into the modification furnace and quartz was simultaneously added into the molten BFS as modification agent. The melt was then electric heated to 1500–1550 °C with graphite electrode. The melt with proper temperature was then produced into slag wool fibers through high-speed centrifugation method.

Results and Discussion

Modification of BFS

The acidity coefficient M_k of BFS used in this study was 1.0 and M_k of slag wool is usually kept at approximately 1.2. Therefore, the modification of BFS with high silica/alumina materials to raise the acidity coefficient is essential for the production of slag wool. Chinese national standard "Rock wool thermal insulation products for building applications (GB/T 19,686-2015)" regulates that an acidity coefficient $M_k \geq 1.6$ is required for rock wool products. In mineral wool industries, high acidity coefficient normally implies better quality of the wool products. Hence, high acidity coefficient slag wool should be investigated to compete with rock wool. Samples modified with different proportion of quartz and M_k of 1.2, 1.4, 1.6 and 1.8 were listed in Table 2.

Table 2 Samples modified with different proportion of quartz

Sample	M_k	Proportion of quartz (mass ratio, %)	Chemical composition (mass ratio, %)			
			SiO_2	Al_2O_3	CaO	MgO
1	1.20	16.0	41.56	11.21	38.99	4.86
2	1.40	23.0	46.19	10.37	35.75	4.46
3	1.60	28.7	49.95	9.69	33.10	4.13
4	1.80	33.7	53.25	9.09	30.79	3.84

The mass ratio of SiO_2 in quartz is 94.77% and that makes quartz a widely applied modification for the adjusting of M_k of slag wool. It can be seen that the addition of quartz increases with the increasing of M_k and an approximate linear relationship indicated that the addition of quartz significantly affected the M_k of the samples. SiO_2 increases while Al_2O_3, CaO and MgO decreases with the increasing of quartz due to the high SiO_2 content of quartz.

Viscosity of the melt of sample 1–4 were tested by RTW-08 and the results is depicted in Fig. 1. It can be seen that the viscosity of the samples increased with the increasing of M_k. Besides, high temperature decreases the viscosity of the samples. Normally, viscosity of the silicate melt is significant affected by the connection degree of glass structure network. Glass viscosity is directly affected by the function of oxides presented in the chemical composition (glass former SiO_2, glass modifier CaO and MgO, glass intermediary Al_2O_3). Al_2O_3 can become glass former by forming tetrahedral coordination similar to SiO_2 in silicate glass system. Glass structure network formed by Si-O tetrahedrons is crucial for the mechanical properties and chemical stability of the slag wool. High SiO_2 content enhances the connection degree of glass structure network, which is beneficial for the properties and chemical stability of slag wool. However, increasing quartz addition has an adverse influence on the melting and homogenization of the melt. The proper viscosity of the melt for slag wool production is 1–3 Pa s. Hence, melt melted by sample 1–3 with temperature exceeding 1400 °C is the ideal melt for the production of slag wool. An appropriate range was determined and labeled in Fig. 1 with dot lines considering the viscosity and temperature variations. It can be seen that slag wool fibers can be produced by all samples with quartz proportion varies from 16.0 to 33.7%. The optimal temperature range of the melt should be 1350–1450 °C for sample 1, 1400–1500 °C for sample 2 and 3, 1450–1550 °C for sample 4, respectively. For the pilot trial, 1450 °C was selected as the forming temperature of the melt spinning into fibers.

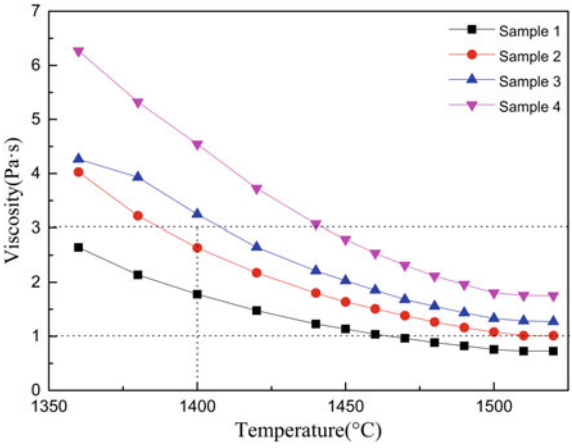

Fig. 1 Viscosity of the melt of samples

Preparation of Slag Wool Fibers

In the pilot trial, BFS were modified by different proportion of quartz. Molten BFS flowed into the modification furnace through slag runner after discharged from blast furnace. The molten BFS flow was controlled by a specialized diversion baffle. Modification agent quartz was simultaneously and homogeneously added into the modification furnace with the preset proportion. The mixture of the molten BFS and quartz was then electric heated to 1500–1550 °C with graphite electrode and then produced into slag wool fibers through high-speed centrifugation method. In traditional cupola furnace method, the coal consumption is 350–800 kg/t slag wool and waste gases containing SO_2 and NO_x were also generated. In the pilot trial, the sensible heat in molten BFS was applied as the main energy source and electrical energy was used as supplementary. Total energy consumption and production costs decreased by 50–70% compared with traditional cupola furnace method. This method provides an energy-saving and emission-reduction technology for the direct utilization of molten BFS.

The melt falls onto the rotating discs of the centrifuge machine under gravity. Fibers are formed from the molten film on the discs. The formation of the fibers depends on the comprehensive effect of the inertial, viscous and surface tension forces of the melt film.

Normally, there is an approximate 50–100 °C temperature drop from the melt outlet to the rotating discs of the centrifuge machine. The ideal tapping temperature are 1450–1550 °C for sample 1–3 and 1500–1600 °C for sample 4, respectively. The rotating speed for disc 1–4 are 2500–3500, 3000–4000, 3500–5000, 3500–5000 r/min, respectively. The melt was high-centrifuged into slag wool fibers and then the fibers were blown into the collection chamber to produce slag wool products.

Characterization of Fibers

The average diameter and shot content of the produced slag wools were tested and shown in Table 3.

A fraction of the melt which has not been transformed into fibers remains in the form of solidified shots, which causes the incomplete fiberization and the deterioration of the properties of the slag wool products. The quality of the slag wool

Table 3 Average diameter and shot content of slag wools

	1	2	3	4	National standard
Average diameter (μm)	4.5	4.9	5.6	6.4	≤ 6.0
Shot content (%)	5.5	5.8	6.2	6.8	≤ 7.0

products is highly related to the structure of the fibers and the shot content in the slag wool [11].

It can be seen that the average diameter and shot content increase from sample 1 to sample 4 when the M_k of the melt increases. This is due to the increasing of viscosity of the melt from sample 1 to sample 4. The increasing of average diameter and shot content deteriorate the mechanical properties of the slag wool products. Low viscosity is beneficial for the melting and homogenization of the mixture of BFS and quartz. The viscosity decreasing means the increasing of fluidity of the melt and fine fibers with small average diameter and low shot content can be produced. The average diameter 6.4 μm of sample 4 exceeded Chinese national standard.

Phase identification of the slag wool fibers was conducted using X-ray diffraction (XRD, M21X apparatus, Cu Kα radiation, MAC Science Co. Ltd., Japan). The XRD spectra of the produced fibers is shown in Fig. 2. The amorphous curve without crystalline peak illustrates the vitreous structure of the fibers. The fibers were fast cooled during the centrifuge process and thus the amorphous phase can be obtained. The amorphous structure contributes to the excellent acoustic and thermal insulation properties of the slag wool products [12].

Dark white translucent and highly interweaved fibers were produced for sample 1–4 in the pilot trial. Microstructure of the fibers were observed by scanning electron microscope (SEM, ZeissEVO-18, Germany) and SEM images of slag wool fibers of sample 3 were depicted in Fig. 3. Figure 3a (SEM image of 500x) shows porous structure formed by intensively interweaved fibers, which explains the superb thermo-acoustic insulation properties of the slag wool products. It can be seen that small black shots attached to or entrapped by the slender fibers (marked with a dotted circle in Fig. 3a). Figure 3b (SEM image of 2000x) shows smooth surface without crackles and holes of the fibers and thus ensures the physical and mechanical properties of the slag wool products.

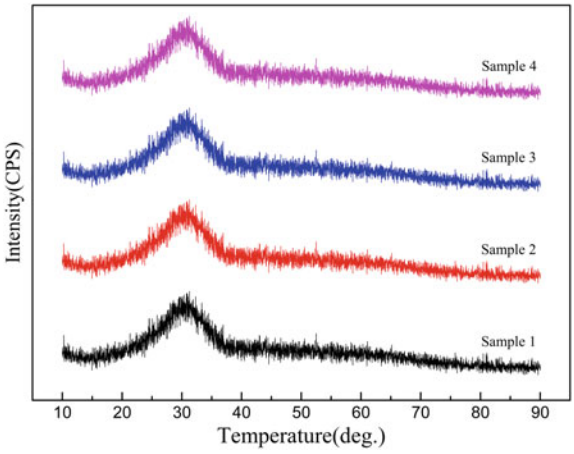

Fig. 2 XRD spectra of slag wool fibers of samples

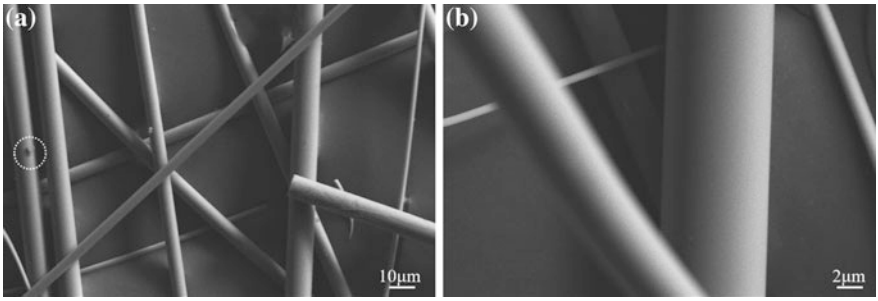

Fig. 3 SEM images of slag wool fibers of sample 3

Conclusions

Slag wool fibers with acidity coefficient 1.2, 1.4, 1.6 and 1.8 were produced with molten BFS after modification with quartz. Quartz proportion increases with the increasing of M_k from sample 1 to 4 and the approximate linear relationship indicated that quartz addition significantly affected the M_k of the samples. Slag wool fibers can be produced by all samples with quartz proportion varies from 16.0–33.7%. Melt at 1450 °C with the viscosity range of 1–3 Pa s was selected as the forming temperature of the melt spinning into fibers. The sensible heat in molten BFS was the main energy source and electrical energy was used as supplementary. Total energy consumption and production costs could be decreased by 50–70% compared with traditional cupola furnace method. The rotating speed for disc 1–4 are 2500–3500, 3000–4000, 3500–5000, 3500–5000 r/min, respectively and fibers with qualified average diameter and shot content were successfully produced. The amorphous structure contributes to the excellent acoustic and thermal insulation properties of the slag wool products. Porous structure formed by intensively interweaved fibers also explains the superb thermo-acoustic insulation properties of the slag wool products. This technology provides an energy-saving and emission-reduction method for the direct utilization of molten blast furnace slag.

References

1. Zhang H, Wang H, Zhu X et al (2013) A review of waste heat recovery technologies towards molten slag in steel industry. Appl Energy 112:956–966
2. Bisio G (1997) Energy recovery from molten slag and exploitation of the recovered energy. Energy 22(5):501–509
3. Barati M, Esfahani S, Utigard TA (2011) Energy recovery from high temperature slags. Energy 36(9):5440–5449
4. Xie D, Jahanshahi S (2008) Waste heat recovery from molten slags. In: Proceedings of the 4th international congress on science and technology of steelmaking, Gifu, Japan, vol 68. pp 674677

5. Zhao D, Zhang Z, Liu L et al (2015) Investigation on slag fiber characteristics: Mechanical property and anti-corrosion performance. Ceram Int 41(4):5677–5687
6. Zhao D, Zhang Z, Liu L et al (2015) A novel kinematic model for molten slag fiberization: Prediction of slag fiber properties. Metall. Mater Trans B 46(2):993–1001
7. Leth-Miller R, Jensen AD, Jensen J et al (2005) Comparative study of reactivity to CO_2 of cokes used in stone wool production. Fuel Process Technol 86(5):551–563
8. Leth-Miller R, Jensen AD, Glarborg P et al (2003) Investigation of a mineral melting cupola furnace. Part I. Experimental work. Ind Eng Chem Res 42(26):6872–6879
9. Leth-Miller R, Jensen AD, Glarborg P et al (2003) Investigation of a mineral melting cupola furnace. Part II. Mathematical modeling. Ind Eng Chem Res 42(26):6880–6892
10. Zhao D, Zhang Z, Tang X et al (2014) Preparation of slag wool by integrated waste-heat recovery and resource recycling of molten blast furnace slags: from fundamental to industrial application. Energies 7(5):3121–3135
11. Blagojevič B, Širok B, Hočevar M (2009) Cooling of the fibres in mineral wool produced by a double-disc spinning machine. Ceramics-Silikáty 53(1):25–30
12. Smedskjaer MM, Solvang M, Yue Y (2010) Crystallisation behaviour and high-temperature stability of stone wool fibres. J Eur Ceram Soc 30(6):1287–1295

Reduction Behavior of Ternary Calcium Ferrites for $CaO–Fe_2O_3–MgO$ System

Senwei Xuan, Xuewei Lv, Kai Tang, Chengyi Ding, Gang Li and Chenguang Bai

Abstract Sinter is an important iron-bearing material charged into blast furnace. Calcium ferrite (CF) is one of the most significant liquid phases in fluxed sinter. The isothermal reduction kinetics of CF and CF8M ($n(CaO):n(Fe_2O_3) = 1$, $wt\%(MgO) = 8$) with 30% CO and 70% N_2 gas mixtures at 1123, 1173, and 1223 K were investigated through thermogravimetric analysis in this study. Rate analysis illuminates that the reduction processes of CF and CF8M are mainly expressed as a typical two-stage reaction. Sharp analysis indicates that CF and CF8M reduction is expressed by the Avrami–Erofeev equation presenting a 2D shrinking layer reaction. The apparent activation energy values of CF and CF8M reduction are 46.9 and 31.8 kJ mol^{-1} individually based on model-free method.

Keywords Calcium ferrite · Magnesia · Isothermal reduction kinetics Apparent activation energy

Introduction

In iron ore sintering process, calcium ferrite is one of the most common liquid phases, which has crucial effect on coke ratio in blast furnace ironmaking process. As a raw material of blast furnace, magnesia play a significant role in reducibility and strength of furnace burden. Hence, the effect of magnesia was deeply investigated by various studies during the past decades [1–3]. Kimura et al. [4] investigated the effect of magnesia on liquid phase of $CaO–SiO_2–FeO_x$ system at 1573 K and found that the liquid area shrinks by addition of MgO. Kalenga et al. [5] reported that increasing magnesia concentration in sinter increases the amount of the spinel and glassy phases. Li et al. [6] explored the effects of magnesia behaviors on softening–melting properties of high basicity sinter and found that magnesia

S. Xuan · X. Lv (✉) · K. Tang · C. Ding · G. Li · C. Bai
College of Materials Science and Engineering, Chongqing University, Chongqing 400044, China
e-mail: lvxuewei@163.com

B. Li et al. (eds.), *Characterization of Minerals, Metals, and Materials 2018*, The Minerals, Metals & Materials Series,
https://doi.org/10.1007/978-3-319-72484-3_13

mainly exists in wustite as FeO–MgO solid solution. Zhang et al. [7] conducted laboratory pot-grate sintering tests and discovered magnesia has positive effects on sinter low temperature degradation. The reduction of samples in previous studies was chemically regarded as the solid–gas reduction of iron oxides [8–10]. The reduction route of iron oxides has been explored by many studies. However, many researchers adopted iron ore samples to investigate influence of magnesia content so that the resulted conclusions influenced by many factors were difficult to agree with each other and explanations with the model function derived by thermal kinetics are lacking. This study attempts to improve the understanding of these aspects.

Experimental

Experimental Scheme

Experimental equipment used in this study are listed in Table 1.

The isothermal TGA was conducted using Setaram analyzer (Setsys Evo TG-DTA 1750) in this study. Samples CF and CF8M (20 mg) in alumina crucible were heated to 1123, 1173, and 1223 K at 15 K/min in N_2 (>99.99%) atmosphere, respectively. Then the temperature remained unchanged with atmosphere transformed into 30% CO (>99.99%) and 70% N_2 gas mixtures. TGA data were obtained in the isothermal reduction stage.

Materials

Calcium carbonate ($\geq$99.99%) and hematite (α-Fe_2O_3, $\geq$ 99.99%) were mixed uniformly in a 1:1 mol ratio with addition of 0 and 8 wt% magnesia. The mixed samples were then pressed into cylindrical-shape samples with 10 MPa pressure. The roasting process was performed on a $MoSi_2$ furnace where the samples were first heated from room temperature to 900 °C and maintained for 1 h to decompose calcium carbonate to calcium oxide. The samples were further heated up to 1200 °C and held for 10 h. Finally, the reacted samples were ground into powder (<100 μm).

Prior to the TG measurement, the phase composition of samples were confirmed by XRD (D/max2500/PC (Cu Kα)) with a scan rate of $4°\cdot min^{-1}$. The XRD results

Table 1 Experimental equipment in this study 1

Equipment	Model	Supplier
Thermal gravimetric analyzer	TG-DSC	Setaram®
Mass flowmeter	CS200A	Hua Chuang®
Electronic balance	BSA124S	Sartorius®

were shown in Fig. 1. The reaction results of the $CaO–Fe_2O_3–MgO$ system in the roasting process can be described as follows:

$$CaO + Fe_2O_3 + MgO \rightarrow CaO \cdot Fe_2O_3 + 2CaO \cdot Fe_2O_3 + MgO \cdot Fe_2O_3 \quad (1)$$

Theoretical Basis

Reduction degree is defined as the ratio of removed oxygen mass at a fixed time t to the theoretically removed oxygen mass from iron oxide, which can be expressed as

$$\alpha = \frac{\Delta m_t}{\Delta m_0} \quad (2)$$

where α is the reduction degree, and Δm_t and Δm_0 refer to the removed oxygen mass at a fixed time t and the theoretically removed oxygen mass from iron oxide respectively. In the reduction of $CaO–Fe_2O_3–SiO_2$ system, the removed oxygen is only from phases containing iron oxides. For instance, Δm_0 accounts for 22.22 and 20.58% of the total mass for CF and CF8M, respectively.

The basic kinetics equation that describes the relationship of reduction rate and time can be shown as

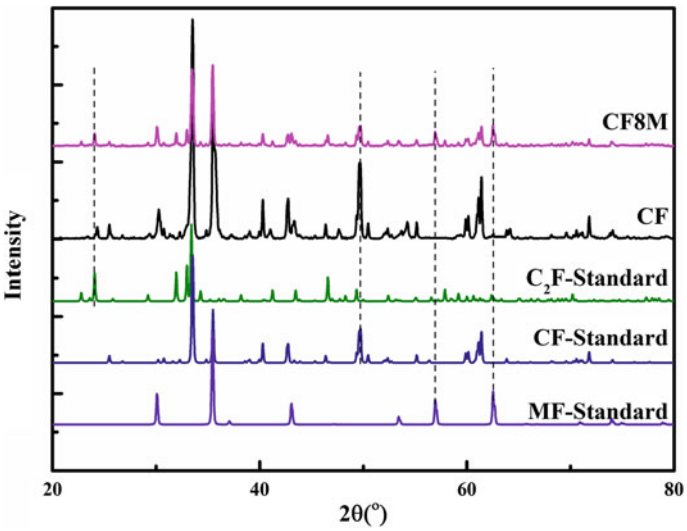

Fig. 1 XRD patterns of CF and CF8M samples

$$\frac{d\alpha}{dt} = k(T)f(\alpha) \tag{3}$$

where dα/dt is the reduction rate, and $k(T)$ and $f(\alpha)$ are the rate constant and model function of the reduction reaction. $f(\alpha)$ is influenced by the reaction mechanism. $k(T)$ is determined by the Arrhenius equation:

$$k(T) = A\exp\left(\frac{-E}{RT}\right) \tag{4}$$

where A is the pre-exponential factor, E is the apparent activation energy, and R is the gas constant [8.314 J/(mol·K)]. Equation (2) can be further expressed as

$$\frac{d\alpha}{dt} = A\ \exp\left(\frac{-E}{RT}\right)f(\alpha) \tag{5}$$

As the reduction degree α is a constant, ln $f(\alpha)$ remains unchanged. Therefore, the activation energy can be calculated as

$$E = -R\frac{d\left(\ln\frac{d\alpha}{dt}\right)}{d\left(\frac{1}{T}\right)}. \tag{6}$$

Model function $G(\alpha)$ was obtained to describe the relationship of reaction degree with time, nine normal functions [11] expressing the solid-state reaction was shown in Table 2. Function A_2 and A_3 were obtained from the nucleation process (crystallization) and can be also applied to the shrinking core reaction. As the model function can't be obtained directly, Sharp [12, 13] defined a non-dimensional parameter $y(\alpha)$ to target model function.

$$y(\alpha) = \frac{G(\alpha)}{G(0.5)} = \frac{kt}{kt_{0.5}} = \frac{t}{t_{0.5}} \tag{7}$$

where $G(0.5)$ refers to a fixed $G(\alpha)$ with $\alpha = 0.5$, and $t_{0.5}$ is the time corresponding to $\alpha = 0.5$.The curves described by the plots of $y(\alpha)$ against α are based on the normal solid reactions called standard curves. Experimental data [$\alpha_i, t_i/t_{0.5}(i = 1,2,\ldots l)$] can be easily obtained through TGA. The corresponding $G(\alpha)$ can be identified when the experimental data match one of the standard curves. As the Sharp analysis was derived when the transition of reaction rate peak approximately occurs when $\alpha = 0.5$. According to the rate change of CF and CF8A reduction, $y(\alpha)$ was set as $t/t_{0.1}$, $t/t_{0.2}$ for CF and CF8M, respectively.

Table 2 Model function $G(\alpha)$ for normal solid-state reactions

Symbol		Kinetic models	G(a)	n
Diffusion models [14, 15]	$D_1(a)$	One-dimensional diffusion	$a^2 = kt$	0.62
	$D_2(a)$	Two-dimensional diffusion, cylindrical symmetry	$(1 - a)\ln(1 - a) + a = kt$	0.57
	$D_3(a)$	Three-dimensional diffusion, spherical symmetry, N = 3	$[1 - (1 - a)^{1/3}]^2 = kt$	0.54
	$D_4(a)$	Three-dimensional diffusion, cylindrical symmetry	$(1 - 2/3a) - (1 - a)^{2/3} = kt$	0.57
Reaction-order	$F_1(a)$	Random nucleation and subsequent growth, N = 1, M = 1	$-\ln(1 - a) = kt$	1.00
Geometrical contraction	$R_2(a)$	Phase boundary reaction, cylindrical symmetry, N = 1/2	$1 - (1-a)^{1/2} = kt$	1.11
	$R_3(a)$	Phase boundary reaction, spherical symmetry, N = 1/3	$1 - (1 - a)^{1/3} = kt$	1.07
Nucleation models [16–18]	$A_2(a)$	Random nucleation and subsequent growth, N = 1/2, M = 2	$[-\ln(1 - a)]^{1/2} = kt$	2.00
	$A_3(a)$	Random nucleation and subsequent growth, N = 1/3, M = 3	$[-\ln(1 - a)]^{1/3} = kt$	3.00

Results and Discussion

Reduction Degree and Reduction Rate

The reduction degree of samples CF and CF8M with the change of time during the isothermal reaction stage that calculated by TG data were shown in Fig. 2. The results indicate that reduction degree is obviously promoted with rise in

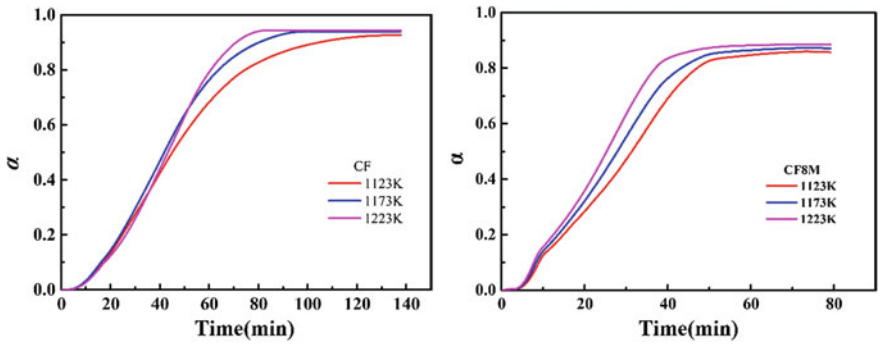

Fig. 2 Reduction degree of samples at 1123, 1173, and 1223 K

temperature. With the increasing of magnesia content, the MF and C_2F gradually increasing which inhibited the reducibility and CF gradually decreasing. Therefore, the total reduction degree presented a slight increase as alumina content increase. There was little distinction of the reduction degree among temperatures during the initial stages (before 50 min) for CF. But for CF8M, temperature barely had impact on the reduction degree for CF8M in the first 10 min.

Reduction rates of samples CF and CF8M at 1123, 1173 and 1223 K were shown in Fig. 3. The results show that the reduction process of CF and CF8M samples has two stages. The reduction degree is about 0–15% during the first stage where Fe_2O_3 is converted into Fe_3O_4 and the reduction degree is about 0–20% during the second stage where Fe_3O_4 is further reduced into Fe.

Apparent Activation Energy for Reduction of CF and CF8M Samples

Apparent activation energy was calculated by the slope of the plots of ln(da/dt) against 1/T shown in Fig. 4. The calculated values were presented in Table 3. Given that sample reduction was combined with several reaction stages and gas diffusion, activation energy was regarded as the apparent value that reflected the comprehensive influence on the reduction process. The results revealed that sample reduction tends to be easy with the addition of 8% magnesia in the Fe_2O_3–CaO system. In addition, the apparent activation energy increased gradually as a reduction reaction proceeds. Gas switching from pure N_2 to N_2 and CO mixtures result in the samples not being reduced by the target CO content during the initial stage. Thus, reduction degrees above 0.3 samples were selected for the calculation.

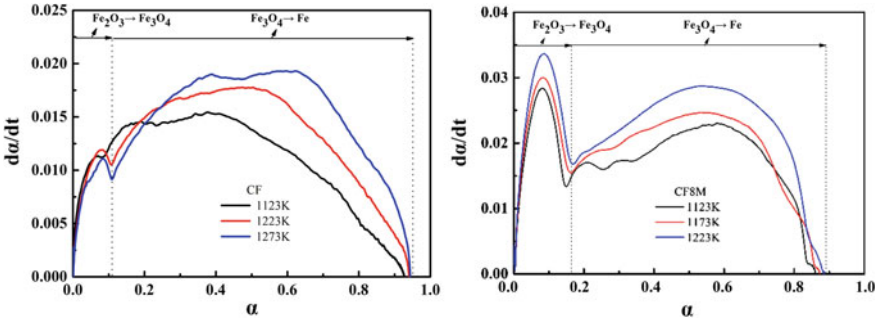

Fig. 3 Reduction rate of samples CF and CF8M

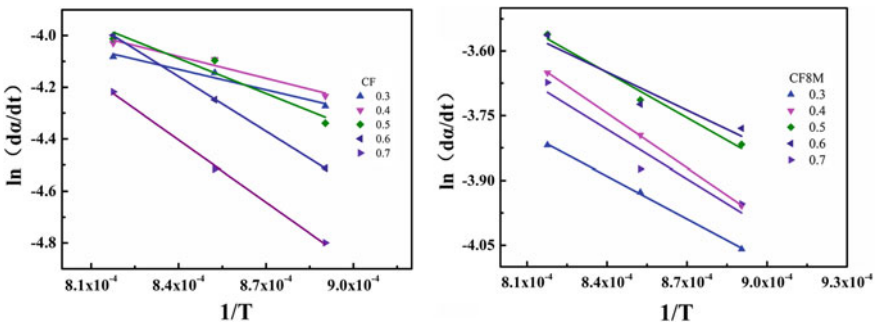

Fig. 4 ln(dα/dt) against 1/T of CF and CF8M samples

Table 3 Apparent activation energy of CF and CF8M samples

	0.3	0.4	0.5	0.6	0.7	Avg.
CF	20.3	23.1	30.9	52.8	67.5	38.9
CF8M	27.5	35.1	29.0	24.5	31.8	29.6

Model Function Results

Sharp analysis is a method by defining non-dimensional parameter $y(\alpha)$ to target G (α). The relevance of $y(\alpha)$ to α for CF and CF8M at various temperature were shown in Fig. 5. The results indicate that the experimental data y(a) values for samples CF and CF8M reduction mostly lie in the standard curve corresponding to function A_2. The reduction of CF and CF8M can be described by the mechanism of 2D shrinking layer reaction merely.

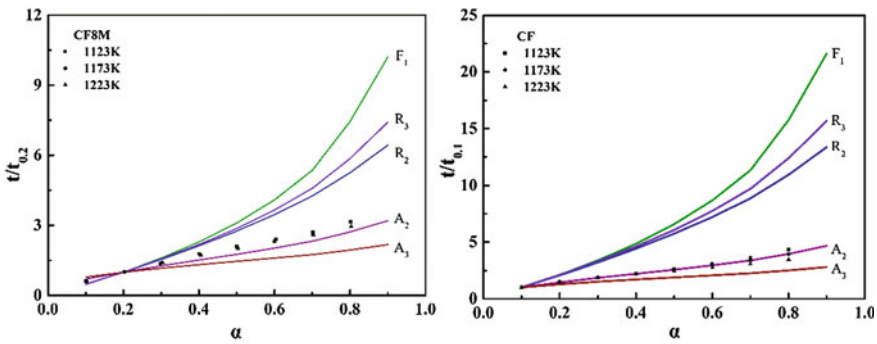

Fig. 5 Standard curves and experimental data based on Sharp analysis for CF and CF8M samples

Conclusions

The isothermal reduction kinetics of CF and CF8M samples were investigated by TG measurement with 30% CO and 70% N_2 gas mixtures. This study implies the reducibility of phases in the Fe_2O_3-CaO system by revealing the reduction rate and apparent activation energy. CF with 8% magnesia addition showed better reducibility and the reduction mechanisms were examined through Sharp analysis. The following conclusions were drawn by this study:

(1) The reduction rate analysis indicated that reduction of samples CF and CF8M comprises two stages during the whole reduction degrees.
(2) The apparent activation energy of reduction of samples CF and CF8M based on the model-free method are equal to 46.9 and 31.8 kJ/mol. Sample reduction tends to be easy with the addition of 8% magnesia in the Fe_2O_3–CaO system.
(3) According to Sharp analysis, the reduction of samples CF and CF8M were described by the Avrami–Erofeev equation with 2D reaction.

References

1. Strassburger JH (1969) Blast furnace-theory and practice. Gordon and Breach Science Publishers, New York, pp 211–215
2. Panigrahy SC, Verstraeten P, Dilewijns J (1984) Influence of MgO addition on mineralogy of iron ore sinter. Metall Trans B 15(1):23–32
3. Shigaki I, Sawada M, Tsuchiya O, Yoshioka K, Takahashi T (1984) Study of primary melt formation and transition mechanism to final slag of sintered ore. Tetsu-To-Hagane 70(16):2208–2215
4. Kimura H, Ogawa T, Kakiki M, Matsumoto A, Tsukihashi F (2005) Effect of Al_2O_3 and MgO additions on liquidus for the CaO–SiO_2–FeO_x system at 1573 K. ISIJ Int 45(4):506–512
5. Kalenga MK, Garbers-Craig AM (2010) Investigation into how the magnesia, silica, and alumina contents of iron ore sinter influence its mineralogy and properties. J South Afr Inst Min Metall 110(8):447–456
6. Li T, Sun C, Liu X, Song S, Wang Q (2017) The effects of MgO and Al2O3 behaviors on softening–melting properties of high basicity sinter. Ironmaking Steelmaking 2017(2):1–9
7. Zhang M, Andrade MW (2016) Effect of MgO and basicity on microstructure and metallurgical properties of iron ore sinter. In: Characterization of minerals, metals, and materials 2016, proceedings symposium, pp 67–174
8. Dutta SK, Ghosh A (1993) Kinetics of gaseous reduction of iron ore fines. ISIJ Int 33(11):1168–1173
9. Kang HW, Chung WS, Murayama T (1998) Effect of iron ore size on kinetics of gaseous reduction. ISIJ Int 38(2):109–115
10. Unal A, Bradshaw AV (1983) Rate processes and structural changes in gaseous reduction of hematite particles to magnetite. Metall Trans B 14(4):743–752
11. Hancock JD, Sharp JH (1972) Method of comparing solid–state kinetic data and its application to the decomposition of kaolinite, brucite, and $BaCO_3$. J Am Ceram Soc 55(55):74–77
12. Brown ME, Dollimore D, Galwey AK (1980) Reactions in the solid state, vol 22. Elsevier, Amsterdam

13. Sharp JH, Brindley GW, Narahari BN (1966) Numerical data for some commonly used solid state reaction equations. J Am Ceram Soc 49(7):379–382
14. Tamhankar SS, Doraiswamy LK (1979) Analysis of solid–solid reactions: a review. AIChE J 25(4):561–582
15. Ginstling AM, Brounshtein BI (1950) On diffusion kinetics in chemical reactions taking place in spherical powder grains. Zhur Priklad Khim 23
16. Avrami M (1939) Kinetics of phase change. I general theory. J Chem Phys 7(12):1103–1112
17. Avrami M (1940) Kinetics of phase change. II transformation–time relations for random distribution of nuclei. J Chem Phys 8(2):212–224
18. Avrami M (1941) Granulation, phase change, and microstructure kinetics of phase change. III. J Chem Phys 9(2):177–184

Propagation of Power Ultrasound in Calcium Ferrite Melt

Ruirui Wei, Xueqing Li and Mingrui Yang

Abstract Ultrasonic vibration was introduced into calcium ferrite (CF) melt in order to develop a new sintering process. Based on the acoustic refraction and reflection principles, ultrasonic propagation between amplitude transformer and CF melt has been analyzed and discussed. In addition, numerical simulation of ultrasonic propagation in CF melt has also been carried out using finite element method. The distribution of acoustic pressure in CF melt were obtained, and the effects of ultrasonic power and frequency on acoustic pressure distribution were also investigated. The results show that increasing ultrasonic power promotes the acoustic pressure amplitude in the CF melt, while increasing frequency decrease the acoustic pressure amplitude. The acoustic pressure amplitude with the frequency closer to the resonant frequency may get the best cavitation effect because its average acoustic pressure is greater than those of others.

Keywords Calcium ferrite · Finite element method · Ultrasonic propagation

Introduction

In China, blast furnace (BF) technology occupies the absolute dominant position in the production of iron-making process. Sinter is one of the main raw materials in BF iron-making process, which takes about 70% of the iron-bearing materials. The quality of sinter has a direct impact on the productivity of blast furnace, and it affects the yield and quality of the pig iron. In recent years, the domestic iron and steel enterprises have attached great importance to the use of low-grade iron ore due to the price fluctuation of imported iron ores, constantly consumption of high-grade iron ore, and falling profits of iron and steel enterprises. Therefore, iron ores with higher gangue content are used in sintering, which results in chemical composition

R. Wei (✉) · X. Li · M. Yang
School of Materials Science and Engineering, Chongqing University, Chongqing 400044, China
e-mail: wrui1990@outlook.com

B. Li et al. (eds.), *Characterization of Minerals, Metals, and Materials 2018*, The Minerals, Metals & Materials Series,
https://doi.org/10.1007/978-3-319-72484-3_14

fluctuation in the raw material, restraining the assimilation process and bringing many difficulties to sinter production [1].

The ore-forming process during sintering involves a series of complex physical and chemical processes, the most important of which are solid-phase reaction, liquid formation, cooling and consolidation. It is worth noting that the heating times employed in sintering at high temperature are usually very short, and the chemical reaction process is very slow because the reaction rate is controlled by the diffusion process [2]. Therefore, many researchers are focused on how to promote the chemical reaction in the sintering process, thereby to improve the quality of sinter.

Ultrasonic vibration has been widely used in the solidification [3–6] and chemical reaction [7–10] of metals and alloys due to its cavitation effect and acoustic streaming effect [4, 5], which aims to refine the grains and accelerate the chemical reaction rate. Regretfully, the application of power ultrasound in the sintering process has not been reported. Calcium ferrite is the base to produce silico-ferrite of calcium, and aluminum (SFCA) in the sintering process [11]. The authors have been studied the effect of power ultrasound on the solid reaction between CaO and Fe_2O_3 in the previous work, the results indicated that power ultrasound can accelerate the chemical reaction, and promote the formation of calcium ferrite (CF) phase [11]. Therefore, as a series work, the effect of power ultrasound on the CF melt will be studied. In this work, the effect of different parameters on the acoustic field was studied to optimize ultrasonic parameters for the experimental study of solidification process.

Numerical Models

When the ultrasonic waves are introduced to the CF melt, the bubbles are produced due to the expansion and compression of power ultrasound periodically. With the propagation of power ultrasound, the bubbles continue grow up. When the acoustic pressure induced by power ultrasound is high enough, the bubbles may collapse and form an instantaneous high temperature and high pressure area. These will break the formed dendrite and produce more nuclei, thus the grains are refined. Therefore, the acoustic pressure in the melt greatly influences the results of ultrasonic cavitation.

In this work, the acoustic pressure distribution was calculated using the Helmholtz equation (1) [12]:

$$\nabla\left(\frac{1}{\rho}\nabla p\right) - \frac{\omega^2}{\rho c^2}p = 0 \tag{1}$$

where ρ denotes the density of melt (kg/m^3), ω denotes the angular frequency (rad/s), c denotes the sound speed in the melt (m/s), p denotes the acoustic pressure (Pa).

Equation (1) was solved by the finite element method. Figure 1 shows the geometrical model and the relevant boundary condition. The liquid was set as CF melt.

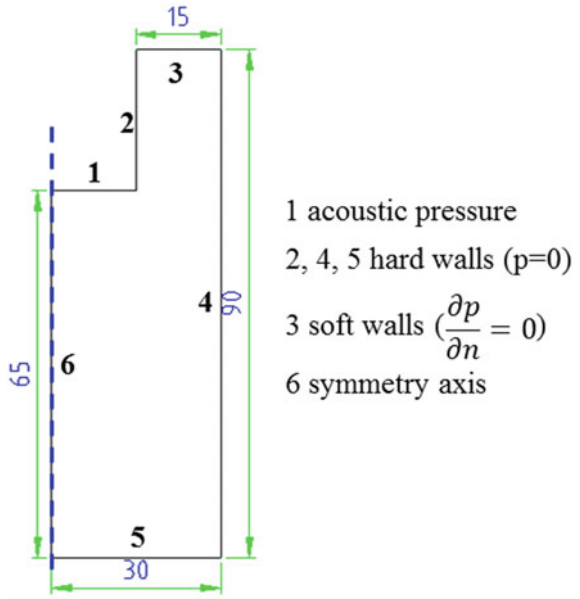

Fig. 1 Geometrical model and the related boundary conditions using in the calculation

In present work, only 25% of the full ultrasonic power, W, was consumed. Thus the acoustic radiation pressure of the emitter can be given [12]:

$$p_{emitter} = \sqrt{\frac{25\% \cdot W}{\pi r_{emitter}^2}}(2\rho_{emitter}c_{emitter}) \tag{2}$$

where $\rho_{emitter}$ denotes the density of emitter (kg/m^3), $c_{emitter}$ denotes the sound velocity in the emitter (m/s), and $r_{emitter}$ denotes the radius of the emitter (m). Thus, p_0 can be obtained following Snell's law:

$$\frac{p_0}{p_{emitter}} = \frac{2\rho c}{\rho c + \rho_{emitter}c_{emitter}} \tag{3}$$

Equation (4) was used to calculate the sound velocity in the melt [13]:

$$c = (\sigma/(6.33 \times 10^{-10}\rho))^{2/3} \tag{4}$$

where σ denotes the surface tension of melt, for CF, the surface tension is 558 N/m [14].

Table 1 Characteristic properties of CF melt and emitter

Properties	Melt	Emitter
Density, kg/m^3	4850	8570
Sound velocity, m/s	3208	3400

Characteristics of the CF melt and emitter can be found in Table 1.

Results and Discussion

COMSOL Multiphysics software was used to calculate the distribution of acoustic field in the melt. Figure 2 shows the distribution of acoustic pressure amplitude in the CF melt at different ultrasonic power. In general, the change of the acoustic pressure amplitude at different ultrasonic power is consistent. The acoustic pressure amplitude in the ultrasonic probe is higher than that of in the others points. It can be seen that the acoustic pressure amplitude decreases to zero and then increases along the axis periodically with the increase of the distance. For different ultrasonic power, the acoustic pressure increases in the same point with increasing the ultrasonic power. These results indicate that increasing ultrasonic power can increase the acoustic pressure amplitude, thereby promote the cavitation effect, which is consistent with the results of the previous study [12].

Figure 3 shows the distribution of acoustic pressure in the CF melt at different frequencies. The change of the acoustic pressure amplitude is obvious different. It can be seen that the acoustic pressure amplitude decreases and then increases along the axis. For different frequency, the acoustic pressure amplitude obviously decreases in the same site with decreasing of frequency. The acoustic pressure amplitude in the ultrasonic probe with 15 kHz frequency is smaller than that at the bottle of the melt, while the frequency is higher than 20 kHz, the acoustic pressure amplitude is greater than that at the bottle of the melt, and the average acoustic pressure amplitude with 20 kHz is higher than that of others. These results mainly caused by the resonance behavior between the CF melt and ultrasonic system, the resonant frequency in the CF melt is closer to 20 kHz. These results indicate that low frequency ultrasonic waves will be beneficial to improve the ultrasonic effect, and the frequency close to the resonant frequency maybe the best under the ultrasonic treatment.

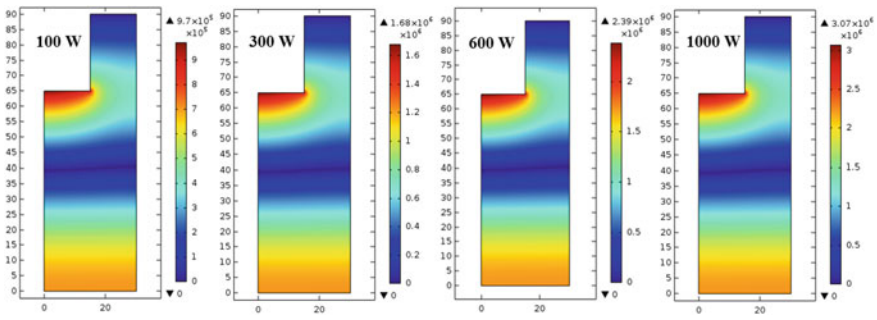

Fig. 2 Distribution of acoustic pressure amplitude in the CF melt at different ultrasonic powers

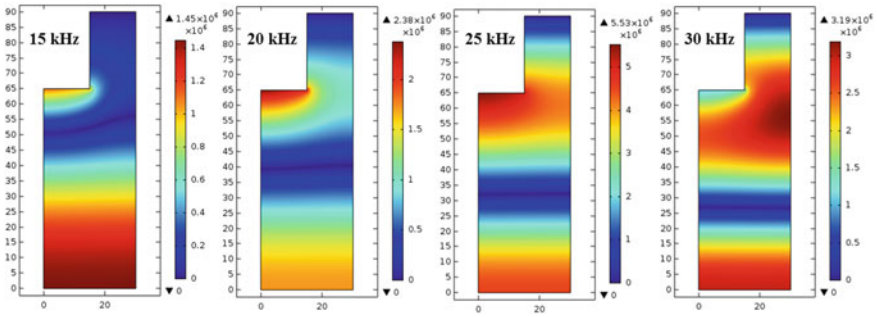

Fig. 3 Distribution of acoustic pressure amplitude in the CF melt at different frequencies

Conclusions

The finite element method was used in this work to study the effect of ultrasonic power and frequency in calcium ferrite (CF) melt. With the increase of ultrasonic power, the acoustic pressure amplitude increases in the CF melt, larger ultrasonic power can improve the cavitation effect of power ultrasound. With the increase of frequency, the acoustic pressure amplitude obviously decreases. However, the acoustic pressure amplitude closed the resonant frequency may obtain the best cavitation effect due to its average acoustic pressure is greater than the others.

Acknowledgements This study was performed with the financial support of Natural Science Fund outstanding youth project funding (No. 51522403) and Chongqing Youth Science and Technology Talent Training Project (cstc2014kjrc-qnrc90001).

References

1. Lv X, Bai C, Deng Q, Huang X, Qiu G (2011) Behavior of liquid phase formation during iron ores sintering. ISIJ Int 51(5):722–727
2. Bergman B (1986) Solid-state reactions between CaO powder and Fe_2O_3. J Am Ceram Soc 69(8):608–611
3. Atamanenko TV, Eskin DG, Zhang L, Katgerman L (2010) Criteria of grain refinement induced by ultrasonic melt treatment of aluminum alloys containing Zr and Ti. Mater Trans B 41(8):2056–2066
4. Jian X, Xu H, Meek TT, Han Q (2005) Effect of power ultrasound on solidification of aluminum A356 alloy. Mater Lett 59(2):190–193
5. Zhang X, Kang J, Wang S, Ma J, Huang T (2015) The effect of ultrasonic processing on solidification microstructure and heat transfer in stainless steel melt. Ultrason Sonochem 27(1):307–315
6. Chen R, Zheng D, Ma T, Ding H, Su Y, Guo J, Fu H (2017) Effects of ultrasonic vibration on the microstructure and mechanical properties of high alloying TiAl. Sci Rep 7:41463
7. Sriraman MR, Babu SS, Short M (2010) Bonding characteristics during very high power ultrasonic additive manufacturing of copper. Scripta Mater 62(8):560–563

8. Dehoff RR, Babu SS (2010) Characterization of interfacial microstructures in 3003 aluminum alloy blocks fabricated by ultrasonic additive manufacturing. Acta Mater 58(13):4305–4315
9. Sajjadi B, Raman AAA, Ibrahim S (2015) A comparative fluid flow characterisation in a low frequency/high power sonoreactor and mechanical stirred vessel. Ultrason Sonochem 27:359
10. Cui Y, Xu CL, Han Q (2006) Effect of ultrasonic vibration on unmixed zone formation. Scripta Mater 55(11):975–978
11. Wei R, Lv X, Yang M, Xu J (2017) Effect of ultrasonic vibration treatment on solid-state reactions between Fe_2O_3 and CaO. Ultrason Sonochem 38:281–288
12. Shao Z, Le Q, Zhang Z, Cui J (2011) A new method of semi-continuous casting of AZ80 Mg alloy billets by a combination of electromagnetic and ultrasonic fields. Mater Design 32(8): 4216–4224
13. Blairs S (2006) Correlation between surface tension, density, and sound velocity of liquid metals. J Colloid Interf Sci 302(1):312–314
14. Saito N, Hori N, Nakashima K, Mori K (2003) Viscosity of blast furnace type slags. Mater Trans B 34(5):509–516

Part VI
Characterization of Polymer and Composite Materials

Dynamic-Mechanical Analysis of Epoxy Composites Reinforced with PALF Fibers

Gabriel O. Glória, Maria Carolina A. Teles, Felipe L. Périsse, Carlos Maurício F. Vieira, Sergio Neves Monteiro, Frederico M. Margem and Maycon Gomes

Abstract The society is increasingly the concern about the ambiental impacts, and demand for eco-friendly materials. The composites reinforced with synthetic fibers are been replaced by composites reinforced with natural fibers because of the environmental advantages. Besides the environmental advantages, those fibers have economical and properties advantages, like the low density and cost. Composites with up to 30% of PALF fibers were tested. The analyzed parameters were the loss modulus, the storage modulus and the delta tangent. The test was conducted in the temperature interval from 25 to 195 °C in a DMA equipment operating at 1 Hz of frequency under a nitrogen flow. The results showed that the incorporation of continuous and aligned PALF fibers tends to increase the viscoelastic stiffness of the epoxy matrix. Contrasting this, minor changes occurred in both the glass transition temperature and the damping capacity of the structure as measured by the tan delta peaks.

Keywords PALF fibers · DMA test · Composites · Natural fibers

G. O. Glória (✉) · M. C. A. Teles · F. L. Périsse · C. M. F. Vieira
Advanced Materials Laboratory, LAMAV, UENF—State University of the Northern Rio de Janeiro, UENF, Av. Alberto Lamego, 2000, 28013-602 Campos dos Goytacazes, Brazil
e-mail: gabrieloliveiragloria@hotmail.com

S. N. Monteiro
Department of Materials Science, IME—Military Institute of Engineering, Praça General Tibúrcio, 80, 22290-270 Rio de Janeiro, Brazil

F. M. Margem
Faculdade Redentor, Rodovia BR 356, Nº 25, 22290-270 Itaperuna RJ, Brazil

M. Gomes
IFF-Instituro Federal Fluminense, R. Dr. Siqueira, 273—Parque Tamandaré, 28030-131 Campos dos Goytacazes—RJ, Brazil

B. Li et al. (eds.), *Characterization of Minerals, Metals, and Materials 2018*, The Minerals, Metals & Materials Series,
https://doi.org/10.1007/978-3-319-72484-3_15

Introduction

Due to growing concern about the ambient impacts caused by the society, new materials that are eco-friendly. In this context the lignocellulosic fibers, natural fibers extracted from cellulose-containing, appears like an option to substitute the more expensive, non-recyclable and energy-intense synthetic fibers in polymer composites. The lignocellulosic fibers are abundant in our planet, biodegradable, recyclable and neutral with respect to carbon dioxide emission, associated with global warming and greenhouse effect [1–3]. In fact, composites reinforced with traditional natural fibers such as coconut, sisal, jute, hemp, etc.…are already on the market in substitution for common glass fiber automobile components [4–6]. Technical aspects could also be in favor of the natural fibers that are softer and, consequently, less abrasive to processing equipments. Furthermore, for some lignocellulosic fibers, the mechanical properties can be superior to the corresponding one of glass fiber composites [2, 7].

Therefore, the objective of this work was to investigate the dynamic mechanical (DMA) behavior of epoxy matrix composites reinforced with up to 30% in volume of continuous and aligned PALF fibers in a wide temperature interval. This evaluation was carried out through the determination of the temperature dependence of the DMA parameters.

Experimental Procedure

The basic material used in this work was the PALF fiber supplied by Desigan Natural Fibers and a diglycidyl ether of the bisphenol A (DGEBA) epoxy resin and TETA hardener (trietylene tetramine) was used as matrix.

One hundred PALF fibers, shown in Fig. 1, were randomly selected from the bundle, the equivalent diameter corresponding to the average between the larger and smaller (90° rotation) cross section dimensions at five locations for each fiber, was measured in a profile projector Nikon 6C.

Figure 2 presents histogram corresponding to the distribution of diameter of the as-received PALF fibers. The equivalent diameter of each fiber was actually the average value obtained by 10 different measurements performed in a profile projector, at five distinct locations (two with 90° rotation at each location).

The histogram in Fig. 2 reveals a relatively large variation in the diameter, which is a consequence of the non-uniform physical characteristics of a lignocellulosic fiber [1, 3, 5–8]. The diameter range was large, varying between 0.10 and 0.28 mm with an average of 0.20 mm.

In this work, the specimens have dimensions of 50 × 13 × 5 mm, for the DMA's tests. Initially the PALF fibers were lay down inside silicone molds with the nominal dimensions, where different volume fractions of 0, 10, 20, 30% of continuous and aligned fibers were used for each specimen. A still fluid epoxy resin

Fig. 1 A bundle of PALF fibers

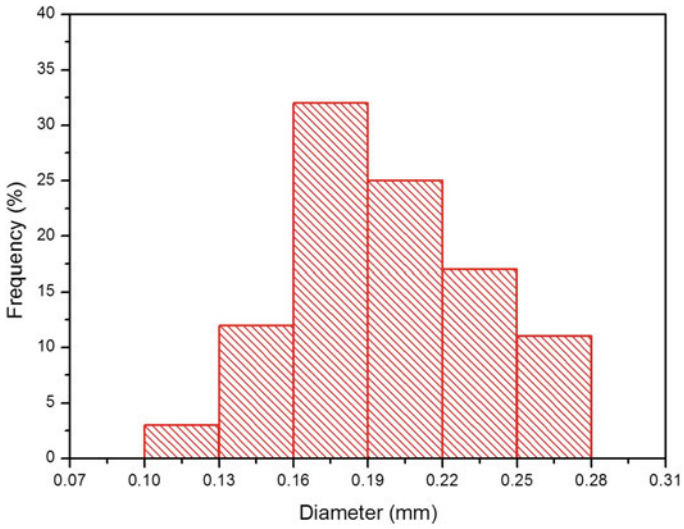

Fig. 2 Histogram for the distribution of diameter's PALF fibers

was poured into the molds to fabricate the composites. These composites specimens were cured for 24 h at room temperature.

Each specimen was tested in a DMA TA instruments Q/800 operating in a three points flexural mode at 1 Hz of frequency and heating rate of 3 °C/min under nitrogen atmosphere. The storage modulus, E', loss modulus, E", and tangent delta, tan δ, curves were simultaneously registered from 20 to 180 °C.

Results and Discussion

In order to evaluate the effect of PALF fiber incorporation into the epoxy matrix, the composites of PALF fibers with epoxy matrix prepared were analyzed in the same way as the neat epoxy. Their respective DMA curves are shown in Figs. 3, 4, 5. These figures show only the second run curves for the 10, 20 and 30 vol.% of PALF fiber composites, respectively. Corresponding curves of the first run were not presented, but the results related will be commented afterwards.

The interpretation of the DMA graphs in Fig. 4 implies that the PALF fiber incorporation results in a reduction of the lower limit of the Tg for the epoxy matrix.

Another relevant result obtained from Fig. 4, is the displacement to lower temperatures of the composites tan peaks with respect to that of the neat epoxy, with a difference about 10 °C. Since the tan peak corresponds to the upper limit of the epoxy matrix Tg, the incorporation of PALF fibers up to 30 vol. % results in a low fiber/matrix interaction due to the difficult in developing effective molecular bonds. This should prematurely disrupt the crystallinity of the epoxy matrix.

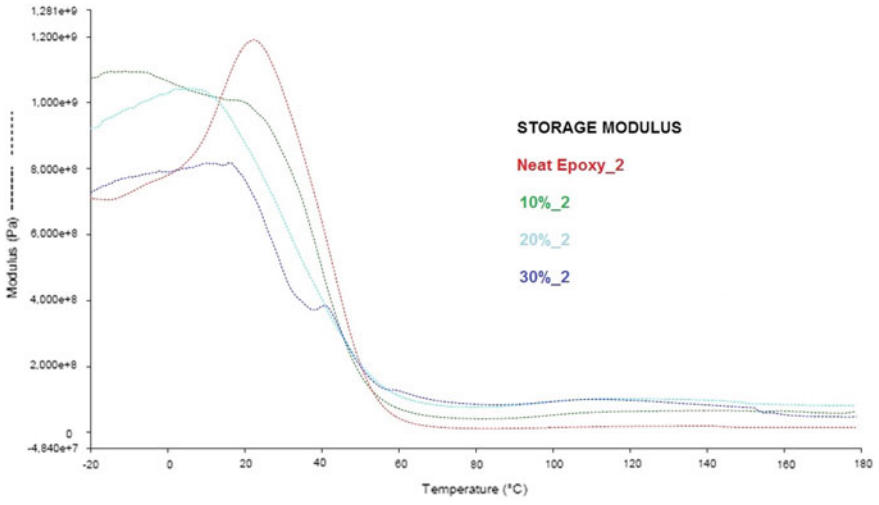

Fig. 3 Storage modulus curves for 0, 10, 20 and 30% of volume fraction of PALF fibers

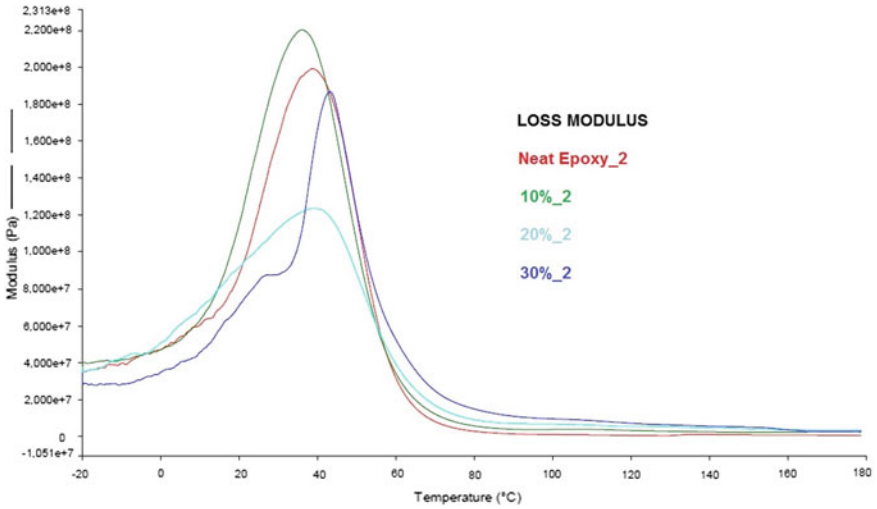

Fig. 4 Loss modulus curves for 0, 10, 20 and 30% of volume fraction of PALF fibers

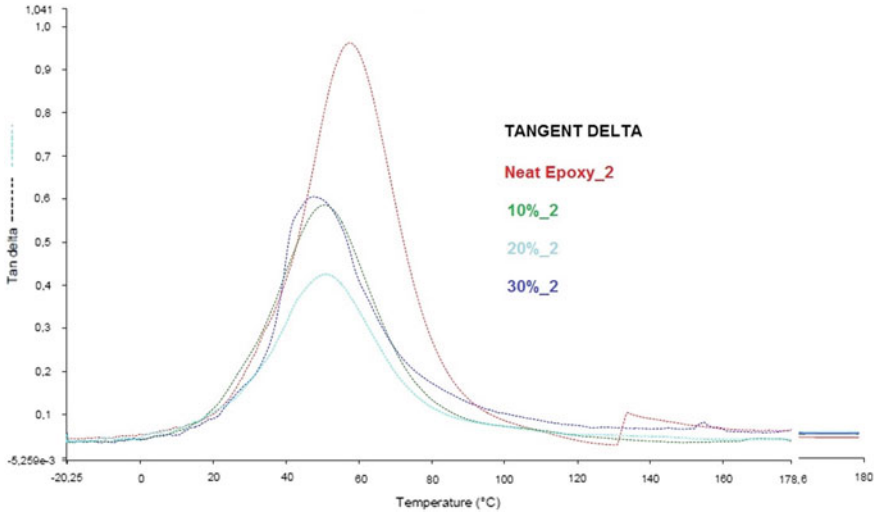

Fig. 5 Tangent delta curves for 0, 10, 20 and 30% of volume fraction of PALF fibers

Furthermore, the level of E' in the composites' first stage is significantly below that of the neat epoxy, even for composites with 20 and 30% of natural fibers, for the second run, where it is possible to see first an increase in the elastic modulus and after a decrease, as expected. Since E' is directly related to the material's capacity to support mechanical loads with recoverable viscoelastic deformation [9], comparatively lower E' indicates that the PALF fiber composites are less stiff than the neat epoxy.

Similar results were reported by Nair et al. [9] in short cut sisal fibers reinforced polystyrene matrix composites. These authors attributed the reduction in the neat polymeric matrix tan peak to the presence of residual solvent in their composites. However, another possible explanation in the present case could be the influence of PALF fibers is disrupting the epoxy structure at lower temperature, i.e., the PALF fiber contributes to prematurely uncrystallize the epoxy chains. The same rationale could be extended to the temperature of the loss of modulus, E", peaks, corresponding to the damping capacity of the composite structure, that is displaced to lower values with PALF fiber incorporation. As a general remark, it is suggested that the PALF fiber sensibly affects the DMA parameters of epoxy composites because of the disruption that it causes on the epoxy macromolecular structure.

It's important to mention that the different behavior of the storage modulus and tangent delta for the composite with 20% of fibers can be related to possible pores in the internal structure of the composite.

Conclusion

- A preliminary analysis of the dynamic-mechanical parameters of epoxy matrix incorporated with continuous and aligned PALF fibers showed a significant effect of samples second run, as compared to the first heating run.
- After the second DMA run up to 180 °C, not only the neat epoxy but also the PALF fiber composites suffered considerable increase in both the lower and upper limits of the glass transition temperature. This is apparently related to the curing process, which was not completed until the second run.
- The introduction of PALF fibers in the epoxy matrix also affects the Tg and causes sensible reduction in both the viscoelastic stiffness and the damping capacity of the composites as compared to the epoxy matrix. It is suggested that a possible reason would be the weak viscoelastic interaction between the PALF fibers and the epoxy macromolecules.

Acknowledgements The authors thank for the support provided by the Brazilian agencies: CNPq, CAPES, and FAPERJ.

References

1. Nabi Sahed D, Jog JP (1999) Natural fiber polymer composites: a review. Adv Polym Technol 18:221–274
2. Mohanty AK, Misra M, Hinrichsen G (2000) Biofibers, biodegradable polymers and biocomposites: an overview. Macromol Mat Eng 276(277):1–24
3. Bledzki AK, Gassan J (1999) Composites reinforced with cellulose-based fibers. Prog Polym Sci 4:221–274

4. Suddell BC, Evans WJ, Isaac, DH, Crosky AA (2002) A survey into the application of natural fibre composites in the automobile industry. In: Proceedings of the 4th international symposium on natural polymers and composites—ISNAPol (São Pedro, SP, Brazil, May, 2002), pp 455–461
5. Marsh G (2003) Next step for automotive materials. Mater Today 6(4):36–43
6. Hill S (1997) Cars that grow on trees. New Sci 153(2067):36–39
7. Wambua P, Ivens I, Verpoest I (2003) Natural fibers: can they replace glass and fibre reinforced plastics? Compos Sci Technol 63:1259–1264
8. d'Almeida JRM, Aquino RCMP, Monteiro SN (2006) Tensile mechanical properties, morphological aspects and chemical characterization of Piassava (Attalea funifera) fibers. Compos Part A 37:1473–1479
9. Nair KCM, Thomas S, Groeninckx G (2001) Thermal and dynamic mechanical analysis of polystyrene composites reinforced with short sisal fibres. Compos Sci Technol 61:2519–2529

Characterization of PCBs from Obsolete Computers Aiming the Recovery of Precious Metals

Mariana Alves de Carvalho, Marcos Paulo Kohler Caldas, Jorge Alberto Soares Tenório and Denise Crocce Romano Espinosa

Abstract The massive application of electrical and electronic equipments increased the production and industry development, which leads to a rising environmental and economic problem: the increase of e-waste's generation. The main cause to explain this problem is the combination between the diversification of electric and electronic device's applications and programmed obsolescence, which promotes a high generation the so-called waste electrical and electronic equipments (WEEE). Printed circuit boards (PCBs) are present in almost all WEEE and their heterogenous composition have a considerable amount of metals, including some precious ones. It is necessary to think about viable alternatives for the destination of WEEE, mostly PCBs'. Recycling is an environmental friendly purpose for PCBs' destination, combined with economic advantage from the recovery of metals. The choice of correct process to recycling depends on the composition of the PCBs, so the correct characterization is required. This work aims to characterize two different PCBs from obsolete computers: motherboard and memory board, concluding that they have 35.5 and 18.92% of metals, respectively, including precious metals as silver and gold. Also, memory board has 0.122% of these precious metals to the detriment of 0.047% from motherboard.

Keywords WEEE · Recycling · PCB · Characterization · Precious metals

M. A. de Carvalho (✉) · M. P. K. Caldas · J. A. S. Tenório · D. C. R. Espinosa
LAREX (Laboratório de Reciclagem, Tratamento de Resíduos
e Extração) – Department of Chemical Engineering, Polytechnic School
of University of São Paulo, Rua do Lago, 250, 2nd floor, São Paulo 05508-080, Brazil
e-mail: carvalhomariana@usp.br

M. P. K. Caldas
e-mail: marcospaulo@usp.br

J. A. S. Tenório
e-mail: jtenorio@usp.br

D. C. R. Espinosa
e-mail: espinosa@usp.br

B. Li et al. (eds.), *Characterization of Minerals, Metals, and Materials 2018*, The Minerals, Metals & Materials Series,
https://doi.org/10.1007/978-3-319-72484-3_16

Introduction

Production of electric and electronic equipments (EEE) has had, in past years until now, an exponential growth while their applications in society also became distinct [1]. On the other hand, the technologic advance is responsible by a phenomenon called programmed obsolescence, which leads to the reduce of life cycle for the EEE [2, 3]. One alarming consequence is the increase in the amount of the so called WEEE (Waste electrical and electronic equipments), electric and electronic equipments after their life cycle which demands correct strategies to final deposition without cause any damage to environment and human health [4]. Intending to contribute in terms of call the attention of society and purpose actions to mitigate the negative effects of WEEE's production and final deposition, European Parliament enacted two directives to contribute with the management of WEEE [5] and the use of hazardous substances in fabrication process of electric and electronic equipments [6].

Printed circuit boards (PCBs) are present in almost all EEE and, because of it, represent a large volume of the WEEE [4]. PCBs' composition is complex because the constituent materials—ceramics, polymers and metals—have heterogeneous origin and different proportion. Metallic fraction varies around 30% of the board and is composed of a lot of metals, including Cu, Fe, Al, Ni, Zn, Sn, precious metals as Ag, Au and Pd, and potentially toxic metals as Hg, Cd and Pb [1, 7].

The combination between the composition of PCBs and the high volume generated every year demands that, after the life cycle, it is necessary to give to the PCBs the correct treatment to prevent the direct contact with the ground, which can cause the contamination of local ecosystems and human health damages, and also the transport by water bodies to more distant places. Because of this environmental concern, the recycling of WEEE represents an alternative to the treatment of end-of-life PCBs and another WEEE [8]. Beyond, in economic sector, recycling is also attractive because of the opportunity of recover the metals contained in them. This recovery implies in the preservation of natural resources, because the use of recycled metals instead of virgin metals reduces the demand of extractive activity of the ores [7].

Precious metals as Ag and Au are contained in PCBs due to their characteristics as stable materials and with exceptional properties as high performance conductors [9]. Besides, because of their high market value, they represent a high percent of the intrinsic value of the residue, even with their low proportion—less than 1% in mass—if compared with another metals, as Cu, Al and Fe. Thus, the residue is considered a promisor secondary source of precious metals in detriment of the metal ores [1, 10].

The recycling of PCBs may use many processes, and the choice of which is better depends on the main objective and characteristics of the residue. Aiming the recovery of metals, it is possible to use hydrometallurgical processes [11], pyrometallurgical [2] processes and biohydrometallurgical processes [1]. All of them have advantages that can be take in consideration and limitations that can be

avoided. To achieve the success in any process adopted, it is necessary to know details of the process but, mostly, to know well the residue in terms of composition.

This work intends to characterize two different PCBs from obsolete computers—memory board and motherboard—aiming the recovery of precious metals by hydrometallurgical routes.

Materials and Methods

PCBs—memory board and motherboard from obsolete computers—were ceded by Centro de Descarte e Reúso de Resíduos de Informática da Universidade de São Paulo (CEDIR/USP). Lead free boards were used due to the substitution of lead in the weld by silver. High sized parts, mostly of motherboard, were manually removed. Then, the boards were comminuted, quartered and characterized with digestion in aqua regia and ICP-OES analysis, and fire loss test to determine the fractions of ceramic, polymeric and metallic materials, and also to identify which metals were contained in metallic fraction. Figure 1 shows the fluxogram with the methodology adopted in this work:

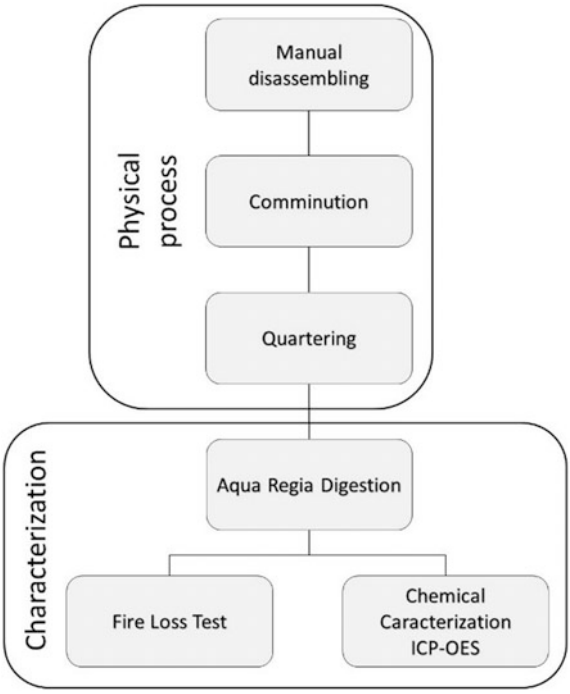

Fig. 1 Fluxogram of boards' physical processing and characterization

Physical Processing

To promote the liberation of the material and the increase of surface area, the PCBs passed through a comminution stage. The comminution was performed using two mills in sequence: the first was a knife mill with a 9 mm grid (RONE FA2305) and the second was a hammer mill (Astecma MDM 18/18) with a 2 mm grid. The boards were weighed before the process, between the two mills and after the second mill to evaluate loss of materials in each stage. After the comminution, the boards were quartered to be homogeneously divided in fractions containing 20 ± 5 g.

Characterization

Aqua Regia Digestion

From the quartered sample, one fraction containing 5 g was solubilized in 100 mL of aqua regia, in 1:20 of solid-liquid ratio. The digestion occurred in ambient temperature for 24 h. Then, the solution was filtered in quantitative paper fast filtering and porosity of 0.75 μm, resulting in two fractions. The liquid fraction—liquor, containing all metals dissolved—was sent to chemical analysis. Solid fraction was washed using deionized water and dried in fumehood for 24 h and temperature of 60 ± 5 °C, ant then was weighed in analytical balance and sent to fire loss test.

Fire Loss Test

The solid fraction was transferred to a porcelain bracelet and weighed in analytical balance. After this, it was put in a muffle oven under heating rate of 10 °C/min until reach the temperature of 800 °C, and then maintained for 1 h. The muffle was turned off to the cooling of the sample naturally until ambient temperature, so the sample was weighed again.

Chemical Characterization ICP-OES

To identify and quantify the metals contained in each board, a sample of 10 mL from the liquor obtained after aqua regia digestion was collected and sent to chemical analysis in ICP-OES.

Results and Discussion

Physical Processing

The weighing after the knife mill showed material's loss of 0.22% and, after the hammer mill, material loss of 1.30%. Overall material's loss calculated was 1.51% and is important to notice that this is a good result, representing low loss of material, mostly small size particles.

Characterization

Aqua Regia Digestion

From the weighing after the digestion, it was possible to know the amount of insoluble material. The difference between the initial mass and the mass of insoluble material—ceramic and polymeric materials—give the mass of soluble material, which corresponds to the amount of metal. For the memory board, the amount of soluble and insoluble material is 18.9 and 81.1%, respectively. Motherboard has 35.5% of soluble and 64.5% of insoluble material.

Fire Loss Test

The difference between the mass of solid fraction before and after the fire loss test corresponds to the polymeric material on the boards. Combining the result of aqua regia digestion and fire loss test, Fig. 2 shows the amount of each type of material for memory board and motherboard:

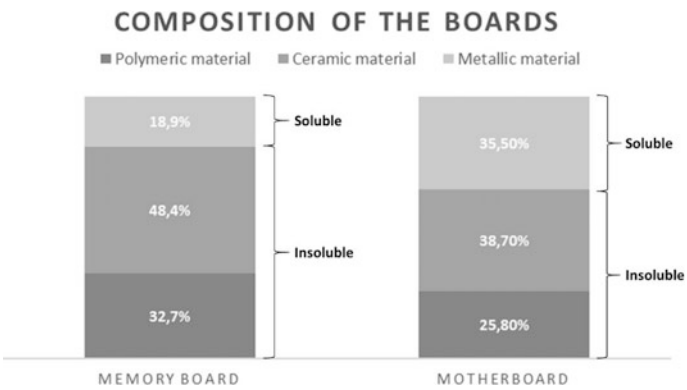

Fig. 2 Composition of memory board and motherboard in each type of material

In both boards, the main material in composition is ceramic, followed by polymeric material in memory board and metallic material in motherboard. Memory board has more insoluble material—ceramic and polymeric—than metallic material, comparing with motherboard.

Chemical Characterization ICP-OES

The following metals were analyzed: Ag, Al, Au, Cu, Fe, Ni, Sn and Zn. The result is shown in Fig. 3:

It is possible to notice that the main metal in the composition of both motherboard and memory board is similar in terms of de proportion of constituent materials. Cu is the main metal because of its exceptional property as conductor. Motherboard also has a significative amount of Fe in front of the other metals, while memory board presents other metals—as Al, Fe and Sn—in similar amounts. Ni and Zn are presents in low amounts for both boards.

In less significative amounts it is possible to find precious metals as Au and Ag, representing together 0122% of memory board and 0047% of motherboard. Considering only the absolute value, it seems like to be a low amount which makes the recovery seems unattractive. But if the market value of the two metals is take for consideration, the recovery becomes economically attractive.

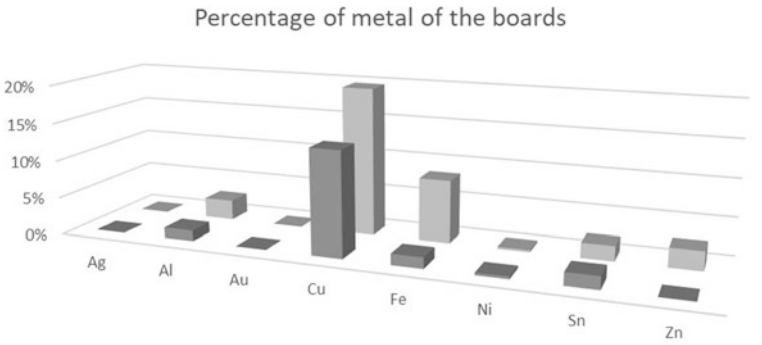

	Ag	Al	Au	Cu	Fe	Ni	Sn	Zn
Memory board	0,053%	1,43%	0,069%	13,83%	1,47%	0,32%	1,70%	0,043%
Motherboard	0,045%	2,66%	0,002%	19,65%	8,34%	0,27%	1,99%	2,550%

Fig. 3 Percentage of metals of memory board and motherboard

Conclusion

The characterization of Printed Circuit Boards from obsolete computers in terms of determine the percentage of each constituent material, mostly metallic material and which are these metals is important to choose the correct treatment in recycling them. Physical processing to prepare the boards for chemical processing were successfully conducted, with low loss of material, preserving mostly small sized particles. About characterization, motherboard has more metals in its composition than memory board, but main metal in both of them is Copper, followed by Iron, Aluminum and Tin. In lower concentrations, there are precious metals as silver and gold that can be recovered using physical and chemical methods to aggregate market value to the recycling process.

Acknowledgements The authors gratefully acknowledge the financial support given by Conselho Nacional de Desenvolvimento Científico e Tecnológico (CNPq) through master grant (131479/2017-2).

References

1. Ilyas S, Ruan C, Bhatti HN, Ghauri MA, Anwar MA (2010) Column bioleaching of metals from electronic scrap. Hydrometallurgy 101(3–4):135–140. https://doi.org/10.1016/j.hydromet.2009.12.007
2. Cayumil R, Khanna R, Rajarao R, Mukherjee OS, Sahajwalla V (2016) Concentration of precious metals during their recovery from electronic waste. Waste Manag 57:121–130. https://doi.org/10.1016/j.wasman.2015.12.004
3. Oh CJ, Lee SO, Yang HS, Ha TJ, Kim MJ (2003) Selective leaching of valuable metals from waste printed circuit boards. J Air Waste Manag Assoc 53(7):897–902. https://doi.org/10.1080/10473289.2003.10466230
4. Havlik T, Orac D, Petranikova M, Miskufova A (2011) Hydrometallurgical treatment of used printed circuit boards after thermal treatment. Waste Manag 31(7):1542–1546. https://doi.org/10.1016/j.wasman.2011.02.012
5. European Parliament and of the Council (2003) Directive 2002/96/EC of the European Parliament and of the Council on waste electrical and electronic equipment (WEEE). In: Official Journal of the European Union. http://eur-lex.europa.eu/legal-content/EN/TXT/?uri=celex%3A32012L0019. Accessed 14 Aug 2017
6. European Parliament and of the Council (2003) Directive 2002/95/EC of the European Parliament and of the Council on the restriction of the use of certain hazardous substances in electrical and electronic equipment (RoHS). In: Official Journal of the European Union. http://eur-lex.europa.eu/legal-content/EN/TXT/?uri=CELEX:32002L0095. Accessed 14 Aug 2017
7. Kumari A, Jha MK, Lee JC, Singh RP (2016) Clean process for recovery of metals and recycling of acid from the leach liquor PCBs. J Clean Prod 112:4826–4834. https://doi.org/10.1016/j.jclepro.2015.08.018
8. Robinson BH (2009) E- waste: An assessment of global production and environmental impacts. Sci Total Environ 408(2):183–191. https://doi.org/10.1016/j.scitotenv.2009.09.044
9. Cui J, Zhang L (2008) Metallurgical recovery of metals from electronic waste: a review. J Hazard Mater 158(2–3):228–256. https://doi.org/10.1016/j.jhazmat.2008.02.001

10. Tuncuk A, Stazi V, Akcil A, Yazici EY, Deveci H (2012) Aqueous metal recovery techniques from e-scrap: hydrometallurgy in recycling. Miner Eng 25(1):28–37. https://doi.org/10.1016/j.mineng.2011.09.019
11. Jing-ying L, Xiu-li X, Wen-quan L (2012) Thiourea leaching gold and silver from the printed circuit boards of waste mobile phones. Waste Manag 32(6):1209–1212. https://doi.org/10.1016/j.wasman.2012.01.026

Izod Impact Test Comparative Analysis of Epoxy and Polyester Matrix Composites Reinforced with Hemp Fibers

Lucas de A. Pontes, Janaína da S. Vieira, Dhyemila de P. Mantovani, Sergio Neves Monteiro, Carlos Maurício F. Vieira, Frederico M. Margem, Lázaro A. Rohen and Anna C. C. Neves

Abstract The interest in composites with natural fibers is due, among other factors, to the growing worldwide concern with the preservation of environment and renewable raw materials. The natural fibers have many particular properties that make them an attractive alternative to traditional synthetic fibers. The advantages of using these fibers are: low cost, renewability, biodegradability, low toxicity, abundance and specific strength. The searching for new suitable, economically viable and technologically advanced materials justifies the accomplishment of this work that aims at comparing the mechanical behavior of polyester matrix composites with epoxy matrix composites reinforced with hemp fibers Izod impact tested. The specimens with dimensions: 10 × 63 × 12.7 mm, made in different volume fractions of fiber: 0–30 vol%. The samples were tested at PANTEC pendulum model XC-50 located at LAMAV/UENF. With this research was possible to analyse the mechanical properties of these two new materials.

Keywords Izod impact test · Polyester · Epoxy · Hemp fiber · Composites

L. de A. Pontes · J. da S. Vieira (✉) · D. de P. Mantovani · C. M. F. Vieira
L. A. Rohen · A. C. C. Neves
Advanced Materials Laboratory LAMAV, UENF—State University of the Northern Rio de Janeiro UENF, Av. Alberto Lamego 2000, Campos dos Goytacazes 28013-602, Brazil
e-mail: Janaina.s.vieira@hotmail.com

S. N. Monteiro
Department of Materials Science, IME—Military Institute of Engineering, Praça General Tibúrcio 80, Rio de Janeiro 22290-270, Brazil

F. M. Margem
Faculdade Redentor, Rodovia BR 356, nº 25, Itaperuna, RJ 22290-270, Brazil

B. Li et al. (eds.), *Characterization of Minerals, Metals, and Materials 2018*, The Minerals, Metals & Materials Series,
https://doi.org/10.1007/978-3-319-72484-3_17

Introduction

Owing to worldwide problems related to climate changes and pollution, Environmental issues are additionally gaining attention. Natural fibers are renewable, biodegradable and recyclable, and this is nowadays a major advantage for them. By contrast, to glass fiber composites that cannot be recovered, natural fiber composites can be completely burnt to produce energy. Moreover, lignocellulosic fibers are neutral with respect to CO_2 emission, the main responsible for global warming.

Especially lignocellulosic fibers, the natural fibers obtained from plants (Table 1), offer economical environmental and technical advantages in comparison to synthetic fibers for application as the reinforcement of polymeric composites. Low cost is certainly one important incentive for the industry, and it has caused the use of lignocellulosic fibers because they usually have a commercial price around five times lower than that of glass fiber, the cheapest among the synthetic fibers.

Nowadays the synthetic fibers are been replaced by the natural ones, particularly the common glass fiber, as reinforcement of polymeric composites in many engineering applications, such as, automobile interior components, cyclist helmets, housing panels and windmill fins [2–5]. The lignocellulosic fibers obtained from vegetables offer social, economical, environmental and technical benefits [6, 7], in particular a higher impact resistance.

These fibers are naturally flexible, while the glass fiber have a brittle characteristic. in a situation of a crash event the flexible ones absorbs more energy than the brittle ones. This is why the natural fibers can be used in automobile parts such as the head-rest and the interior front panel, parts that should not have a brittle rupture during an accident, because in this case them should be sufficiently soft and flexible to absorb the impact energy without splitting into sharp pieces, to avoid injuring the passengers [7].

The hemp fiber, although strong and flexible [8] has not yet been applied in composites for automobile components. Actually, the fibers obtained from the petiole of the hemp palm tree commonly used to fabricate ropes and baskets owing to its high strength. This has motivated the study of the mechanical characteristic of the fibers.

The impact resistance of continuous and aligned fiber reinforcing polymeric composites has yet to be evaluated, in spite of existing works on the properties of hemp fiber composites [9, 10]. Therefore, the objective of the present work was to

Table 1 Classification of lignocellulosic fibers according to origin [1]

Origin	Lignocellulosic fiber
Leaf	Abaca, Cantala, Curaua, Sisal
Seed	Cotton
Steam	Ramie, Linen, Hemp, Jute
Fruit	Cairo, Sumaúma
Herb	Alfalfa, Sugarcane Bagasse, Bamboo
Stalk	Banana and Straw

access and compare the toughness through the energy absorbed by notched Izod Impact specimens of epoxy and polyester composites reinforced with different amounts of continuous hemp fibers.

Experimental Procedure

In this work, the material used was untreated hemp fiber extracted from the stem hemp plant and epoxy resin. Were performed a statistical analysis on one hundred fibers randomly removed from the as-received the lot. Figure 1 shows the histogram for the distribution of hemp fiber diameters by considering 6 diameter intervals. From this distribution, presented elsewhere an average diameter of 0.065 mm was found for the as-received lot.

Several other hemp fibers were cleaned in water and dried at 60 °C in a stove to be used as composite reinforcement. Continuous and aligned fibers were laid down, in separate amounts of 10, 20, and 30% volume, mixed with still fluid unsaturated epoxy and polyester resin, in a mold made of steel with 146 × 127 mm and 10 mm of thickness. Epoxy resin type commercial diglycidyl ether of bisphenol A (DGEBA) cured with triethylene tetramine (TETA) in stoichiometric proportion of 13 parts of hardener to 100 parts of still liquid resin was poured into the hemp fibers in the mold. The polyester ones were prepared using unsaturated orthophitalic polyester resin mixed with 0.5% of methyl ethyl- ketone as hardener of still liquid resin. A 24 h cure at room temperature was allowed for these composite samples. After unmolded, the samples were cut following the ASTM D256 standard. Ten specimens for each percentage of hemp fiber composite were impact tested in a PANTEC pendulum, Fig. 2, set in the Izod configuration.

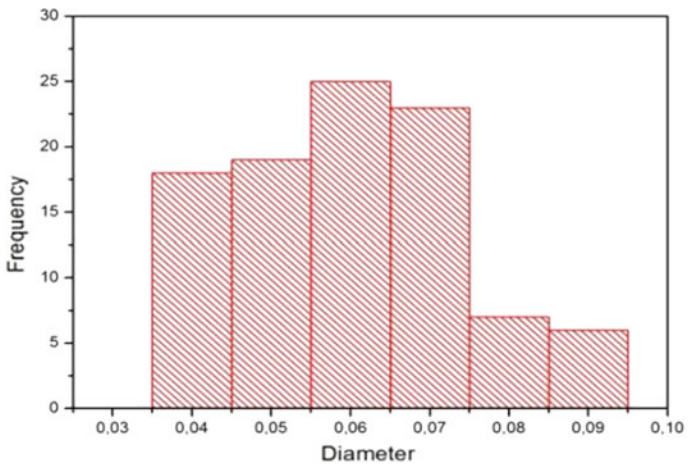

Fig. 1 Distribution histogram for six diameter intervals

Fig. 2 Izod equipment

Results and Discussion

The macrostructural appearance of broken specimens with different amounts of hemp fibers, from 0 to 30% in volume, are shown in Fig. 3. It can be noticed that the epoxy matrix without the addition of hemp fiber is brittle and the impact-generated crack propagates without being arrested until the specimen separates. However, for any proportion of hemp fiber the initial propagating crack is blocked and the rupture migrates to the fiber/matrix interface.

Important factors related to the impact fracture characteristic of polymeric reinforced with long and aligned natural fibers are relevant. Interface strength between a hydrophilic natural fiber is relatively low, and a hydrophobic polymeric matrix contributes to an ineffective load transfer from the matrix to a longer fiber.

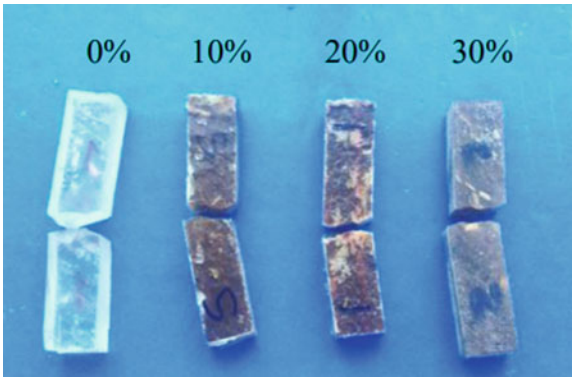

Fig. 3 Typical ruptured specimens of epoxy composites reinforced with hemp fibers by Izod impact tests

Table 2 Izod impact energy for epoxy matrix composites reinforced with hemp fibers

Fiber content (%)	Impact energy (J/m)
0	23.07 ± 6.42
10	29.09 ± 3.91
20	36.56 ± 9.38
30	47.99 ± 5.36

These results not only in a relatively greater fracture surface but also higher impact energy needed for the rupture. The impact energy obtained in the Izod impact tests of epoxy matrix composites reinforced with different volume fractions of fibers hemp are shown in Table 2.

From the data in Table 1, the graph of the energy absorbed in the Izod impact versus the corresponding volume fraction of hemp fibers in the epoxy matrix was plotted, as shown in Fig. 4.

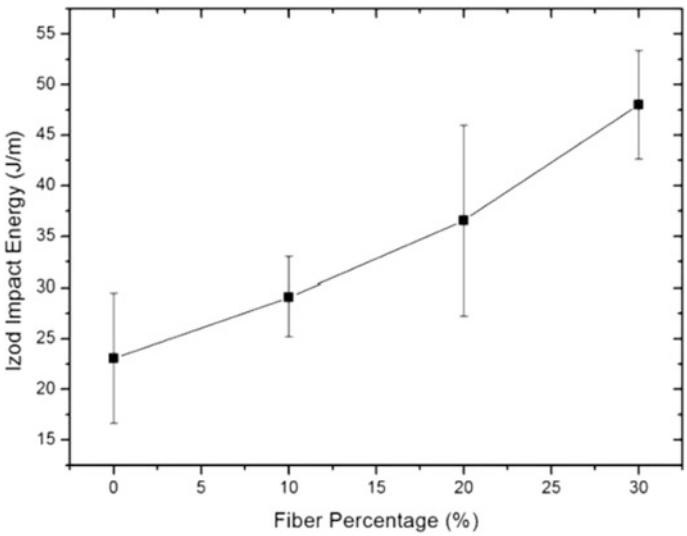

Fig. 4 Variation of the Izod impact energy with the amount of fiber in the epoxy composites

Due to the heterogeneous nature of these fibers, causing substantial dispersion in the composites properties, other lignocellulosic fibers present the same behavior [5]. It is possible to interpret the increase of impact energy (even considering the error bars), as following a linear relationship. Indeed, for most lignocellulosic fibers, the increase in the Izod impact energy is directly related to the increase in the fiber volume fraction [10].

The cracks had propagated along the fiber/matrix interface causing the fiber separation from the epoxy but not the fiber rupture. This effect increases the cracks trajectory through the composite, creating greater impact energy. Similar behavior

was also observed in the pullout tests [11]. Thus, the composites absorb relatively larger amounts of energy, leading to an increase in the impact resistance. Figure 5 shows the typical fracture surface of a 30% hemp fiber composite caused by an Izod impact test.

With low magnification, Fig. 5a, the surface region where the fibers are bending, instead of breaking, can be observed. With higher magnification, Fig. 5b, one sees the interface fiber/matrix where a crack is propagating. The crack "river pattern" is observed at the left side of Fig. 5b.

Figure 5b also shows a detail of the interface between the epoxy matrix and a hemp fiber, especially signs of adhesion between them. Some cracks may be observed, however, propagating through the fiber/matrix interface. This behavior confirms the mechanism of rupture between the hemp fiber and epoxy matrix associated with low interfacial resistance, resulting in greater impact energy.

Table 3 presents the results of Izod impact tests of polyester matrix composites reinforced with different volume fractions of hemp fibers.

Based on the results shown in Table 3, the variation of the Izod impact energy with the amount of hemp fiber in the polyester composite is shown in Fig. 6.

In this figure it should be noticed that the hemp fiber incorporation into the matrix significantly improves the impact toughness of the composite. This improvement can be considered almost as increase with respect to the amount of hemp fibers.

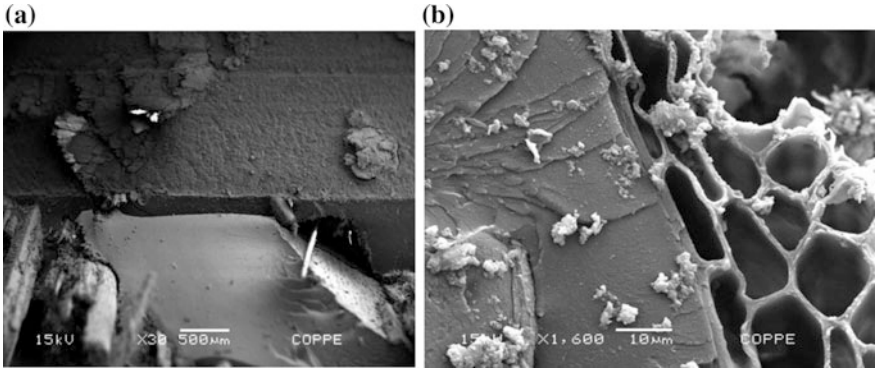

Fig. 5 SEM micrograph of the fracture for a 30% hemp composite. **a** 30×; **b** 1600×

Table 3 Izod impact energy for polyester composites reinforced with hemp fibers

Volume fraction of hemp fiber (%)	Izod impact energy (J/m)
0	14.9 ± 0.60
10	78.7 ± 2.58
20	87.1 ± 7.51
30	139.05 ± 8.21

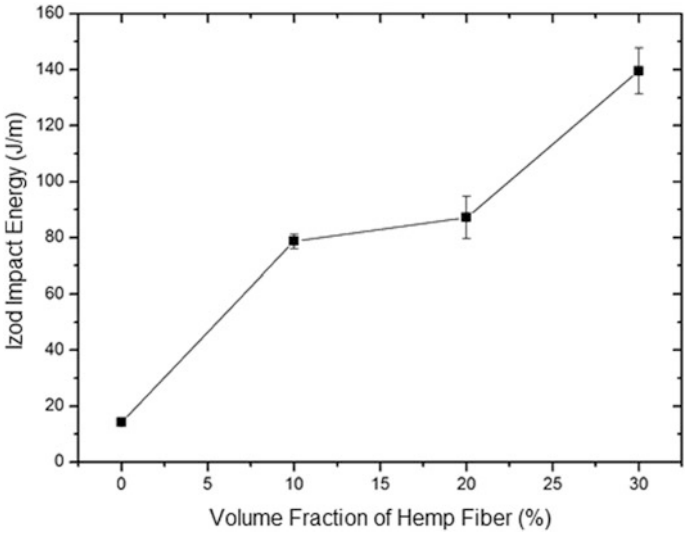

Fig. 6 Izod impact energy as a function of different volume fractions of hemp fiber

The relatively high dispersion of values, given by the standard deviation associated with the higher fiber percentage points in Fig. 6, is a well known heterogeneous characteristic of the lignocellulosic fibers [12]. The values shown in this figure are consistent with results reported in the literature [12, 13]. The reinforcement of a polymeric matrix with both synthetic [14, 15] and natural [16, 17] fibers increases the impact toughness of the composite.

In this work, using aligned hemp fibers, the impact toughness of 139.05. J/m for 30% long hemp fibers. The greater impact resistance of the polyester in comparison with the polypropylene matrix could be one reason for the superior performance found in the present work. However, there are other important factors related to the impact fracture characteristic of polymeric reinforced with long and aligned natural fibers.

The relatively low interface strength between a hydrophilic natural fiber and a hydrophobic polymeric matrix contributes to an ineffective load transfer from the matrix to a longer fiber. This characteristic allow the system to absorb more energy because of the flexibility of the fiber that slide out of the matrix but do not breaks, what amplifies the energy needed to rupture the specimen [17]. The macroscopic aspects of the typical specimen ruptured by Izod impact tests are shown in Fig. 7. In this figure it should be noted that the incorporation of fiber results in a completely different rupture shape with respect to pure polyester (0% fiber) in which a totally transversal rupture occurs.

Even with 10% of fiber, the rupture is no longer completely transversal. This indicates that the cracks nucleated at the notch will initially propagate transversally through the matrix, as expected in a monolithic polymer. However, when the crack reaches a fiber, the rupture will proceed through the interface. As a consequence, after

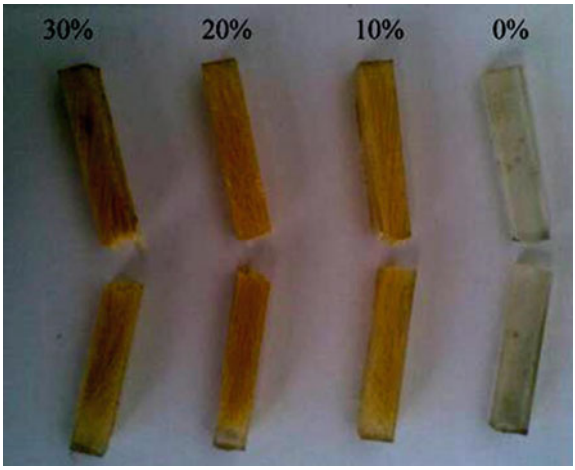

Fig. 7 Typical ruptured specimens of polyester composites reinforced with hemp fibers by Izod impact tests

the Izod hammer hit the specimen, some long fibers will be pulled out from the matrix but will not break, simply bend. In fact, for volume fractions of fiber above 10%, some specimens are not separated at all. For these amounts of fibers, part of the specimen was bent enough to allow the hammer to continue its trajectory carrying away the specimen without breaking it into pieces, which is expected in a Izod test. The value of the impact toughness in this case cannot be compared with others in which the specimen is totally split apart. Anyway, the fact that a specimen is not completely separated in two parts underestimates the impact toughness. In other words, had all the fibers been broken, the adsorbed impact energy would be even higher.

Conclusion

- The hemp fiber incorporation in the polymeric matrix reinforced the composite material, and showed a linear increase in the absorbed Izod impact energy, the results displays some significant dispersion commonly associated to the non uniform nature of the lignocellulosic fiber, and the presence of pores, defects and impurity occurs during the specimen fabrication.
- There is a significant increase in energy absorbed in Izod impact tests with the incorporation of hemp fibers in an epoxy matrix composite.
- The weak interface between the hemp fibers and the epoxy matrix contributes greatly to increase the impact energy by changing the cracks trajectory in the composite. Most of this increase in toughness is apparently due to the low hemp fiber/epoxy matrix interfacial shear stress. This results in a higher absorbed energy as a consequence of a longitudinal propagation of the cracks throughout the interface, which generates larger rupture areas, as compared to a transversal fracture.

- There is a significant increase in energy absorbed in Izod impact tests with the incorporation of hemp fibers in a polyester matrix composite. The weak interface between the hemp fibers and the polyester matrix contributes greatly to increase the impact energy by changing the cracks trajectory in the composite. Most of this increase in toughness is apparently due to the low hemp fiber/polyester matrix interfacial shear stress. This results in a higher absorbed energy as a consequence of a longitudinal propagation of the cracks throughout the interface, which generates larger rupture areas, as compared to a transversal fracture.

Acknowledgements The authors thank for the support provided by the Brazilian agencies: CNPq, CAPES, and FAPERJ.

References

1. Kalia S, Kaith BS, Kaur I (2009) Pretreatment of natural fibers and then application as reinforcing material in polymer composites—a review. Polym Eng Sci 49(7):1253–1272
2. Aquino RCMP, Almeida JRM, Monteiro SN (2005) Análise do Compósito de Piaçava/Resina poliéster, como substituto da Madeira. In: 60° Congresso Anual da Associação Brasileira de Metalurgia e Materiais—ABM, 24-27 de julho de 2006, Belo Horizonte, MG, Brasil
3. Hull D, Clyne TW (1996) An introduction to composite materials, 2a edn. Cambridge University Press, Cambridge
4. Monteiro SN, Costa LL, Santafé HPG (2008) Tenacidade ao impacto Charpy de compósito epoxídico reforçado com fibras de coco. In: CBECIMAT—CONGRESSO BRASILEIRO DE ENGENHARIA E CIÊNCIA DOS MATERIAIS, outubro de 2008, Porto de Galinha—PE—Brasil, pp 1–12
5. Bledzki AK, Gassan J (1999) Composites reinforced with cellulose-based fibres. Prog Polym Sci 24:221–274
6. Monteiro SN, Lopes FPD, Ferreira AS, Nascimento DCO (2009) Natural fiber polymer matrix composites: cheaper, tougher and environmentally friendly. JOM 61(1):17–22
7. Leão AL, Carvalho FX, Frollini E (1997) Lignocellulose-plastics composites, plastic composite. USP & UNESP, São Paulo
8. Joseph A, Sreekala MS, Oomens Z, Koshy P, Tohomas SA (2002) A comparison of the mechanical properties of phenol formaldehyde composites reinforced with banana fibre and glass fibres. Compos Sci Technol 62:1857–68
9. Monteiro SN, Lopes FPD (2007) Ensaios de impacto em compósito polimérico reforçado com fibras de curauá—In: 62° CONGRESSO ANUAL DO CONGRESSO ANUAL DA ASSOCIAÇÃO BRASILEIRA DE METALURGIA E MATERIAIS, ABM, julho de 2007, Vitória, ES. pp 1–10
10. Yue CY, Looi HC, Quel MY (2005) Assessment of fibre-matrix adhesion and interfacial properties using the pullout test. Int J Adhes Adhes 15:73–80
11. Monteiro SN, Margem FM, Neto JB (2010) Evaluation of the interfacial strength of ramie fibers in polyester matrix composites. In: TMS 2010 annual meeting & exhibition, 14–18 Feb 2010. Washington State Convention Center, Seattle, WA
12. Crocker J (2008) Natural materials innovative natural composites. Mater Tecnolo 2–3: 174–178
13. Nair KCM, Diwan SM, Thomas S (1996) Tensile properties of short sisal fiber reinforced polystyrene composites. J Appl Polym Sci 60(9):1483–1497

14. Joseph PV, Joseph K, Thomas S (2002) Short sisal fiber reinforced polypropylene composites: the role of interface modification on ultimate properties. Compos Interf 92(2):171–205
15. Monteiro SN, Inacio WP, Lopes, FPD, Costa LL, Santos LFL Jr (2009) Characterization of the critical length of sisal fibers for polyester composite reinforcement. In: Proceedings of characterization of minerals, metals & materials—TMS conference San Francisco, USA, March, pp 1–8
16. Fu SY, Lauke B, Mäder E, Hu X, Yue CY (1999) Fracture resistance of short-glass-fiber-reinforced and short-carbon-fiber-reinforced poly-propylene under charpy impact load and dependence on processing. J Mater Process Technol 89(90):501–507
17. Monteiro SN, Aquino RCMP, Lopes FPD, Carvalho EA, d'Almeida JRM (2006) Charpy impact notch toughness of piassava fibers reinforced polyester matrix composites. Rev Mater 11(3):204–210 (in Portuguese)

Synthesis of Polymeric Hydrogel Loaded with Antibiotic Drug for Wound Healing Applications

Angélica Tamião Zafalon, Vinícius Juvino dos Santos, Fernanda Esposito, Nilton Lincopan, Vijaya Rangari, Ademar B. Lugão and Duclerc Fernandes Parra

Abstract Polymeric hydrogels are natural or synthetic systems, which have gained interest due to their high biocompatibility with soft tissues. These types of hydrogels have been used for wound dressing as a drug delivery system. Here in this study the polymeric hydrogels based wound healing systems were prepared using poly (N-vinyl-2-pyrrolidone) (PVP), poly (ethylene glycol) (PEG), agar and neomycin drug followed by gamma irradiation to promote crosslinking and sterilization. The influence of irradiation process with 25 kGy dose was investigated. The gel fraction and maximum swelling were estimated using physicochemical methods and found about 95% gel fraction and 1100% swelling after 8 h of immersion. Neomycin released from hydrogel was carried out by Liquid Chromatography-Mass Spectrometry method and the drug concentration remained constant for 48 h. Hydrogel/neomycin exhibited antibacterial effects against *Staphylococcus aureus*. With these results, it can be inferred that hydrogel/neomycin is a suitable candidate for wound dressing.

Keywords Hydrogel · Polymeric material · PVP · Wound dressing Neomycin

A. T. Zafalon (✉) · V. J. dos Santos · A. B. Lugão · D. F. Parra
Nuclear and Energy Research Institute, IPEN-CNEN/SP, Cidade Universitária, Av. Prof. Lineu Prestes, 2242, São Paulo, SP 05508-000, Brazil
e-mail: angelicatamiao@gmail.com

F. Esposito · N. Lincopan
Institute of Biomedical Sciences, ICB-USP, Cidade Universitária, Av. Prof. Lineu Prestes, 2415, São Paulo, SP 05508-900, Brazil

V. Rangari
Department of Materials Science and Engineering, Tuskegee University, Tuskegee, AL 36088, USA

B. Li et al. (eds.), *Characterization of Minerals, Metals, and Materials 2018*, The Minerals, Metals & Materials Series,
https://doi.org/10.1007/978-3-319-72484-3_18

Introduction

Hydrogels are insoluble three-dimensional structures, with soft and elastic consistency. They are crosslinked polymers with high capacity to absorb water and swell without losing its integrity [1–3]. The synthesis of hydrogels with crosslinked polymers can be prepared by ionizing radiation process. Ionizing radiation source commonly used for hydrogel membranes is from ^{60}Co gamma source and involves crosslinking of molecules, scission mechanisms and modification of rheological characteristics of three-dimensional network. Advantages of radiation processes are the sterilization, polymer crosslinking and the no use of toxic reactants or catalysts during the polymerization process [4–11].

Currently, hydrogels are used in dressings as transdermal drug delivery systems. They provide a moist environment at the wound, accelerated healing, act as barrier against microorganisms, prevention of fluid loss from wound, reduce the dosing frequency and ensure the presence of drug exposure at infected wound area continuously [12–16]. PVP hydrogel is formed from synthetic polymer with high polarity, amphoteric characteristics, electrical properties, complexing ability, stability, processability, high transparency, good biocompatibility and non-toxicity in nature. These characteristics are in high demand for pharmaceutical industrial application of polymer [7]. The PVP may be used alone, however, to increase its versatility, researchers have blended it with other polymers, nanoparticles and antibiotic carriers for therapeutic membranes for wounds [17, 18]. Incorporation of drug in hydrogel is of current interest to develop more efficient wound healing system [19, 20]. Neomycin is one of such antibiotic drug with aminoglycoside antibiotic, which has broad spectrum activity, produced by *Streptomyces fradiae* and consists of two main components, neomycin B and C. It has high polarity, solubility in water, low volatility and capability of topical use for treatment and prophylaxis of skin infections, including traumatic wounds and burns [21, 22].

Chronic wound infections are difficult to treat due to low blood perfusion and systemic drugs have been seen to have low effectiveness. Often, antibiotic resistant bacteria lead to increase mortality and morbidity especially in debilitated patients [18]. The necessity for developing new techniques for the treatment of wounds and overcome bacterial resistance are the motivation for this research. In this study, PVP based hydrogels loaded with neomycin drug using gamma irradiation method were prepared and characterized. It was found that gamma irradiation methods improved crosslinking and sterilization.

Experimental

Materials

PVP k90 (Mw 360,000) was purchased from Exodo Cientifica, neomycin was obtained from Sigma Aldrich, polietilenoglicol 300 (PEG 300) was provided from Synth and agar was supplied from Oxoid. The chemical structure of neomycin is shown in Fig. 1.

Materials Sample Preparation and Irradiation

PVP polymer (6 wt%) was mixed with an appropriate amount of deionized water and kept for 24 h at room temperature to complete dissolution. This mixture was heated at 80–85 °C and added agar (1.5%), PEG (0.45%) and Neomycin (0.5%). This hot mixture was slowly poured in a custom built rectangular plastic molds and dried at room temperature. These hydrogels were further exposed to the gamma irradiation in ^{60}Co source using a 25 kGy dose and 6 kGy/h dose rate.

Determination of Gel Fraction

Extraction of the sol fraction was carried out by Soxhlet apparatus for 6 h using water as solvent. Then dried at 50 °C to a constant weight. The gel fraction was determined gravimetrically by using the following equation.

$$G = (Wg/Wo) \times 100\% \quad (1)$$

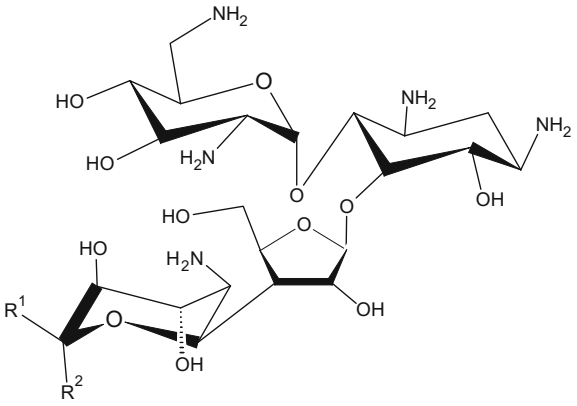

Fig. 1 Chemical structure of the neomycin.
R1 = CH2NH2, R2 = H2

where *G* is the gel fraction (%), *Wg* the weight of sample after extraction and *Wo*, before.

Swelling Behavior

Hydrogels were dried to constant weight. After they were immersed in distilled water and weighed each hour for 10, 24, 48 and 72 h. The water absorption was calculated as follows:

$$S = (Ws - Wo/Wo) \times 100\% \quad (2)$$

where *S* is water absorption, *Ws* weight swollen sample, *Wo* is the weight of initial gel sample.

Characterization of the Hydrogels

Hydrogels were lyophilized before characterization by Fourier Transform Infrared (FTIR) spectroscopy using KBr pellet prepared by mixing KBr with dried hydrogels samples (10:1 w/w). The TGA analysis was carried out using a Mettler-Toledo TGA/SDTA 851 under inert atmosphere of N_2 from 25 to 600 °C at heating rate of 10 °C min^{-1}. The DSC experiments were carried out using Mettler-Toledo 822e under inert atmosphere of N_2 from 25 to 600 °C at heating rate of 10 °C min^{-1}.

Drug Release

Hydrogels samples were placed in beakers and immersed in 100 mL distilled water and incubated at 37 °C under agitation of 80 rpm. 2 mL aliquots were retained at times intervals of 2, 5, 8, 10 and 15 min, 1, 1.5, 2, 4, 8, 24, and 48 h, and were replaced by 2 mL of distilled water at aliquot. These samples were further analyzed by LC—MS/MS.

LC–MS/MS Analysis and Standard Solution Preparation

HPLC analysis were carried out using Agilent Technologies 1290 Infinity. The chromatographic experiments were performed using an Aquasil C18 column, 100 × 2.1 mm, 5 μ. A mixture of acetonitrile/formic acid mobile phase was applied. The MS–MS system used was AB Sciex 3200 Q Trap equipped with an

electrospray interface (ESI). MS data were recorded in the full scan mode from 250 to 620 m/z. The standard of neomycin was weighed into volumetric flasks and dissolved with the distilled water to produce stock solution at concentration 1 mg mL^{-1} and successive dilutions were carried out to obtain five required concentration (20, 50, 100, 200 and 400 μg mL^{-1}).

Microbiological Test

The efficiency of the hydrogel was tested against Gran positive bacteria *S. aureus* (ATCC 6835). Colonies were incubated at 37 °C in tube to an approximate concentration of 10^8 colony forming units (CFU/mL) and after inoculated in Mueller Hinton agar in Petri dishes [19]. Circular disc hydrogel (control) and hydrogel/neomycin were placed on the bacteria lawn. The dishes were incubated overnight at 37 °C and the antimicrobial activity was observed and zone of inhibition around the disk was measured using ruler.

Results and Discussion

Hydrogel

Synthesis of hydrogel was carried out by gamma radiation in ^{60}Co gamma ray at 25 kGy. The crosslinking induced by ionizing radiation was shown to be a suitable method for the synthesis of hydrogel, inducing the formation of insoluble three-dimensional structure. The technique has advantages such as easy to control the process and relatively low cost process [9, 10] The crosslinking density is proportional to radiation dose, it could be seen hydrogel produced at low dose are smoother than hydrogel produced at high doses. The 25 kGy dose is optimal to ensure the formation of insoluble three-dimensional structure with excellent fluid affinity, elasticity and sufficient to concomitant sterilization of the membrane [21–24].

After irradiation process, gel fraction was determined. The gel fraction (%) of hydrogel and hydrogel/neomycin, both estimated at around 95% gel fraction. The variation of the gel fraction at two different compositions are not significantly different, this indicates that the neomycin did not modify the crosslinking density of the polymer.

Swelling

One of most important characteristic of a hydrogel is swelling capacity without losing its form and the water cannot be removed from hydrogel under pressure [25]. Several parameters affect the swelling ratio such as hydrophilicity attributed to the presence of hydrophilic groups on the polymer chain, stiffness, polymer concentration, plasticizer and irradiation dose. Theses factors modify average molecular weight crosslinks and thus the spaces between them. This influences the structure and water absorption [1, 5, 20]. The swelling can be explained in steps. Swelling increased rapidly during the first period in contact with solution due to the porosity of the crosslinked polymer, enabling water to diffuse rapidly. This relaxation of the polymer chains allows diffusion of the water into the hydrogel interface until saturation, in this moment the maximum swelling is achieved [25]. This makes the structure stable for fluid retention and integrity of wound dressing [1, 5, 9, 26]. The results of swelling of hydrogel as a function of time in distilled water at room temperature can be observed in Fig. 2. The water penetrated and diffused into the hydrogel rapidly in the first few hours and the maximum swelling reached equilibrium about 1100% after 24 h of immersion. Maximum swelling value can be observed above 1000% from expected results with hydrogel at 6% PVP. It is seen that PVP polymer has hydrophilic groups which allow absorption, however, inversely the increase in PVP concentration decreases swelling due to increased crosslinking density by ionizing radiation [5, 26].

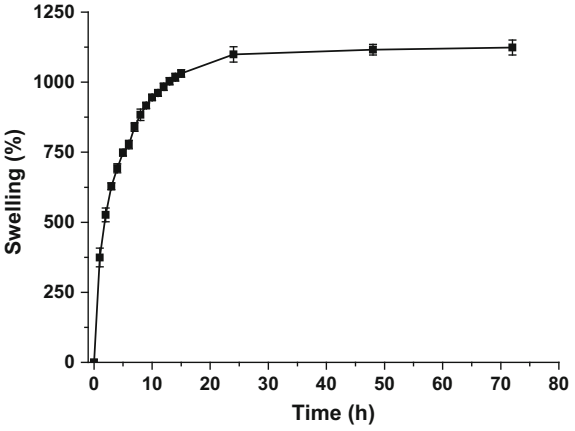

Fig. 2 Swelling curve of hydrogels PVP/Neomycin, obtained by gamma irradiation at 25 kGy

Characterization of the Hydrogel

FTIR

Functional groups of the hydrogel and composition were characterized by FTIR. Figure 3 shows some characteristic peaks of PVP at 1286 cm^{-1} for C–N stretching vibration of amid group, presence of C=O stretching adsorption peaks in 1652 cm^{-1}. According to the literature, vibration carbonyl stretching around 1650 and 1680 cm^{-1} is assigned to the presence of PVP. Peaks between from 3000 to 3500 cm^{-1} are attributed to water presence [27, 28].

Thermal Behavior—Thermogravimetric (TGA)

Thermogravimetry was used to investigate the thermal stability of the composite hydrogel. The TGA curve shows two distinct steps of loss mass, as illustrated in Fig. 4.

These results suggest that during the first step of the thermal degradation, from 25 to 250 °C, the weight loss is due a dehydration process of the water contained in such hydrophilic hydrogels. During the second stage, from 250 to 450 °C, there are the decomposition of the side groups and branches of the hydrogels. In temperature above 450 °C, the weight loss due to the main chain scission of polymeric chain, which resulted in rapid decomposition into carbon dioxide and volatile hydrocarbons. Results show that the hydrogels are thermally stable at temperature up to about 350 °C, which are suitable for most practical uses. The 50% weight loss at above 400 °C is observed and it is assigned to the degradation of hydrogel [29].

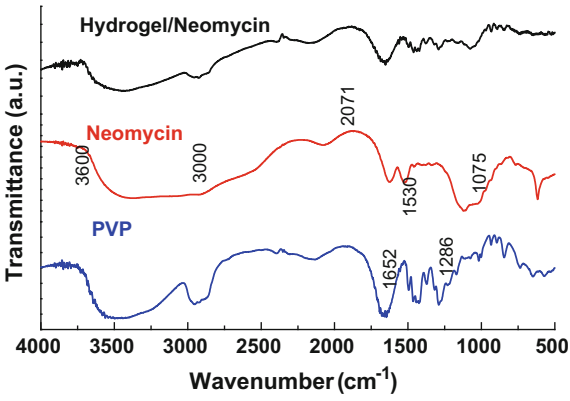

Fig. 3 FTIR spectrum of hydrogel/neomycin, synthesized by gamma irradiation, dose 25 kGy; PVP and neomycin powder

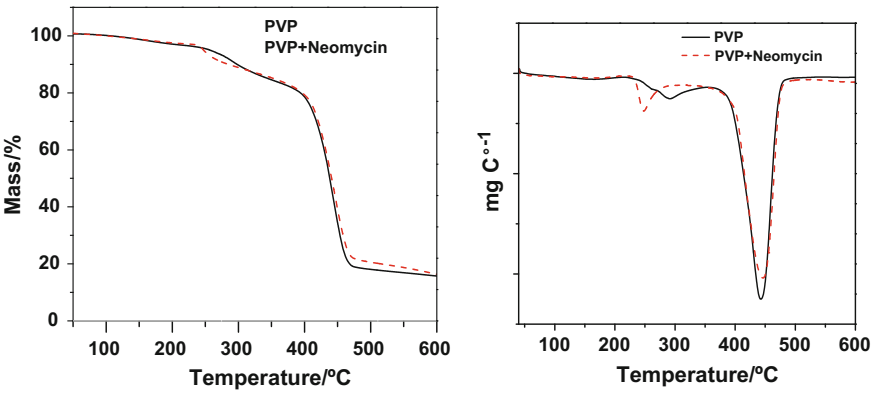

Fig. 4 TGA and DSC curves PVP/neomycin and PVP

Drug Release

LC—MS/MS Method

In this method, a solution of neomycin sulfate at concentration of 10 μg ml^{-1} was studied. The retention time of the neomycin was at 3 min. A neomycin sulfate solution was injected in LC–MS full scan positive ion mode to recognize fragmentation pattern. Peak at 612.3 m/z was attributed to the protonated molecular ion of neomycin [M + H] + (the precursor ion), and five others peaks corresponded to the protonated ions resulting from the proposed fragmentation scheme as presented in Fig. 5 with 615 m/z as the precursor ion. In Fig. 5, it can be observed fragment ions at 259, 277, 293, 323 and 455 m/z [30, 31].

The reference method described in the European and US Pharmacopoeia (USP) is the bioassay method or turbidimetric test, but this method has a low efficiency and reproducibility [30, 32]. Other analytical methods may be used such as the HPLC-MS/MS [33].

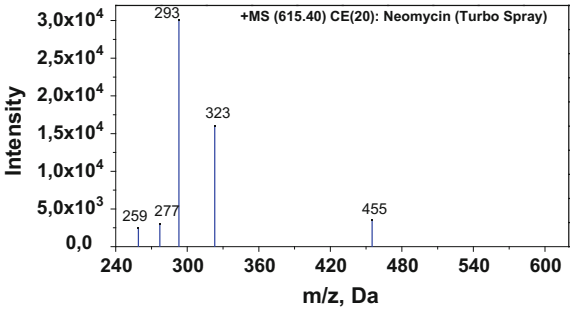

Fig. 5 LC–MS full scan positive ion mode to recognize neomycin fragmentation

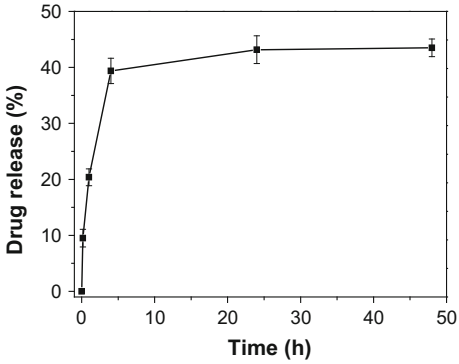

Fig. 6 Kinect of neomycin release in matrices of hydrogel obtained by gamma irradiation

Figure 6 shows the neomycin release from hydrogel evaluated for 48 h. It was observed a fast release of neomycin in the early hours of experiment with the maximum release concentration at 8 h and remained stable up to 48 h. Through this study it can be inferred, the release rate of drug is related to its interaction with three-dimensional network fluid retention. Once neomycin is water soluble, strong interactions with hydrophilic PVP [21, 34]. When water penetrates and diffuses into the hydrogel a relaxation of structure occurs, increasing pore size, which enables neomycin to be released from the system [35]. The result indicates that release neomycin from hydrogel was about 40% and occurred at a prolonged duration, which is required for the development of a dressing with controlled drug release system. With this improvement, the wound dressing is effective to remain on the wound for a longer duration without losing drug efficacy.

Growth Inhibition Test

Growth inhibition tests were performed by disk diffusion method against *S. aureus* strains in triplicate (control, sample 1, 2 and 4). Bacterial was inoculated in Mueller Hinton agar and circular discs hydrogels were carefully placed on the Petri plates. After 24 h incubated, the hydrogel/neomycin exhibited clear zone of inhibition around the disc, obtained strong antibacterial effects compared with the sample without drug.

In Fig. 7 can be observed zone of inhibition in samples 2, 3 and 4, with 22 ± 1 mm diameters. While the control sample (1), without the antibiotic did not present halo. Theses results indicate that the neomycin was released from hydrogel, diffused in agar and bound of to the DNA structure of the bacteria resulting cell lysis. Therefore, the hydrogel could be used in the treatment for infected wounds.

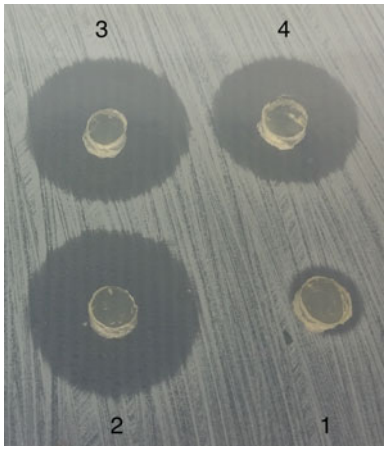

Fig. 7 Antibacterial activity of hydrogel loaded neomycin against *S. aureus* after 24 h of incubation at 37 °C in Mueller Hinton agar. The experiment was carried out in triplicate

Conclusion

The hydrogels obtained by gamma radiation are widely studied due to their potential medical applications. Hydrogels/neomycin have been formulated, characterized and have shown excellent transparency, elasticity, optimal swelling, sustained release of neomycin and consistent antibacterial activity. The presence of neomycin did not affect the physical structure and properties of the hydrogel. TGA analyses and FTIR spectra indicated thermally stability of these hydrogels and showed characteristics peaks of PVP and neomycin.

The drug delivery system released the antibiotic shortly after application of the hydrogel, and reached equilibrium after 8 h. This indicates the formulation and method for producing PVP hydrogel loaded with neomycin are suitable for controlled drug release for wound healing applications. It was observed that hydrogel/neomycin showed antibacterial activity against *S. aureus*. These results were significant and suggest that hydrogel/neomycin are promising candidate for wound treatment application an alternative to conventional topical dressing.

Acknowledgements FAPESP and CAPES for financial support.

References

1. Peppas NA, Huang T, Torres-Lugo M, Wand JH, Zhang J (2000) Physicochemical foundations and structural design of hydrogels in medicine and biology. Annu Rev Biomed Eng 2:9–29
2. Peppas NA, Bures P, Leobandurg W, Ichikawa H (2000) Hydrogels in pharmaceutical formulations. Eur J Pharm Biopharm 50:27–46
3. Dragan ES (2014) Design and application of interpenetrating polymer network hydrogels. A rev Chem Eng J 243:572–590

4. Wictterle O, Lim D (1960) Hydrophilic gels for biological use. Nature 185:117–118
5. Ajji Z, Othman I, Rosiak JM (2005) Production of hydrogel wound dressing using gamma radiation. Nucl Instr Meth Phys Res 229:375–380
6. Villanova JCO, Rodrigo LO, Armando SC (2014) Aplicação farmacêutica de polímeros. Polímeros 20:51–64
7. Halake K, Birajdar M, Kim B, Bae H, Lee C, Kim YJ, Kim S, Ahs S, Lee J (2014) Recent application developments of water-soluble synthetic polymer. Ind Eng Chem Res 20:3913–3918
8. Singh B, Bala R (2014) Polysaccharide based hydrogels as controled drug delivery system for GIT câncer. Int J Biol Macromol 65:524–533
9. Skorupska E, Jeziorna A, Kazmierski S, Potrzebowski MJ (2014) Recent progress in solid-state NMR studies of drugs confiner within drug delivery systems. Solid State Sci 58:2–16
10. Kadlubowski S, Henke A, Ulanski P, Rosiak JM (2010) Hydrogels of polyvinylpyrrolidone (PVP) and poly(acrylic acid) (PAA) synthesized by radiation induced crosslinking of homopolymers. Radiat Phys Chem 79:261–266
11. Hackl EV, Khutoryanskiy VV, Ermolina I (2017) Hydrogels based on copolymers of 2-hydroxyethylmethacrylate and 2-hydroxyethylacrylate as a delivery system for protein: interactions with lysozyme. J Appl Polym Sci 134:1–13
12. Lipsky BA, Hoey C (2009) Topical antimicrobial therapy for treating chronic wounds. Clin Infect Dis 49:1541–1549
13. Frykberg RG, Banks J (2015) Challenges in the treatment of chronic wounds. Adv Wound Care 4:560–582
14. Singh B, Sharma S, Dhiman A (2017) Acacia gum polysaccharide based hydrogel wound dressings: synthesis, characterization, drug delivery and biomedical properties. Carbohydr Polym 165:294–303
15. Yasasvini S, Anusa RS, VedhaHari BN, Prabhu PC, RamyaDevi D (2017) Topical hydrogel matrix loaded with Simvastatin microparticles for enhanced wound healing activity. Mater Sci Eng C 72:60–167
16. Singh B, Varshney L, Francis S, Rajneesh (2017) Synthesis and characterization of tragacanth gum based hydrogels by radiation method for use in wound dressing application. Radiat Phys Chem 135:94–105
17. Gottlieb R, Schimidt T, Arndt RT (2005) Synthesis of temperature sensitive hydrogel blends by high energy irradiation. Nucl Instr Meth Phys Res 236:236–371
18. Huh AJ, Kwon YJ (2011) Nanoantibiotics: a new paradign for treating infections diseases using nanomaterials in the antibiotics resistant era. J Control Release 156:128–145
19. Bazzaz BSF, Khamene B, Behabadi MJ (2014) Preparation, characterization and antimicrobial study of a hydrogel (soft contact lens) material impregnated with silver nanoparticules. Cont Lens Anterior Eye 37:149–152
20. Rosiak JM, Ulanski P, Pajensky LA, Yoshii F, Makuuchi K (1995) Radiation formation of hydrogels for biomedical purpose. Some remarks and comments. Radiat Phys Chem 46:161–168
21. Kilic AG, Malci S, Çelikbiçak O, Sahiner N, Salih B (2005) Gold recovery onto poly (acrylamide-allylthiourea) hydrogels synthesized by treating with gamma radiation. Anal Chim Acta 547:18–25
22. ISO 11137 (2013) Sterilization of health care products radiation—International Organization for Standardization. https://www.iso.org/standard/51238.html. Accessed 10 may 2017
23. Lugao AB, Rogero SO, Malmonge SM (2002) Rheological behaviour of irradiated wound dressing poly(vinyl pyrrolidone) hydrogels. Radiat Phys and Chem 63:543–546
24. Lugao AB, Malmonge S (2001) Use of radiation in the production of hydrogels. Nucl Instr Meth Phys Res 185:37–42
25. Sood S, Gupta VK, Agarwal S, Pathania DKD (2017) Controlled release of antibiotic amoxicillin drug using carboxymethyl cellulose-cl-poly (lactic acid-co-itaconic acid) hydrogel. Int J Biol Macromol 101:612–620

26. Adl-Alla SG, El-Din HMN, El-Naggar AWM (2007) Structure and swelling-release behavior of poly(vinyl pyrrolidona) (PVP) and acrylic acid (AAc) copolymer hydrogel prepared by gamma irradiation. Eur Polym J 43:2987–2998
27. Dergunov SA, Nam IK, Mun GA, Nurkeeva ZS, Shaikhutdinov EM (2005) Radiation synthesis and characterization of stimuli-sensitivechitosan–polyvinyl pyrrolidone hydrogels. Radiat Phys Chem 72:619–623
28. Swathi V, Vidyavathi M, Prasad TNVKV, Kumar RVS (2013) Design, characterization and evaluation of metallic nano biocomposites of neomycin. J Appl Sol Chem Model 2:136–144
29. Abd El-Mohdy HL, Hegazy EA, El-Nesr EM, El-Wahab MA (2013) Metal sorption behavior of polu (N-vinyl-2-pyrrolidone)/(acrylic acid-co-styrene) hydrogel synthesized by gamma radiation. J Environ Chem Eng 1:328–338
30. Oertel R, Renner V, Kirch W (2004) Determination of neomycin by LC-tandem mass spectrometry using hydrophilic interation chromatography. J Pharm Biomed Anal 35:633–638
31. Stypulkowska K, Blazewicz A, Fijalek Z, Warowna-grzeskiewicz M, Srebrzynska K (2013) Determination of neomycin and related substances in pharmaceutical preparation by reversed—phase high performance liquid chromatography with mas spectrometry and charged aerosol detection. J Pharm Biomed Anal 76:207–214
32. United States Pharmacopoeia (2009) The National formulary, Official Monographs, Neomycin Sulfate, USP 32, Convention, Rockville, MD
33. Apyari VV, Dmitrienko SG, Arkhipova VV, Atnagulov AG, Gorbunova MV, Zolotov YA (2013) Label-free nanoparticles for the determination of neomycin. Spectrochim Acta A Mol Biomol Spectrosc 115:416–420
34. Nitanan T, Akkaramongkolporn P, Rojanarata T, Ngawhirunpat T, Opanasopit P (2013) Neomycin-loaded poly(styrene sulfonic acid-co-maleic acid) (PSSA-MA)/polyvinyl alcohol (PVA) ion exchange nanofibers for wound dressing materials. Int J Pharm 448:71–78
35. Choi JS, Kim DW, Kim DS, Kim JO, Yong CS, Cho KH, Youn YS, Jin SG, Choi HG (2016) Novel neomycin sulfate-loaded hydrogel dressing with enhanced physical dressing properties and wound-curing effect. Drug Deliv 23(8):2806–2812

Comparative Mechanical Analysis of Epoxy Composite Reinforced with Malva/Jute Hybrid Fabric by Izod and Charpy Impact Test

Janaína da S. Vieira, Felipe P. D. Lopes, Ygor M. de Moraes, Sergio N. Monteiro, Frederico M. Margem, Jean Igor Margem and Djalma Souza

Abstract Synthetic fibers have been used for many years to attend the demands required by the technological fields. However, the use of them has been questioned due to the impact on the environment. In this way, the natural fibers have received extensive attention, in particular hybrid fabrics of natural fibers to reinforce environmentally friendly polymer matrix composites. Thus, the present work has the objective of evaluating and comparing the mechanical properties of composites formed by hybrid fabric with 70% Malva—30% Jute in epoxy polymer matrix. The tests carried out are the Charpy and Izod Impact Tests, with specimens of 10, 20 and 30% in volume of hybrid fabric environmentally friendly into polymer matrix composites at room temperature. The 30% samples had the best results, functioning as an efficient reinforcement.

Keywords Hybrid fabric · Malva · Jute · Impact tests · Epoxy Polyester

J. da S. Vieira (✉) · F. P. D. Lopes · Y. M. de Moraes · D. Souza
Advanced Materials Laboratory, LAMAV, State University of the Northern Rio de Janeiro, UENF, Av. Alberto Lamego, 2000, Campos dos Goytacazes 28013-602, Brazil
e-mail: janaina.s.vieira@hotmail.com

S. N. Monteiro
Instituto Militar de Engenharia, IME, Praça Gen. Tibúrcio, nº 80 Urca, Rio de Janeiro, RJ 22290-270, Brazil
e-mail: snevesmonteiro@gmail.com

F. M. Margem · J. I. Margem
Faculdade Redentor Rodovia, BR 356. n° 25, Itaperuna, RJ 28.300-000, Brazil

B. Li et al. (eds.), *Characterization of Minerals, Metals, and Materials 2018*, The Minerals, Metals & Materials Series,
https://doi.org/10.1007/978-3-319-72484-3_19

Introduction

The first known composite material used by human was clay reinforced by tree branches some 3000 years ago. However, materials with better performance have been intensively used and developed, reducing interest in natural fiber composites [1].

Recently, the use of natural fiber composites began to gain in popularity in engineering applications, because of their properties, such as low density, low cost and easy workability, and more importantly it come from renewable sources and are biodegradable [2]. Certain natural fibers have already been used in the automotive sector [3, 4].

However, the down side of natural fibers include they are hydrophilic while the polymer matrices are hydrophobic, thereby making it more difficult to bond well with the resin [5]. The objective of this work is to analyze the Izod and Charpy impact resistance of the epoxy composites with hybrid blanket—70% of Malva fibers and 30% Jute fibers.

Experimental Procedures

Materials

The materials used in this work were the commercial epoxy resin DGEBA /TETA, from the company Resinpoxy and the 70% Malva /30% Jute hybrid fabric (MJHF) was purchased from the company Permantec localized in California. In Fig. 1 it can be seen the 70% Malva /30% Jute hybrid blanket.

The weight average formula, Eq. 1, was used to determine the density hybrid malva/jute fabric.

Fig. 1 The 70% malva /30% jute hybrid blanket

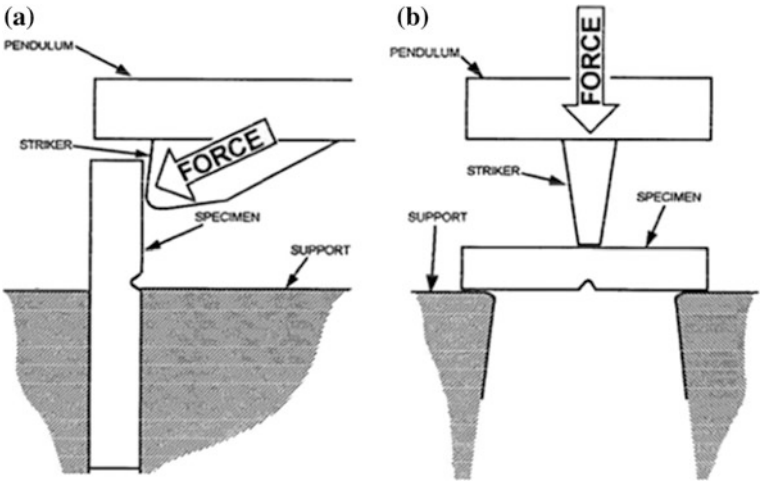

Fig. 2 The Izod **a** and the Charpy **b** impact test methods

$$X_w = \sum_{i=1}^{n} \frac{x_i w_i}{w_i} \tag{1}$$

Impact Test

According to the ASTM D 256-84, there are significant differences between both tests, Izod and Charpy impact test, that can lead to distinct results [6]. These differences are shown in Fig. 2.

This figure reveals that the Charpy specimen, with a minimum length of 124 mm, is freestanding on the support during the impact with a hammer, which strikes exactly at the opposite side of the notch, Fig. 2b. By contrast, the Izod specimen has a maximum length of 63 mm and it is fixed to the support during the impact, Fig. 2a, which strikes at a point 22 mm away from the notch. In practice, the Izod test simulates better the actual situation of a component fixed into a system, which is hit at a point away from a stress concentrators as groves or flange. The test was done through using the Pantec model XC-50 machine with hammer 2,7 J at room temperature.

Procedures

For the perform of the tests, ten specimens for each percentage of fiber were made.

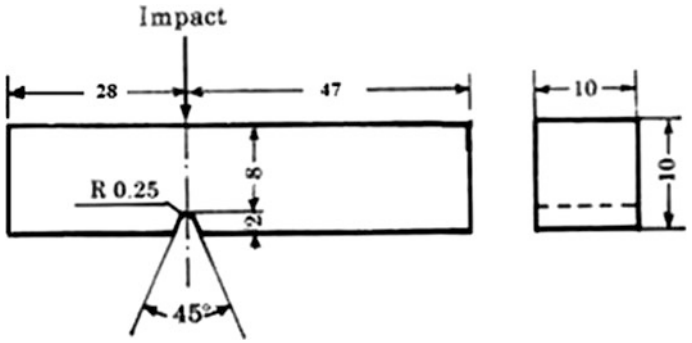

Fig. 3 Izod test standard specimen

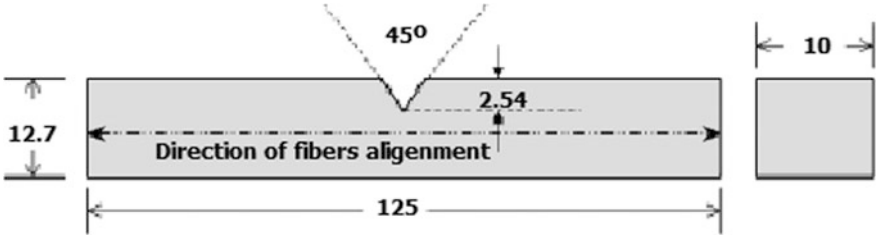

Fig. 4 Charpy test standard specimen

ASTM D256/ISO R180 and ASTM D6110 were followed in performing Izod impact test and Charpy impact test.

Fabric was cut to 62 × 12.7 mm in size to prepare the composites with 10, 20 and 30% MJHF, the fabric was then soaked with bisphenol A (DGEBA) cured diglycidyl ether (TETA) epoxy resin in the stereometric ratio of 13 parts of hardener to 100 parts of resin. The matrix was subjected to press with 2.5 tons for 24 h.

After curing, the specimens were cut according to ASTM D256 (Fig. 3), sanded, measured, numbered and subsequently subjected to the Izod impact test. And according to ASTM D6110 (Fig. 4), they were sanded, measured, numbered and subsequently subjected to the Charpy impact test.

Fiber Surface Analysis

The surface of representative specimen was analyzed by scanning electron microscopy (SEM).

Results

Table 1 presents the result of the hybrid fabric density based on percentage of its constituents fibers.

Table 2 shows the average of the Izod and Charpy impact test results on 100% epoxy, 10, 20 and 30% MJHF.

Based on the results presented in Table 2, the variation of the Izod impact energy with the changing of the specimens is shown in Fig. 5.

Based on the results presented in Table 2, the variation of the Charpy impact energy with the according to the specimens types is shown in Fig. 6.

In this figure, it is noted that the incorporation of hybrid fabric in the epoxy matrix significantly improves the impact strength of the composite. The relatively high dispersion of the values given by the error bars associated with higher fiber percentage points is a well-known characteristic of non-uniform lignocellulosic fibers [9].

Table 1 Hybrid fabric density

Material	Density (g/cm^3)	References
Malva	1.04	Margem [7]
Jute	1.30	Bledzki and Gassan [8]
Malva/jute hybrid fabric	1.12	This work

Table 2 Average of the Izod and charpy impact test results

MFHF percentage (%)	Izod impact energy (J/m)	Charpy impact energy (J/m)
0	31 ± 3.9	22 ± 3.6
10	112 ± 8.6	98 ± 9.8
20	148 ± 12.8	158 ± 11.8
30	198 ± 11.5	186 ± 15

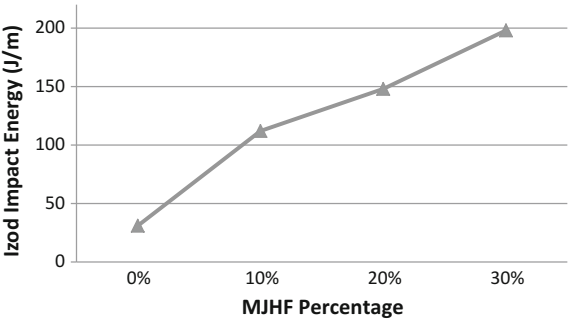

Fig. 5 Graph of the Izod impact test results in function of different reinforcement percentages

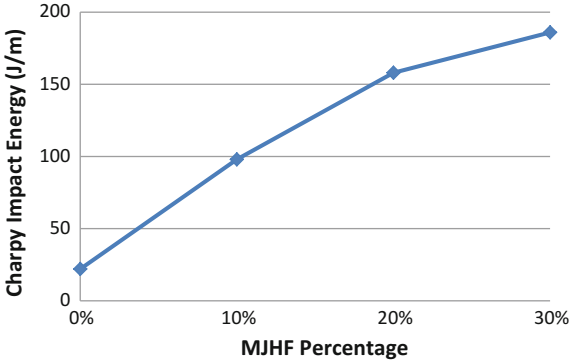

Fig. 6 Graph of the charpy impact test results in function of different reinforcement percentages

Limitation the interface interaction between polymeric matrix, hydrophobic, and the fabric, hydrophilic, contributes to an ineffective charge transfer from the matrix to natural fibers.

The incorporation of MJHF results in a marked change with respect to the pure epoxy (0% MJHF) where a transverse rupture occurs fully. This indicates that the nucleated cracks in the slot initially spread transversely across the epoxy matrix, as it is expected in a monolithic polymer [10]. However, when the front of the crack reaches a fiber, the break will continue through the interface. As a result, after the Izod hammer hitting the sample, some fibers will be pulled out of the matrix, but due to their compliance, it will not break, but simply fold. This feature allows the system to absorb more energy due to the flexibility of the fiber that slides out of the matrix, which amplifies the energy needed to break the sample [11, 12].

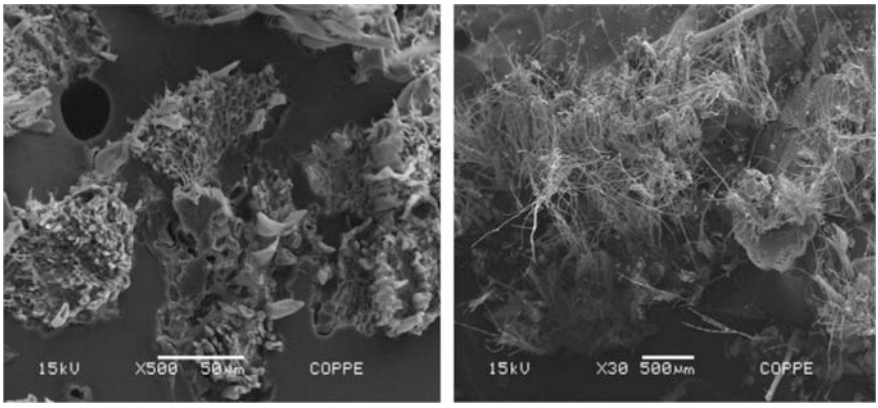

Fig. 7 Scanning electron microscopy (SEM) of the MJHF with ×500 and ×30

Figure 7 shows Scanning Electron Microscopy (SEM) investigation.

Figure 7 shows the fiber imperfections, voids and irregularities in the all fractures surface.

Conclusions

- Compared to pure epoxy specimen, composites of epoxy matrix, exhibit a significant increase in resistance when reinforced with Malva/Jute hybrid fabric.
- This increase is due to the low interfacial shear strength of the tensioned epoxy matrix /fabric. This results in increased energy absorbed when longitudinal cracks along the interface, which leads to larger areas of rupture compared to a transverse fracture.

References

1. Sapuan SM, Maleque MA (2005) Design and fabrication of natural woven fabric reinforced epoxy composite for household telephone stand. Mater Des 26:65–71
2. Joshi SV, Drzal LT, Mohanty AK, Arora S (2004) Are natural fibre composites environmentally superior to glass fibre reinforced composites? Compos Pat A 35:371–376
3. Monteiro SN, Ferreira AS, Lopes FPD (2008) A comparative study of curaua fiber reinforced epoxy matrix composites as building materials. In: Proceedings of the global symposium on recycling, waste treatment and clean technology—REWAS2008 (Cancun, Mexico, October 2008) 1653–1658
4. Monteiro SN, Satyanarayana KG, Lopes FPD (2010) High strength natural fibers for improved polymer matrix. Mat Sci Forum 638–642:961–966
5. Monteiro SN, Lopes FPD, Ferreira AS, Nascimento DCO (2009) Natural fiber polymer matrix composites: cheaper, tougher and environmentally friendly. JOM 61(1):17–22
6. ASTM D 256-84 (1984) Standard test method for impact resistance of plastic and electrical insulating materials. ASTM, USA, pp 81–102
7. Margem JI (2013) Estudo Das Características Estruturais E Propriedades De Compósitos Poliméricos Reforçados Com Fibras De Malva. Campos dos Goytacazes. Thesis [Doctorate degree] - UENF
8. Bledzki AK, Gassan J (1999) Composite reinforced with cellulose based fibres. Prog Polym Sci 24:221–274
9. Satyanarayana KG, Sukumaran K, Kulkarni AG, Pillai SGK, Rohatgi PK (1999) Fabrication and properties of natural fibre-reinforced polyester composites. Composites 17:329–333
10. Monteiro SN, Costa LL, Terrones LAH (2008) Annual meeting & exhibition conference: characterization of minerals, metals, and materials (TMS). New Orleans 09–13 Mar 2008. In: Proceeding… New Orleans 2008. Loisiana (USA), p 1
11. Fu SY, Lauke B, Mäder E, Hu X, Yue CY (1999) Fracture resistance of short-glass-fiber-reinforced and short-carbon-fiber-reinforced polypropylene under charpy impact load and its dependence on processing. J Mater Process Technol 89(90):501
12. Leão AL, Tan IH, Caraschi JC (1998) International conference on advanced composites. Hurghada 15–18 Dec 1998. In: Proceeding… Hurghada 1998. Egypt, p 557

Comparison Between Epoxy Matrix Composites Reinforced with Ramie Fabric Under Pressure and Vacuum

Caroline G. de Oliveira, Janine F. de Deus, Felipe P. D. Lopes, Lucas A. Pontes, Frederico M. Margem and Sérgio N. Monteiro

Abstract For decades, natural fibers have been studied as an economical and environmentally viable alternative to use instead of some types of synthetic fibers, for example fiberglass. To find the best way to make composites, the investigations shall be under various configurations, which is extremely important to understand the potentialities and facilities. To aim the comparison of impact performance of epoxy matrix composites reinforced with ramie fabric, the composites were produced by two different methodologies: under pressure and vacuum. The results show that the composites produced under pressure have greater resistance to both the Charpy and Izod Impact than under vacuum conditions.

Keywords Natural fibers · Composites · Impact resistance · Izod Charpy

C. G. de Oliveira (✉) · J. F. de Deus · F. P. D. Lopes · L. A. Pontes
Advanced Materials Laboratory, LAMAV, State University of the Northern Rio de Janeiro, UENF, Av. Alberto Lamego, 2000, Campos dos Goytacazes RJ 28013-602, Brasil
e-mail: caroline.oliveyra@gmail.com

J. F. de Deus
e-mail: janinefd@globo.com

F. P. D. Lopes
e-mail: felipeperisse@gmail.com

L. A. Pontes
e-mail: lucasdealmeidapontes@gmail.com

F. M. Margem
Faculdade Redentor Rodovia, BR 356. n° 25, Itaperuna, RJ-28 300-000, Brasil
e-mail: fmargem@gmail.com

S. N. Monteiro
InstitutoMilitar de Engenharia, IME, Praça Gen. Tibúrcio, n° 80 Urca, Rio de Janeiro, RJ 22290-270, Brasil
e-mail: snevesmoteiro@gmail.com

B. Li et al. (eds.), *Characterization of Minerals, Metals, and Materials 2018*, The Minerals, Metals & Materials Series,
https://doi.org/10.1007/978-3-319-72484-3_20

Introduction

In the current world scenario, factors such as technological development, population growth and increasing industrial activities in the last decades, lead to a growing concern with global issues like worldwide pollution and climate changes [1]. This makes the search for sustainable solutions associated with high-performance a global trend. With this regard, the replacement of synthetic materials by natural ones is a promising alternative. In the past decades, natural lignocellulosic fibers, obtained from plants widely cultivated around the world, have emerged as a potential alternative to the use of synthetic fibers as polymer matrix reinforcement.

Several studies in the last decade demonstrated that natural lignocellulosic fiber composites result in cheaper, lighter and more resistant materials when compared to fiberglass composites, steadily used in many engineering sectors [2, 3]. Besides that, they are environmentally friendly, biodegradable, renewable and less abrasive to processing equipment. It worth noting that, unless glass fibers, the natural fibers present CO_2 neutrality and are not toxic to the operators [4–10].

Among the natural fibers, ramie (Boehmeria nivea) is one of the most resistant, which can reach a tensile strength higher than 1000 MPa [5] and elastic modulus of 44 GPa [11]. Moreover, epoxy matrix composites reinforced with ramie fibers reached 102.26 MPa for 30% of fibers in tensile tests. Another possible configuration for the use of natural fiber is as its fabric (Fig. 1), instead of its aligned fibers. The fabric provides multidirectional reinforcement and also grants the introduction of higher volume fraction of reinforcement material. This new structure, considering the use of ramie fabric, has already been tested for bulletproof panels and jackets [12].

One of the most common industrial applications of natural fibers composites nowadays is in the automotive industry, which already widely applies them in various internal parts, such as front and door panels, package trays, seat backs, head-rest, and trunk liners [13, 14]. In this regard, the natural flexibility of natural fibers can be considered an important technical advantage. In a situation of a crash

Fig. 1 As-received ramie fabric

event, the flexible natural fibers are able to absorb more energy than the glass fibers, which have brittle behavior. It avoids that automobile parts, such as the interior front panel, have a brittle rupture during an accident, splitting into sharp pieces and injuring the passengers [15]. Thus, it is extremely important to investigate the response of natural fiber composites to a range of stresses, in order to enable its use in more industry sectors.

Aiming to further improve the performance of the natural fiber composites, this work studied the performance of composites reinforced with ramie fabric under Izod and Charpy stresses, manufactured in two configurations: under pressure and under vacuum. The comparison between both materials revealed that the composites produced under vacuum presented higher impact resistance, leading to conclude that, so far, vacuum is the most efficient manufacturing methodology.

Experimental Procedures

The ramie fabric was purchased from a Chinese company Rose Natural Healthy Items Wholesale. The epoxy DEGEBA/TETA resin was supplied by Resinpoxy. First, the ramie fabric was manually cleaned for the removal of solid waste from the transport. Then, two methodologies were adopted for the production of the test specimens: under pressure and under vacuum.

In the first methodology (under pressure), the fabric was cut in the impact molds format and then dried in an oven at 120 °C for about 1 h. After, the epoxy resin was mixed with the catalyst/hardener DEGEBA/TETA according to the manufacturer's instructions and the fabric layers were pressed with enough quantity of resin to guarantee total impregnation. Then new layers of still liquid resin and ramie fabric were alternated into the Charpy and Izod impact molds. The specimens were cured for 24 h at room temperature. Both Izod and Charpy impact tests were carried out in a pendulum Pantec set to the respective configurations.

In the second methodology (under vacuum), the fabric was cut in 15 cm × 13 cm rectangles and then dried in an oven at 120 °C for about 1 h and the epoxy resin was mixed with the catalyst/hardener DEGEBA/TETA according to the manufacturer's instructions. The first layer of ramie fabric was positioned into the mold and embedded in resin; the subsequent layers were then positioned and the procedure was repeated until the last layer were placed. After, the perforated film, the absorbent film and the peel ply were positioned and the system was sealed with tacky tape. Finally, the system was subjected to vacuum with the aid of a vacuum pump (Fig. 2). The cure lasted 24 h at room temperature and the specimens were cut from the plate into the Charpy and Izod specimens dimensions. Both Izod and Charpy impact tests were carried out in a pendulum Pantec set to the respective configurations.

For both methodologies, the percentage of ramie fabric is 35% in volume.

The tested specimens were metallized and analyzed by scanning electron microscoping (SEM) under a voltage of 15 kV for the electron beam.

Fig. 2 Under vacuum methodology set

Results and Discussion

The macroscopic analysis of the Charpy test specimens for both methodologies shows that the fracture was transversal to its thickness, with small deviations in some cases, characterizing a brittle fracture. It can also be observed that the rupture of the specimen was complete without fabric involvement, indicating that the pull out effect (reinforcement sliding out of the matrix before the fibers break) does not occur (Fig. 3).

The results show that both methodologies are effective in reinforcing the epoxy matrix under impact stress. The values obtained by the tests can be seen in Table 1.

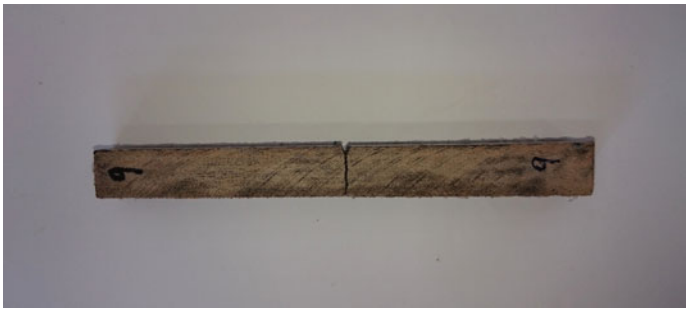

Fig. 3 Specimen after charpy impact test

The introduction of the fabric increased by more than ten times the impact resistance of the material for the under pressure methodology, and by more than five times for the under vacuum methodology, compared to the neat epoxy matrix and considering the statistic error. This increase in impact strength can be attributed to fabric layers acting as a barrier to crack propagation, making it necessary to provide a much higher amount of energy to rupture the composite than to break the epoxy, which offers low resistance to the propagation of cracks, characteristic of thermosetting resins [16].

Although the methodology of production under pressure is effective reinforcing the epoxy matrix, this methodology does not guarantee the complete elimination of micro air bubbles from the arrangement of the fabric layers, in fact: in some cases it can trap the microbubbles. The continuous application of vacuum ensures not only the complete impregnation of the fabric by the resin, but also the elimination of practically all microbubbles present. This explains why the impact resistance is lower in the composite produced under vacuum: the elimination of practically all the micro air bubbles increases the adhesion between the fabric and the matrix, making the material more compact and more rigid. It means that the crack propagation occurs in a shorter trajectory, requiring less energy to rupture the material.

Although natural fibers (including ramie fiber) generally exhibit low adhesion to the matrix, slipping does not occur in this case. This is possibly due to the interwoven configuration of the fabric, which contributes to the fabric being retained in the matrix. While fibers aligned to the direction of stress tend to slip from the matrix, the transverse fibers (at 90°) do not undergo this effect and help to retain the fabric in the matrix. In this way, the fabric fibers rupture without slipping from the matrix. It can be evidenced in Fig. 4.

It can be seen in Fig. 4a that the fabric fibers ruptured approximately parallel to the point where the matrix fractured, which evidences that the pull out effect did not occur. It is also possible to observe the characteristic marks of the brittle fracture, called “river patterns” and how the fibers deviate the propagation of the crack. This deviation is even more evident in Fig. 4b.

The Izod impact tests have shown very similar results. In Fig. 5 it can be seen the fracture of Izod impact test specimen, which is typically brittle with some deviations and with total rupture of the matrix and the fabric.

The results, just like in the Charpy test, showed that both methodologies are effective as reinforcement for the epoxy matrix, increasing its impact resistance. It was also observed that the composites produced under vacuum presented an impact

Table 1 Charpy impact resistance for the epoxy matrix and for the reinforced composite with ramie fabric for both methodologies

Material	Charpy impact resistance (J/m)
Epoxy matrix	23.09 ± 4.78
Composite under pressure	252.56 ± 28.40
Composite under vacuum	8536 ± 1156

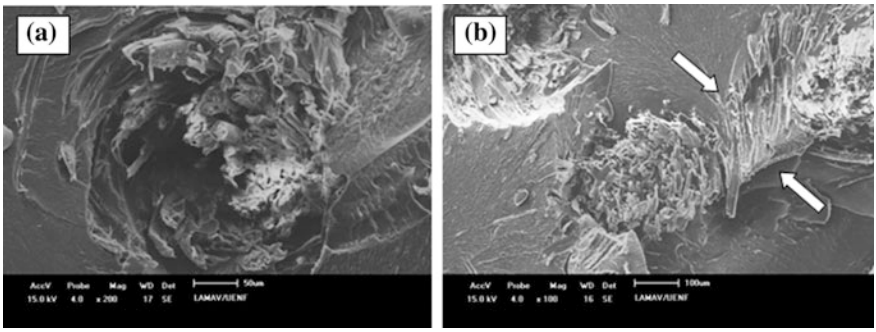

Fig. 4 Micrograph of the fracture surface of the reinforced composite with ramie fabric after the charpy impact test with **a** 200× and **b** 100× magnification

Fig. 5 Specimen after Izod impact test

resistance about 4.5 times greater than the neat matrix and the composites produced under pressure presented a resistance about 8 times greater, considering the statistic error. The results obtained from the Izod impact test can be seen in Table 2.

Figure 6 shows the micrographs of Izod impact specimens after the test, where it can be seen that, when encountering the fibers of the fabric, the crack is deviating. It may also be observed that the fibers of the fabric break at approximately the same height as the matrix, confirming that the slip between the matrix and the fiber does not occur also for the Izod impact test.

The difference in reinforcement ratio in the two types of test is probably due to the difference in stress application and hence the difference in the response of the

Table 2 Izod impact resistance for the epoxy matrix and for the reinforced composite with ramie fabric for both methodologies

Material	Izod impact resistance (J/m)
Epoxy matrix	1964 ± 501
Composite under pressure	114.78 ± 22.60
Composite under vacuum	5673 ± 1014

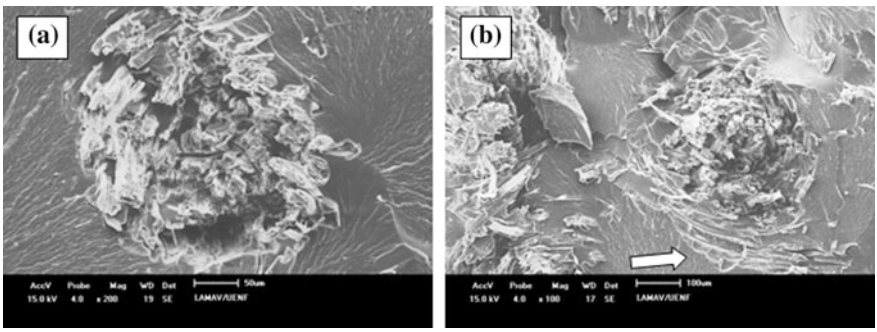

Fig. 6 Micrograph of the fracture surface of the reinforced composite with ramie fabric after the Izod impact test with **a** 200× and **b** 100× magnification

material to two different stresses. However, it is noteworthy that in both cases the presence of the fabric significantly increased the epoxy matrix impact resistance and again in both cases the composites produced under pressure have presented higher values for this property than those produced under vacuum.

Conclusions

- The introduction of the ramie fabric showed to be effective in increasing the epoxy matrix impact resistance (both Charpy and Izod), demonstrating a higher gain in the Charpy impact resistance.
- The composites produced under pressure showed to be even more effective as a reinforcement material, presenting higher values of impact resistance when compared to those produced under vacuum.
- The adhesion between the fabric and the matrix is considerable and the pull-out effect does not occur. The fabric fibers serve as barriers, deflecting the crack during its propagation.

Acknowledgements The authors thank to the Brazilian agencies: CNPq, CAPES, FAPERJ.

References

1. Gore A (2006) An inconvenient truth. The planetary emergency of global warming and what we can do about it. Rodale Press, Emmaus, PA
2. Wambua P, Ivens I, Verpoest I (2003) Natural fibers: can they replace glass in fibre reinforced plastics? Compos Sci Technol 63:1259–64

3. Monteiro SN, Lopes FPD, Ferreira AS, Nascimento DCO (2009) Natural fiber polymer matrix composites: cheaper, tougher and environmentally friendly. JOM 61:17–22
4. Summerscales J, Dissanayake N, Virk AS, Hall W (2010) A review of bastfibres and their composites. Compos Part A 41:1329–44
5. Monteiro SN, Lopes FPD, Barbosa AP, Bevitori AB, Silva IL, Costa LL (2011) Natural lignocellulosic fibers as engineering materials—an overview. Metall Mater Trans A 42: 2963–74
6. Faruk O, Bledzki AK, Fink H-P, Sain M (2012) Biocomposites reinforced with natural fibers: 2000–2010. Progr Polym Sci 37:1552–96
7. Shah DU (2013) Developing plant fibre composites for structural applications by optimizing composite parameters: a critical review. J Mater Sci 48:6083–107
8. Thakur VK, Thakur MK, Gupta RK (2014) Review: raw natural fibers based polymer composites. Intern J Polym Anal Charact 19:256–71
9. Güven O, Monteiro SN, Moura EAB, Drelich JW (2016) Re-emerging field of lignocellulosic fiber-polymer composites and ionizing radiation technology in their formulation. Polym Rev 56:702–36
10. Pickering KL, Efendy MGA, Le TM (2016) A review of recent developments in natural fibre composites and their mechanical performance. Compos Part A 83:98–112
11. Satyanarayana KG, Guimarães JL, Wypych F (2007) Studies on lignocellulosic fibers of Brazil. Part I: Source, production, morphology, properties and applications. Compos Part A, 38:1694–709
12. Bevitori, AB, da Silva, IL, Simonassi, NT, Oliveira CG, Margem FM, Monteiro SN (2013) Tensile behavior of epoxy composites reinforced with continuous and aligned ramie fibers. In: Proceedings of the characterization of materials metals and materials—TMS annual meeting San Antonio, TX, USA, March, 2013 pp 465–71
13. Holbery J, Houston D (2006) Natural-fiber-reinforced polymer composites in automotive applications. JOM 58:80–6
14. Zah R, Hischier R, Leao AL, Braun I (2007) Curauá fibers in the automobile industry – a sustainability assessment. J Clean Prod 15:1032–40
15. Joshi SV, Drzal LT, Mohanty AK, Arora S (2004) Are natural fiber composites environmentally superior to glass fiber reinforced composites? Compos Part A 2004 35:371–6
16. Mallick CK (2007) Fiber-reinforced composites—materials, manufacturing and design. LLC, Boca Raton, FL

Charpy Impact Test in Polyester Matrix Composites Reinforced with Hybrid Blanket of the Jute and Malva Fibers

Jean Igor Margem, Ygor Macabu de Moraes, Frederico Muylaert Margem, Sergio Neves Monteiro and Marina Rangel Margem

Abstract Natural fibers presents interfacial characteristics with polymeric matrices that favor a high impact energy absorption by the composite structure. The objective of this work was then to assess the charpy impact resistance of polymeric composites reinforced with one or two layers of batt jute and malva fibers. The results showed a remarkable increase in the notch toughness with increasing layers of jute blankets and malva. This can be attributed to a preferential debonding of the fiber/matrix interface, which contributes to an elevated absorbed energy.

Keywords Charpy testing · Hybrid blanket of the jute and malva Composite · Polyester matrix · Notch toughness

Introduction

Natural fibers with high cellulose content, known as lignocellulosic fibers, become firmly established as a potential replacement for the search field of synthetic fibers, particularly glass fiber [1].

J. I. Margem (✉)
Instituto de Ensino Superiores do Censa, ISECENSA, Rua Salvador Correa, nº 139, Campos dos Goytacazes, Rio de Janeiro 28035-310, Brazil
e-mail: igormargem@gmail.com

Y. M. de Moraes · F. M. Margem
LAMAV, State University of the Northern Rio de Janeiro, UENF, Av. Alberto Lamego, nº 2000, Campos dos Goytacazes 28013-602, Brazil

S. N. Monteiro
Instituto Militar de Engenharia, IME, Praça Gen. Tibúrcio, nº 80, Urca, Rio de Janeiro, RJ 22290-270, Brazil

M. R. Margem
Universidade Federal Fluminense, UFF, Rua Miguel de Frias nº 9, segundo andar, Icaraí, Niterói, Rio de Janeiro, RJ 24220-900, Brazil

B. Li et al. (eds.), *Characterization of Minerals, Metals, and Materials 2018*, The Minerals, Metals & Materials Series,
https://doi.org/10.1007/978-3-319-72484-3_21

The use of natural fibers to replace the existing, present especially in aircraft and cars, is motivated by several advantages such as good toughness and less abrasion equipment used in processing composite [2–6].

Among these features is the low cost and lightweight. In addition, unlike the glass fibers [7] lignocellulosic fibers are relatively flat and the processing procedures produce less wear on equipment. The environmental issue is another point in favor of natural fibers, which are renewable, recyclable, biodegradable and neutral with regard to CO_2 emissions [8, 9].

The incorporation of banana fibers in polymeric matrices of composite was 30 investigated [10, 11, 12] and found to have significant properties. These properties 31 are directly related to the microstructure of the fiber as well as the physical and 32 chemical characteristics present in any lignocellulosic fiber [13–17].

The objective of this study was a preliminary assessment through different measures Charpy impact energy, together with the micro structural characteristics associated with the fracture of polyester matrix composites with blanket of the jute and malva fibers.

Experimental Procedure

The materials used in this work were blanket of the jute and malva fibers which was Acquired by a producer, Pematec Triangel, from the Southeast region of Brazil (Fig. 1).

The blanket comprises 40% jute fiber and 60% of Malva fiber. The fiber of jute (*Corchorus capsularis*) is a vegetable textile fibers, this woody herb reaches 3–4 m in height and its stalk is approximately 20 mm. It is used mainly in sacks industry, due to resistance and strength of its fiber is also used in the furniture industry.

Fig. 1 Blanket of the jute and malva fibers

Already Malva fiber belongs to a botanical genus of several species of herbaceous Malvaceae family, is distributed geographically by tropical, subtropical and temperate regions, the leaves are alternate, lobed and usually slaps and measure half to 5 cm. Its raw material is mainly used in the wireless industry and natural fibers packaging [16, 17].

The polyester resin still liquid, together with 0.5% catalyst based on methyl ethyl ketone, was poured into the one and two layers of the blanket inside the mold. The composite thus formed was allowed to cure for 24 h at room temperature. The plates of each composite were then cut according to the direction of fiber alignment in bars measuring 10 × 125 × 12.7 mm were used as basis for preparation of test samples Charpy impact test according to ASTM D256 [18–20].

The samples were assayed in a pendulum of the Charpy brand Pantec in configuration belonging to the LAMAV UENF. The impact energy was obtained in power hammer with 11 J for composites. For each condition, relative to a certain fraction of fibers, 10 specimens were used and the results were statistically interpreted (Fig. 2).

The impact fracture surface of the specimens was gold sputtered and analyzed by scanning electron microscopy, SEM, in a model SSX-500 Shimadzu microscope with secondary electrons imaging at an accelerating voltage of 15 kV.

Results and Discussion

Table 1 shows the results of the values of Charpy impact energy with their respective standard deviations for pure polyester and composites with up to two batt layers.

Based on the results of Table 1, the change in Charpy impact energy with layers of the blanket this shown in Figs. 3 and 4.

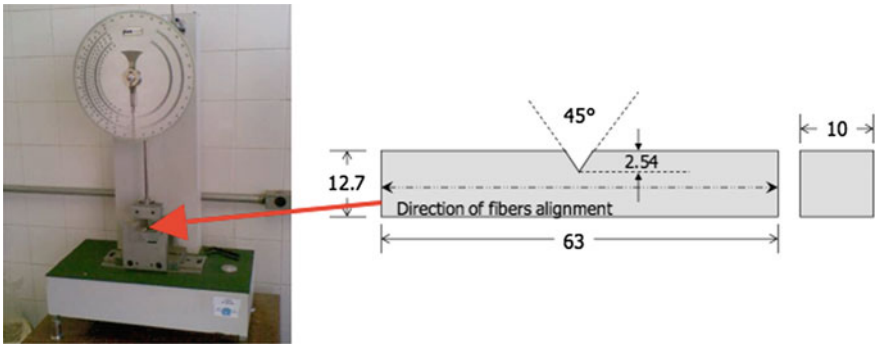

Fig. 2 Charpy equipment and standard specimen schematic

Table 1 Energy impact charpy for polyester matrix reinforced with blanket of the jute and malva fibers

Layers of the blanket of jute and malva fibers	Charpy impact energy (J/m)
0	22.9 ± 6.19
1	38.7 ± 28.96
2	58.9 ± 41.87

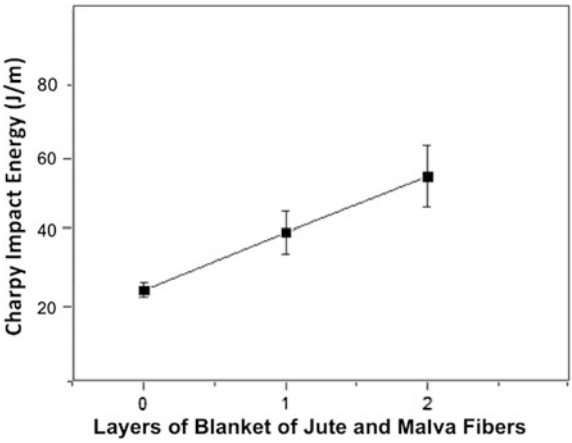

Fig. 3 Charpy impact energy as a function of the amount of blanket of the jute and malva fibers

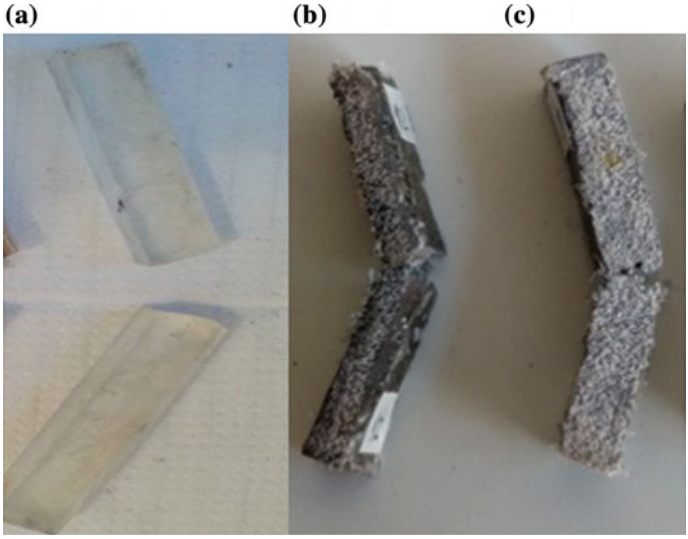

Fig. 4 Macrostructural aspects of charpy impact rupture polyester matrix composites with net polyester **a** one layers **b** and two layers **c** of the jute and malva blanket incorporated

Conclusions

- Polyester matrix composites reinforced with jute and malva blanket, show a linear increase in toughness as measured by Charpy impact test.
- Increase in toughness is apparently due to the low shear stress at the interface between the blanket of jute and malva and polyester matrix.
- The increase energy absorbed due to propagation of longitudinal cracks through the interface generates a larger fracture area when compared to the simple transverse fracture.
- The incorporation of one or two layers of the blanket of jute and malva is associated with incomplete specimens fracture due to the jute and malva fibers that curves but no rupture during impact.

Acknowledgements The authors thank the support to this investigation by the Brazilian agencies: CNPQ, CAPES, FAPERJ and TECNORTE/FERNORTE.

References

1. Bledzki AK, Gassan J (1999) Composites reinforced with cellulose-based fibres. Prog Polym Sci 24:221–274
2. Nabi Sahed D, Jog JP (1999) Natural fiber polymer composites: a review. Adv Polym Technol 18:221–274
3. Mohanty AK, Misra M, Hinrichsen G (2000) Biofibres, biodegradable polymers and biocomposites: an overview. Macromol Mater Eng 276:1–24
4. Crocker J (2008) Natural materials innovative natural composites. Mater Technol 2–3(3): 174–178
5. Monteiro SN, Lopes FPD, Ferreira AS, Nascimento DCO (2009) Natural fiber polymer matrix composites: cheaper, tougher and environmentally friendly. JOM 61(1):17–22
6. Gore A (2006) An inconvenient truth. The planetary emergency of global warming and what we can do about it. Rodale Press, Emmaus, PA
7. Peijs T (2000) Natural fibers based composites. Mater Technol 15:281–285
8. Wambua P, Ivens I, Verpoest I (2003) Natural fibers: can they replace glass and fiber reinforced plastic? Compos Sci Technol 63:1259–1264
9. Mohanty AK, Misra M, Drzal LT (2002) Sustainable biocomposites from renewable resources: opportunities and challenges in the green materials world. J Polym Environ 10: 19–26
10. Satyanarayana KG, Sukumaran K, Kulkarni AG, Pillai SKG, Rohatgi PK (1999) Fabrication and properties of natural fibre-reinforced polyester composites. Composites 17:329–333
11. Callister WD Jr (2000) Materials science and engineering—an introduction, 5a Edição, Wiley, Nova York
12. Fu SY, Lauke B, Mäder E, Hu X, Yue CY (1999) Fracture resistance of short-glass-fiber-reinforced and short-carbon-fiber-reinforced poly-propylene under charpy impact load and dependence on processing. J Mater Process Technol 89–90:501–507
13. Leão AL, Tan IH, Caraschi JC (1998) Curaua fiber—a tropical natural fiber from Amazon—potential and applications in composites. In: International conference on advanced composites, Hurghada, Egito, Maio, 1998, pp 557–564

14. Monteiro SN, Costa LL, Lopes FPD, Terrones LAH (2008) Characterization of the impact resistance of coir fiber reinforced polyester composites. In: Mineral, metals & materials characterization symposium—TMS conference, New Orleans, LA, USA, Março, 2008, pp 1–6
15. Yue CY, Looi HC, Quek MY (1995) Assessment of fibre-matrix adhesion and interfacial properties using the pullout test. Int J Adhes Adhes 15:73–80
16. Margem JI, Monteiro SN, Margem FM, Ribeiro CG, Moraes Y (2017) Izod impact tests in polyester matrix composites reinforced with blanket of the malva and jute fibers. In: Characterization of minerals, metals, and materials—soft materials—TMS conference, San Diego, CA, USA, February, 2017, pp 89–90
17. Margem JI, Monteiro SN, Margem FM, Ribeiro CG, Moraes Y (2016) Tensile strength tests in epoxy composites with high incorporation of malva fibers. In: Characterization of minerals, metals, and materials—composites—TMS 145th conference, Nashville, Tennessee, USA, February, 2016, p 174
18. Margem JI, Monteiro SN, Margem FM, Ribeiro CG, Moraes Y (2015) Photoacoustic thermal characterization of malva fibers. In: Characterization of minerals, metals, and materials—soft materials—TMS 144th conference, Orlando, Florida, USA, March, 2015, pp 215–216
19. Margem JI, Monteiro SN, Margem FM, Margem M, Ribeiro CG, Gomes V (2015) Pullout tests behavior of epoxy matrix reinforced with malva fibers. In: Characterization of minerals, metals, and materials—soft materials—TMS 144th conference, Orlando, Florida, USA, March, 2015, p 261
20. Margem JI Monteiro SN, Margem FM, Margem M, Gomes V (2014) Charpy impact tests in epoxy matrix composites reinforced with malva fibers. In: Characterization of minerals, metals, and materials—characterization of soft materials I—TMS 143rd conference, San Diego Convention Center, California, USA, February, 2014, p 214

Part VII
Analysis of Surfaces and Interfaces

Applications of Aberration-Corrected Low-Energy Electron Microscopy for Metal Surfaces

Zheng Wei, Tao Li, Meng Li, Xueli Cao, Hanying Wen, Guodong Shi, Lei Yu, Lin Zhu, Wen-xin Tang and Chenguang Bai

Abstract Low energy electron microscopy and photoemission electron microscopy (LEEM/PEEM), as powerful in-situ surface-sensitive electron microscopy, find wide applications in surface physics, chemistry and catalysis. The high reflectivity of incident low-energy electrons (0–100 eV), allows it to image the surface structures in the topmost few atomic layers within less than one second, while the sample can be heated up to 1200 °C in real time which is potentially very useful in metallurgy and materials fields. A unique three-prism aberration correction (ac-) LEEM was commissioned successfully in Chongqing University, with a lateral resolution below 2 nm. A multiple gas source in the ac-LEEM system was installed as well, which allowed us to observe chemical reactions of nanoscale mineral powders on metallic substrates. In this paper, the latest results on the applications of this three-prism ac-LEEM on oxidation and reduction processes on copper and iron polycrystalline surfaces are demonstrated.

Keywords Metal · Mineral · Low-energy electron microscopy (LEEM) Photoelectron microscopy (PEEM) · Mirror electron microscopy(MEM) Micro-Low-energy electron diffraction (μ-LEED)

Introduction

Low energy electron microscopy (LEEM) and photoemission electron microscopy (PEEM) are powerful tools in surface and interface science to investigate surface dynamics in real time and real space [1]. In contrast to the well-known scanning

Z. Wei · T. Li · M. Li · X. Cao · H. Wen · G. Shi · L. Yu
L. Zhu · W. Tang (✉) · C. Bai (✉)
College of Materials Science and Engineering, Chongqing University, Chongqing 400044, China
e-mail: wenxintang@cqu.edu.cn

C. Bai
e-mail: bguang@cqu.edu.cn

B. Li et al. (eds.), *Characterization of Minerals, Metals, and Materials 2018*, The Minerals, Metals & Materials Series,
https://doi.org/10.1007/978-3-319-72484-3_22

electron microscopy (SEM) and transmission electron microscopy (TEM), the impact of electron energy on the surfaces in LEEM/PEEM is in an extremely low range of 0–100 eV. The low electron energy not only ensures their surface-sensitivity, but also allows the LEEM/PEEM setups to collect all the electrons emitted from surfaces with cathode lens consisting of both the sample and objective lens. Furthermore, the LEEM can resolve single atomic steps on the surfaces, and different surface structures and domain orientations within the same terraces, thanks to the quantum interference effects of the elastically back-scattered electrons. Thus, LEEM and PEEM are the most effective and powerful tools to study various dynamical processes on the surfaces, such as the epitaxial growth of new materials, the phase transitions, the chemical reactions, the self-assembly of atoms or molecules, the melting-crystallization processes, etc.

Besides the intensive applications in basic surface physics, PEEM finds a wide range of more technology-oriented applications ranging from minerals to electronic devices. Although the compositions, morphologies, and crystal orientations are very complicated in general materials, the PEEM has been applied to investigate the synthetic lamellar clay mineral flakes [2], the oxidization processes in pyrite (FeS_2) [3], the grain growth of a TiAlZr alloy [4], the martensitic phase transition in CuZnAl and NiTiCu shape memory alloys [5], etc. However, there is few LEEM experiment reported on applied materials. It is due to the difficulty of aligning the incident electron beam on the rough surfaces, which has been avoided in the PEEM experiments mentioned above.

In this paper, the preliminary LEEM/PEEM research results in metallurgical process would be presented. Two important substrates, polycrystalline copper films and polycrystalline Fe plates, could be chosen. The oxidation of polycrystalline copper in air and its reduction in atomic hydrogen atmosphere at the topmost few atomic layers will be demonstrated in LEEM. Furthermore, the segregation of impurity atoms from the bulk of a polycrystalline iron plates also will be shown.

Experimental Setup

Recently, tremendous progress has been achieved in aberration corrected (ac-) LEEM, with a lateral spatial resolution of 1.4 nm [6]. However, all LEEM instruments available today are working with continuous electron sources. A new ac-LEEM instrument capable of integrating multiple electron sources has been built up successfully in Chongqing University, China [7].

Figure 1a shows a side-view photograph of the actual three magnetic prism array (MPAs) ac-LEEM setup. Besides the installed standard cold field emission gun (FEG), an ultrafast spin-polarized electron gun (SP-Gun), and a scanning electron column (Gun-II) can be introduced to the MPA3 in the near future. The setup can be operated in two modes: LEEM and PEEM. In the LEEM mode, the highly coherent electrons field emitted from the cold FEG will be deflected by 90° twice sequentially by MPA3 and MPA1, shown in Fig. 1b, and impact on the biased sample with a

small landing energy of 0–100 eV. The aberrations of the back-scattered electrons can be greatly reduced, via the electron mirror, as indicated in Fig. 1, before they enter the projective lens and hit the MCP detector eventually. In the PEEM mode, either a UV-lamp (indicated in Fig. 1a) or a focused HeI/HeII SPECS UVS-300 light source (installed in the back of MPAs and could not be shown) is used as the excitation source to eject photoelectrons from surface via photoelectric effects.

The LEEM sample manipulator has six degrees of freedom (X, Y, Z, two tilts and azimuth) operated under full computer control, and can operate in a wide temperature range of −90–1200 °C. Sample preparation and characterization are further enhanced in a separated preparation (Pre-) chamber by including of new components such as plasma sources, an atomic hydrogen source for III–V and II–VI surface cleaning. A high HT-STM is also integrated into the same ultra-high-vacuum (UHV) system. The samples can be transferred under UHV to either the ac-LEEM or the HT-STM chamber via the transfer and preparation chamber. HT-STM can provide atomic resolution at high temperature around 1000 K. Thus in-situ surface dynamics over a lateral scale of 20 µm–2 nm (ac-LEEM) and 1 µm–0.02 nm (HT-STM) can be investigated.

The sub-monolayer Ag deposited in-situ on clean Si(111)-(7 × 7) surfaces with a substrate temperature of 500 °C was taken as an example to show the ability of

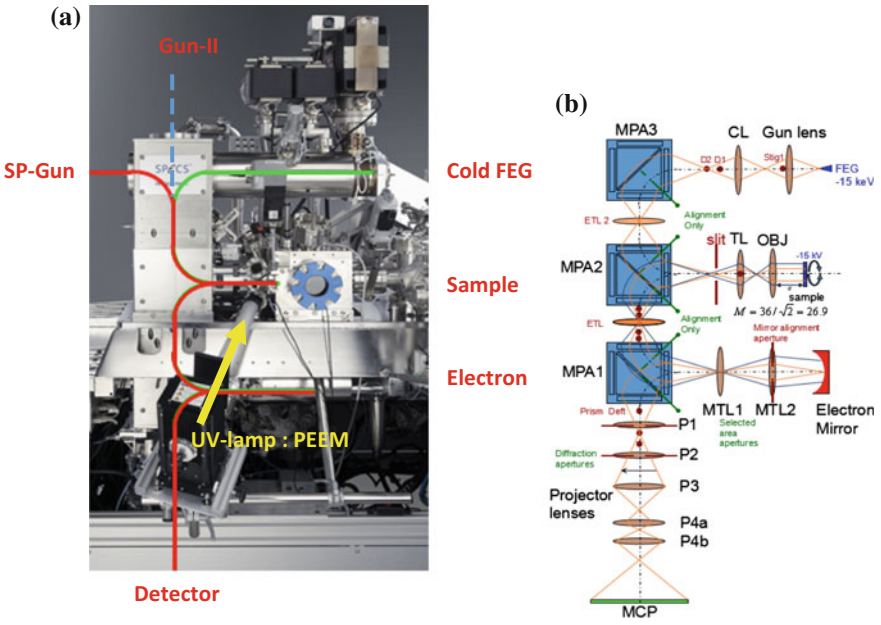

Fig. 1 **a** is the photograph of the actual three-MPA ac-LEEM and **b** is the corresponding electron-optics in side-view

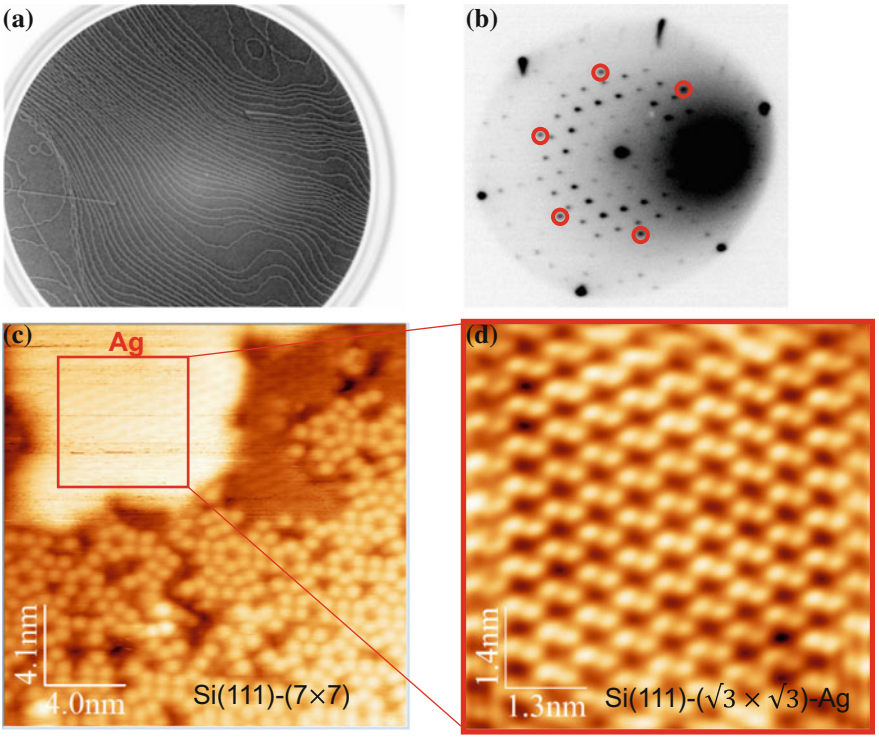

Fig. 2 Sub-monolayer Ag deposited on the heated Si(111)-(7 × 7) surface at 500 °C. **a** ac-LEEM image resolved the atomic steps, dislocations, and large islands. Electron energy was 45 eV, FoV=10 μm; **b** The corresponding LEED image was dominated by the diffraction spots of the Si (111)-(7 × 7) substrate. The diffraction spots of the reconstructed Ag single-atomic-layer, Si(111)-($\sqrt{3}\times\sqrt{3}$)-Ag, were indicated by red circles; **c** and **d** were STM images reflect the atomic structures of both reconstructed surfaces. I_t = 0.1nA, V_t = 1.8 V

the ac-LEEM/HT-STM platform. The single atomic steps, two dislocations, and several large islands are clearly resolved in the ac-LEEM image,shown in Fig. 2a, with an electron landing energy of 45 eV and a field of view (FoV) as large as 10 μm. The corresponding surface reconstructed phases of the uncovered Si(111)-(7 × 7) and single-atomic-layer of Ag on Si(111), Si(111)-($\sqrt{3}$ × $\sqrt{3}$)-Ag, can be identified in the corresponding LEED pattern, shown in Fig. 2b. Although the ×7 spots dominated the LEED pattern, the ×$\sqrt{3}$ spots due to the monolayer Ag were clearly resolved and labelled as red circles. The morphology and atomic structures of the monolayer Ag islands on Si(111) can be clearly resolved in the STM images, shown in Fig. 2c, d).

Results of Polycrystalline Copper Foils

Polycrystalline Cu foils are the most popular substrates to grow high-quality graphene layers. It is well known that the oxidation and reduction of Cu surfaces play important roles in the growth mechanisms. However, the morphology, work function variations and atomic structures of the topmost three to four layers are out of the capability of the scanning electron microscopy and transmission electron microscopy, since both techniques are bulk-sensitive.

Two polycrystalline Cu foils was investigated systematically, that have been electro-chemically etched in NaOH solutions with different times of 30 s and 3 min, as shown in Figs. 3 and 4, respectively. Longer etching time in the solution resulted in much higher quality of clean Cu surfaces, as shown in the LEEM images of Fig. 4b. Only one grain boundary (GB) was observed in Fig. 4b. In contrast, hundreds of GBs were observed in Fig. 3a with much shorter etching time. These GBs are much clearly resolved in the LEEM images of Fig. 4b, rather than the PEEM images of Fig. 4a, due to the much stronger elastically scattered electron signals in comparing with the corresponding photoelectron intensities in PEEM image. Much fine features can be observed in LEEM images, thus, only the LEEM images are concentrated on in the following discussions.

The oxidized layer of copper foils was clearly resolved in the low-energy electron diffraction pattern at micrometer scale (μ-LEED), as acquired in region-c of Fig. 4b and shown in Fig. 4c. In contrast, the clean Cu parts of region-d show typical μ-LEED pattern of clean Cu(100) surface. The oxidized layer can be partially removed even with a very small amount of atomic hydrogen introduced into the pre-chamber with a base pressure of 1×10^{-8} Pa, as revealed in the central part of Fig. 3b. The atomic hydrogen not only removed the oxygen atoms from oxidation layer, but also induced the formation of large terraces of Cu islands.

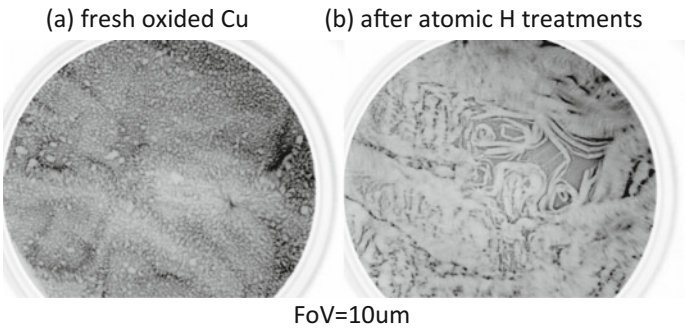

Fig. 3 The LEEM images of polycrystalline Cu foils. **a** before and **b** after atomic hydrogen treatments. The polycrystalline Cu was etched in NaOH solutions for 30 s before introduced into the UHV system

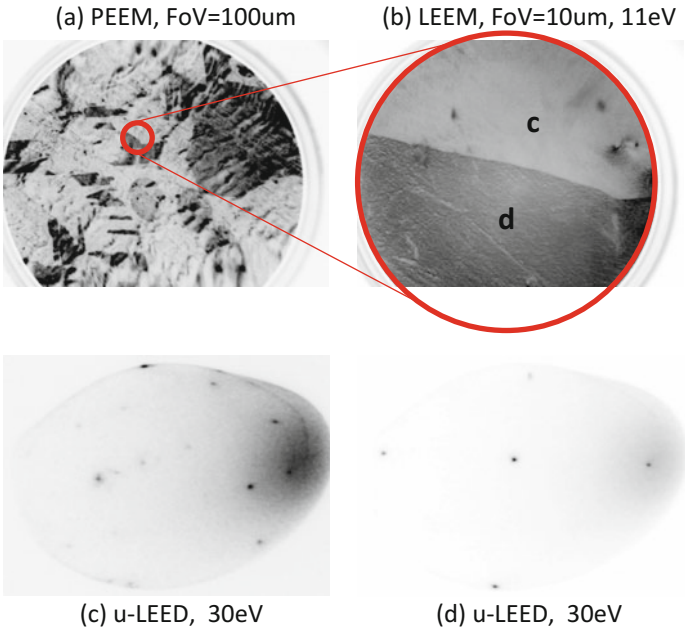

Fig. 4 **a** PEEM and **b** LEEM image of polycrystalline Cu foil, that was etched in NaOH solutions for 3 min. The PEEM image much large patches of clean Cu surface, in comparing with Cu foils in Fig. 3. The atomic structures of oxidized copper and clean copper were indicated in the μ-LEED patterns of **c** and **d**

Results of Polycrystalline Iron Plates

Iron is notoriously difficult to be cleaned, due to the high concentrations of non-metallic impurities, particularly carbon and sulfur. A polycrystalline iron surfaces was successfully cleaned via repeated cycles of argon ion sputtering and annealing in UHV.

Figure 5a shows a typical LEEM image of the polycrystalline iron surfaces after just two cycles of sputtering/annealing. Small terraces were observed in a field of view (FoV) of 10 μm, with an average terrace width around 1 μm. A blurred LEED spots was observed with incident electron energy of 16 eV, as shown in Fig. 5b. Once the incident electron energy varied from tens of eV to 0 eV, all the incident electrons will be reflected from the surfaces. In this case, the surface acts as a mirror to the incident electrons [8]. This special LEEM mode with zero incident energy is named as mirror electron mode (MEM). It is worth noting that much fine features can be observed in MEM image of Fig. 5c, in comparing with the LEEM image of Fig. 5a. The extra features in MEM image were mostly due to the roughening of the polycrystalline iron surface, since the impurity atoms precipitated from the bulk into the terraces effectively.

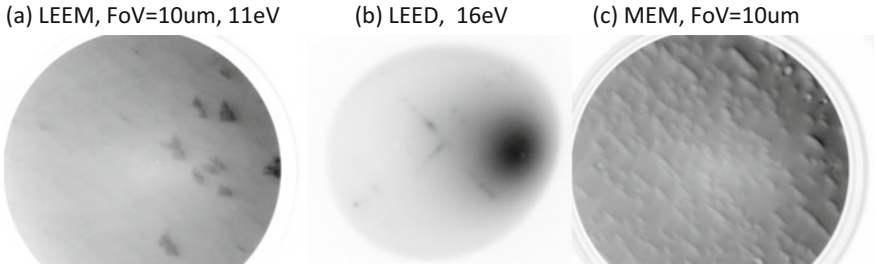

Fig. 5 **a** The LEEM images of 'dirty' polycrystalline Fe surfaces with few sputtering/annealing cycles; **b** The corresponding LEED pattern; **c** The MEM image of the same region, which reflects more much morphology features of the surfaces

The morphology and quality of the iron surfaces was monitored in the high sensitivity of MEM mode, after intervals of sputtering/annealing cycles. Figures 6 show different regions of the iron surfaces after tens of cleaning cycles. In comparing with the MEM image in Fig. 5c, the average terrace width had been increased from less than 1 μm to 5 μm, while the populations of the impurity atoms pinned in the GBs have been greatly reduced. In Fig. 6d, no single precipitation region is observed. The polycrystalline iron crystal has been cleaned to a large extent.

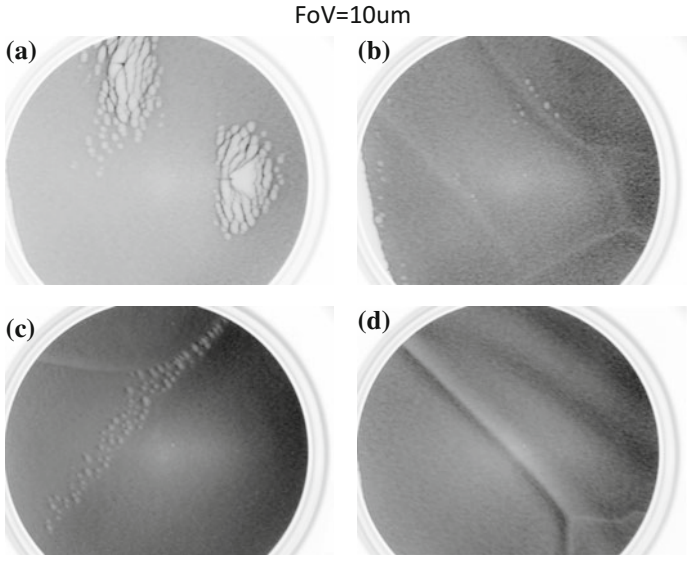

Fig. 6 The typical MEM images of 'clean' polycrystalline Fe surfaces after many sputtering/cleaning cycles

Conclusions and Outlooks

In summary, it is clear that the LEEM is a powerful tool to characterize the oxidized and reduced polycrystalline copper foil, the segregation and morphology of polycrystalline iron surface at intervals of cleaning cycles. In the present stage, the oxidation and reduction processes were performed in a separated pre-chamber. Now a multiple gas source are being tested, which is installed directly in the ac-LEEM chamber. It allows the introduction of four different gases/mixed gases simultaneously onto surfaces. Once the multiple gas source is fully commissioned, the dynamic processes on metallic and mineral surfaces would be monitored in-situ. The dynamic processes of iron oxidation and reduction would be monitored vividly, from which the key parameters related to the diffusion processes, such as the activation energies, the initial reaction sites, would be drawn quantitatively.

Acknowledgements This work was financially supported by the National Natural Science Foundation of China (No. A04-11227802, No. 51234010, No. 11774039), 985 Key National University Funding at Chongqing University (No. 0211001104414, No. 0211001104423, No. 0211001104478) and Science and Technology Innovation Projects at Chongqing University (No. 0211005202084). We acknowledge Dr. Xin Li and Prof. Guilin Wu for providing the polycrystalline copper and iron samples, respectively.

References

1. Bauer E (2014) Surface microscopy with low energy electron. Springer, New York, NY
2. Vantelon D et al (2009) An XPEEM study of structural cation distribution in swelling clays. I. Synthetic trioctahedral smectites. Phys Chem Minerals 36:593–602. https://doi.org/10.1007/s00269-009-0304-4
3. Chandra AP, Gerson AR (2010) The mechanisms of pyrite oxidation and leaching. A fundamental perspective. Surf Sci Rep 65:293–315. https://doi.org/10.1016/j.surfrep.2010.08.003
4. Marsh SP et al (1993) On the kinetics of shrinking grains. Acta Metall Mater 41:297–304. https://doi.org/10.1016/0956-7151(93)90360-5
5. Xiong G et al (2006) In situ photoelectron emission microscopy of a thermally induced martensitic transformation in a CuZnAl shape memory alloy. Appl Phys Lett 88:091910. https://doi.org/10.1063/1.2177450
6. Tromp RM et al (2013) A new aberration-corrected, energy-filtered LEEM/PEEM instrument II. Operation and results. Ultramicroscopy 127:25–39. https://doi.org/10.1016/j.ultramic.2012.07.016
7. Wan W et al (2017) Design and commissioning of an aberration-corrected ultrafast spin-polarized low energy electron microscope with multiple electron sources. Ultramicroscopy 174:89–96. https://doi.org/10.1016/j.ultramic.2016.12.019
8. Tang WX et al (2011) Ga droplet surface dynamics during Langmuir evaporation of GaAs. IBM J Res Dev 55:10. https://doi.org/10.1147/JRD.2011.2158762

ZnO Thin Films of Flowered-Fibrous Micro/Nanowebs on Glass Substrates Using the Spray Pyrolysis Method

Shadia J. Ikhmayies

Abstract Zinc oxide (ZnO) flowered-fibrous micro/nanowebs were produced as thin films on glass substrates at 350 °C using the low cost spray pyrolysis (SP) method. The films were characterized using the XRD diffraction, scanning electron microscopy (SEM), and X-ray energy dispersive spectroscopy (EDS). Hexagonal structure was confirmed from X-ray diffractogram, which showed preferential orientation along the (002) line. SEM images showed two dimensional flowered-fibrous micro/nanowebs, and EDS elemental analysis revealed the presence of chlorine in the films in addition to zinc and oxygen. The obtained morphology is important for optoelectronic device industry and solar cells, where it provides large surface area that helps light harvesting.

Keywords ZnO · Micro/nano webs · Solar cells · Spray pyrolysis
XRD · SEM

Introduction

Zinc oxide (ZnO) is an inexpensive II–IV compound semiconductor with a direct bandgap of 3.37 eV and high exciton binding energy of 60 meV at room temperature [1, 2]. Because of its unique optical and electronic properties, ZnO attracted considerable attention in recent decades. ZnO micro/nanostructures have been used in different applications, such as sensors [3], photocatalysis [4–8], and solar cells [9, 10] such as dye-sensitized solar cells DSSCs [11] and thin film solar cells. Characteristics and practical performance of ZnO in all applications are strongly dependent on the size and shape of the produced particles or structures. Hence, much effort had been devoted to controllably synthesize the material with specific functionality [8]. Accordingly, it is highly desirable to seek a novel and

S. J. Ikhmayies (✉)
Faculty of Science, Department of Physics, Al Isra University, Amman 11622, Jordan
e-mail: shadia_ikhmayies@yahoo.com

B. Li et al. (eds.), *Characterization of Minerals, Metals, and Materials 2018*, The Minerals, Metals & Materials Series,
https://doi.org/10.1007/978-3-319-72484-3_23

facile route to synthesize ZnO micro/nanostructures with tunable size and morphology [11].

ZnO micro/nano structures can be prepared by several growth methods such as the vapor–liquid–solid method (VLS) [12], chemical vapor deposition (CVD) [13], pulsed laser deposition (PLD) [14], magnetron sputtering [15], sol–gel [16], hydrothermal method [17], and spray pyrolysis (SP) [18–27] method. However, for simplicity, low cost, and large-scale production, the SP method was preferred in this research. In this work ZnO flowered-fibrous micro/nanowebs were produced on glass substrates as thin films using $ZnCl_2$ as the starting material and the spray pyrolysis method without using any catalyst or surfactant.

Experimental Procedure

Flowered-fibrous zinc oxide (ZnO) thin films were deposited on glass substrates of dimensions 60 × 26 × 1 mm^3 at a substrate temperature of 350 ± 5 °C using the spray pyrolysis (SP) method. Zinc chloride ($ZnCl_2$) of purity 99% is used as the precursor, where 2.5 g of $ZnCl_2$ is dissolved in 60 ml of distilled water to get a solution of concentration 0.03 M. Before use, glass substrates were pre cleaned by soap, rinsed in distilled water, and then they were dried by lens paper. Spraying of the solution has been done vertically, and intermittently. At the end of the deposition process, the heater is turned off, and the films were left on the heater to cool gradually to room temperature.

Structure and phase of the films were studied using X-ray diffraction (XRD), which was carried out using SHIMADZU XRD-7000 diffractometer utilizing X-Ray Cu K_α radiation (λ = 1.54 A°). The step size and scan speed were 0.02° and 2°/min respectively. The measurements are taken in the continuous 2θ mode in the range 20–65° using a current of 30 mA and voltage of 40 kV. Morphology and elemental composition were explored using scanning electron microscopy (SEM) by an FEI scanning electron microscope (SEM) (Inspect F 50) operating at 20 kV, and equipped with EDS apparatus. The thickness of the films is around 1 μm and it was estimated using the SEM microscope.

Results and Discussion

The structure and phase of the as-deposited, flowered-fibrous ZnO thin films was analyzed by X-ray diffraction, where Fig. 1 displays the diffractogram of one of the films. The film is polycrystalline with hexagonal (wurtzite) structure. All of the diffraction peaks were indexed by the corresponding Miller indices and shown in the figure. These represent reflections from the planes (100), (002), (101) and (102), (110) and (103). The preferential orientation along the c-axis is indicated by the plane (002), where this plane has the highest energy of formations. As the figure

shows, there are no impurity peaks in the diffractogram, which indicates the formation of pure products.

Figure 2 displays the SEM images of two films, where the films show a flowered-fibrous web structure. Such morphology provides high surface area, and suggests the possibility of the light harvesting mechanism, which is a prerequisite for solar cells and optoelectronic device applications. These webs are composed of fibers of different lengths and diameters that are linked in a complex but beautiful way to form two dimensional flowers of different shapes which are also interlinked to other flowers. The flowers in Fig. 2a are different from those in Fig. 2b despite the fact that they are prepared at the same time with the same deposition parameters. The fibers in Fig. 2a are thinner, softer, and more crowded, and they form the interior parts of the flower surrounding the center of the flower which appears as a cluster. The web in Fig. 2a appears as a decorative piece of cloth. In Fig. 2b the web consists of flowers that have larger clusters at the center, and the diameters of the fibers are larger and they are longer, and they can be named petals. These flowers are not surrounded by a decoration, they are less beautiful, and they are linked together in a complicated way. Self assembling appears in different places in Fig. 2b.

Figure 3 displays the X-ray energy dispersive spectrum (EDS) of one of the as-deposited films, and the inset SEM image shows the position A at which the measurement was recorded. EDS analysis confirmed the presence of elemental zinc, oxygen, and chlorine signals. The vertical axis displays the number of x-ray counts although the horizontal axis displays energy in KeV. The atomic percentages of zinc, oxygen, and chlorine were found to be 39.65 ± 2.3, 58.83 ± 4.9, and 1.52 ± 0.1 at.% respectively. The ratio of Zn:O is 0.67, while that in ZnO compound is 1. The explanation of this discrepancy is that: First, part of detected oxygen is incorporated in the glass substrates as SiO_2, where the EDS system includes it in the measurements. Second, the EDS system can't give accurate values for concentrations of light elements like oxygen, and the tolerance in the oxygen

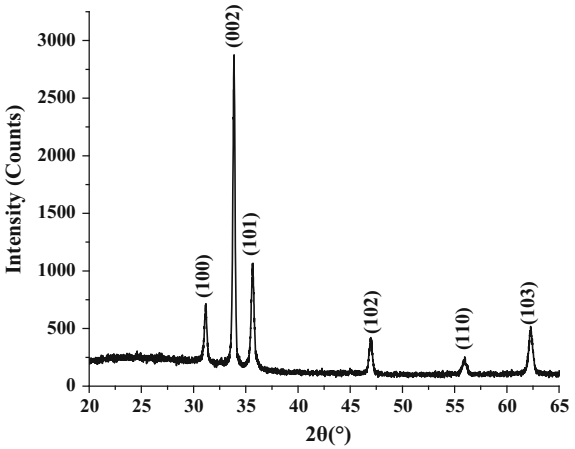

Fig. 1 XRD diffractogram of an as-deposited ZnO film

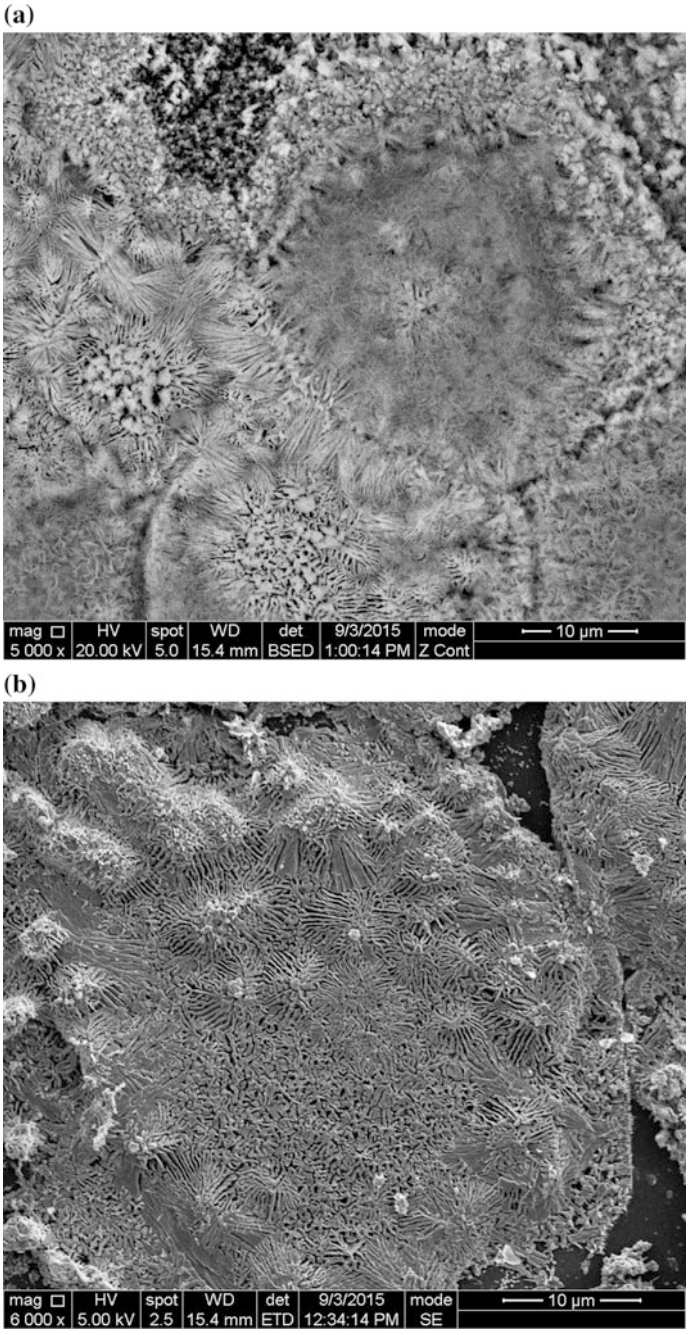

Fig. 2 SEM images of two ZnO films on glass substrates where the flowered-fibrous web in **a** differs from that in **b** despite the fact that deposition parameters are the same

concentration is the largest one as seen in the EDS report. Hence, it may be expected that the films are deficient in oxygen, and not rich in oxygen. The ratio of Cl:O is 0.026, and this small ratio means that chlorine works as a dopant in the films, where it replaces oxygen in ZnO crystal lattice. When this happens the n-type conductivity of the films increases, which is required for the use of the films as a transparent conducting oxide and/or a window layer in thin film solar cells.

Conclusions

ZnO flowered-fibrous webs were synthesized as thin films on glass substrates using $ZnCl_2$ as the precursor, and the spray pyrolysis (SP) method without using any catalyst or surfactant. XRD diffraction revealed the hexagonal structure of the films, and SEM images showed flowered-fibrous micro/nanowebs. This important morphology provides large surface area, which helps in light harvesting, which is a prerequisite for solar cells and optoelectronic device applications. EDS elemental analysis showed that the films contain chlorine in addition to Zn and O.

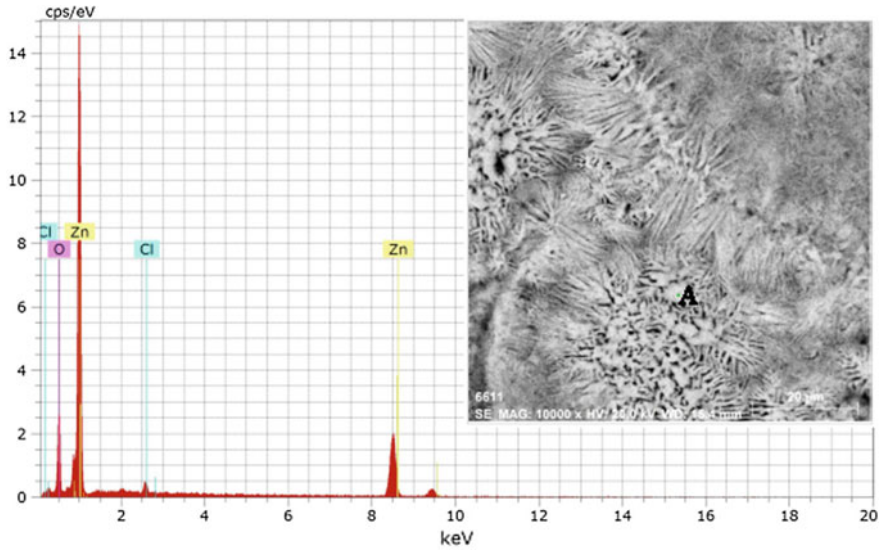

Fig. 3 EDS spectrum of an as-deposited ZnO film. The inset SEM image shows point A at which the measurement was recorded

References

1. Cho S et al (2010) Formation of amorphous zinc citrate spheres and their conversion to crystalline ZnO nanostructures. Langmuir 27:371–378
2. Wu J, Xue D (2011) Progress of science and technology of ZnO as advanced material. Sci Adv Mater 3:127–149
3. Kim J, Yong K (2011) Mechanism study of ZnO nanorod-bundle sensors for H_2S gas sensing. J Phys Chem C 115:7218–7224
4. Li H et al (2011) Fabrication of ordered flower-like ZnO nanostructures by a microwave and ultrasonic combined technique and their enhanced photocatalytic activity. Mater Lett 65:3440–3443
5. Lai Y, Meng M, Yu Y (2010) One-step synthesis, characterizations and mechanistic study of nanosheets-constructed fluffy ZnO and Ag/ZnO spheres used for rhodamine B photodegradation. Appl Catal B: Environ 100(3–4):491–501
6. Milao TM, de Mendonca VR, Araujo VD, Avansi W, Ribeiro C, Longo E, Bernardi MI (2012) Microwave hydrothermal synthesis and photocatalytic performance of ZnO and *M*: ZnO nanostructures (*M* = V, Fe, Co). Sci Adv Mater 4:54–60
7. Roselin LS, Selvin R (2011) Photocatalytic degradation of reactive orange 16 dye in a ZnO coated thin film flow photoreactor. Sci Adv Mater 3:251–258
8. Liao Y, Xie C, Liu Y, Huang Q (2013) Enhancement of photocatalytic property of ZnO for gaseous formaldehyde degradation by modifying morphology and crystal defect. J Alloys Comp 550:190–197
9. Ko SH, Lee D, Kang HW, Nam KH, Yeo JY, Hong SJ, Grigoropoulos CP, Sung HJ (2011) Nanoforest of hydrothermally grown hierarchical ZnO nanowires for a high efficiency dye-sensitized solar cell. Nano Lett 11(2):666–671
10. Ling T, Song JG, Chen XY, Yang J, Qiao SZ, Du XW (2013) Comparison of ZnO and TiO_2 nanowires for photoanode of dye-sensitized solar cells. J Alloys Comp 546:307–313
11. Kao M-C, Chen H-Z, Young S-L, Lin C-C, Kung C-Y (2012) Structure and photovoltaic properties of ZnO nanowire for dye-sensitized solar cells. Nanoscale Res Lett 7:260
12. Huang MH, Mao S, Feick H, Yan HQ, Wu YY, Kind H, Weber E, Russo R, Yang PD (2001) Room-temperature ultraviolet nanowire nanolasers. Science 292(8):1897–1899
13. Xiang B, Wang PW, Zhang XZ, Dayeh SA, Aplin DPR, Soci C, Yu DP, Wang DL (2007) Rational synthesis of p-type zinc oxide nanowire arrays using simple chemical vapor deposition. Nano Lett 7(2):323–328
14. Sun Y, Fuge GM, Ashfold MNR (2004) Growth of aligned ZnO nanorod arrays by catalyst-free pulsed laser deposition methods. Chem Phys Lett 396(1–3):21–26
15. Kluth O, Schöpe G, Hüpkes J, Agashe C, Müller J, Rech B (2003) Modified Thornton model for magnetron sputtered zinc oxide: film structure and etching behavior. Thin Solid Films 442:80–85
16. Ohyama M, Kozuka H, Yoko T (1998) Sol-gel preparation of transparent and conductive aluminum-doped zinc oxide films with highly preferential crystal orientation. J Am Ceram Soc 81:1622–1632
17. Ekthammathat N, Phuruangrat A, Thongtem S, Thongtem T (2015) Hydrothermal-assisted synthesis and photoluminescence of ZnO microrods. Dig J Nanomater Biostruct 10(1):149–153
18. Ikhmayies Shadia (2016) Synthesis of ZnO microrods by the spray pyrolysis technique. J Electron Mater 45(8):3964–3969
19. Ikhmayies SJ, Abu El-Haija NM, Ahmad-Bitar RN (2014) A comparison between different ohmic contacts for ZnO thin films. J Semicond 36(3):033005-1-6
20. Ikhmayies SJ, Abu El-Haija NM, Ahmad-Bitar RN (2010) Electrical and optical properties of ZnO:Al thin film prepared by the spray pyrolysis technique. Phys Scr 81(1):015703

21. Ikhmayies SJ, Abu El-Haija NM, Ahmad-Bitar RN (2010) Characterization of undoped spray-deposited ZnO thin films of photovoltaic applications. FDMP: Fluid Dyn Mater Proces 6(2):165–178
22. Ikhmayies SJ, Abu El-Haija NM, Ahmad-Bitar RN (2010) The Influence of annealing in nitrogen atmosphere on the electrical, optical and structural properties of spray- deposited ZnO thin films. FDMP: Fluid Dyn Mater Proces 6(2):219–232
23. Ikhmayies SJ, Zbib MB (2017) Spray pyrolysis synthesis of ZnO micro/nanorods on glass substrate. J Electron Mater 46(10):5629–5634
24. Ikhmayies SJ (2017) Formation of three dimensional ZnO micro flowers from self assembled ZnO micro discs. Metall Mater Trans 48(8):3625–3629
25. Ikhmayies SJ, Zbib MB (2017) Synthesis of ZnO hexagonal micro discs on glass substrates using the spray pyrolysis technique. J Electron Mater 46(7):3982–3986
26. Juwhari HK, Ikhmayies SJ, Lahlouh B (2017) Room temperature photoluminescence of spray-deposited ZnO thin films on glass substrates. Int J Hydrog Energy 42:17741–17747
27. Ikhmayies SJ (2017) Synthesis of ZnO micro prisms on glass substrates by the spray pyrolysis method. In: Characterization of minerals, metals, and materials 2017, part of the the minerals, metals & materials series book series (MMMS), pp 131–138

Intergranular Cracking of High Strength Extruded Brass Alloys

A. Vazdirvanidis and G. Pantazopoulos

Abstract In this paper, a failure analysis investigation is presented concerning the intergranular cracking of three different diameter (Ø26.6, Ø10.8, Ø8.5 mm) high strength brass rods which failed after extrusion. Optical, Scanning Electron Microscopy and Electron Backscatter Diffraction are employed in order to reveal the mechanisms and the root causes of the failures. The microstructural characteristics, exhibited by the brass rods, pertaining mainly to phase, grain structure, size and distribution of intermetallic particles, are considered to exert a detrimental effect, impairing the mechanical properties, facilitating the environmentally-induced degradation and assisting the occurrence of brittle fractures. Revision of preheating and extrusion conditions could be further implemented in order to minimize the risk of such failure in the future.

Keywords Brass alloy · Brittle fracture · Extrusion · EBSD

Introduction

Copper alloys exhibit the well-known "intermediate temperature embrittlement" which is related with intergranular segregation of alloying additions or impurities and the presence of Pb in leaded alloys [1, 2]. Ductility trough may occur in a large range of temperatures and it is aggravated in case of high Pb concentration alloys may be brittle even at room temperatures [2]. Grain boundary decohesion provoked by liquid/solid metal embrittlement (LME/SMIE) phenomena occurred due to manufacturing and/or service conditions were also reported [3, 4]. For SMIE by internal phases in the microstructure, voids are initiated at the matrix-particles

A. Vazdirvanidis (✉) · G. Pantazopoulos
ELKEME Hellenic Research Centre for Metals S.A,
56th km Athens—Lamia National Road, 32011 Oinofyta Viotias, Greece
e-mail: avazdirvanidis@elkeme.vionet.gr

G. Pantazopoulos
e-mail: gpantaz@elkeme.vionet.gr

B. Li et al. (eds.), *Characterization of Minerals, Metals, and Materials 2018*, The Minerals, Metals & Materials Series,
https://doi.org/10.1007/978-3-319-72484-3_24

interface, and grow by an adsorption-induced decohesion or dislocation emission mechanism [4]. Cavities appeared, at areas of prior particles' positions, while the embrittling constituent diffuses to crack tips and forms thin films on the fracture surface. Deformation during the process, especially during void coalescence, occurs to some extent behind the crack tip and produces slip steps on the fracture surface [4]. LME by internal phases can produce a similar appearance of surfaces. Lead surface-self-diffusion can occur at high rates even at room temperature, and would be relatively fast at higher temperatures assisting to crack propagation and embrittlement. Crack growth becomes practically unstable when crack has travelled over the quarter of the wall thickness. Moreover, the effect of high angle grain boundaries in triple junctions is also considered factor contributing to local high dislocation density pile-ups and stress accumulation resulting in lowering of the critical intergranular fracture stress and cracking evolution [5].

In the present article three different case studies of fractured extruded brass high-alloy bars are examined in order to shed more light on the conditions and root-causes that adversely affect ductility, creating production delays and quality problems to the respective industrial plants. The samples of the study are the following:

- CW713R alloy, Ø26.6 mm bar,
- C6782 alloy, Ø10.8 mm bar, and
- CW721R, Ø8.5 mm bar.

Experimental Procedure

Microstructure evaluation was conducted in mounted sections parallel to the extrusion direction. Metallographic examination was performed employing a Nikon Epiphot 300 inverted optical microscope while SEM evaluation was conducted using a FEI XL40 SFEG scanning electron microscope using Secondary (SE) and Backscattered Electron (BSE) detectors coupled with an EDAX Energy Dispersive X-ray Spectroscopy (EDS) Apollo XF Silicon Drift Detector (SDD) of 60 mm^2 area. The microstructure was assessed after immersion etching using $FeCl_3$ solution.

EBSD scans were collected employing a high speed Hikari EDAX camera at 70° tilt position, using hexagonal grid with 1.0 μm step, resulting in >500 k individual orientation measurements. The SEM conditions for the scans were accelerating voltage of 20 kV at working distance 10 mm. The data obtained for the scans were of high quality with indexing success >95%. Post processing was applied to clean up the data (grain dilation). The data analysis was realized using Orientation Imaging Microscopy analysis software.

Results and Discussion

Microstructure

The microstructure consisted of a single β-brass (CuZn) phase as the results of EBSD scans showed for all the studied alloys.

CW713R alloy, Ø26.6 mm bar

In Ø26.6 mm bar, a hairline crack aligned parallel to extrusion direction was observed. It propagated to the centre of the bar following an intergranular path which coincided with the locations of brittle, CuFeMnSi second phase particles and also locally segregated Pb regions (Figs. 1 and 2). The grain structure was fully recrystallized with a mean grain size of 35 μm. Second phase particles exhibited an

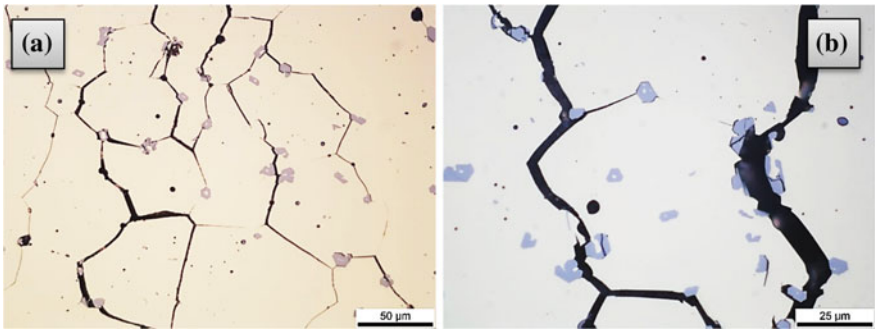

Fig. 1 **a**, **b** Optical micrographs, longitudinal section showing the crack propagation through brittle intermetallic particles network on the CW713R, Ø26.6 bar

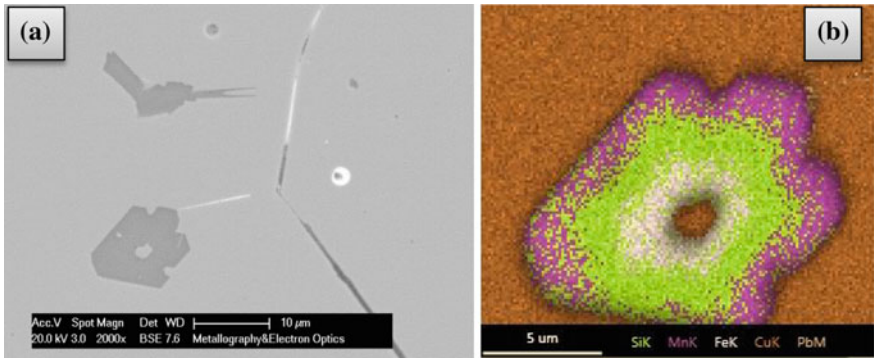

Fig. 2 **a** Electron micrograph showing grain boundary separation due to Pb segregation. **b** EDS mapping of Si, Mn, Fe and Cu of an intermetallic particle indicating formation through peritectic reaction

intensively cored structure consisting of a Cu core and successive "shells" of Fe, Si and Mn formed around it. This type of structure is met in peritectic reactions when the liquid and solid phases are no longer in close contact since atomic diffusion is impeded through the developed shell of the produced solid-phase. The respective phenomenon is known as surrounding or enveloping.

C6782 alloy, Ø10.8 mm bar

The detected crack on Ø10.8 mm bar differed from the previous case study in that it was oriented transverse to extrusion direction according to the details of Fig. 3. It extended to the centre of the round bar following an intergranular crack path mode.

Brittle, second phase particles, assisting in crack propagation, were identified as Fe–Mn–Si, (low concentrations of C, Cu, Zn, Ni were found as well) exhibiting an elongated morphology contrary to the respective second phase particles of Ø26.6 mm bar which were almost equiaxed (Fig. 4). Smaller needle-shaped particles corresponding to Mn–Si–Zn were also found dispersed in the matrix. The contribution of Pb to crack propagation was lower due to the lower degree of segregation and average "island" size of Pb particles on the grain boundaries.

CW721R, Ø8.5 mm bar

The detected crack in Ø8.5 mm bar was also transverse to extrusion direction as shown in Fig. 5. The crack had a depth of ~3.3 mm, intergranular mode and the development of secondary cracking (also intergranular) was observed as well. The fracture surface exhibited a high concentration of Pb particles which significantly contributed to the formation of low energy crack propagation paths (Fig. 6). Longitudinal cross-section revealed initiation of multiple surface secondary cracks adjacent to the main crack (Fig. 7). It seems that one of the parallel cracks was allowed to develop due to locally existing favouring stress concentration conditions after extrusion process.

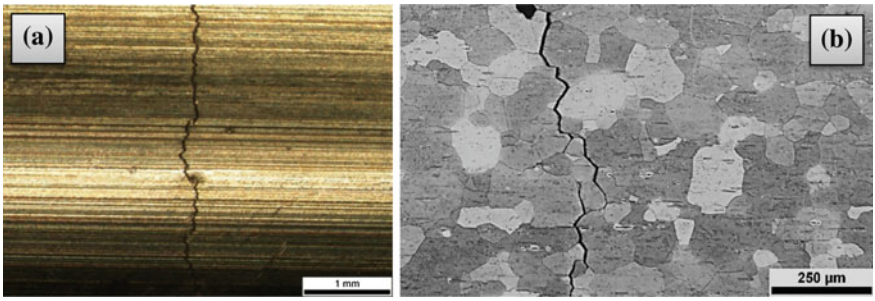

Fig. 3 **a** Stereoscopic micrograph of the surface crack on the C6782, Ø10.8 bar. **b** Optical micrographs, longitudinal section showing the intergranular crack propagation through the β-phase grain boundaries

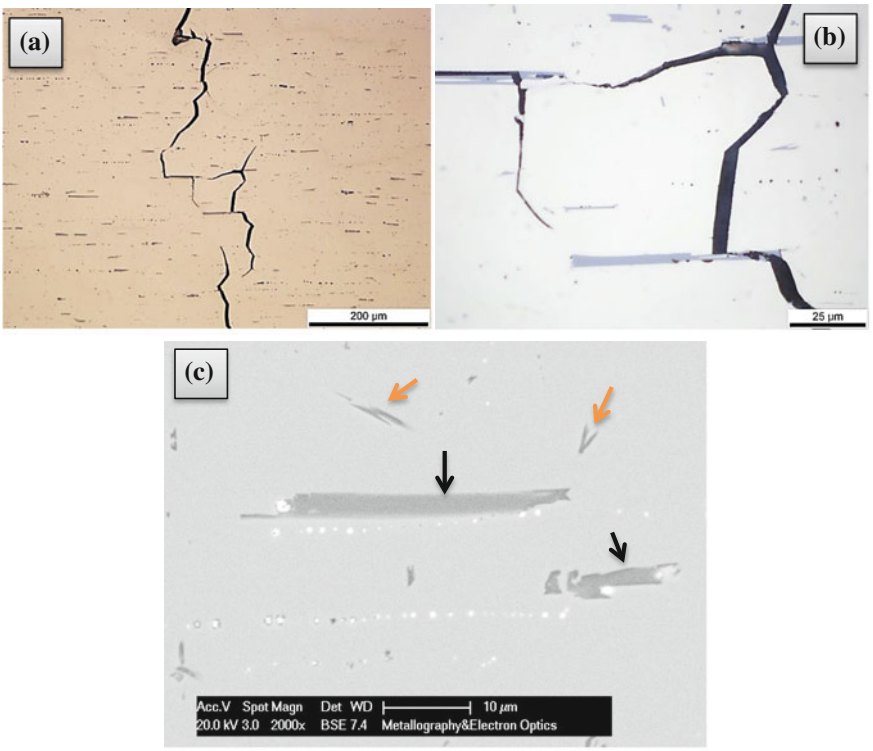

FeMnSi particles (black arrows)	
Element	Weight %
C	18.55
Si	18.30
Mn	26.69
Fe	30.55
Ni	0.21
Cu	3.66
Zn	2.05

MnSiZn particles (orange arrows)	
Element	Weight %
C	18.70
Al	0.07
Si	11.92
Mn	32.69
Fe	2.18
Ni	0.71
Cu	20.50
Zn	13.23

Fig. 4 **a**, **b** Optical micrographs, longitudinal section showing the crack propagation through the brittle intermetallic particles' network. **c** Electron micrograph showing two types of intermetallic particles dispersed in the matrix (see approximate compositions in the respective tables)

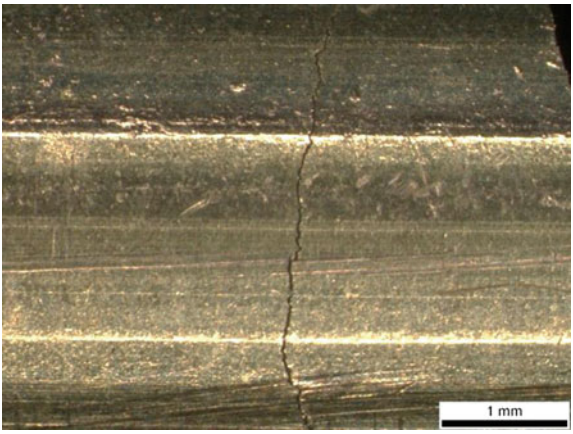

Fig. 5 Stereoscopic micrograph of the surface crack on the CW721R, Ø8.5 bar

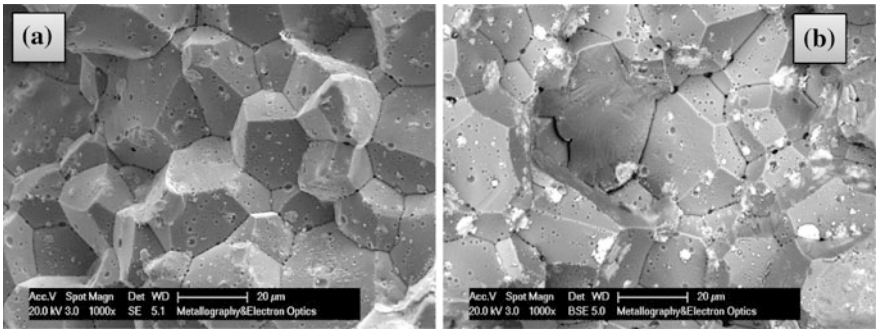

Fig. 6 **a**, **b** SE and BSE electron micrographs of the fracture surface. Note the Pb islands dispersed on the fracture facets and prior grain boundaries. Local voids are also present signifying prior Pb particle positions

EDS analyses revealed that the second phase particles found in the crack path consisted of Fe, Mn, P, Cr, Mg, Cu and Zn.

Texture

EBSD analysis for all samples was performed transverse to extrusion direction. Representative results presented in Fig. 8 for C6782, Ø10.8 bar showed preferably [101] directions of the equiaxed recrystallized grains aligned parallel to extrusion direction as this is indicated by IPF map and plots. The presence of high angle grain

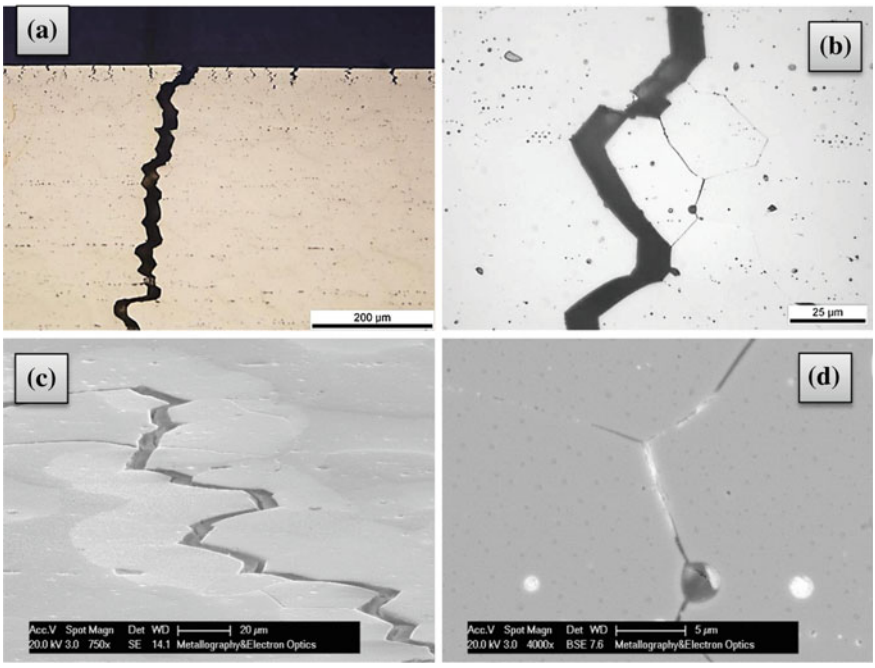

Fig. 7 **a**, **b** Optical and **c** tilted electron micrographs, longitudinal section showing the crack propagation mode. **d** Electron micrograph revealing grain boundary Pb segregation and decohesion

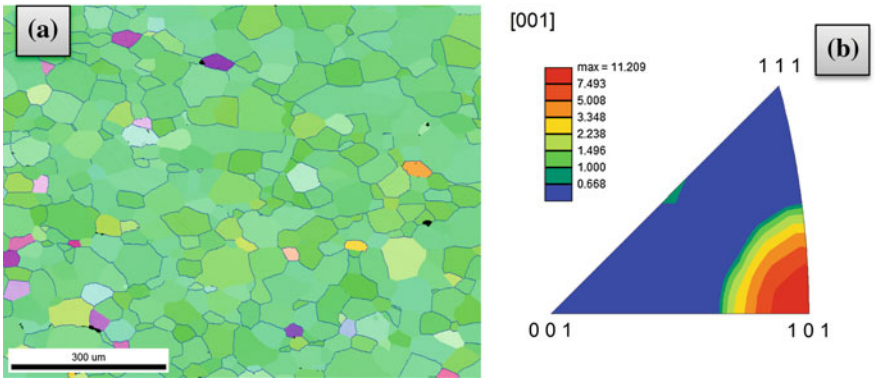

Fig. 8 **a** EBSD IPF map showing crystals orientation, transverse section, high angle (>30°) grain boundaries are highlighted, **b** respective [001] IPF plot showing high relative intensity of [101] directions

boundaries (larger than 30°) is obvious and could be an additional factor contributing to the sensitization of the grain boundaries, especially at the locations of triple joints. Mean grain size was calculated 40 μm by EBSD.

Conclusions

In the present workunexpected low ductility failures during brass alloy extrusion were documented through optical and scanning electron microscopy. The fractures exhibited a typical intergranular mode which is consistent to the following synergistic embrittling factors: LME/SMIE, intense intermetallic phase particle (Mn–Fe–Si based phases) density and high angle boundaries. It is considered that in a medium temperature region ($\sim$300–500 °C) secondary microstructural constituents are associated with grain boundary sensitization and unexpected brittle fracture occurrence. Moreover, the presence of high angle grain boundaries on the dynamically recrystallized grains, as it was aquired by EBSD analysis, is also an additional factor which plays a contributing role to the development of intergranular cracking without noticeableprior plastic deformation in all the examined alloy bars.

References

1. Laporte V, Mortensen A (2009) Intermediate temperature embrittlement of copper alloys. Int Mater Rev 54:94–116
2. Wolley DJ, Fox AG (1988) The embrittlement of leaded and unleaded $\alpha + \beta$ (60–40 brasses in the temperature range 300–500 °C. J Mater Sci Lett 7:763–765
3. Pantazopoulos G, Vazdirvanidis A (2008) Failure analysis of a fractured leaded-brass (CuZn39Pb3) extruded hexagonal rod. J Fail Anal Prev 8:218–222
4. Lynch SP (2008) Failures of structures and components by metal-induced embrittlement. J Fail Anal Prev 8:259–274
5. Bond D, Zikry M (2017) Microstructural Modeling of intergranular fracture in tricrystals with random low- and high-angle grain boundaries. JOM 69:856–862

Part VIII
Mechanical Behaviors of Materials

Determination of Microstructure-Based Constitutive Models Using Temperature Rise Distribution in Plane Strain Machining

Juan Camilo Osorio, Sepideh Abolghasem and Juan Pablo Casas Rodriguez

Abstract Predicting flow stress at high strain-rates is a desirable practice for material behavior characterization. Sub-grain size has shown a huge influence in cutting forces and the workpiece surface finish determination during orthogonal cutting process. Hence, a prediction of flow stress as a function of thermomechanical conditions and sub-grain size is of great important which is studied in this work for OFHC copper. The principal thermomechanical conditions being strain, strain-rate and the accompanying temperature rise are characterized in Plane Strain Machining (PSM) and the resulting microstructure, sub-grain size, is quantified. Material maximum flow stress (a constitutive model) as a function of thermomechanical conditions and sub-grain size is predicted considering a saturated state in microstructure using optimization algorithms for reaching the validated temperature rise based on modified Hahn's model. Evaluated models suggest a major influence of strain-rate and dislocation in temperature rise estimation and flow stress prediction leading to consideration of mechanical failure phenomenon involved in machining-based manufacturing processes.

Keywords Metal cutting process · Severe plastic deformation · Ultrafine grained microstructure

J. C. Osorio (✉) · J. P. C. Rodriguez
Departamento de Ingeniería Mecánica, Universidad de Los Andes, Carrera 1a No. 18A-10, Bogotá, Colombia
e-mail: c.osorio10@uniandes.edu.co

S. Abolghasem
Departamento de Ingeniería Industrial, Universidad de Los Andes, Carrera 1a No. 18A-10, Bogotá, Colombia

B. Li et al. (eds.), *Characterization of Minerals, Metals, and Materials 2018*, The Minerals, Metals & Materials Series,
https://doi.org/10.1007/978-3-319-72484-3_25

Introduction

High Rate Severe Plastic Deformation (HRSPD) imposes severe strain and severe strain-rate resulting in Ultra-fine grained microstructure which has been found to entail enhanced properties such as the strength, wear, fretting and fatigue which are shown to be substantially improved relative to their coarse-grained counterparts [1, 2]. Hence, these discoveries have motivated the exploration of material behavior uncertainties in HRSPD of bulk metals, which involves complex thermomechanical conditions with the advantage of not changing the chemical composition of the obtained chips and machined surfaces. It is vital to optimize these enhanced microstructure properties, which requires understanding of the microstructure transformations as well as the behavior of the material as a function of strain, strain-rate and temperature. It has been found that the microstructure of the chip formed during HRSPD is a consequence of interaction of large strain and high strain-rate scaling with the temperature rise in the deformation zone [3]. The main objective of this work is to establish a microstructure-base constitutive model to estimate the flow stress through calculating the temperature rise during chip formation. This effort will offer an estimate of stress as a function of strain, strain-rate and temperature $\sigma(\varepsilon, \dot{\varepsilon}, T)$. We use plane strain machining (PSM) as our experimental framework due to the conveniences it offers by providing an open deformation zone in utilizing digital image correlation (DIC) of high-speed images of the deformation zone to measure the strain-rate in addition to the temperature rise measurement using infrared thermography [4]. Furthermore, using PSM we apply HRSPD in chip, which can transmit large range of strain and strain-rate in a single deformation pass in a range of material system. Most of the study till date has been accomplished in a very low strain-rate range ($\sim$0.1/s to 10/s), except for few recent works where strain-rates of the order of 10^3/s were utilized resulting in fascinating property combinations [4–7]. Comparing HRSPD processing conditions with these constitutive models, we lack a suitable relationship to bridge the gap among the thermomechanical conditions, resulting microstructure and the flow stress in machining-based manufacturing processes.

Experimental Methods

We utilized Plane Strain Machining (PSM), as shown in Fig. 1a where a condition of orthogonal cutting was performed. This configuration was used to measure thermomechanical properties using imaging and analytical methods. Different cutting conditions including chip thickness ratio (a_0/a_c), velocity (V) and rake angle (α) from 0º to 40º were modified to achieve different strain and strain-rate values. These conditions are listed in Table 1 corresponding to four rake angles (α = 0°, 20°, 30° and 40°) and four different machining speeds (viz. Low (L) = 50 mm/s; Med (M) = 550 mm/s; Medium-High (MH) = 750 mm/s and High

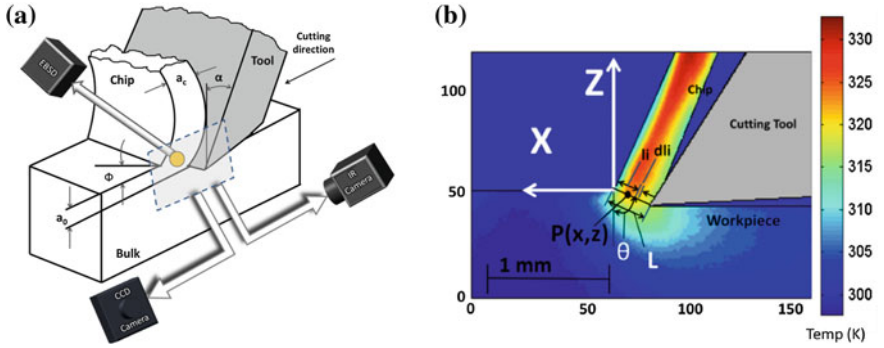

Fig. 1 **a** Schematic of the plane strain machining (PSM) process. **b** Infrared thermograph for 30 M sample

Table 1 Machining parameters for different deformation conditions

Sample condition	V [mm/s]	α [°]	φ [°]	Ɛ	$\dot{\varepsilon}$ [1/s]	T_m	T_c	δ_c
0 L	50	0	3.8	8.7	60	322	363	0.28
0 M	550	0	5.6	5.9	940	–	454	0.38
0 MH	750	0	5.95	5.6	1240	–	464	0.39
20 L	50	20	3.22	5.9	80	342	346	0.35
20 M	550	20	4.34	3.9	1290	378	412	0.42
20 MH	750	20	4.5	3.6	1740	–	416	0.43
20 H	1250	20	5	3.4	3130	–	439	0.44
30 L	50	30	7.7	4	100	319	332	0.40
30 M	550	30	11.4	2.6	1740	–	379	0.45
30 MH	750	30	11.8	2.5	2290	–	385	0.45
30 H	1250	30	12.3	2.3	4030	–	402	0.46
40 L	50	40	11.2	2.6	140	324	321	0.44
40 M	550	40	13.6	2.1	1930	336	367	0.46
40 MH	750	40	14	2	2520	339	372	0.46
40 H	1250	40	15.8	1.8	4680	–	381	0.47

(H) = 1250 mm/s). Samples were denoted 0 L, 0 M, 0 MH, etc. where the numbers represent the rake angle and the letters L, M, MH and H refer to the machining speeds.

Results and Discussion

In machining, the imposed strains vary with the rake angle α as [4]:

$$\varepsilon = \frac{\gamma}{\sqrt{3}} = \frac{\cos\alpha}{\sqrt{3}\sin\phi\cos(\phi-\alpha)} \tag{1}$$

where ϕ is the inclination of the shear plane (Fig. 1a) and α is the rake angle of the tool. The strain-rates were obtained using the Oxley and Hastings relation as [4]:

$$\dot{\varepsilon} = C\frac{V\cos\alpha\sin\phi}{\cos(\phi-\alpha)a_0} \tag{2}$$

The constant "C" is directly measured as 2.77 (V in mm/s and a_0 in mm) using high-speed images of the deformation zone captured by means of a CCD camera combined with Digital Imaging Correlation (DIC) on the sequence of images (see Ref. [4] for more details). The values for the effective strain and the strain-rates are listed in Table 1. The temperature rise was measured using infrared (IR) thermography and IR camera (FLIR A325). To obtain the thermograph analogous to the Fig. 1b, a plate of commercially pure copper was machined at various rake angles and at various cutting velocities. The calibration process is explained in detail in [4]. Measured temperatures are listed as T_m in Table 1 and are compared with T_c that is calculated using the expression found in [4].

$$\int_{T_0}^{T_c} \frac{\rho C_p(T)}{1-\left(\frac{T-T_r}{T_m-T_r}\right)^m} = (1-\beta)\left(A\varepsilon + \frac{B}{n+1}\varepsilon^{n+1}\right)\left(1 + C\ln{}^{\dot{\varepsilon}}/_{\dot{\varepsilon}_0}\right) \tag{3}$$

To build the model it is necessary to predict the temperature rise in the deformation zone. The temperature in the deformation zone is not an independent variable, but a function of machining geometry, strain and the constitutive behavior of the material. The imposed shear strain in HRSPD controls the amount of temperature generated in the deformation zone. This heat is partitioned between the bulk workpiece and the chip. We can intuitively foresee that the higher the shear strain and the strain-rate, the higher the temperature in the deformation zone. The fraction of heat taken away by the bulk is strongly dependent on the deformation configuration. In this paper, the configuration of machining geometry as shown in Fig. 1b can be approximated by a moving heat source problem, which is characterized by an inclined heat source across which mass transport occurs. Therefore, the temperature in the deformation zone and its distribution around the deformation zone can be solved using modified Hahn's model as given in [8, 9]. However, the temperature in the deformation zone also modifies the constitutive behavior, thus interacting with the accommodation of the shear strain and the strain-rates, which manifests in the wide variety of deformed microstructures obtained here.

During machining, the heat generated in the deformation zone occurs in response to volumetric heat generation, that is produce by elastic, plastic and material failure energy release as [10].

$$u_s = \int_0^{\varepsilon} \sigma(\varepsilon, \dot{\varepsilon}, T) d\varepsilon \tag{4}$$

where $\sigma(\varepsilon, \dot{\varepsilon}, T)$ is the flow stress of the material that can be back calculated knowing the temperature, the strain and strain rate conditions during any deformation process.

The derivation for $\sigma(\varepsilon, \dot{\varepsilon}, T)$ as a function of the central deformation variables is explained in [11], where effective strain-rate is directly proportional to dislocation velocity varying with as:

$$\dot{\varepsilon} = \dot{\varepsilon}_0 e^{-\frac{G}{kT}} \tag{5}$$

in which the optimality conditions require $\dot{\varepsilon}_0$ to be a constant equal to one. In this equation, the activation energy G is expressed in the following from [11].

$$G = G_o - \int_0^{\tau_{th}} A^* b d\tau'_{th} \tag{6}$$

where G_0 is the reference Gibbs energy at T = 0, A^* is the activation area and τ_{th} is the thermal component of shear stress. Assuming all samples are at a saturated stress (A^* is stress independent), G can be simplified to:

$$G = G_0 - Ab\tau_{th} \tag{7}$$

Combining Eqs. 4 and 6 and noting that $\sigma_{th} = m\tau_{th}$, stress can be written as:

$$\sigma_{th} = \frac{mG_0}{Ab}\left[1 + \frac{kT}{G_0}\ln\left(\frac{\dot{\varepsilon}}{\rho}\right)\right] \tag{8}$$

where m is the orientation factor having the value of $\sqrt{3}$ based on Von Mises model [11]. As it is shown in [12], when a saturated state is being analyzed, dislocation density (ρ) and sub-grain size (δ) can be related using the principle of scaling, that results in $\delta\sqrt{\rho} = q_c$ [11] and hence a proportional relation between A^* and δ can be concluded ($A^* \propto \delta$) [12]. Considering this proportionality, the flow stress that depends on the sub-grain size, can be rewritten as:

$$\sigma = E\left(\frac{1}{\delta}\right)\left[1 + C_1 T \ln\left(\frac{\dot{\varepsilon}}{\rho}\right)\right] + D \tag{9}$$

Using $\delta\sqrt{\rho} = q_c$ and rewriting it in the form $\frac{1}{\rho} = C_3\delta^2$ we can present the flow stress as:

$$\sigma = E\left(\frac{1}{\delta}\right)\left[1 + C_1 T \ln\left(C_3 \dot{\varepsilon} \delta^2\right)\right] + D \tag{10}$$

where E, C_1, C_3, D are all constants.

As this work focus on sub-grain size based constitutive models and flow stress calculation, it is necessary to stablish a relationship between cutting conditions and saturated sub-grain size. To do this a Taylor series expansion function is developed for which the detail procedure can be found in [4], written as a function of two variables R and ε [4]:

$$\delta_c = \delta_0 + \frac{\partial \delta_r}{\partial \in} \in + \frac{\partial \delta_r}{\partial R} R + \frac{\delta^2 \delta_r}{\partial \in \partial R} \in R \tag{11}$$

This expression ignores all high order terms in ε and R second-order effects are negligible. We can write the sub-grain size across all area of thermomechanical conditions as [4]:

$$\delta_c = 0.25 - 0.03 \in + 0.058R + 0.0003 \in R \tag{12}$$

The variable R is defined as a temporally dependent rate function [4]:

$$R = \left(\frac{Gb^3}{\kappa T} + \eta\right)\left(\frac{1}{\ln(C_1) + \ln(Z)}\right) \tag{13}$$

where Z is the Zener-Hollomon parameter describing strain-rate and temperature as $Z = \dot{\varepsilon} e^{Q/RT}$ where $\dot{\varepsilon}$ is the effective strain-rate, Q the activation energy ($Q = 197\,\text{kJ mol}^{-1}$ for self-diffusivity of Cu [13]), R the gas constant and T the absolute deformation temperature.

Developing the relationship between grain size and the central variables of deformation, we can proceed in constructing the model using the equation for flow stress. In this model, workpiece is the semi-infinite medium while the deformation zone is the oblique plane heat source moving with cutting velocity U. Taking the origin at the intersection of the band heat source and the surface of the un-machined work-piece (see Infrared image in Fig. 1b), the temperature rise at any point $P(x, z)$ on the work piece is given by [8, 9]:

$$\Delta T_P = \frac{q_{pl}}{2\pi\lambda} \int_{l_i}^{L} e^{-(x - l_i \sin\theta)V/2a} \left\{ K_o \left[\frac{V}{2a}\sqrt{(x - l_i \sin\theta)^2 + (z - l_i \cos\theta)^2}\right] + K_o \left[\frac{V}{2a}\sqrt{(x - l_i \sin\theta)^2 + (z + l_i \cos\theta)^2}\right] dl_i \right\} \tag{14}$$

where x-axis is in the direction of the moving tool and z-axis points away from the chip. The angle θ is defined as the angle between the heat source and z-axis (see the Fig. 1b for orientation of coordinates and explanation of various terms). In above equation $\sqrt{(x - l_i \sin\theta)^2 + (z - l_i \sin\theta)^2}$ and $\sqrt{(x - l_i \sin\theta)^2 + (z + l_i \sin\theta)^2}$ are the distances of the point $P(x, z)$ from the primary heat source and the image source (chip and tool intersection) respectively, λ the thermal conductivity, a thermal diffusivity, K_0 the modified Bessel function of the second kind zeroth order, q_{pl} $\left[\frac{J}{mm^2 s}\right]$ the intensity of heat liberation of the band heat source calculated from $q_{pl} = u_s U \sin\phi$.

The two models described above (microstructure base model for stress calculation and modified Hahn's model for temperature calculation) [8, 9] setup a thermomechanical and microstructurally coupled problem where we need to know the temperature rise to calculate the shear strength values, which in turn is required to calculate the temperature rise. To solve this problem, we consider an iterative procedure where error between the calculated and measured temperature is minimized to achieve appropriate constants (Fig. 2). First, it is necessary to determine the sub-grain size using the calculated temperature allowing us to calculate the homologous stress. Then we use the modified Hahn's model to calculate the temperature rise for the conditions for which the temperature has been measured through IR thermography. After the temperature rise is calculated, the error between experimental and calculated temperature rise is minimized to find the flow stress equation constants. As this procedure does not depend on the flow stress equation or the constitutive model, it could essentially be utilized to calculate any constitutive model constants. This error is minimized using a genetic algorithm found in Matlab. The flow chart is shown in Fig. 2 and the calculated stress is compared with

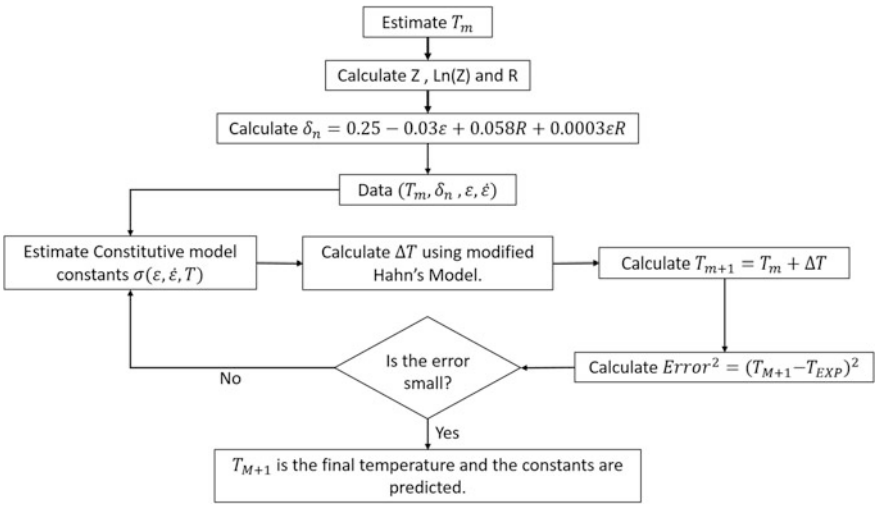

Fig. 2 Methodology for material characterization using temperature rise

other constitutive models in Figs. 3 and 4. For the maximum flow stress equation, the parameters are obtained as E = 64.12 MPa mm, $C_1 = 7.17 \times 10^{-4}\mathrm{K}^{-1}$, $C_3 = 89.97$ s mm^{-2} and $D = 293.05$ MPa.

All constants where predicted using the higher strain and strain-rate cutting conditions. This consideration gives more accuracy for strain-rate depended models as materials are subjected to HRSPD. Furthermore, to verify our model we have evaluated the flow stress for the maximum deformation data points using Johnson Cook [14] (Eq. 15), Cowper Symonds [15] (Eq. 16), and Zerilli Armstrong [12] (Eq. 17) as follows:

$$\sigma = (A + B\varepsilon^n)\left(1 + C\ln\left(\dot{\varepsilon}/\dot{\varepsilon}_0\right)\right)\left(1 - \left(\frac{T - T_r}{T_m - T_r}\right)^m\right) \tag{15}$$

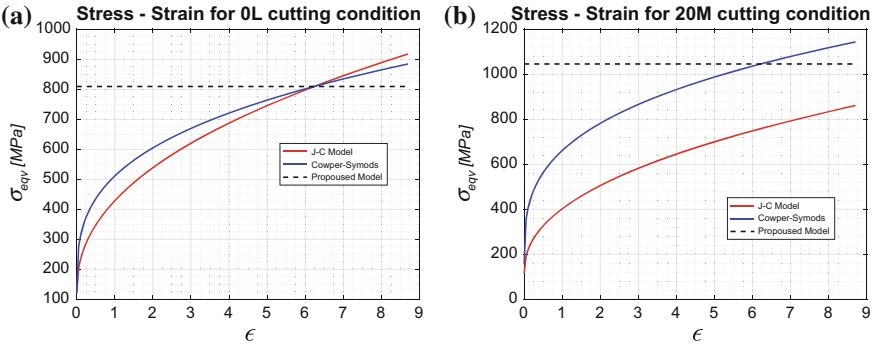

Fig. 3 Stress strain curve for Johnson-Cook [14] model, Cowper–Symonds [15] compared with calculated flow stress. **a** Comparison for 0 L cutting condition. **b** Comparison for 20 M cutting condition

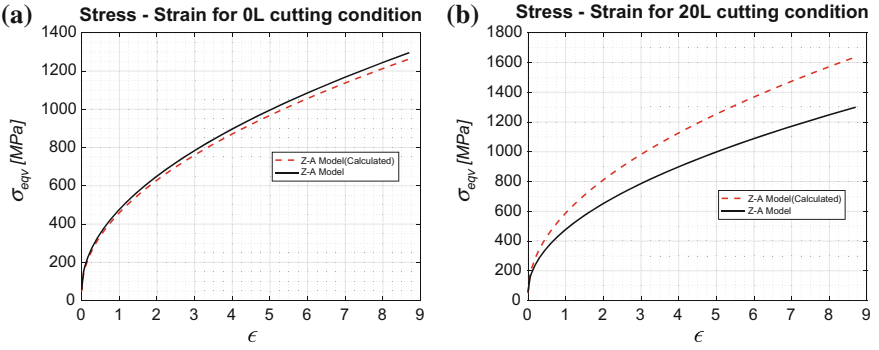

Fig. 4 Comparison between Zerilli–Amstrong model found in [12] and Zerilli–Amstrong model calculated in this work

$$\sigma = (A + B\varepsilon^n)\left(1 + \left(\frac{\dot{\varepsilon}}{C}\right)^{1/P}\right) \tag{16}$$

The iterative method was verified calculating Zerilli–Amstrong model constants using temperature rise and compering them to Z–A constants found in [12] (Fig. 4). For this model five constants where predicted $\Delta\sigma_g, C_2, C_3, C_4, K$ as:

$$\sigma = \Delta\sigma_G + C_2\varepsilon^{1/2}e^{(-c_3T + c_4T\ln\dot{\varepsilon})} + k\delta^{-1/2} \tag{17}$$

Figure 3 shows the maximum stress achieved for 0 and 20 L cutting conditions. In this cutting condition the predicted maximum flow stress is similar to the maximum stress calculated using the Z–A Model [12] and the C–S model found in [15]. As the proposed model is not stress dependent, it only represents the maximum stress achieved during cutting process for a specific strain. Hence, an accurate comparison between the proposed maximum flow stress model and the constitutive CS and JC models should be in a determined strain condition. Here 8% of error is achieve with respect to CS material model and 11% with respect to JC material model.

Error between models can be explained considering that the proposed model is not strain dependent, which leads to a poor estimation of the energy release u_s and material model constants. On the other hand, the error with respect to CS model should be smaller as the constants predicted for this model were determined using an inverse Taylor impact model achieving strain-rates of 10^5 s^{-1} (see more detail in [15]).

Material model constants for Z–A were calculated using the same process described above. Model constants are estimated as $\Delta\sigma'_G = 41.45$ MPa, $C_2 = 883$ MPa, $C_3 = 0.0036$ MPa, $C_4 = 0.000346$ MPa, $K = 4.44$ MPa mm^2 which are material parameters in Eq. 17. The obtained model in this work is compared with Z–A model in Fig. 4 for 0 and 20 L conditions.

Prediction of a couple elastic–plastic model requires many variables and phenomenon to be considered. During orthogonal cutting process, ductile materials experience elastic, plastic deformation and failure due to extreme deformation. During ductile failure elastic modulus is degenerated as elastic energy is lost to generate dislocation movements leading to micro voids and micro fractures. In Z–A model there is no failure model coupled and hence in temperature rise calculation, there is extra energy (in the energy term (u_s)) that turns into heat due to extra plastic energy since it is assumed to be completely plastic. To understand this phenomenon, we must consider the second law of thermodynamics for a continuum material [16] as:

$$\sigma_{ij}\dot{\varepsilon}^p_{ij} - \dot{w}_s + Y_{ij}\dot{D}_{ij} - \frac{q_i T_{,i}}{T} \geq 0 \tag{18}$$

This means the sum of the dissipation due to plastic power ($\sigma_{ij}\dot{\varepsilon}^{p}_{ij}$) minus the stored energy density as Plastic Energy ($\dot{w}_s$) plus the dissipation due to damage ($Y_{ij}\dot{D}_{ij}$), is transformed into heat $\left(\frac{q_i T_{,i}}{T}\right)$ [16]. This explains the error between the calculated Z–A model and the model constants found in [12], as the cutting process couples damage and plasticity and in this case the dissipation due to damage is not considered. Therefore there is more plastic energy included in the model. Moreover, dislocations are proportional to strain-rate, and damage is directly related with dislocations. Hence, as the strain-rate increases it increases the error between the models as the damage term is not added to heat generation, and temperature rise is sub predicted. Consequently, the material generates more energy duo to plastic deformation. However, if a damage model is coupled, the term $\dot{w}_s$ will be considerably reduced and the damage term in heat equation ($Y_{ij}\dot{D}_{ij}$) will take a key role in the analysis of heat generation and temperature rise.

Conclusion

We established a microstructure-based method to predict an fcc material behavior simulating the workpiece as a semi-infinite medium while the deformation zone is the oblique plane heat source moving with cutting velocity. This allows us to couple the constitutive or flow stress equation with geometry and thermal properties of the material, considering the energy released during an elastic–plastic deformation process. A maximum stress model was calculated considering a saturated condition for sub-grain size. We obtained the result for flow stress in good agreement with other constitutive models found in [13–15]. It was proved that constants for different constitutive models can be predicted using the modified Hahn's model [8, 9] allowing to predict material behavior with almost no error. However, as the metal cutting process involves elastic–plastic deformation and material failure, it is necessary to take the effect of mechanical failure of material into consideration for establishing the constitutive models at high strain-rates.

Acknowledgements In this study, we acknowledge the funding support from Colciencias grant code 120474557650 and the 2017 grant from school of engineering at Universidad de los Andes, Bogotá, Colombia.

References

1. Denguir LA, Outeiro JC, Fromentin G, Vignal V, Besnard R (2016) Orthogonal cutting simulation of OFHC copper using a new constitutive model considering the state of stress and the microstructure effects. Procedia CIRP 46:238–241

2. Rahman MA, Rahman M, Kumar AS (2017) Modelling of flow stress by correlating the material grain size and chip thickness in ultra-precision machining. Int J Mach Tools Manuf 123:57–75
3. Shekhar S, Abolghasem S, Basu S, Cai J, Shankar MR (2012) Effect of severe plastic deformation in machining elucidated via rate-strain-microstructure mappings. J Manuf Sci Eng 134(3):31008
4. Abolghasem S, Basu S, Shekhar S, Cai J, Shankar MR (2012) Mapping subgrain sizes resulting from severe simple shear deformation. Acta Mater 60(1):376–386
5. Basu S, Abolghasem S, Shankar MR (2013) Mechanics of intermittent plasticity punctuated by fracture during shear deformation of Mg alloys at near-ambient temperatures. Metall Mater Trans A Phys Metall Mater Sci 44(10):4558–4566
6. Abolghasem S, Basu S, Shankar MR (2013) Quantifying the progression of dynamic recrystallization in severe shear deformation at high strain rates. J Mater Res 28(15):2056–2069
7. Shekhar S, Cai J, Basu S, Abolghasem S, Shankar MR (2011) Effect of strain rate in severe plastic deformation on microstructure refinement and stored energies. J Mater Res 26(3):395–406
8. Journal of Theoretical and Applied Mechanics (2013) Development of a thermal model in the metal cutting, pp 553–567
9. Komanduri R, Hou ZB (2000) Thermal modeling of the metal cutting process Part I—temperature rise distribution due to shear plane heat source. Int J Mech Sci 42(9):1715–1752
10. Kapoor R, Nemat-Nasser S (1998) Determination of temperature rise during high strain rate deformation. Mech Mater 27:1–12
11. Zerilli FJ (2004) Dislocation mechanics-based constitutive equations. Met Mater Trans A 35 (9):2547–2555
12. Zerilli FJ, Armstrong RW (1987) Dislocation-mechanics-based constitutive relations for material dynamics calculations. J Appl Phys 61(5):1816–1825
13. Mahadevan D (2007) Experimental determination of velocity and strain rate fields in metal cutting of OFHC copper
14. Denguir LA, Outeiro JC, Fromentin G, Vignal V, Besnard R (2017) A physical-based constitutive model for surface integrity prediction in machining of OFHC copper. J Mater Process Technol 248(April):143–160
15. Hernandez C, Maranon A, Ashcroft IA, Casas-Rodriguez JP (2012) Inverse methods for the mechanical characterization of materials at high strain rates, vol. 4022. Freiburg, Germany, pp. 1–6
16. Lemaitre J, Desmorat R (2005) Engineering Damage Mechanics. Springer, Berlin

Precipitating Behaviour of Second Phase Particles in Lightweight Fe–Mn–Al–C–N Stainless Steel

Wei Hou, Xiaoyu Han, Jingtao Wang and Jun Bao

Abstract Lightweight stainless steel has widely potential applications in many fields, such as automobile, ship, submarine manufacturing and aerospace. The properties of lightweight stainless steel are significantly affected by the precipitating behaviour of second phase particles. In this paper, the precipitating behaviour was investigated by XRD, DSC in the process of heating and thermodynamic calculation combining the Miedema's and Chou's model. The XRD results indicate that there are five types of phases in lightweight Fe–Mn–Al–C–N stainless steel: ferrite, FeAl, AlMn, AlN and Mn_4N. The DSC results show that the precipitating temperature of FeAl, Mn_4N is 1260, 1031 °C, respectively, corresponding to the thermodynamic calculation. Besides, The DSC measurement reflects the precipitating temperature of AlMn and austenite is 934 and 600 °C.

Keywords Lightweight stainless steel · Second phase particles
Precipitating temperature · Thermodynamic calculation

Introduction

Lightweight stainless steel based on the high aluminum concentration has very attractive properties [1–5], such as low density, high melting temperature, high thermal conductivity, very good oxidation resistance ability and hot corrosion resistance, which have been playing an active role for the application in high temperature and corrosive environments due to the ability to form protective Al_2O_3 scales [6–8]. This type of steel has attracted considerable attentions as a potential candidate for structural and coatings applications at elevated temperatures, and can become a promising substitute for traditional stainless steels in the foreseeable future. The researches of the addition of aluminum to the stainless steels have

W. Hou (✉) · X. Han · J. Wang · J. Bao
College of Materials Science and Engineering, Chongqing University, Chongqing 400044, China
e-mail: cquhouwei@163.com

B. Li et al. (eds.), *Characterization of Minerals, Metals, and Materials 2018*, The Minerals, Metals & Materials Series,
https://doi.org/10.1007/978-3-319-72484-3_26

been widely reported, Ham et al. obtained that lightweight Fe-10.2%Al-34.4% Mn-0.76%C stainless steel has lower densities over S30210, and also showed good processability and excellent oxidation resistance performance even at 815 °C [9]. Zhu et al. [10] have researched the corrosion resistance and corrosion film on the interface of Fe-31%Mn-8%Al alloys, results showed that the addition of aluminum is the key factor to the corrosion resistance of this Fe–Mn based alloy. Russia and Japan have developed lightweight Fe–Mn–Al stainless steel in succession and this steel has been applied to submarine manufacturing benefitting from their corrosion and flushing resistance in seawater. In addition, compared with the chromium nickel stainless steel and copper alloy, this steel has lower cost and density [11]. However, the properties of lightweight stainless steel could be significantly influenced by the formation and distribution behaviors of the second phase particles. Chang et al. [12] have reported that smaller nanocrystalline AlN phase can led to higher surface hardness and better corrosion resistance. Nevertheless, if AlN phase has severely precipitated at the crystal boundary, it could wreck the continuity of the base and accelerate the forming and expanding of the cracks thus decreasing the strength of the steels. So, it is necessary and crucial to study the precipitating behaviors of the second phase particles in lightweight stainless steel.

In the present study, the theoretical calculation, which is based on the Miedema's and Chou's model [13–15], combines with experiments by means of precise method of XRD and DSC technique in the process of heating were used to explore the precipitating behavior of second phase particles in lightweight Fe–Mn–Al–C–N stainless steel Please note that the equations have been renumbered to maintain sequential order..

Experimental Procedure

Sample Preparation

In the experiments of smelting, 45# steel ingot, silicon iron, Mn–Fe alloy containing N, graphite and aluminum were employed. The smelting process was performed with the use of a 25 kg vacuum induction melting furnace. The experiment began with introducing 45# steel sample (of pre-specified mass) to the melting pot placed in the induction coil of the furnace. Given that these alloy materials and addition agents will be added to the pot during the melting process step by step, the furnace is always kept open and nitrogen gas is top-blown to protect melts from oxidation. When the test was completed, liquid metal was poured into the cooled mold. When it solidified and the furnace cooled down, the furnace chamber was opened and the steel sample was analyzed for the chemical composition. The chemical compositions of the steel were analyzed by XRF-1800 X-ray fluorescence spectrometer and the results were presented in Table 1.

Phase of the melted samples were characterized by a Rigaku D/max 2500/PC X-ray diffractometer (XRD) using Cu Kα. Scanning was carried out at an angular

Table 1 The chemical composition of lightweight Fe–Mn–Al–C–N stainless steel

Element	Al	Si	Mn	C	N	Fe
wt (%)	14.969	1.01	8.366	0.650	0.200	74.805

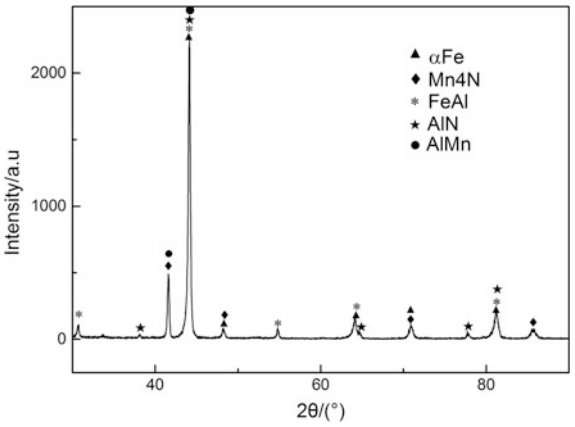

Fig. 1 XRD patterns of the Fe–Mn–Al–C–N lightweight stainless steel

range from 10° to 90° and scan rate of 4°/min. MDI Jade 5.0 was utilized to analyze the intensity data obtained by XRD analysis. Figure 1 shows the XRD patterns of the lightweight Fe–Mn–Al–C–N stainless steel. Careful examination of the diffraction pattern revealed the presence of the Mn_4N, FeAl, AlN, AlMn phases in addition to αFe.

The Differential Scanning Calorimetry

The differential scanning calorimetry (DSC) tests were carried by NETZSCH STA 449F3 differential thermal analyzer. The test samples in an alumina crucible were heated from room temperature to 1500 °C at a rate of 20 K/min in Ar (20 ml/min) protective atmosphere. Meanwhile Ar as reactant gases were blown into the furnace at 50 ml/min to enable complete reaction with the samples at the temperature rise period. To exclude the influence of the system error from the thermal analyzer and the buoyance force from the gas, a blank test was conducted under the same elimination conditions with no samples in alumina crucibles. It is noticeable that activation energy for the main exothermic reaction was obtained by using DSC measurement. Figure 2 expressed the DSC curve of the Fe–Mn–Al–C–N lightweight stainless steel in the continuous heating process, in which there exists around 6 endothermic peaks (peaks F, E, D, C, B, A in order). The peak E, C, and B correspond to the phase transition of austenite, Mn_4N, and FeAl, respectively and the peak F, and A coincide with the heat absorption of water evaporation and the

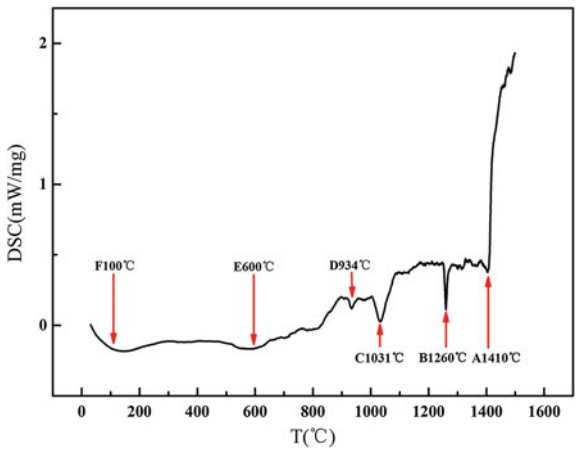

Fig. 2 Thermal analysis results of Fe–Mn–Al–C–N lightweight stainless steel

melting process of the experimental of steel. Previous investigations have shown the phase transition temperature of AlMn ranges from 900 to 1005 °C, and combining the Aluminum-Manganese(Al–Mn) binary phase diagram [16] with the experimental results from XRD analysis, the existence of the AlMn phases could be identified. Analogically, peak D corresponds to the phase transition temperature of AlMn phase.

Thermodynamic Calculation

The Precipitating Behaviour of AlN and Fe_3C in the Solidification Process

The melting point of lightweight Fe–Mn–Al–C–N stainless steel was estimated by:

$$T = T_{iron} - \sum \Delta T_i \times x_i \% \tag{1}$$

where T is the temperature of the liquid phase in the solidification process, T_{iron} is the melting point of pure iron, ΔT_i is the decreased solidifying point temperature of the addition of i elements (1 wt%) to the steel (presented in Table 2) and x_i % is the content of i elements in the steel, as presented in Table 2.

Substituting these parameters into Eq. (1), the melting point of the experiment use of steel is 1420 °C, in accordance with the result of experimental measurement from DSC.

the Gibbs energy of AlN can be written as:

Table 2 The information of $x_i\%$ and ΔT_i in the lightweight Fe–Mn–Al–C–N stainless steel

Elements	Fe	C	Mn	Al	N
ΔT_i	–	65	5	3	90
$x_i\%$	75.81	0.65	8.37	14.97	0.2

$$[\mathrm{Al}] + [\mathrm{N}] = \mathrm{AlN}_{(S)} \Delta G_{\mathrm{AlN}} = -393880 + 119.547T \tag{2}$$

According to Eq. (2), when T = 1420 °C, the result can be obtained: $\Delta G_{\mathrm{AlN}} = -204895 < 0$

Analogically,

$$3\mathrm{Fe}_l + [\mathrm{C}] = \mathrm{Fe_3C}_{(S)} \Delta G_{\mathrm{Fe_3C}} = -159302 + 70.82T = -39403 < 0 \tag{3}$$

From the results of thermodynamic calculations, the precipitation phases of AlN and Fe_3C can meet the thermodynamic requirements, so AlN and Fe_3C could be precipitated in thermodynamic respect. However, according to the thermodynamic principle, a phase is more prone to form as it has a lower Gibbs energy of formation. It can be observed that the Gibbs energy of formation of Fe_3C is considerably higher than AlN, so the precipitates of AlN were nucleated preferentially. Meanwhile, the AlN phase was identified rather than Fe_3C in the XRD experimental results, which correspond to the results of the thermodynamic calculations.

The Precipitating Behaviour of FeAl and Mn_4N in the Solidification Process

The Miedema's model is widely used for estimating the formation enthalpy of binary compounds [17–20]. The Miedema model is expressed as

$$\Delta H_{\mathrm{ij}} = f_{ij} \frac{x_i \left[1 + \mu_i x_j (\varphi_i - \varphi_j)\right] x_j \left[1 + \mu_j x_i (\varphi_j - \varphi_i)\right]}{x_i V_i^{2/3} \left[1 + \mu_i x_j (\varphi_i - \varphi_j)\right] + x_i V_i^{2/3} \left[1 + \mu_j x_i (\varphi_j - \varphi_i)\right]} \tag{4}$$

With f_{ij} defined as

$$f_{ij} = 2pV_i^{2/3} V_{\mathrm{j}}^{2/3} \frac{\left\{ q \Big/ p \left[\left(n_{ws}^{1/3}\right)_j - \left(n_{ws}^{1/3}\right)_i \right]^2 - (\varphi_i - \varphi_j)^2 - \alpha(\gamma/p) \right\}}{\left(n_{ws}^{1/3}\right)_i + \left(n_{ws}^{1/3}\right)_j} \tag{5}$$

where ΔH_{ij} is the formation enthalpy of binary alloy, n_{ws}^i and n_{ws}^j are electron density parameter of i and j elements, φ_{i} and φ_{j} are electronegativity for i and j elements, α, μ, γ, p and q are empirical parameters associated with the electronegativity, electronic properties and so on of solute atoms. In liquid metal,

$\alpha = 0.73$, in solid solution, $\alpha = 1$. The values of p and q depend on the type of metals forming the alloy/intermetallic compound. In general, the value of p is taken as 14.2 for metals with valency higher than 2, and 10.7 for metals with valency of 1 or 2. The p/q ratio is maintained at 9.4. The factor γ takes the values 8 and 0 for intermetallics and solid solutions, respectively. The values of $n_{ws}^{1/3}$, φ, V, μ are as shown in Table 3.

In a binary system, the relation between G_{ij}^{E} and ΔH_{ij}, and S_{ij}^{E} is given by $G_{ij}^{E} = \Delta H_{ij} - TS_{ij}^{E}$, where T is the absolute temperature of the system, since the melting point of individual component is at least above 1000 K, according to the data of DSC. So S_{ij}^{E} is much smaller than the absolute value of ΔH_{ij}. Analogically, $G_{ij}^{E} = \Delta H_{ij}$. Considering the results of experimental measurement from DSC, only Fe–Al, Mn–N and Al–Mn are calculated by substituting these parameters into Eqs. (2) and (3). The formation enthalpies and excess partial molar free energies of Fe–Al, Mn–N and Al–Mn binary alloy system are as shown in Table 4.

From the results of thermodynamic calculations, the formation enthalpies of Fe–Al, Mn–N and Al–Mn binary alloy system can meet the thermodynamic requirements, so the phases formed by Fe–Al, Mn–N and Al–Mn binary alloy system could be precipitated in thermodynamic respect. The formation enthalpies of Mn–N phase are the lowest, as the chemical bonding in MnN is a combination of ionic Mn–N.

The Gibbs free energy of the solution system could be changed if other atoms there exist, which will interact with the original system. The Gibbs free energy of quinary systems can be estimated if formation enthalpies of binary systems and the activities of the quinary Fe–Mn–Al–C–N system as known, but only a part of the activities can be measured by experiment. In this work, based on binary Miedma's model and Chou's model for multicomponent systems, the theoretical formula was derived by coupling with excess entropy introduced by free volume theory for a series of thermodynamic properties. In particular, in combinations with several basic thermodynamic relations, the activity coefficient of a solute at infinite dilution solution, $\ln\gamma_1$ in liquid iron-based system.

Based on the Miedema model, an extrapolation model which is available to quinary Fe–Mn–Al–C–N system is proposed by the Chou's model. The model can be described as

Table 3 The value of φ, $n_{ws}^{1/3}$, $V^{2/3}$ and μ in Miedema model

Element	φ	$n_{ws}^{1/3}$	$V^{2/3}$	μ
Cr	4.65	1.73	3.74	0.10
Mn	4.45	1.61	3.78	0.04
Fe	3.103	1.77	3.69	0.10
Al	4.2	1.39	4.64	0.07
C	6.24	1.77	2.20	0.04
N	6.86	1.65	2.56	0.04

Table 4 The ΔH (kJ/mol) and $\bar{G}_i^E$ (kJ/mol) of i-j binary alloy

i-j	x_i	0.1	0.2	0.3	0.4	0.5	0.6	0.7	0.8	0.9
Fe–Al	ΔH	−7.3046	−13.1410	−17.4571	−20.1979	−21.3048	−20.7154	−18.3634	−14.1780	−8.0838
	$\bar{G}_i^E$	−81.7990	−81.1895	−78.4052	−73.4617	−66.3791	−57.1829	−44.9047	−32.5826	−17.2627
Mn–Al	ΔH	−9.7656	−17.6381	−23.5265	−27.3333	−28.9540	−28.2757	−24.1773	−19.5280	−11.1865
	$\bar{G}_i^E$	−109.1080	−108.5787	−104.2101	−98.9690	−89.8263	−77.7577	−62.7458	−44.7806	−23.8617
Mn–N	ΔH	−44.8988	−81.1152	−104.6192	−119.5343	−123.1083	−116.6863	−100.6848	−74.5701	−41.8383
	$\bar{G}_i^E$	−493.1099	−469.8826	−437.2475	−397.4540	−350.5616	−296.4080	−234.6825	−163.1089	−86.9021

$$X_{j(ij)} = x_j + \sum_{k \neq i,j} x_k \tag{6}$$

With

$$\bar{G}_i^E = G^E + \left(\frac{\partial G^E}{\partial x_i}\right)_{x[j,k]} - \sum_{j=1}^{k-1} x_j \left(\frac{\partial G^E}{\partial x_j}\right)_{x[j,k]} \tag{7}$$

Analogically, with $\ln \gamma_1$ defined as

$$\begin{aligned} \ln \gamma_1 = {} & \frac{x_2}{1-x_1} \ln \gamma_{1(12)} + \frac{x_3}{1-x_1} \ln \gamma_{1(13)} + \frac{x_4}{1-x_1} \ln \gamma_{1(14)} + \frac{x_5}{1-x_1} \ln \gamma_{1(15)} \\ & - \frac{x_2 x_3}{(1-x_2)^2} \ln \gamma_{2(23)} - \frac{x_2 x_4}{(1-x_2)^2} \ln \gamma_{2(24)} - \frac{x_2 x_5}{(1-x_2)^2} \ln \gamma_{2(25)} - \frac{x_3 x_4}{(1-x_3)^2} \\ & \ln \gamma_{3(34)} - \frac{x_3 x_5}{(1-x_3)^2} \ln \gamma_{3(35)} - \frac{x_4 x_5}{(1-x_4)^2} \ln \gamma_{4(45)} \end{aligned} \tag{8}$$

where x_i, x_j, x_k are mole fractions of quinary constituents is the quinary alloy.

The Gibbs energy of AlN can be written in the Gess's Law format:

$$Fe + [Al] = FeAl \;\; \Delta G_{FeAl} = -27.72 + 0.0187T \tag{9}$$

When $\Delta G_{FeAl} = 0$, according to Eq. (9) the precipitation temperature of FeAl was calculated as 1210 °C.

Analogically,

$$4Mn + 0.5N_2 = Mn_4N_{(S)} \;\; \Delta G_{Mn_4N} = -87.661 + 0.06516T \tag{10}$$

When $\Delta G_{Mn4N} = 0$, according to Eq. (10) the precipitation temperature of Mn_4N was calculated as 1072 °C.

From the results of thermodynamic calculations, the precipitating temperature of FeAl, Mn_4N is 1210, 1072 °C, respectively, corresponding to the results of experimental measurement from DSC, indicating that the thermodynamic calculations can well describe the precipitating behaviour of second phase particles in the experimental use of steel.

Conclusions

In the present study, the thermodynamic characteristics and formation mechanism of second phases in the Fe–Mn–Al–C–N system are investigated, and following conclusion are summarized:

(1) From the results of the experiments, the phase composition of the Fe–Mn–Al–C–N system steel are ferrite, FeAl, AlMn, AlN and Mn_4N phases.
(2) The precipitating temperature of FeAl, Mn_4N, AlMn and austenite is 1260, 1031, 934, and 600 °C, respectively, corresponding to the theoretical calculation results.

References

1. Szczucka-Lasota B, Formanek B et al (2005) Oxidation models of the growth of corrosion products on the intermetallic coatings strengthened by a fine dispersive Al_2O_3. J Mater Process Technol 164–165(4):935–939
2. Totemeier TC et al (2003) Mechanical and physical properties of high-velocity oxy-fuel-sprayed iron aluminide coatings. Metall Mater Trans A 34(10):2223–2231
3. Jimenez JA et al (1995) Relationship between microstructure and texture in Fe-25%Cr-5%Al ribbons produced by planar flow casting. Scr Metall Mater 33(7):1027–1031
4. Lee JH et al (2005) Microstructure evolution in directionally solidified Fe-18Cr stainless stees. Mater Sci Eng A 413–414:30
5. Kim HC et al (2005) Formation of AlN in the N added 18Cr ferritic stainless steels. Mater Sci Forum 428–431
6. Wang CH et al (2011) Biocompatibility of metal carbides on Fe-Al-Mn-based alloys. J Alloy Compd 509(3):691–696
7. López D et al (2007) Corrosion–erosion behaviour of austenitic and martensitic high nitrogen stainless steels. Wear 263(1–6):347–354
8. Degallaix S et al (1986) Mechanical behaviour of high-nitrogen stainless steels. Mater Sci Technol 2:946–950
9. Ham JL et al (1958) Manganese joins Aluminium to give strong stainless. Prod Eng 29(52):50
10. Zhu XM et al (1996) corrosion performance and passive film of an austenitic Fe-Mn-Al alloy. J Chin Soc Corros Prot 16(4):275–280
11. Aperador WA et al (2013) Evaluation of erosion-corrosion resistance in Fe-Mn-Al austenitic steels. Mater Res-Ibero-am J Mater 16(2):447–452
12. Chang KM et al (2014) Effects of gas nitriding pressure on the formation of nanocrystalline AlN in plasma nitride Fe-9Al-28Mn-1.8C alloy. Surf Coat Technol 254(18):313–318
13. Ding X et al (1999) Thermodynamic calculation for alloy systems. Metall Mater Trans B 30 (2):271–277
14. Ray PK et al (2010) Applications of an extended Miedema's model for ternary alloys. J Alloy Compd 489(2):357–361
15. Kang YB et al (2012) Thermodynamic evaluations and optimizations of binary Mg-light Rare Earth (La, Ce, Pr, Nd, Sm) systems. Calphad-Comput Coupling of Phase Diagrams Thermochem 38(5):100–116
16. Schaefer RJ et al (1986) Formation and stability range of the G phase in the Al-Mn system. Scr Metall 20(10):1439–1444
17. Goncalver AP et al (1996) Extended miedema model: predicting the formation enthalpies of intermetallic phases with more than two elements. Phys B 228(2–4):289–294
18. Ouyang YF et al (2006) Formation enthalpies of Fe-Al-RE ternary alloys calculated with a geometric model and Miedema's theory. J Alloy Compd 416(1–2):148–154
19. Zhang L et al (2014) Amorphous forming ranges of Al-Fe-Nd-Zr system predicted by Miedema and geometrical model. Rare Earth 32(4):343–351
20. Miedema AR et al (1980) Cohesion in alloys-fundamentals of a semi-empirical model. Physica B+c 100(1):1–28

Local Texture Evolution and Mechanical Performance of Ultra-High-Speed Friction Stir Weld of AA 6111-T4 Sheets

Jingyi Zhang, Yuri Hovanski, Piyush Upadhyay and David P. Field

Abstract Friction stir welding has gained wide interest in industry and drawn large research attention due to its high level of automation and superior joint performance. In this study we further expand the welding parameters to be of magnitudes higher than those previously reported to lower the cost and enable high volume joint production. Sound butt-joints were produced with aluminum alloy 6111-T4 blanks with welding speeds up to 6000 mm/min. Tensile tests of the joint pieces show >97% joint efficiency in terms of ultimate tensile strength. The T4 natural aging and grain refinement is found to contribute to the superior joint properties. Electron backscatter diffraction (EBSD) analysis is used to qualitatively study the local shear texture inside the nugget zones of the welds. The shear texture result is a good indicator of the material flow directions in the nugget zones. The flow directions behind the rotation tool are found to be flattened towards the top surface of the workpiece when the welding speed is increased, suggesting intense material mixing and transportation along the longitudinal welding direction (WD).

Keywords High-Speed · FSW · AA6111 · Texture · EBSD · Tensile Mechanical · Butt-joint

J. Zhang (✉) · D. P. Field
School of Mechanical and Materials Engineering,
Washington State University, Pullman, WA 99163, USA
e-mail: jingyi.zhang2@wsu.edu

Y. Hovanski
Manufacturing Engineering Technology, Brigham Young University,
Provo, UT 84602, USA

P. Upadhyay
Pacific Northwest National Lab, Richland, WA 99352, USA

B. Li et al. (eds.), *Characterization of Minerals, Metals, and Materials 2018*, The Minerals, Metals & Materials Series,
https://doi.org/10.1007/978-3-319-72484-3_27

Introduction

There are a large number of published studies about the friction stir welding (FSW) process, its forming mechanisms, and evaluation of the products [1–9]. The technology was first developed as a next generation joining method for aluminum alloys. Many intrinsic features of FSW directly lead to advantages of FSW in joining aluminum alloys, especially heat-treatable aluminum alloys. The process is a solid state joining process which means no material melting is involved; only the immediate neighboring materials in the workpiece along the weld seam are softened by friction heat and adiabatic heat and then mechanically mixed. This reduction of heat input is beneficial in preserving the high level of strength in heat-treatable aluminum alloys because the major strengthening mechanism in these types of alloys is precipitate strengthening [5, 10–15]. Holding heat-treatable aluminum alloys at higher temperatures for extended periods of time as required by traditional fusion welding will lead to growth or dissolution of the strengthening precipitates intentionally introduced by previous heat-treatment steps.

However, there are still some limiting factors in the application and understanding of FSW in aluminum alloys. The complex material flow field and asymmetric microstructures have been examined in many papers and some empirical descriptions are commonly accepted. No general rule of thumb is established to predict the behavior of joint product given the welding parameters. The complicated material flow field is still a black box even with some attempts to experimentally trace or numerically simulate the process. Another shortcoming of FSW is the relatively slow welding speed, usually on the level of tens to hundreds of millimeters per minute. The slower joining speed limits the use of FSW in industry as it increases the cost of manufacturing and the production period. To investigate the possibility of further increasing the welding speed and the effect on mechanical performance of the products we increased our welding speed to 6000 mm/min, comparable to the commercially available speeds of laser welding.

A statistical study was performed with the body of literature available on web of science to better understand the current landscape of research on FSW, specifically butt joining of heat-treatable aluminum alloys. The papers that are peer-reviewed publications, with experimental studies of butt joint FSW on heat-treatable (sometimes referred to as high-strength) aluminum alloys were searched and selected on April 17th, 2017 and yields 544 items. The abstracts and keywords of these studies were exported as a text body and the frequency of each unique word were counted. The most frequent words that are related to material properties are: “ductility”, “formability”, “residual stress”, “corrosion”, “microstructure”, “texture”, “mechanical”, “toughness”, “fatigue”, and “hardness”. The count of papers that included these words in their abstract is perceived as an indicator of how extensive the subject has been studied and is summarized in Fig. 1(left). To investigate the range of welding parameters in FSW, 50 random papers in the selected body were read and the highest welding speed and rotation speed

combination used are summarized in Fig. 1(right) as small open circles [5, 16–33]. The vast majority of these parameters fell in the red triangle marked on the image with welding speeds lower than 2000 mm/min and rotation rates lower than 2000 rpm. In this study we used parameters marked by the solid orange squares, with ultra-high welding speeds up to 6000 mm/min at rotation rates of 4500 rpm.

Materials and Methods

The base material (BM) used in this study is 2.7 mm thick commercial aluminum alloy AA6111-T4 sheet. The sheet form of AA6111 is commonly used for outer autobody panels in automobile applications. The designation T4 indicates that the material is naturally aged, reaching a lower strength but preserving most of the ductility. Three sets of FSW butt joints were made with the welding speed and rotation rate combination of: weld #1 (3000 mm/min, 4000 rpm), weld #2 (4500 mm/min, 4250 rpm), weld #3 (6000 mm/min, 4500 rpm). The welding direction is perpendicular to the rolling direction of the sheet. Sub-sized rectangular tensile specimens designed following ASTM B557 were machined perpendicular to the welding direction with the weld located in the center of the gauge. The gauge section is 25.4 mm in length and 6.35 mm in width. Metallographic samples of the cross sections of the welds were prepared and etched with 10% NaOH for optical examination. The same samples were then mechanically polished for EBSD acquisition. A FE-SEM with 20 kV accelerating voltage was used to collect EBSD patterns from the cross sections of all welds. The EBSD scans were then analyzed with OIM software, no data cleanup was applied for the scans used in texture analysis.

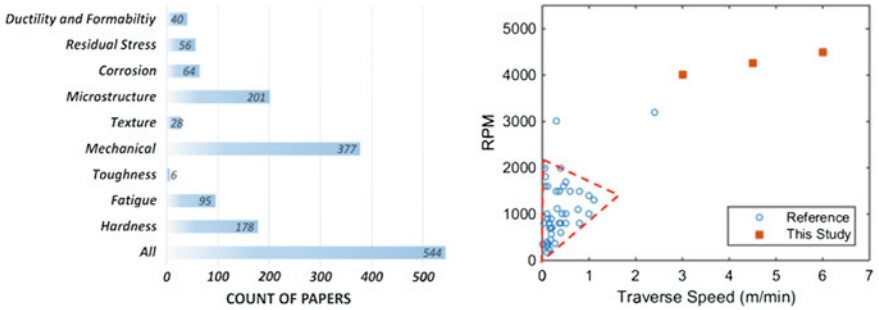

Fig. 1 Summary of the current landscape of study on FSW heat-treatable aluminum alloys. Left: the most studied properties and the counts of papers for each property. Right: the distribution of welding speeds and rotation rates in the literature and in this study

Results and Discussion

Tensile Test

The results from tensile tests are presented in Figs. 2 and 3. The locations of fracture can be observed in Fig. 2 on the left. The samples in this image from top to bottom are the base material (BM) sample, weld #1 sample, weld #2 sample and weld #3 sample. There is no fracture observed in the nugget zone. Typical engineering stress-strain curves obtained from the tensile tests are presented in Fig. 2 on the right. The three samples with a weld have very similar stress-strain curves, and are almost the same as the BM curve before yielding. All samples with a weld have a clear reduction in elongation at break compared to BM. The important data exported from the stress-strain curves in Fig. 2 are plotted in Fig. 3. The weld samples have a higher yield strength, lower UTS, and similar Young's modulus to the BM samples (all within 5%). The UTS joint efficiencies are all above 97%. The elongation at break drops significantly from 29.9% without weld to 21% with a friction stir weld, which yields about 70% efficiency in elongation.

Microstructure and Microtexture

The microstructure on the cross sections near the welds were examined with both light microscopy and EBSD method (Fig. 4). The two techniques both show severe microstructure gradient between the base material and the nugget zones. In the optical images the weld nuggets reveal much smaller grain sizes than in the BM. Alternating layers of grains with different contrast can be seen in the nugget zones close to the advancing side. The orientation maps in Fig. 4 provide a rough impression of the local texture in and around the welds, with the colors corresponding to the inverse pole figure orientation relative to the welding direction. The

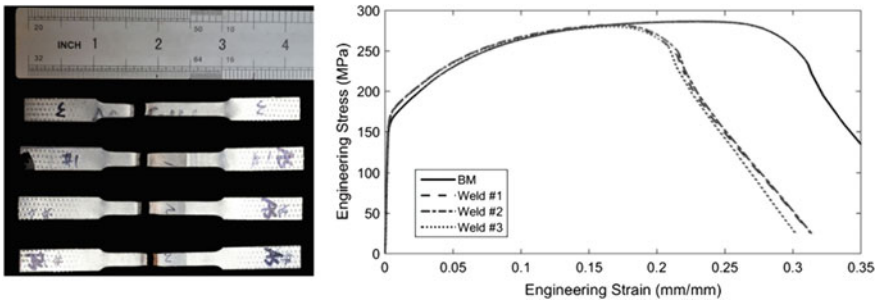

Fig. 2 Raw tensile results. Left: broken tensile samples after tests. Right: the representative engineering stress and strain curves of the welded tensile samples compared with the BM sample

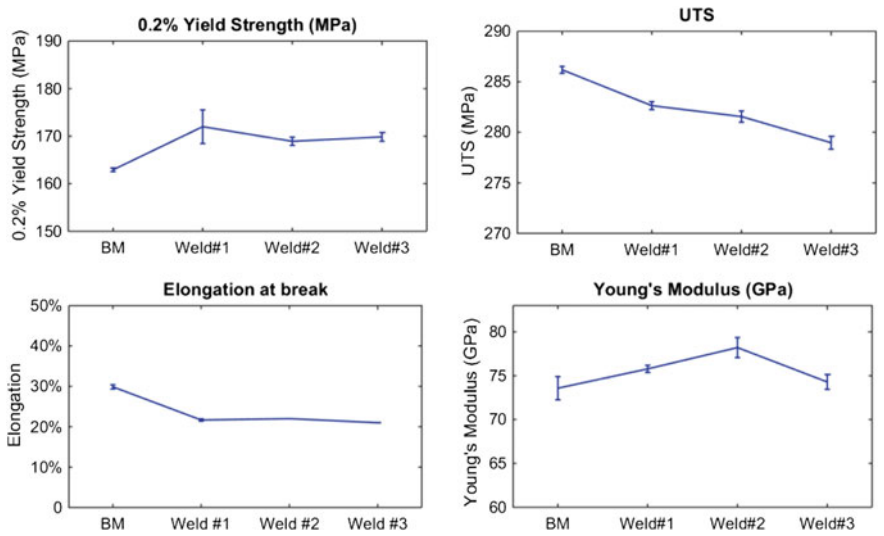

Fig. 3 Summary of key results derived from the tensile tests. Top left: yield strength; top right: ultimate tensile strength; bottom left: elongation at break; bottom right: Young's modulus

alternating layers inside the nugget zones in the optical images are also observed in the EBSD orientation maps and appear to have a layered texture structure.

All the nugget zones have very fine recrystallized grains. The nugget center of the welds have average grain diameters of 5–7 μm while the average grain diameter in the BM is 50 μm. The distribution of grain sizes in the nugget zones of the three welds are mapped out in Fig. 5. The x-axis in Fig. 5 is the distance from the weld center, with the advancing side (AS) to the left and the retreating side (RS) to the right. The y-axis is the relative depth through the thickness of the sheet, where 0 represents the middle layer and positive values are closer to the top surface of the sheet. The units for both axes are in mm.

The faster welds have smaller grains in the nugget zones compared to the slower welds. This is because with higher welding speeds and larger traverse distance per revolution, heat generation per unit length of weld is reduced and cooling rate after joint formation is increased. The overall cooler conditions and faster cooling rates lead to less grain growth after recrystallization.

The texture in the nugget zones of FSW aluminum alloys is commonly observed to be of simple shear type. Typically observed components are partial B fibers and C components. The local shear directions across the nugget zone were found to trace the outer shape of the rotating tool pin, usually bowl-shaped hovering over the cylindrical tool pin. The shear direction at the weld center behind the center of tool pin was found to be 70° away from the top surface. The upper part of the weld is closer to the tool shoulder and has shear directions angled more towards the top surface. To check if the high speed welds follow the general observations made in the much slower welds, continuous local fine scans of the center layer of the weld

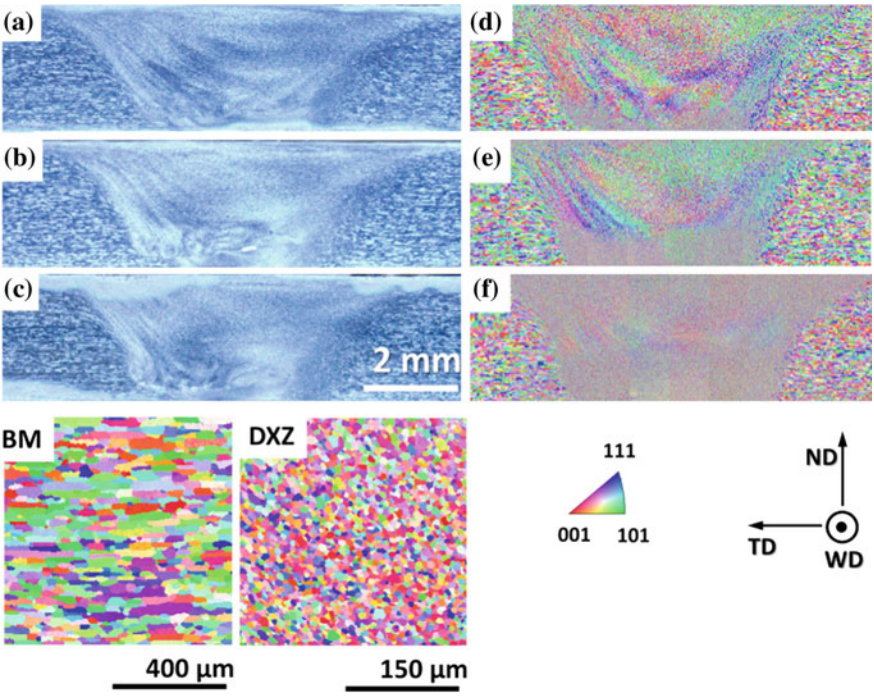

Fig. 4 Microstructure of the welds. Images **a–c** are the optical images of the cross section of weld #1, weld #2 and weld #3 respectively. The images **d–f** are the corresponding orientation maps with grain orientation colored with respect to the welding direction. The bottom two orientaion maps are BM: base material cross section microstructure, and DXZ: nugget zone center microstructure in weld #2

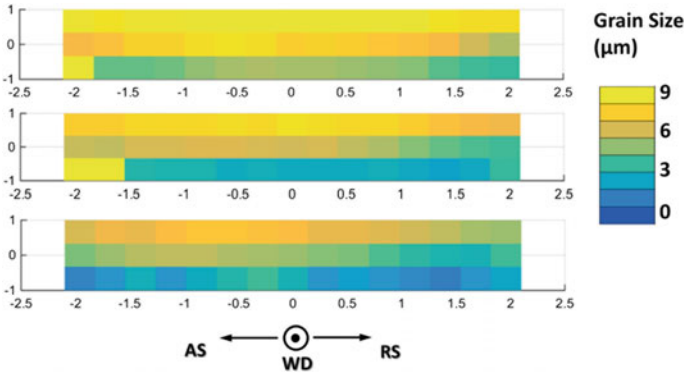

Fig. 5 Grain size mapping in the nugget zones. From top to bottom are nugget zone maps of weld #1, weld #2 and weld #3 respectively

#1 and weld #3 nuggets were collected. Pole figures every 300 μm were calculated, and are listed in Fig. 6. The pole figures on the top row are from the center layer of weld #1 and the pole figures on the bottom row are from the center layer of weld #3 nugget zone. The pole figures are arranged by their physical location from the advancing side (AS) to the retreating side (RS) of the weld from left to right. All pole figures show some extent of fcc shear texture and have gradually rotated pole directions in neighboring locations.

The local shear direction in aluminum can be tracked by recording the rotation matrix when rotating the local crystal orientations so that the shear textures are matched with the ideal fcc shear texture. A backwards spatial rotation using the same rotation matrix can give the shear direction as indicated by the texture information with respect to the spatial coordinates in the workpiece. The derived shear directions on each location in the nugget zones are summarized in the plot in the bottom box of Fig. 6a shows the shear directions across the nugget for weld #1 and Fig. 6b shows the local shear directions across the nugget for weld #3. The black dotted line marks the circular shape of the backside of the tool pin surface. Previous studies generally observed that material shear directions follow this semicircular shape. The blue line segments are local shear directions obtained by the rotation of each pole figures as mentioned above. The line thickness is scaled with the maximum texture intensity (or shear texture strength) at each location. Note that these lines only provide information about local material flow directions and do not provide knowledge about the material flow velocity. Both welds have a majority of shear directions tracing the semicircle with a considerable vertical

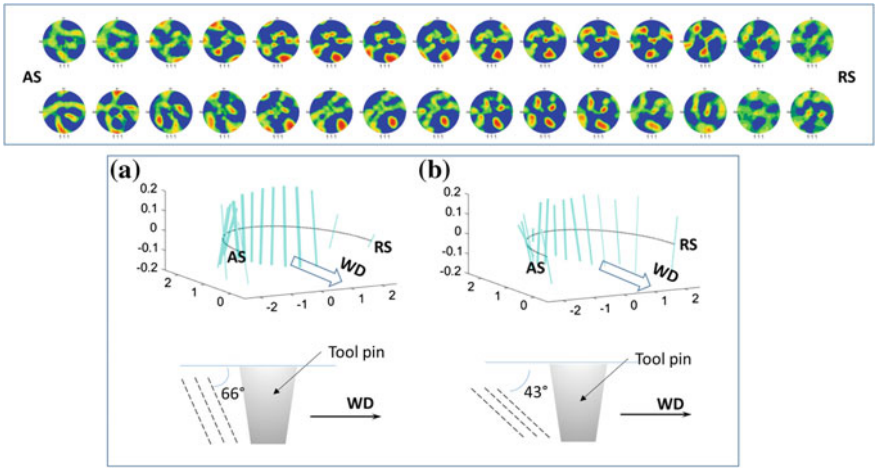

Fig. 6 The local texture analysis in weld nugget zones of weld #1 and weld #3. The top box list the local pole figures in the nugget zones of weld #1 and weld #3 from AS to RS, in the cross-section view plane. The bottom box is the illustration of the shear directions derived from the pole figures. **a** Summary of the local shear directions around the back circular surface of weld #1. **b** Summary of the shear directions around the back circular surface of tool in weld #3

component indicating upward lifting/mixing of material. The shear directions in the faster weld (weld #3) are more flattened toward the top surface as we suspected. To quantify the direction difference in the two welds, shear direction at the center of the weld (i.e. directly behind the tool) are selected and their tilt angles from the top surfaces are found to be 66° and 43° for weld #1 and weld #3 respectively. Illustrations of material flow directions behind the tool are sketched in the bottom of Fig. 6. The smaller tilt angle from top surface in faster weld #3 suggest the faster moving tool has more of a "dragging" effect on the mixing of material along the welding direction. This change in flow (shear) direction suggests that with higher welding speed, more longitudinal material mixing can be expected. There may also be larger longitudinal residual stress after welding.

Conclusions

High-speed (up to 6000 mm/min) FSW butt joints of AA6111-T4 were made with good mechanical performance. The weld efficiency is 97% in terms of UTS. The high level of tensile strength is due to the starting naturally aged T4 temper and grain refinement during the FSW process. The yield strength and Young's modulus are both kept on the same level regardless of the presence of a weld. The elongation at break was reduced from 29.9% in the base material to about 21% when a FSW weld is present. The complex microstructures in and near the welds are recorded with both light microscopy and EBSD. The texture in nugget zones are found to be mainly of fcc simple shear texture, as observed in the literature. The local texture variation in the nugget zones was analyzed to reveal the local material flow directions. Using spatial rotation to match shear texture frame with real sample space we found out the local shear direction and used this direction as a representation of the last step material flow inside nugget zone. The higher welding speed resulted in the "flattening" of material flow directions toward the top surface. This change in flow direction indicates that higher welding speed leads to more material transportation and mixing along the welding direction.

References

1. Thomas WM, Nicolas ED, Needham JC, Murch MG, Temple-Smith P, Dawes CJ 1991
2. Li Y, Murr LE, McClure JC (1999) Mate Sci and Eng A Struct Mater Prop Microstruct Process 271:213–223
3. Sato YS, Kokawa H (2001) Metall Mater Trans A 32:3023–3031
4. Sato YS, Kokawa H, Ikeda K, Enomoto M, Jogan S, Hashimoto T (2001) Metall Mater Trans A Phys Metall Mater Sci 32:941–948
5. Li WY, Jiang RR, Zhang ZH, Ma YE (2013) Adv Eng Mater 15:1051–1058
6. Hovanski Y, Upadhyay P, Carsley J, Luzanski T, Carlson B, Eisenmenger M, Soulami A, Marshall D, Landino B, Hartfield-Wunsch S (2015) JOM 67:1045–1053

7. Zapata J, Toro M, López D (2016) J Mater Process Technol 229:121–127
8. Zhou L, Wang T, Zhou WL, Li ZY, Huang YX, Feng JC (2016) J Mater Eng Perform 25:2542–2550
9. Zhang J, Upadhyay P, Hovanski Y, Field DP (2017) High-speed FSW aluminum alloy 7075 microstructure and corrosion properties. In: Hovanski Y, Mishra R, Sato Y, Upadhyay P, Yan D (eds) Friction stir welding and processing IX. Springer International Publishing, Cham, pp 125–135
10. Ericsson M, Sandstrom R (2003) Int J Fatigue 25:1379–1387
11. Peel M, Steuwer A, Preuss M, Withers PJ (2003) Acta Mater 51:4791–4801
12. Rodrigues DM, Leitão C, Louro R, Gouveia H, Loureiro A (2010) Sci Technol Weld Join 15:676–681
13. Palanivel R, Koshy Mathews P, Murugan N, Dinaharan I (2012) Mater Des 40:7–16
14. Barenji RV (2016) Proc Inst Mech Eng Part L J Mater Des Appl 230:663–673
15. Nam ND, Dai LT, Mathesh M, Bian MZ, Thu VTH (2016) Mater Chem Phys 173:7–11
16. Donne CD, Braun R, Staniek G, Jung A, Kaysser WA (1998) Materialwiss Werkstofftech 29:609–617
17. Staron P, Koçak M, Williams S, Wescott A (2004) Physica B 350:E491–E493
18. Cavaliere P, Cerri E, Squillace A (2005) J Mater Sci 40:3669–3676
19. Liu HJ, Fujii H, Nogi K (2005) J Mater Sci 40:3297–3299
20. Chen YC, Liu HJ, Feng JC (2006) J Mater Sci 41:297–299
21. Paglia C, Jata K, Buchheit R (2007) Mater Corros 58:737–750
22. Motohashi Y, Sakuma T, Goloborodko A, Ito T, Itoh G (2008) Materialwiss Werkstofftech 39:275–278
23. Fratini L, Buffa G, Shivpuri R (2009) Int J Adv Manuf Technol 43:664–670
24. Ramulu PJ, Narayanan RG, Kailas SV, Reddy J (2013) Int J Adv Manuf Technol 65:1515–1528
25. Fehrenbacher A, Duffie NA, Ferrier NJ, Pfefferkorn FE, Zinn MR (2014) Int J Adv Manuf Technol 71:165–179
26. Costa MI, Rodrigues DM, Leitao C (2015) Int J Adv Manuf Technol 79:719–727
27. Chen SJ, Li H, Lu S, Ni RY, Dong JH (2016) Int J Adv Manuf Technol 86:337–346
28. He J, Ling ZM, Li HM (2016) Int J Adv Manuf Technol 84:1953–1961
29. Ji SD, Meng XC, Li ZW, Ma L, Gao SS (2016) Int J Adv Manuf Technol 84:2391–2399
30. Ji SD, Meng XC, Ma L, Gao SS (2016) Int J Adv Manuf Technol 87:3051–3058
31. Papahn H, Bahemmat P, Haghpanahi M (2016) Int J Adv Manuf Technol 83:1003–1012
32. Chen SJ, Zhou Y, Xue JR, Ni RY, Guo Y, Dong JH (2017) J Mater Eng Perform 26:1337–1345
33. Liu H, Liu X, Wang X, Wang T, Yang S (2017) Int J Adv Manuf Technol 88:3139–3149

Part IX
Characterization of Powder Materials

Characterization of HPGR Pre-treated Sinter Feed

Mingming Zhang, Udaya Bhaskar Kodukula and Marcelo Andrade

Abstract The physical and chemical properties of sinter feed are important factors that determine the productivity and quality of sinter product. In this study the feasibility of treating sinter feed by high pressure grinding rolls (HPGR) is investigated for selective cracks generation exploiting weak zones along grain boundaries of poor quality iron ores without generating much fines. The pre-treated sinter feed was characterized for size distribution, surface area, contact angle, and SEM analyses. The characterization results indicated that surface area of the pre-treated sinter feed sample increased about 20%. Pot-grate sintering tests results also indicated improvement on cold permeability, sintering yield and productivity, sinter Tumbler index, and low temperature degradation index (LTD) after HPGR pre-treatment.

Keywords High pressure grinding rolls · Iron ores · Sintering

Introduction

Sinter plants for integrated steel mills have been facing challenges to increase sinter productivity with declining quality of raw materials and demanding environmental regulations [1]. In addition, major iron ore suppliers have been not only gradually decreasing amount of iron ores that has high ferrous grade, and good sintering properties, but also pushing new iron ores with poor sintering performance. There is an increasing trend for silica in typical sintering feeds as shown in Fig. 1 and it has been considered as an unavoidable trend in the future. With the recovery of iron ore price, this demands innovative use of cheaper iron sources, while still maintaining the quality and productivity standards.

M. Zhang (✉) · U. B. Kodukula · M. Andrade
ArcelorMittal Global R&D, East Chicago, IN 46312, USA
e-mail: Mingming.Zhang@arcelormittal.com

B. Li et al. (eds.), *Characterization of Minerals, Metals, and Materials 2018*, The Minerals, Metals & Materials Series,
https://doi.org/10.1007/978-3-319-72484-3_28

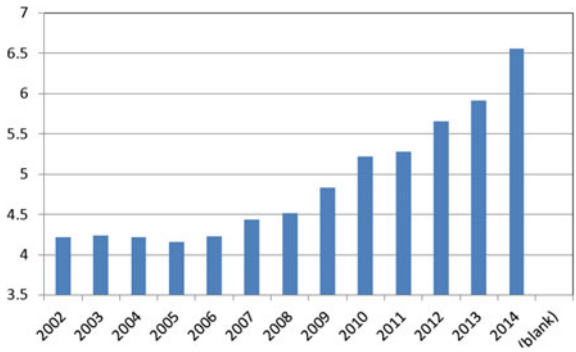

Fig. 1 Historical evolution of silica content of a typical sintering feed used at sinter plant

There have been some reported studies of using high pressure grinding rolls (HPGR) to treat poor quality iron ores for pelletizing and sintering. The influence of HPRG pre-treatment of iron ore concentrate on sintering and pelletizing performance has been reported recently [2–4]. Results of mini-sintering tests showed that assimilation temperature of iron concentrate fines decreased from 1230 to 1220 °C and assimilation time was shortened from 10 to 5 min when the iron concentrate fines was pretreated by HPGR. Sinter pot tests showed that the yield of sinter increased from 60 to 73%, tumble index increased from 44 to 47%. However, the HPGR treated iron ore concentrates need to be fully characterized to understand the mechanism of the improvement of granulation property and reactivity in solid state reaction.

Experimental

Feed Materials

Iron ore samples from a Brazilian mining production plant was used as feed material for the HPGR experiments. The iron ore consisted about 32% of the −0.1 mm fraction, with F80 = 1.5 mm and F50 = 0.6 mm. The iron ore is a very hard and mechanically competent material with a Bond's work index of 19.6 kW h/ton. Approximately 12 kg of charge was used for each batch experiment. The moisture level of the as-received iron ore sample was found to be close to 7.0%.

Grinding Tests

HPGR tests were performed at University of Utah using a laboratory HPGR unit with studded surface rolls measuring 200 mm in diameter and 100 mm in width. To isolate the center product from the less representative edge product the unit was

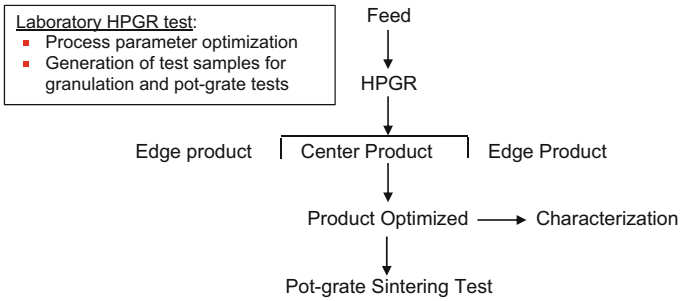

Fig. 2 Simplified flowsheet of the laboratory HPGR test

equipped with a discharge splitter arrangement. The products were collected manually, disregarding the part of product stream originating from the very beginning and very end of the batch. The edge product was collected to determine the throughput of the press, but only the center product was used in further testing and analysis. Experiments with different feed moisture, roller speed, operating gap and pressure were conducted. Following the HPGR batch tests, representative samples of the center product from each batch were subjected to further characterization. Simplified flowsheet of the HPGR circuit is given in Fig. 2.

Characterization of Iron Ore Samples

The specific surface area of the iron ore samples was measured using a BET SA-9600 surface area analyzer (Horiba, New Jersey, USA). All the iron ore samples were measured using nitrogen at the temperature of 77 K. For the measurement of particle size, the sieve sizing method and the laser diffraction method were used. The laser diffractometer used in this study was a Cilas 1190 laser particle size analyzer (Madison, WI, USA). Contact angle measurement were made using a CAM-PLUS contact angle meter (ChemInstruments, Fairfield, OH, USA).

Results and Discussion

The results of this study are organized in three separate but interrelated sections. The first section discusses the size distribution of feed materials and HPGR product, whereas the second part addresses the characterization of HPGR product in terms of surface area, particle morphologies, permeability and contact angle. The third section presents the results of pot-grate sintering test results using the HPGR treated iron ores.

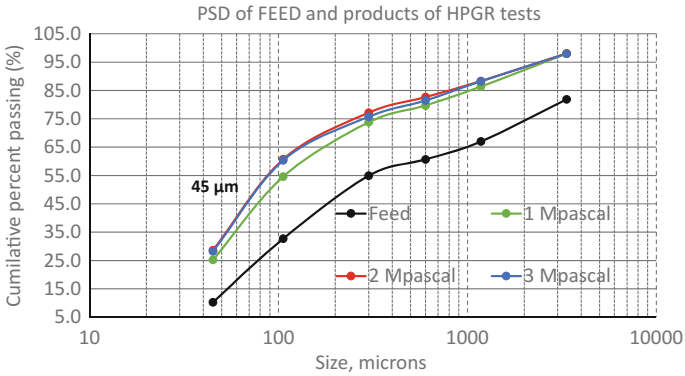

Fig. 3 Sieving analysis of iron ore before and after HPGR treatment

Operating Pressure and HPGR Product Size Distribution

The main HPGR operating parameters, such as specific operating pressure, roller speed, operating gap, throughput and specific energy consumption, were registered in each batch test. Figure 3 presents the size distribution of feed and products at three levels of specific operating pressure. The operating pressure, obviously, it affects product size distribution. The test results indicated that higher pressure resulted in higher size reduction ratio. However, there is a marginal difference in the size distribution between the products run at 2 Mpascal and 3 Mpascal, though larger flakes were observed at higher pressure. To achieve desired size reduction ratio while avoiding too much flakes in products, 2 Mpascal pressure was selected for continuous HPGR production for sinter pot tests.

Characterization of HPGR Product

Figure 4 and 5 show the morphology of the iron ore samples before (A. Feed) and after HPGR treatment (B. HPGR product). It is observed that the particle surface turns to be more irregular, with more internal microcracks, sharp corners and edges appearing after HPGR grinding. The rougher shape brings more inter-particles contact areas and consequently brings higher mechanical strength. Rough shaped particles with lots of crystal defects also exhibit advantages in granulation and sintering owing to enhancement in surface activity during mechano-chemical activation by HPGR. Mechanic energy during high pressure compression is stored in the concentrate grains in the form of chemical energy and surface energy [5, 6].

Granulation and pot-grade sintering tests were conducted to evaluate the impacts of HPGR treatment on sintering performance. The comparison of moisture, surface

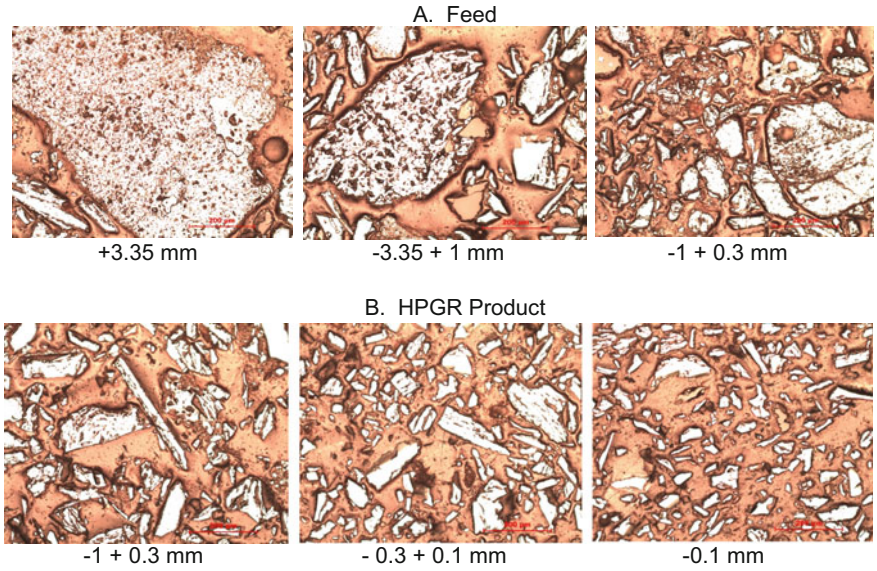

Fig. 4 Optical micrographs of iron ore before and after HPGR treatment

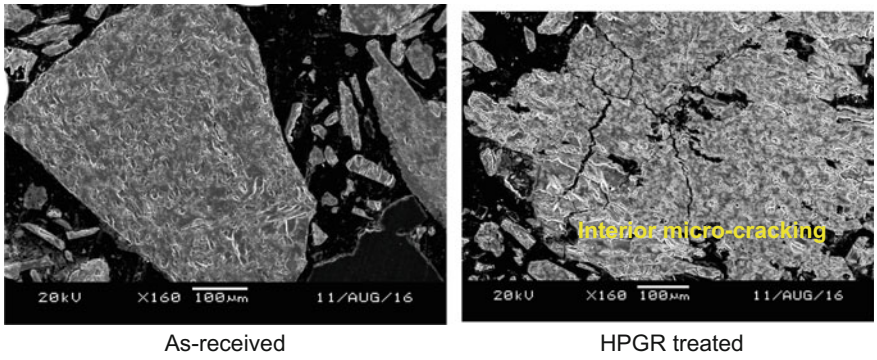

Fig. 5 SEM micrographs of iron ore grains before and after HPGR treatment

area, cold permeability and contact angle before and after HPGR treatment are shown in Table 1. As shown in the table, the physical properties of iron ore samples changed significantly. After HPGR treatment, the iron ore sample showed about 20% increase in surface area and the cold permeability was improved about 18%. The contact angle measurement also indicates that the HPGR treated iron ore samples turned out to be more hydrophilic than iron ore samples without HPGR treatment, which is a condition for enhanced wettability and in turn better granulation.

Table 1 HPGR pre-treatment of iron ore samples

Parameters	Unit	As received	HPGR treated	±, %
Moisture	wt%	7.8	5.6	−28.2
BET surface area	m^2/gram	8.69	10.54	21.3
Cold permeability[a]	JPU	38.65	45.79	18.5
Contact angle	degree	90	82	−8.9

Pot-Grate Sintering Test Results

Figure 6 shows the comparison of pot-grate sintering test results using iron ore samples with and without HPGR treatment. Comparing with baseline (without HPGR treatment), sintering test using HPGR treated iron ore resulted in significant improvement on cold permeability and sinter low temperature degradation (LTD) index with an average of about 20% improvement. In addiiton to the improved sinter LTD, sinter yield, Tumbler and productivity improvement are also observed with an average of 3% increase.

HPGR activation of iron ores can be attributed to increase in the surface area without generating much ultrafines (< 45 μm). Selective breakage along the grain boundaries due to inter-particle compressive forces left micro-cracks and hydrophilic surfaces on particles and resulted enhanced granulability during the granulation process. This resulted in high bed porosity and permeability and in turn the quality and productivity.

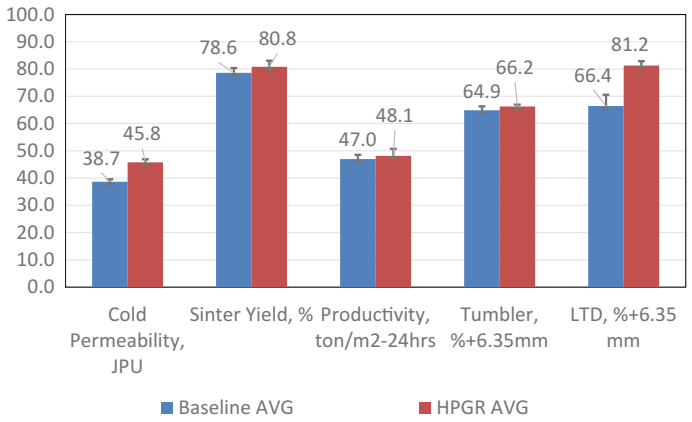

Fig. 6 Pot-grate sintering test results using HPGR treated iron ore

Conclusions

The characterization of iron ore samples before and after HPGR treatment by various methods and its indication on the particle size/morphology, surface area, contact angle and sintering performance were discussed in this study. The conclusions can be summarized as follows,

(1) The homogeneity of the particle size was studied by comparing the results of laser diffraction, optical micrograph and that of SEM observation, the conclusions of the two measurements agree well. The shapes of the particles influence the specific surface area apparently, the samples with like-slice and like layer particles have high specific surface area.
(2) The specific surface areas of the iron ore sample increased about 21% after HPGR treatment.
(3) The cold permeability and pot-grate sintering test results show that cold permeability and sinter low temperature degradation (LTD) index increased about 20% with HPGR treatment. Further, the treatment improved sinter yield, Tumbler and productivity with an average of 3%.
(4) Application of HPGR increased granulation through improved surface area and activation sites and in turn improved sinter bed permeability and overall sinter productivity.

Acknowledgements The authors would like to thank ArcelorMittal Global R&D management for their permission to publish this work.

References

1. Noldin JH Jr et al (2015) Trends in ironmaking given the new reality of iron ore and coal resources. AISTech 2015 Proceedings, 366–375
2. Chen X-L et al (2014) Study on pre-granulation technology for strengthening sintering of high proportion iron ore concentrate. In: 5th International Symposium on High Temperature Metallurgical Processing, TMS, Warrendale, pp. 401–408
3. Jiang et al (2012) Strengthening the sintering of iron concentrate fines by high pressure roller grinding. In: 3th International Symposium on High Temperature Metallurgical Processing, TMS, Warrendale, pp. 211–220
4. Zhu D, Yang C, Pan J, Zhong Y (2015) Improving the pelletization of chromite concentrate by HPGR and its mechanism. In: Jiang T, Hwang J-Y, Alvear GRFF, Yücel O, Mao X, Sohn HY, Ma N, Mackey PJ, Battle TP (eds) 6th International Symposium on High-Temperature Metallurgical Processing, TMS, Warrendale
5. van der Meer FP (2015) Pellet feed grinding by HPGR. Miner Eng 73:21–30
6. Abazarpoor A, Halali M (2017) Investigation on the particle size and shape of iron ore pellet feed using ball mill and HPGR grinding methods. Physicochem Probl Miner Process 53 (2):908–919

Thermogravimetric Analysis on Reduction Behavior of Powdery Dicalcium Ferrite

Chengyi Ding, Xuewei Lv, Gang Li, Chenguang Bai, Senwei Xuan, Kai Tang and Yang Xu

Abstract Dicalcium ferrite ($2CaO{\cdot}Fe_2O_3$, C_2F) is one of the most significant bonding phase of fluxed sinters. Reduction of C_2F was investigated via thermal kinetics analysis. The isothermal reduction behavior of C_2F by 30% H_2 and 70% N_2 at 1123 K (850 °C), 1173 K (900 °C), and 1223 K (950 °C) were discussed by thermogravimetric analysis in this paper. The results revealed that the C_2F reduction was typical one-step reaction. The apparent activation energy of the C_2F reduction was 27.40 kJ/mol. The rate-determining steps of the C_2F reduction were the first inner gas diffusion, then the inner gas diffusion and interface chemical reaction mixed controlling. The ln-ln analysis implied that the C_2F reduction was described by the Avrami–Erofeev (A-E) equation, thus appeared as a 2D A-E equation kinetics reaction.

Keywords Dicalcium ferrite · Hydrogen · Isothermal reduction kinetics Apparent activation energy · Model function

Introduction

The ironmaking and steelmaking industries have become the largest source of CO_2 emission, especially because of the blast furnace (BF) process. Injection of natural gas into the tuyere raceway of a BF can effectively decrease the use of coke, as well as reduce CO_2 emission. Therefore, the reduction behavior of sinters, which account for 60% of the raw materials charged into the BF process under H_2, is important for natural gas utilization. The $CaO–Fe_2O_3$ systems principally comprising dicalcium ferrite ($2CaO{\cdot}Fe_2O_3$, C_2F), calcium ferrite ($CaO{\cdot}Fe_2O_3$, CF), and calcium diferrite ($CaO{\cdot}2Fe_2O_3$, CF_2), are the main bonding phases in fluxed sinters. To characterize the ternary or even quaternary calcium ferrite, study on binary

C. Ding · X. Lv (✉) · G. Li · C. Bai · S. Xuan · K. Tang · Y. Xu
College of Materials Science and Engineering, Chongqing University, 400044 Chongqing, China
e-mail: lvxuewei@163.com

B. Li et al. (eds.), *Characterization of Minerals, Metals, and Materials 2018*, The Minerals, Metals & Materials Series,
https://doi.org/10.1007/978-3-319-72484-3_29

$CaO–Fe_2O_3$ systems, which contain simplified phase compositions appears so vital. The phase structure and morphology of C_2F were extensively discussed, and some consensus was reached in previous work [1–3]. The reducibility of C_2F was essentially caused by the chemical composition and micro-structure of the contained multi-phases. The analysis of the reduction behavior of C_2F under the atmosphere condition in the upper area of the blast furnace requires further research. The reduction of the C_2F bonding phase in iron ore sinters in the blast furnace was a typical gas–solid reaction. Ganguly [4] revealed that CF is reduced with a number of reaction steps and concluded that the $CaO–FeO–Fe_2O_3$ ternary system stably exists in the formation of calcium ferrites in the H_2–CO atmosphere. Geassy [5] reported that Fe_2O_3 reduction doped with CaO by CO at 1173–1473 K is controlled by the combined effect of gaseous diffusion and interfacial chemical reaction during the initial stage. Du [6] found that the reduction of C_2F in H_2 is more dependent on temperature compared with CF; the reduction rate of C_2F and CF increases with temperature up to a transition point (>1373 K), above which a decrease occurs because of softening and densification of samples. The reduction kinetics of C_2F including reduction degree, rates, apparent activation energy, and model function were fully investigated in this study.

Experimental Procedure

Materials

C_2F samples were prepared from $CaCO_3$ ($\geq$ 99.99%, <100 μm) and Fe_2O_3 (α-Fe_2O_3, $\geq$ 99.99%, <100 μm) with 2:1 molar ratios, respectively. The powdery raw materials were uniformly mixed and then pressed into cylindrical samples. The samples were roasted in a furnace with the heating element $MoSi_2$ at 1173 K for 1 h to completely decompose $CaCO_3$ to CaO and then increased to 1473 K for 20 h to allow complete formation of C_2F. The entire process was performed in air atmosphere. The samples were ground into powder (<100 μm) for further investigations.

TG Analysis

TG measurement of C_2F reduction was conducted by using a Setaram analyzer (Model Setsys Evo TG-DTA 1750, Setaram Instrumentation). Samples (20 mg) were heated from room temperature to 1123 K (850 °C), 1173 K (900 °C), and 1223 K (950 °C) in N_2 ($\geq$ 99.999%) atmosphere at a heating rate of 15 K/min, then switching to gas mixtures of 30% H_2 ($\geq$ 99.999%) and 70% N_2 at a flow rate of 20 ml/min for 70 min to enable complete reaction with the samples at the isothermal stage. To exclude the influence of the system error from the thermal

analyzer and the buoyance force from the gas mixtures, a blank test was conducted under the same elimination conditions with only empty alumina crucibles. Weight loss was obtained during the isothermal reduction stage, from which the TG data of the blank test were deduced. Each experiment was conducted for two times to have the average data for final calculations.

Results and Discussion

Reduction Degree and Reduction Rate

Reduction degree is defined as the ratio of removed oxygen mass at a fixed time t to the theoretically removed oxygen mass from the iron oxide. It can be expressed as follows:

$$\alpha = \frac{\Delta m_t}{\Delta m_0}, \tag{1}$$

where α is the reduction degree; and Δm_t and Δm_0 refer to the removed oxygen mass at fixed time t and the theoretically removed oxygen mass from the iron oxide, respectively.

The reduction degrees of the C_2F samples at 1123 K (850 °C), 1173 K (900 °C), and 1223 K (950 °C) are shown in Fig. 1. The results indicated that the reduction degree obviously increased in the middle of the reduction stages for samples.

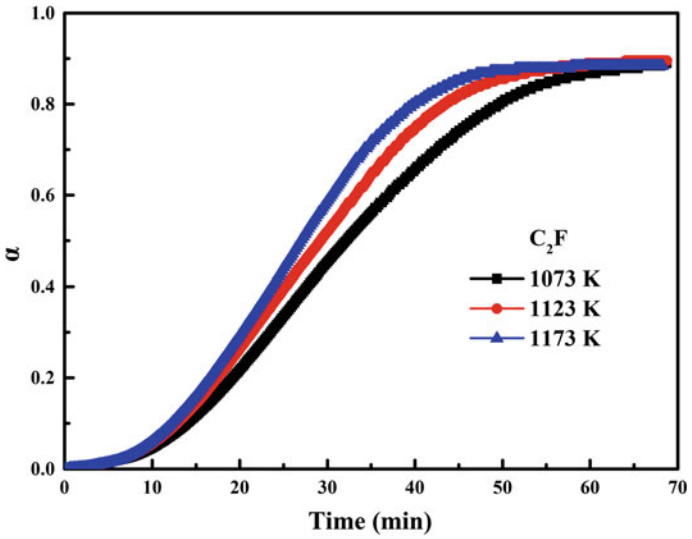

Fig. 1 Reduction degree of C_2F at 1123 K (850 °C), 1173 K (900 °C), and 1223 K (950 °C)

The reduction rates dα/dt for C_2F at 1123 K (850 °C), 1173 K (900 °C), and 1223 K (950 °C) are illustrated in Fig. 2. Reduced samples of C_2F at 1173 K at some fixed time were examined through XRD measurement. Samples at two reduction time points that correspond to $\alpha = 0.1$ and 0.5 for C_2F were selected to investigate their phase compositions. The reduction rates at three temperatures and XRD patterns of the reduced samples at a fixed reduction degree at 1173 K for C_2F are shown in Fig. 2. The figure shows that CaO and Fe (F) mainly exist in the products of C_2F reduction, and the content of the two produced phases is higher when $\alpha = 0.5$ than that when $\alpha = 0.1$. Therefore, the reduction routes of C_2F can be described as follows:

$$C_2F \rightarrow Fe. \tag{2}$$

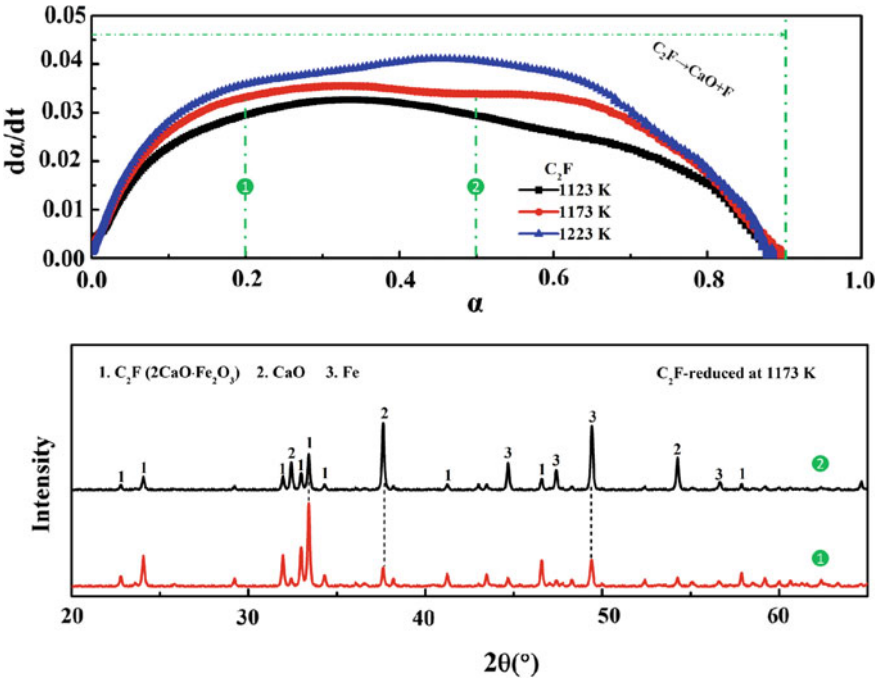

Fig. 2 Reduction rate of C_2F at 1123 K (850 °C), 1173 K (900 °C), and 1223 K (950 °C), and XRD patterns of the reduced samples at fixed time for C_2F and reduction at 1173 K

Apparent Activation Energy and Rate–determining Step for C_2F Reduction

The basic kinetic equation [7] that describes the relationship between the reduction rate and time can be expressed as follows:

$$\frac{d\alpha}{dt} = k(T)f(\alpha), \tag{3}$$

where dα/dt is the reduction rate and $k(T)$ and $f(\alpha)$ are the rate constant and model function of the reduction reaction, respectively. $f(\alpha)$ is influenced by the reaction mechanism, and $k(T)$ is determined by the following Arrhenius equation:

$$k(T) = A\exp\left(\frac{-E}{RT}\right), \tag{4}$$

where A is the pre-exponential factor, E is the apparent activation energy, and R is the gas constant [8.314 J/(mol·K)]. Equation (3) can be further expressed as follows:

$$\frac{d\alpha}{dt} = A\exp\left(\frac{-E}{RT}\right)f(\alpha). \tag{5}$$

Given that the reduction degree α is a constant, ln $f(\alpha)$ remains unchanged. Therefore, the activation energy can be calculated as follows:

$$E = -R\frac{d\left(\ln\frac{d\alpha}{dt}\right)}{d\left(\frac{1}{T}\right)}. \tag{6}$$

The method to calculate activation energy can eliminate the limit from the model function and is called the model–free method [8]. $f(\alpha)$ is usually not easily obtained. $G(\alpha)$, which is the integral function of $f(\alpha)$, can be described as follows:

$$G(\alpha) = \int_0^{\alpha}\frac{d\alpha}{f(\alpha)} = \int_0^{t}A\exp\left(\frac{-E}{RT}\right)dt = k(T)t. \tag{7}$$

The apparent activation energy was calculated by the slope of the plots of ln(dα/dt) against 1/T, and the results are expressed in Table 1. The H_2 content

Table 1 Apparent activation energy of C_2F

E/(kJ/mol)							
α	0.3	0.4	0.5	0.6	0.7	0.8	Avg
C_2F	17.62	24.84	34.08	39.70	31.81	16.35	27.40

Table 2 Relationship of rate-determining step and activation energy of iron oxide

E/(kJ/mol)	Rate-determining step
8–16	Inner gas diffusion
29–42	Inner gas diffusion and interface chemical reaction mixed
60–67	Interface chemical reaction
>90	Solid diffusion

cannot reach the target value at the initial stage of hematite and CF reduction because of the gas switching from N_2 to H_2 and N_2 mixed atmosphere. In addition, the activation energy may not reflect the real energy change. Thus, reduction degrees from 0.3 to 0.8 were selected for the calculation. The average values of activation energy for the C_2F reductions were 27.40 kJ/mol. As the reaction progresses, the reaction becomes more difficult as the activation energy increases with the increasing reduction degree (<0.6).

The connection of the rate-determining step to the activation energy was investigated by Nasr [9], as shown in Table 2. The apparent activation energy of the C_2F reductions lay between 17.62 to 39.70 kJ/mol. The rate-determining steps of the C_2F reductions were the first inner gas diffusion, then the inner gas diffusion and interface chemical reaction mixed controlling.

Model Function Results

According to the Avrami-Erofeev [10–12] equation, the reduction degree α can be expressed by the following relationship of time t and rate constant k:

$$1 - \alpha = \exp^{-kt^n}, \tag{8}$$

where n refers to the Avrami exponent. By obtaining the double natural logarithm on either side of the equal sign of Eq. (8), we can formulate the following equation:

$$\ln[-\ln(1-\alpha)] = n \ln t + \ln k. \tag{9}$$

The Avrami exponent n can be obtained by the slope of the fitted line of $\ln[-\ln(1-\alpha)]$ against $\ln t$. For example,

$$n = \frac{d\{\ln[-\ln(1-\alpha)]\}}{d \ln t}. \tag{10}$$

The value of n is directly related to $G(\alpha)$, which means that $G(\alpha)$ can be determined by first obtaining the value of n. Table 3 shows the corresponding relationship between $G(\alpha)$ and n and its reaction mechanism. The Avrami exponent n is related to the functions corresponding to nine solid-state reactions, which can

Table 3 Relationship between $G(\alpha)$ and n for normal solid reactions and its reaction mechanism

Function	$G(\alpha)$	n	Mechanism
$D_1(\alpha)$	α^2	0.62	One-dimensional diffusion
$D_2(\alpha)$	$(1-\alpha)\ln(1-\alpha)+\alpha$	0.57	Two-dimensional diffusion (bidimensional particle shape)
$D_3(\alpha)$	$[1-(1-\alpha)^{1/3}]^2$	0.54	Three-dimensional diffusion (tridimensional particle shape) Jander equation [13]
$D_4(\alpha)$	$(1-2/3\alpha)-(1-\alpha)^{2/3}$	0.57	Three-dimensional diffusion (tridimensional particle shape) Ginstling-Brounshtein equation [14]
$F_1(\alpha)$	$-\ln(1-\alpha)$	1	Bimolecular decay law (instantaneous nucleation and unidimensional growth)
$R_2(\alpha)$	$1-(1-\alpha)^{1/2}$	1.11	Phase boundary controlled reaction (contracting area, i.e., bidimensional shape)
$R_3(\alpha)$	$1-(1-\alpha)^{1/3}$	1.07	Phase boundary controlled reaction (contracting volume, i.e., tridimensional shape)
$A_2(\alpha)$	$[-\ln(1-\alpha)]^{1/2}$	2	Random instant nucleation and two-dimensional growth of nuclei (Avrami-Erofeev equation [10, 11])
$A_3(\alpha)$	$[-\ln(1-\alpha)]^{1/3}$	3	Random instant nucleation and three-dimensional growth of nuclei (Avrami-Erofeev equation)

be expressed as diffusion controlled, reaction-rate controlled, and first-order kinetics controlled in mechanisms or follow the equations of Avrami and Erofeev.

Figure 3 shows the relationship between $\ln[-\ln(1-\alpha)]$ and $\ln t$ for the C_2F samples, and the Avrami exponent n was calculated. The results revealed that the n corresponding to the C_2F samples reduction at 1123 K (850 °C), 1173 K (900 °C), and 1223 K (950 °C) lay at 2.05, 2.06, and 2.08, respectively, thereby indicating the reduction of the C_2F samples as described by function A_2. Functions A_2 and A_3 were obtained from the nucleation process (crystallization) and can also be applied to the reduction reaction. Function A_2 can express the 2D reduction reaction and function A_3 can express a 3D reaction. Moreover, the reaction determined by A_2 appears in a plane, whereas that of A_3 is a cylinder.

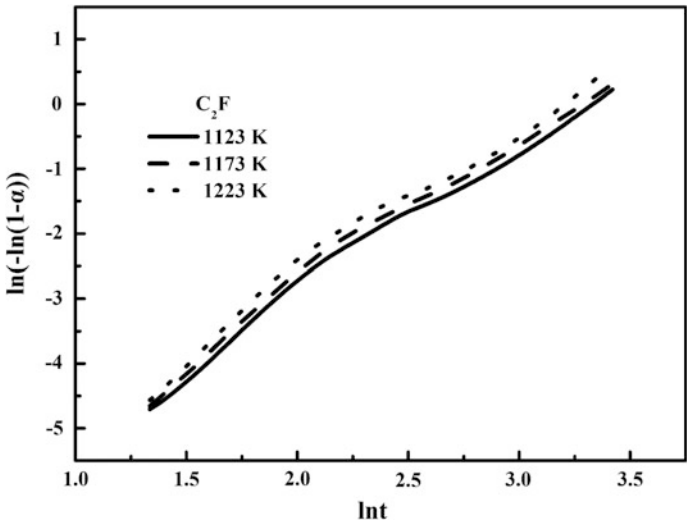

Fig. 3 ln[−ln(1 −α)] versus lnt at 1123 K (850 °C), 1173 K (900 °C), and 1223 K (950 °C) based on ln-ln analysis for C_2F

Conclusions

The isothermal reduction kinetics of C_2F was investigated via TG measurement with 30% H_2 and 70% N_2 gas mixtures. The reduction degree and rate of C_2F were further discussed. The reduction mechanisms of C_2F were examined through ln-ln analysis. The following conclusions were summarized.

1. The reduction rate analysis indicated that the reduction of the C_2F was typical one-step.
2. The apparent activation energy values of the reduction process of the C_2F was 27.40 kJ/mol. The rate-determining steps of the C_2F reductions were the first inner gas diffusion, then the inner gas diffusion and interface chemical reaction mixed controlling.
3. The ln-ln method implied that the reduction of C_2F was described by the of Avrami–Erofeev function and appeared as a 2D reaction.

Acknowledgements The authors are grateful for the financial support provided by the Natural Science Foundation of China (51234010 and 51522403).

References

1. Phillips B, Muan A (2006) Phase equilibria in the system CaO-iron oxide-SiO_2, in air. J Am Ceram Soc 42(9):413–423
2. Ding C, Lv X, Chen Y et al (2015) Non-isothermal crystallization kinetics for CaO–Fe_2O_3 system. J Therm Anal Calorim 124(1):509–518
3. Sosman RB, Merwin HE (1916) Preliminary report on the system, lime: ferric oxide. Wash Acad Sci J 6(15):532–537
4. Ganguly S (1991) A study of gaseous reduction of calcium ferrites. Ph.D. thesis, The University of Queensland
5. El-Geassy AA (1996) Reduction of CaO and/or MgO-doped Fe_2O_3 compacts with carbon-monoxide at 1173-1473 K. ISIJ Int 36:1344–1353
6. Du S, Sichen N, Staffansson LI (1988) Reduction of calcium ferrites by hydrogen in the temperature interval 1191–1426 K. Scand J Metall 17(5):232–238
7. Mccune RC, Wynblatt P (2010) Calcium segregation to a magnesium oxide (100) surface. J Am Ceram Soc 66(2):111–117
8. Vyazovkin S, Wight CA (1999) Model-free and model-fitting approaches to kinetic analysis of isothermal and non-isothermal data. Thermochim Acta 340:53–68
9. Nasr MI, Khedr MH, El-Geassy AA, Omar AA (1995) Effect of nickel oxide doping on the kinetics and mechanism of iron oxide reduction. ISIJ Int 35(9):1043–1049
10. Avrami M (1939) Kinetics of phase change. I general theory. J Chem Phys 7(12):1103–1112
11. Avrami M (1940) Kinetics of phase change: II. transformation—time relation for random distribution of nuclei. J Chem Phys 8(2):212–224
12. Avrami M (1940) Granulation, phase change, and microstructure kinetics of phase change.III. J Chem Phys 9(2):177–184
13. Tamhankar SS, Doraiswamy LK (1979) Analysis of solid–solid reactions: a review. AIChE J 25(4):561–582
14. Ginstling AM, Brounshtein BI (1950) On diffusion kinetics in chemical reactions taking place in spherical powder grains. Zhur Priklad, Khim, p 23

Study on Application of Iron Ore Fine in Pelletizing

Gele Qing, Yunqing Tian, Weidong Zhang, Xiaopeng Wang, Wenbin Huang, Xiangjuan Dong and Ming Li

Abstract Pellet production requires iron ore concentrates have fine particle size, high specific surface area and good balling performance, so iron ore concentrates appropriate for pelletizing is limited compared to sintering. In order to extend the iron ore resources for pelletizing, the iron ore fines for sinter are studied in this paper. The effect of grinded iron ores on pelletizing, roasting and pellet quality were studied in this paper. The bond grinding index of iron ore fine is between 12.5 and 16.98 kwh/t. The grinded iron ore fine has good balling performance, the drop number and compressive strength of green pellet were improved with increase of grinded iron ore fine ratio. The compressive strength of roasted pellets were decreased with increase of grinded iron ore fine ratio, however it can be reached 2500 $N.P^{-1}$ while proportioned with more than 80% of magnetite iron ore concentrate.

Keywords Iron ore fine · Pellet · Bond grinding index · Compressive strength

Introduction

Pellet has the advantages of high iron grade, high compressive strength, uniform particle size and good metallurgical properties compared to sinter, which is benifical for blast furnace to improve technical and economical indexes [1, 2]. The pellet production needs iron ore concentrates with fine grain size, good balling and roasting performance. However the iron ore resources appropriate for pelletizing is limited, which is restricting the further development of domestic pellet process. The energy consumption of pellet process is lower 50% than that of sinter process, and pellet process is more environmental friendly than sinter. So the development of

G. Qing (✉) · Y. Tian · W. Zhang
Shougang Research Institute of Technology, Beijing 100043, China
e-mail: qinggele_68@163.com

X. Wang · W. Huang · X. Dong · M. Li
Shougang Jingtang United Iron & Steel CO., Ltd., Hebei 063200, China

B. Li et al. (eds.), *Characterization of Minerals, Metals, and Materials 2018*, The Minerals, Metals & Materials Series,
https://doi.org/10.1007/978-3-319-72484-3_30

pellet is becoming more important. There is abundant resource in iron ore fine and price is lower than iron ore concentrates for pelletizing [3, 4]. So in order to extend the resource appropriate for pelletizing, the grindability, as well as balling and roasting performances of six typical iron ore fines usually used for sintering were studied in this paper.

Materials and Experimental Methods

Table 1 shows the main chemical composition of the iron ore fines used in experiment. The iron grade of iron ore fine A is 66%, SiO_2 content is 2.01%, the iron grade of iron ore fine B is 61.5%, SiO_2 content is 3.6%. The bond grinding index of each iron ore fine was tested first. Then the iron ore fines grinded by ball mill. The balling and roasting performance of each grinded iron ore fine were studied, and the effect of it on magnetite iron ore concentrate pelletizing were studied together. Table 2 shows the chemical composition and grain size of magnetite. The balling of green pellets were carried out in the pelletizing disc with Φ800 mm. The pelletizing time is 10 min. After balling the green pellets with size of 10–12.5 mm were screened out and tested the indexes of drop number, compressive strength and bursting temperature. The green pellets were roasted in experimental pot. After roasting the compressive strength of pellets were examined.

Grindablity of Iron Ore Fine

Table 3 shows the results of bond grinding index of six iron ore fines. The bond grinding index of iron ore fine A and iron ore fine E is 16.98 and 16.56 kwh/t respectively. The bond grinding index of iron ore fine D and iron ore fine F are low, which is 12.88 and 13.21 kwh/t respectively. The bond grinding index of normal iron ore is between 11.2 and 19 kwh/t [5].

Table 1 Chemical composition of iron ore (%)

Item	TFe	FeO	SiO_2	Al_2O_3	CaO	MgO	P	S
A	66.0	0.20	2.01	1.91	0.19	0.19	0.055	0.011
B	61.50	0.69	3.60	2.31	0.15	0.29	0.098	0.021
C	59.61	0.33	5.51	2.81	0.27	0.12	0.096	0.012
D	62.75	0.40	3.93	2.09	0.16	0.15	0.10	0.011
E	60.66	1.01	6.96	1.89	0.94	0.13	0.076	0.015
F	57.72	0.44	5.27	1.68	0.61	0.12	0.065	0.010

Table 2 Chemical composition of magnetite (%)

Item	TFe	FeO	SiO_2	Al_2O_3	CaO	MgO	P	S	LOI
Magnetite	69.32	29.12	1.73	0.39	0.45	0.51	0.009	0.19	−2.45

Table 3 Bond grinding index of iron ore fines

Name	Bond grinding index, kWh/t
A	16.98
B	14.20
C	14.13
D	12.88
E	16.56
F	13.21

In order to study the feasibility of iron ore fines used in pellet production, the iron ore fines were grinded by ball mill first and then agglomerated and roasted. The iron ore fines grinded until the mesh 200 was reached 80%, Table 4 shows the grain size of the grinded iron ore fine.

Pelletizing Performance of Grinded Iron Ore Fine

The balling tests were carried out using single grinded iron ore and the mixed iron ore with different ratio of magnetite. The bentonite was used as binder and the proportion was 1.5%. Figures 1 and 2 show the drop number and compressive strength of green pellets respectively. The grinded iron ore has good balling performance, the shatter index as drop number and compressive strength of green pellets made by grinded iron ore are higher than the pellet made by single magnetite. The drop number of green pellets agglomerated by iron ore fines A, B, C were reached 15 times/0.5 m and compressive strength reached 12 $N.P^{-1}$. Figures 3 and 4 show the drop number and compressive strength of green pellets made by magnetite mixed with grinded iron ore fine. With increase of grinded iron

Table 4 Grain size of grinded iron ore (%)

Grain size (mesh)	>80	80–120	120–140	140–160	160–180	180–200	<200
A	0.73	2.34	2.15	6.34	3.64	4.35	80.45
B	1.23	3.45	2.31	5.23	2.86	5.36	80.12
C	0.97	3.01	3.12	3.68	4.23	2.65	82.34
D	1.78	1.87	3.77	3.56	3.56	5.09	80.37
E	1.02	2.67	4.53	3.55	2.67	4.33	81.23
F	0.67	3.45	1.97	4.79	4.59	3.89	80.64

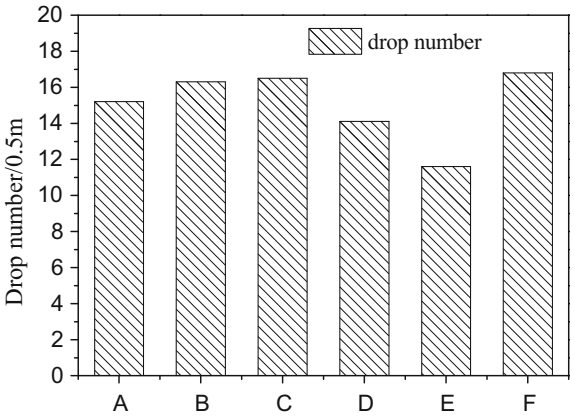

Fig. 1 Drop number of green pellet made green pellet by single grinded iron ore

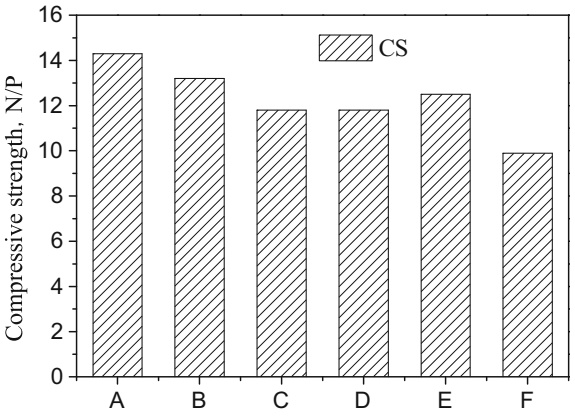

Fig. 2 Compressive strength of made by single grinded iron ore

ore fine ratio the drop number and compressive strength of green pellets were increased. When the magnetite proportioned with 30% of grinded iron ore fine A, the drop number was increased from 4.0 times/0.5 m to 6.8 times/0.5 m. The drop number was increased to 10.1 times/0.5 m while added 30% of iron ore fine F. The compressive strength of green pellet was increased from 8.12 to 11.4 N/P when added by 30% of iron ore fine A, and increased to 10.78 N/P when added by 30% of iron ore fine E. It is illustrated that the grinded iron ore fine can improve the quality of green pellet significantly.

The grinded iron ore fine except A will influence the bursting temperature of green pellets. The results are shown in Table 5. The bursting temperature of green pellets made by iron ore fine B, C, F were decreased to 450 °C. The bursting temperatures of green pellets can be improved while added by magnetite, which can be increased to 600 °C when the ratio of magnetite was reached 80%. The iron ore fine A has little effect of pellet bursting temperature.

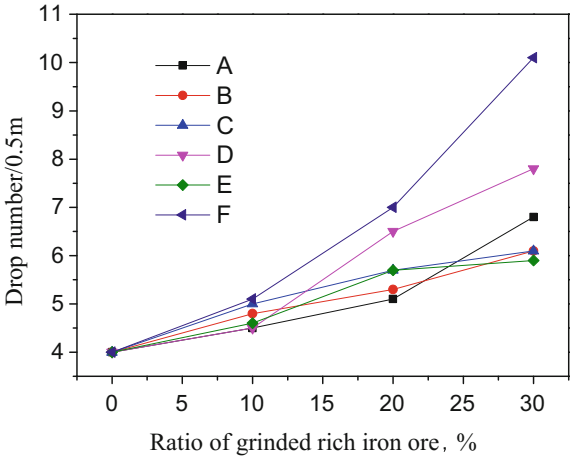

Fig. 3 Drop number of green pellet made pellet by mixed iron ore

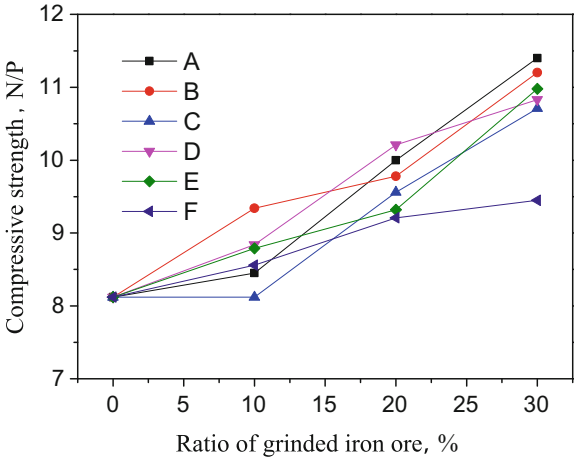

Fig. 4 Compressive strength of green made by mixed iron ore

Table 5 Bursting temperature of green pellets (°C)

Ratio %	A	B	C	D	E	F
0	>650	>650	>650	>650	>650	>650
10	>650	650	650	650	650	640
20	>650	600	600	640	650	630
30	>650	540	580	590	600	540
100	>650	480	450	550	480	450

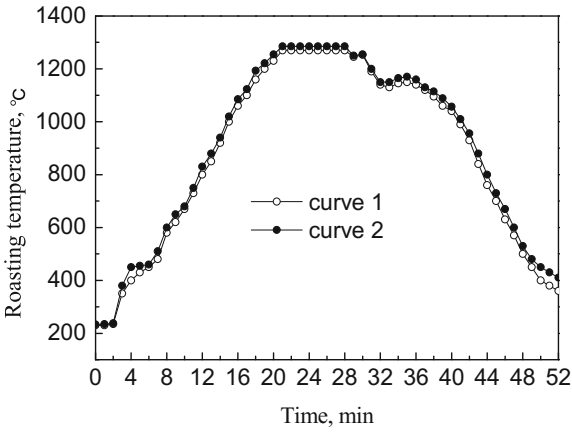

Fig. 5 Temperature and time of roasting experiment

Roasting Performance of Grinded Iron Ore Fine

Green pellets made by single grinded iron ore fine and mixed iron ores were roasted in experimental pot. The temperature and time of roasting experiment are shown in Fig. 5. The green pellets were roasted under two different firing temperature. The highest roasting temperature of curve 1 was 1270 °C and curve 2 was 1280 °C. The roasting process include drying, preheating, firing, soaking and cooling. The total roasting time was 52 min. After roasting, the compressive strength of each pellet was tested.

Figure 6 shows the compressive strength of roasted pellet. The compressive strength of pellet made by iron ore fine is high, which was reached 3000 N/P, it is show in Fig. 6a. This shows that iron ore fine A has little effect on pellet compressive strength. The other iron ore fines will affect the pellet compressive strength. The compressive strength of pellet made by single iron ore B, C, D, E, F

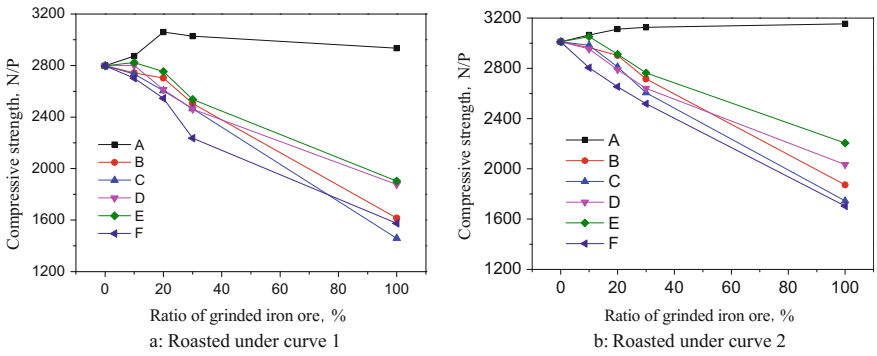

Fig. 6 Compressive strength of roasted pellet

was lower than 2000 N/P. The compressive strength of pellet can be improved when added by magnetite iron ore concentrate. The compressive strength of pellets were reached 2500 N/P when the proportion of grinded iron ore fine B, C, D, E, F was lower than 20%. If the roasting temperature is increased, the compressve strength of pellet can be increased, which is shown in Fig. 6b.

Conclusions

(1) The bond grinding index of iron ore fine is similar to normal iron ore. The bond grinding index of iron ore fine A and E is 16.98 and 16.56 kwh/t, and iron ore fine B and C is 13.21 and 12.88 kwh/t respectively.
(2) The grinded iron ore fine has good balling performance. The shatter index as drop number and compressive strength of green pellet can be improved by with increase of grinded iron ore fine ratio.
(3) The iron ore fine A has little effect on green pellet bursting temperature, other iron ore fines will decrease the bursting temperature of green pellet, however it can be reached 600 °C while the proportion is lowere than 20%.
(4) The iron ore fine A has little influence on pellet compressive strength, which can be reached 3000 N/P. The compressive strength of roasted pellet made by single iron ore fine B, C, D, E, F is lower, however it can be reached 2500 N/P when proportioned by more than 80% of magnetite iron ore concentrate. Increase of roasting temperature also will improve the pellet compressive strength.

References

1. Lampke JP, Silge S (2008) Agglomeration by pelletizing discs-an important process in times of rising worldwide demand for iron ore. Aufbereitungs-Technik Min Process 49(8):4–12
2. Zhu DQ et al (2008) Use of vale hematite pellet feed in Chinese pelletizing plants. Paper presented at the 3rd International Meeting on Ironmaking and 2nd International Symposium on Iron Ore, Saỉõ Paulo, Brazil, 472–476, September 2004
3. Umadevi T, Sampath Kumar MG, Kumar S (2008) Influence of raw material particle size on quality of pellets. Ironmaking Steelmaking 35(5):327–337
4. Fan XH, et al (2009) Study on the suitable temperature of oxidized pellets roasting. Paper presented at the Proceedings of the 5th International Congress on the Science and Technology of Ironmaking, Shanghai, China, 320–324 October 2009
5. Wu JM (2005) Progress in research and application of bond grinding index. Nonferrous Metall Equip 35(3):5–9

Characterization of Different Clays for the Optimization of Mixtures for the Production of Ceramic Artifacts

A. R. G. Azevedo, J. Alexandre, E. B. Zanelato, M. T. Marvila, L. G. Pedroti, G. C. Xavier, D. P. Santos, S. N. Monteiro and M. S. Peixoto

Abstract The *Baixada Campista* is a region located in the municipality of Campos dos Goytacazes and is known as an important pole producing ceramic artifacts in Brazil. The clay used in this production is usually extracted from different layers of the region itself undergoing a pretreatment process. The objective of this work was to characterize the different soils (A, B and C), from different layers of the reservoir, in order to characterize the different physical and chemical characteristics (granulometry, determination of Atterberg limits, moisture and chemical analysis). To optimize, using the simplex methodology, properties such as mechanical strength, porosity and linear retraction. The results pointed to an optimum proportion of the clays studied so that the properties meet the Brazilian technical norms, being the proportion of 30% of soil A, 30% of soil B and 40% of soil C well.

Keywords Clays · Ceramic artifacts · Simplex methodology

A. R. G. Azevedo · J. Alexandre · E. B. Zanelato · M. T. Marvila · G. C. Xavier · D. P. Santos
LECIV—Civil Engineering Laboratory, UENF—State University of the Northern Rio de Janeiro, Av. Alberto Lamego, 2000, Campos dos Goytacazes, Rio de Janeiro 28013-602, Brazil

A. R. G. Azevedo (✉) · M. S. Peixoto
IFF—Federal Institute Fluminese, DIRINF—Directorate of Infrastructure Rectory, St. Cel. Valter Kramer, 357—Parque Vera Cruz, Campos dos Goytacazes, Rio de Janeiro 28080-565, Brazil
e-mail: afonso.garcez91@gmail.com

L. G. Pedroti
Federal University of Viçosa, UFV. Av. Peter Henry Rolfs, S/N—Campus Universty, Viçosa, Minas Gerais 36570-000, Brazil

S. N. Monteiro
Department of Materials Science, IME—Military Institute of Engineering, Square General Tibúrcio, 80, Rio de Janeiro 22290-270, Brazil

B. Li et al. (eds.), *Characterization of Minerals, Metals, and Materials 2018*, The Minerals, Metals & Materials Series,
https://doi.org/10.1007/978-3-319-72484-3_31

Introduction

The municipality of Campos dos Goytacazes, located in the northern region of the state of Rio de Janeiro, especially the region of the *Baixada Campista*, has one of the great highlights in its economy the red ceramic industry. Currently, according to data from the Campos Ceramists' Union (2015), the red ceramic industry that forms part of Campos dos Goytacazes industrial park consists of more than 100 unionized ceramics, which generate approximately four thousand direct jobs, with an estimated production of six million pieces per month, which makes the region the second largest Brazilian industrial park in red ceramics [1].

Study for characterization of clays in the Campos dos Goytacazes region showed different clays coming from fields located at the lower camped pole and performing chemical analysis, X-ray diffraction, differential thermal analysis, thermogravimetric analysis, particle size analysis and determination of physical-mechanical properties in test specimens molded with the studied ceramic masses [1]. The two authors concluded that clays found in the studied region are predominantly kaolinitic, and that can be used to manufacture massive bricks and ceramic blocks without problems. However, both authors concluded that for the manufacture of tiles and coatings, it is necessary to carry out a study in the formulation of the ceramic masses used, since for these types of materials the required minimum properties were not obtained or were very close to the limits established by norm [2].

Other studied showed of the ceramic masses of the Campos dos Goytacazes municipality, in order to verify the feasibility of the incorporation of residues for the production of ceramic artifacts clays used in this region [3]. One of the conclusions obtained by the authors is that it becomes evident the necessity of the planning of mixtures so that more satisfactory results are obtained in the properties of the studied ceramics [4].

More modern studies show the importance of experimental planning, since the outstanding studies did not succeed in their conclusions because of poor choice in the traits to be studied [5]. Proper planning would eliminate this problem. Researches shows faced the same problem in choosing the dosages to be studied in his work, since the author performed a little effective experimental planning, which caused some traces lost by the author [6]. In this context, the purpose of this work is to characterize three clay samples used in the Campos ceramics and mainly to use the simplex network blends planning to create a rational dosing methodology for the ceramic masses to be used in red ceramic artifacts [7].

The simplex method is a set of statistical planning and analysis techniques used in mathematical modeling of responses. It consists in varying the proportions of the components of a mixture, keeping its total quantity constant. Thus, the response value changes when changes are made to the relative proportions of the components [2]. The simplex space corresponds to the response surface for experimental data, or also to the response points of an experiment planning. Briefly, the method relates the parameters to the responses of the analyzed system.

In this work, three types of ceramic mass commonly used in the camper descent will be used, named by A, B and C. Therefore, a simplex network will be used in the triangular form, where each of the vertices represents one of the components that will be studied. To obtain the network response surface it is necessary to use one of the mathematical models available in the planning. For this work will be used the linear, quadratic and simple cubic models.

Materials and Methods

Samples were collected and named as samples A, B and C. Samples were characterized by the following tests, which were the stages of sun drying, dewatering and homogenization:

- Granulometric Analysis;
- Specific grain mass, Liquidity and Plasticity limits;
- Identification of clay minerals with X-ray diffraction.

After the characterization phase of the materials, samples were prepared by varying the proportions of materials A, B and C in order to verify the most important technological properties for ceramic materials, namely: breaking stress and water absorption at temperature of 850 °C. Both tests are performed in accordance with Brazilian standards [8, 9]. The variation of the proportion of materials is defined according to the methodology proposed by simplex itself, where material A becomes associated with variable X_1, material B to X_2 and the material C to X_3. It is noteworthy that other intermediate traits were proposed in order to statistically refine the model. The fractions studied and their respective nomenclatures are indicated in Table 1.

With the test specimens and the tests, it was possible to obtain the response surface through simplex network planning, which indicates the proportions of materials A, B and C should be used in order to obtain the best technological characteristics for the ceramic products.

Results

The particle size distribution curve of samples A, B and C is shown in Fig. 1. Analyzing the distributions, it is easy to see that material A has a higher proportion of larger particles, whereas material C has the highest proportions of fine particles. This is of great importance for the planning of experimental mixtures, since, because they have different granulometry, the materials need to be compensated in order to obtain the mixture with the greatest possible packaging.

Table 1 Nomenclature of the traits studied

Nomenclature	Proportion of material A (%)	Proportion of material B (%)	Proportion of material C (%)
X_1	100	0	0
X_2	0	100	0
X_3	0	0	100
X_{12}	50	50	0
X_{13}	50	0	50
X_{23}	0	50	50
X_{123}	33.33	33.33	33.33
X_{1123}	50	25	25
X_{1223}	25	50	25
X_{1233}	25	25	50
X_{112}	66.67	33.33	0
X_{113}	66.67	0	33.33
X_{122}	33.33	66.67	0
X_{223}	0	66.67	33.33
X_{133}	33.33	0	66.67
X_{233}	0	33.33	66.67

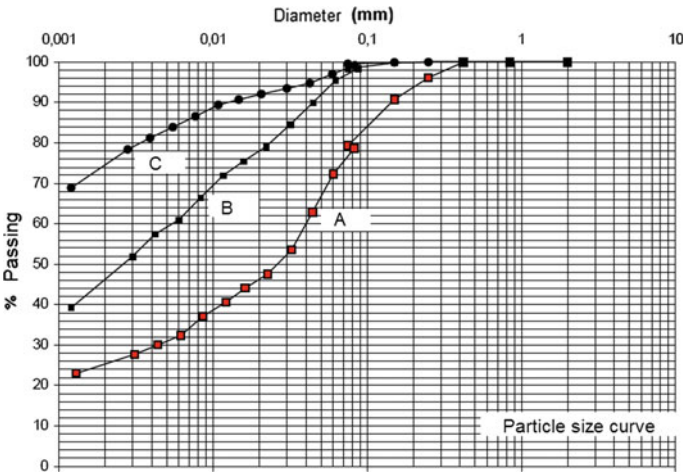

Fig. 1 Granulometric distribution curve of samples A, B and C

The specific mass of the grains for the studied samples is presented in Table 2. It is extremely important to know these parameters, since it varies according to the mineralogical constituent of the soil particles. It is known that for most soils the value varies between 2.65 and 2.85 g/cm^3, decreasing to soils containing high organic matter content, harmful to the manufacture of ceramic pieces, and increased

Table 2 Parameters found for samples

Sample	Specific mass (g/cm^3)	LL (%)	LP (%)	IP (%)
A	2.68	44	27	17
B	2.65	64	28	36
C	2.62	76	37	39

to soils rich in oxides of iron. In the case of the samples studied, the specific mass value did not show significant variations, being in a range of 2.65 g/cm^3.

The limits of Atteberg, which correspond to the limit of liquidity and plasticity limit, indicate parameters of soil workability. The liquidity limit (LL) can be defined as the moisture content for which the soil passes from the plastic state to the liquid state while the plasticity limit (LP) indicates the moisture where the soil begins to fracture when mold it. It is extremely important to know these values of moisture so that in the molding of the ceramic pieces, no excess water or scarcity is used [3]. The limits found for the studied samples are shown in Table 2, where it is possible to see that soil A presents lower plasticity parameters, while soil C can be considered the most plastic among the studies. It is important to note that the use of a tool that performs the planning of the mixtures of the three samples studied is essential to find the trait that will provide the best technological properties for the ceramic pieces to be manufactured.

Analyzing Fig. 2, which demonstrates the X-ray diffractograms for the three samples studied, it is apparent that the predominant clay in the samples studied is kaolinite. This fact bought what the bibliographical already predicted, according to works of Alexandre (2001) and Vieira (2000). It is of great interest to prove the predominance of kaolinite clay, because as widely published by the bibliographical, since this clay is heat treated around 550 °C, metacaulinite is formed, a compound of great interest for presenting excellent technological parameters for ceramics [10].

After the mechanical strength and water absorption tests were carried out for the specimens burned at 850 °C, the data and results obtained were treated in a simplex

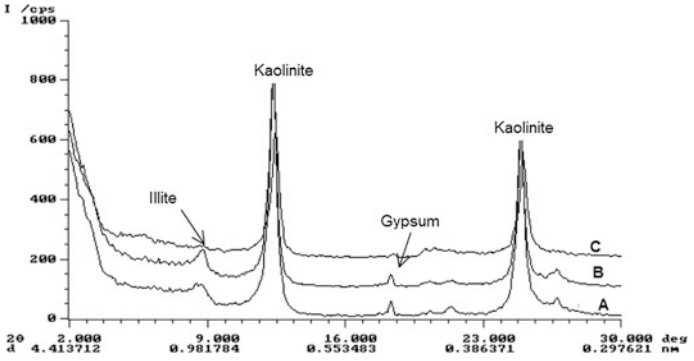

Fig. 2 X-ray diffraction of samples A, B and C

Table 3 Mechanical resistance of the models studied at 850 °C

Nomenclature	Observed value (kgf/cm^2)	Linear model (kgf/cm^2)	Quadratic model (kgf/cm^2)	Cubic model (kgf/cm^2)
X_1	17.19	17.19	17.19	17.19
X_2	44.77	44.77	44.77	44.77
X_3	60.27	60.27	60.27	60.27
X_{12}	31.30	30.98	31.30	31.15
X_{13}	27.77	27.80	27.77	27.77
X_{23}	52.50	52.50	52.50	52.50
X_{123}	34.10	40.74	35.88	34.10
X_{1123}	23.30	28.96	24.17	23.29
X_{1223}	40.60	42.75	41.56	40.63
X_{1233}	42.20	50.50	45.62	44.66
X_{112}	28.60	26.38	26.50	26.60
X_{113}	23.50	31.54	21.84	21.88
X_{122}	28.60	35.57	35.63	35.69
X_{223}	49.30	49.93	49.93	49.93
X_{133}	36.70	45.91	36.14	36.12
X_{233}	50.40	55.10	55.10	55.10
Average waste		4.84	2.24	1.91

methodology. Tables 3 and 4 present the results for mechanical resistance and water absorption at the burning temperature of 850 °C respectively. Figures 3 and 4 present the response surface that best suited the parameters mechanical strength and water absorption, respectively. For the mechanical resistance parameter, the model that best fit was the cubic, as can be observed by the mean of the residues. For the parameter water absorption and specific mass, the quadratic model provided a very low average of residues, and therefore the cubic model was not calculated for this parameter. It is also worth noting that the parameter water absorption was better adjusted with the linear model, as seen by the average of the residues [11].

The calculations in Table 3 were performed applying the expressions described below that came from applying the simplex methodology.

$$y_{linear} = 17.19 * X_1 + 44.77 * X_2 + 60.27 * X_3$$

$$y_{quadratic} = 17.19 * X_1 + 44.77 * X_2 + 60.27 * X_3 - 44.22 * X_1 * X_3$$

$$y_{cubic} = 17.19 * X_1 + 44.7 * X_2 + 60.27 * X_3 - 44.22 * X_1 * X_3 - 52.17 * X_1 * X_2 * X_3$$

The calculations in Table 4 were performed applying the expressions described below that came from applying the simplex methodology. For this parameter, the cubic model was not calculated, since the linear model presented greater adjustment than the quadratic model.

Table 4 Water absorption of the models studied at 850 °C

Nomenclature	Observed value (%)	Linear model (%)	Quadratic model (%)
X_1	19.86	19.86	19.86
X_2	23.10	23.10	23.10
X_3	25.20	25.20	25.20
X_{12}	21.90	21.49	21.49
X_{13}	23.40	22.54	23.39
X_{23}	24.90	24.18	24.89
X_{123}	22.96	22.73	23.44
X_{1123}	20.80	21.30	21.76
X_{1223}	23.00	22.93	23.35
X_{1233}	24.70	23.98	24.67
X_{112}	20.80	20.94	20.94
X_{113}	20.90	21.64	22.41
X_{122}	20.60	22.04	22.04
X_{223}	21.80	23.82	24.47
X_{133}	22.60	23.44	24.19
X_{233}	23.40	24.53	25.16
Average waste		0.70	1.09

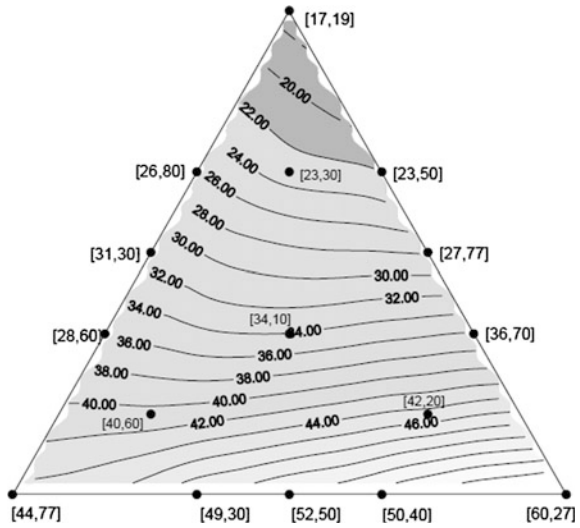

Fig. 3 Surface of response of the simple cubic model for the parameter mechanical resistance

$$y_{linear} = 19.86 * X_1 + 23.13 * X_2 + 25.23 * X_3$$

$$y_{quadratic} = 19.86 * X_1 + 23.13 * X_2 + 25.23 * X_3 + 3.77 * X_1 * X_3 + 2.60 * X_2 * X_3$$

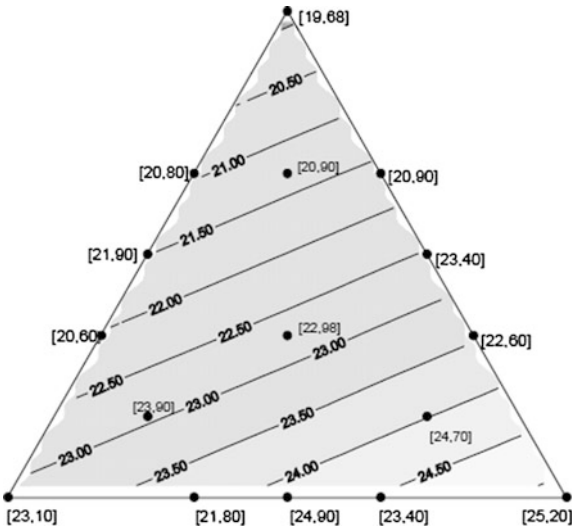

Fig. 4 Response surface of the linear model for the parameter water absorption

Based on the results obtained by the tables and the response surfaces of the simplex, the effectiveness of the simplex network planning for the analysis and prediction of the technological parameters of the ceramic pieces is proved. By analyzing the optimal regions obtained, it is easy to see that material C contributes most to mechanical strength, while material A helps in reducing water absorption, while material B exhibits intermediate behavior between the two. A ceramic material with good technological properties will be obtained if the correct proportion between these materials is realized. Several traces can be used, being obtained through the equations resulting from the simplex methodology. A possible trace would be 30% of A, 30% of B and 40% of C, which would result in values of resistance and water absorption compatible with the recommended values [2, 11].

Conclusion

After the study of the methodology of clay samples in simplex network can be concluded:

- The characterization of samples A, B and C of clayey soils typically used in camellary ceramics demonstrates what has been studied by researchers such as Alexandre (2000) and Vieira (2001), that the clays of the region are typically kaolinitic and have a great granulometric variation and the Atteberg boundaries.
- Because of this large size range and liquidity and plasticity limits, it is necessary to use some kind of mix planning in order to obtain better technological parameters for the ceramic materials produced.

- The use of planning in simplex networks allows a better interpretation and prediction of these parameters using mathematical and statistical models, as observed when analyzing the mixture of samples A, B and C and to analyze the mechanical resistance and water absorption properties.
- The effectiveness of using simplex modeling to predict the technological parameters of ceramics is effectively proven in this way.

References

1. Alexandre J, Toledo R, Saboya F, Pereira M (2004) The use of Simplex design to predict the mechanical properties of brick ceramic. Ceramic 47:236–241
2. Vieira CMF, Holanda JNF, Pinatti DG (2008) Caracterization of red ceramic body used in the production of bricks in the region of Campos dos Goytacazes – RJ. Ceramic 46:458–468
3. Babisk MP, Vidal FWH, Ribeiro WS, Aguiar MC, Gadioli MCB, Vieira CM (2012) Incorporation of quartzitos residue in red ceramics. Holos 6:169–177
4. Nicolite M, Delaqua GCG, Amaral LF, Vernilli F, Vieira CMF (2016) Effect of incorporation of residue from alumina production adjustments step in ceramic properties. 60° Brazilian Ceramic Congress, pp 614–621
5. Oliveira YL, Junior ZL, Ancelmo L, Soares RAL (2016) Reuse of study of ceramic tile waste (grog) in formulation dough for blocks ceramic. 60° Brazilian Ceramic Congress, pp 468–479
6. Barroso MDB, Marinho RMM, Pereira FM, Santos IS, Melo PS (2016) Evaluation of the incorporation of cariri stone in masses of ceramics tiles. 22° Brazilian Congress of Engineering and Materials Science, pp 2368–2378
7. Tironi A, Trezzza MA, Scian AN, Irassar EFI (2012) Incorporation of calcined clays in mortars: porous structure and compressive strength. Procedia Mater Sci 1:366–373
8. Brazilian Association of Technical Norms—ABNT NBR 15270-1 (2005) Ceramic components part 1: hollow ceramic blocks for non load-bearing masonry—Terminology and requirements (in Portuguese)
9. Brazilian Association of Technical Norms –ABNT NBR 15310, 2009, Ceramic componentes —Ceramic roof tiles—Terminology, requirementes and testing methods (in Portuguese)
10. de Azevedo ARG et al (2015) Evaluation of the Industrial Raw Material Used for Ceramic Production in São José de Ubá. State of Rio de Janeiro, Brazil, Mater Sci Forum 820:3–7
11. Silva AC, Méxas MP, Quelhas OLG (2017) Restrictive factors in implementation of clean technologies in red ceramic industries. J Clean Prod 168:441–451

Part X
Mineral Processing and Analysis

Structural, Spectroscopic, Magnetic, and Thermal Characterizations of a Magnetite Ore from the Nagaland Region, India

Ritayan Chatterjee, Dinabandhu Ghosh, Surajit Biswas, Sandeep Agarwal, P. K. Mukhopadhyay and Saikat K. Kuila

Abstract An Indian magnetite ore from the Nagaland region was characterized by powder X-ray diffraction, spectroscopies (ultraviolet-visible and Raman), high temperature magnetization and thermal analysis. A Rietveld refinement of the diffraction data revealed that the principal phase present in the sample is magnetite with partial substitution of Fe with Mg (mainly) and Cr, leading to the chemical formula of $MgCr_{0.2}Fe_{1.8}O_4$. The UV-visible spectra of the sample in MeCN solution showed three distinct peaks. The lower region bands are due to metal-oxygen charge transitions and the other band is for d-d transition of iron. Raman spectral study at room temperature gave four characteristics bands of magnetite. The sample underwent a magnetic transition at high temperature and the thermomagnetization curve shows hysteresis during cooling cycle which indicates the possibility of first order structural transition at high temperature. The thermal property of the concentrate was studied by differential scanning calorimetric technique.

Keywords XRD · UV-vis · Raman spectroscopy · High temperature magnetization · Magnetite ore

R. Chatterjee (✉) · S. Agarwal
School of Applied Sciences, Haldia Institute of Technology, Haldia 721657, West Bengal, India
e-mail: ritayanchatterjee@gmail.com; ritayanc@research.jdvu.ac.in; ritayan.chatterjee@heritageit.edu; ritayan@hithaldia.in

R. Chatterjee · D. Ghosh · S. K. Kuila
Department of Metallurgical and Materials Engineering, Jadavpur University, Kolkata 700032, India

R. Chatterjee
Department of Physics, Heritage Institute of Technology Kolkata, East Kolkata Township, Kolkata 700107, India

S. Biswas
Department of Chemistry, Jadavpur University, Kolkata 700032, India

B. Li et al. (eds.), *Characterization of Minerals, Metals, and Materials 2018*, The Minerals, Metals & Materials Series,
https://doi.org/10.1007/978-3-319-72484-3_32

Introduction

Indian Bureau of Mines has set a target of 180 million tons per year of steel production as published in the report of 'Iron and steel vision 2020' [1]. To reach this goal, existing practice of iron extraction in India from hematite alone is not sufficient. India has a big reservoir of magnetite ore, in lumps and fines; however, this stock is still mostly unused [2]. Utilization of this huge magnetite stock should be an important step to fulfill the target. Even though the reduction of magnetite to iron, is more difficult than hematite reduction where magnetite is an intermediate product, works have been reported on successful hydrogen reduction where high and low grade magnetite was used as starting material [3–7]. Due to the huge demand of steel, and since the remaining stock of high grade hematite ore is dwindling, the low grade ores are going to draw more attention in the upcoming researches. The coarser hematite ore fines are used mainly in sintering and fines with less than 0.05 mm particle size are used for pelletization, to be subsequently fed to the conventional blast furnace (BF) [4] and direct reduction (DR) [3, 5–7] processes. A detailed characterization is necessary to select the appropriate ore beneficiation process, for a particular iron ore, on the basis of adjustable basicity index. Detailed characterization studies of Indian iron ores are still not adequate [2, 8, 9]. Especially, the role of characterization is more crucial for the low grade ores. In the present work, an attempt was made to characterize a low-grade magnetite ore, collected from Nagaland, India, by powder X-ray diffraction (XRD), ultraviolet-visible (UV-Vis) and Raman spectroscopies, high temperature magnetization and thermal analysis.

S. Biswas
Department of Chemistry, University of Kalyani, Kalyani, Nadia 741235, West Bengal, India

S. Agarwal
Key Lab of Magnetic Materials and Devices, Ningbo Institute of Materials Technology and Engineering, Chinese Academy of Sciences, Zhejiang 315201, Ningbo, People's Republic of China

S. Agarwal · P. K. Mukhopadhyay
CMP, Department of Condensed Matter Physics and Material Sciences, S. N. Bose National Centre for Basic Sciences, Salt Lake, Kolkata 700106, India

S. K. Kuila
Department of Metallurgical and Materials Engineering, Indian Institute of Technology Kharagpur, Kharagpur 721302, West Bengal, India

Experimental

The magnetite ore was crushed to powder and subjected to X-ray diffraction (XRD) using a Bruker D8 Advance X-ray diffraction unit. The powder diffraction data was taken in the 2θ range of 20° to 80° using Bragg-Brentano geometry and Cu-K_α radiation. A Rietveld refinement was carried out over the XRD data in JANA2006 program [10] using the LeBail algorithm [11]. Ultraviolet (UV)-visible (vis) absorption spectra of the ore fines were recorded by a JASCO V-630 spectrophotometer. Experiments were carried out in 1 cm × 1 cm quartz cuvette containing 2 mL of phosphate buffer. Raman spectra of the ore fine were recorded with the help of a T64000 J-Y Horiba spectrometer at 514.5 nm laser excitation (green light) and scan duration of 30 s. A Lake Shore 7400™ vibrating sample magnetometer with high temperature oven was used for magnetic measurements. The magnetic property was measured at and above room temperature to determine its magnetic transition temperature. A large quantity of sample was crushed into powder and mixed well to ensure that the magnetic property was not an outcome of sample inhomogeneity. The ore powder was encapsulated in a Teflon tape and magnetic measurements were performed in a high temperature furnace. A magnetic field of 0.001 T was applied and thermo-magnetization measurement was performed on the sample from room temperature up to 800 °C. The sample was then cooled back to room temperature and the same measurements were repeated in the cooling leg. The thermal phenomena occurring during heating of the ore were examined by a PerkinElmer Pyris Diamond differential scanning calorimeter (DSC). Alpha alumina powder was taken as the reference material.

Results and Discussion

X-Ray Diffraction of Magnetite Ore

XRD showed cubic magnetite, with cell parameter, $a \approx 0.83$ nm and space group Fd-3m. But the fit was not satisfactory for the Fe_3O_4 phase after introducing the atom coordinates. The atom coordinates as found in the database [12] for Fe_3O_4 are presented in Table 1.

The refinement with the atom coordinates returned a poor goodness of fitting (GOF) value of 1.90 with the reliability index parameters Rp = 2.76, Rwp = 3.92

Table 1 Atom coordinates of Fe_3O_4 (Pearson's crystal data entry number 1910832)

Site	Elements	Wyck.	Sym. (m)	x	y	z
FeB	Fe	16d	−3	1/2	1/2	1/2
FeA	Fe	8a	−43	1/8	1/8	1/8
O	O	32e	0.3	0.25470	0.25470	0.25470

(*R*p and *R*wp are profile *R* factor and weighted profile *R* factor, respectively). According to the energy-dispersive X-ray spectroscopic (EDS) result of the same ore, reported elsewhere [3], the major impurities present in the ore are Cr, Mg and Ni, besides the commonly found impurities of Si and Al. Hence the existence of Cr^{3+} impurity in Fe_3O_4 is likely. Therefore, the Rietveld refinement of the powder XRD pattern for $Cr_{0.1}Fe_{2.9}O_4$ phase was carried out and the result was even less satisfactory with the GOF value of 2.20 (*R*p = 3.29, *R*wp = 4.53). The Cr^{3+}-containing phase having the same cell parameters and symmetry possesses the atom coordinates as given in Table 2 [12].

In contrast, the fit for the principal phase is quite satisfactory after introducing the atomic coordinates of the phase containing both Cr^{3+} and Mg^{2+} impurities with the phase formula of $MgCr_{0.2}Fe_{1.8}O_4$. The GOF value thus obtained was 1.64, with *R* factors, *R*p = 2.33, *R*wp = 3.37. The Rietveld refinement of the powder XRD pattern of the magnetite ore for $MgCr_{0.2}Fe_{1.8}O_4$ is shown in Fig. 1. Red points represent the experimental values and black solid line depicts the calculated values. Vertical bars show the positions of the calculated Bragg reflections, and blue solid line at the bottom is the difference between the experimental and the calculated values. The profile at the major peak positions at 2θ values of 35.5°, 62.9° are nicely fitted, although the fitting at less intense peaks at 30.2°, 43.3°, 57.2° are not as satisfactory. The atom coordinates as found in the database [12, 13] for $MgCr_{0.2}Fe_{1.8}O_4$ are given in Table 3.

The refined values of the cell parameters and the space group with the *R* factors (*R* factors predict the quality of Rietveld fit to a powder diffraction pattern) are shown in Table 4.

Peak appearing at 25.3° is unindexed, supposedly due to a silica or alumina-based impurity phase or due to the presence of an iron-bearing hydroxide minerals, such as goethite (FeO(OH)).

Spectroscopic Studies of Magnetite Ore

1. *UV–visible spectroscopy*

The UV-Vis spectra of sample taken after ultra-sonicating the ore powder in MeCN solvent, is shown in Fig. 2. It shows one sharp peak at 252 nm and two distinct broad peaks at 318 and 970 nm, respectively. (The last one is not included in the

Table 2 Atom coordinates of $Cr_{0.1}Fe_{2.9}O_4$ (Pearson's crystal data entry number 382596)

Site	Elements	Wyck.	Sym. (m)	*x*	*y*	*z*
O1	O	32*e*	0.3	0.2378	0.2378	0.2378
M1	0.950Fe + 0.050Cr	16*c*	−3	0	0	0
Fe1	Fe	8*b*	−43	3/8	3/8	3/8

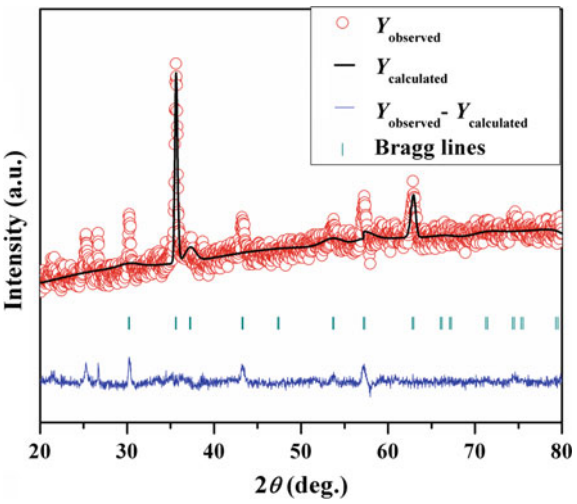

Fig. 1 Rietveld refinement pattern for $MgCr_{0.2}Fe_{1.8}O_4$ based on powder XRD at room temperature of the magnetite ore ($Y_{observed}$ is the experimental value and $Y_{calculated}$ is the calculated value)

Table 3 Atom coordinates of $MgCr_{0.2}Fe_{1.8}O_4$ (Pearson's crystal data entry number 553509)

Site	Elements	Wyck.	Sym.(m)	*x*	*y*	*z*
M1	0.8Fe + 0.2Mg	8*a*	−43	0	0	0
M2	0.5Fe + 0.4Mg + 0.1Cr	16*d*	−3	5/8	5/8	5/8
O	O	32*e*	0.3	0.377	0.377	0.377

Table 4 Rietveld refinement for $MgCr_{0.2}Fe_{1.8}O_4$ based on powder XRD pattern

Phase	Cell parameters	Space group	*R* factors
$MgCr_{0.2}Fe_{1.8}O_4$	*a* = 0.8363283 nm, *b* = 0.8363283 nm, *c* = 0.8363283 nm; α = 90°, β = 90°, γ = 90°	*Fd*-3*m*	*R*(obs) = 5.20 wR (obs) = 4.08 *R* (all) = 7.74 wR (all) = 4.11

Note R and wR indicate reliability index parameters; "obs" indicates observed reflections; "all" indicates all reflections, both strong and weak

figure). The lower region bands at 252 and 318 nm are due to the metal-oxygen charge transition. The band at 970 nm is for d-d transition of iron.

2. *Raman spectroscopy*

Raman spectra of the ore containing $MgCr_{0.2}Fe_{1.8}O_4$ as principal phase, is shown in Fig. 3. It consists of four characteristic peaks of magnetite at 306, 417, 590, 698 cm^{-1} respectively [14, 15]. The four Raman shifts and their corresponding symmetry modes are given in Table 5.

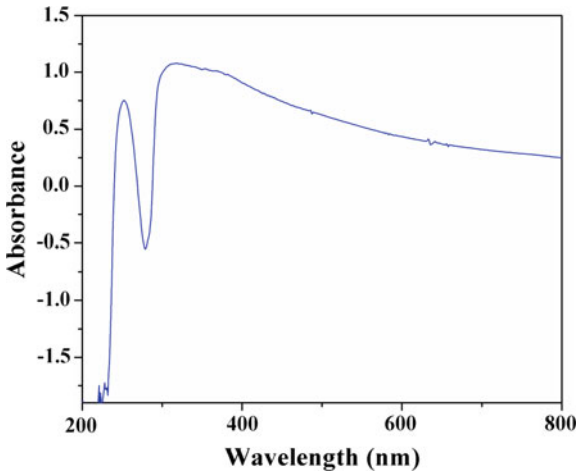

Fig. 2 UV-Visible spectra of the magnetite ore containing mainly $MgCr_{0.2}Fe_{1.8}O_4$, dispersed in MeCN

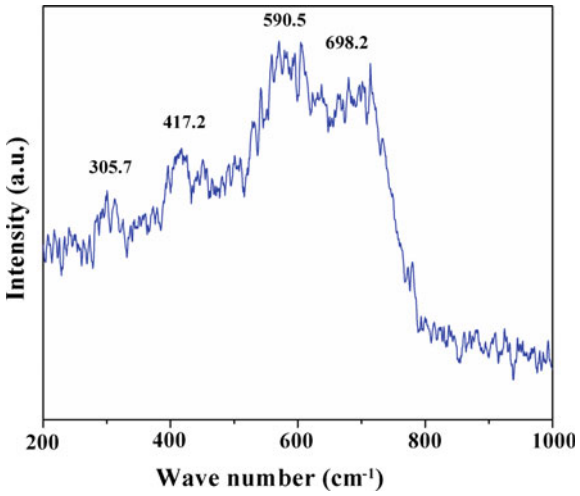

Fig. 3 Raman spectra of the magnetite ore containing mainly $MgCr_{0.2}Fe_{1.8}O_4$

Table 5 Raman wavenumbers and assignments

Raman shift (cm^{-1})	Symmetry mode
306	E_g (Fe–O sym. bend)
417	T_{2g} (Fe–O asym. bend)
590	T_{2g} (Fe–O asym. bend)
698	A_{1g} (Fe–O sym. str)

Magnetization and Thermal Analysis of Magnetite Ore

To examine the thermal stability of the ore in a semi inert (mildly oxidizing) atmosphere, the sample was heated at a rate of 15 °C min^{-1} from room temperature to 900 °C in a steady flow of nitrogen gas in a differential scanning calorimeter with a vertical furnace. The DSC result is shown in Fig. 4. The first thermal event that is observed occurs at 300 °C where the onset of an exothermic peak appears. It corresponds to magnetite to maghemite (γ-Fe_2O_3) transition [16]. The next thermal phenomenon occurs at 450 °C, where the onset of a little sharper exothermic peak appears. The peak corresponds to maghemite to hematite transition [16]. The effect of heating of the ore in hydrogen atmosphere at different isotherms between 700 and 1000 °C had been thoroughly studied earlier [3].

Because magnetite is a naturally occurring magnetic material which undergoes phase transition at higher temperature, the magnetic characterization for the ore sample is vital. Magnetic measurement performed on the ore from room temperature till 800 °C in the magnetic field of 0.001 T during heating and cooling is shown in Fig. 5a. The curve displays complex behavior and a rise in magnetization is seen above 300 °C, as shown in the magnified view in the inset of Fig. 5a. The rise in magnetization occurs because of the magnetite to maghemite (γ-Fe_2O_3) transition as can be seen in the DSC curve, discussed earlier. Beyond this, the magnetization of the sample keeps increasing till 430 °C and drops to near zero between 525 and 550 °C. The drop in magnetization occurs due to maghemite to hematite transition as observed in the DSC curve. Hematite is antiferromagnetic or weakly ferromagnetic, which results in drop in magnetization [17]. The cooling and heating curve also displays thermal hysteresis above 300 °C. This occurs because of the first order transition in the sample. The isothermal magnetization curves as measured in virgin sample and sample heated to 800 °C and cooled in a magnetic field of 0.001 T, are shown in the Fig. 5b. The magnetization of the sample increased after it was heated to 800 °C. The coercive field of the sample also

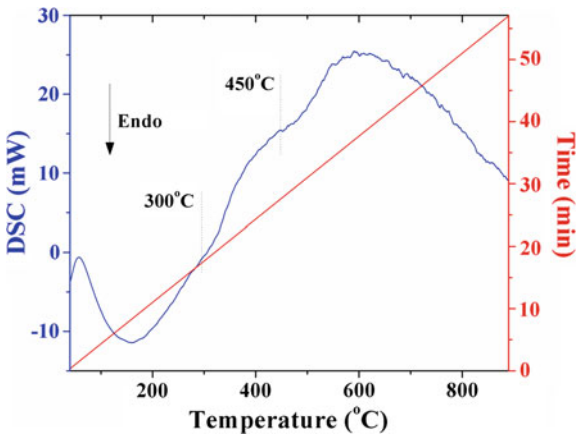

Fig. 4 DSC plot of magnetite ore powder heated from room temperature to 900 °C in nitrogen atmosphere

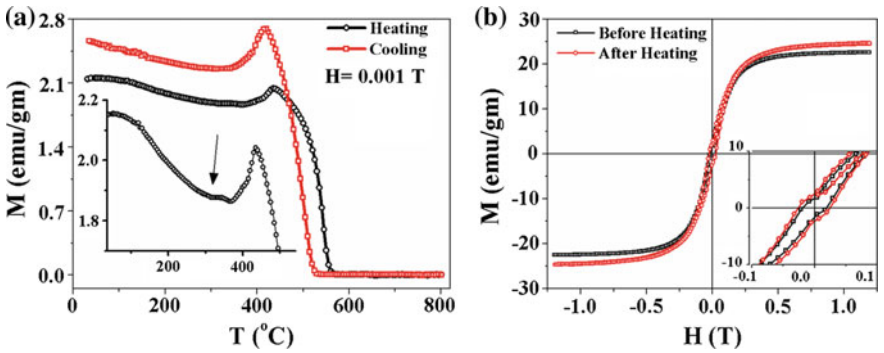

Fig. 5 **a** Magnetic measurement performed on the magnetite ore from room temperature till 800 °C in the magnetic field of 0.001 T during heating and cooling. In the inset, the magnified view of the heating curve. **b** Isothermal magnetization measurement performed at room temperature on the virgin sample (Black) and sample after heating to 800 °C

increased. The sample displayed symmetric double shifted loop. Such loop has previously been reported in the system with competing ferromagnetic/antiferromagnetic interaction, but mostly at low temperatures [18]. The appearance of such double shifted loop at room temperature indicates a strong competing interaction in the sample.

Conclusions

The ore was characterized by Rietveld refinement of powder XRD, magnetic transition at high temperature, thermal property analysis based on DSC data during heating, UV-vis and Raman spectra. The Rietveld refinement revealed that the principal phase present in the ore is cubic magnetite with Cr^{3+} and Mg^{2+} impurities, bearing a chemical formula $MgCr_{0.2}Fe_{1.8}O_4$. The cell parameters and the symmetry of the phase are $a = b = c = 0.8363283$ nm, $\alpha = \beta = \gamma = 90°$ and $Fd\text{-}3m$. Three distinct peaks were observed in the UV-vis spectra of the ore fines dispersed in MeCN solution. The lower region bands are due to metal-oxygen charge transitions and the higher band, due to d-d transition of iron. Raman spectral study at room temperature gave four characteristics bands of magnetite. The sample undergoes multiple magnetic transitions at high temperature which occur due to magnetite to maghemite and maghemite to hematite transitions at 300 and 450 °C, respectively.

References

1. Indian Bureau of Mines, Indian Iron Ore Resources and Exploitation, Iron & Steel Vision 2020, pp 13–35
2. Sinha M et al (2015) Mineralogy of iron ores of different alumina levels from Singhbhum Belt and their implication on sintering process. J Miner Mater Charact Eng 3:180–193
3. Kuila SK, Chatterjee R, Ghosh D (2016) Kinetics of hydrogen reduction of magnetite ore. Int J Hydrogen Energy 41:9256–9266
4. Biswas AK (1981) Principles of blast furnace ironmaking: theory and practice. Cootha Publishing House, Brisbane
5. Wang H, Sohn HY (2013) Hydrogen reduction kinetics of magnetite concentrate particles relevant to a novel flash ironmaking process. Metall Mater Trans B 44(1):133–145
6. Ishizaki K, Nagata K, Hayashi T (2007) Localized heating and reduction of magnetite ore with coal in composite pellets using microwave irradiation. ISIJ Int 47(6):817–822
7. Zhu DQ et al (2007) One-step direct reduction of damp milled magnetite concentrate pellets. Iron Steel 10:001
8. Samanta S, Mukherjee S, Dey R (2014) Oxidation behaviour and phase characterization of titaniferous magnetite ore of eastern India. Trans Nonferrous Met Soc China 24(9):2976–2985
9. Das D et al (1992) Mössbauer, XRD and positron annihilation studies on natural magnetite and hematite ore from Ari Dongri, Central India. Bull Mater Sci 15(2):161–170
10. Petrícek V, Dusek M, Palatinus L (2014) Crystallographic computing system JANA2006: general features. Zeitschriftfür Kristallogr Cryst Mater 229(5):345–352
11. Le Bail A, Duroy H, Fourquet JL (1988) Ab-initio structure determination of LiSbWO6 by X-ray powder diffraction. Mater Res Bull 23(3):447–452
12. Villars P, Cenzual K (2010) Pearson's crystal data: crystal structure database for inorganic compounds (on DVD), ASM International®, Materials Park, Ohio, USA Release, 2009/10
13. Kirichok PP, Antoshchuk AI (1977) Controlling the properties of magnesium ferrite by doping with Al^{3+}, Cr^{3+}, Sc^{3+}, In^{3+}. Izvestiya Akademii Nauk SSSR Neorganicheskie Materialy 13(7):1327–1330
14. Shebanova ON, Lazor P (2003) Raman spectroscopic study of magnetite ($FeFe_2O_4$): a new assignment for the vibrational spectrum. J Solid State Chem 174(2):424–430
15. Legodi MA, De Waal D (2007) The preparation of magnetite, goethite, hematite and maghemite of pigment quality from mill scale iron waste. Dyes Pigm 74(1):161–168
16. Lauer HV Jr et al (2001) Characterization of the thermal properties of magnetite using differential scanning calorimetry. In: Lunar and Planetary Science Conference, vol 32
17. Özdemir Ö, Dunlop DJ, Berquo TS (2008) Morin transition in hematite: size dependence and thermal hysteresis. Geochem Geophys Geosyst 9(10):1–12
18. Agarwal S, Banerjee S, Mukhopadhyay PK (2013) Crossover of spin glass characteristics as a function of field in an NiMnSnAl alloy. J Appl Phys 114(13), 133904

Humic Acid-Based Silica Composite Aerogels—A Preliminary Study

Guihong Han, Chaolei Lv, Yongsheng Zhang and Wei Wang

Abstract Silica aerogels are promising in many applications because of their excellent properties. However, the real applications of pure silica aerogels are limited because of their fragile network structure. We have prepared silica aerogel composites using humic acid as a composite material for improving the performance of silica aerogels and valorization of humic acid. The silica hydrogel composite was prepared using sodium silicate as a precursor and humic acid as a composite material by acid-base catalysis and sol-gel method. The hydrogel was followed by freeze-drying to obtain composite aerogel. The microstructures, specific surface area, and functional groups of silica and composite aerogel were characterized using scanning electron microscope (SEM), brunauer-emmett-teller (BET) and fourier transform infrared spectrometer (FTIR). The results demonstrated that the specific surface area of the silica composite aerogel was 307 m^2/g under the condition of pH at 6, the mass ratio of silicon to humic acid (HA) at 3.82 and the molar ratio of N, N-dimethylformamide (DMF) to silicon at 0.9. X-ray diffraction (XRD) showed that the silica (composite) aerogels were amorphous. Thermogravimetric analysis (TGA) revealed that the silica aerogels lost weight from 150 to 250 °C and humic acid decomposed between 350 and 500 °C, and then the mass of the sample remained stable.

Keywords Silica aerogel · Humic acid · Composite aerogels

G. Han · C. Lv · W. Wang
Henan Province Industrial Technology Research Institute of Resources and Materials, Zhengzhou University, 100 Science Avenue, Zhengzhou 450001, People's Republic of China
e-mail: guihong_han@126.com

G. Han · Y. Zhang (✉)
School of Chemical Engineering and Energy, Zhengzhou University, 100 Science Avenue, Zhengzhou 450001, People's Republic of China
e-mail: yzhang@zzu.edu.cn

B. Li et al. (eds.), *Characterization of Minerals, Metals, and Materials 2018*, The Minerals, Metals & Materials Series,
https://doi.org/10.1007/978-3-319-72484-3_33

Introduction

Aerogel is a kind of low-density solid materials, and most common aerogels are silica and carbon aerogels. Because the fragility of the porous network structure of aerogels, the aerogels may collapse under the pressure, losing its unique properties and limiting its applications. Silica aerogels are necessary to combine with other materials in the practical applications to prepare the network skeleton that supports the aerogels structure, obtaining the aerogel composites with practical significance [1].

There have been many reports on the silica aerogel composites. Fernández et al. [2] added TiO_2 to the silica aerogels to improve its biological activity, while the anti-fracture of the aerogels remained constant and the Young's modulus increased steadily against the strain. Martinez et al. [3] applied the nonwoven polyester fiber blankets as a composite material and tetraethyl orthosilicate (TEOS) as the precursor. The prepared composite aerogel exhibited good mechanical properties and low thermal conductivity (0.015–0.018 W/mK). Humic acid, an organic macromolecule, is widely distributed throughout the ecosystem. Humic acid contains carboxyl, phenollic hydroxyl, and alcoholic hydroxyl groups etc., while its methoxide content is low [4]. Humic acid molecules have a certain adsorption capacity. Humic acid can interact with many organic and inorganic matters [5]. However, humic acid has not been reported as a composite component of the silica aerogel.

Sodium silicate was selected as a cost-effective silicon precursor, and humic acid was taken as a composite material in this work. Silica and composite aerogels were prepared using sol-gel and freeze-drying method. The microstructures, specific surface area, and functional groups of silica and composite aerogel were characterized by SEM, BET, FTIR, XRD and TGA.

Experimental

1. Materials

Na_2SiO_3 (AR), Sinopharm Chemical Reagent Co. Ltd.; DMF (AR, 99.5%), NaOH (AR, 96%), Tianjin Kermel Chemical Reagent Co. Ltd.; sulfuric acid (AR, 95 $\sim$ 98%), Luoyang Haohua Chemical Reagent Co. Ltd.; HA (fulvic acid, FA $\geq$ 90%), Shanghai Aladdin Bio-Chem Technology Co., Ltd were all used as received.

2. Preparation of silica and composite aerogels

2 g of sodium silicate and 30 mL of distilled water were mixed to form a sodium silicate solution. DMF was used as the dry control chemical additive (DCCA) [6, 7]. Then sulfuric acid (2 mol/L) was added to the sodium silicate solution until the pH reached 1–2. The mixtures were hydrolyzed for 10 min when a certain amount

of humic acid was added into the solution. Then sodium hydroxide solution (1 mol/L) was added dropwise to the solution until the pH reached 5.5, 6.0, 6.5 and 7.0 respectively. The above steps were operated under magnetic stirring, forming the hydrogel. The hydrogel was washed three times per day using distilled water before it was freeze-dried to obtain the aerogel powder.

3. **Characterization of the samples**

The infrared spectra of the samples were measured at 4 cm^{-1} resolution in the range of 4000–400 cm^{-1} on a PerkinElmer Spectrum Two FTIR spectrometer in this paper. The microstructure and particle distribution of the samples were observed by Zeiss/Auriga FIB SEM. The thermal stability was measured by a Q50 thermogravimetric analyzer under a constant N_2 flow 100 mL/min with a temperature rate of 10 °C/min. Nitrogen adsorption-desorption isotherms were measured on a multi-station extended automatic surface and porosity analyzer (ASAP2460, USA) after the samples were degassed in vacuum at 150 °C for at least 12 h. The X-ray diffraction patterns of the samples were recorded on a Bruker Diffractometer (D8 Advance), using Cu-Kα radiation (40 kV, 30 mA). The samples were scanned from 5° to 70°, with a step speed of 0.02°/s.

Results and Discussions

Figure 1 shows how the gel time varies along with the pH values. In general, the gel time decreases while pH value increases. When pH is 5.5, the gel time is almost 29 min, which is too long for the preparation. When pH is 7.0, the solution gelled without time slot, which does not allow enough time for framework formation. As such, the gel pH at 6 is taken in the following study.

The curve (a) in Fig. 2 shows the infrared spectrum of the silica aerogel without humic acid. The peaks near 1043, 794, 475 cm^{-1} are attributed to Si–O–Si anti-symmetric stretching vibration, symmetrical stretching vibration and bending vibration, respectively. The curves (b, c and d) are the infrared spectrum of the silica

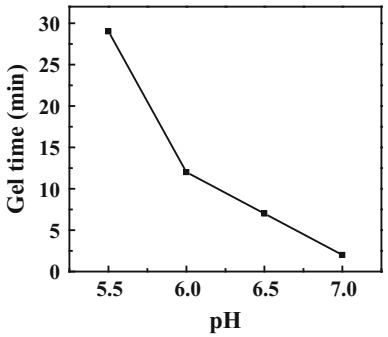

Fig. 1 Effect of pH on gel time

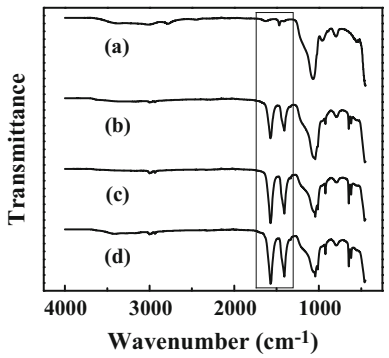

Fig. 2 FTIR of different humic acid content **a** 0 g; **b** 0.06 g; **c** 0.12 g; **d** 0.16 g

composite aerogel obtained by the combination of humic acid. The peak near 1408 cm^{-1} corresponds to the vibration peak of the hydroxyl groups from humic acid and the peak near 1575 cm^{-1} is the aromatic ring C=C skeleton vibration of humic acid. Si–O–Si anti-symmetrical stretching vibration, symmetrical stretching vibration and bending vibration peaks are showed at 1043, 794, and 475 cm^{-1}. The hydroxyl groups and aromatic ring C=C skeleton vibration of humic acid are observed from curves (b, c, d) except curve (a), indicating that humic acid has been combined with silica aerogel. The intensities of the peaks near 1408 and 1575 cm^{-1} increase with humic acid content from 0.06 to 0.16 g (curves (b), (c), (d)). Since curves (c) and (d) demonstrate the same intensity at 1408 and 1575 cm^{-1}, 0.12 g of humic acid is sufficient for the above mentioned preparation, i.e. w(Si)/w(HA) = 3.82.

Figure 3 demonstrates the gel time of sodium silicate solution and the specific surface area of silica composite aerogel. Five ratios of n(DMF):n(Si) were investigated from 0.3, 0.45, 0.9 to 1.2, corresponding to 0.19, 0.28, 0.56 and 0.75 mL DMF. The dry control chemical additive, DMF, prolonged the gel time from 1 to 13 min. The specific surface area increased along with the DMF content and reached the maximum of 307 m^2/g at n(DMF)/n(Si) of 0.9. The specific surface area was slightly smaller than the specific surface area of the aerogel prepared by Cai et al. [8] which was 474 m^2/g. Therefore, the n(DMF):n(Si) at 0.9 was taken in the following study.

Figure 4a shows the SEM images of silica aerogel with n(H_2O)/n(Si) at 100. It can be observed that the aerogel particles are homogeneous and isotropic, because the cross-linking and irregular growth of Si–O–Si chains formed the crisscrossing skeleton network and the micro-pores between the skeletal network structures. Figure 4b shows the SEM graphs of silica composite aerogel at n(H_2O)/n(Si) = 100, w(Si)/w(HA) = 3.82. Because of the combined humic acid, the surface of composite aerogels Composite aerogels presents finer pore size. The surface contains a lot of pores and it is expected that composite aerogel has higher specific surface area than its counterpart silica aerogel, which will be studied in the future work.

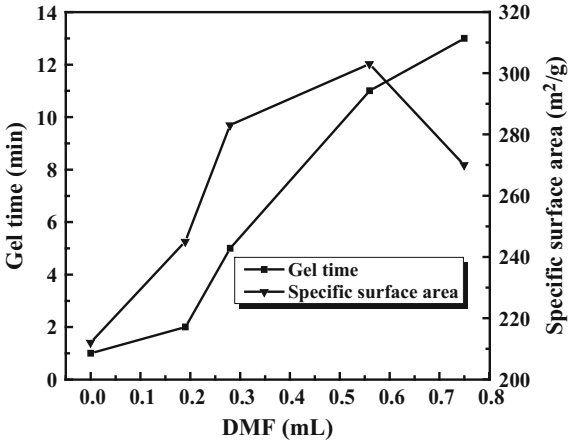

Fig. 3 Effect of DMF on gel time and specific surface area of silica composite aerogel (pH = 6, *w*(Si)/*w*(HA) = 3.82)

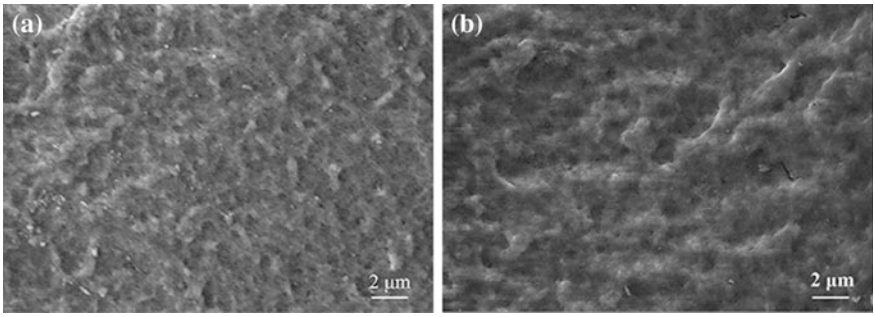

Fig. 4 SEM images of silica aerogel (**a**) and silica composite aerogel (**b**) (*w*(Si)/*w*(HA) = 3.82) (pH = 6, n(DMF):n(Si) = 0.9)

Figure 5 shows the XRD patterns of silica aerogel and silica composite aerogel. Neither silica aerogel nor the composite silica aerogel shows obvious crystallization peak, except the dispersion peak near 22°. This indicates that the prepared aerogels are amorphous.

A very significant, substantial loss of about 15% was observed between 150 and 250 °C (Fig. 6a). Because the aerogel surface has a large amount of hydroxyl groups, a large number of hydroxyl groups bonded to each other and lost H_2O. The weight remained stable after 250 °C. Curve (b) shows 7% mass loss between 150 and 250 °C for the same reason as curve (a). There was another substantial loss of mass, about 23%, between 350 and 500 °C, because of the decomposition of the humic acid. Therefore, residual weight fraction of curve (b) was lower than that of (a), because of the decomposition of humic acid at high temperatures.

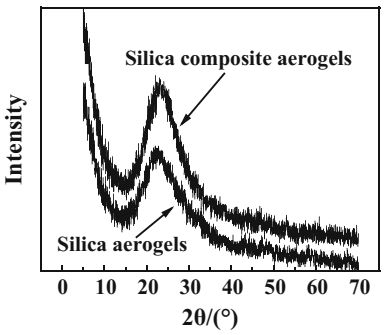

Fig. 5 Comparison of XRD of silica aerogel and silica composite aerogel

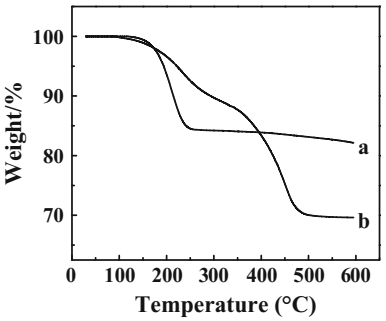

Fig. 6 Thermal stability of silica aerogel (**a**) and silica composite aerogel (**b**) *w*(Si)/*w* (HA) = 3.82

Conclusions

The silica composite aerogel was designed and prepared for the cost-effectiveness, enhanced mechanical properties and valorization of humic acid in this paper. With the sol-gel process and freeze-drying, silica aerogel was directly combined with humic acid. The reaction conditions, microstructures, specific surface area, crystal form and functional groups of silica and composite aerogels Composite aerogels were characterized by SEM, BET, FTIR, XRD and TGA. The main conclusions are as follows: The pH value was optimized to be 6–6.5 according to the gel time of sodium silicate solution. The specific surface area of the sample changed along with the content of DMF and HA and reached the maximum of 307 m^2/g at n(DMF)/n(Si) = 0.9, pH = 6, *w*(Si):*w*(HA) = 3.82 in this work. The silica (composite) aerogels were amorphous. The silica aerogels lost weight from 150 to 250 °C and humic acid decomposed between 350 and 500 °C, and then the weight was unchanged.

References

1. Leventis N et al (2002) Nanoengineering strong silica aerogels. Nano letters 2(9):957–960
2. Fernández JAT et al (2008). Improvement of the bioactivity of organic–inorganic hybrid aerogels/wollastonite composites with TiO_2. J Sol-Gel Sci Technol 45(3):261–267
3. Martinez RG et al (2016) Thermal assessment of ambient pressure dried silica aerogel composite boards at laboratory and field scale. Energy and Buildings 128:111–118
4. Li L et al (2009) Flexible nanofiber-reinforced aerogel (xerogel) synthesis, manufacture, and characterization. ACS Appl Mater Interfaces 1(11):2491–2501
5. Schnitzer M (1978) Humic substances: chemistry and reactions. Dev Soil Sci 8:1–64
6. Lenza RFS et al (2015) Preparation of sol-gel silica samples modified with drying control chemical additives. J Non-Cryst Solids 423:35–40
7. He S et al (2015) Synthesis and characterization of silica aerogels dried under ambient pressure bed on water glass. J Non-Cryst Solids 410:58–64
8. Cai J et al (2012) Cellulose–silica nanocomposite aerogels by in situ formation of silica in cellulose gel. Angewandte Chemie 124(9):2118–2121

Characterization of Non-Covalently Functionalized Halloysite

Danae Lopes Francisco, Lucilene Betega de Paiva, Wagner Aldeia, Ademar B. Lugão and Esperidiana A. B. Moura

Abstract The inorganic nanotube halloysite (HNT) is a promising type of natural occurring filler for polymers. Its characteristics, such as high aspect ratio (10–50), small size, and high strength (elastic modulus—140 GPa) suggest that HNTs have a potential use in high-performance polymer nanocomposites. Compared to other nanoclays and nanosilica the relatively low content of hydroxyl groups on their surfaces makes HNTs relatively hydrophobic, although, sometimes, this is not sufficient for guaranty a good interfacial adhesion in composite systems. Further hydrophobic treatment is required to improve HNTs compatibility with polymer matrixes, maximizing interfacial interactions. In the present study, different percentages of EPB (2,2-(1,2-ethene diyldi-4,1-phenylene) bisbenzoxazole) was used to perform a non-covalent functionalization of halloysite, based on electron transfer interactions. The functionalization is characterized by specific surface area (BET), thermogravimetric analysis (TG) and water/toluene extraction experiment.

Keywords Halloysite · EPB · BET · TG

Introduction

Extensive research about halloysite (HNT) began in the 1940s and has regained attention in recent years. HNT is a natural multiple-walled inorganic nanotube (1D), with a geometry similar to that of carbon nanotubes (CNTs). Its chemical formula is

D. L. Francisco (✉) · L. B. de Paiva · W. Aldeia
IPT, Group for Bionanomanufacturing, Laboratory of Chemical Process and Particle Technology, Institute for Technological Research of State of São Paulo, São Paulo, Brazil
e-mail: danae_lopes@hotmail.com

D. L. Francisco · A. B. Lugão · E. A. B. Moura
Center for Chemical and Environmental Technology (CQMA), Nuclear and Energy Research Institute, São Paulo, SP, Brazil

B. Li et al. (eds.), *Characterization of Minerals, Metals, and Materials 2018*, The Minerals, Metals & Materials Series,
https://doi.org/10.1007/978-3-319-72484-3_34

similar to that of kaolinite, represented by $Al_2Si_2O_5(OH)_4{\cdot}nH_2O$, where n can vary from 0 to 2, representing dehydrated and hydrated halloysite, respectively [1–3].

The halloysite nanotubes (HNTs) vary from size depending on the crystallization conditions and on their geological origin. Some of their main characteristics, such as tubular microstructure, reduced size, high aspect ratio (10–50), high mechanical strength (elastic modulus—140 GPa) have raised interest for its application in polymers, resulting in high-performance polymer nanocomposites [4–10].

Most of the aluminols (Al-OH) groups are located in the inner part of the halloysite, while on the outer surface the siloxane group (Si–O–Si) is present with a few silanols/aluminols on the edges of the sheets. The relatively small amount of hydroxyl groups (O–H) on halloysite surface makes it relatively hydrophobic when compared to other nanoclays and nanosilica. Sometimes, the halloysite natural hydrophobicity is not sufficient for interfacial adhesion in the composites, so it is necessary to proceed with HNTs hydrophobic treatment, prior to its incorporation into polymers, maximizing the interfacial interactions [1, 2].

Halloysite functionalization can be divided into two main groups: covalent functionalization and non-covalent functionalization [1]. In the present study, a non-covalent functionalization based on electron transfer interactions using EPB (2,2-(1,2-ethene diyldi-4,1-phenylene) bisbenzoxazole) as functionalizer is evaluated.

Experimental

Materials

Halloysite nanotubes; CAS number 1332-58-7, chemical formula $Al_2Si_2O_5(OH)_4{\cdot}2H_2O$, molecular weight of 294.19 g/mol, true specific gravity of 2.53 g/ml, diameter between 30 and 70 nm, and length between 1 and 3 μm, purchased from Sigma Aldrich.

The non-covalent functionalizer 2,2′-(1,2-ethene diyldi-4,1-phenylene) bisbenzoxazole (EPB); CAS number 1533-45-5, empirical formula $C_{28}H_{18}N_2O_2$, molecular weight of 414.45 g/mol and melting point higher than 300 °C, purchased from Sigma Aldrich.

Functionalization of HNTs

Different percentages of EPB were used to functionalize halloysite, as shown in Table 1, by blending both mechanically. The HNTs were previously dehumidified at a temperature of 80 °C for 24 h.

Table 1 Composition of studied samples

Samples	Halloysite (wt%)	EPB (wt%)
100H	100	0
99,75HE	99.75	0.25
95HE	95	5
90HE	90	10

Characterization

Water/Toluene Extraction Experiment

The extraction experiment was used to verify the hydrophobicity of pristine halloysite and of functionalized halloysite. In separated glass tubes were added about 0.2 g of each composition of the studied samples. First it was added 10 mL of toluene followed by bath sonication for 10 min, further 10 mL of deionized water was added and followed for more 10 min of bath sonication. Observation on retention of the samples was made after rest.

Thermogravimetric Analysis (TG)

Thermogravimetric analysis was carried out on a Mettler Toledo TGA/DSC1 from 25 to 1000 °C, at a heating rate of 10 °C/min, under N_2 flow. Two TG assays were performed for each sample, with a mass about 15 mg.

BET Method

The specific surface area of the samples was determined by Brunauer, Emmett and Taller (BET) isotherms with a Micromeritics Gemini V. The samples were previously dehumidified under vacuum at a temperature of 60 °C.

Results and Discussion

Water/Toluene Extraction Experiment

The hydrophilicity tests using toluene and water (Fig. 1) shows that HNTs do not undergo swelling in water and have a more hydrophilic character since it stays in the water phase. The functionalized HNTs increased their affinity with toluene and

presented a shift to the toluene phase, indicating that there is an interaction between EPB and HNTs.

Thermogravimetric Analysis (TG)

Table 2 shows the results of the thermogravimetric analysis. The mass loss in the range of temperature between 25 and 100 °C is related to the release of physically adsorbed water. The pristine HNT (100H) shows the highest mass loss. Samples functionalized with EPB showed a lower mass loss in this region, indicating that functionalization is responsible for changing HNT characteristic, lowering its affinity for free water adsorption. In the second range of temperature (100–250 °C) occurs HNT interlamellar water loss. Functionalized HNTs also present a lower mass loss than pristine nanotubes in this region, which may be attributed to the presence of the functionalizer in its structure. In the range of temperature between 250 and 650 °C, functionalized samples present a greater mass loss than the pristine halloysite, indicating the degradation of the functionalizer EPB. Similar tendencies were observed by Pontón et al. [11] for functionalized titanate nanotubes.

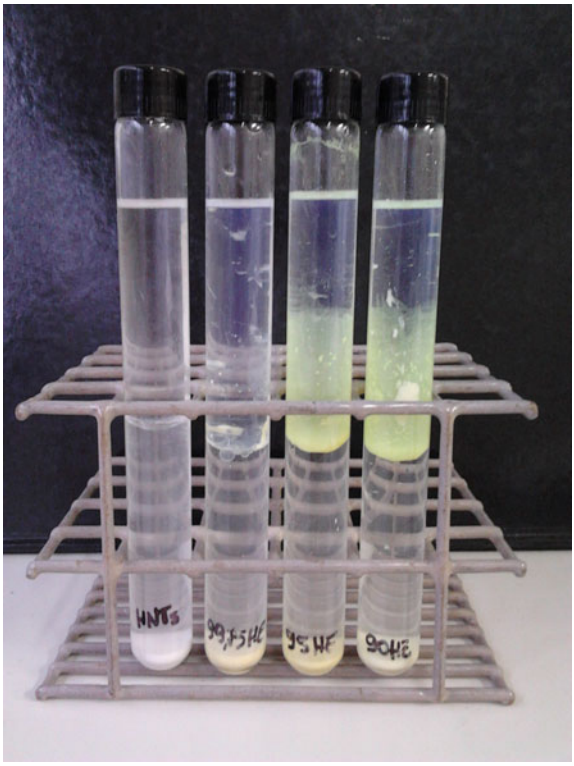

Fig. 1 Water/toluene hydrophilicity test of samples 100H (HNTs), 99,75HE, 95HE and 90HE

Table 2 Results of thermogravimetric analysis of pristine HNT and of functionalized HNTs with different percentages of EPB (99,75HE, 95HE, 90HE)

Sample	25–100 (°C) wt (%)	100–250 (°C) wt (%)	250–650 (°C) wt (%)
100H	2.09 ± 0.34	3.62 ± 0.55	16.27 ± 0.50
99,75HE	1.96 ± 0.01	3.08 ± 0.01	16.44 ± 0.36
95HE	1.52 ± 0.49	2.42 ± 0.60	19.61 ± 0.13
90HE	1.76 ± 0.76	2.84 ± 1.21	24.08 ± 0.55

Brunauer-Emmett-Teller (BET) Surface Area Analysis

The results obtained by BET method (Fig. 2; Table 3) shows that the surface area tends to decrease with the increase of EPB percentage in HNT, other authors also observed the same effect for functionalized halloysite [12, 13].

Table 3 shows that the C constant tends to decrease for samples with a higher amount of EPB showing that there is an effective interaction between halloysite surface and EPB. The higher change is observed for the sample 90HE, prepared

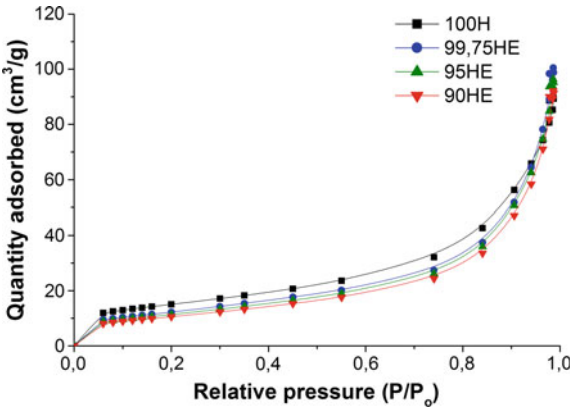

Fig. 2 BET curves of pristine HNT (100H) and of functionalized HNTs with different percentages of EPB (99,75HE, 95HE, 90HE)

Table 3 BET surface area and C constant for pristine HNT (100H) and functionalized HNT with different percentages of EPB (99,75HE, 95HE and 90HE)

Sample	BET surface area (m^2/g)	BET C value
100H	53.72	154.94
99,75 HE	44.03	107.09
95HE	41.04	101.37
90HE	38.18	95.37

with the higher amount of EBP (10 wt%). The C constant is related to the interaction of the adsorbed nitrogen molecules and the halloysite surface. The higher the C value, the higher the interaction energy between the nitrogen and Al-OH and Si–OH groups in HNT surface [12].

Conclusion

The electron-deficiency of HNT due to its metal atoms, such as aluminum, and ferrous, allows HNTs to accept foreign electron on their empty orbital, so when HNTs are blended with electron-rich species, electron transferring to HNTs can occur. In the present study the organic EPB, with a conjugated structure, is the electron-rich species and increasing the amount of this functionalizer in HNT the interaction between them became more evident and an effective electron transferring may be occurred. The hydrophilic character of HNT change to a more hydrophobic one, shifting the functionalized HNTs to toluene phase, as observed in the water/toluene extraction experiment. The mass loss related to the release of physically adsorbed water became smaller with the functionalization, indicating a lowering affinity for water in functionalized HNTs. The BET surface area was reduced with the functionalization.

References

1. Liu M, Jia Z, Jia D, Zhou C (2014) Recent advance in research on halloysite nanotubes-polymer nanocomposite. Prog Polym Sci 39:1498–1525
2. Du M, Guo B, Jia D (2010) Newly emerging applications of halloysite nanotubes: a review. Polym Int 59:574–582
3. Yi Z, Aidong T, Huaming Y, Ouyang J (2016) Applications and interfaces of halloysite nanocomposites. Appl Clay Sci 119:8–17
4. Hedicke-Höchstotter K, Lim GT, Altstädt V (2009) Novel polyamide nanocomposites based on silicate nanotubes of the mineral halloysite. Compos Sci Technol 69:330–334
5. Erdogan AR, Kaygusuz I, Kaynak C (2014) Influences of aminosilanization of halloysite nanotubes on the mechanical properties of polyamide-6 nanocomposites. Polym Compos 35:1350–1361
6. Guo B, Zou Q, Lei Y, Du M, Liu M, Jia D (2009) Crystallization behavior of polyamide 6/halloysite nanotubes nanocomposites. Thermochim Acta 484:48–56
7. Guo B, Zou Q, Lei Y, Jia D (2009) Structure and performance of polyamide 6/halloysite nanotubes nanocomposite. Polym J 41:835–842
8. Handge UA, Höchstötter KH, Altstädt V (2010) Composites of polyamide 6 and silicate nanotubes of the mineral halloysite: Influence of molecular weight on thermal, mechanical and rheological properties. Polymer 51:2690–2699
9. Prashantha K, Lacrampe M-F, Krawczak P (2013) Highly dispersed polyamide-11/halloysite nanocomposites: thermal, rheological, optical, dielectric, and mechanical properties. J Appl Polym Sci 130:313–321

10. Lecouvet B, Gutierrez J, Sclavons M, Bailly C (2011) Structure-property relationship in polyamide 12/halloysite nanotube composites. Polym Degrad Stab 96:226–235
11. Pontón PI, d'Almeida JRM, Marinkovic BA, Savíc SM, Mancic L, Rey NA, Morgado E Jr, Rizzo FC (2014) The effects of the chemical composition of titanate nanotubes and solvent type on 3-aminopropyltriethoxysilane grafting efficiency. Appl Surf Sci 301:315–322
12. Peixoto AF, Fernandes AC, Pereira C, Pires J, Freire C (2016) Physicochemical characterization of organosilylated halloysite clay nanotubes. Microporous Mesoporous Mater 219:145–154
13. Liu M, Guo B, Mingliang DDJ (2008) The Role of Interactions between Halloysite Nanotubesand 2,2′-(1,2-Ethenediyldi-4,1-phenylene) Bisbenzoxazole in Halloysite Reinforced Polypropylene Composites. Polym J 40:1087–1093

Synchrotron-Based XRD and XANES Study of Bornite Leached by Mesophilic Mixed Bacteria

Xingxing Wang, Maoxing Hong, Rui Liao, Chunxiao Zhao, Shichao Yu, Jun Wang, Hongbo Zhao and Min Gan

Abstract In this study, bioleaching experiments, synchrotron X-ray Diffraction (SR-XRD), X-ray absorption near edge structure (XANES) and X-ray Photoelectron Spectroscopy (XPS) were conducted to investigate the intermediates and surface species of bornite leached by mesophilic mixed bacteria of *Leptospirillum ferriphilum*, *Acidithiobacillus caldus* and *Sulfobacillus thermosulfidooxidans*. CuS, $Cu_9Fe_9S_{16}$ and S_8 were the main intermediate species during bornite bioleaching by mesophilic mixed bacteria, and $CuFeS_2$ was also detected. The surface species of S^{2-} and S_2^{2-} would be polymerized to S_n^{2-} during bioleaching. The formation of element sulfur and the increase of its content were confirmed by the fitted results of XPS spectra. The presence of polysulfide and element sulfur did not inhibit the bornite bioleaching. The formations of CuS and $CuFeS_2$ were confirmed by the results of Cu *K*-edge XANES spectra.

X. Wang (✉) · M. Hong · R. Liao · C. Zhao · S. Yu · J. Wang · H. Zhao · M. Gan
School of Minerals Processing & Bioengineering, Central South University, Changsha, Hunan, People's Republic of China
e-mail: wangxingxing@csu.edu.cn

M. Hong
e-mail: 619980916@qq.com

R. Liao
e-mail: 442435954@qq.com

C. Zhao
e-mail: 1729462165@qq.com

S. Yu
e-mail: yushichao@csu.edu.cn

J. Wang
e-mail: wjwq2000@126.com

H. Zhao
e-mail: alexandercsu@126.com

M. Gan
e-mail: ganmin0803@sina.com

B. Li et al. (eds.), *Characterization of Minerals, Metals, and Materials 2018*, The Minerals, Metals & Materials Series,
https://doi.org/10.1007/978-3-319-72484-3_35

Keywords Bornite · Bioleaching · Mesophilic mixed bacteria
Chemical speciation · Synchrotron · XRD · XANES · XPS

Introduction

Bornite is an important source of copper [1, 2], following chalcopyrite and chalcocite in economic importance [3], so the development of bornite processing can bring huge economic benefits. Bioleaching is a simple, lower cost and eco-friendly technology, which has been widely used in leaching low grade copper and complex ores [4, 5]. The dissolution mechanism during bornite leaching is still ambiguous. Some researchers have investigated the dissolution process during bornite leaching with different conditions [6–8]. Dutrizac found that the dissolution of synthetic bornite in acidified ferric sulfate solution in the temperature range 40–90 °C obeys a linear rate law. Nature and synthetic bornite dissolve by the same process and at essentially the same rate. Nonstoichiometric bornite ($Cu_{5-x}FeS_4$), chalcopyrite ($CuFeS_2$) and covellite (CuS) were formed during the leaching of bornite in either ferric chloride or ferric sulfate media, and then nonstoichiometric bornite converted to Cu_3FeS_4. Pesic also found the formation of covellite and chalcopyrite during the dissolution of bornite in sulfuric acid using oxygen as oxidant, but without the X-ray data of Cu_3FeS_4. Buckley et al. [9] investigated the anodic oxidation of bornite and found that an iron-free copper sulfide of Cu_5S_4 was formed.

The report about bornite bioleaching was relatively few, particularly in respect of intermediates evolutions during bornite bioleaching by bacteria. Zhao et al. [10] investigated the electrochemical dissolution of bornite in acid culture medium and found that covellite was the main intermediate specie during the bornite bioleaching. Covellite was detected as a secondary phase during bornite bioleaching by *A. ferrooxidans* with or without ferrous iron. Sulfur and jarosite were also found in the process [11]. For the ambiguous dissolution process of bornite bioleaching, this study aims to investigate the intermediates transformation during bornite bioleaching by mesophilic mixed bacteria of *L. ferriphilum*, *A. caldus* and *S. thermosulfidooxidans*.

Materials and Methods

Minerals

Bornite samples were obtained from Meizhou, Guangdong Province, China. Chemical analysis showed that the bornite sample contained (w/w) 61.81% Cu, 9.70% Fe, 21.18% S. Synchrotron-XRD result indicated that bornite used in the study were of high purity.

Microorganisms and Bioleaching Experiments

Domesticated cultivation of mixed bacteria of *L. ferriphilum*, *A. caldus* and *L. ferriphilum*, *A. caldus* and *S. thermosulfidooxidans* was conducted in an aeration beaker include 40 g mineral and 2 L 9 K basic salt medium, which did not include $FeSO_4 \cdot 7H_2O$ and S. Planktonic cells were collected from bacteria solution in logarithmic phase by centrifugation, then the collected bacteria used for bioleaching experiments. Bioleaching were conducted in 250 mL flasks containing 100 mL sterilized basal medium. 2 mL bacteria cultures and 2 g minerals were added in each flask, then which incubated at 45 °C and 170 rpm on a rotary shaker. The initial cell concentration was higher than 1.0×10^7 cells/mL. The pH was adjusted daily to 1.70 ± 0.03 with sulfuric acid. Evaporation losses was compensated periodically by adding distilled water. During the bioleaching process, the variation of pH values, redox potentials, and the concentration of ferric, ferrous and copper were measured.

Analysis Methods

The mineralogical components of bornite samples and leaching residues were analyzed by synchrotron-XRD at beamline BL14B1 of the Shanghai Synchrotron Radiation Facility (SSRF) with a wavelength of 0.6887 Å. All XPS spectra were calibrated by C 1 s peak at 284.8 eV. XPS PEAK 4.1 software was used for fitted the XPS peaks. Sulfur *2p* peaks occur as doublets (S $2p_{3/2}$ and S $2p_{1/2}$) because of spin orbit splitting. Only the S $2p_{3/2}$ peaks are displayed in the figures for clarity. The Cu and Fe *K*-edge XANES data were conducted in transmission mode at beamline 1W1B of Beijing Synchrotron Radiation Facility (BSRF), Beijing, China. The near edge part of the Cu or Fe *K*-edge X-ray absorption spectra was collected with a step of 1 eV and dwell time of 1 s in appropriate energy range.

Results and Discussion

Figure 1 shows the variations of solution ORP and copper extractions during bioleaching of bornite. It indicated that the solution ORP increased slowly in the first two days, and then successively increased from 303.6 to 405.9 mV. The variation of copper extractions presented a similar pattern. The copper extractions increased rapidly in the last two days.

SR-XRD analysis (Fig. 2) indicates that before copper extractions reached 11.25%, the bornite was the main species of leached residue. The results showed that only small amount bornite dissolved in the first two days, and the crystal structure of bornite has not changed. The results were consistent with the lower

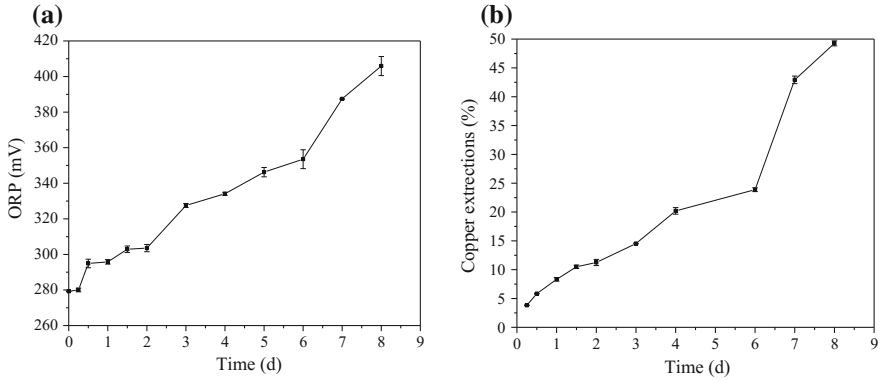

Fig. 1 Variations of solution ORP (**a**) and copper extractions (**b**) during bioleaching

copper extractions in the first two days as showed in Fig. 1(b). Small amount of covellite (CuS, PDF#78-0877) and element sulfur (S_8, PDF#85-0799) was formed in earlier bioleaching process. A peak represented geerite (Cu_8S_5, PDF#33-0491) was detected. When the copper extractions reached 11.25%, the higher intensity peak of Cu_8S_5 appeared with the disappearance of two bornite peak (2θ = 12.484 and 20.468). The peaks of bornite and Cu_8S_5 all disappeared at the copper extractions of 14.54%, while CuS became the main specie. The change of the peak indicated that Cu_8S_5 may convert to CuS. The cooper extractions increased significantly from day 6 to day 7, meanwhile, the SR-XRD pattern has changed significantly. Large amount of element sulfur and mooihoekite ($Cu_9Fe_9S_{16}$, PDF#27-0164) formed and two CuS peak (2θ = 12.704 and 20.833) disappeared. When the copper extractions reached 44.84%, a peak (2θ = 13.117) represented chalcopyrite ($CuFeS_2$, PDF#33-0491) and a peak (2θ = 12.948) represented isocubanite ($CuFe_2S_3$, PDF#81-1738) were detected (Fig. 3).

The results of copper extractions and SR-XRD analysis indicated that the dissolution of bornite bioleaching in this study occurs in three stages. Firstly, only small amount bornite dissolved in the first two days and small amount CuS and S_8 were formed. Secondary, crystal structure of bornite changed significantly. With the dissolution of bornite, a large amount of CuS was formed. Thirdly, with the dissolution of CuS a large amount of $Cu_9Fe_9S_{16}$ was formed (Fig. 4).

The fitted results of XPS spectra suggested that the amount of S^{2-} species of bornite bulk decreased with time. The amount of S_2^{2-} species also decreased during bioleaching. The variation of the amount of S^{2-} and S_2^{2-} is consistent with the dissolution of bornite. The amount of S_n^{2-}/S^0 species increased with time from 28.15 to 49.96%, which were consistent with the results of SR-XRD. These changes confirm that S^{2-} and S_2^{2-} were polymerized to S_n^{2-} [12]. In combination with the results of copper extractions, indicated that the presence of polysulfide did not inhibit the bornite bioleaching. The amount of sulfate increased from 1.59 to

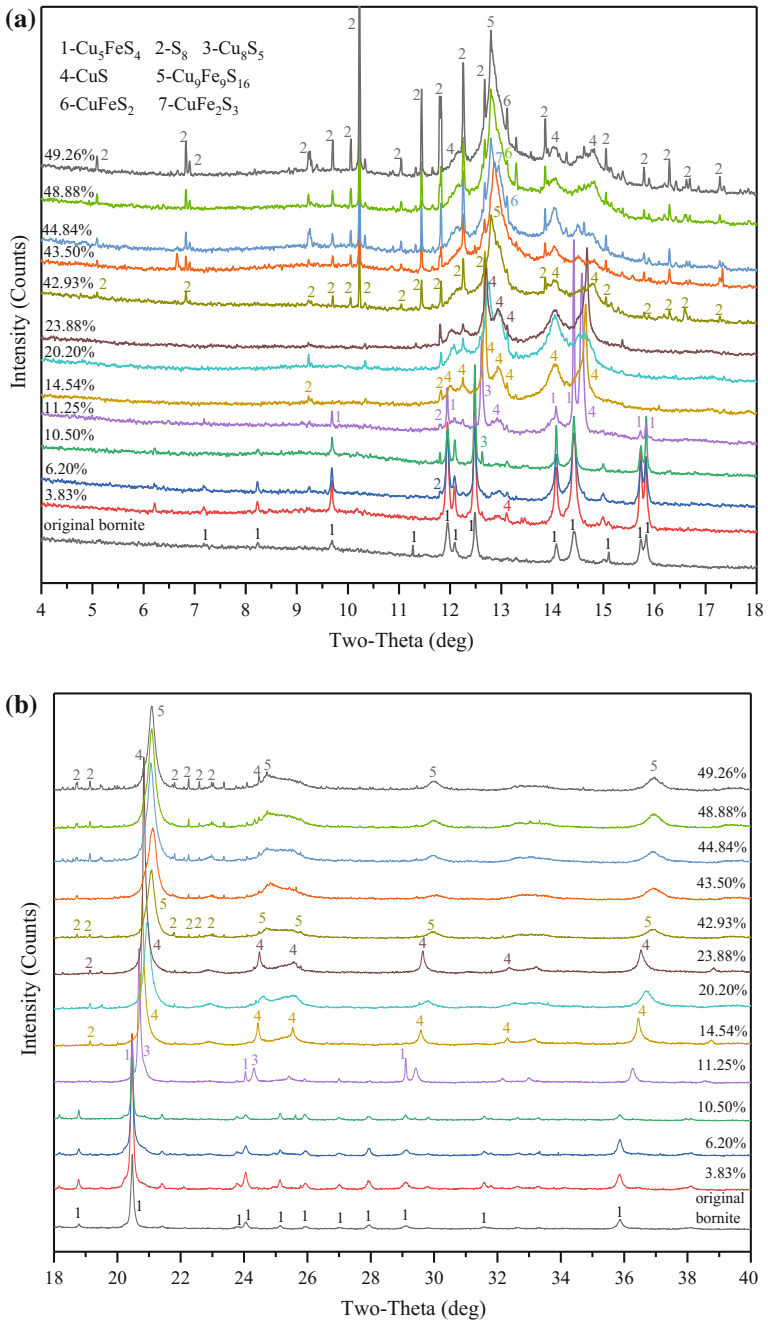

Fig. 2 SR-XRD analysis of bioleaching residue: **a** Two-Theta = 4°–18°, **b** Two-Theta = 18°–40°

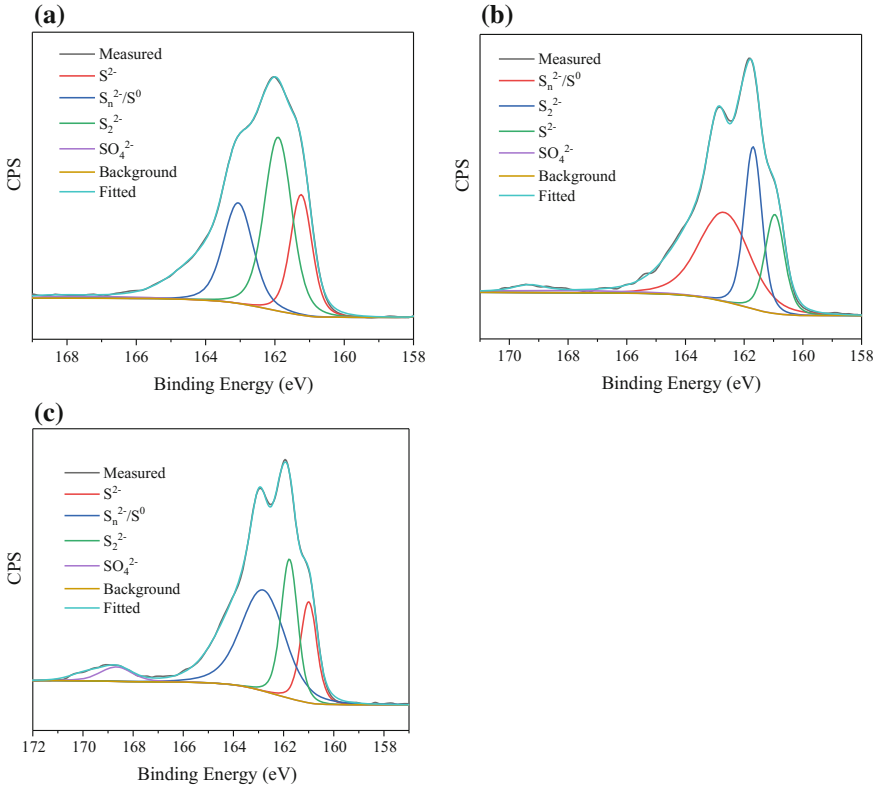

Fig. 3 S $2p_{3/2}$ XPS spectra of bioleaching residue: **a** copper extractions = 8.71%, **b** copper extractions = 14.37%, **c** copper extractions = 42.79%

5.20% during bioleaching, which may represent an increase of the amount of jarosite (Tables 1, 2).

The fitting results of Cu *K*-edge XANES spectra showed the presence of covellite and chalcopyrite, which indicated that bornite would convert to covellite and chalcopyrite during bioleaching. In the earlier period of bioleaching, covellite was the main intermediate species. With the bioleaching of bornite, the amount of covellite and chalcopyrite increased obviously. The Fe *K*-edge XANES spectra of sample with 49.26% copper extractions showed a very great difference with the other two samples, which indicated that the intermediate species had undergone massive changes. The appearance of the peak at 7130 eV represented the formation of jarosite.

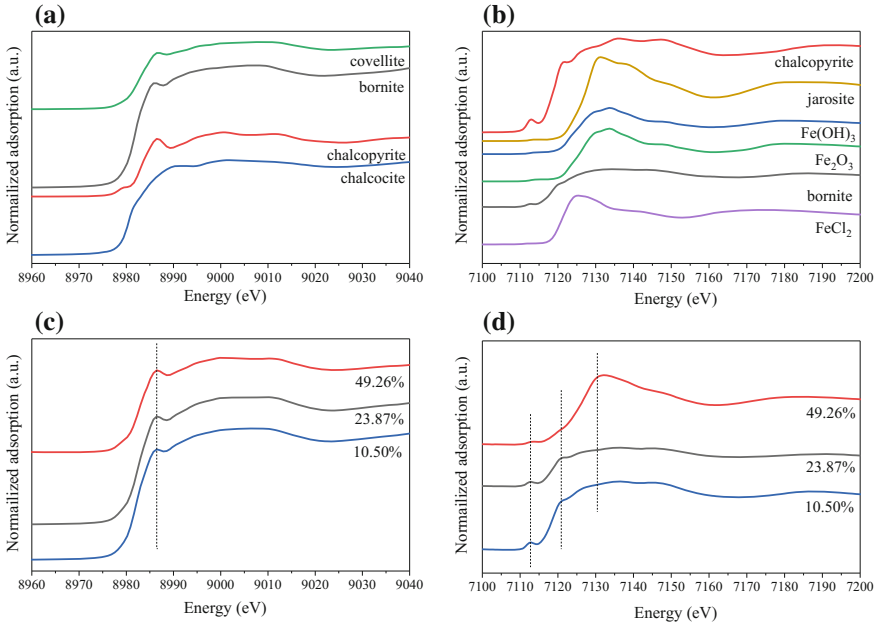

Fig. 4 Cu *K*-edge XANES spectra (**a**, **c**) and Fe *K*-edge XANES spectra (**b**, **d**) of reference samples (**a**, **b**) and bioleaching residue (**c**, **d**)

Table 1 Proportion of different surface sulfur contents in bioleaching residue (%)

Samples (with different copper extractions)	S^{2-}	S_2^{2-}	S_n^{2-}/S^0	SO_4^{2-}
8.71%	24.87	45.39	28.15	1.59
14.37%	20.18	29.49	46.74	3.59
42.79%	18.63	26.20	49.96	5.20

Table 2 Fitted results of Cu *K*-edge XANES spectra of bioleaching residue (%)

Samples (with different copper extractions)	Bornite	Chalcopyrite	Covellite
10.50%	53.5	–	46.5
23.87%	29.8	13.0	57.2
49.26%	23.2	25.5	51.4

Conclusion

The intermediates and surface species of bornite leached by mesophilic mixed bacteria of *L. ferriphilum*, *A. caldus* and *S. thermosulfidooxidans* was investigated by bioleaching experiments, SR-XRD, Cu *K*-edge and Fe *K*-edge XANES and XPS. The SR-XRD results showed that CuS, $Cu_9Fe_9S_{16}$ and S_8 were the main intermediate species during bornite bioleaching by mesophilic mixed bacteria, and $CuFeS_2$ was also detected. The surface species of S^{2-} and $S_2{}^{2-}$ would be polymerized to S_n^{2-} during bioleaching. The formation of element sulfur and the increase of its content were confirmed by the fitted results of XPS spectra. The presence of polysulfide and element sulfur did not inhibit the bornite bioleaching. The formations of CuS and $CuFeS_2$ were confirmed by the results of Cu *K*-edge XANES spectra.

Acknowledgements This work was supported by the National Natural Science Foundation of China (project No. 51374248 and No. 51774332), the Program for New Century Excellent Talents in University (project No. NCET-13-0595), the Open Funds of SSRF (No. 2016-SSRF-PT-005985) and the Open Funds of BSRF (No. 2017-BEPC-PT-000653) and the Fundamental Research Funds for the Central Universities of Central South University.

References

1. Ferraz LFC, Verde LCL, Vicentini R et al (2011) Ferric iron uptake genes are differentially expressed in the presence of copper sulfides in *Acidithiobacillus ferrooxidans* strain Lr. Antonie Van Leeuwenhoek 99(3):609–617
2. Bevilaqua DI, Diéz-Perez C, Fugivara S et al (2003) Characterization of Bornite (Cu_5fes_4) electrodes in the presence of the bacterium *Acidithiobacillus ferrooxidans*. J Braz Chem Soc 14(4):637–644
3. Pesic B, Olson FA (1983) Leaching of bornite in acidified ferric chloride solutions. Metall Trans B 14(4):577–588
4. Brierley JA, Brierley CL (2001) Present and future commercial applications of biohydrometallurgy. Hydrometallurgy 59(2):233–239
5. Rawlings DE, Johnson DB (2007) Biomining. New York: Springer, Berlin
6. Dutrizac JE, Macdonald RJC, Ingraham TR (1970) The kinetics of dissolution of bornite in acidified ferric sulfate solutions. Metall Trans 1(1):225–231
7. Dutrizac JE, Chen TT, Jambor JL (1985) Mineralogical changes occurring during the ferric lon leaching of bornite. Metall Trans B 16(4):679–693
8. Pesic B, Olson FA (1984) Dissolution of bornite in sulfuric acid using oxygen as oxidant. Hydrometallurgy 12(2):195–215
9. Buckley AN, Hamilton IC, Woods R (1984) Investigation of the surface oxidation of bornite by linear potential sweep voltammetry and X-Ray photoelectron spectroscopy. J Appl Electrochem 14(1):63–74
10. Zhao H-B, Hu M-H, Li Y-N et al (2015) Comparison of electrochemical dissolution of chalcopyrite and bornite in acid culture medium. Trans Nonferrous Met Soc China 25(1):303–313
11. Bevilaqua D, Garcia O Jr, Tuovinen OH (2010) Oxidative dissolution of bornite by *Acidithiobacillus ferrooxidans*. Process Biochem 45(1):101–106
12. Harmer SL, Thomas JE, Fornasiero D et al (2006) The evolution of surface layers formed during chalcopyrite leaching. Geochim Cosmochim Acta 70(17):4392–4402

Adsorption and Surface Area of Modified Bentonite Used as Bleaching Clay

C. G. Bastos Andrade, S. M. Toffoli and F. R. Valenzuela Diaz

Abstract The modification of structural clays by chemical processes is a common method. It usually uses strong inorganic acid attacks, aiming at improving the clay's properties and applications. Among the applications are its use in clay-polymer nanocomposites, cosmetics, medicines, and bleaching clays. Tests using acid attack to modified Brazilian bentonites were successfully performed and, resulted in significant improvement in the clay properties. This paper discusses the use of a Brazilian bentonite modified by acid attack as bleaching clay. The treated bentonite samples were characterized by XRF, specific surface area (BET) and SEM/EDS. The treated clay exhibited improved bleaching capacity for Brazilian nut oil and other Amazonian oils.

Keywords Acid attack · Bentonite · Bleaching clays · Clay · Nanotechnology

Introduction

The terms "bleaching clay", "bleaching earth", "clarifying clay", or "clay adsorbent" are defined in the oil industry as clays that, in their natural state, or after chemical or thermal activation, have the property of adsorbing the dissolved coloring material present in mineral, vegetable and animal oils. Bleaching clays are generally categorized into three types: fuller's earth, activated clays, and activated bauxites [1–3]. Clays used as raw materials for obtaining acid activated clays are the ones which, in natural state, have a low decolorizing power, but develop a high decolorizing power after acid treatment. Generally, these materials are calcium bentonites, that is, essentially montmorillonitic clays with calcium as the predominantly saturating cation. The acid activation works to convert montmorillonite into acid montmorillonite by replacing sodium, potassium, and calcium (sometimes,

C. G. Bastos Andrade (✉) · S. M. Toffoli · F. R. Valenzuela Diaz
Department of Metallurgical and Materials Engineering, Polytechnic School, University of Sao Paulo, Sao Paulo, SP, Brazil
e-mail: gianesic@usp.br

B. Li et al. (eds.), *Characterization of Minerals, Metals, and Materials 2018*, The Minerals, Metals & Materials Series,
https://doi.org/10.1007/978-3-319-72484-3_36

also magnesium) with the cation hydrogen or hydroxonium, and also to reduce the magnesium, iron, and aluminum content. During the activation process, the hydroxonium is partially replaced by structural Al^{3+}, with partial destruction of the mineral clay structure. The acid activation is also used to increase the specific surface area and the apparent porosity of clays [4–6]. Several research groups have been studying treatments to apply to modified clays using inorganic acids at high concentrations and temperatures, aiming at the bleaching and purification of the clays, for bleaching processes in the food industry [7–12]. Polycationic bentonites are widely used in modification processes, since they consist of montmorillonitic clays wherein the predominated interlayer cation is calcium. On the other hand, there is another type of montmorillonite, industrially called sodic bentonite, with a negative response to acid attack [13–16]. The Brazilian bentonite from Vitoria da Conquista, Bahia, is a polycationic bentonite which has high iron content, and exhibits green color [17–21]. This paper discusses the application of this latter bentonite, modified by acid attack, as bleaching clay. The samples were characterized by XRF, specific surface area BET, and SEM/EDS, and their bleaching capacities for some Amazonian oils were studied.

Experimental

Materials

The clay sample was supplied by ARGILAB (Applied Clays Laboratory) clays collection. It is a bentonite from Brazilian northwestern region, modified by acid attack using Dr. Bastos Andrade's and Dr. Valenzuela-Diaz's, from University of Sao Paulo, MAT methodology (patent pending). The selected Amazonian oils were açaí oil, passion fruit oil, and Brazilian nut oil.

Methods

Initially, the modified clay sample was sieved in #200 mesh. Afterwards, it was dried at 60 °C for 24 h. The purified oils were obtained by using the same amount of commercial activated clay and modified clay by MAT methodology. The purification of the Amazonian oils was performed by a simplified bleaching test: the clay samples were added to 20 mL of filtered oils in a glass vessel, homogenized by stirring, and then treated at 90 °C for 48 h. After being cooled to 22 °C, the samples were centrifuged at 3000 rpm for 5 min. The specific surface area was measured by the N_2-BET method, Micromeritics ASAP 2020 analyzer. The semi-quantitative chemical composition of the modified clay sample was measured by X-ray fluorescence (XRF), using TBL rock standards as a parameter. The XRF

spectrometer was a Panalytical Axios Advanced. Images and energy dispersive X-ray spectra (EDS) were obtained using a scanning electron microscope (SEM) Philips XL30—EDAX INSPECT 50. The oil absorbance capacity, before and after purification, was obtained using a spectrophotometer FEMTO 700 Plus, at 440 nm. The bleaching efficiency was calculated as the percentage of the absorbance decrease with reference to the unpurified filtered oil. The oils kinematic viscosities were determined by measuring the time that 10 mL of oil, at 22 °C, flowed down a plastic funnel with a 1 mm aperture.

Results and Discussion

Microcopy images of bentonite samples treated with purified water, and submitted to MAT process, are shown in Figs. 1 and 2. It is possible to observe the agglomerated, lamellar structure, of the clays, presenting agglomerates with irregular forms. The bentonite sample modified by water and MAT process show agglomerates of similar sizes, and no apparent destruction of the smectite crystal structures after modification was observed.

Figure 3 presents the EDS spectrum of the bentonite sample treated with purified water. It is possible to observe the presence of Si, O, Al, Fe, and Mg, in accordance to which is expected for a montmorillonite [14]. The presence of gold is explained by the required thin coating of the sample surface, necessary to perform the analysis of non-conductive materials.

Figure 4 present the EDS spectrum of the clay sample modified by MAT process. It is possible to observe the indication of bentonite purification, since the

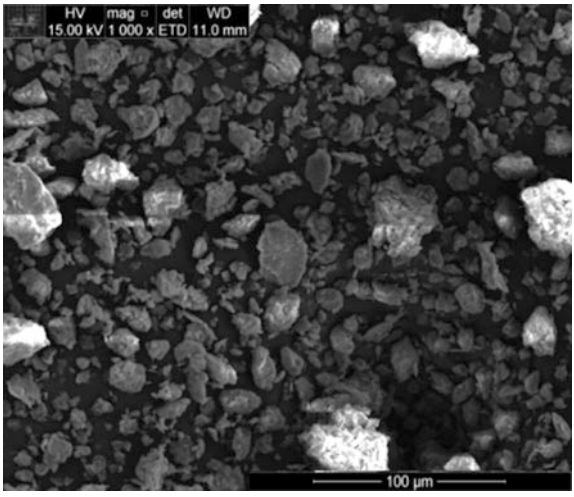

Fig. 1 SEM image of bentonite sample treated with water

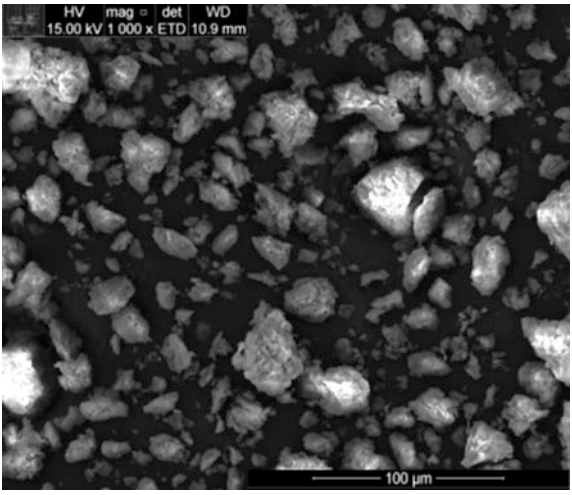

Fig. 2 SEM image of bentonite sample modified by MAT process

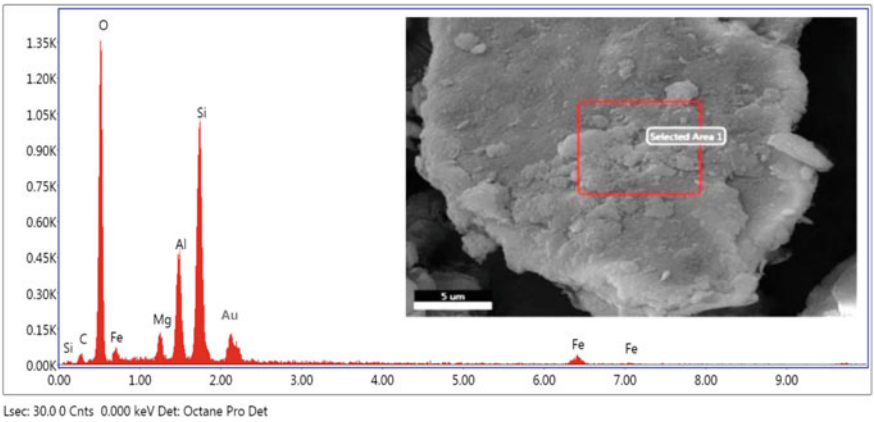

Fig. 3 EDS spectrum of the bentonite sample treated with H_2O

height of the metals peaks were reduced, although remaining a short peak relative to aluminum.

Table 1 presents the XRF results, expressed in percentage of oxides. It is observed an elevated presence of metallic oxides. In the sample treated with water, 83% of all the oxides are comprised of SiO_2, Al_2O_3, and Fe_2O_3. In sample modified by MAT it is possible to observe the reduction of all oxide contents, but silica. In accordance with literature, bentonites without any treatment, present at least 75% of these metallic oxides and rest is being organic matter and/or other minerals [12, 14, 19].

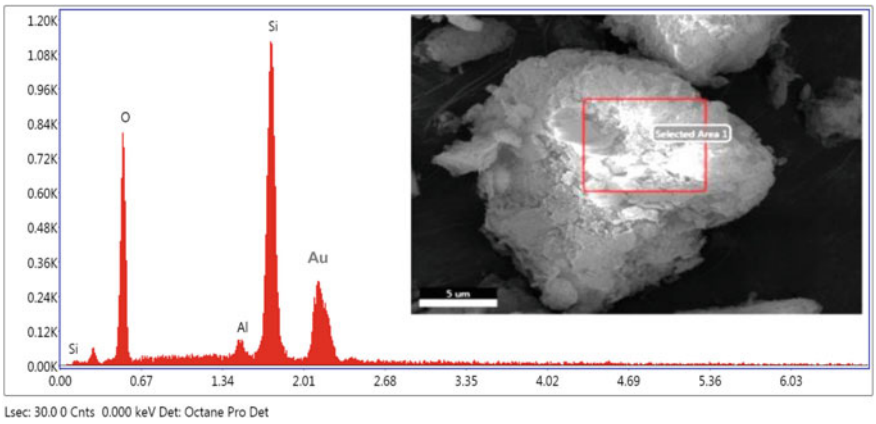

Fig. 4 EDS spectrum of bentonite sample modified by MAT process

Table 1 XRF results of the bentonite submitted to treatment (semi-quantitative analysis, values in percentage of oxides)

Sample	SiO_2	Al_2O_3	Fe_2O_3	MnO	MgO	CaO	Na_2O	K_2O	TiO_2	P_2O_5	LOI
H_2O	54.7	19.8	8.06	<0.10	3.73	0.20	0.10	<0.10	0.36	<0.10	13.5
MAT	64.1	15.9	5.08	<0.10	2.11	0.18	<0.10	<0.10	0.43	<0.10	13.0

The specific surface area, measured for the bentonite sample treated with water, was 28 m^2/g and for the bentonite modified by MAT, of 213 m^2/g, indicating a dramatic increase of more than 650%. This high value indicates a great potential of the MAT treated clay to be used as a bleaching clay [8, 12]. The BET pore diameter increased, from the water treated sample, to the MAT sample, from 6.8 to 7.6 nm.

In Figs. 5, 6 and 7 it is possible to observe the bleaching of Amazonian oils samples "in-natura", purified with the commercial activated clay, and also purified with the MAT modified clay. It is possible to observe a minimum difference in

oil sample purified with modified clay (0.75 g) | oil sample "in natura" | oil sample purified with commercial clay (0.75 g) | oil sample purified with commercial clay (1.50 g)

Fig. 5 Images of "in natura" and purified açaí oil

oil sample purified with modified clay (0.75 g) | oil sample "in natura" | oil sample purified with commercial clay (0.75 g) | oil sample purified with commercial clay (1.50 g)

Fig. 6 Images of "in natura" and purified Brazilian nut oil

oil sample purified with modified clay (0.75 g) | oil sample "in natura" | oil sample purified with commercial clay (0.75 g) | oil sample purified with commercial clay (1.50 g)

Fig. 7 Images of "in natura" and purified passion fruit oil

color between purified oils samples using commercial bleaching clay and modified clay by MAT. In all samples was obtained a good bleaching of Amazonian oils "in natura".

Tables 2 and 3 present the bleaching efficiency values of bentonite samples, commercial, and MAT modified. The obtained values for the modified clay were similar to those obtained with the commercial activated clay. The açaí oil is very dark, and for the wavelength used (440 nm, yellow color) the efficiency for all samples was null. However, in Fig. 5 it is possible to observe a light bleaching obtained with both the commercial and MAT clays.

For Brazilian nut oil purified with 0.75 g of commercial and MAT clays, it is possible to observe the same bleaching efficiency. Doubling the quantity of

Table 2 Bleaching efficiency of Brazilian nut oil "in natura", and purified

Brazilian nut oil		Efficiency (%)
"in natura"		–
Purified with	Modified clay (0.75 g)	19.0
	Commercial clay (0.75 g)	19.0
	Commercial clay (1.50 g)	13.0

Table 3 Bleaching efficiency of passion fruit oil "in natura" and purified

Passion fruit oil		Efficiency(%)
"in natura"		–
Purified with	Modified clay (0.75 g)	36.0
	Commercial clay (0.75 g)	22.0
	Commercial clay (1.50 g)	1.2

Table 4 Kinematic viscosity of the açaí oil "in natura", and purified

Açaí oil		Kinematic viscosity (in seconds)
"in natura"		115
Purified with	Modified clay (0.75 g)	123
	Commercial clay (0.75 g)	147
	Commercial clay (1.50 g)	132

commercial clay resulted in a great decrease in efficiency, most likely because the centrifugation wasn't capable to separate all the clay from the oil.

Therefore, the best bleaching efficiencies were achieved for the passion fruit oil, with 36% for the clay modified by MAT process, against 22% for the commercial bleaching clay. As for the Brazilian nut oil, increasing the quantity of clay results in a lower efficiency value.

Tables 4, 5 and 6 present the kinematic viscosity results of the Amazonian oils "in natura", purified with commercial activated bentonite, and modified by MAT process. For açaí oil, all the activated samples presented higher viscosity values compared to samples "in natura". The probable reason for that is the presence of residual clay, even after the centrifugation stage. For the Brazilian nut oil, all of the

Table 5 Kinematic viscosity of the Brazilian nut oil "in natura" and purified

Brazilian nut oil		Kinematic viscosity (in seconds)
"in natura"		148
Purified with	Modified clay (0.75 g)	127
	Commercial clay (0.75 g)	140
	Commercial clay (1.50 g)	129

Table 6 Kinematic viscosity of the passion fruit oil "in natura" and purified

Passion fruit oil		Kinematic viscosity (in seconds)
"in natura"		127
Purified with	Modified clay (0.75 g)	118
	Commercial clay (0.75 g)	105
	Commercial clay (1.50 g)	133

treated samples presented lower viscosity values after purification, indicating a good efficiency of the purification process. For the passion fruit, with the exception of the 1.5 g commercial treated sample, were obtained reduced viscosities values compared to the sample "in natura", and also indicates a good efficiency of the purification process.

Conclusions

Scanning electron microscopy images of the MAT clay sample and the water treated clay sample, revealed that they presented similar agglomerate sizes and no indication of significant destruction of the smectite crystal structures after the modification process. The MAT process also caused the reduction in the level of the metallic oxides in the clay, according to both FRX and EDS analyses. The BET specific surface area increased dramatically because of the MAT treatment and further investigation is demanded for understanding the microstructural changes, but it is a strong indicative of the great potential of using the MAT clay as a bleaching clay. The passion fruit and Brazilian nut oils presented excellent bleaching when the MAT clay was employed as bleaching agent. However, another wavelength of the testing light is necessary, in order to measure the bleaching efficiency of dark oils, like the açaí oil, although it was possible to visually observe oil bleaching caused by the clay samples. In terms of the viscosity of the samples, the presence of a residual amount of clay even after centrifugation is the possible cause for the viscosity increase and bleaching efficiency decrease observed in samples which were purified using higher amounts of clay. In conclusion, the process efficiency could be observed by the good bleaching of all Amazonian oils purified with MAT clay (0.75 g), as well as by the kinematic viscosity reduction. Therefore, it is possible to say that the MAT clay may be considered a revelation as a green alternative for the production of bleaching clays to be used in industrial bleaching processes.

Acknowledgements This work was supported by the São Paulo State Research Foundation—FAPESP, and by the CNPq—National Council for Scientific and Technological Development.

References

1. Nutting PG (1943) Adsorbent clays, their distribution, properties, production, and uses. U.S. Geological Survey Bulletin 928C. United States Government Printing Office, Washington
2. Grim RE (1962) Applied clay mineralogy. McGraw-Hill, New York
3. Souza Santos P (1975) Ciência e Tecnologia de Argilas, Aplicada às Argilas Brasileiras e Aplicações, vol 1–2. Edgar Blücher, Sao Paulo
4. Coelho ACV et al (2007) Argilas especiais: argilas quimicamente modificadas - uma revisão. Quim Nova 30(5):1282–1294

5. Souza-Santos P (1975) Tecnologia de Argilas, vol 1. Edgard Blücher, EDUSP, Sao Paulo
6. Teixeira-Neto E, Teixeira-Neto AA (2009) Modificação química de argilas: desafios científicos e tecnológicos para obtenção de novos produtos com maior valor agregado. Quim Nova 32(3):809–817
7. Folleto EL et al (2001) Obtenção e caracterização de materiais argilosos quimicamente ativados para utilização no descoramento de óleo vegetal. Mater Res 4(3):211–215
8. Valenzuela-Diaz FR, Souza Santos P (2001) Studies on the acid activation of Brazilian smetctite clays. Quim Nova 24(3):345–353
9. Barauna OS (2006) Processo de adsorção de pigmentos de óleo vegetal com argilas esmectíticas ácido-ativadas. Ph.D. thesis, Universidade Estadual de Campinas
10. Guerra DL et al (2006) Influence of the acid activation of pillared smectites from Amazon (Brazil) in adsorption process with butylamine. Polyhedron 25:2880–2890
11. Morales-Carrera A et al (2009) Argilas bentoníticas da Península de Santa Elena, Equador: pilarização, ativação ácida e seu uso como descolorante de óleo de soja. Quim Nova 32 (9):2287–2293
12. Bastos-Andrade CG (2016) Brazilian Bentonites submitted to mild acid attacks aiming industrial use. Ph.D. thesis, University of Sao Paulo
13. Grim RE (1968) Clay mineralogy, 2nd edn. McGraw-Hill Book, New York
14. Souza-Santos P (1992) Ciência e Tecnologia de Argilas, vol 1, 2a edn. Edgar Blücher, Sao Paulo
15. Flessner U et al (2001) A study of the surface acidity of acid-treated montmorillonite clay catalysis. JMC A Chemical 168:247–256
16. Folleto EL et al (2001) Influência do tipo de ácido usado e da sua concentração na ativação de uma argila bentonítica. Cerâmica 47(304):208–211
17. Abreu SF (1973) Recursos minerais do Brasil, vol 1, 2a edn. Edgard Blücher, Sao Paulo
18. Grim RE (1978) Bentonites. Elsevier, Amsterdam
19. Valenzuela-Diaz FR et al (1992) A Importância das argilas industriais brasileiras. Quím Ind 42:33–37
20. Valenzuela-Diaz FR (1994) Preparação a nível de laboratório de algumas argilas esmectíticas organofílicas. Ph.D. thesis, Universidade de Sao Paulo
21. Rodrigues MGF et al (2006) Obtenção e caracterização de materiais argilosos quimicamente ativados para utilização em catálise. Cerâmica 52:260–263

Investigation for Removal of Organic Carbon from Carbonaceous Copper Sulphide Ore and Improving the Recovery of Copper Through Flotation

Refilwe S. Magwaneng, Kazutoshi Haga, Altansukh Batnasan, Atsushi Shibayama, Masato Kosugi, Ryo Kawarabuki, Kohei Mitsuhashi and Masanobu Kawata

Abstract An investigation on improving copper and iron recovery by removal of organic carbon and carbonaceous gangue mineral through flotation was carried out. The ore contains chalcopyrite and bornite as valuable minerals, and dolomite and calcite as carbonaceous gangue minerals. The chemical composition of the ore indicates that grade of 2.08 and 5.37 mass% for copper and iron respectively, while carbon was 3.70 mass%. The total organic carbon in the feed was recorded as 2.02 mass%. The presence of these gangue minerals is detrimental to copper and iron recovery during flotation. Therefore a two stage flotation study was carried out to remove hydrophobic carbon and carbonaceous material from ore and to improve copper and iron recovery. The objective of the study was to find effective and selective flotation conditions which can eliminate gangue minerals from valuable minerals and improve quality (grade) and recovery of copper and iron. The obtained results could be used to develop a flotation circuit for recovering copper and iron from carbonaceous sulphide ores.

Keywords Organic carbon · Carbonaceous material · Copper · Iron Flotation

R. S. Magwaneng (✉) · A. Batnasan · A. Shibayama
Department of Earth Resource Engineering and Environmental Science, Graduate School of International Resource Sciences, Akita University, Akita 010-8502, Japan
e-mail: fyfymags@gmail.com

K. Haga
Department of Materials Science, Applied Chemistry Course, Graduate School of Engineering Science, Akita University, Akita 010-8502, Japan

M. Kosugi · R. Kawarabuki · K. Mitsuhashi · M. Kawata
Nittetsu Mining Co. Ltd., Tokyo, Japan

B. Li et al. (eds.), *Characterization of Minerals, Metals, and Materials 2018*, The Minerals, Metals & Materials Series,
https://doi.org/10.1007/978-3-319-72484-3_37

Introduction

Over the years, the depletion of high-grade deposits has presented significant challenges in the processing of low-grade deposits with complex mineralogy. Particularly, the recovery of copper and iron is quite challenging and unsatisfactory in carbonaceous sulphide ores. Previous confidential reports and cursory mineralogical characteristic of the ore indicate that the chalcopyrite and bornite host the copper and iron minerals. Their grain size distribution ranges from coarse grains to fine grains with an assemblage of organic carbon and carbonaceous minerals. The degree of liberation is therefore necessary during the milling process and is a critical parameter in determining the flotation efficiency [1].

The presence of organic carbon and carbonaceous material hinders the production of quality flotation concentrates, therefore resulting in a decrease in beneficiation efficiency [2]. Numerous studies on the elimination of have been carried out as pre-flotation stages before continued processing such as pyro metallurgy and hydrometallurgy [3–5]. Before evaluating organic carbon removal from copper ores, extensive mineralogical studies indicated that none of the traditional reasons based on liberation provided an adequate explanation on the poor separation. Other explanations for these observations were simply the variable composition and amount of organic component of a single type of ore [6–9].

In this paper, a two-stage flotation processing method consisting of pre-flotation of carbonaceous feed and main flotation of tailings from pre-flotation stage was discussed. Consideration was mainly made to the optimization of reagents used on the removal of organic components and clay minerals from sulphide. Therefore, the main issues in this paper are: (i) the elimination of organic carbon and carbonaceous minerals (ii) optimization of reagents (collectors and frother) for recovery of Cu and Fe.

Experimental

Materials and Methods

Initially, the ore samples received were stored in a freezer to minimize oxidation effects. To determine the chemical composition of the carbonaceous sulphide ore, measurements were determined by inductively coupled plasma-optical spectrometry (ICP-OES, SPS5510 SII Hitachi High-Tech Science Corporation, Japan) and X-Ray Fluorescence Spectrometry (XRF, ZSX Primus II Rigaku). As indicated in Table 1, the sample consist of 2.08 mass% of copper, 4.94 mass% of iron and 38.6 mass% of SiO_2 including other elements such as aluminum (Al), calcium (Ca), and magnesium (Mg). The total carbon (C_{TC}) and total organic carbon (TOC) were determined based on combustive oxidation and infrared analysis method using

Table 1 Chemical composition of the carbonaceous sulphide ore

	Al	Ca	Cu	Fe	Mg	C_{TC}	SiO_2	TOC
Grade (mass%)	1.84	12.16	2.08	5.37	4.03	3.69	38.6	2.02

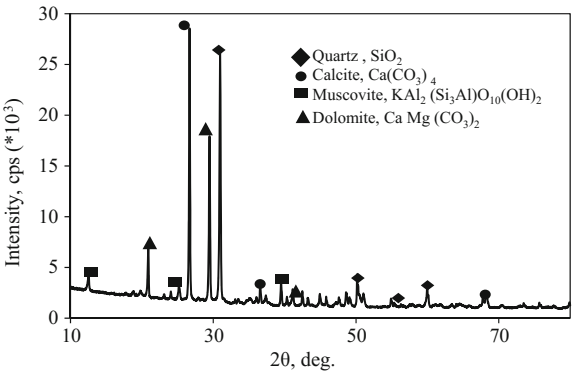

Fig. 1 XRD pattern of a carbonaceous sulphide ore

Sumigraph Nitrogen-Carbon-Hydrogen analyzer (NCH-22A) and included in Table 1 of the chemical analysis by ICP-OES.

Mineralogical studies by X-ray diffraction diffractometer (XRD, RINT-2200 V Rigaku) indicated the presence of calcite ($CaCO_3$), dolomite (Ca, Mg $(CO_3)_2$), chlorite ($(Mg{\cdot}Fe)_6(Si, Al)_4O_{10}(OH)_8$), mica ($Al_2$, K_2O_6Si) and quartz (SiO_2) as shown in Fig. 1.

Flotation

The scope of the experiment covered two stages: the first stage involved a pre-treatment study that focused on the removal of carbonaceous materials from the feed. A chemical reagent of methyl-isobutyl carbinol (MIBC, $C_6H_{14}O$) was used as a frother based on its hydrophobic interactions with carbonaceous material. In addition, an emulsion of MIBC and kerosene was considered to determine an optimum reagent dosage to minimize consumption of reagent used. The effect of particle size distribution on the elimination of organic carbon, in the pre-flotation stage for carbonaceous materials and clay minerals from the ore was investigated. After each experiment, froth was collect and slurry was filtered using 120 mm filter, and the solid samples obtained were dried in an oven at 70 °C for 24 h. The chemical compositions of the samples were determined by ICP-OES after digesting them in aqua regia.

In the second stage flotation as a main flotation, the pre-flotation tailings were used. Potassium amyl xanthate (PAX, C5H11OCSSK) and dithiophosphate (Aero3477) were used for the recovery of Cu and Fe.

The flotation experiments were conducted using a laboratory mechanical flotation machine (US 590-001C) equipped with 0.25 L flotation cell. The flotation time during the stage 1 and stage 2 was kept at 5 and 10 min, respectively, while other parameters such as slurry pH, conditioning time and stirring speed were kept constant at 8, 10% pulp density and 700 r/min, respectively.

Results and Discussion

Pre-treatment of Carbonaceous Sulphide Ore to Eliminate Organic Carbon and Carbonaceous Material

The effects of particle size on the removal of organic carbon and carbonaceous material was investigated. Additionally, for the purpose of frother optimization MIBC and an emulsion of MIBC and kerosene was carried out. Kerosene acts as a supportive aid for improved delivery of frother admission to carbon hydrophobicity [4]. In this case, the tailings obtained are fundamentally important in ascertaining that more sulphide is contained for further processing. The recovery and grade aid in determining the efficiency of carrying out pre-flotation experiment.

The results shown in Figs. 2 and 3 indicate that particle size has an impact in the recovery of Cu and Fe. In the particle size range of 75–52 μm, recovery of copper was achieved at 89.29% with grade of 5.71 mass%, (Fig. 2). Iron recovery was recorded at 92.43% with a grade of 6.03 mass% (Fig. 3). This observation was attributed to the distribution of sulphide minerals in a particle size range of 75–52 μm. According to the results, addition of 200 g/t of MIBC resulted in the increase in the recovery and grade of Cu and Fe respectively. The addition of kerosene as a means of improving frother administration and increasing carbon material flotation indicated a compromised quality grade for tailing. Results shown in Figs. 2 and 3 indicate that grade of 2.58 and 4.98 mass% for Cu and Fe when 200:600 g/t MIBC and kerosene emulsion was used despite their higher recoveries of 88 and 89% for Cu and Fe respectively. Therefore, it is expected that copper and iron could be lost to the pre-concentrate in conjunction to carbon removal, and confirming the poor selectivity of kerosene in separating carbon from sulphide ores (Table 2).

The amounts of total organic carbon (TOC) in the tailings under various particle size ranges and different frother dosages are shown in Fig. 4. For this case, the presence of TOC in the tailing indicates that some of the carbonaceous materials are not particularly hydrophobic. At the optimized conditions, which are particle size of 75–52 μm, MIBC dosage of 200 g/t, flotation time of 10 min, stirring speed of 700 r/min, and slurry pH of 8, the amount of total carbon (C_{TC}) was reduced from

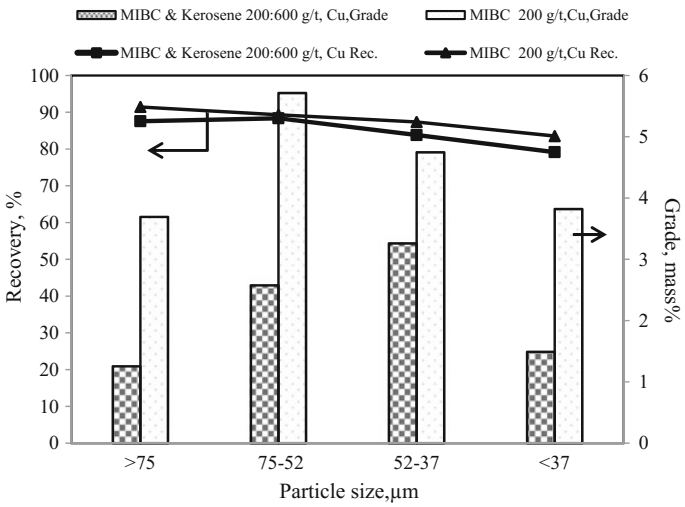

Fig. 2 The effects of particle size on grade and recovery of copper. (Collector: MIBC and emulsion of MIBC + kerosene, 200 g/t and 200:600 g/t respectively, Flotation time: 10 min, pulp density 10%, and slurry pH 8)

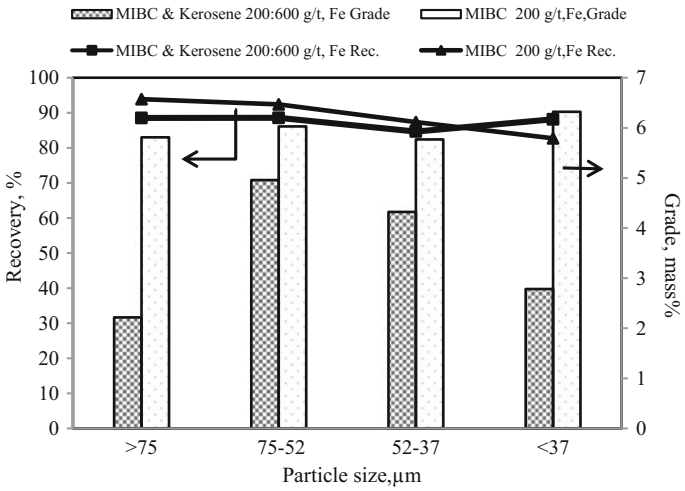

Fig. 3 The effects of particle size on grade and recovery of iron. (Collector: MIBC and emulsion of MIBC + kerosene, 200 g/t and 200:600 g/t respectively, Flotation time: 10 min, pulp density 10%, and slurry pH 8)

3.69 to 2.61% with minimal Cu and Fe losses (Table 3). The results revealed that separation of organic matter during pre-flotation is possible and tailings could be further taken for the main flotation process where selectivity could be improved by collector.

Table 2 Contents of copper and iron in concentrate after pre-flotation. (Flotation time: 10 min, pulp density 10%, and slurry pH 8)

	MIBC and kerosene 200:600 g/t, Cu		MIBC 200 g/t, Cu		MIBC and kerosene 200:600 g/t, Cu		MIBC 200 g/t, Cu	
	Grade assay (mass%)				Recovery (%)			
	Cu	Fe	Cu	Fe	Cu	Fe	Cu	Fe
>75	1.39	2.63	2.42	3.82	12.44	11.46	8.58	6.09
75–52	3.71	4.98	2.56	4.08	11.63	11.42	10.71	7.57
52–37	3.26	4.30	2.57	4.51	16.19	15.33	12.64	12.63
<37	2.99	4.32	2.56	4.00	20.84	11.85	16.48	17.28

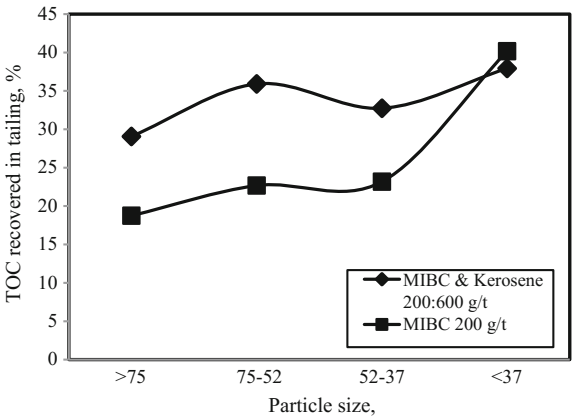

Fig. 4 Total organic carbon (TOC) recovered in tailings versus particle size. (Flotation time: 10 min, pulp density 10%, slurry pH 8, D_{50} = 70 µm, frother 200 g/t MIBC and 200:600 g/t MIBC and kerosene emulsion)

Main Flotation Circuit

The flotation experiments were performed using tailings as feed from the pre-flotation sulphide ore. Under slurry pH of 8, flotation time of 10 and 5 min conditioning, stirring speed of 700 r/min and 200 g/t of MIBC as frother. The main flotation circuit test was directed at maximizing recovery and grade of the Cu and Fe from pre-flotation tailings. Hence the performed tests were intended to investigate the role of different collector and their dosage on recovery of Cu and Fe in the pre-flotation tailings. The results for the main flotation are shown in Figs. 5 and 6, respectively. It is shown that a gradual increase in copper recovery attributed to the increase of collector dosage (AERO 3477). The maximum flotation recovery was obtained at 57.6% while the grade of copper was 5.8 mass% with 240 g/t AERO 3477 (Fig. 5).

Table 3 Chemical composition of concentrate and tailing after pre-flotation. (Flotation time: 10 min, pulp density 10%, and slurry pH 8)

Grade assay (mass%)						Distribution (%)		
Parameter	Product	wt%	Cu	Fe	C_{TC}	Cu	Fe	C_{TC}
MIBC 200 g/t	Conc.	4.76	4.56	4.08	5.91	10.42	7.19	9.94
	Tail	92.43	5.71	6.03	2.61	89.58	92.54	65.39
MIBC and kerosene 200:600 g/t	Conc.	14.46	4.38	7.24	3.63	30.44	19.48	14.23
	Tail	83.39	2.02	4.96	3.81	81.11	76.95	86.12

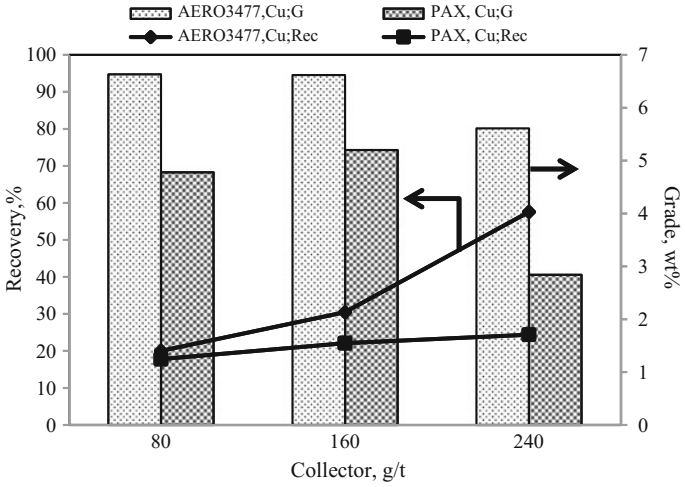

Fig. 5 Effects of collector dosage on the recovery of copper. (Flotation time: 10 min, pulp density 10%, slurry pH 8)

Figure 6 shows the influence of collector dosage on the recovery and grade of Fe, under conditions of 10% pulp density, slurry pH of 8 for 10 min flotation. The recovery of iron increased gradually with increase in collector dosage from 80 to 240 g/t, whereas PAX had no effect on the recovery of Fe. Generally, low grade concentrates for Cu and Fe were obtained therefore suggesting that organic carbon and carbonaceous minerals that have remained in the tailings were a result of increase of collector consumption. Despite the fact that PAX is commonly used to render sulphide hydrophobicity, low recoveries for Cu and Fe suggest that multi-mineral system and liquid phase are an important factor that needs to be highly accessed. The presence of middling in the system is one of the major concerns carried from pre-flotation stage to main flotation stage.

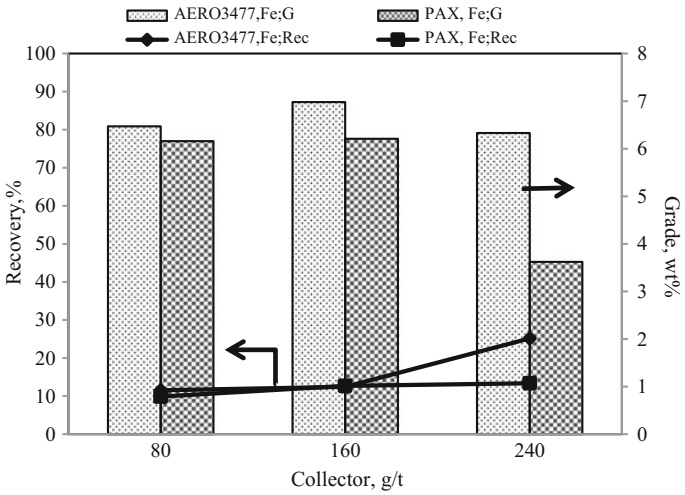

Fig. 6 Effects of collector dosage on the grade of iron (Flotation time: 10 min, pulp density 10%, slurry pH 8)

Conclusion

The results obtained show that there is a possibility for separating organic and carbonaceous material from sulphide minerals. The experimental results are summarized as follows:

Pre-flotation stage

- Total carbon (C_{TC}) was reduced from 3.69 to 2.61% in the optimized condition which were particle size range of 75–52 μm, MIBC dosage of 200 g/t, slurry pH of 8 and flotation time of 10 min.
- The pre-flotation concentrates are suggested to further scavenger flotation cell to maximize copper and iron recovery.

Main Flotation

- Relatively low recoveries of 57.6 and 25.17% for Cu and Fe were obtained from the flotation of pre-flotation tailings.
- The organic and carbonaceous materials that form in middling with sulphide minerals warrant difficulty in selective separation by use of collector. It is suggested that further liberation needs to be considered and addition of cleaner flotation cells would be added to optimize the recovery and upgrade of Cu and Fe.

Acknowledgements This work was financially supported by JSPS Leading Program "New Frontier Leader Program for Rare-metals and Resources" in Akita University. We are grateful to

the Nittetsu Co. Ltd. Company for providing us with the samples for performing this study and allowing for publication of results in this paper.

References

1. Luszczkiewicz A, Chmielewski T (2008) Acid treatment of copper sulfide middlings and rougher concentrate in the flotation circuit of carbonate ores. Int J Miner Process 88:45–52
2. Sousa R, Futuro A, Pires CS, Leite MM (2017) Froth flotation of Aljustrel complex ore. Physiochem Probl Miner Process 53:758–769
3. Smith T, Lin D, Lacouture B, Anderson G (2008) Removal of carbon with a Jameson cell at Red Dog Mine. In: Paper presented at the 40th annual meeting of the Canadian mineral processors. Ottawa, Ontario, Canada, 22–24 Jan 2008
4. Koneiczny A, Pawlos W, Krzeminska M, Kaleta R, Kurzydlo P (2013) Evaluation of organic carbon separation from copper ore by pre-flotation. Physiochem Probl Miner Process 49 (1):189–201
5. Gredelj S, Zanin M, Grano SR (2009) Selective flotation of carbon in the Pb–Zn carbonaceous sulphide ores of Century mine. Zinifex Miner Eng 22:279–288
6. Tabatabaei RH, Nagaraj DR, Vianna SM, Napier-Munn TJY (2014) The effect of non-sulphide gangue minerals on the flotation of sulphide minerals from Carlin-type gold ores. Miner Eng 60:26–32
7. Wieniewskin A, Skorupska B (2016) Technology of polish copper ore beneficiation-perspectives from the past experience. In: Paper presented at minerals engineering conference 2016. Swieradow-Zdroj, Lower Silesia, Poland, 25–28 Sept 2016
8. Bulatovic SM (2007) Handbook of flotation reagents. Elsevier, Boulevard
9. Kowalczuk PB, Zaleska E, Danczak O (2015) Flotation of carbonaceous copper shale-quartz mixture with poly (ethylene glycol) alkyl ethers. Trans Nonferrous Met Soc China 25:314–318

Part XI
Nanostructure and Characterization of Materials

Microwave Synthesis of Co–Ni Ferrite/Graphene Nanocomposite for Microwave Absorption

Zhiwei Peng, Jianhui Peng, Xiaolong Lin, Zhizhong Li, Zhongping Zhu, Guanghui Li and Tao Jiang

Abstract As the absorbing material composed of sole carbon is difficult to meet the comprehensive requirements of microwave applications, preparation of carbonaceous nanocomposite materials becomes an effective method to increase microwave absorption properties. In this study, a novel nanocomposite composed of Co–Ni ferrite and graphene was synthesized via a simple and rapid microwave hydrothermal method in just a few minutes. It was demonstrated that the minimum microwave reflection loss of the composite of 3 mm thickness with a low filling ratio (20 wt%) reached −13.1 dB at 17.2 GHz with an effective absorption bandwidth of 3.1 GHz. The good performance of the composite was believed to be a result of high dielectric loss of graphene associated with a multi-dielectric relaxation process and magnetic loss of the ferrite mainly originated from natural ferromagnetic resonance.

Keywords Graphene · Microwave-assisted synthesis · Magnetic ferrite Electromagnetic parameters · Absorbing materials

Introduction

Microwave absorption materials are widely used in the television, broadcast, radar, microwave anechoic chamber and electronic devices. [1]. Graphene, periodic honeycomb shaped new carbon material [2], becomes a potential nanoscale building block for new absorbing materials due to its outstanding properties. The two dimensional conjugate structure of graphene [3] contributes to its high dielectric loss, low density, special surface properties, etc. [4]. However, its remarkable dielectric loss ability and non-magnetic feature lead to poor impedance matching and thus a low attenuation property in microwave absorption [5–7].

Z. Peng · J. Peng · X. Lin · Z. Li · Z. Zhu (✉) · G. Li · T. Jiang
School of Minerals Processing and Bioengineering, Central South University, Changsha 410083, Hunan, China
e-mail: zhuzp@csu.edu.cn

B. Li et al. (eds.), *Characterization of Minerals, Metals, and Materials 2018*, The Minerals, Metals & Materials Series,
https://doi.org/10.1007/978-3-319-72484-3_38

In order to improve microwave absorption properties, one of the effective approaches is to load magnetic materials, typically ferrites, on graphene [8–10]. For example, when reduced graphene oxide (r-GO) was coated with Fe_3O_4 through a co-precipitation method, the reflection loss (RL) value of rGO/Fe_3O_4 composite (filling ratio = 8 wt%) reached −47.9 dB at 10.1 GHz with the effective absorption bandwidth (RL < −10 dB) ranging from 6.5 to 10.3 GHz (coating layer thickness of 2.0 mm) [8]. Other ferrites are also used for improving the magnetic performance of graphene matrix composite. A recent study showed that rugby-shaped $CoFe_2O_4$/graphene composites via a vapor diffusion method had the minimum RL of −39.0 dB (filling ratio = 60 wt%) at 10.9 GHz and corresponding effective absorption bandwidth was 4.7 GHz at 2.0 mm [9]. Another report demonstrated that $NiFe_2O_4$ nanorod/graphene composites of 2.0 mm thickness (filling ratio of 60 wt%), prepared by an ionic liquid assisted one-step hydrothermal approach, achieved minimum RL of −29.2 dB with the effective absorption bandwidth of 4.4 GHz [10]. The good microwave absorption performance of those composites was largely attributed to enhanced electron transmission when two or more ions replacing Fe cations within the spinel structure [11]. For this mechanism, it is anticipated that Co–Ni ferrites may be another promising candidate to be assembled onto graphene for further improvement of absorption performance

In this paper, a novel composite constituted by $Co_{0.5}Ni_{0.5}Fe_2O_4$ and graphene was synthesized via microwave hydrothermal method in just several minutes. The minimum RL of the composite of 3.0 mm thickness reached −13.1 dB at 17.2 GHz with an effective absorption bandwidth of 3.1 GHz.

Experimental

Materials

All chemical reagents used in this experiment, including natural graphite powder (<48 μm), sulphuric acid (H_2SO_4), potassium permanganate ($KMnO_4$), sodium nitrate ($NaNO_3$), hydrogen peroxide (H_2O_2), cobalt acetate ($Co(OAc)_2$), nickel acetate ($Ni(OAc)_2$), ferrous chloride ($FeCl_2$), ammonia ($NH_3{\cdot}H_2O$), and ethanol were of analytical grade and used as received without further purification.

Preparation of $Co_{0.5}Ni_{0.5}Fe_2O_4$/Graphene Composite

For preparation of $Co_{0.5}Ni_{0.5}Fe_2O_4$/graphene composite, 2.0 mmol of $FeCl_2$, 0.5 mmol of $Co(OAc)_2$ and 0.5 mmol of $Ni(OAc)_2$ were mixed and dissolved in 80 mL of distilled water under magnetic stirring. Subsequently, 50 mg of GO, which was preliminarily prepared by the Hummers method using the natural

graphite powder as starting material [12], was added into the above solution under ultrasonic treatment to form a homogeneous solution. The mixture was stirred for 4 h at room temperature. The pH value of the suspension was adjusted to 10 by adding $NH_3 \cdot H_2O$. The mixture was stirred for 1 h at room temperature. Then, the reaction mixture was heated at 160 °C in a microwave reactor at power of 500 W for 25 min. The resultant precipitate was filtered, washed with deionized water and ethanol, and finally dried in a vacuum oven at 70 °C for 12 h.

Characterization of $Co_{0.5}Ni_{0.5}Fe_2O_4$/Graphene Composite

The electromagnetic parameters (permittivity and permeability) of the composite were measured with an AV3629 vector network analyzer using the coaxial line method. Samples were first prepared by homogeneously mixing the nanocomposite with paraffin (the weight content of the as-prepared powder was about 20 wt%), and then the mixture was pressed into a toroid with an inner diameter of 3.0 mm, an outer diameter of 7.0 mm and a height of 2.0 mm. Subsequently, the samples were embedded into a copper holder and connected between the waveguide flanges of the instrument for measurement of the parameters.

To assess the microwave absorption performance of $Co_{0.5}Ni_{0.5}Fe_2O_4$/graphene composite, its reflection loss (RL) was calculated by the following equations [13, 14]:

$$\mathrm{RL(dB)} = 20 \times \log\left|\frac{Z_{in} - Z_0}{Z_{in} + Z_0}\right| \tag{1}$$

$$Z_{\mathrm{in}} = Z_0 \times \sqrt{\frac{\mu_r}{\varepsilon_r}} \times \mathrm{Tanh}\left[\mathrm{j} \times \frac{2 \times \pi \times \mathrm{f} \times \mathrm{d}}{\mathrm{c}} \times \sqrt{\mu_r \times \varepsilon_r}\right] \tag{2}$$

$$Z_0 = \sqrt{\frac{\mu_0}{\varepsilon_0}} \tag{3}$$

where Z_{in} is the input impedance of the absorber, Z_0 is the input impedance of the free space, ε_r ($\varepsilon_r = \varepsilon_r' - \mathrm{j}\varepsilon_r''$) is the complex relative permittivity of the absorber, μ_r ($\mu_r = \mu_r' - \mathrm{j}\mu_r''$) is the complex relative permeability of the absorber, c is the velocity of electromagnetic waves in free space, f is the frequency and d is the absorber layer thickness.

Results and Discussion

Electromagnetic Absorption Properties

Figure 1a shows the real part (ε_r') and imaginary part (ε_r'') of the complex relative permittivity of $Co_{0.5}Ni_{0.5}Fe_2O_4$/graphene composite. It is revealed that the ε_r' value decreased gradually from 2.89 to 2.59 and the ε_r'' value increased from 0.003 to 0.479, respectively, in the frequency range of 2–18 GHz. Figure 1b shows the real part (μ_r') and imaginary part (μ_r'') of the complex relative permeability of $Co_{0.5}Ni_{0.5}Fe_2O_4$/graphene composite. It reveals that the values of μ_r' were in the range of 0.95–1.11 over 2–18 GHz and the μ_r'' values exhibited a major peak at 10.16 GHz and a minor peak at around 4.64 GHz. From Fig. 1c, it is found that most of the values of the dielectric loss tangent (tan $\delta\varepsilon_r$) were larger than the values of the magnetic loss tangent (tan $\delta\mu_r$) from 2 to 18 GHz, except the frequency ranges of 4.48–6.40 and 9.60–10.88 GHz. Therefore, we can conclude that the electromagnetic wave attenuation mechanism of $Co_{0.5}Ni_{0.5}Fe_2O_4$/graphene composite was mainly ascribed to electrical loss in the frequency range of 2–18 GHz. The higher tan $\delta\mu_r$ values than the tan $\delta\varepsilon_r$ values were associated with the two peaks of the μ_r'' value in Fig. 1b.

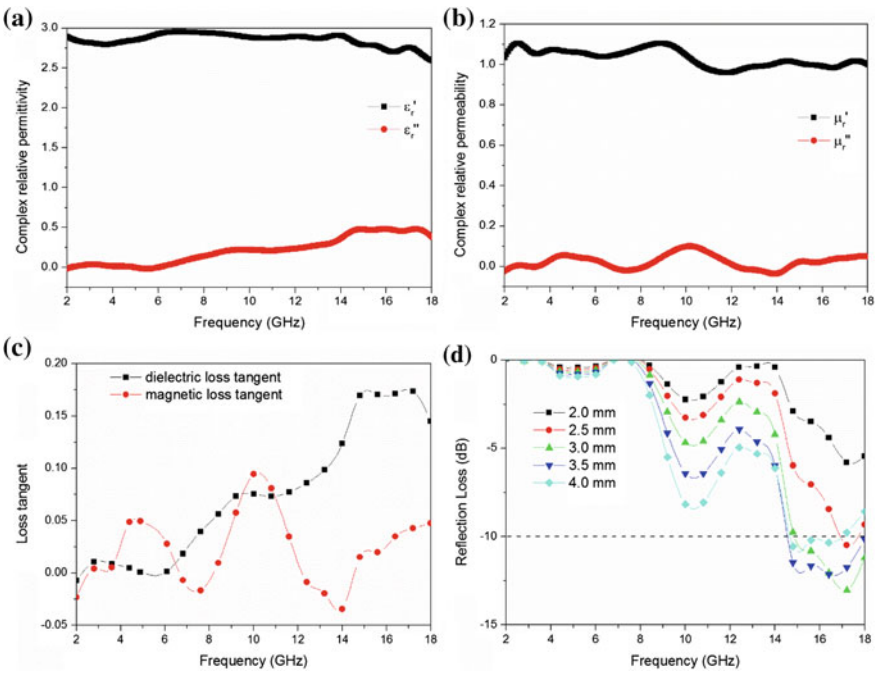

Fig. 1 Complex relative permittivity (**a**), complex relative permeability (**b**), loss tangent (**c**) and reflection loss (**d**) of $Co_{0.5}Ni_{0.5}Fe_2O_4$/graphene composite

Figure 1d shows the RL curves of $Co_{0.5}Ni_{0.5}Fe_2O_4$/graphene composite with different thicknesses. Its minimum RL was up to −13.1 dB at 17.2 GHz, and the bandwidth corresponding to the RL values below −10 dB (90% of electromagnetic wave absorption) was 3.1 GHz (from 14.9 to 18.0 GHz) with a thickness of 3.0 mm. In addition, the minimum RL values obviously decreased first and then increased with increasing the layer thickness.

To investigate the possible mechanism of the enhanced microwave absorption properties of $Co_{0.5}Ni_{0.5}Fe_2O_4$/graphene composite, the Cole-Cole semicircle curve and the values C_0 [μ_r'' $(\mu_r')^{-2}f^{-1}$] versus frequency are presented in Fig. 2. As for the Debye dipolar relaxation, the complex relative permittivity can be expressed by the following equation [15]:

$$\varepsilon_r = \varepsilon_\infty + \frac{\varepsilon_s - \varepsilon_\infty}{1 + j2\pi f\tau} = \varepsilon_r' - j\varepsilon_r'' \tag{4}$$

where f, ε_s, ε_∞ and τ are the frequency, static permittivity, relative dielectric permittivity at the high-frequency limit, and polarization relaxation time, respectively. Thus, ε_r' and ε_r'' can be described by the following equations:

$$\varepsilon_r' = \varepsilon_\infty + \frac{\varepsilon_s - \varepsilon_\infty}{1 + (2\pi f)^2\tau^2} \tag{5}$$

$$\varepsilon_r'' = \frac{2\pi f\tau(\varepsilon_s - \varepsilon_\infty)}{1 + (2\pi f)^2\tau^2} \tag{6}$$

According to Eqs. (5) and (6), the relationship between ε_r' and ε_r'' can be deduced as follows:

$$\left(\varepsilon_r' - \varepsilon_\infty\right)^2 + \left(\varepsilon_r''\right)^2 = (\varepsilon_s - \varepsilon_\infty)^2 \tag{7}$$

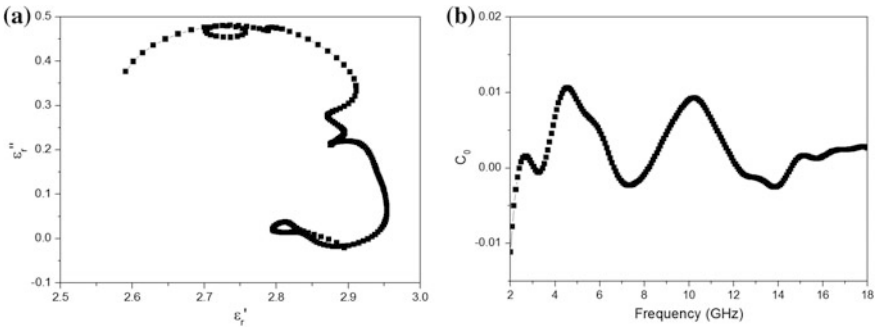

Fig. 2 Cole-Cole curves (**a**) and C_0 versus frequency curve of $Co_{0.5}Ni_{0.5}Fe_2O_4$/graphene composite (**b**)

Thus, the curve of ε_r' versus ε_r'' is a single semicircle, which is generally called the Cole-Cole semicircle. Each semicircle corresponds to one Debye relaxation process. Figure 2a shows the ε_r'–ε_r'' curve of $Co_{0.5}Ni_{0.5}Fe_2O_4$/graphene in the frequency range from 2 to 18 GHz. The curve of ε_r' versus ε_r'' shows that $Co_{0.5}Ni_{0.5}Fe_2O_4$/graphene composite had a distinct segment of three semicircles, demonstrating that the composites had multi-dielectric relaxation processes. In other words, the Debye relaxation process played a key role in improving the dielectric properties of $Co_{0.5}Ni_{0.5}Fe_2O_4$/graphene composite. In general, the microwave magnetic loss of magnetic materials originates mainly from hysteresis, domain wall resonance, natural ferromagnetic resonance, and the eddy current effect [16]. The hysteresis loss comes from irreversible magnetization and is negligible in a weak applied field. The domain wall resonance occurs only in multidomain materials and usually in the 1–100 MHz range [17]. In this study, the complex relative permeability was measured in the frequency range of 2–18 GHz. Therefore, hysteresis and domain wall resonance were not the main factors that led to magnetic loss of the composite. Instead, only natural ferromagnetic resonance or the eddy current effect might contribute to the microwave magnetic loss. If the eddy current effect occurs at the absorber, the C_0 ($C_0 = \mu_r''(\mu_r')^{-2}f^{-1} = 2\pi\mu_0\sigma d^{2/3}$) will be a constant when the frequency varies. It is shown in Fig. 2b that these C_0 values were not constant with the increasing frequency. Therefore, the magnetic loss of the composite was considered to be originated from natural ferromagnetic resonance.

The mechanism of excellent electromagnetic absorbing performance for $Co_{0.5}Ni_{0.5}Fe_2O_4$/graphene composite was investigated in detail (Fig. 3). The excellent wave absorption properties and wider absorption bandwidth of $Co_{0.5}Ni_{0.5}Fe_2O_4$/graphene composite can be explained as follows. Firstly, the remarkable dielectric loss ability of graphene was conducive to absorbing electromagnetic waves. Loading $Co_{0.5}Ni_{0.5}Fe_2O_4$ nanoparticles not only effectively reduced the excessive dielectric loss of graphene but also enhance good magnetic properties of the composite, contributing to impedance matching. More interfaces and defects could be induced after the introduction of $Co_{0.5}Ni_{0.5}Fe_2O_4$ nanoparticles, which caused more interface polarization [18]. Secondly, the multiple reflection could occur at defect of the graphene and $Co_{0.5}Ni_{0.5}Fe_2O_4$ nanoparticles, extending the propagative routes of electromagnetic wave. In addition, the natural resonances produced by $Co_{0.5}Ni_{0.5}Fe_2O_4$ could greatly increase magnetic losses and convert electromagnetic energy into thermal energy, thus absorbing electromagnetic waves.

Compared with other absorbers, the $Co_{0.5}Ni_{0.5}Fe_2O_4$/graphene composite exhibited significantly enhanced electromagnetic absorbing ability, as shown in Table 1. Furthermore, it was only 20 wt% of the filling ratio for the $Co_{0.5}Ni_{0.5}Fe_2O_4$/graphene composite. The above results demonstrated that the $Co_{0.5}Ni_{0.5}Fe_2O_4$/graphene composite had strong absorption, wide absorption bandwidth and light weight.

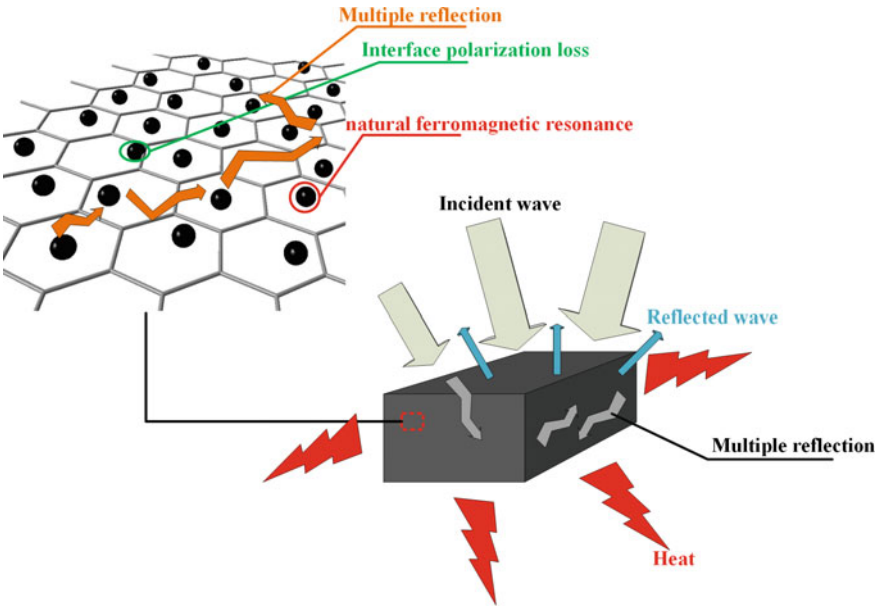

Fig. 3 Possible electromagnetic absorbing mechanism of the $Co_{0.5}Ni_{0.5}Fe_2O_4$/graphene composite

Table 1 Electromagnetic absorption performance of similar absorbers

Sample (name)	RL_{min} (dB)	Bandwidth (≤ -10.0 dB) (GHZ)	Filling ratio (wt%)	Thickness (mm)	Adhesive matrix	References
$Co_{0.2}Ni_{0.4}Zn_{0.4}Fe_2O_4$	−17.4	3.8	30	5.0	Paraffin	[19]
$Ni_{0.12}Mn_{0.38}Zn_{0.5}Fe_2O_4$	−32	3.0	90	6.0	Polymeric epoxy resin	[20]
$Ni_{0.5}Zn_{0.5}Fe_2O_4$	−11	2.0	80	3.5	Wax	[21]
Porous graphene/Fe_3O_4	−48.5	3.4	30	3.2	Paraffin	[22]
$CoFe_2O_4$ hollow sphere/graphene	−22.5	3.1	60	3.0	Paraffin	[23]
$NiFe_2O_4$ nanorod/ graphene	−23.9	3.9	60	3.0	Paraffin	[10]
$Co_{0.5}Ni_{0.5}Fe_2O_4$/ graphene	−13.1	3.1	20	3.0	Paraffin	This work

Conclusions

A $Co_{0.5}Ni_{0.5}Fe_2O_4$/graphene composite was synthesized via a simple and rapid microwave method. It was shown that the $Co_{0.5}Ni_{0.5}Fe_2O_4$/graphene composite had good dielectric and magnetic properties. The minimum RL of $Co_{0.5}Ni_{0.5}Fe_2O_4$/

graphene composite was −13.1 dB at 17.2 GHz and the absorption bandwidth with the reflection loss below −10 dB was 3.1 GHz with a thickness of 3.0 mm. The good performance of the composite was attributed to the high dielectric loss of graphene in association with multi-dielectric relaxation processes and magnetic loss of the ferrite mainly originated from natural ferromagnetic resonance.

Acknowledgements This work was partially supported by the National Natural Science Foundation of China under Grant 51774337, the innovation-driven Program of Central South University under Grant 2016CXS021 and the Shenghua Lieying Program of Central South University under Grant 502035001.

References

1. Wu X, Che Y (1992) Foreign microwave absorbing materials. National University of Defense Technology press
2. Geim AK, Novoselov KS (2007) The rise of graphene. Nat Mater 6:183–191
3. Loh KP, Bao Q, Ang PK, Yang J (2010) The chemistry of graphene. J Mater Chem 20:2277–2289
4. Ma E, Li J, Zhao N, Liu E, He C, Shi C (2013) Preparation of reduced graphene oxide/Fe_3O_4 nanocomposite and its microwave electromagnetic properties. Mater Lett 91:209–212
5. Lv H, Ji G, Li X, Chang X, Wang M, Zhang H, Du Y (2015) Microwave absorbing properties and enhanced infrared reflectance of FeAl mixture synthesized by two-step ball-milling method. J Magn Magn Mater 374:225–229
6. Shang C, Ji G, Liu W, Zhang X, Lv H, Du Y (2015) One-pot in situ molten salt synthesis of octahedral Fe_3O_4 for efficient microwave absorption application. Rsc Adv 5:80450–80456
7. Zhao B, Shao G, Fan B, Zhao W, Zhang R (2015) Facile synthesis and enhanced microwave absorption properties of novel hierarchical heterostructures based on a Ni microsphere-CuO nano-rice core-shell composite. Phys Chem Chem Phys 17:6044–6052
8. Zhang H, Xie A, Wang C, Wang H, Shen Y, Tian X (2014) Room temperature fabrication of an RGO–Fe_3O_4 composite hydrogel and its excellent wave absorption properties. Rsc Adv 4:14441–14446
9. Zhang S, Jiao Q, Hua J, Li J, Zhao Y, Li H, Wu Q (2015) Vapor diffusion synthesis of rugby-shaped $CoFe_2O_4$/graphene composites as absorbing materials. J Alloy Compd 630:195–201
10. Fu M, Jiao Q, Zhao Y (2013) Preparation of $NiFe_2O_4$ nanorod–graphene composites via an ionic liquid assisted one-step hydrothermal approach and their microwave absorbing properties. J Mater Chem A 1:5577–5586
11. Ji R, Cao C, Chen Z, Zhai H, Bai J (2014) Solvothermal synthesis of $Co_xFe_{3-x}O_4$ spheres and their microwave absorption properties. J Mater Chem C 2:5944–5953
12. Hummers WS, Offeman RE (1958) Preparation of graphitic oxide. J Am Chem Soc 80:1339
13. Wang LN, Jia XL, Li YF, Yang F, Zhang LQ, Liu LP (2014) Synthesis and microwave absorption property of flexible magnetic film based on graphene oxide/carbon nanotubes and Fe_3O_4 nanoparticles. J Mater Chem A 2:14940–14946
14. Kim SS, Jo SB, Gueon KI, Choi KK, Kim JM, Churn KS (1991) Complex permeability and permittivity and microwave absorption of ferrite-rubber composite at X-band frequencies. IEEE Trans Magn 27:5462–5464
15. Zhao B, Zhao WY, Shao G, Fan BB, Zhang R (2015) Morphology-control synthesis of a core-shell structured NiCu alloy with tunable electromagnetic-wave absorption capabilities. ACS Appl Mater Interfaces 7:12951–12960

16. Peng Z, Hwang JY (2015) Microwave-assisted metallurgy. Int Mater Rev 60:30–63
17. Wu M, Zhang Y, Hui S, Xiao T, Ge S, Hines W, Budnick J, Taylor G (2002) Microwave magnetic properties of $Co_{50}/(SiO_2)_{50}$ nanoparticles. Appl Phys Lett 80:4404–4406
18. Qu B, Zhu C, Li C, Zhang X, Chen Y (2016) Coupling hollow Fe_3O_4-Fe nanoparticles with graphene sheets for high-performance electromagnetic wave absorbing material. ACS Appl Mater Interfaces 8:3730–3735
19. Liu P, Yao Z, Ng, VMH, Zhou J, Yang Z, Kong L (2017) Enhanced microwave absorption properties of double-layer absorbers based on spherical NiO and $Co_{0.2}Ni_{0.4}Zn_{0.4}Fe_2O_4$ ferrite composites. Acta Metallurgica Sinica https://doi.org/10.1007/s40195-017-0612-5
20. Tong SY, Wu JM, Tung MJ, Ko WS, Huang YT, Wang YP (2012) Effect of Ni concentration on electromagnetic wave absorption of (Ni, Mn, Zn)Fe_2O_4/resin particulate composites. J Alloy Compd 525:143–148
21. Bueno AR, Gregori ML, No´brega MCS (2008) Microwave-absorbing properties of $Ni_{0.50-x}Zn_{0.50-x}Me_{2x}Fe_2O_4$ (Me = Cu, Mn, Mg) ferrite-wax composite in X-band frequencies. J Magn Magn Mater 320:864–870
22. Zheng Y, Wang X, Wei S, Zhang B, Yu M, Zhao W, Liu J (2017) Fabrication of porous graphene-Fe_3O_4 hybrid composites with outstanding microwave absorption performance. Compos A 95:237–247
23. Fu M, Jiao Q, Zhao Y, Li H (2014) Vapor diffusion synthesis of $CoFe_2O_4$ hollow sphere/graphene composites as absorbing materials. J Mater Chem A 2:735–744

Evaluation of Urea Encapsulation by Microcapsules of PHB/MMT and PHB/OMMT Nanocomposites

J. C. Arjona, F. R. Valenzuela-Diaz, H. Wiebeck, S. H. Wang and M. G. Silva-Valenzuela

Abstract Urea is the most used nitrogen fertilizer around the world being responsible for many environmental problems. Preparation of microcapsules from biodegradable polymer has been reported as a main system to sustain active substances, finding application in different areas. The objective of this work was to sustain urea in nanocomposite microcapsules of poly(3-hidroxybutyrate) (PHB) reinforced with a smectite Brazilian clay in its natural (MMT) and modified (OMMT) form. PHB/MMT and PHB/OMMT microcapsules were obtained by w/o/w emulsion. Characterization were performed by XRD and optical microscopy. Structural and morphological differences observed by XRD and optical microscopy shown that PHB/OMMT microcapsules are smaller than PHB/MMT microcapsules, with average size diameter ranging ~ 49 μm. Results indicate that PHB/OMMT microcapsules present more defects and fractures than PHB/MMT microcapsules.

Keywords Microencapsulation · Brazilian clay · Urea · PHB

Introduction

Microcapsules can become a solution to a lot of environmental problems, one of them is caused by exceed of fertilizers in the agriculture, which is responsible for river, air and soil contamination beside some species of animals. Because of that urea encapsulation is so important: it is the most used fertilizer with nitrogen in Brazil [1]. Studies showed the benefits of encapsulate urea through polymer microcapsules: the low density of polymer and the study of urea release that can be better controlled and studied when compared with other materials [2].

J. C. Arjona (✉) · F. R. Valenzuela-Diaz · H. Wiebeck · S. H. Wang
M. G. Silva-Valenzuela
Metalurgic and Materials Engineer Department, Polytechnic School of University of São Paulo, Avenida Prof. Mello Moraes 2463, São Paulo 05508-030, Brazil
e-mail: jessica.arjona@usp.br

B. Li et al. (eds.), *Characterization of Minerals, Metals, and Materials 2018*, The Minerals, Metals & Materials Series,
https://doi.org/10.1007/978-3-319-72484-3_39

PHB is a great option to make these microcapsules: it is a biopolymer and biodegradable, consequently it will be not responsible for more contaminations or solid waste in the environment [3]. Besides that, less urea would be necessary to the same quantity of plantation, consequently this arrangement would be really important to all the world, since there are predictions that in less of 50 years the consume of food will double and the number of productive land will decrease [4].

To improve mechanical and thermal properties of PHB, a clay can be incorporated to this polymer [5]. Frequently, montmorillonite is a kind of clay utilized as nanometric load. To enhance the interaction between inorganic particles and polymer matrix, it is usual modify the clay surface with ammonium quaternary salt, creating a organoclay (OMMT) [6].

In this paper, we used a physical-chemical method of emulsion-diffusion of solvent to obtain microcapsules. It is a method widely applied for encapsulation of drugs, mainly water-soluble drugs. The efficiency of this process depends on material core of microcapsules, the drug that will be encapsulated and other parameters like rate of mixing and solvents [7].

Materials and Methods

Materials

It was used a Brazilian Northeast smectite, from Vitoria da Conquista, Bahia-Brazil. Poly(3-hydroxybutyric acid) (PHB) of molecular weight approximative 600,000 g/mol was supplied by PHB Industrial S/A—Brazil. Urea (99.5%), hexadecyl trimethyl ammonium chloride ($C_{19}H_{44}NCl$) in aqueous solution (50%), and sodium carbonate (99.5%) were commercially available.

Methods

Clay purification

The smectite utilized in the present work was purified before used. Firstly, an aqueous dispersion of the clay (15% w/w) was made by mixing at 14,000 rpm for 20 min. After resting, the solution showed three phases with different colors, which were carefully separated. One of these phases, the intermediate phase, here denominated MMT, was used in the composition of the PHB/clay nanocomposite systems used to obtain microcapsules.

Clay organophilization

A clay dispersion (4% w/w) was prepared and mixed at 14,000 rpm for 20 min. Then, it was made a cation exchange using Na_2CO_3 at 1500 rpm for 20 min. After that, the ammonium quaternary salt solution (50% w/w) was dropped in the clay dispersion and it was mixed at 1500 rpm for 30 min, and then left to rest overnight. Thereafter, the supernatant was removed from the dispersion and the clay was washed with 3 L of distilled water, under vacuum. The resulting organoclay was dried at 60 °C for 24 h and sieved through a 200-mesh sieve.

Obtaining PHB/MMT and PHB/OMMT nanocomposites

Nanocomposites were obtained by solution method. Chloroform was used as the solvent to prepare both the 0.4% (w/w) clay (MMT and OMMT) dispersions and 3.6% (w/w) PHB solution, which were mixed using a magnetic stirrer, the clay dispersions for 3 h at room temperature, and PHB solution for 30 min at 40 °C. After, PHB solution was dropped in the clay dispersion under magnetic stirring.

Obtaining encapsulated microcapsules

Microcapsules were obtained by emulsion-diffusion method. First, an emulsion w/o was prepared mixing urea (10%) aqueous solution in nanocomposite solution and PVA (0.5% w/w) aqueous solution by magnetic stirrer at 150 rpm, for 2 min. This emulsion was slowly dropped in a PVA (0.5% w/w) solution that was mixing by mechanical stirring at 1500 rpm during the dropping and for more 25 min. Microcapsules were obtained in the bottom of beaker.

XRD

A Rigaku MiniFlex600 X-ray diffractometer system with KCuα radiation was used to perform XRD analyses. Scans were recorded in the range of $2\Theta = 2°–60°$ at 2°/min with an X-ray tube operated at 30 kV and 10 mA.

Optical microscopy

A Zeiss Stereo microscope model Stemi2000 was used to verify morphology and size distribution of microcapsules. Images were made utilizing 100 × zoom.

Results and Discussion

XRD

The purified clay (MMT), organoclay (OMMT) and microcapsules (PHB, PHB/MMT and PHB/OMMT) with and without urea encapsulated were analyzed by X-ray diffraction and the spectra of these materials are illustrated in Fig. 1. The basal spacing d(001) = 1.4 nm for MMT shifted to 1.8 nm for OMMT indicating higher gallery space and more affinity with polymer matrix [6]. All the

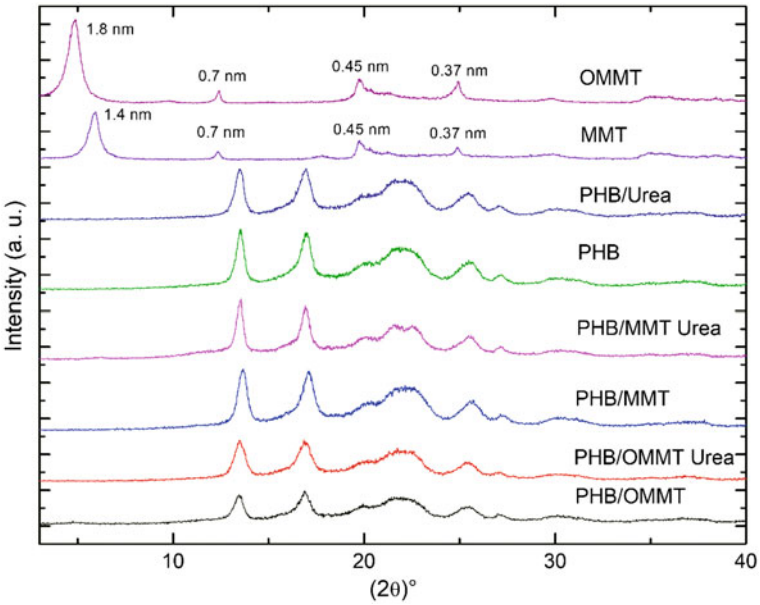

Fig. 1 XRD of microcapsules, clay and organoclay

nanocomposites do not present the d(001) clay peak indicating the obtaining of nanocomposite [8].

Besides that, the crystallinity of PHB increased with MMT addition and it occurs due the rise of heterophase nucleation points in the moment that microcapsules are precipitating on bottom of Becker [5]. However, OMMT addition reduces peaks intensity, indicating crystallinity decreased, which may be related with the rise of exfoliation of OMMT in PHB, what hinder polymer chain to organize in the spherullites due the interaction between polymer and organoclay [8].

Furthermore, urea encapsulation has reduced crystallinity of PHB in PHB/MMT while has raised of PHB/OMMT. Besides of that, the peaks form of PHB and its nanocomposites is quite similar, what indicates the crystallization occurs on the same way whether montmorillonite be present or not [9].

Optical Microscopy

Figure 2 shows morphology and size of microcapsules with and without urea encapsulated: they are spherical and uniform, further urea encapsulation has risen their size. Medium diameters of PHB, PHB/MMT and PHB/OMMT are, respectively, 40.6 ± 13, 52.8 ± 16 and 49.4 ± 12 μm. When urea is added to obtaining microcapsules, they growth to 47.4 ± 14, 54.7 ± 22 and 70.5 ± 26 μm,

respectively, what may be an indication of urea encapsulation. PHB microcapsules showed smaller medium size distribution, but PHB/OMMT showed bigger average size when urea was encapsulated suggesting better encapsulation efficiency [7].

Graphs were made to analyze the average size distribution of microcapsules, which are showed in Fig. 3. The quantity of microcapsules was normalized, in the range of 0–1, for better comparison among them. They all present a short range of size, from $\sim$20 µm to $\sim$100 µm, and the most of them is around 50 µm. It is a distribution similar to what was expected [10, 11]: comparable to normal curve with a region with more quantity of size and less microcapsules bigger or smaller [12].

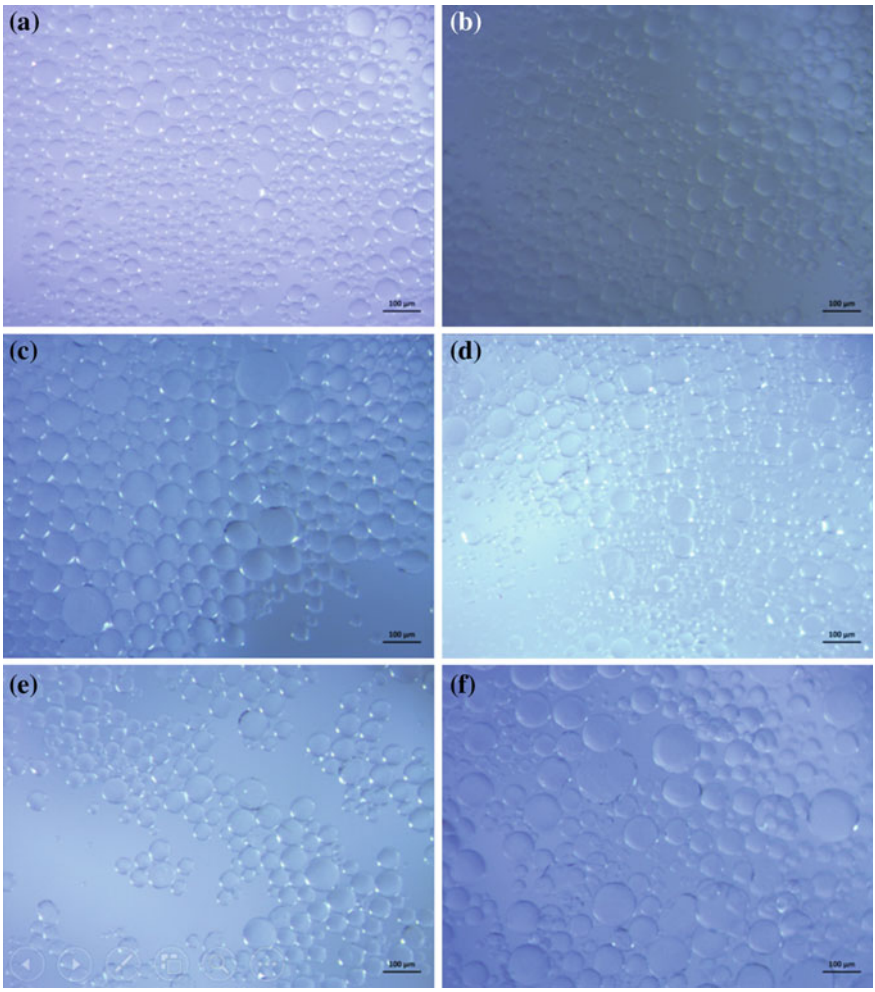

Fig. 2 Images by optical microscopy of microcapsules of **a** PHB, **b** PHB sustaining urea, **c** PHB/MMT, **d** PHB/MMTsustaining urea, **e** PHB/OMMT and **f** PHB/OMMT sustaining urea

PHB ones showed more strait distribution and the urea encapsulation made all the distribution of size wider.

As XRD showed, PHB/OMMT microcapsules presented less crystallinity than the PHB/MMT, which might have an effect on their mechanical properties, as illustrate in the Fig. 4. PHB/OMMT with and without urea encapsulated have presented more fracture and defects in their surfaces, what were not seen in the other kinds of microcapsules. And it can be explaining because as organoclays have more interaction with polymer, probably more OMMT was incorporated than

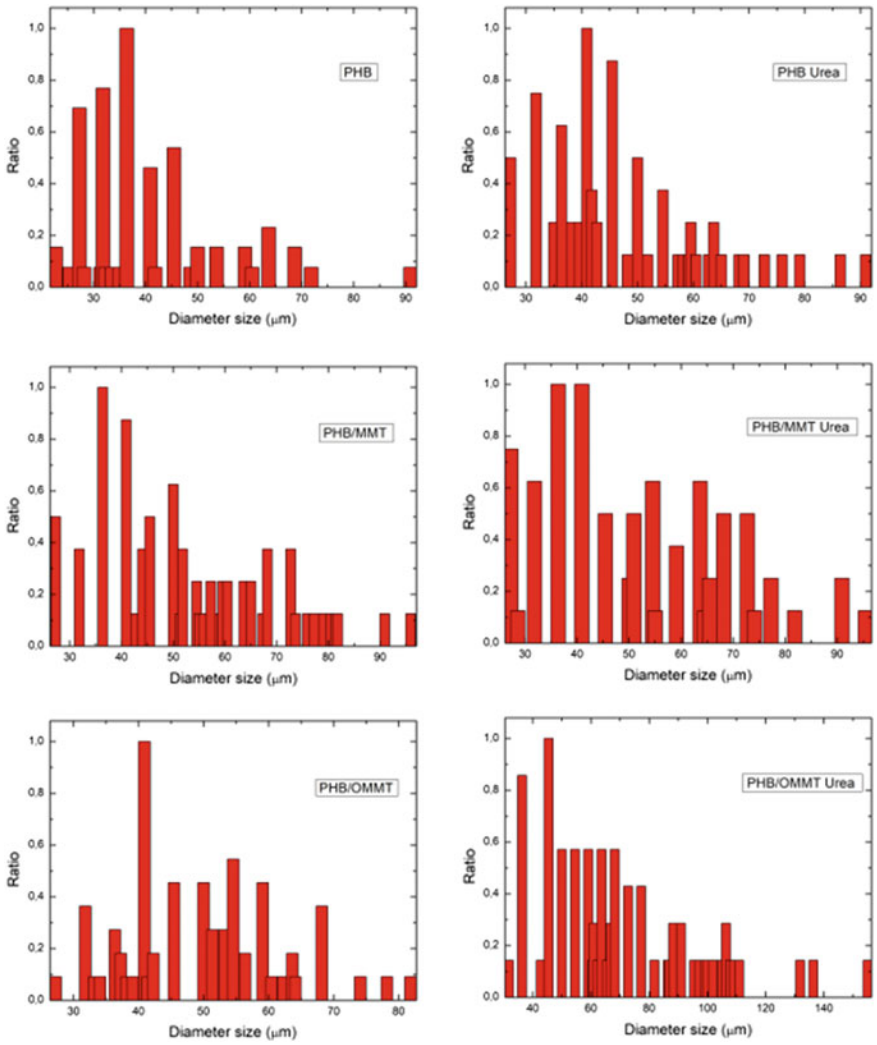

Fig. 3 Ratio of diameter size distribution of microcapsules

MMT, then it can be beyond the percolated limit and consequently reduce the mechanical properties [13].

Conclusion

XRD showed the obtaining of nanocomposites for PHB/MMT and PHB/OMMT, however PHB has its crystallinity declined when OMMT had been exfoliated in the polymeric matrix, which can be related to the reducing of mechanical properties of PHB/OMMT microcapsules, which presented fractures and defects surface. Nevertheless, microcapsules of PHB and nanocomposites showed spherical form and a good diameter size distribution.

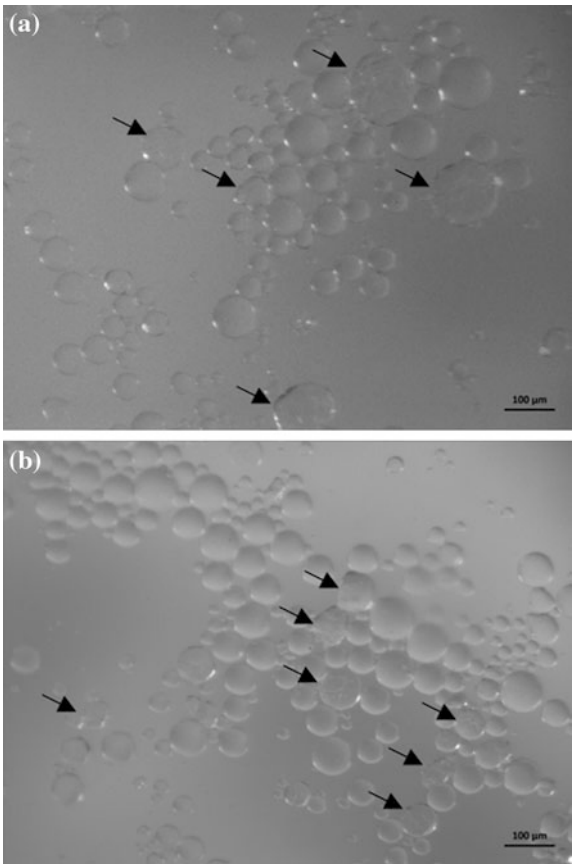

Fig. 4 Optical microscopy of **a** PHB/OMMT microcapsules and **b** PHB/OMMT microcapsules encapsulated with urea

Acknowledgements The authors are grateful to FAPESP for financial support of 12/51871-9 and 11/50027-7 projects. One of us (JCA) thanks to Coordination for Improvement of Higher Education Personnel (CAPES) for master's scholarship.

References

1. Civardi EA, Nunes A, Neto DS, Ragagnin VA, Godoy ER, Brod E (2011) Ureia De Liberação Lenta Aplicada Superficialmente E Ureia Comum Incorporada Ao Solo No Rendimento Do Milho. Agropec Trop 41(1):52–59. https://doi.org/10.5216/pat.v41i1.8146
2. Chien SH, Prochnow LI, Cantarella H (2009) Advances in agronomy. Elsevier, Burlington
3. Kansiz M, Billman-Jacobe H, McNaughton D (2000) Quantitative determination of the biodegradable polymer Poly(beta-Hydroxybutyrate) in a recombinant *Escherichia coli* strain by use of mid-infrared spectroscopy and multivariative statistics. Appl Environ Microbiol 66 (8):3415–3420. https://doi.org/10.1128/AEM.66.8.3415-3420.2000
4. Azeem B, Kushaari K, Man ZB, Basit A, Thanh TH (2014) Review on materials & methods to produce controlled release coated urea fertilizer. J. Control. Release 181(1):11–21. https://doi.org/10.1016/j.jconrel.2014.02.020
5. Botana A, Mollo M, Eisenberg P, Torres Sanchez RM (2010) Effect of modified montmorillonite on biodegradable PHB nanocomposites. Appl Clay Sci 47(3–4):263–270. https://doi.org/10.1016/j.clay.2009.11.001
6. de Paiva LB, Morales AR, Valenzuela Díaz FR (2008) Organoclays: properties: preparation and applications. Appl Clay Sci 42(1–2):8–24. https://doi.org/10.1016/j.clay.2008.02.006
7. Li M, Rouaud O, Poncelet D (2008) Microencapsulation by solvent evaporation: state of the art for process engineering approaches. Int J Pharm 363(1–2):26–39. https://doi.org/10.1016/j.ijpharm.2008.07.018
8. Bruno M, Tavares MIB, Motta LM, Miguez E, Preto M, Fernandez AOF (2008) Evaluation of PHB/ clay nanocomposite by spin-lattice relaxation time. Mater Res 11(4):483–485
9. Puglia D, Fortunati E, D'Amico DA, Manfredi LB, Cyras VP, Kenny JM (2014) Influence of organically modified clays on the properties and disintegrability in compost of solution cast poly(3-hydroxybutyrate) films. Polym Degrad Stab 99(1):127–135. https://doi.org/10.1016/j.polymdegradstab.2013.11.013
10. Brown EN, Kessler MR, Sottos NR, White SR (2003) In situ poly(urea-formaldehyde) microencapsulation of dicyclopentadiene. J Microencapsul 20(6):719–730. https://doi.org/10.1080/0265204031000154160
11. Zernov AL, Ivanov EA, Makhina TK, Myshkina VL, Samsonova OV, Feofanov AV, Volkov AV, Gazhva JV, Muraev AA, Ryabova VM, Shaitan KV, Ivanov SY, Bonartseva GA, Bonartsev AP (2015) Microcapsules of poly(3-hydroxybutyrate) for sustained protein release. Sovremennye Tehnologii v Medicine 7(4):50–56. https://doi.org/10.17691/stm2015.7.4.06
12. Moinard-Chécot D, Chevalier Y, Briançon S, Beney L, Fessi H (2008) Mechanism of nanocapsules formation by the emulsion-diffusion process. J Colloid Interface Sci 317 (2):458–468. https://doi.org/10.1016/j.jcis.2007.09.081
13. Pavlidou S, Papaspyrides CD (2008) A review on polymer-layered silicate nanocomposites. Prog Polym Sci 33(12):1119–1198. https://doi.org/10.1016/j.progpolymsci.2008.07.008

Part XII
Thermal Processing and Analysis

Buildup Formation Mechanism of Carbon Sleeve in Continuous Annealing Furnace for Silicon Steel

Mingsheng He, Guohua Xie, Xuecheng Gong, Wangzhi Zhou, Jing Zhang and Jian Xu

Abstract Graphite, which has a unique stack structure that enables a small friction coefficient, is used as one kind of the best hearth rolls to support and convey silicon steel strip in continuous annealing furnace. However, the buildup formation in/on the surface of carbon sleeve has always been a worldwide difficulty in the silicon steel industry. Based on the analysis of the microstructure, topography and composition of the buildups, combined with simulation experiments, the mechanism of forming buildups is discussed. The results show that buildups experience the process from nucleating to growing-up, and buildups are formed by nano liquid phase sintering (NLPS). Meanwhile, some countermeasures to reduce or prevent the formation of the buildups are proposed.

Keywords Silicon steel · Buildup · Mechanism · Continuous annealing Carbon sleeve

Introduction

Silicon steel strips are used in the core of a generator, a motor, a small size transformer and the like. Generally, silicon steel strip by hot or/and cold rolling process is decarburized, re-crystallized and annealed in continuous roller-hearth annealing furnace. Carbon sleeve is the most important kind of hearth rolls in the annealing furnace to support and convey silicon steel strips [1, 2]. Under the condition of the high temperature and H_2–N_2–H_2O weak oxidation or H_2–N_2 strong reducing atmosphere in the annealing furnace, buildups adhered (AD-buildup) to the surface of the carbon sleeve or buildups embedded (ED-buildup) in the surface of the carbon sleeve can form after using for a period of time, especially during the production of high-grade non-oriented silicon steel and some low- and medium-grade non-oriented silicon steel containing low melting point metal,

M. He (✉) · G. Xie · X. Gong · W. Zhou · J. Zhang · J. Xu
Wuhan Iron and Steel Co., Ltd., Wuhan 430080, China
e-mail: hms03@mails.thu.edu.cn

B. Li et al. (eds.), *Characterization of Minerals, Metals, and Materials 2018*, The Minerals, Metals & Materials Series,
https://doi.org/10.1007/978-3-319-72484-3_40

ED-buildups are much easier to form. Once buildups come into being in/on the surface of carbon sleeve, they will easily indent, bruise and scratch the surface of steel strip, which seriously affects the quality of steel strip surface and even causes degraded or waste products [3]. The quality and life time of carbon sleeve have been troubling the production of continuous annealing line for silicon steel for worldwide iron and steel enterprises [1].

In recent years, it has greatly attracted research attentions to buildup formation cause and mechanism of carbon sleeve. Many researchers and specialists think that the following three points are the main causes of buildup formation for silicon steel strip during continuous annealing [4–7]: (1) Each kind of damage and defect (oxidization, grain boundary etching, score, pit or the like) is formed on the roll surface; (2) A formation of metal particles due to reduction of an oxide under a reducible atmosphere and an activation of metals; (3) Some oxides for example, Fe_2O_3, Fe_3O_4, FeO, SiO_2, Al_2O_3 and MnO are subjected to a solid phase reaction with each other. In general, iron and its oxides particles can not react with other oxides without external force at 800–950 °C, even below 800 °C to form very hard buildups. This study was to discuss the real reason and mechanism of buildup formation of carbon sleeve.

Materials and Methods

In order to determine the microstructure and compositions of buildups, the buildups are sectioned along radial or axial direction, inlaid, ground, and polished. And then the as-prepared samples were observed and analyzed by a scanning electron microscope (SEM, Quanta 400, FEI Co., Netherland) equipped with energy-dispersive X-ray spectroscopy (EDS).

Online sintering experiments: (1) Nano-Fe_2O_3 powder with an average particle size of 30 nm was put into the alumina crucible; (2) The crucible was placed in the zone easy to form buildups in continuous annealing furnace; (3) The sintering samples were taken out from the furnace after about three months, and the microstructures of sinter body of nano-Fe_2O_3 powder were examined.

Results and Discussions

Topography and Composition of Buildups

Figure 1 shows the ED-buildups forming in the surface of carbon sleeve during the decarburizing and annealing for non-oriented silicon steel strips. Figure 1a–c are the photos of ED-buildups in the surface of carbon sleeve in low- and medium-temperature zone of the annealing furnace. Figure 1d is the photo of

ED-buildup in the surface of carbon sleeve in high temperature zone of the annealing furnace. ED-buildups may be in different shapes, such as cylinder-like, cone-like, barrel-like, and truncated cone-like. Most of the ED-buildups are in cylinder shape, and the axial direction of buildups parallels to that of carbon sleeve. Generally speaking, ED-buildups in low- and medium-temperature zone are bigger than high-temperature zone. Meanwhile, the size and shape of ED-buildups have relations to the pore size and shape in the surface of carbon sleeve [1, 2].

Figure 2 shows the AD-buildups forming on the surface of carbon sleeve during the decarburizing and annealing for non-oriented silicon steel strips. Some AD-buildups are in flaky or willow leaf shapes (Fig. 2a), others are completely irregular in shape (Fig. 2b), and the formation of the buildups has no regularity.

Figure 3a is the cross section SEM micrograph of the ED-buildup along radial direction (Perpendicular to the axis of the carbon sleeve) in the low-temperature zone (LTZ) of annealing furnace; Fig. 3b is the longitudinal section SEM micrograph of the ED-buildup along axial direction (Parallel to the axis of the carbon sleeve) in the high-temperature zone (HTZ). As shown in Fig. 3a, it can be seen that the buildup is composed of light and deep color belts in alternately dark and bright annular concentric circles [1]. As shown in Fig. 3b, it can be seen that the HTZ buildup also has dark and bright annular structure same to the LTZ buildup.

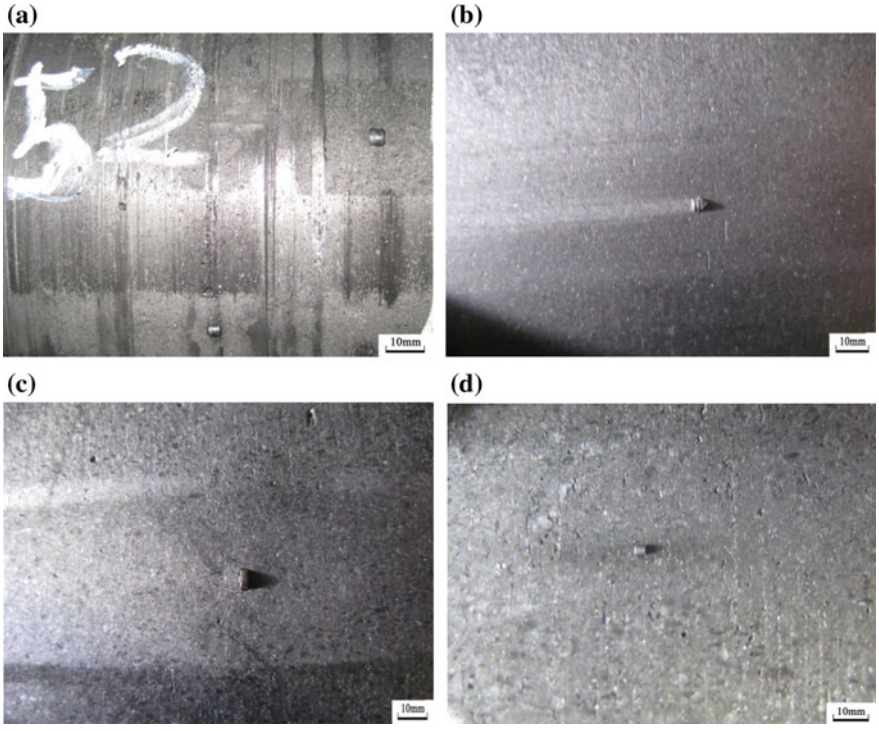

Fig. 1 Photos of ED-buildups in the surface of carbon sleeve

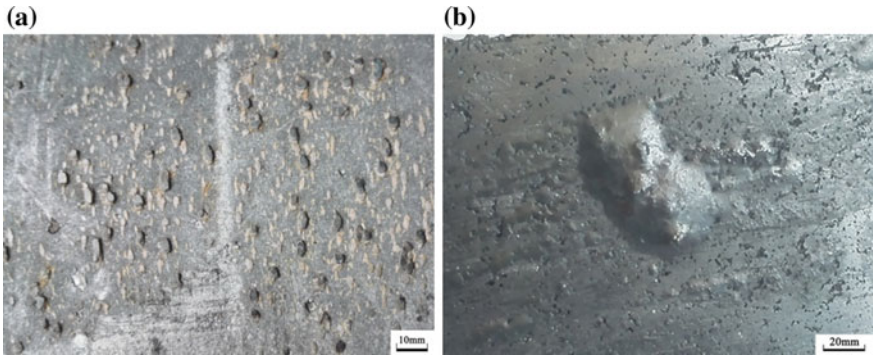

Fig. 2 Photos of AD-buildups on the surface of carbon sleeve: **a** flaky or willow leaf shapes; **b** irregular shapes

Therefore, the ED-buildup is formed gradually in the surface pore of carbon sleeve from layer to layer by accumulation. With the continuous growth of the buildup to a certain size, the buildup may have friction and wear with silicon steel strip. And then the buildup will further accelerate growth. Finally, the buildups can indent, bruise and scratch the surface of steel strip.

Figure 3c shows a ball-like ED-buildup forming in the surface pore of carbon sleeve, which is just bringing into contact with steel strip, but almost having no friction and wear with the strip. It was proved that the nucleation of buildup was formed in the surface pore of carbon sleeve and grown up gradually.

Figure 3d shows AD-buildups on the surface of carbon sleeve, which is irregular in shape. Although the AD-buildups were formed occasionally, it may result in the surface defects of steel strip. Once an AD-buildup was formed, it was very difficult to eliminate it by grinding rollers.

Figure 4a, b are the cross section partially enlarged SEM micrographs of the LTZ ED-buildup along radial direction of carbon sleeve. Figure 4c, d are the longitudinal section SEM micrographs of the HTZ ED-buildup along axial direction of carbon sleeve. Figure 4e, f are the partially enlarged SEM micrographs of the ED-buildup without abrasion in the surface of carbon sleeve and the AD-buildup on the surface of carbon sleeve, respectively. As shown in Fig. 4a, it can be seen that the grain sizes mostly fall in a range of 20–30 μm. However, the grain sizes (Fig. 4e, f) are only a few microns, even below 1 μm (Fig. 4b).

Figure 5a, b are respective EDS spectrums of the light belt and deep color belt of the LTZ ED-buildup. The EDS spectrum (Fig. 5a) of light color belt shows strong peaks of Fe and weak peaks of Al, Si, C and O. However, the EDS spectrum (Fig. 5b) of deep color belt shows strong peaks of Al, O, Fe, Si and weak peaks of Na, Mg and P. Figure 5c, d are respective EDS spectrums of the light color and deep color position of the HTZ ED-buildup. The EDS spectrum (Fig. 5c) of light color position shows strong peaks of Fe and weak peaks of Si. The EDS spectrum (Fig. 5d) of deep color position shows strong peaks of Si and weak peaks of Fe, Al,

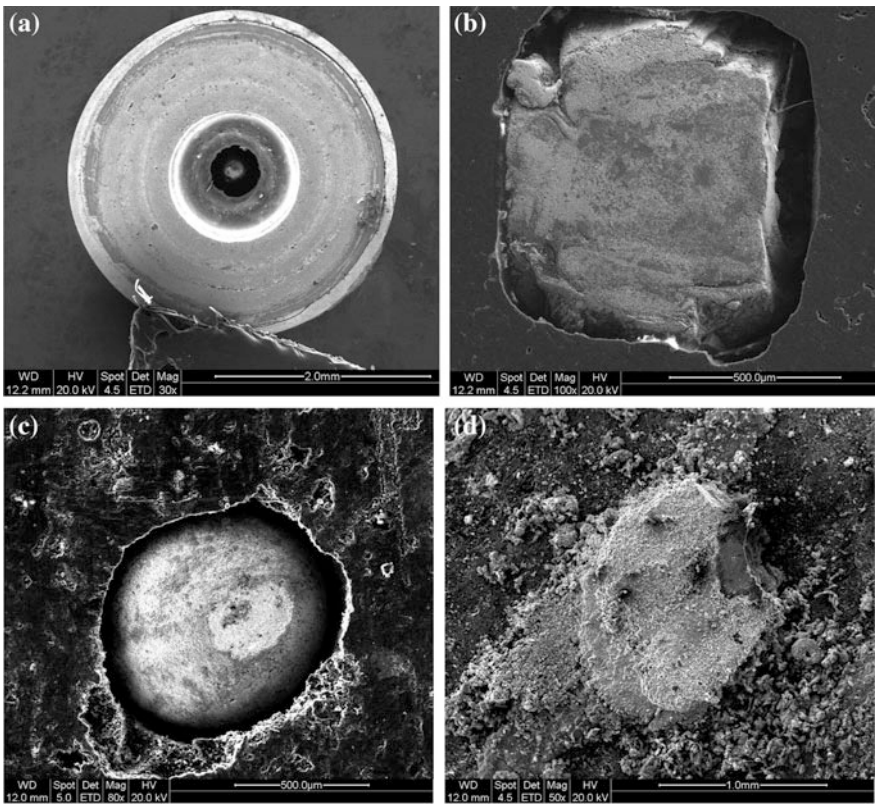

Fig. 3 SEM micrographs of the buildups: general view. **a** Cross section along radial direction; **b** longitudinal section along axial direction; **c** no friction and wear with steel strip; **d** AD-buildup

O, and Mn. Figure 5e, f are respective EDS spectrums of the light belt and deep color belt of the LTZ AD-buildup. The EDS spectrum (Fig. 5e) of light color position shows strong peaks of Fe, P and weak peaks of C and O in the AD-buildup. Nevertheless, the EDS spectrum (Fig. 5f) of deep color position shows strong peaks of Fe and weak peaks of Mn, P and O.

The results show that the main components of buildups are iron, a small amount of iron oxide, and oxides of Mn, Al, Si, or some compound oxides. Phosphorus content of some AD-buildups and ED-buildups of low- and medium-temperature carbon sleeve is relatively high [8]. Phosphate is widely used as an antioxidant in the production of low- and medium-temperature carbon sleeve. Meanwhile, phosphate is a high-temperature binder commonly used in various industries. Phosphate antioxidants can promote or accelerate the formation of buildups for low- and medium-temperature carbon sleeve during the continuous annealing of non-oriented silicon steel strips.

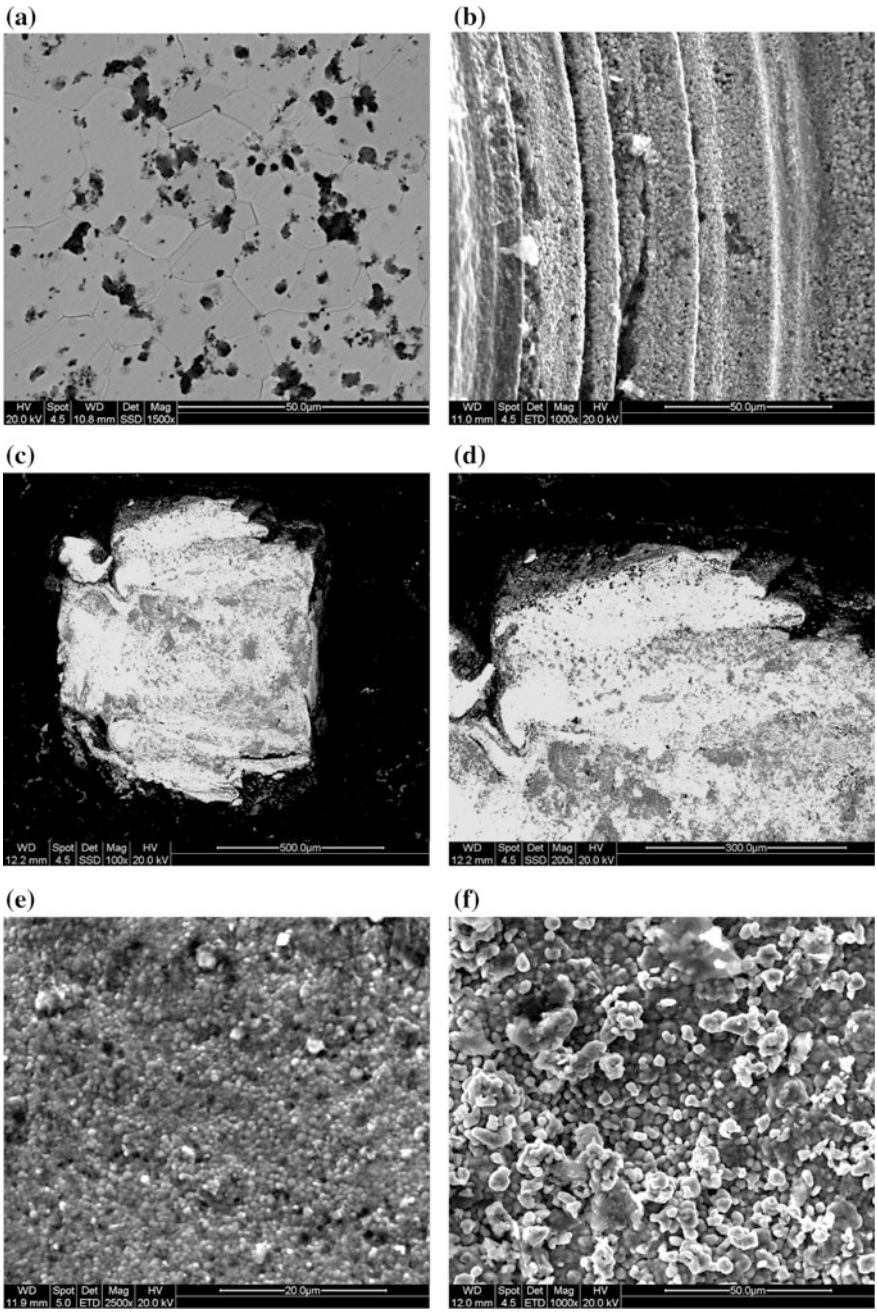

Fig. 4 SEM micrographs of the buildups: partially enlarged. **a** and **b** Along radial direction; **c** and **d** along axial direction; **e** no friction and wear with steel strip; **f** AD-buildup

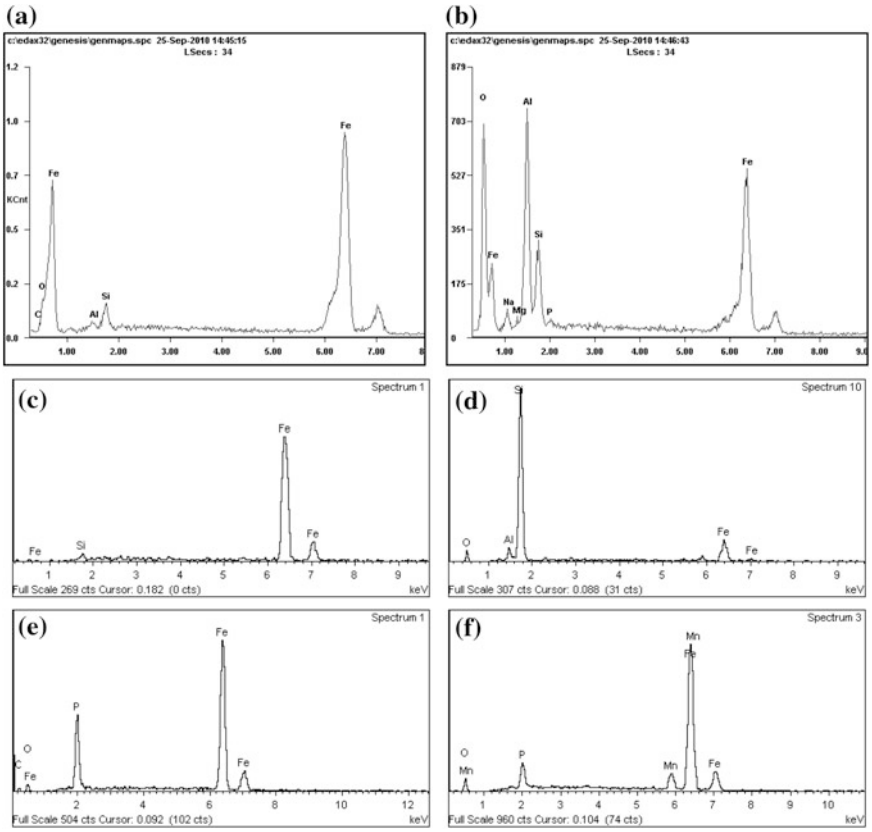

Fig. 5 EDS spectrums at different positions of the buildup. **a** Light color belt and **b** deep color belt in the LTZ; **c** light color and **d** deep color positions in the HTZ; **e** light grey and **f** dark grey position of AD-buildup

Causes for Buildup Formation of Carbon Sleeve

According to the results of analysis on the microstructure, topography and composition of the buildups, it can be seen that ED-buildups in the surface of the carbon sleeve experienced the "nucleation-growing up" process and the main components were iron, a small amount of binary oxides or compound oxides, and phosphide. Obviously, the two necessary conditions for ED-buildup formation were: (1) there exist big pores in the surface of carbon sleeve; (2) rich material sources such as iron scale, iron rust, greasy dirt, dust, etc [1, 2]. AD-buildups without regularity were formed on the surface of the carbon sleeve because of phosphate antioxidant, high temperature and special atmosphere in annealing furnace.

Graphite is chemically inert in non-oxygen media. At normal temperature and pressure, graphite does not make any chemical reactions except the long-term

immersion in nitric acid, hydrofluoric acid or in fluorine, bromine and other strong oxidizing atmosphere leads to form intercalation compounds slowly. Graphite is not subject to any acid, alkali and salt corrosion and does not react with any organic compound. However, due to complex procedures and processes of producing carbon sleeves together with porous material itself, it is inevitable to form bigger holes ore pores in the surface during production and processing.

Generally speaking, graphitization degree of carbon sleeve is over 70%. Although the surface of carbon sleeve is smooth after soaking of various chemical substances and processing, graphite begin to react with water vapor over 700 °C. The carbon in silicon steel has great influence on the magnetic. Carbon not only strongly inhibits grain growth, but also expands γ phase zone. Hence, the excessive amount of carbon makes the shift quantity of two phases α and γ increase in normalizing treatment, refine crystal structure, and cause the increase in iron loss. One of the important purposes of the annealing to the finished product of silicon steel is decarburization. Therefore, holes or pores inevitably appear due to oxidation during the use of carbon sleeves in continuous annealing furnace for silicon steel. As a result, these holes or pores provide the necessary conditions for stubborn ED-buildups to form. When there are larger pores together with rich iron scale, iron rust, greasy dirt, dust, and other material sources, the stubborn ED-buildups could form in a relatively short time.

Many other factors influence buildup formation of carbon sleeves, such as atmosphere, dew point, uncleanness of alkali wash, outer-sync of the actual speed of carbon sleeves and the running line speed of steel strip, uncleanness of inside furnace, etc.

Buildup Formation Mechanism

The buildup has iron content from 70 to 95%. All the dense buildups are made up of micron sized particles, even smaller particles, and harder than silicon steel strip. However, how to form so dense and hard buildups without external force at 800–950 °C, even below 800 °C? It is well-known that the melting point is related to the size of the nanoparticle, and the smaller particles, the lower melting point. Based on investigation and analysis of the microstructure, topography and composition of the buildups, an idea was proposed that the buildup could be formed by liquid phase sintering of nano-Fe powder. Nevertheless, it was impossible that there were a great deal of nano-Fe powder on the surface of silicon steel trip or in the annealing furnace. Nano-Fe powder could come from nano-Fe_2O_3 or other nano-oxides of iron powder by the reduction of hydrogen or carbon.

Online simulation experiments were conducted in annealing furnace for silicon steel strip. Alumina crucibles containing nano-Fe_2O_3 powder were placed in different zone of annealing furnace. The results showed that all the powder had been completely sintered to form dense and hard sintering bulk after about three months. The microstructures and composition (Fig. 6) of sinter bulk were examined by

SEM and EDX. The grain sizes mostly fall in a range of 20–40 μm (Fig. 6b, c), and the chemical composition is only iron (Fig. 6d). The experimental results show that buildups experience the process from nucleating to growing-up, and buildups are formed by nano liquid phase sintering (NLPS).

Measures to Control and Reduce Buildups Formation

According to the present production technology, equipment and conditions, it is impossible to completely eliminate buildups, but it is possible to take some process control in technology or preventive measures to reduce buildups formation in continuous annealing furnace for silicon steel [1, 2]. The smaller pores in the surface of carbon sleeve are, and the less material sources for forming buildups such

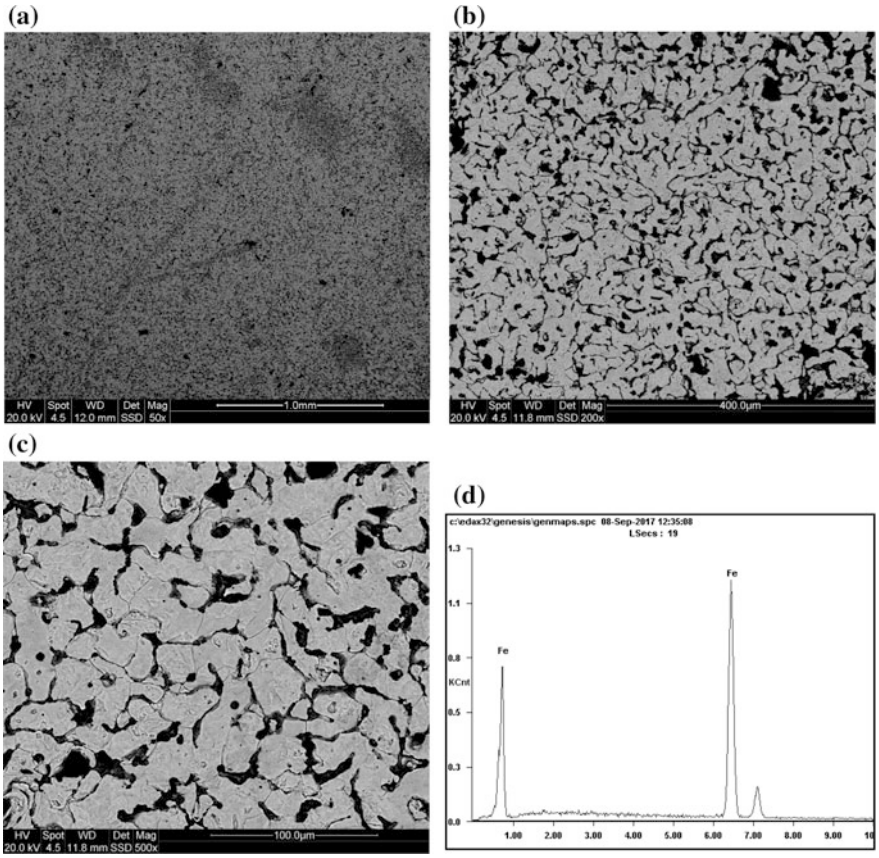

Fig. 6 SEM micrographs and EDS spectrum **d** of sinter bulk. **a** General view; (**b**) and **c** partially enlarged

as iron scale, iron rust, iron oxidation, greasy dirt on the surface of silicon steel strip are, the less the possibility of buildup formation is. In order to control and reduce buildup formation, extend the service life of carbon sleeve, the following methods and measures are proposed:

(1) Further improve the surface quality of carbon sleeve and enhance its oxidation resistance, wear resistance, and buildup formation resistance;
(2) Improve descaling equipment and process, strengthen the pickling, and reduce iron scale;
(3) Strictly monitor atmosphere and dew point to prevent steel strip oxidation;
(4) Strengthen the cleanness of steel strip and alkaline wash to reduce iron rust, greasy dirt;
(5) Clean dust regularly in continuous annealing furnace;
(6) Use the adjusting steel roll with good surface quality;
(7) Arrange the production properly;
(8) Monitor and correct the motor of carbon sleeves and adjust the inconsistent roller speed of carbon sleeves in time.

Conclusions

Buildups experience the process from nucleating to growing-up, and buildups are formed by nano liquid phase sintering. The pore sizes and shapes in the surface of carbon sleeve determine the sizes and shapes of ED-buildups. Phosphate antioxidants can promote or accelerate the formation of buildups for low- and medium-temperature carbon sleeve during the continuous annealing of non-oriented silicon steel. It is feasible and effective to take some process control in technology or preventive measures to reduce buildups formation and extend the service life of carbon sleeve and improve the production quality and production efficiency for silicon steel.

References

1. He MS, Peng SJ, Xue GF et al (2011) Cause analysis about buildup formation of carbon sleeve in continuous annealing furnace for silicon steel. Adv Mater Res 317–319:1954–1959
2. He MS, Peng SJ, Xue GF et al (2015) Cause analysis on buildup formation of carbon sleeve in continuous annealing furnace for non-oriented silicon steel produced by CSP process. Charact Miner Metals Mater 2015:587–593
3. He MS, Peng SJ, Xue GF et al (2012) Cause analysis about breakage of carbon sleeve in continuous annealing furnace for silicon steel. Iron Steel Res 40:24–27
4. Midorikawa S, Katoh S (2003) Cermet powder for sprayed coating excellent in build-up resistance and roll having sprayed coating thereon. US. Patent 6,572,518B1, 3 June 2003

5. Nakahira A, Harada Y, Mifune N (1991) Roll for use in heat treating furnace and method of producing the same. US. Patent 5,070,587, 10 Dec 1991
6. Midorikawa S, Yamada T, Nakazato K (2001) Development of Surface-modifying technologies by thermal spraying of process rolls in steel production process. Kawasaki Steel Tech Rep 45:57–63
7. Matthews S, James B (2010) Review of Thermal spray coating applications in the steel industry: part 1—hardware in steel making to the continuous annealing process. J Therm Spray Technol 19(6):1267–1276
8. He MS, Luo ZH, Xue GF et al (2015) Carbon sleeve for silicon steel in continuous annealing furnace. Metallurgical Industry Press, Beijing

Pulse Parameter Characterization in Microdrilling of Maraging Steel 300 Alloy

Yeole Shivraj Narayan, Nunna Nagabhushana Ramesh, Banoth Balu Naik and Alluru Ramya

Abstract MicroEDM process is mainly used for producing miniaturized features like microholes on different types of materials that are hard to cut and difficult to machine. One typical application of microEDM process is microhole drilling operation. Choice and utilization of optimum pulse parameters is of utmost importance for achieving superior surface quality and higher machining rates. However, the process is characterized by low machining rates and considerable overcut as compared to conventional EDM drilling. An attempt is made to investigate the effect of pulse parameters on maraging steel 300 alloy during microEDM drilling. Parameters like pulse on time, pulse off time, voltage and current are explored through 09 experiments replicated thrice using Taguchi method. Machining characteristics like material removal rate and overcut are studied while drilling micro holes of 500 μm diameter using brass electrode. Evaluation of microhardness after microdrilling is also performed. It is found that pulse on time and current influenced the machining characteristics. Minimal change is observed in the microhardness of the alloy after microdrilling.

Keywords MicroEDM · Microholes · Material removal rate · Overcut Microhardness · Maraging steel 300 alloy · Taguchi method · Signal-to-noise ratio

Y. Shivraj Narayan (✉) · A. Ramya
Department of Mechanical Engineering, VNR VJIET, Hyderabad 500090, Telangana, India
e-mail: shivrajyeole@vnrvjiet.in

A. Ramya
e-mail: ramya1989_alluru@yahoo.com

N. Nagabhushana Ramesh
Department of Mechanical Engineering, Anurag Group of Institutions, Hyderabad 500088, Telangana, India
e-mail: nunna.nb@gmail.com

B. Balu Naik
Department of Mechanical Engineering, JNTU College of Engineering, Hyderabad 500085, Telangana, India
e-mail: banothbn@rediffmail.com

B. Li et al. (eds.), *Characterization of Minerals, Metals, and Materials 2018*, The Minerals, Metals & Materials Series,
https://doi.org/10.1007/978-3-319-72484-3_41

Nomenclature

I	Discharge current (A)
MRR	Material removal rate (mm^3/min)
η *or S/N*	Signal-to-noise ratio (dB)
OC	Overcut (μm)
T_{On}	Pulse on time (μs)
T_{Off}	Pulse off time (μs)
V	Voltage (V)
I	Current (A)
HV	Vickers hardness number

Introduction

Manufacturing of miniaturized components in the size range of 1–999 μm is called as micromachining [1]. Micro-Electric Discharge Machining (Micro-EDM) or simply micro-EDM, is a variant of electrical discharge machining (EDM) process but fundamentally similar to it. The work material is removed by a series of rapidly recurring spark discharges between the tool electrode and the workpiece. The two electrodes are separated by a dielectric medium that is initially nonconductive. When the electrodes come closer to each other, dielectric strength of medium breaks down and the medium becomes conductive resulting in the generation of sparks between the electrodes. The thermal energy released is used for removing the material by melting and evaporation process. The released energy can be accurately controlled for machining micro-features on any electrically conductive material. Parameters like type of pulse generator, the resolution of the axes of movement and diameter of the electrode distinguishes micro-EDM from EDM. In micro-EDM, pulse generator produces very small pulses within pulse duration of a few micro seconds or nano seconds. Therefore, micro-EDM utilizes low discharge energies ($\sim 10^{-6}$ to 10^{-9} J) to remove small volumes ($\sim$0.05–500 μm^3) of material. This process can machine any type of conductive and semi-conductive materials with high surface accuracy irrespective of material hardness. It is favored especially for the machining of difficult-to-cut material due to its high efficiency and precision. Small volumetric material removal of micro-EDM provides ample opportunities in the manufacturing and fabrication of micro-dies and micro-structure such as micro holes, micro slot, and micro gears etc. [2]. Micro-EDM can be used for different operations like micro-EDM drilling, micro-EDM milling, micro-EDM die sinking, micro-EDM contouring, micro-EDM dressing, and micro-wire EDM grinding (micro-WEDG). Various miniaturized parts and components such as holes, nozzles and gears, used extensively in micro-electro-mechanical systems (MEMS), biomedical applications, automotive industry, and defense industry, are machined using this process [3].

Kuneida et al. [4] have shown the prospects of micro-EDM technology by interrelating recent achievements in fundamental studies on EDM with the newly developed advanced application technologies. Micro-EDM has got the capability of machining complex shapes onto any conductive material with very low forces. The forces are very small because the electrode and the workpiece do not come into contact during the machining process, thus, providing advantages to both the electrode and the workpiece. Low set-up cost, high aspect ratio, enhanced precision and large design freedom are other advantages of this process. Since, micro-EDM is a contactless material removal process; generally observed problems during machining like mechanical stress, chatter and vibration are eliminated. Therefore, micro-EDM is very effective and efficient process in the areas of micromachining and fabrication. Even though it offers multiple advantages, micro-EDM is known to be a slow machining process with the higher tool wear rate. Shape inaccuracies in the micro machined features are the resultant of tool wear. Another drawback is the formation of a heat affected layer on the machined surface. Since it is impossible to remove all the molten part of the workpiece, a thin layer of molten material remains on the workpiece surface, which re-solidifies during cooling [2]. The schematic of experimental setup used in the micro EDM drilling process is shown in Fig. 1. It consists of single-discharge RC circuit with one end connected to the electrode and the other to the workpiece. Dielectric medium is used for insulation as well as for flushing out the debris after machining [3]. Electrode and workpiece are separated with a very small gap, called as inter-electrode gap wherein the discharging of the pulsed arc occurs. The electrode shape is copied with an offset equal to the gap size and the liquid is selected to minimize the gap to obtain precise machining. A certain gap width is needed to avoid short circuiting especially for electrodes that are sensitive to vibration. Initially, a high voltage current is needed to discharge in order to overcome the dielectric breakdown strength of the small gap.

A channel of plasma (ionized and electrically conductive gas with high temperature) is formed between the electrodes and its further development depends on the discharge durations. Discharge occurs at high frequencies between 10^3 and 10^6 Hz since the metal removal per discharge is very small. For every pulse, discharge occurs at a particular location where the electrode materials are

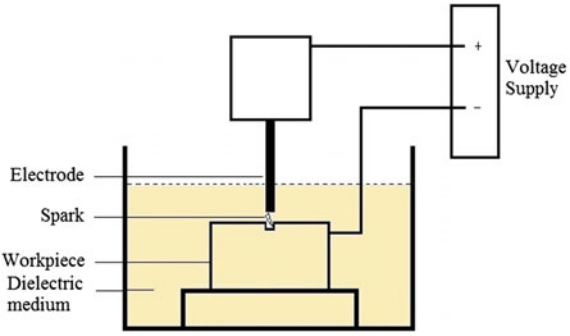

Fig. 1 Schematic of micro-EDM drilling process

evaporated or ejected in the molten phase then a small crater is generated both on the electrode and workpiece surfaces. The removed material is then cooled and re-solidified in the dielectric liquid forming several hundreds of spherical debris particles which will be flushed away from the gap by the dielectric flow. The temperature of the plasma and the electrode surfaces that is in contact of the plasma rapidly drops at the end of the discharge duration, resulting in the recombination of ions and electrons and also the recovery of the dielectric breakdown strength. It is important for the next pulse discharge to occur at a spot distanced sufficiently far from the previous discharge location so as to obtain stable condition in EDM. This is because the previous location will result in having a small gap and it is contaminated with debris particles which may weaken the dielectric breakdown strength of the liquid. The time interval for the next discharge pulse should be long so that the plasma that is generated by the previous discharge can be fully de-ionized and the dielectric breakdown strength around the previous discharge location can be recovered by the time the next voltage charge is applied. If discharge occur at the same location, it results in thermal overheating and non-uniform erosion of the workpiece. Achieving maximum MRR with minimum overcut and surface roughness is desired in EDM operations [5].

Problem Definition

MicroEDM is essentially a sparking process which is inherently difficult to control thereby achieving accurate feature is a tough task. Such a process consumes very little energy, so the machining rates are also lower. Drilling of micro holes with aspect ratio ranging from high to ultra-high range is an area of current research. Nowadays microholes are extensively used in various applications in aerospace, medical, automotive sectors. This justifies the need to drill good quality and high aspect ratio microholes with superior machining rates on hard and difficult to cut materials like maraging steel 300 alloy. However, in order to achieve it, many variables need to be controlled effectively that affect the quality of holes. This work investigates experimentally the effect of various process parameter combinations on material removal rate and overcut in micro-EDM drilling of maraging steel 300 alloy using Taguchi methodology. The effect of various process parameters and microhardness of micro drilled hole surfaces on a maraging steel 300 alloy are studied and discussed elaborately.

Experimental Procedure

M/s. Toolcraft India made high precision micro-EDM machine tool V40506 is used for experimental investigation on maraging steel 300 alloy. Machine tool employs RC-type pulse generator and has the ability of performing variety of operations like

micro-drilling, micro milling etc. Maraging steel 300 alloy is used as the work material because of its excellent properties and applicability in various sectors. Workpiece dimensions are 55 mm × 20 mm × 5 mm. Chemical composition of the workpiece is shown in Table 1.

Tool (electrode) material used is brass. Deionized water is used as dielectric to avoid the formation of carbon that occurs due to the use of kerosene in EDM process. Pulse parameters used are pulse on time, pulse off time, voltage and current. Experiments are carried out using L_9 (3^4) orthogonal array based on Taguchi design [6–8]. Three replicates of L_9 OA are performed. Table 2 shows the various settings of machining parameters used in the experimentation. Figure 2 shows the 27 micro holes drilled on maraging steel 300 alloy using brass electrode of 500 µm diameter.

Output Factors and Their Estimation

Material removal rate In micro-EDM, sparks are produced between the workpiece and tool during machining. Each spark produces a tiny crater along the cutting path by melting and vaporization, thus eroding the workpiece to the shape of the tool. Material Removal Rate (MRR) is calculated by considering the weight of the workpiece before and after micro drilling as shown below in Eq. 1 [6].

$$\text{MRR} = \frac{W_b - W_a}{t \times \rho} \left(\text{mm}^3/\text{min}\right) \tag{1}$$

where

W_b Weight of workpiece before machining, g
W_a Weight of workpiece after machining, g
t Machining time, min
ρ Density of maraging steel 300 alloy = 8.1 g/cm^3

Overcut It is the discharge by which the machined hole in the workpiece exceeds the tool electrode size and is determined by both the initiating voltage and the discharge energy. EDMed cavities produced are always larger than the electrode. This difference is called as overcut (OC). OC is expressed as half the difference of diameter of the hole produced to the tool electrode diameter as shown in Eq. 2, [9].

$$\text{OC} = \frac{Dw - De}{2} \tag{2}$$

where

Dw Diameter of hole produced in the workpiece, µm
De Diameter of tool electrode, µm

Table 1 Composition of maraging steel 300 alloy

Composition	Fe	Ni	Co	Mo	Ti	Al	Mn	Si	C	P	S
Weight %	67.50	18.21	8.34	5.12	0.61	0.069	0.061	0.056	0.026	0.005	0.004

Table 2 Machining parameters

Control factors	Level 1	Level 2	Level 3
Pulse on time (μs)	1	5	9
Pulse off time (μs)	3	6	9
Voltage (V)	30	60	90
Current (A)	3	4	5

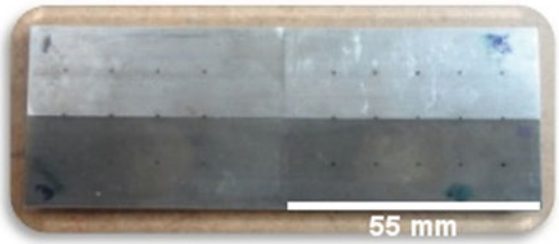

Fig. 2 Microholes drilled on maraging steel 300 alloy

Table 3 Material removal rate in drilling of microholes

Exp. Nos.	Factors				Average MRR (mm^3/min)
	T_{On} (μs)	T_{Off} (μs)	V (V)	I (A)	
1	1	3	30	3	44.331
2	1	6	60	4	44.349
3	1	9	90	5	44.356
4	5	3	60	5	44.342
5	5	6	90	3	44.325
6	5	9	30	4	44.352
7	9	3	90	4	44.303
8	9	6	30	5	44.389
9	9	9	60	3	44.315
					$\mu = 44.340$ & $\sigma = 0.025$

Results and Discussions

Average results of 27 experiments for material removal rate and overcut are presented in Tables 3 and 4 respectively.

Table 4 Overcut in the microholes

Exp. Nos.	Factors				Average OC (μm)
	T_{On} (μs)	T_{Off} (μs)	V (V)	I (A)	
1	1	3	30	3	71.57
2	1	6	60	4	47.81
3	1	9	90	5	9.17
4	5	3	60	5	36.17
5	5	6	90	3	21.35
6	5	9	30	4	86.76
7	9	3	90	4	76.76
8	9	6	30	5	82.04
9	9	9	60	3	53.43
					$\mu = 53.89$ & $\sigma = 27.65$

Effect of Process Parameters on MRR

Material removal rate is recorded for the 27 microholes in terms of weight of the workpiece before and after the microdrilling operation. Table 3 indicates the average MRR of the 27 microholes with a mean of $\mu = 44.340$ mm^3/min and standard deviation of $\sigma = 0.025$ mm^3/min. It is observed that MRR is highest when pulse on time is at 9 μs, pulse off time is at level 6 μs, voltage is at 30 V and discharge current is at 5 A.

In comparison to other alloys, MRR for maraging steel 300 alloy is observed to be more as anticipated due to its low melting point.

Figure 3 shows the effect of pulse parameters on micro hole drilling of 500 μm diameter holes on maraging steel 300 alloy. Increasing pulse on time makes the spark plasma channel larger in size. But this results in reduction of energy density in the channel area. Also, it reduces the energy consumed per unit area by workpiece. Although energy supplied by the plasma dissolves the work material, it lacks the required bursting pressure for flushing of the molten metal. Residual debris gets stuck and is carried away by the flowing dielectric thus decreasing the MRR. MRR initially increases and then decreases with increasing pulse off time. With higher pulse off times, properly energized sparks are not generated thereby reducing MRR. Mixed response is observed in the case of increasing voltage. MRR initially decreases and then increases with increasing voltage. MRR is increasing with increase in current as it increases the spark energy.

Effect of Process Parameters on OC

Overcut is measured in terms of the average diameter at the entry and exit of the 27 micro holes.

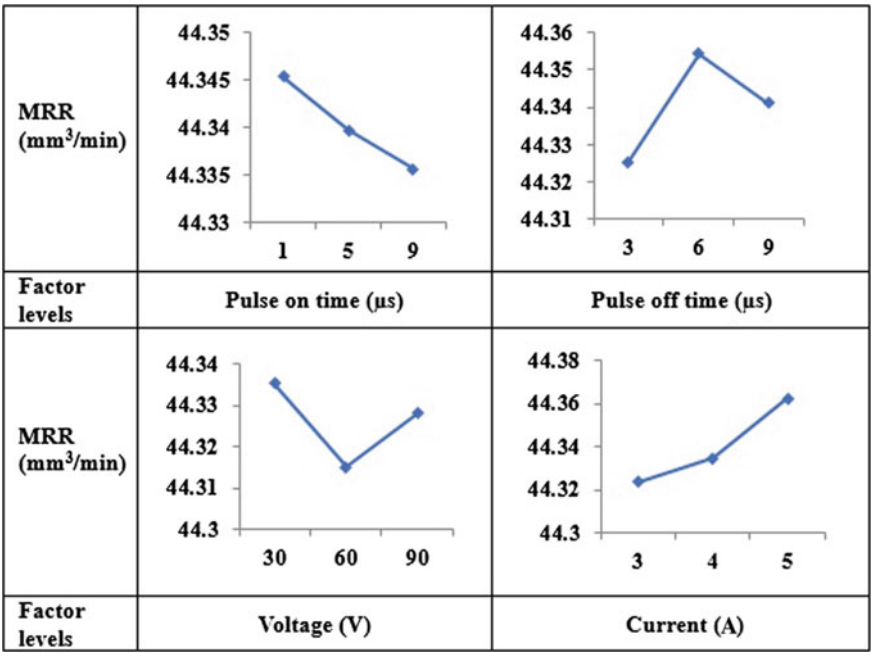

Fig. 3 Effect of process parameters on material removal rate

Table 4 indicates the average overcut values of the 27 microholes with a mean of $\mu = 53.89$ µm and standard deviation of $\sigma = 27.65$ µm. Least overcut of 9.17 µm is obtained at pulse-on time of 1 µs, pulse-off-time at 9 µs, voltage of 90 V and discharge current is at level 5 A. Similarly, a maximum overcut of 86.76 µm is witnessed at machining conditions of high pulse on time, medium pulse off time, medium current and low voltage respectively. Figure 4 shows the effect of process parameters on the overcut. Overcut is observed to increase with increasing pulse times. Prolong pulse on duration significantly increase overcut because of the extension of plasma channel at the areas surrounding the micro tool. Overcut rises with increasing pulse on time and drops with increasing pulse off time. However, voltage and current exhibited interesting results. Overcut is seen to increase initially and decrease later with increase in voltage and current levels. One of main reasons for overcut to exist is improper conveying of the dielectric liquid. Because of this, diameter at the entry of micro hole expands. Other reason could be the debris accumulated near the edges of the micro holes. This results in initiation of secondary sparking which causes larger entrance diameter.

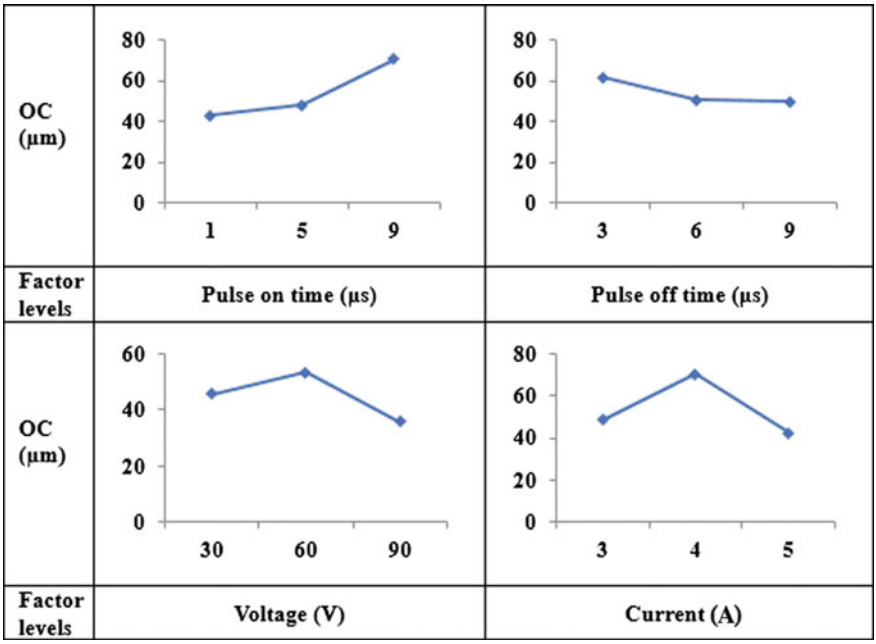

Fig. 4 Effect of process parameters on overcut

Evaluation of Microhardness

Microhardness is the hardness of the substance measured by a diamond point indenter that penetrates microscopic areas [10]. Vickers hardness tester is used for the measurement of microhardness on the surfaces of the microholes drilled on maraging steel 300 alloy using microEDM process. The Vickers hardness test consists of indenting the test material with a diamond indenter, in the form of a right pyramid with a square base and an angle of 136° between opposite faces subjected to a load of 1–100 kgf. Full load is normally applied for 10–15 s. The two diagonals of the indentation left in the surface of the material after removal of the load are measured using a microscope and their average calculated. The area of the sloping surface of the indentation is calculated using Eq. 3.

$$HV = \frac{2F\ \sin\left(\frac{136^\circ}{2}\right)}{d^2} \quad or \quad HV = 1.854\frac{F}{d^2}\ approximately \tag{3}$$

where

HV Vickers hardness
F Load in kgf
d Arithmetic mean of two diagonals d_1 and d_2 (mm)

Vickers hardness test allows to take extremely accurate readings using one type of indenter for all types of metals and surface treatments. Figure 5a,b shows the Vickers hardness tester used in the evaluation and schematic of the diamond indenter respectively. The phenomenon of severe thermal cycles in microEDM process results in higher microhardness on the top layer of the eroded surfaces. It is normal to anticipate such microhardness at the eroded surfaces. Three different settings of current are used in the experimentation, so microhardness is measured at low and high current conditions i.e., 3 A and 5 A. Microhardness values at these settings are measured on the surfaces of microEDM drilled holes of 500 µm diameter and are shown in Table 5.

As compared to base material hardness of 540 HV, there is minimal change in the microhardness level of the surfaces of microholes drilled at low current and high current conditions.

Figure 6 shows the effect of pulse parameters on the microhardness of surfaces of microdrilled holes. An increase in microhardness with increasing pulse times and current is observed whereas voltage displayed a random effect. MicroEDM surfaces display increased microhardness to some extent (minimal) than base metal hardness due to the use of deionized water which avoids the occurrence of carburization [11]. Thus, the quenching effect of water dielectric is observed to be more effective in microEDM.

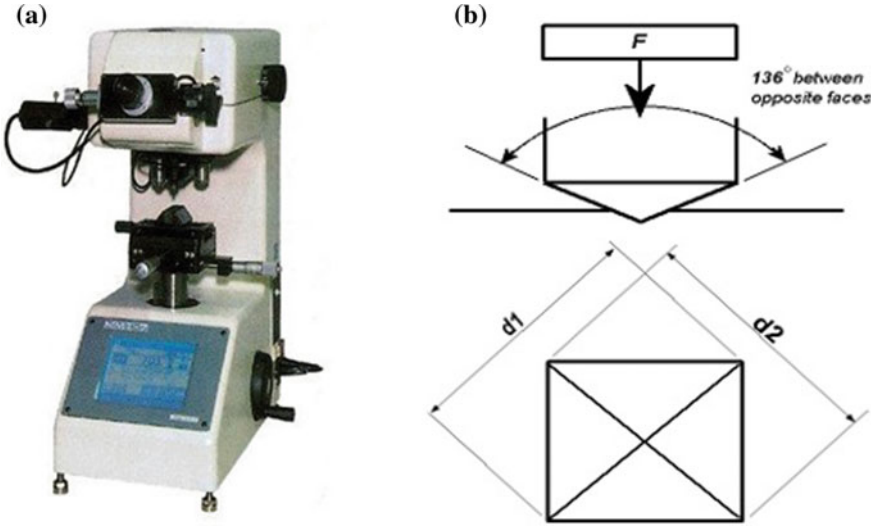

Fig. 5 **a** Vickers hardness tester, **b** Schematic of diamond indenter

Table 5 Microhardness readings

Tool material: brass	Work material: maraging steel 300 alloy (540 HV)
Machining parameters	Microhardness (HV)
Low current (3 A)	556
High current (5 A)	570

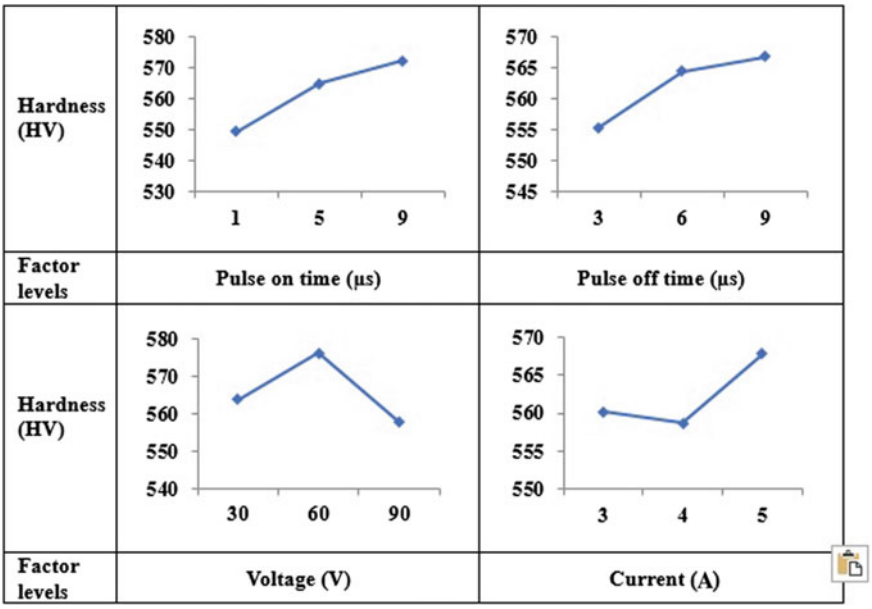

Fig. 6 Response graph of factor effects on microhardness

Conclusions

Following broad conclusions are drawn from this experimental investigation.

- In general, higher MRR is achieved at higher levels of current. However, random effect is observed in case of pulse off time and voltage parameters whereas MRR is decreasing with increasing pulse on time.
- MRR of maraging steel 300 alloy is significantly higher due to its low melting point.
- Accuracy of microholes, in terms of overcut, is found to be guided mainly by pulse on time and current. Higher current and prolong pulse on period significantly increase the extension of plasma channel at the areas surrounding the tool electrode thereby increasing overcut. Pulse off time and voltage have shown random effect. Accuracy of holes drilled in microEDM process is higher.

- Microhardness of microholes drilled in microEDM process is influenced mainly by pulse on time and current. Microhardness is found to increase with increasing pulse on time and current. It is believed that the quenching effect of water dielectric may be more effective in microEDM.
- There is minimal change in the microhardness value of maraging steel 300 alloy after microdrilling operation.

Acknowledgements The authors express their gratitude to M/s. Sharp Tools & M/s. Krushi Engineers Hyderabad for extending help and support in carrying out the experimentation. Special thanks are due to ARCI Hyderabad and Defence Metallurgical Research Laboratory Hyderabad for allowing to use their facilities for analysis purpose. Last but not the least; the authors thank all those who contributed directly or indirectly in executing the project.

References

1. Masuzawa T, Tonshoff HK (1997) Three-dimensional micromachining by machine tools. Ann CIRP 46(2):621–628
2. Bleys P, Kruth J, Lauwers B (2004) Sensing and compensation of tool wear in milling EDM. J Mater Process Technol 149:139–146
3. Mahendran S et al (2010) A review of micro EDM. Paper presented at the International Multiconference of Engineers and Computer Scientists Hong Kong, 17–19 Mar 2010
4. Kuneida M, Lauwers B, Rajurkar KP, Schumacher BM (2005) Advancing EDM through fundamental insight into the process. CIRP Ann Manuf Technol 54:64–87
5. Khan AA (2008) Electrode wear and material removal rate during EDM of aluminium and mild steel using copper and brass electrodes. Int J Adv Manuf Technol 39:482–487
6. Jesudas T, Arunachalam M (2011) Study on influence of process parameters in micro-electrical discharge machining (μ-EDM). Eur J Sci Res 59(1):115–122
7. Phadke MD (1989) Quality engineering using robust design. Pearson Education, New Delhi, pp 133–148
8. Ross PJ (2005) Taguchi techniques for quality engineering. McGraw-Hill, New York, pp 203–244
9. Rasheed MS (2013) Comparison of micro-holes produced by micro-EDM with laser machining. Int J Sci Eng 1(3):14–18
10. Hardness Testing Procedure. Defence Metallurgical Research Laboratory, Hyderabad
11. Lee SH, Li X (2003) Study of the surface integrity of the machined workpiece in the EDM of tungsten carbide. J Mater Proces Technol 139:315–321

Characterization of Coke-Making Coals of High Reactivity from Northwest China

Qiang Wu, Zizong Zhu, Guojing Shi, Feng Wang and Yangyang Xie

Abstract The coal chars from northwestern part of China are characterized with high reactivity and low strength after reaction. Four type of coke-making coals selected from northwestern part of China were studied by proximate analysis, ultimate analysis, vitrinite reflectance analysis, and FTIR with curve-fitting analysis to obtain information on their chemical composition and chemical structure. The results show that the studied coals have relatively high values of final contraction of coke residue index (x) and relatively low values of maximum thickness of plastic layer (y) and average vitrinite reflectance. Based on the curve-fitting analysis of FTIR spectra, the aliphatic carbon (C_{al}), the aromatic carbon (C_{ar}), and the molecular structural parameters such as CH_2/CH_3, f_a, H_{al}/H_{ar}, and $(R/C)_u$ are determined. The results of curve-fitting analysis indicate that the studied coals are characterized by a large amount of oxygen-containing functional groups and aliphatic side chains.

Keywords Coke-making coal · High reactivity · Vitrinite reflectance FTIR · Structural parameters

Introduction

The late Jurassic coke-making coals, from Xinjiang province in China, have relatively high value of volatile matter and relatively low content of ash, sulfur and phosphorus in comparison with normal coke-making coals of similar rank [1]. Furthermore, the coke made from Xinjiang Aiwergou coke-making coals contains high reactivity (CRI > 70%) and low strength after reaction (CSR < 25%) compared to the coke produced by normal coke-making coals at the similar rank [2]. To meet hot metal production requirement at Xinjiang, the coal blend was prepared by

Q. Wu · Z. Zhu (✉) · G. Shi · F. Wang · Y. Xie
College of Material Science and Engineering, Chongqing University, Chongqing 400044, China
e-mail: zhuzizong@163.com

B. Li et al. (eds.), *Characterization of Minerals, Metals, and Materials 2018*, The Minerals, Metals & Materials Series,
https://doi.org/10.1007/978-3-319-72484-3_42

adding high quality coke-making coals obtained from remote coalfield, resulting in an increase in hot metal cost. The steelmaking companies located at Xinjiang have already begun to research the specificity of Xinjiang coke to reduce the cost of coke. The coke quality is influenced by the characteristics of coal blend and carbonization condition. In addition, the coal blend composition plays a predominant role in determining the coke quality [3]. So the characterization of Xinjiang coke-making coal is a critical way to reveal the high reactivity of Xinjiang coke. There have been many approaches to investigate the heterogeneity of coal [4, 5].

The most widely used parameter for maturity determination is vitrinite reflectance, which play an important role in categorizing coal [6]. FTIR is also commonly used to characterize the chemical structure of coal. In addition, some structure parameters obtained from the FTIR pattern can be also used to assess the grade of maturation of coal [7, 8]. The information on the functional groups of coal can be inferred by FTIR technique [9]. In previous work, the FTIR with curve-fitting analysis can be also used to determine aromaticity and structure information of coal [6–10].

In this study, the objectives were to characterize structural features of Chinese Xinjiang coke-making coal, and investigate the reason why the coke formed by Xinjiang coke-making coals has high reactivity by using FTIR.

Experimental

Materials

Four coke-making coal samples varying in rank from gas coal to lean coal were collected from the Kubai coalfield in the Northwest China plate. With the increase of carbon content, the coal samples are identified as follows: gas coal (XJ-QM), rich coal (XJ-FM), coking coal (XJ-JM), and lean coal (XJ-SM). All collected samples were immediately placed in a polyethylene bag filled with nitrogen to minimize oxidation and contamination. These coal samples were milled to less than 3 mm and dried for 2 h at 80 °C in a flow of N_2 before use. Proximate analysis and ultimate analysis were carried out following China Standard GB/T 212-2008 and GB/T 214-2007, respectively. The plastic layer index of coal samples were measured in accordance with China Standard GB/T479-2000. The measurement of coal caking index ($G_{R.I}$) was carried out according to the National Standard of China (GB/T 5447-85), which is based on that of Roga index [11]. The random vitrinite reflectance ($R_{o,ran}$) was measured according to the Chinese national standard issued in 2008 (GB/T 6948-2008).

FTIR Analysis

FTIR were measured on a Nicolet iS5 FT-IR spectrometer at a resolution of 4 cm^{-1}. Samples for the FTIR measurement were prepared by mixing 1 mg of coal sample (particle size of ~76 μm) with 200 mg of KBr and the mixture was pressed to form a pellet under 10 MPa pressure for 2 min. Meanwhile, the duplicate pellets of each sample were used and were dried under vacuum for 48 h to remove the perturbations of water to the spectrum.

Results and Discussion

Characterization Data of Coals

The properties of the coal samples are listed in Table 1. As shown in the table, the Xinjiang coke-making coals have relatively low content of sulfur and ash yield (A_d), which benefit the operation of blast furnace. The values of volatile matter (V_{daf}), fixed carbon (FC_{ad}) and caking indexes ($G_{R.I}$) in Xinjiang coke-making coal samples keeps the normal level as shown in Table 1. However, Xinjiang coke-making coals have relatively low value of the maximum thickness of plastic layer (y), suggesting that Xinjiang coke-making coals might be formed to a certain amount of plastic mass in the coking process while it is unstable. Moreover, the relatively high value of the final contraction of coke residue (x) in the Xinjiang coke-making coals could be observed in Table 1. It may understand that the high value of x in coal samples will result in a decrease of coke quality because much amount of cracks will generate into the coke.

Vitrinite Reflectance

Figure 1 shows random distribution graphs of vitrinite reflectance in the studied coals. As can be seen from the figure, the average vitrinite reflectance ($\overline{R}_{o,ran}$) is the weighted average of $R_{o,\ ran}$, which increases from 0.68% (XJ-QM) to 1.54% (XJ-SM) with the increase of coalification. The average maximum vitrinite reflectance values ($\overline{R}_{o,max}$) were calculated from the Eq. 1 [12], which can be used to measure of the grade of metamorphism in the coal.

$$\overline{R}_{o,max} = 1.0645\ \overline{R}_{o,ran} \tag{1}$$

Obviously, the $\overline{R}_{o,max}$ values of XJ-FM and XJ-JM are 0.94 and 1.11%, which lower than the commonly used rich coal and coking coal, respectively, indicating that the coalification of XJ-FM and XJ-JM is lower than that of commonly used rich

Table 1 Basic characteristics of coal samples

	XJ-QM	XJ-FM	XJ-JM	XJ-SM
Proximate analysis (wt%)				
A_d	6.76	6.94	9.27	9.75
V_{daf}	40.03	32.31	26.52	19.12
FC_{ad}	54.76	62.80	66.08	71.67
Process analysis				
$G_{R.I}$	88	101	89	46
y/mm	12.4	25.6	12.5	8.5
x/mm	38.8	22.4	31.3	38.1
Ultimate analysis (wt%)				
C	75.93	83.20	84.41	88.08
H	5.33	5.19	4.94	4.13
N	1.33	1.54	1.28	1.34
S	0.50	0.57	0.51	0.50
O[a]	16.91	9.50	8.86	5.95

A ash yield; *d* dry basis; *V* volatile matter; *daf* dry and ash-free; *FC* fixed carbon; *ad* air-dry basis; $G_{R.I}$ caking index; *y* maximum thickness of plastic layer; *x* final contraction of coke residue

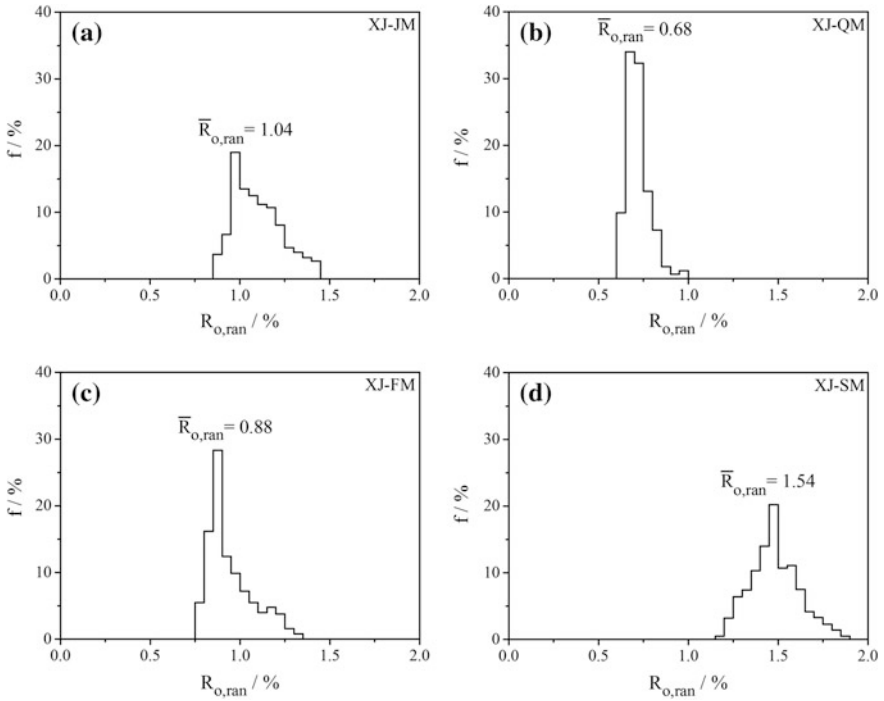

Fig. 1 Graphs of vitrinite reflectance random distribution. **a** XJ-QM, **b** XJ-FM, **c** XJ-JM, and **d** XJ-SM

coal and coking coal. XJ-QM and XJ-SM have also the relative low values of $\overline{R}_{o,max}$, which is 0.72 and 1.64%. On the whole, the $\overline{R}_{o,max}$ value of studied coals lower than that of commonly used coke-making coals, which leads to produce the higher reactivity coke and is against for coke-making industry.

FTIR Spectral Characteristics of Studied Coal Samples

Figure 2 shows the FTIR spectra of the four coals where some trends can be observed. The spectra are broadly similar, consisting of primarily of aromatic nuclei, aliphatic side-chains, oxygen-containing groups, and mineral bands [13]. However, their intensities of absorption bands vary significantly, indicating considerably structural difference among coals of different ranks. According to the literatures [5, 8, 14–16], the 2800–3000 cm^{-1} zone correspond to aliphatic C–H stretching modes, 1000–1800 cm^{-1} zone correspond to oxygen containing functional groups bending modes, and 700–900 cm^{-1} region correspond to aromatics bending modes. In order to gain information on structural parameters, the spectra were studied by curve-fitting analysis used by Origin® 9.1 software.

As shown in Fig. 2, the oxygenated functional groups of the samples are displayed by the three highest bands at 3300–3700 and 1000–1800 cm^{-1} regions, indicating that Xinjiang coke-making coal have a large number of oxygen-containing functional groups. In addition, the intensity bands of these oxygen-containing functional groups decrease slightly with increasing the coalification due to magmatic intrusion modification chemical structures of coal. The XJ-FM and XJ-SM have two high intensity bands at approximately 1062 and 525 cm^{-1} attributed to mineral matter (SiO_2), while the corresponding intensity

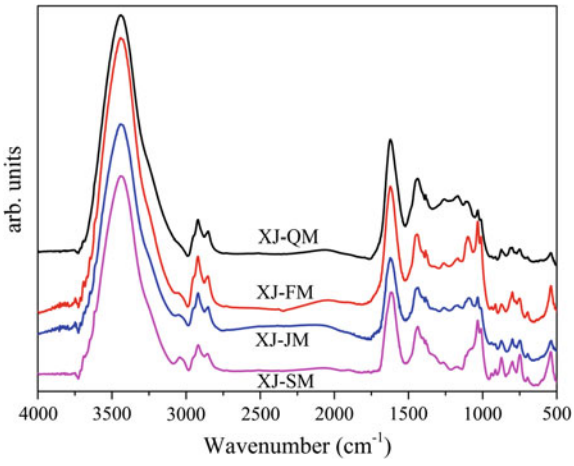

Fig. 2 4000–500 cm^{-1} normalized FTIR spectra of the four studied coal samples

bands of the XJ-QM and XJ-JM are largely decreased, suggesting a relatively lower SiO_2 content in XJ-QM and XJ-JM than XJ-FM and XJ-SM.

The aliphatic (H_{al}) and aromatic (H_{ar}) hydrogen contents were calculated from the integrated absorbance areas of the bands at 2800–3000 cm^{-1} and 700–900 cm^{-1}, respectively. The extinction coefficients used for converting integrated absorbance areas to concentration units were 684 and 744 abs cm^{-1} mg cm^{-2} for the studied coals, respectively.

The apparent aromaticity (f_a) of the samples was estimated according to the Eq. 2 [17].

$$f_a = 1 - \left(\frac{H_{al}}{H}\right)\left(\frac{H}{C}\right)\left(\frac{C_{al}}{H_{al}}\right) \tag{2}$$

where, H/C is the hydrogen–carbon atomic ratio calculated from elemental analysis, H_{al}/H is the fraction of total hydrogen present as aliphatic hydrogen, and H_{al}/C_{al} is hydrogen–carbon atomic ratio for aliphatic groups, which is generally taken to be 1.8 for coals [18].

According to previous works [19], the number of rings of atomic carbon in the monomer (that is the degree of aromatic ring condensation) can be established by using a structural parameter $(R/C)_u$.

$$\left(\frac{R}{C}\right)_u = 1 - \frac{f_a}{2} - \frac{(H/C)}{2} \tag{3}$$

The parameter CH_2/CH_3 represents for length of aliphatic side-chains, which was obtained according to Eq. 4 by de-convolution of the region from 2800 to 3000 cm^{-1} (Fig. 3). If this parameter value is higher, it is possible to infer that the aliphatic side-chains are longer [20].

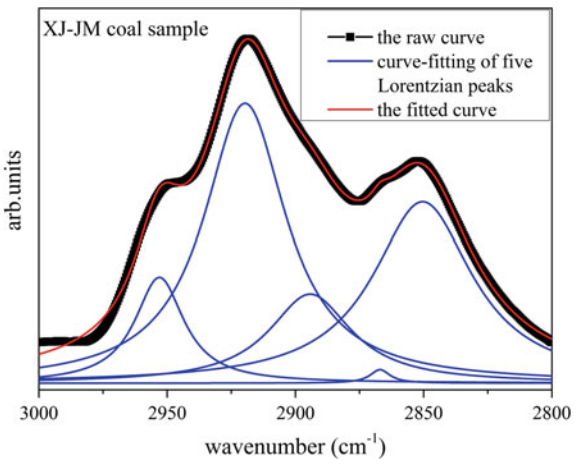

Fig. 3 Curve-fitted FTIR spectrum of the aliphatic C–H stretching bands for XJ-JM

Table 2 Structural parameters deduced from the FTIR measurements

Samples	H_{al}/H_{ar}	CH_2/CH_3	f_a	$(R/C)_u$	C_{al} (wt%)	C_{ar} (wt%)
XJ-QM	3.11	2.45	0.681	0.258	24.22	51.71
XJ-FM	2.28	3.14	0.705	0.264	24.54	58.66
XJ-JM	1.79	3.46	0.764	0.276	19.92	64.49
XJ-SM	0.83	4.51	0.863	0.295	12.07	76.01

$$\frac{CH_2}{CH_3} = \frac{A_{2922\ cm^{-1}}}{A_{2952\ cm^{-1}}} \tag{4}$$

The structure parameters for FTIR are calculated according to Eqs. 2−4 and are given in Table 2. The results show that the values of H_{al}/H_{ar} and C_{al} of studied coals decrease from XJ-QM to XJ-JM and then both fall drastically with increasing the content of carbon, suggesting the content of aliphatic decrease from XJ-QM to XJ-SM. The CH_2/CH_3 values increase with the coalification (in Table 2) indicates that methylene groups increased from XJ-QM to XJ-SM. This is probably due to a loss of alkyl chains and the conversion of hydro-aromatic methyl structures to aromatic rings or the branched aliphatic structures [8]. However, all of the studied coals have a relatively high CH_2/CH_3 value, indicating that Xinjiang coke-making coal have a length of the aliphatic chains [6, 7]. As shown in Table 2, f_a, $(R/C)_u$, and C_{ar} increase with the increase of carbon content in the studied coals. These observations are in good agreement with previous studies that the increase of aromaticity in thermally metamorphosed coal is mainly due to its higher content of polynuclear aromatic [21–23]. On the whole, these structure parameters change slightly in the evolution stage from XJ-QM to XJ-JM, indicating that XJ-FM and XJ-JM have a relatively low degree of metamorphism, resulting in Xinjiang coke with high reactivity.

Conclusions

In this paper, the basic characteristics and structure parameters of Xinjiang coke-making coal were investigated. The main conclusions are summarized as follows: (1) With the increase of coal ranks, the aromaticity and average maximum vitrinite reflectance increase, whereas aliphatic and oxygen-containing groups decrease. (2) Xinjiang coke-making coals contain many oxygen-containing groups and relatively long aliphatic side-chains, especially XJ-FM and XJ-JM. (3) Xinjiang coke-making coals have a relatively low grade of metamorphism. This is considered to be an important factor that responsible for the high reactive Xinjiang coke, which is also confirmed by relatively low value of y and the relatively high value of x in the studied coals.

Acknowledgements This research was supported by The National Natural Science Foundation of China (51044005) and The Key Project of Science and Technology of Chongqing (CSTS.2010AB4084).

References

1. Huang WH, Yang Q, Tang XY (2010) Distribution features of coal for coking resource in China and deep part potential analysis. Coal Geol China 22(5):4–6 (in Chinese)
2. Zhang N (2013) Xinjiang coking coal supply and demand outlook. Sci Technol Inform 20:469 (in Chinese)
3. Barranco R, Patrick J, Snape C (2007) Impact of low-cost filler material on coke quality. Fuel 86:2179–2185
4. Li W, Zhu Y, Chen S, Zhou Y (2013) Research on the structural characteristics of vitrinite in different coal ranks. Fuel 107(9):647–652
5. Ibarra J, Munoz E, Moliner R (1996) FTIR study of the evolution of coal structure during the coalification process. Org Geochem 24(6):725–735
6. Davis A, Kuehn DW, Starsinic M, Coleman MM, Painter PC (1981) Concerning the application of FT-IR to the study of coal: A critical assessment of band assignments and the application of spectral analysis programs. Appl Spectrosc 35(5):475–485
7. Orrego-Ruiz JA, Cabanzo R, Mejia-Ospino E (2011) Study of Colombian coals using photoacoustic Fourier transform infrared spectroscopy. Int J Coal Geol 85(3):307–310
8. Wu D, Liu GJ, Sun RY (2013) Investigation of structural characteristics of thermally metamorphosed coal by FTIR spectroscopy and X-ray diffraction. Energy Fuels 27(10):5823–5830
9. Baysal M, Yurum A, Yildiz B, Yürüm Y (2016) Structure of some western Anatolia coals investigated by FTIR, Raman, 13 °C solid state NMR spectroscopy and X-ray diffraction. Int J Coal Geol 163:166–176
10. Li W, Zhu YM, Wang G (2016) Characterization of coalification jumps during high rank coal chemical structure evolution. Fuel 185:298–304
11. Shui HF, Li HP, Chang HT (2011) Modification of sub-bituminous coal by steam treatment: caking and coking properties. Fuel Process Technol 92(12):2299–2304
12. He XM et al (2010) Coal chemistry. Metallurgical Industry Press, Beijing, pp 152–153 (in Chinese)
13. Yan J, Bai Z, Bai J, Guo Z (2014) Effects of organic solvent treatment on the chemical structure and pyrolysis reactivity of brown coal. Fuel 128(4):39–45
14. Bodoev NV, Guet JM, Gruber R, Dolgopolov NI, Wilhelm JC (1996) FTIR and XRD analysis of sapropelitic coals. Fuel 75(7):839–842
15. Jones JM, Pourkashanian M, Rena CD, Williams A (1999) Modelling the relationship of coal structure to char porosity. Fuel 78(14):1737–1744
16. Alvarez R, Clemente C, Gomez-Limon D (2003) The influence of nitric acid oxidation of low rank coal and its impact on coal structure. Fuel 82:2007–2015
17. Brown JK, Ladner WR (1960) Hydrogen distribution in coal-like materials by high resolution nuclear magnetic resonance spectroscopy. Fuel 39:87–96
18. Ibarra J, Moliner R, Bonet AJ (1994) FTIR investigation on char formation during the early stages of coal pyrolysis. Fuel 73(6):918–924
19. Kastner J, Pichler T, Kuzmany H, Curran S, Blau W (1994) Resonance Raman and Infrared spectroscopy of carbon nanotubes. Chem Phys Lett 221:53–61
20. Saikia B, Boruah RK, Gogoi PK (2007) XRD and FT-IR investigation of sub-bituminous Assam coals. B Mater Sci 30(4):421–427

21. Zerda TW, John A, Chmura K (1981) Raman studies of coals. Fuel 60(5):375–384
22. Sadezky A, Muckenhuber H, Grothe H, Niessner R, Pöschl U (2005) Raman microspectroscopy of soot and related carbonaceous materials: Spectral analysis and structural information. Carbon 43(8):1731–1736
23. Semmler J, Yang PW, Craford GE (1991) Gas chromatography/Fourier transform infrared studies of gas-phase polynuclear aromatic hydrocarbons. Vib Spectrosc 2(4):189–203

The Anodic Behavior of Electro-deoxidation of Titanium Dioxide in Calcium Chloride Molten Salt

Pingsheng Lai, Meilong Hu, Leizhang Gao, Zhengfeng Qu and Chenguang Bai

Abstract Since Fray-Farthing-Chen (FFC) Cambridge process was proposed in 2000 for electrochemical extraction of titanium from titanium oxide, a great quantity of research has been carried out to investigate the mechanism of the electro-reduction of the process. Results show that the intermediate products of perovskite phases are inevitable during the electro-deoxidation process. In this paper, a new perspective focus on the anodic behavior was applied. The behavior of the graphite anode with different times has been investigated. Although the main anodic process in the electrolysis is the oxygen evolution by means of the CO_2. The interphases of calcium species appeared on the cathode are closely related with chlorine ions in the molten $CaCl_2$. In addition, the released CO_2 from the anode is related with the formation of $CaCO_3$ which floated on the surface of the molten salt.

Keywords Anodic behavior · Electro-deoxidation · Titanium dioxide

Introduction

Electrochemical reduction of various solid metal oxides to their respective metals has been successfully carried out in $CaCl_2$-based molten salts at mild temperatures (500–1000 °C) by many researchers since 2000 [1–5], and has received much attention due to its simplicity and economic and environmental advantages [6–9]. This process, known as the Fray-Farthing-Chen (FFC) Cambridge Process,. is usually carried out by applying a constant cell voltage between typically a cathode fabricated from the metal oxides and a carbon or graphite anode. During the electrolysis, the metal oxides is reduced to the metal or intermetallic compound at cathode. The electro-deoxidation is accompanied by the release of O^{2-} ions which

P. Lai · M. Hu (✉) · L. Gao · Z. Qu · C. Bai
School of Materials Science and Engineering, Chongqing University, Chongqing 400044, China
e-mail: hml@cqu.edu.cn

B. Li et al. (eds.), *Characterization of Minerals, Metals, and Materials 2018*, The Minerals, Metals & Materials Series,
https://doi.org/10.1007/978-3-319-72484-3_43

transport through the molten salts by diffusion and convection, and then discharge at the graphite anode to form mainly the CO_2 or CO gas.

Researchers has put efforts into the extraction of titanium from TiO_2 due to its large economic and environmental advantages which is compared to the traditional Kroll process. As what mentioned before, the titanium is produced in cathode via electro-deoxidation of TiO_2. Therefore, most of the researches are focus on the cathodic reactions in order to understanding the mechanism of the electro-deoxidation process. Chen et al. [2] firstly proposed that the reaction pathway of the electro-reduction is $TiO_2 \rightarrow Ti_2O_3 \rightarrow TiO \rightarrow Ti$ in 2000. Dring [10] found the Ti_3O_5 phase during the electro-deoxidation process. Substantly, Schwandt [11, 12] reported that the electrochemical reduction goes through special stages which include the formation and decomposition of calcium titanates, and it can be expressed as $TiO_2 \rightarrow CaTiO_3 + Ti_xO_y \rightarrow CaTi_2O_4 \rightarrow TiO \rightarrow Ti$. In these studies, the anodic reaction takes place as follows:

$$2O^{2-} + C \rightarrow CO_2 + 4e^-$$

$$O^{2-} + C \rightarrow CO + 2e^-$$

Admittedly, the graphite anode captures the O^{2-} discharged from cathode and react to form CO_2 or CO. However, few attention was put into the anodic behavior during the electrochemical reduction. Such as the amount and rate of the gas released, and the consumption of the anode in different stages during the electrochemical reduction process.

This paper reports the preliminary findings from studies of graphite electrodes (anode) in molten $CaCl_2$ in conjunction with electro-reduction of TiO_2 pellets counter electrode (cathode), and a new perspective focus on the anodic behavior was applied.

Experimental

Materials

Analytical grade anhydrous $CaCl_2$ (99%, purity) was used as electrolyte in this work, and TiO_2 (99%, purity) powder was uniaxially pressed in a press with 6–7 Mpa to make pellets with 10 mm in diameter and 5 mm in thickness. The TiO_2 pellets were sintered at 900 °C in air for 2 h and cooled to the room temperature.

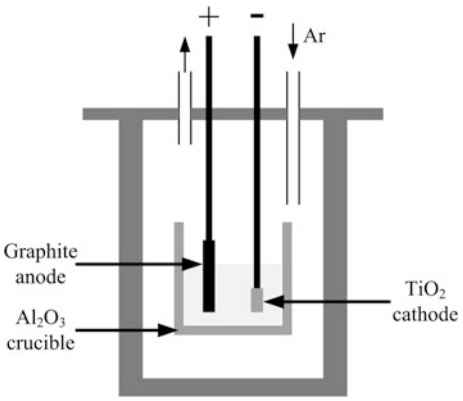

Fig. 1 The schematic diagram of electrolytic apparatus

Experimental Procedure

An electrolysis cell was installed in a sealed reactor which was vacuumed and thoroughly controlled with high purity Ar gas. The TiO_2 pellets was wrapped by molybdenum wire and attached to the stainless steel rod, which was served as cathode. Graphite rods were selected to use as anode.

Before the experiments, the anhydrous $CaCl_2$ was dried in an oven with the temperature of 100 °C for 2 h and 300 °C for 3 h. After cooling to room temperature, the $CaCl_2$ was put in a alumina crucible (100 mm in internal diameter, 100 mm in height) which was dried at 150 °C before. Pre-electrolysis was carried at 850 °C for 2 h with 2 V to remove moisture and other redox-active impurities with graphite anode and stainless steel cathode. The reactor was heated at a constant rate of 3 °C/min by the furnace with argon flow of 120 ml/min until reaching the target temperature. Figure 1 shows the schematic diagram of electrolytic apparatus.

When reaching the experimental temperature (900 °C), the prepared TiO_2 cathode and graphite anode were placed to the alumina crucible and lowered into the molten salt. The gas released from the reactor was collected and passed into starch potassium iodide solution. A constant potential of 3.2 V was inflicted between the electrode. The experiments were terminated by 6, 8, 10, 12, 14, 18, 24 h, respectively. After electrolysis for a designated time, the anode and cathode were removed from the furnace, cooled in argon, washed in distilled water. The products were characterized by X-ray diffraction spectroscopy (XRD, RigakD/Max-2500).

Results and Discussion

The Consumption of the Graphite Anode

The anodic behavior of the graphite anode has been investigated by series experiments. Figure 2 shows the morphology of the graphite anode after electrolysis with

different times when using TiO_2 as the counter cathode. Dramatically, the all graphite anodes have different level consumption at different times. When electrolyzing no more than 10 h, the diameter of immerged graphite anode has little decrease and the surface has no obvious change, which is compared to the upside not immerged. Other than that, the surface of the anode is smooth. When taking insight into the graphite anode electrolyzing for more than 10 h, the surface of the immerged anode is rough and has more serious consumption with electrolysis time increasing.

There is no doubt that the consumption of the graphite is caused by the reaction between the graphite anode and O^{2-} dissolved in molten salt, it can be expressed as:

$$C + O^{2-} - 2e^{-} \rightarrow CO$$

$$C + 2O^{2-} - 4e^{-} \rightarrow CO_2 \quad \text{or} \quad C + CO_2 \rightarrow 2CO$$

Therefore, we can judge that there is little CO_2 or CO released at the anode in the initial 10 h from the morphology of the graphite anode. In other words, little O^{2-} discharged from the TiO_2 cathode at the initial 10 h don't transfer to the anode and don't have reactions, so CO_2 or CO hardly release at the anode. As mentioned above, many researches indicate that the electrochemical reduction of TiO_2 goes through special stages which include the formation and decomposition of calcium titanates. Firstly, the TiO_2 cathode obtains the electrons supplied by constant

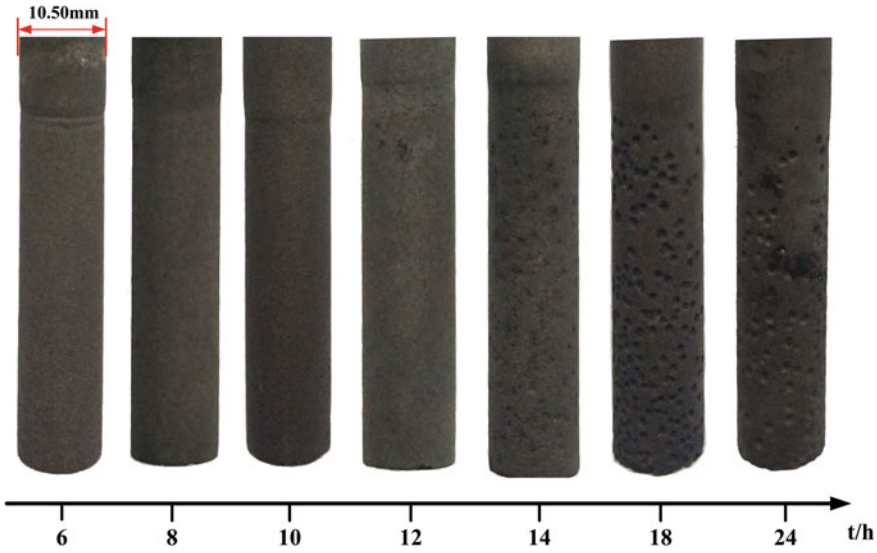

Fig. 2 Photographs of the graphite anode with TiO_2 counter cathode after electrolysis for different times

potential and discharges O^{2-}. Then, the O^{2-} and Ca^{2+} dissolved in molten salt react with the prior TiO_2 to generate $CaTiO_3$. At this stage, the corresponding reaction can be expressed as follows:

Cathode:

$$TiO_2 + (4 - 2x)e^- \rightarrow TiO_x + (2 - x)O^{2-}$$

$$Ca^{2+} + O^{2-} + TiO_2 \rightarrow CaTiO_3$$

Anode:

$$2Cl^- - 2e^- \rightarrow Cl_2$$

The anodic reaction is the discharge of the chlorine in order to balance the charge in the molten salt because Ca^{2+} is consumed to form the $CaTiO_3$. At this period, maybe there is no O^{2-} transferred to the anode. This issue can be clarified by ways of the controlled experiments. The gas released at anode was obtained and connected to a bottle which contains starch potassium iodide solution. As shown in Fig. 3, it shows that there exists chlorine released from the anode at the first 4 h, but didn't detect later.

The changes of the gas released at the anode in conjunction with the consumption of the graphite anode, can help us determine the chemical reactions taking place at the graphite anode, which contributes to understand the cathodic behavior. At the beginning, the initial TiO_2 cathode convert to $CaTiO_3$ and titanium suboxides by the potential and molten salt. At this time, little O^{2-} is released at the anode. However, a large number of Cl^- are discharged to balance the consumption of Ca^{2+} which is consumed to form $CaTiO_3$ on the anode. Thus the graphite anode was consumed little on the surface during this period. Subsequently, the new formed $CaTiO_3$ will also be electrolyzed to titanium suboxides. The graphite anode is consumed and CO_2 or CO released gradually and the rate of gases released is slow

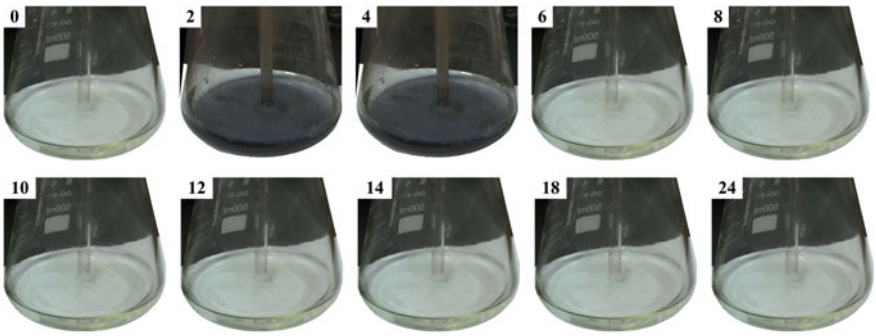

Fig. 3 The change of the collected gas at various electrolysis time (the number in the figures means the electrolysis time)

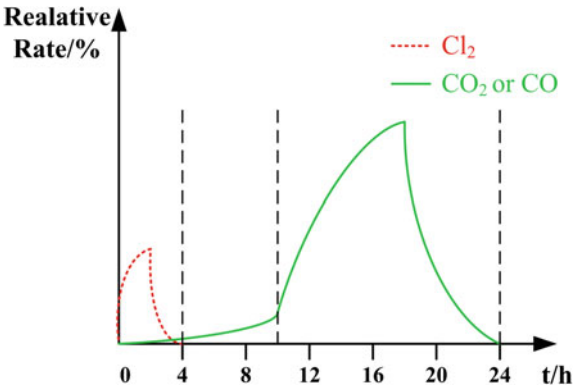

Fig. 4 The released gas and the discharge rate during different electrolysis period

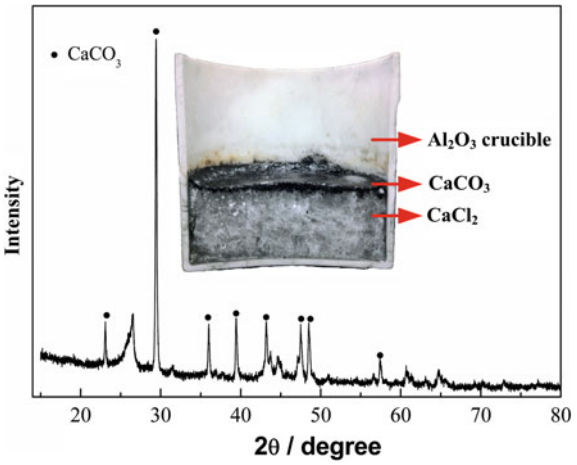

Fig. 5 XRD patterns of the black floating powder on the surface of molten salt

at this period. Finally, the titanium suboxides are reduced to Ti and discharge a large number of O^{2-} which transfer to the anode and releases as CO_2 or CO. The graphite anode is consumed seriously, which leads the anodic surface rough. Figure 4 describes the released gas and the discharge rate during different electrolysis period.

The Gases Released at Graphite Anode

At the experimental process, we found that there was a thick layer of floating powder on the surface of the molten salt. Figure 5 shows the cooled $CaCl_2$ molten salt and the XRD patterns of the floating powder. The analysis result indicates that the main phase of the floating power is almost $CaCO_3$. Based on the analysis above,

it is certain that there are both Cl_2 and CO_2 or CO release at the anode. In conjunction with the phase composition, it can be concluded that the released CO_2 may dissolve in the molten salt and take place chemical reaction with the dissolved CaO produced from $CaTiO_3$. This phenomena is also investigated by the other study [13]. It can be expressed as follows:

$$CO_2 + O^{2-} \rightarrow {CO_3}^{2-}$$

$${CO_3}^{2-} + Ca^{2+} \rightarrow CaCO_3$$

Conclusions

The anodic behavior of electro-deoxidation of titanium dioxide in calcium chloride molten salt has been investigated. The main conclusions are obtained as follows:

(1) Both of Cl_2 and CO_2 or CO are released from the graphite anode. At the beginning of electrolysis, Cl_2 is first released at the anode with little CO_2. Then, Cl_2 disappeared and the amount of CO_2 or CO increase gradually. The formed CO_2 can also dissolve in molten salt and react to generate the $CaCO_3$.
(2) Corresponding to the consumption degree of the graphite anode, the changes of gases during the electrolysis can be obtained.
(3) Based on the analysis of gas change and the consumption degree of the graphite anode, the reaction pathway of electro-oxidation of TiO_2 is $TiO_2 \rightarrow CaTiO_3 \rightarrow Ti_xO_y \rightarrow Ti$.

Acknowledgements The authors acknowledge gratefully the financial support from the National Natural Science Foundation of China (Grant No. 51674054 and Grant No. 51234010).

References

1. Xiao W, Wang D (2014) ChemInform abstract: the electrochemical reduction processes of solid compounds in high temperature molten salts. Chem Soc Rev 45(10):3215–3228
2. Chen GZ, Fray DJ, Farthing TW (2000) Direct electrochemical reduction of titanium dioxide to titanium in molten calcium chloride. Nature 32(2):361–364
3. Abdelkader AM, Kilby KT, Cox A et al (2013) DC voltammetry of electro-deoxidation of solid oxides. Chem Rev 113(5):2863–2886
4. Suzuki RO, Ono K, Teranuma K (2003) Calciothermic reduction of titanium oxide and in situ electrolysis in molten $CaCl_2$. Metall Mater Trans B 34(3):287–295
5. Chen GZ, Fray DJ (2001) Cathodic refining in molten salts: removal of oxygen, sulfur and selenium from static and flowing molten copper. J Appl Electrochem 31(2):155–164
6. Yasuda K, Nohira T, Hagiwara R et al (2008) Direct electrolytic reduction of solid SiO in molten $CaCl_2$ for the production of solar grade silicon. Electrochim Acta 53(1):106–110

7. Kar P, Evans JW (2008) A model for the electrochemical reduction of metal oxides in molten salt electrolytes. Electrochim Acta 54(2):835–843
8. Sang MJ, Hur JM, Hong SS et al (2008) An electrochemical reduction of uranium oxide in the advanced spent-fuel conditioning process. Nucl Technol 162(2):184–191
9. Wu T, Jin X, Xiao W et al (2010) Thin pellets: fast electrochemical preparation of capacitor tantalum powders. Chem Mater 19(2):153–160
10. Dring K, Dashwood R, Inman D (2005) Voltammetry of titanium dioxide in molten calcium chloride at 900 °C. J Electrochem Soc 152:104–113
11. Schwandt C, Fray DJ (2005) Determination of the kinetic pathway in the electrochemical reduction of titanium dioxide in molten calcium chloride. Electrochim Acta 51:66–76
12. Schwandt C, Alexander DTL, Fray DJ (2009) The electro-deoxidation of porous titanium dioxide precursors in molten calcium chloride under cathodic potential control. Electrochim Acta 54:3819–3829
13. Hu L, Song Y, Jiao S et al (2016) Direct conversion of greenhouse gas CO_2 into graphene via molten salts electrolysis. ChemSusChem 9(6):588

Part XIII
Poster Session

Addition of Dregs in Mixed Mortar: Evaluation of Physical and Mechanical Properties

Rodrigo Felipe Santos, Rita de Cássia Silva Sant'ana Alvarenga, Beatryz Mendes, José Maria Carvalho, Leonardo Pedroti and Afonso Azevedo

Abstract The dregs is a waste from the cellulose production, and its reuse is an effective way to reduce environmental impacts. Researches have already been done to incorporate it into building materials. The present work aimed at incorporating dregs in the production of mortar to replace hydrated lime. The methodology adopted was the Simplex network with ten sampling points, varying the amount of cement, sand, and dregs. Each mix was submitted to flexural strength, compressive strength, apparent mass density and water absorption by capillarity tests. The results were analyzed by the software Minitab, obtaining the influence of each component in the mixture. The best results were observed in mixes with a higher proportion of cement and less of residue when it was analyzed the flexural and compressive strengths. Larger rates of apparent mass density and water absorption were noticed with a greater amount of dregs. The experimental design also allowed the obtainment of mixture ratios from predetermined values of the tested properties and indicated that the addition of dregs in mortar could be an alternative to civil construction.

Keywords Dregs · Mortar · Simplex · Environment · Civil construction

Introduction

The production of paper and cellulose generates many kinds of residues that can be dangerous to the environment. One of them is a gray waste called dregs that contains in its composition the quicklime [1]. It is also rich in calcium carbonate ($CaCO_3$), which can generate quicklime in the presence of heat. So, this residue can be a promising usage in the production of mix mortar with a partial or total replacement of the conventional lime. Moreover, the incorporation of dregs in

R. F. Santos · R. de Cássia Silva Sant'ana Alvarenga · B. Mendes (✉)
J. M. Carvalho · L. Pedroti · A. Azevedo
Viçosa, Brazil
e-mail: beacm03@gmail.com

B. Li et al. (eds.), *Characterization of Minerals, Metals, and Materials 2018*, The Minerals, Metals & Materials Series,
https://doi.org/10.1007/978-3-319-72484-3_44

building materials would be an alternative to reduce the costs and to avoid environmental impact.

One way to work with residues is using an experimental design, such as the Simplex design. This methodology allows fewer tests and time, besides it permits the determination of the reliability of the experiment and the learning of the interaction between mixture components [2]. After a literature review, it was found many works using dregs in different materials, including in mortar [3–7]. However, any of these researches made use of the Simplex design.

Therefore, in this work, it was made an experimental design to incorporate dregs in a mix mortar replacing the lime. In the end, it is hoped to obtain equations and response surfaces that describe the influences of each mixture components in the mortar. And in this way, it is expected to found a proper application of dregs in civil construction, allowing a cheaper mortar and less available residue to contaminate the environment.

Materials and Methods

Materials

The mixed mortar was made with the dregs replacing the hydrated lime. This residue was produced by CENIBRA, an important cellulose and paper company located in Belo Oriente—Brazil. The other components of the mortar were: cement Portland CP II-F–32 of the company TUPI, Carandaí—Brazil; natural sand from the Piranga River, Porto Firme—Brazil; and water from the supply network of the Federal University of Viçosa (UFV).

Methods

As the statistical analyses would be performed with three components, the amount of water was fixed in all the mixtures types. Furthermore, the ratios of cement, dregs, and sand (Fig. 1) were determined to keep a space sub-region of a typical Simplex triangle of ternary mixtures; in other words, a Simplex triangle with restrictions.

The program Minitab® 17.1.0 was used for the experimental lineation and response surfaces generation. The {3, 2} Simplex-Lattice design with axial and central points was adopted. The components percent for each ratio used in experimental lineation are presented in Table 1.

Once determined each ratio, the residue and the aggregate were prepared for use. The dregs was crushed for half an hour in a ball mill, and so it was passed through a 0.85 mm sieve. In case of sand, it was only passed through a 4.76 mm sieve.

Fig. 1 Sand, dregs, and cement for the confection of the mortar, respectively

Table 1 Measurements used in the experimental design

Trace	Original components (%)			Pseudo-components		
	Cement	Sand	Dregs	Cement	Sand	Dregs
1	12.00	81.00	7.00	1	0	0
2	8.50	84.50	7.00	1/2	1/2	0
3	8.50	81.00	10.50	1/2	0	1/2
4	5.00	88.00	7.00	0	1	0
5	5.00	84.50	10.50	0	1/2	1/2
6	5.00	81.00	14.00	0	0	1
7	7.33	83.33	9.33	1/3	1/3	1/3
8	9.67	82.17	8.17	2/3	1/6	1/6
9	6.17	85.67	8.17	1/6	2/3	1/6
10	6.17	82.17	11.67	1/6	1/6	2/3

In the next step prismatic specimens was made according to the ABNT NBR 13279:2005 [8], with dimensions 4 cm × 4 cm × 16 cm. The paste preparation and the flow table determination were made according to the ABNT NBR 13276:2005 [9].

Table 2 Results of the realized tests

Trace	Flexural strength (MPa)	Compressive strength (MPa)	Apparent mass density (Kg/m^3)	Water absorption (g/cm^2 min$^{1/2}$)
1	2.22	5.97	1914.17	4.60
2	0.90	2.55	1850.20	19.53
3	1.07	2.90	1816.15	17.37
4	0.28	0.89	1767.00	30.57
5	0.33	1.13	1777.89	32.93
6	0.21	0.94	1707.54	34.63
7	0.74	2.04	1829.77	19.53
8	1.36	3.57	1842.78	17.30
9	0.52	1.59	1781.03	32.63
10	0.53	1.78	1791.07	27.50

The flexural and compressive strength tests were performed according to the ABNT NBR 13279:2005 [3]. The specimens were tested at 3, 28, and 63 days. The capillarity water absorption test was made according to the ABNT NBR 15259:2005 [10] and the apparent mass density test was performed according to the ABNT NBR 13280:2005 [11], using three specimens for each ratio at the age of 28 days.

With the results obtained from these tests (Table 2), the dregs mortar's properties design was progressed. The lineation was performed by a completely randomized design and without repetitions. The values used in lineation corresponded to the averages obtained in the tests.

For each mortar property, linear, quadratic and special cubic models were generated by Minitab. The choice between one of them was made accordingly the following parameters: determination coefficient (R^2), determination of prediction coefficient (R^2 pred) and sum of squares of prediction errors (PRESS).

Results and Discussion

Since the water amount was fixed and the other components were limited for the experiment, a large variation of the consistency between the ratios was observed. After seven different restrictions, it was adopted a range of 5–12% of cement, 81–88% of sand and 7–14% of dregs (percentage related to dry weight of mortar). For these specifications, the mortar flow table results were between 182 and 310 mm. Although it still was a significant variation, this was accepted to continue working with a ternary blend, varying only three components and keeping the others fixed.

The results of the realized tests are shown in Table 2. And the chosen models to each property are shown in Table 3. Their choices were made according to the *p*-

Table 3 Results of variance analysis for the adopted models

Properties	Regression	*p*-value	R^2 (%)	R^2 pred (%)	Press
Flexural strength	Quadratic	0.002	99.90	98.79	0.041287
Compressive strength	Quadratic	0.016	99.58	93.09	1.48716
Water absorption coefficient	Linear	0.000	93.15	86.77	109.373
Apparent mass density	Linear	0.000	90.58	76.70	6638.02

Table 4 Equations generated to analyze each property

Properties	Equation
Flexural strength	$y = 2.214\,x_1' + 0.288\,x_2' + 0.212\,x_3' - 1.319\,x_1'\,x_2' - 0.520\,x_1'\,x_3' + 0.409\,x_2'\,x_3'$
Compressive strength	$y = 5.913\,x_1' + 0.920\,x_2' + 0.984\,x_3' - 3.433\,x_1'\,x_2' - 2.121\,x_1'\,x_3' + 1.121\,x_2'\,x_3'$
Water absorption coefficient	$y = 5.160\,x_1' + 32.771\,x_2' + 33.049\,x_3'$
Apparent mass density	$y = 1911\,x_1' + 1780\,x_2' + 1732\,x_3'$

value, R^2, R^2 pred, and PRESS. In Table 4, the math equations are presented, where it being x_1', x_2' and x_3' the amount in pseudo-components of cement, sand, and dregs respectively. It is worth highlighting that the analysis was made in terms of pseudo-components to keep low levels of multicollinearity.

The obtained equations to flexural and compressive strength demonstrate that the cement is more influent on these properties. So, an increase in the cement amount has a higher effect on the gain of strength. The sand and the dregs, on the other hand, have a weaker influence on this property. Regarding the nonlinear terms, the interactions cement-sand and cement-dregs are antagonistic, and the interaction sand-dregs is synergic. Accordingly to the nonlinear coefficients, it was possible to conclude that the increase of dregs amounts in place of sand provide a gain of strength.

Figures 2 and 3 represent the response surface to the flexural and compressive strength, and they show the influence of the components in mixer mortar, as explained in the last paragraph.

In the linear model adopted to the water absorption coefficient, it is perceived that R^2 and R^2 pred are lower and the value of PRESS is high when compared with the values obtained to the strengths. Thus, it was decided to accept this model but highlighting that its prediction is not so accurate than the obtained to the previous characteristics. Observing the response surface (Fig. 4), it perceived that mixtures with a larger amount of dregs have an effect of capillarity more accented. It was also perceived that the dregs and the sand contribute approximately equal to the water absorption, what can be seen by the similar coefficients in the model equation

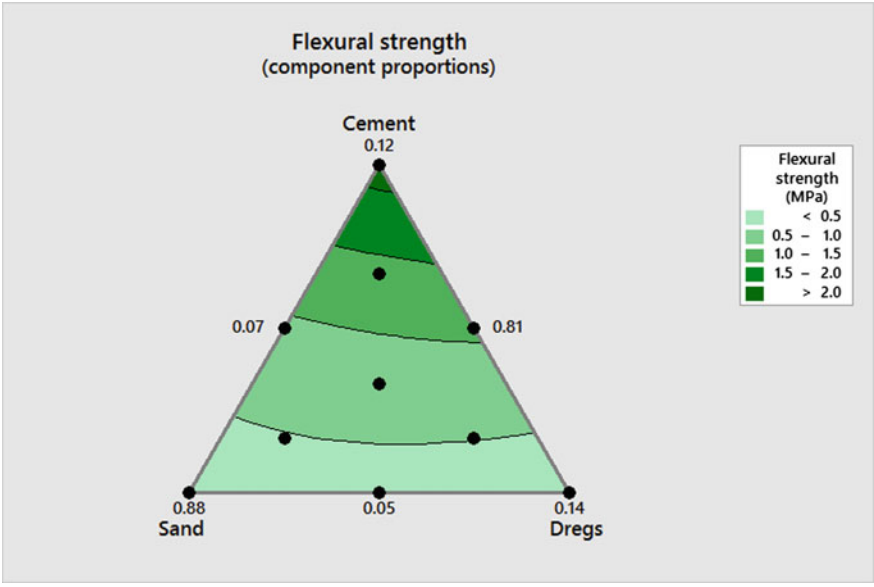

Fig. 2 Response surface of the quadratic model for flexural strength (MPa) at 28 days

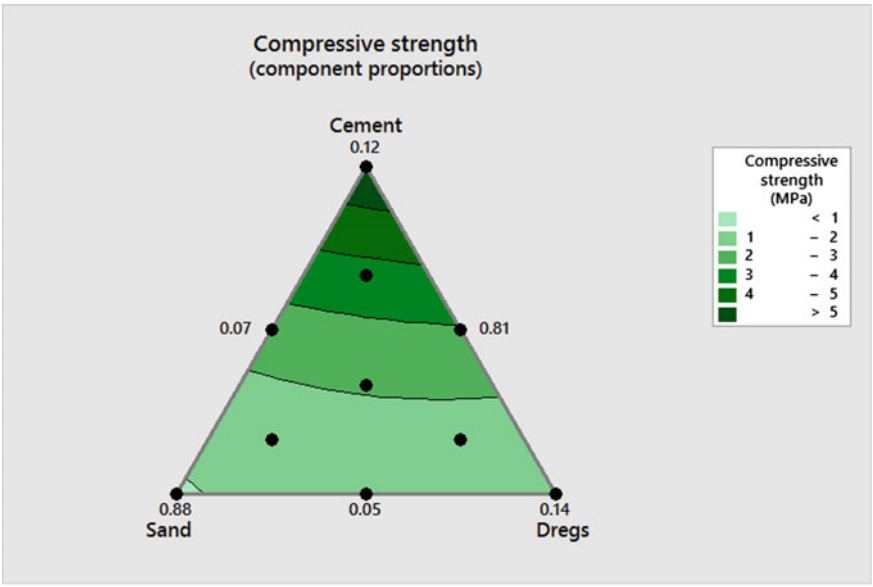

Fig. 3 Response surface of the quadratic model for compressive strength (MPa) at 28 days

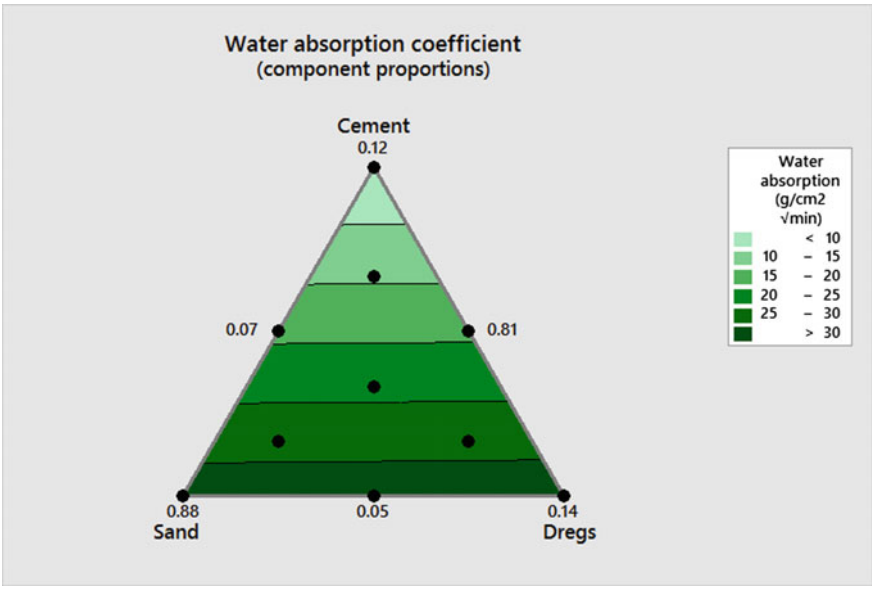

Fig. 4 Response surface of the linear model for capillary water absorption

(32.771 to the sand and 33.049 to the dregs) and by the curves of the response surface of Fig. 4.

When the mortar is covering surfaces, one of its necessary proprieties is the impermeability to water, especially in cases of an external covering. Nevertheless, the water can move by capillaries of mortar [12]. Therefore, mortars with high capillarity are not very interesting, thus being necessary more attention while dregs is added to the mixture.

To the apparent mass density was adjusted a linear model as done to the water absorption coefficient. In comparison to the models of other properties, this one had less precision to estimate the influence of the different components in the mixture. However, this model can be used and reveals that the dregs has a lesser impact on the apparent mass density. So, increasing the amount of the residue provide a more lightweight mortar. This characteristic can be attractive in some applications when it is desired construction units with less weight.

In Fig. 5 is presented the response surface to the apparent mass density.

The ABNT NBR 13281:2005 code [13] classifies mortar in some categories accordingly the properties range. Thus, according to the desired application to the mortar and the intended category, it is only necessary to use a ratio of mortar contained in the analyzed Simplex region.

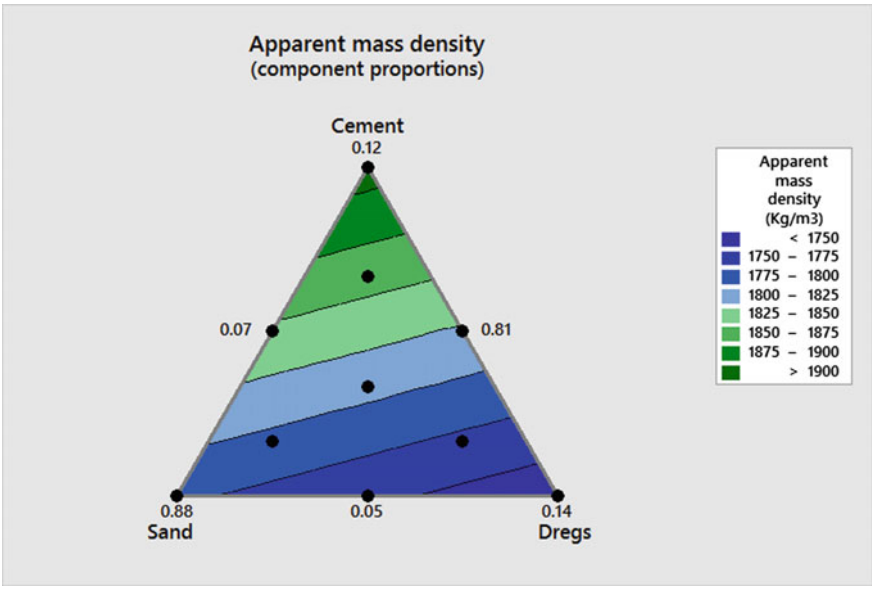

Fig. 5 Response surface of the linear model for apparent mass density

Conclusion

Through this work, it can be concluded that the use of dregs in replacement of hydrated lime is feasible, as long as the amount of residue is moderate. A larger amount of dregs substantially decreases the mortar strength and increases the water absorption. Other observed behavior was the reduction of mortar mass density with the greater presence of dregs, which can be interesting on some occasions.

Since it was obtained equations that relate the amount of each component with the value of certain mortar property, it is possible to manipulate the ratio proportion of the components and, hence, to obtain a mortar with a desirable characteristic. And also to fit in the created product in the different classifications of the ABNT NBR 13281:2005 [13]. However, it is applicable only to the sub-region of the analyzed Simplex triangle, in other words, extrapolations are not allowed.

The fixation of the water amount generates a broad range of mortar consistencies, which can be a problem when there was not a compatibility between the desired mortar property and its use in the building site. Thus, new studies emphasizing the relation water amount-consistency in different ratios of mixed mortar with dregs would be necessary to complement this work and to make possible the optimization of this product.

Lastly, it was concluded that the observed results were satisfactory concerning incorporation of a residue in a construction material. The produced mortar will have an environment appeal and, also, due to the lower costs can attend social buildings.

Acknowledgements The authors want to thank the FAPEMIG for the support provided to this investigation.

References

1. CENIBRA (2009) Caracterização de resíduos industriais. CENIBRA, Belo Oriente
2. Barros Neto B, Spacino IS, Bruns RE (2007) Como fazer experimentos: pesquisa e desenvolvimento na ciência e na indústria. UNICAMP, Campinas
3. Ribeiro AP (2010) Avaliação do uso de resíduos sólidos inorgânicos da produção de celulose em materiais cerâmicos. Doctoral thesis, Universidade de São Paulo
4. Villain L (2008) Pulping wastes and abandoned mine remediation: application of green liquor dregs and other pulping by products to the solidification/stabilization of copper mine tailings. Master's thesis, Luleå University of Technology
5. Medeiros CJ et al, Calagem superficial com resíduo alcalino na indústria de papel e celulose em um solo altamente tamponado. Rev Bras Ciênc Solo. http://dx.doi.org/10.15871/1517-8595/rbpa.v16n4p423-431
6. Marques et al. (2014) Potencialidades do uso de resíduos de celulose (dregs/grits) como agregado em argamassas. Rev Bras Produtos Agroindust. ISSN: 1517-8595
7. Zanella et al. (2014) Durability of mixed mortar lining containing dregs-grits. American Journal of Environmental Science. https://doi.org/10.3844/ajessp.2014.44.47
8. ABNT NBR 13279 (2005) Argamassa para assentamento e revestimento de paredes e tetos—determinação da resistência à tração na flexão e à compressão. ABNT, Rio de Janeiro
9. ABNT NBR 13276 (2005) Argamassa para assentamento e revestimento de paredes e tetos—preparo da mistura e determinação do índice de consistência. ABNT, Rio de Janeiro
10. ABNT NBR 15259 (2005) Argamassa para assentamento e revestimento de paredes e tetos—determinação da absorção de água por capilaridade e do coeficiente de capilaridade. ABNT, Rio de Janeiro
11. ABNT NBR 13280 (2005) Argamassa para assentamento e revestimento de paredes e tetos—determinação da densidade de massa aparente no estado endurecido. ABNT, Rio de Janeiro
12. Silva NG (2006) Argamassa de revestimento de cimento, cal e areia britada de rocha calcária. Master's thesis, Universidade Federal do Paraná
13. ABNT NBR 13281 (2005) Argamassa para assentamento e revestimento de paredes e tetos—requisitos. ABNT, Rio de Janeiro

Adhesion Study at Advanced Ages in Multipurpose Mortars

M. T. Marvila, J. Alexandre, A. R. G. Azevedo, E. B. Zanelato, S. N. Monteiro, G. C. Xavier, M. A. Goulart and B. Mendes

Abstract One of the parameters used in the study of mortars is the adhesion resistance, which indicates how much the mortar adhered to the substrate. The usual study is done at 28 days, to worldwide standardization. Few researchers study the adhesion of mortars to ages other than 28 days. In this scenario, the adhesion strength tests of conventional mortar with a 1:1:6 mass scale (cement, and sand) at 7, 14, 28, 56, 91, 182 and 364 days were performed in order to understand the behavior of this material. The usual characterization tests of the mortars were carried out to correlate the values obtained with the adhesion results. The obtained results demonstrate that the mortar continues to gain resistance with the passage of time. For the trait studied the gain was considerable, indicating that over time the cement continues to hydrate, reacting and contributing to the strength of the material.

Keywords Mortar · Adhesion · Advanced ages

Introduction

Adhesion is one of the most important parameters when analyzing the performance of a multipurpose mortar, which is a type of mortar used for both wall cladding and ceramic tile laying. Although it is a property of great relevance in the studies of this

M. T. Marvila (✉) · J. Alexandre · A. R. G. Azevedo · E. B. Zanelato
G. C. Xavier · M. A. Goulart
Civil Engineering Laboratory, UENF—State University of the Northern Rio de Janeiro, Av. Alberto Lamego, 2000, Campos dos Goytacazes, Rio de Janeiro 28013-602, Brazil
e-mail: markssuel@hotmail.com

S. N. Monteiro
IME—Military Engineering Institute, Rio de Janeiro, RJ, Brazil

B. Mendes
UFV—Federal University of Viçosa, Viçosa, MG, Brazil

B. Li et al. (eds.), *Characterization of Minerals, Metals, and Materials 2018*, The Minerals, Metals & Materials Series,
https://doi.org/10.1007/978-3-319-72484-3_45

type of material, it is extremely complex the understanding about the functioning of the adhesion mechanisms, since several factors interfere in the study of such property.

It is known that four basic mechanisms of adhesion between mortar and porous substrates can be identified, as in the case of blocks and ceramic bricks: first adhesion occurs by initial adhesion between the substrate and the mortar, then the adhesion is processed due to suction capillary, identified by the transport of fine materials to the interface between the two materials, followed by an equilibrium mechanism that occurs between the moisture of the mortar and the substrate studied, and finally the adhesion is due to the hydration of the cement present in the mortar, with formation of a cohesive solid phase between mortar and substrate [1].

Traction adhesion tests are the main parameters for evaluating the performance of multiple use mortars, although there is a great variation in the results found by different authors. These differences can be justified by several factors, which interfere in the execution of the test, and consequently in the comparison of results between different authors, among which can be cited:

- Differences in properties among the mortars studied: factors such as the initial adhesion that the mortar under study has as the substrate, which is strongly influenced by the rheological characteristics of the mortar interfere in the results of adhesion found by different authors [2]. Another factor that also interferes is the water retention that the mortar presents, because it has a great correlation with the suction that the substrate presents.
- Substrate properties: the properties of the substrate interfere with the adhesion mechanisms between this material and mortar, since factors such as porosity, capillary suction and substrate roughness interfere directly with the adhesion values found by different authors.
- Execution of the test: was verified in studies that the parameters of the test interfered directly with the adhesion values found [3]. Factors such as the shape of the specimens used, eccentricity, type of equipment and loading rate cause an unmanage in the results obtained in these tests.
- Impact energy: it is characterized by the kinetic energy with which the portion of mortar thrown reaches the base, and depends on several factors, such as the launching force and the portion of mortar that is thrown on the substrate, which vary from operator to operator. Therefore, it is extremely complicated to compare results of adhesion tests performed by different researchers [2, 4–6].
- Climatic conditions: the conditions of temperature, relative humidity and ventilation directly interfere with the curing conditions that the mortar will suffer, especially for outdoor environments. In this way the comparison between adhesion results obtained for mortars made in different geographic regions is subject to the differentiated climatic conditions of each of these regions [7–9].

Another great factor that interferes in the adhesion resistance between mortar and substrate is the time factor, since the cement present in the mortar continues to undergo the hydration process throughout the ages, even in the advanced ones, which can generate the idea that the mortar will continue to gain resistance over

time. However the weather conditions which will be subject to mortar over time may have the opposite effect on this material. That is, due to rainy conditions and exposure to the sun it may be that the resistance of the mortar actually decreases with the passage of a certain age.

Thus, the objective of this work is to verify and analyze the adhesion strength to the traction of a mortar of multiple external use throughout the advanced ages, with the intention of understanding if the mortar continues to increase its resistance thanks to the hydration of the cement, if the mortar maintains the resistance without changes, or even if mortar presents a decrease in resistance due to exposure to external degradation agents, such as temperature variation, rainfall and sun incidence.

Materials and Methods

Thus, the objective of this work is to verify and analyze the adhesion strength to the traction of a mortar of multiple external use throughout the advanced ages, with the intention of understanding if the mortar continues to increase its resistance thanks to the hydration of the cement, if the mortar maintains the resistance without changes, or even if mortar presents a decrease in resistance due to exposure to external degradation agents, such as temperature variation, rainfall and sun incidence. The mortar in the 1:1:6 (cement: hydrated lime: sand) mortar was characterized according to the parameters required by the Brazilian standards highlighted in Table 1.

After curing times, namely 7, 14, 28, 56, 91, 192 and 364 days, the mortar systems were tested for tensile strength. The adhesion test is performed in the following manner: a chipped masonry wall is performed to receive the coatings and to serve as the substrate in the assay. On this substrate is executed a coat of mortar of the trait studied in the form of a plaster.

After the cure time, a glass saw is used to drill the specimens. According to the Brazilian standard, at least 12 specimens should be analyzed. After the drilling,

Table 1 Characterization of mortar 1:1:6 (cement: hydrated lime: sand)

Parameter	Value obtained	Norm
Relation w/c	0.80	NBR 13276:2016 [10]
Built-in airflow	7.8%	NBR 13278:2005 [11]
Capillarity	13.94	NBR 15259:2005 [12]
Density in hardened state	1.91 g/cm^3	NBR 13280:2005 [13]
Density in the fresh state	2.03 g/cm^3	NBR 13278:2005 [11]
Water retention	93.22%	NBR 13277:2005 [14]
Compressive strength 28 days	4.08 MPa	NBR 13279:2005 [15]
Tensile strength at flexion 28 days	1.12 MPa	NBR 13279:2005 [15]

Fig. 1 Adhesive device

metallic pellets are bonded to each of the specimens using an epoxy adhesive that must have a higher resistance than the coating. After 24 h of application of the adhesive, the test can be performed using a pull-out equipment as shown in Fig. 1. The equipment records the pulling force applied to the mortar to cause its breakage, which force is then converted into resistance.

Results and Discussion

The results of characterization of the mortar used to carry out the tests are indicated in Table 1. As can be seen by analyzing the data in the table, it is a standard mortar commonly used in civil construction.

The results obtained for the twelve specimens of each age, as well as their statistical treatment, are shown in Table 2.

Analyzing the results found for adhesion at different ages and using Duncan's proposed mean difference analysis, it is easy to see that mortar continues to gain resistance to adhesion over different ages. This is because the cement present in this mortar continues to moisturize even at later ages. Therefore, for the region of Campos

Table 2 Data obtained for different ages

Age	7 days	14 days	28 days	56 days	91 days	182 days	364 days
01	0.05	0.12	0.33	0.46	0.51	0.72	0.66
02	0.06	0.08	0.25	0.35	0.40	0.58	0.72
03	0.08	0.08	0.43	0.60	0.39	0.57	0.66
04	0.10	0.15	0.32	0.44	0.38	0.81	0.72
05	0.07	0.06	0.26	0.36	0.48	0.62	0.82
06	0.10	0.08	0.19	0.16	0.48	0.61	0.96
07	0.04	0.10	0.18	0.26	0.47	0.56	0.92
08	0.12	0.06	0.24	0.34	0.43	0.62	0.90
09	0.04	0.07	0.38	0.53	0.53	0.83	0.96
10	0.09	0.16	0.15	0.21	0.38	0.80	1.02
11	0.08	0.06	0.34	0.47	0.51	0.64	1.08
12	0.06	0.13	0.13	0.18	0.32	0.73	1.07
Average	0.07	0.10	0.27	0.36	0.44	0.67	0.88
Duncan	E	E	D	C	C	B	A

dos Goytacazes, under the climatic conditions analyzed, there is no depredation of the resistance and consequently loss of adhesion between substrate and mortar.

Thus, it refutes the idea that the mortar will have loss of resistance due to the climatic actions of temperature, insolation and rain for this specific case of study, since in the present study the hydration of the cement had greater significance in the resistance of the mortars than the action of time.

It is also emphasized that in the first ages, 7 and 14 days, the resistance gain is negligible, since there was no significant difference for the average resistance obtained in these two ages. With this, it is evident that the hydration of the cement is more intense after 14 days, since at 28 days there was a significant gain of tensile strength.

At the age of 56 days until the age of 91 days there was also no significant gain in resistance, which is evidenced by Duncan's analysis. It is likely that during this period the cement hydration has entered the dormancy stage, where the hydration reactions are decelerated. Analyzing the literature, an explanation for this is found: in cement mortars and hydrated lime, late ettringite formation is common due to the compounds that do not react completely in the early ages. This late ettringite reduces the resistance of mortars since its structure is rod-shaped, causing internal stresses detrimental to the material. It is noteworthy that these reactions commonly occur in ages between 60 to 80 days, as observed in this study. After this period, the ettringite decomposes and the cement hydration reaction proceeds [16–18].

After the dormancy period, the mortar again underwent hydration reactions, and its resistance increased until the last analyzed age at 364 days. The graph presented in Fig. 2 demonstrates how it was the tendency of resistance gain to adhesion to mortar, where it is observed that obviously this phenomenon does not follow a

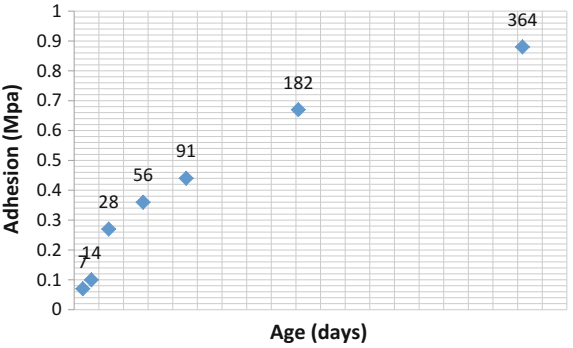

Fig. 2 Resistance to adhesion of the mortar studied

linear trend, since the reactions that modify the resistance of the mortar present great complexity and do not follow trends obvious and simple.

Conclusion

Through this study it was possible to conclude:

- Statistical analysis by the Duncan method for separation of averages shows that the mortar presents resistance gain to adhesion with the advancement of the studied ages.
- The increase in resistance is justified by the hydration of cement that continues to occur even in advanced ages.
- In the early ages, 7 and 14 days, the increase in resistance is negligible, indicating that cement hydration at these early ages has not reached levels of great relevance.
- After the 28 days, it is possible to increase the resistance to the adhesion of the mortar, until the ages of 56 and 91 days when the cement hydration is reduced, it is a period of dormancy in the mortar.
- From the period of 182 days until the last analyzed period, at 364 days, the mortar continued to have a resistance to adhesion.
- For the mortar studied, the hydration of the cement presented a greater contribution than the external factors of insolation, rainfall and temperature variation. This is perceived by the resistance gain that the mortar presented.

References

1. Barbosa W, Borges J, da Silva IJ (2013) Discussion on the classification requirements of NBR 13281 for the water retention test. In: Brazilian symposium on mortar technology, vol 10, SBTA
2. Paes INL (2004) Evaluation of water transport in mortar coatings in the early moments post-application. Doctoral thesis, UnB, p 242
3. Costa EBC, Carasek H (2009) Influence of test parameters on determination of adhesion strength of mortar coatings. Built Environ 9(4):17–35
4. John VM (2003) Rethinking the role of hydrated lime in mortars. In: Brazilian symposium on mortar technology, vol 5, SBTA
5. Loturco B (2004) How to check mortar adhesion.Téchne, vol 88, pp 42–47
6. Dualibe RP, Cavani GR, Oliveira MCB (2005) Influence of the type of projection of the mortar on the tensile strength and water permeability. In: Brazilian symposium on mortar technology, vol 6, SBTA
7. Mehta PK, Monteiro PJM (1994) Concrete: structure, properties and materials. PINI, São Paulo
8. Isehard JLRF (2000) Contribution to the study of the feasibility of curing concrete by solar energy. Doctoral thesis, UFRS, p 162
9. Lorenzetti, UV, Fredel MC, Gleise P (2002) Evaluation of the effectiveness of curing procedures on concrete durability: compressive strength, mass loss and water absorption by capillarity. In: Workshop on construction durability, vol 2
10. Brazilian Association of Technical Norms—ABNT NBR 13276:2016, Mortars applied on walls and ceilings—determination of the consistence index (in Portuguese)
11. Brazilian Association of Technical Norms—ABNT NBR 13278:2005, Mortars applied on walls and ceilings—determination of the specific gravity and the air entrained content in the fresh stage (in Portuguese)
12. Brazilian Association of Technical Norms—ABNT NBR 13277:2005, Mortars applied on walls and ceilings—determination of the water retentivity (in Portuguese)
13. Brazilian Association of Technical Norms—ABNT NBR 13279:2005, Mortars applied on walls and ceilings—determination of the flexural and the compressive strength in the hardened stage (in Portuguese)
14. Brazilian Association of Technical Norms—ABNT NBR 13280:2005, Mortars applied on walls and ceilings—determination of the specific gravity in the hardened stage (in Portuguese)
15. Brazilian Association of Technical Norms—ABNT NBR 15259:2005, Mortars applied on walls and ceilings—determination of water absorption coefficient due to capillary action (in Portuguese)
16. Ikumi T, Segura I, Cavalaro SHP (2017) Influence of early sulfate exposure on the pore network development of mortar. Constr Build Mater 143:33–47
17. Ekolu SO, Thomas MDA, Hooton RD (2006) Pessimum effect of externally applied chlorides on expansion due to delayed ettringite formation: proposed mechanism. Cem Concr Res 36:688–696
18. Talero R (2002) Kinetochemical and morphological differentiation of ettringites by the Le Chatelier-Anstett test. Cem Concr Res 32:707–717

Applications and Opportunities of Nanomaterials in Construction and Infrastructure

Henry A. Colorado, Juan C. Nino and Oscar Restrepo

Abstract New and extraordinary physical-chemical properties of materials at nanoscale open up new applications for the building and infrastructure industry such as structural reinforcements, electronic properties and energy harvesting. Therefore the issues and risks associated with the manufacturing of nanomaterials are now of big concern due to the large volumes and typical processing involved in this industry. This paper presents a discussion and selected applications of nanotechnology in the construction and building materials: from metals and alloys, clay and minerals, ceramics, cement and concrete, asphalt, wood and composites, to finishing systems and some of the most used characterization techniques. Besides the progress in some areas, nanotechnology is just emerging in this field, with many challenges and opportunities, problems unsolved and business opportunities. A discussion regarding the potential health issues and risks of using nanomaterials for workers and the potential environment effects is included as well. New images and diagrams are presented and discussed.

Keywords Cement · Concrete · Composites · Asphalt · Clays Ceramics · Wood · Steel · Characterization · Nanomaterials

H. A. Colorado
CC Compuestos Laboratory, Universidad de Antioquia,
Calle 70 no. 52-21, Medellín, Colombia

J. C. Nino
Materials Science and Engineering Department, University of Florida,
Gainesville, USA

O. Restrepo
Departamento de Ciencia e Ingeniería de Materiales,
National University of Colombia, Medellín, Colombia

H. A. Colorado (✉)
Facultad de Ingeniería, Universidad de Antioquia, Calle 67 # 53-108,
Bloque 20 of 437, Medellín, Colombia
e-mail: henry.colorado@udea.edu.co

B. Li et al. (eds.), *Characterization of Minerals, Metals, and Materials 2018*, The Minerals, Metals & Materials Series,
https://doi.org/10.1007/978-3-319-72484-3_46

Introduction

The physics and chemistry of nanostructured building materials differ from everyday materials due to quantic effects and due to its high surface area to volume ratio. Typical morphologies in nanomaterials are spheres, cylinders and sheets. These materials have changed the technology in an increasing number of applications, and the construction and building materials industry has also been benefit. In this paper, some of the most significant achievements of nanotechnology in the construction and building materials are discussed, not only in the materials developments but also in the most used characterization techniques. The main goal is to show the progress, tendency, and opportunities in this field, in a context not only useful for students, professors and researchers from engineering and natural sciences, but also for industries starting in nanotechnology, or simply for interested readers without background in nanotechnology.

Regarding the main areas of materials from science to engineering, applications and performance of nanomaterials seem to need more research and development than structure, properties, processing and characterization. This is true since most academic community agree in the high potential of nanomaterials to change significantly many aspects of our future. This is represented in Fig. 1a.

Figure 1b shows the construction and building materials from the present paper, mostly organized by their structure. Metals have metallic bond, ceramics can have ionic and covalent, and composites can have combination of different bond types. All can have secondary bonds too. Including organic materials, such as wood, the building materials can be classified as composites.

Materials in the building and construction industry such as cement and concrete (most used man fabricated material) have had a slow evolution in their science and engineering. Today, nanotechnology is rapidly changing this trend and many scientific and business opportunities appeared. On the other hand, areas such as composites have shown a notable development in the last years, as both

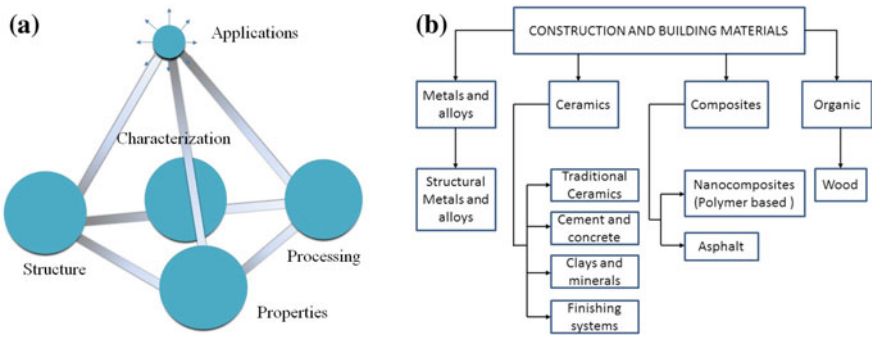

Fig. 1 **a** Diagram showing the applications growing area in nanomaterials; **b** construction and building materials from the present paper

nanocomposites and nanoadditives. In fact, aside with electronic and biomaterials are some of the engines that today drive materials science. As example, other fields such as wood have shown less progress in nanotechnology when compared to composites.

Therefore, in the last years, multiple and significant progress are changing the construction and building materials by a revolution in science and technology driven by nanotechnology. New trends and opportunities are emerging which must be taken into the account of young engineers, companies and researchers.

Materials and Methods

Metals and Metal Alloys in Building and Construction

Copper and steel are undoubtedly the most widely used metals in construction. Steel alloys are used in screws, bolts, as well as in beams and support structures and in particular as reinforcement within concrete concrete where either thick wires (rebars) or meshes are added in order to enhance the mechanical strength of concrete under tension and bending stress fields. The dimension of steel components for construction are typically in the centimeter to meter range and it is the advancement in the understanding of the effect of microstructure on the mechanical properties and corrosion resistance that has enabled the use of nanotechnology to achieve substantial improvements in the performance of metals and its alloys. For example, recent work by Lu et al. [1]. All text references should be consecutively numbered, using square brackets with the period after the reference; for example [1, 2] has shown that in low carbon steels microalloying with 0.1 wt% of niobium, titanium or vanadium results in hardening due to the controlled precipitation of carbides. The size of these carbides ranges between a few nanometers and one micrometer depending on processing conditions. It is important to note that when the size of the precipitates is below 10 nm there is an increase of approximately 200 MPa in the yield strength, which represents roughly a 25% improvement in the mechanical performance. While this is in itself an impressive enhancement, it is perhaps most important to recognize that it well known hardening techniques, like precipitation hardening, have seen a rebirth an expansion as a result of nanotechnology. Being able to characterize the microstructure of alloys and their precipitates in the nanometer scale has open the door for a whole new series of alloys for which the above is but one example.

In the case of copper, it is primarily used for electrical wiring and in piping where the use of polymers is not a desired or viable option. In addition, copper alloys such as brass are used in the weather protection of roofs, doors, siding, and facades due to its high corrosion resistance. Precisely in the field of corrosion Mao et al. [2] has demonstrated that through a process of nanocrystallization of a copper-nickel alloy (70 Cu–30 Ni) yields increased hardness and enhanced

corrosion resistance. For reader interested in reading more about mechanical property enhancement in copper alloys using nanotechnology a number of sources including the work by Hoppel et al. [3] is available in the open literature.

Clays and Minerals

One of the most important aspects of working with clay is the determination of particle size. This is given by the genesis of the minerals that make up its internal composition. Kaolinitic clays, for example, are mainly composed of kaolinite (in Fig. 2a a nanoparticle of kaolinite is shown), halloysite, dickite and other minerals produced by the degradation of metamorphic rocks by effects of weathering. Formation processes allow the clay minerals, in some cases, to have particle sizes in the nanometer range, that is, which do not exceed 100 nm in average size. These sizes are critical in determining the application to these clays. Nanotechnology has now come to stay when using fine-grained clays is about. The interaction at the nanometer scale between particles had found important applications for this type of minerals and rocks.

Working with nanoparticles has allowed to change existing paradigms regarding the surface behavior of clays and thus achieve processing that until recently were not conceived; it is the case of mineral processing, classification processes [4] and concentration of minerals, such as flotation [5, 6]. For the classification and separation of minerals it was reached using banks of hydrocyclones for separating particles of nanometer size from those of micron size and thereby control key parameters in their use, such as chemical surface, which is key in controlling the rheology of slurries and suspensions, critical in the ceramic industry, paint, food, etc. With regard to the concentration of minerals, nanotechnology has advanced

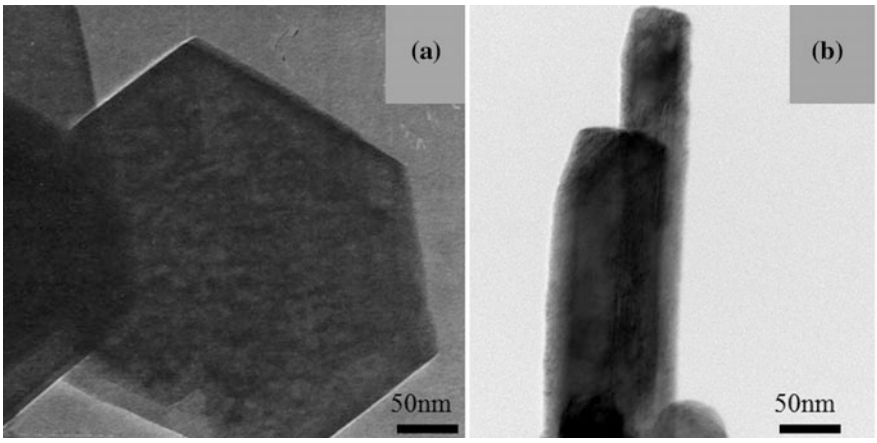

Fig. 2 Transmission electron microscopy (TEM) for **a** Kaolinite, **b** goethite nanocrystals

significantly in processes such as flotation of ultrafine particles; it is the case of feldspar contaminated by quartz or talc mixed with some iron oxide powders, which changed its color which made them suitable for the cosmetics industry. Today this is possible and has been given a major boost to some sites that until very recently were not considered.

Recent Works [7] have let to explain that, when the clay minerals have small size of particle, they could change the color of the clay, thus bleaching processes can be performed successfully performing effective separation of different sizes comprising mineral samples.

With respect to mineral transformation process, nanotechnology has enabled processes on an industrial scale for obtaining nano-sized crystalline structures in order to achieve special applications. Such is the case of the pigment industry [8, 9], coatings industry [10] and decorating industry [11], among others, which, by controlled particle size growth processes, have succeeded in designing products for specific colors, resistance to temperature, weathering, and extreme working conditions, such as acidity or alkalinity. All this thanks to the understanding of the processes of nucleation and growth and control of the technological aspects that allow handling. Figure 2b is a photo taken of goethite nanocrystals (FeO (OH)), used since ancient times as a pigment.

Ceramics

In general ceramic compounds are the materials most widely utilized in construction as described before, however engineering ceramics as those shown in Fig. 3, constitute an important area in modern applications in áreas such as electronic materials or high temperature ceramics. This is not surprising given the fact that clays and minerals used in bricks, stone, marble, granite, sand, as well as cement, and concrete are all ceramics. Since several of these are described in detail elsewhere, in this section only glasses are discussed.

Since its discovery, glass has been used broadly in construction as part of decoration but also as an integral part of the architecture as light management and exterior walls. Of the extensive number of recent advances in glass for building and construction as a result of nanotechnology, it is particularly worth mentioning tempered glass as a result of ionic exchange (also used in smartphones) which exhibit high fracture toughness enabling its use in buildings requiring adequate hurricane and wind damage protection.

Likewise, recent advancements in thin film coatings (i.e. coatings of submicron thickness) have enabled novel applications in the field of smart windows such as thermochromic windows and self-cleaning windows. An example of thermochromic windows (i.e. windows that change color or transparency with temperature changes) is achieved with thin film coatings of vanadium oxide (VO_2). For

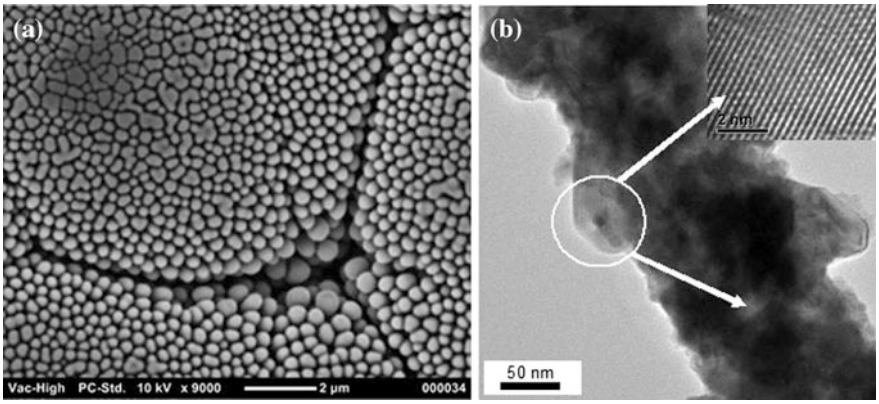

Fig. 3 **a** SEM micrograph revealing the surface morphology of an electrodeposited ceramic coating revealing the nanometer nodular structure; **b** TEM of a $BaTiO_3$ nanofiber synthesized by electrospinning. The inset shows the lattice fringes indicating the crystallinity of the polycrystalline nanofiber. Both images were collected by the Nino Research Group at University of Florida

example, Zhang et al. [12] have shown that a VO_2 coating of 56 nm maintains the transmittance in the visible spectrum combined with a 50% efficiency in blocking the infrared spectrum, which is the highest heating contributor. The development of this type of smart windows and related applications has enabled a leap change in building energy management practices and standards. The recent review by Kamalisarvestani et al. [13] is an excellent source of information in this particular topic.

As mentioned before, another area of recent interest and impact is that of self-cleaning windows. In this type of windows, coatings typically of titanium dioxide [14] or sílica [15] with thicknesses in the 120–150 nm range induce photocatalytic reactions when in contact with dust and other environmental contaminants and the product of these reactions is washed away by the rain thus leaving behind a clean window. It is important to note that there are already a number of commercially available smart window products and its broad use and expanded market share is anticipated. Jelle et al. [16] presents a list of applications for smart windows, discusses state of the art research areas in the field as well as future trends.

Cement and Concrete

Concrete, and cement as its main component, are the most widespread man made materials. These materials are very successful not only for their performance in buildings and infrastructure, but also for the low cost and raw materials availability.

Lastly, cement has been significantly progressing with nanotechnology, mostly because cement is a multiphase material strongly influenced by its components, such as hydrates, at the nanoscale.

On the other hand, since the hydration process is such a complex one that involves a lot of mechanisms and species reacting chemically in different time scales, from seconds to years, some fundamental aspects, at nano and even micro scales, are still unknown. Because of this aspect, nanotechnology will continue driving areas like cementitious materials specifically in the materials characterization and nano-additives.

For instance, the understanding of the main cement phase, the hydrated calcium silicate C–S–H which corresponds to nearly 60% of all hydrates in cement, was a significant progress due to nanotechnology [17]. In addition, researchers reported that C–S–H and other cement phases could be modified with nanotechnology through organic molecules [18] in order to tailor different properties. Moreover, since some cement structures do not have a long order range, identification by traditional methods such as X-ray diffraction (XRD) is very complex and not possible in some cases. However, other techniques such as transmission electron microscopy (TEM) and nuclear magnetic resonance (NMR) enabled us to build a clear atomic structure of C–S–H nano-crystals in the last 25 years [19–22].

Another significant achievement was the development of the third generation of super-plasticizers additives, such as PCE (polycarboxylate ether), used to improve the particle dispersion and to reduce the amount of water in cement (which is known as strength improver).

The accelerated development of nano-additives for concrete enabled the development of a wide varied amount of modified mixtures (see Fig. 4) with high mechanical performance and durability, for applications such as pre-fabricated parts, such as tubes, walls, and beams [23, 24]. Figures 2b, c show portlandite, one of the cement clinker phases. Finally, nanotechnology is also a way to decrease the negative environmental impact and costs in concrete, which is given a new generation of construction and building materials.

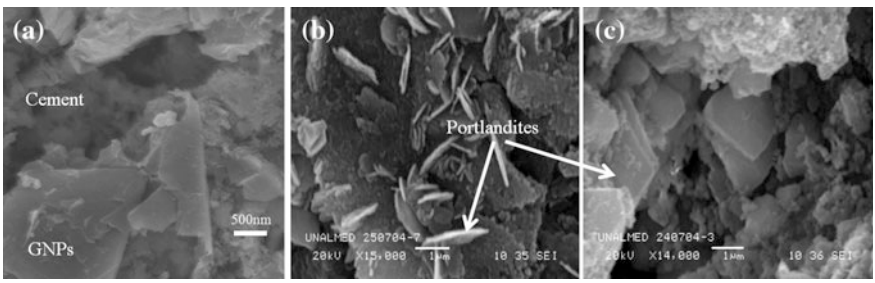

Fig. 4 Images taken with transmission electron microscopy (TEM)) for **a** reinforced concrete with graphite nanoplateles (GNPs), **b** and **c** the nanostructure Portland cement phase portlandite

Asphalt

Besides asphalt pavement is used at large scale in roads of big cities, its macroscopic behavior depends from its properties at micro and nanoscale. Therefore, research showed improvements in durability, fatigue life and routing for asphalt and its admixtures with nanotechnology. This was mainly obtained with nanoadditives (such as nanoclay, carbon nanotubes, and other nanostructures from silica, alumina, magnesium, calcium and titanium dioxide) [25].

As one example of many significant advances in this field, it has been found that nanoclay non-modified (NNM) increases slightly the asphalt viscosity, whereas the same nanoclay modified with a polymer (NMP) slightly decreases the asphalt viscosity. On the other hand, the addition of NNM improved the high temperature stability, whereas the addition of NMP do not produce significant changes, but increases the asphalt recovering. In summary, the addition of NNM in general increases the asphalt recovering [26].

Another good example is the addition of silica nanoparticles to improve fatigue, dynamic modulus, routing strength, and anti-aging behavior [27]. Similarly, a great result found was that adding only 1% of rubber nanopowder obtained by the sulfurization of latex nanoparticles in a dry process, asphalt has a higher cracking and routing strength at low temperatures. Moreover, by adding up to 3% of this powder the softening point can increase from 48.3 to 55.3 °C [28].

The examples shown above shows the great potential that nanotechnology has in the future of asphalt and other related materials.

Wood

Being one of the oldest and most widely used construction materials, it would seem rather incredible that nanotechnology would have enabled key advances even in wood. Nonetheless, same as with almost all materials, the ability to investigate the structure of wood in the nanometer range has yielded a better understanding of the origin of the observed properties and thus has enabled the tailoring and development of new properties and response to external stimuli like environmental conditions and in particular the relative humidity. Humidity control in wood is essential to ensure property homogeneity and in particular to control shape and limit deformations. In general, wood is hydrophilic, that is, it has an affinity for water and it can readily absorb it. Therefore, any modification to the wood characteristics that can make it repel water (hydrophobicity) is of great interest. It is precisely here where nanotechnology has demonstrated promising results. To highlight just one of the numerous works in this area, according to Artus et al. [29] deposition of silicon filaments, between 20 and 50 nm in diameter and 1 μm in length, on the surface of wood results in “superhydrophobicity”, a term used to highlight the extreme repulsion of water with contact angles above 150°, where 0° is indicative of a

hydrophilic surface and 180° indicative of a perfectly hydrophobic surface. This is an impressive and transformative result as it represents a new paradigm in the interaction of water and wood. For additional reading about this and other processes that can be used to modify the properties of wood that are relevant for construction the reader is referred to the review by Wang and Piao [30].

Composite Materials

Nanocomposites are multiphase materials where at least one of its phases has one, two or three dimensions of less than 100 nm. Therefore, many topics of this paper could classify as nanocomposites. Therefore, in this section we will only consider those with polymeric matrix. As one of the many great applications, polymeric nanocomposites are used to repair and rehabilitate damaged construction and structures, such as tubes and bridges [31]. Nanocomposite coatings are required where a fast set material is needed, such as in metallic tubes repair with defects induced by corrosion, in such a way that no flow stopping is needed while tube is repaired, as shown in Fig. 5.

Known nanocomposites also act as fillers, and these can have a very diverse chemical composition (such as nanosilica SiO_2, nanoalumina Al_2O_3, or titanium dioxide TiO_2); nanoclays (such as montmorillonite $(Na,Ca)_{0.3}(Al,Mg)_2(Si_4O_{10})(OH)_2\ nH_2O$); or CNTs and carbón nanofibers [32, 33]. These nanoadditives change the resin rheology, increase the stiffness one gets set, and reduce the difference in the coefficient of thermal expansion between the filler nanocomposite and the substrate (such as in a metallic tube).

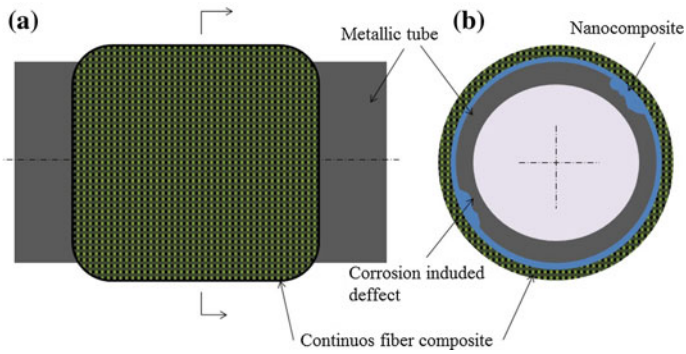

Fig. 5 **a** Typical repaired tube by polymeric nanocomposite resin with continuous fibers; **b** cross sectional detail

Finishing Systems

The application of nanotechnology has allowed the construction industry forward significantly in subjects which until a few years ago were considered finished and completed. This applies to finishing systems and decor. In recent years there has been significant progress in the development of new designs and technologies, which were considered impossible to achieve. Particularly in the ceramic industry it has opened a major way in the design of complex modern formats and techniques used as decorating inkjet [34], application of laser and plasma decoration, and special deposition techniques (PVD, CVD) [35]. New technologies allow very sophisticated decor finishes and the key to all these techniques is precisely the use of nanotechnology, as it has led to the use of products with distinct sizes and tailored particle distributions which has been possible to implement of appropriate technologies. The same has been achieved in the application of cement and concrete finishes, paints, wood and other natural elements, which change significantly their surface appearance, presenting sizes of very fine and controlled in terms of particle distribution.

As for the surface finish of construction products such as cement, concrete, ceramic, wood and other natural products, the use of some nanoparticles, used as additives, has great potential in technological development because these particles applied in small significant portions help to significantly improve the final properties of the paints and varnishes used on them so. Adding ZnO nanoparticles improves significantly the performance against UV radiation of the coating, while the addition of alumina (Al_2O_3) and silica (SiO_2) improves quality of the stripes. Paintings with self-cleaning properties and anti-graffiti eco solvent which dried in about three seconds and turn out to be much cheaper than conventional paints [36].

Installation and Lightweight Construction Systems

On the use of installation systems of building products, as well as light weight construction, nanotechnology also has an important application field that has been growing over the course of the years. The use of nanoparticles of iron oxide thermally activated adhesive materials allows remote start of the drying process by applying an electromagnetic field in the microwave-range radio frequency (1–10 GHz). Also, on completion of the drying process of the adhesive on scales smaller time than conventional processes, the undesirable heating of surrounding areas is reduced [37].

The applications of this kind of technology could be in all those in which it is desired to bond two pieces reducing unwanted heating of adjacent areas, by heating locally the glue. It is also used when it is desired to decrease the drying time of an adhesive, whereupon processes needed to complete valuably reduce welding parts. Furthermore nanoparticles absorb radiation and heat drying glue matrix [38].

Polycarboxylate based additives allow the tailoring of the different functional parts of the molecule to each of the functions needed in the installation materials. Polycarboxylates have a molecular structure composed by a main supported chain structure with free functional groups as side chains, which allow the interaction with the cement for diverse applications, and can be adapted using nanotechnology to the desired functionality [39].

Characterization Techniques

As it has been emphasized throughout, being able to observe and investigate the surface and microstructure of materials in the nanometer scale is perhaps the most important development that has allowed for the vast impact of nanotechnology. In general, any advanced characterization technique, provided the needed resolution, can be used to investigate nanotechnology either directly or indirectly. Nonetheless, without presenting extensive technical working details of the techniques, it is still worth highlighting some microscopy and spectroscopy examples.

(a) Scanning electron microscope (SEM) uses the interaction of a beam of electrons with the material to form an image and it therefore allows for the visualization of the material surface in the nanometer scale (which is smaller than the wavelength of the visible light). The current state of the art SEM have a typical resolution around 2 nm.
(b) Transmission electron microscope (TEM) is similar to SEM but with the difference that the samples utilized are ultrathin (nanometer thickness) and therefore allow the transmission of the electron beam and the image is then formed from the transmitted electrons. State of the art TEM with aberration correction can resolve sample features in the order or 0.1 nm.
(c) Atomic force microscope (AFM) is a scanning instrument that combines laser optics and piezoelectric conduction to detect forces in the order of nanoNewtons through a cantilever probe. The motion of the cantilever can itself be registered with nanometric spatial resolution. This combined force-space precision allows the formation of surface and topographical images of the samples with resolution around 1 nm. Given the versatility of the type of probe that can be used and different the modes of operations (contact or dynamic) AFM is perhaps one of the most widely techniques used in nanotechnology.
(d) X-ray photoelectron spectroscopy (XPS) is a technique that enables the estimation of the stoichiometry of the sample surface with typical resolution around 5 at.%. The unique advantage of XPS relies on the fact that it enables the separate characterization of the first 10 nm of material below the surface. Moreover, with techniques like ion ablation it is possible to remove the atoms between 1 and 8 nm below the surface and thus a detailed analysis of the composition as a function of distance from the surface in the nanometer scale is possible.

For additional information on this and other characterization techniques it is worth consulting volume 10 of the ASM Handbook.

Health Concrete and Environmental Risk for Using Nanomaterials

Nanoparticles and nanomaterials in general as we know have always existed in nature, however, it is just in this time when humans have been creating a lot of them by engineering, and therefore there are questions regarding their effect on the environment and human health. Due to the nanomaterials high surface to volume ratio, they have a highly reactive materials. This enables them as reactive oxygen species (ROS) and free radicals, important mechanisms of nanomaterials, which has an emerging science, the nanotoxicology [40]. ROS have been related with CNTs, carbon fullerenes and metal oxides nanoparticles, resulting in health issues such as inflammations, and protein, DNA and membranes damage [41]. Human body is more exposed in skin, respiratory and gastrointestinal tract due to the semi-open condition of these parts. Hristozov and Malsch [42] have drawn very important conclusions after investigation on the nanoparticles effect on human health. Figure 6 summarizes some of the information presented above. The main routes of exposures for mammals have been classified as dermal, ingestion, inhalation, and ocular. These correspond to the more vulnerable body parts typically more exposed to environment. Also, the main contamination sources are grouped in Fig. 6: combustion, medicine and cosmetics, mining and construction industry, energy, laundry and automobile industries. Particularly in case of construction and building materials industry there are additional issues regarding the final product presentation. Many of the supplied materials are powders that workers and people use at home, nanoparticles have to be stabilized in many ways if companies want to put it on a cement powder mix at store. Major advances are needed until this can be safe for all.

The first conclusion is that with the state of knowledge we have of the topic it is almost impossible to know any collective judgment about the potential risks for exposure to nanomaterials, although most of research show that nanomaterials have different types of hazardous effects on life. This is due to the limited number of studies of effects of nanomaterials in human and environment. Thus, engineering nanoparticles influence on life is even less known [42].

Lee et al. [43] have reported a good review on environmental health and safety considerations of nanoparticles in the construction industry. Research in several nanoparticles show their negative effects, for instance, carbon nanotubes (CNTs) cause pulmonary toxicity and inflammation in mammals [44, 45] associated with cell wall damage. C_{60} fullerenes show antimicrobial activity, which is toxicity to bacteria by an oxidation to cells mechanism [46, 47]. TiO_2 irradiated with UV cause inflammation, cytotoxicity, and DNA damage in mammalian cells [48]. SiO_2

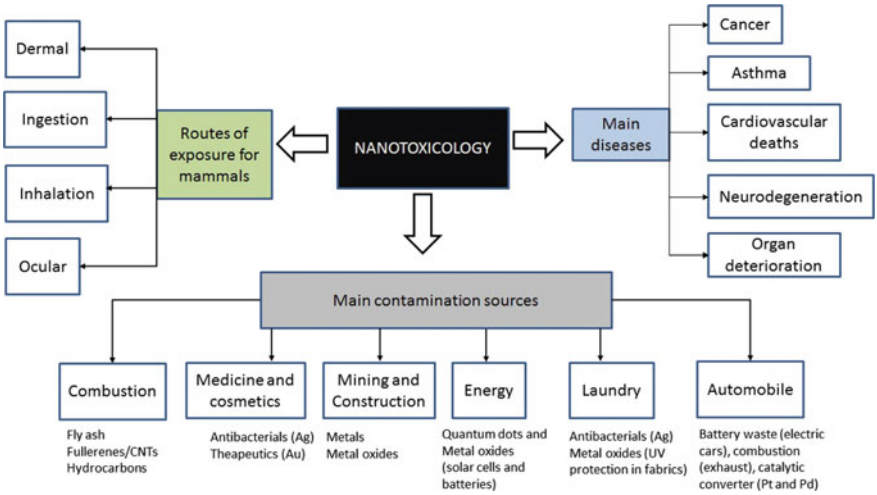

Fig. 6 Nanoparticle health concerns and environmental risks

nanoparticles have been related as carcinogenic [49–50] by causing problems such as membrane damage and tumor necrosis genes in rats. Quantum dots are toxic for both mammalian cells and bacteria due mainly to their hazardous heavy metals content such as cadmium and lead [51]. Copper and copper oxide can cause DNA damage in bacteria, algae, yeasts, mice, and human cells [52]. Figure 6 summarizes many of this examples in the main diseases: cancers, asthma, cardiovascular deaths, neurodegeneration, and multiple organ deterioration.

The second important conclusion relays on the fact that there are many actions and activities that need to be done in order to decrease the negative effects of nanoparticles. Moreover, the degree of their environmental mobility and bioavailability of nanoparticles need to be established.

Summary

Some of the most significant advances in nanotechnology of construction and building materials has been presented in this paper. As shown above, nanotechnology has gone into all different kind of materials and applications, solving old problems and some new challenges that are just emerging. Examples from metals and alloys, clay and minerals, ceramics, cement and concrete, asphalt, wood and composites, to finishing systems and some of the most used characterization techniques are discussed.

Therefore, it is clear to see that this area will be a great tool for construction materials understanding and improving, carrying out the industry to find the limits of materials such as tallest buildings and extreme durability of infrastructure.

Besides the progress, nanotechnology is still an emerging area with many challenges and opportunities, problems unsolved and business opportunities. Some open areas from the materials and processing are: particle agglomeration, scaling up, property repeatability, and interface enhancement.

Finally, nanomaterials effects on health and environment has still not much information to know all its effects. However, most research reveals its negative effects on life. Urgent actions must be taking into the account in order to avoid a public health worldwide problem. The industry of construction and building materials have extra challenges due not only to its large scale but also to the current manufacturing procedures which probably need to be fully redesigned when nanoparticles are used. This is not only an issue, it is a motivating challenge to engineers and scientist to work in new technologies of materials and manufacturing.

References

1. Lu JF, Omotoso O, Wiskel JB, Ivey DG, Henein H (2012) Strengthening mechanisms and their relative contributions to the yield strength of microalloyed steels. Metall Mater Trans A 43A(9):3043–3061. https://doi.org/10.1007/s11661-012-1135-3
2. Mao XY, Li DY, Fang F, Tan RS, Jiang JQ (2011) Application of a simple surface nanocrystallization process to a Cu-30Ni alloy for enhanced resistances to wear and corrosive wear. Wear 271(9-10):1224–1230. https://doi.org/10.1016/j.wear.2010.12.063
3. Hoppel HW, Kautz M, Xu C, Murashkin A, Langdon TG, Valiev RZ, Mughrabi H (2006) An overview: fatigue behaviour of ultrafine-grained metals and alloys. Int J Fatigue 28(9):1001–1010. https://doi.org/10.1016/j.ijfatigue.2005.08.014
4. Saidi M, Maddahian R, Farhanieh B, Afshin H (2012) Modeling of flow field and separation efficiency of a deoiling hydrocyclone using large eddy simulation. Int J Min Process 112–113
5. Aghaiea E, Pazoukib M, Hosseinia MR, Ranjbara M, Ghavipanjeh F (2009) Response surface methodology (RSM) analysis of organic acid production for Kaolin beneficiation by Aspergillus niger. Chem Eng J 147:245–251
6. Yoon R-H, Nagaraj DR, Wang SS, Hildebrand TM (1992) Benefication of kaolin clay by froth flotation using hydroxamate collectors. Min Eng 5(3–5):457–467 (March–May)
7. Jiménez G, María A (2012) Estudio del Efecto de la Fracción de Ultrafinos sobre el Blanqueo de Caolines. Tesis de Maestría. Facultad de Minas. Universidad Nacional de Colombia
8. Giraldo C, Tobón JI, Restrepo Baena OJ (2012) Ultramarine blue pigment: a non-conventional pozzolan. Constr Build Mater 36:305–310
9. Chavarriaga E, Montoya J, Restrepo C, Restrepo O. Synthesis of ceramic nanopigments. In: TMS 2014, 143th annual meeting and exhibition. San Diego, Ca. USA, 16–20 Feb 2014
10. Sancho JP, Restrepo OJ, García P, Ayala J, Fernández B, Verdeja LF (2008) Ultramarine blue from Asturian hard kaolins. Applied Clay Science 41(3–4):133–142
11. Hernández MY, Restrepo O (2014) Sol-gel synthesis $NaCrSi_2O_6$ nanopigments aided by statistical design of experiments. In: TMS 2014, 143th annual meeting and exhibition. San Diego, Ca. USA, 16–20 Feb 2014
12. Zhang ZT, Gao YF, Chen Z, Du J, Cao CX, Kang LT, Luo HJ (2010) Thermochromic VO_2 thin films: solution-based processing, improved optical properties, and lowered phase transformation temperature. Langmuir 26(13):10738–10744. https://doi.org/10.1021/La100515k

13. Kamalisarvestani M, Saidur R, Mekhilef S, Javadi FS (2013) Performance, materials and coating technologies of thermochromic thin films on smart windows. Renew Syst Energ Rev 26:353–364. https://doi.org/10.1016/j.rser.2013.05.038
14. Chabas A, Lombardo T, Cachier H, Pertuisot MH, Oikonomou K, Falcone R, Verita M, Geotti-Bianchini F (2008) Behaviour of self-cleaning glass in urban atmosphere. Build Environ 43(12):2124–2131. https://doi.org/10.1016/j.buildenv.2007.12.008
15. Guan KH (2005) Relationship between photocatalytic activity, hydrophilicity and self-cleaning effect of TiO_2/SiO_2 films. Surf Coat Tech 191(2–3):155–160. https://doi.org/10.1016/j.surfcoat.2004.02.022
16. Jelle BP, Hynd A, Gustavsen A, Arasteh D, Goudey H, Hart R (2012) Fenestration of today and tomorrow: a state-of-the-art review and future research opportunities. Sol Energ Mat Sol C 96(1):1–28. https://doi.org/10.1016/j.solmat.2011.08.010
17. Bittnar Z, Bartos PJM, Nemecek J, Smilauer V, Zeman J (eds) (2009) Nanotechnology in Construction. In: Proceedings of the NICOM3
18. Raki L, Beaudoin JJ, Alizadeh R (2009) Nanotechnology applications for sustainable cement-based products. In: Nanotechnology in Construction 3. Springer Berlin Heidelberg, pp 119–124
19. Cong X, Kirkpatrick RJ (1996) ^{29}Si MAS NMR study of the structure of calcium silicate hydrate. Adv Cement Based Mater 3(3):144–156
20. Richardson IG (1999) The nature of CSH in hardened cements. Cem Concr Res 29(8):1131–1147
21. Richardson IG (2002) Electron microscopy of cements. Structure and Performance of Cements. Spon Press, London
22. Richardson IG (2008) The calcium silicate hydrates. Cem Concr Res 38(2):137–158
23. Peyvandi A, Soroushian P, Balachandra AM, Sobolev K (2013) Enhancement of the durability characteristics of concrete nanocomposite pipes with modified graphite nanoplatelets. Constr Build Mater 47:111–117
24. Colorado HA, Rivera D, Hiel C, Hahn HT, Yang JM (2011) Effect of fly ash and graphite nanoplatelets contents on the compression strength of rapid-setting cement concrete. Society for the advancement of material and process engineering. Sampe, Long Beach-CA, USA
25. Yang Jun, Tighe Susan (2013) A review of advances of nanotechnology in asphalt mixtures. Procedia-Social Behav Sci 96:1269–1276
26. Yao H, You Z, Li L, Shi X, Goh SW, Mills-Beale J, Wingard D (2012) Performance of asphalt binder blended with non-modified and polymer-modified nanoclay. Constr Build Mater 35:159–170
27. Yao H, You Z, Li L, Lee CH, Wingard D, Yap YK, Goh SW (2012) Rheological properties and chemical bonding of asphalt modified with nanosilica. J Mater Civil Eng 25(11):1619–1630
28. Chen SJ, Zhang XN (2012) Mechanics and pavement properties research of nanomaterial modified asphalt. Adv Eng Forum 5
29. Artus GRJ, Jung S, Zimmermann J, Gautschi HP, Marquardt K, Seeger S (2006) Silicone nanofilaments and their application as superhydrophobic coating. Adv Mater 18(20) 2758–2762. https://doi.org/10.1002/adma.200502030
30. Wang CY, Piao C (2011) From hydrophilicity to hydrophobicity: a critical review-part II: hydrophobic conversion. Wood Fiber Sci 43(1):41–56
31. Kessler MR, Goertzen WK (2009) Polymer nanocomposites for infrastructure rehabilitation. In: Nanotechnology in Construction 3. Springer, Berlin, Heidelberg, pp 241–250
32. Bauer M, Kahle O, Landeck S, Uhlig C, Wurzel R (2008) High performance composites using nanotechnology. Adv Mater Res 32:149–152
33. Wang Z, Colorad HA, Guo Z-H, Kim H, Park C-L, Hahn HT, Lee S-G, Lee K-H, Shang Y-Q (2012) Effective functionalization of carbon nanotubes for bisphenol F epoxy matrix composites. Mater Res 15(4):510–516

34. Woo K, Jang D, Kim Y, Moon J (2013) Relationship between printability and rheological behavior of ink-jet conductive inks. Ceram Int 39:7015–7021
35. Dobrzanski LA, Pakułaa D, K˘riz˘ A, Sokovic´ M, Kopac J (2006) Tribological properties of the PVD and CVD coatings deposited onto the nitride tool ceramics. J Mater Process Technol 175:179–185
36. Sato T, Diallo F (2010) Seeding effect of nano-$CaCO_3$ on the hydration of tricalcium silicate. J Transp Res Board, No 2142. Nanotechnol Cement Concrete 1: 61–67
37. Li H, Zhang M, Ou J (2006) Abrasion resistance of concrete containing nano-particles for pavement. Wear 260:1262–1266
38. Comunidad de Madrid (2007) Consejería de Economía e Innovación Tecnológica. Los minerales industriales. El recorrido de los minerales. http://www.uhu.es/jc.caliani/pdf/MinIndustrialesMadrid.pdf
39. Enea D, Guerrini G (2010) Photocatalytic properties of cement-based plasters and paints containing mineral pigments. In: Transportation research record: journal of transportation research board, No 2142. Nanotechnology in cement and concrete vol 1. Transportation Research Board of the National Academies, Washington, DC, pp 52–60
40. How safe is nano? Nanotoxicology, an interdisciplinary challenge. http://phys.org/news/2011-01-safe-nano-nanotoxicology-interdisciplinary.html. Website visited on August 2015
41. Nanotoxicology, assessing the risks of emerging technology. http://followgreenliving.com/nanotoxicology-assessing-risks-emerging-technology/ Website visited on August 2015
42. Slezakova K, Morais S, do Carmo Pereira M (2013) Atmospheric nanoparticles and their impacts on public health
43. Lee J, Shaily M, Alvarez PJJ (2010) Nanomaterials in the construction industry: a review of their applications and environmental health and safety considerations. ACS nano 4(7): 3580–3590
44. Lam CW, James JT, McCluskey R, Arepalli S, Hunter RL (2006) A review of carbon nanotube toxicity and assessment of potential occupational and environmental health risks. Crit Rev Toxicol 36:189–217. https://doi.org/10.1080/10408440600570233
45. Ding LH, Stilwell J, Zhang TT, Elboudwarej O, Jiang H, Selegue JP, Cooke PA, Gray JW, Chen F (2005) Molecular characterization of the cytotoxic mechanism multiwall carbon nanotubes and nano-onions on skin fibroblast. Nano Lett 5:2448–2464. https://doi.org/10.1021/nl051748o
46. Fang J, Lyon DY, Wiesner MR, Dong J, Alvarez PJ (2007) Effect of a fullerene water suspension on bacterial phospholipids and membrane phase behavior. Environ Technol 41:2636–2642. https://doi.org/10.1021/es062181w
47. Lyon DY, Brunet L, Hinkal GW, Wiesner MR, Alvarez PJJ (2008) Antibacterial activity of fullerene water suspensions (nC60) is not due to ROS-mediated damage. Nano Lett 8:1539–1543. https://doi.org/10.1021/nl0726398
48. Handy RD, Henry TB, Scown TM, Johnston BD, Tyler CR (2008) Manufactured Nanoparticles: their uptake and effects on fish-a mechanistic analysis. Ecotoxicology 17:396–409. https://doi.org/10.1007/s10646-008-0205-1
49. Karlsson HL, Cronholm P, Gustafsson J, Moller L (2008) Copper oxide nanoparticles are highly toxic: a comparison between metal oxide nanoparticles and carbon nanotubes. Chem Res Toxicol 21:1726–1732. https://doi.org/10.1021/tx800064j
50. Oberdorster G, Gelein RM, Ferin J, Weiss B (1995) Association of particulate air-pollution and acute mortality involvement of Ultrafine particles. Inhalation Toxicol 7:111–124
51. Park S, Lee YK, Jung M, Kim KH, Chung N, Ahn EK, Lim Y, Lee KH (2007) Cellular toxicity of various inhalable metal nanoparticles on human alveolar epithelial cells. Inhalation Toxicol 19:59–65. http://www.ncbi.nlm.nih.gov/pubmed/17886052
52. Reeves JF, Davies SJ, Dodd NJF, Jha AN (2008) Hydroxyl radicals are associated with titanium dioxide (TiO_2) nanoparticle-induced cytotoxicity and oxidative DNA damage in fish

Automated Optical Serial Sectioning Analysis of Phases in a Medium Carbon Steel

Bryan Turner, Satya Ganti, Bill Davis and Veeraraghavan Sundar

Abstract This work presents a three dimensional microstructural analysis of medium carbon steels, based on serial sectioning using optical microscopy. The microstructural phases considered here are ferrite and pearlite. Typically conventional 2D microscopy is used to analyze these phases (ASTM E112-13 in Standard test methods for determining average grain size. ASTM International, West Conshohocken, PA, 2013), with eddy current (Khan et al. in J Mater Process Technol 200(1):316–318, 2008) or ultrasonic methods (Araújo Freitas et al. in Mater Sci Eng A 527(16):4431–4437, 2010) as alternatives. Medium carbon steel samples were heat treated in a furnace and either slowly cooled in the furnace, or cooled at higher rates. This resulted in different pearlitic microstructures in the samples. The analysis was conducted with Robo-Met.3D®, a fully automated metallography system for serial sectioning. Based on optical microscopy, volume cubes of hundreds of microns on edge were imaged and reconstructed to conduct grain size and phase volume analysis. The system proved capable of collecting image data with high fidelity, and controlled slice thickness in an automated manner. The resultant dataset was useful in visualization and analysis of pearlite and ferrite phases in steel samples.

Keywords Serial sectioning · Grain size analysis · Microstructure
Phase analysis · Medium carbon steels · Metallography · Robo-Met

Materials and Serial Sectioning Methods

Robo-Met.3D is a fully automated metallography system that generates two dimensional optical microstructural data for three dimensional reconstructions and analysis. Common applications of Robo-Met.3D include studying additively

B. Turner · S. Ganti · V. Sundar (✉)
UES Inc., Robo-Met.3D Services, Dayton, OH, USA
e-mail: vsundar@ues.com

B. Davis
WSD Consulting, Cincinnati, OH, USA

B. Li et al. (eds.), *Characterization of Minerals, Metals, and Materials 2018*, The Minerals, Metals & Materials Series,
https://doi.org/10.1007/978-3-319-72484-3_47

manufactured components [4], analysis thermal barrier coatings [5], and fiber orientation effects in ceramic matrix composites [6].

- Material Composition and State

An off-the-shelf, un-heat treated, cold drawn 1045 medium carbon steel (1045 MCS) sample was chosen (as received). Samples were excised from rod, and were conventionally mounted in metallographic mounts ($\sim$38 mm diameter $\times$ 25 mm height) for automated serial sectioning. In this study, two different heat treatments were performed on the samples. The first heat-treated sample was heated to approximately 830 °C and furnace cooled (annealed) for about 12 h until room temperature was attained. The second heat treated sample was heat treated to approximately 830 °C, removed from the furnace and quickly dropped into water (quenched). The three samples were then serial sectioned for microstructural analyses.

- Grinding and Polishing for Serial Sectioning

A typical automated grinding and polishing program for materials of this type involves diamond suspensions of varying sizes—6, 3, 0.25 μ, and finishing with 0.05 μ colloidal silica. Polishing times may be varied automatically to achieve varying rates of material removal. The samples were etched with 2% Nital reagent to enhance contrast. Intermediate and final cleaning steps with water and ethanol are programmed in to keep cross contamination to a minimum.

- Image Acquisition and Processing

Optical images were automatically acquired with the Zeiss Axiovert microscope built into the Robo-Met.3D system. The 2D image tiles from each layer were stitched into montages, registered with the images from the next layer using Fiji software. A mosaic or montage of 2 $\times$ 2 tiles of 500$\times$ images was collated, with a resolution of 0.21 μ along the X and Y axes. A total of 50 slices, or sections were collected. Acquisition parameters are shown in Table 1.

For 2D analysis, single 2D image was segmented using WEKA segmentation filter in Fiji to identify the phases (pearlite—dark, ferrite-bright and martensite—light grey). For 3D analysis, the raw 2D images were stitched and aligned for accurate post-processing. The loaded z-stack of 50 slices was processed with subsampling along Y direction and full resolution along X and Z directions. A 3D isosurface was created without any filtering to extract the volume distribution of the phases. Thresholding was performed on pixel values as for the 2D analyses. A combination of Fiji and ImagePro software suites was used in this analysis.

Table 1 Serial sectioning data acquisition parameters

1045 MCS	Overall magnification	Resolution in x − y (μ)	Sectioning rate (μ/section)	No. of sections analyzed	Dimensions analyzed (μ)
As-received	500×	0.21	1.8	50	451 × 28 × 92
Annealed	500×	0.21	4.6	50	451 × 282 × 230
Quenched	500×	0.21	3.2	50	460 × 290 × 160

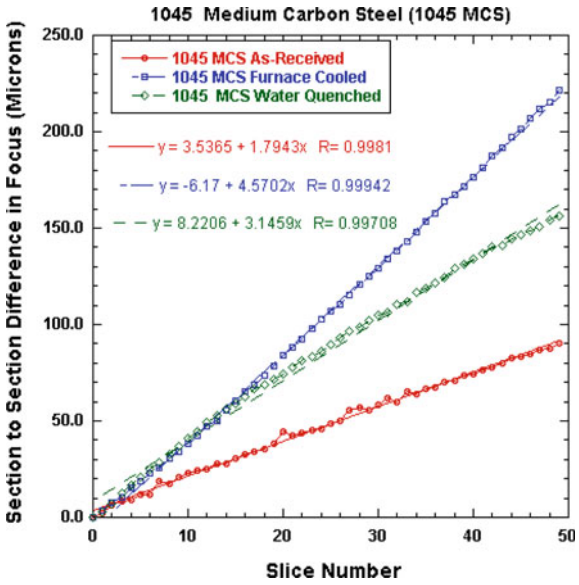

Fig. 1 Material removal plot for 1045 MCS as-received, annealed and quenched samples

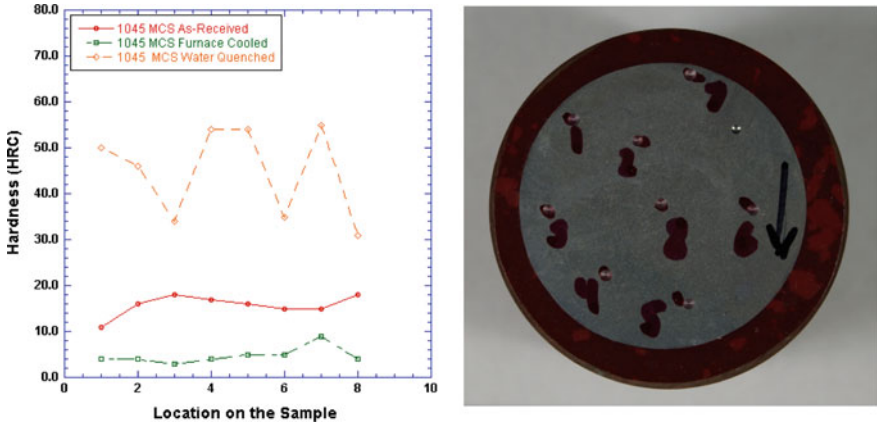

Fig. 2 Rockwell hardness C measurements for 1045 MCS as-received, furnace cooled and water quenched samples (left) and location of eight measurements on the sample (right)

- Linearity of Material Removal Rate

Robo-Met.3D uses z-focus or z-height of the optical microscope for accurate material removal measurements between sections, rather than fiducial marks. As shown in in Fig. 1, a highly linear material removal rate of between 1.8 and 4.6 μ was maintained for all samples.

- Material Hardness

As expected, HRC hardness values were lowest for annealed sample (HRC 4.1), followed by the as-received (HRC 16.4) and water quenched samples (HRC 44.9) as shown in Fig. 2.

Analysis Results

The 2D and 3D image sets (Figs. 3, 4 and 5) were analyzed for the relative fraction of pearlite and ferrite phases. The 3D data may be considered more representative as it minimizes section-dependent variation [7].

Based on the heat-treatment conditions (especially cooling rate), we have observed different percentages of the three phases as shown in Table 2.

The as-received sample showed 71.0% pearlite and 29.0% ferrite, and the annealed sample showed 70.1% pearlite and 29.9% ferrite which approximate with the ideal values of 75.0% pearlite and 25.0% ferrite. Incomplete conversion to about 28% martensite was observed in the quenched material as agitation was not used in the quenching bath. The quenched sample was predominantly pearlitic.

We have also performed preliminary grain size analysis on un-heat-treated sample as shown in Fig. 6. Image-pro premier-3D software is equipped to perform semi-automated (interactive) grain analysis per ASTM E112 standard.

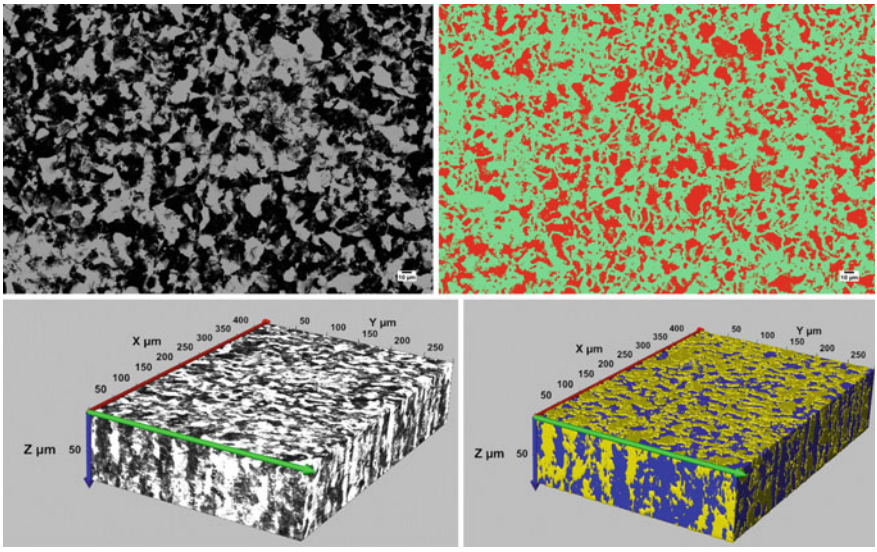

Fig. 3 1045 as-received steel—Top: 2D raw image (left) and WEKA segmented image: pearlite-green, and ferrite-red (right); bottom: 3D image (2D raw images aligned stack of 50 slices) (left) and segmented 3D image (pearlite-yellow; ferrite-blue) (right)

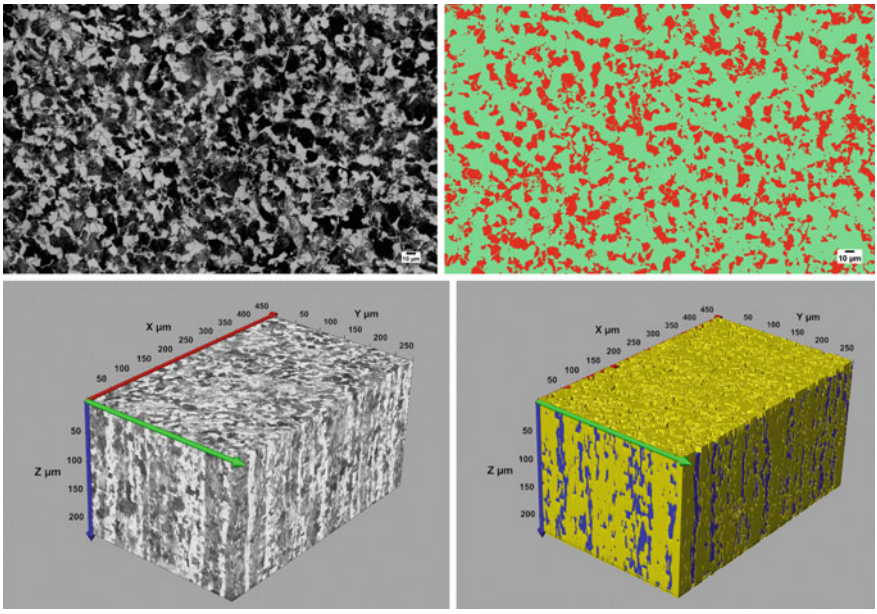

Fig. 4 1045 annealed steel—top: 2D raw image (left) and WEKA segmented image: pearlite-green, and ferrite-red (right); bottom: 3D image (2D raw images aligned stack of 50 slices) (left) and segmented 3D image (pearlite-yellow; ferrite-blue) (right)

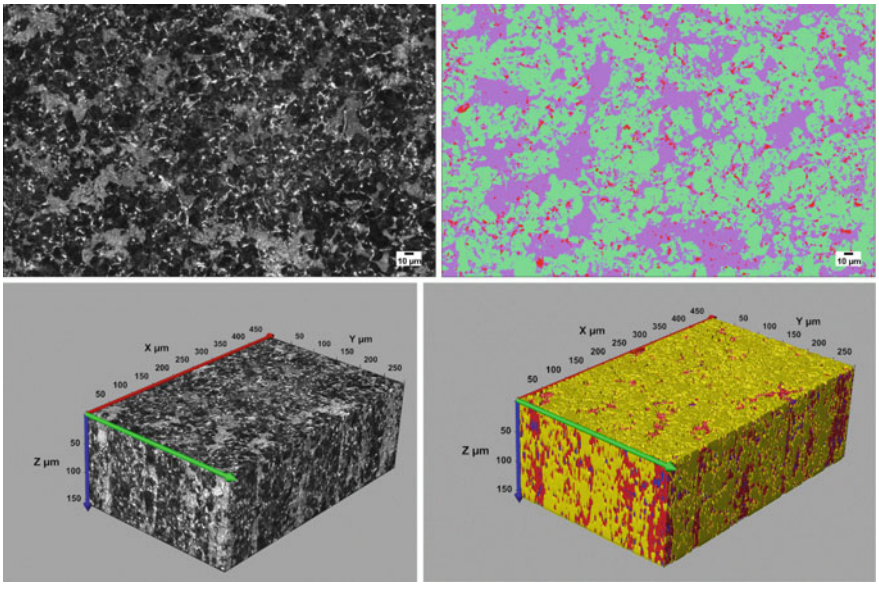

Fig. 5 1045 water quenched steel—top: 2D raw image (left) and WEKA segmented image: pearlite-green, martensite-purple and ferrite-red (right); bottom: 3D image (2D raw images aligned stack of 50 slices) (left) and segmented 3D image (pearlite-yellow; martensite-red; ferrite-blue) (right)

Table 2 Area (2D) and volume(3D) percentages of phases

Material	Phase volume fraction (%)		
1045 medium carbon steel	Pearlite	Ferrite	Martensite
As received	71	29	–
Annealed	70.1	29.9	–
Water quenched	66.2	6.02	27.8

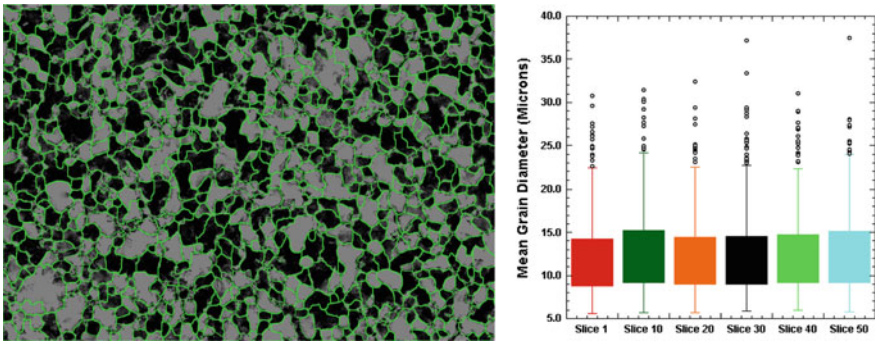

Fig. 6 Grain network outline overlaid on raw image (left); 2D statistical distribution of mean grain diameter (center)

Conclusion

The study successfully demonstrates the use of automated serial sectioning for phase analyses and interactive grain size analyses. The RoboMet.3D®system proved capable of collecting image data with high fidelity, and controlled slice thickness in an automated manner. Experimental results have shown the effect of different heat treatment conditions on the hardness and microstructure of steel. The resultant datasets were useful in visualization and analysis of pearlite, ferrite and martensitic phases in 1045 steel samples.

Further Information

www.ues.com/forums,info@ues.com.

References

1. ASTM E112-13 (2013) Standard test methods for determining average grain size. ASTM International, West Conshohocken, PA www.astm.org

2. Khan SH, Ali F, Khan AN, Iqbal MA (2008) Pearlite determination in plain carbon steel by eddy current method. J Mater Process Technol 200(1):316–318
3. de Araújo Freitas VL, de Albuquerque VHC, de Macedo Silva E, Silva AA, Tavares JMR (2010) Nondestructive characterization of microstructures and determination of elastic properties in plain carbon steel using ultrasonic measurements. Mater Sci Eng A 527 (16):4431–4437
4. Seifi M et al (2016) Microstructure and mechanical properties of Ti-48Al-2Cr-2Nb manufactured via electron beam melting. In: Proceedings of world conference on titanium, 13th. TMS/Wiley, Warrendale, PA/Hoboken, NJ
5. Brake MRW, Hall AC, Madison JD (2017) Designing energy dissipation properties via thermal spray coatings. Surf Coat Technol 310:70–78
6. Bricker S et al (2015) Anomaly detection of microstructural defects in continuous fiber reinforced composites. In: SPIE/IS&T electronic imaging. international society for optics and photonics
7. Ganti S et al (2017) A Comparison of porosity analysis using 2D stereology estimates and 3D serial sectioning for additively manufactured Ti 6Al 2Sn 4Zr 2Mo alloy. Pract Met 54(2):77–94

Characterization of a Brazilian Bentonite for Its Use in the Oil and Gas Industry

Adriana Almeida Cutrim, Margarita Bobadilla, Kleberson R. Oliveira Pereira, Fabio Jose Esper, Guillermo Ruperto Martin Cortes, Maria das Graças da Silva Valenzuela and Francisco R. Valenzuela-Diaz

Abstract Bentonites are an important kind of industrial clays with more than a hundred different uses. In the oil and gas industries they are used as thixotropic additives for drilling fluids and also as sorbents for purification of flows and effluents. Due to the mechanical and thermal properties that they exhibit, bentonites will become in a near future important fillers in clay/polymer nanocomposites which could be used in the oil and gas industry for replacement of various metal components. In this paper a chocolate color bentonite from the state of Paraiba in Brazil was characterized by diverse techniques such as XRD, DSC/TGA, surface area, and cation exchange capacity and it was studied its potential use as thixotropic additive for oil and gas drilling fluids and as sorbents of oils. The bentonite showed good potential for use in those applications.

Keywords Bentonite · Characterization · Oil and gas industry

Introduction

Bentonites are industrial clays, consisting essentially of smectite clay minerals [1]. The smectite clay minerals are mostly hydrated aluminum and magnesium silicates that generally have a lamellar morphology, with diameters of the order of micrometers and thicknesses of the order of one nm. The layers are stacked together

A. A. Cutrim · K. R. Oliveira Pereira
Federal University of Campina Grande, R. Aprígio Veloso, 882—Universitário, Campina Grande, PB, Brazil

M. Bobadilla · M. das Graças da Silva Valenzuela · F. R. Valenzuela-Diaz (✉)
Polytechnic School of University of São Paulo, Av. Professor Mello de Morales, 2643, Sao Paulo, SP 055030, Brazil
e-mail: frrvdiaz@usp.br

F. J. Esper · G. R. M. Cortes
Centro Universitário Estacio, Av. dos Remedios, 810, Vila dos Remédios, São Paulo, SP, Brazil

B. Li et al. (eds.), *Characterization of Minerals, Metals, and Materials 2018*, The Minerals, Metals & Materials Series,
https://doi.org/10.1007/978-3-319-72484-3_48

forming booklets in the c axis (see Fig. 1). Morphologically they are composed of tetrahedra sheets, containing Si^{4+} in the centers of the tetrahedra and O in the vertices. The oxygens join the tetrahedra with each other and with octahedron sheets. These octahedron sheets generally contain Al^{3+} aluminium or Mg^{2+} magnesium at the octahedral centers and the bonds of these cations sharing oxygen with the tetrahedral sheets or, when there is no tetrahedron for shared, with –OH bonds. Due to interstitial substitutions (for example, aluminum by silicium or magnesium by aluminium) the lamellae have a negative surface charge, that is compensated by interlamellar cations that are reversibly exchangeable, providing to bentonites a cation exchange capacity in the range of 80–120 meq.

There are two main types of bentonites, those that swell in water and those that do not swell in water. Bentonites that swell in water have sodium as the predominant interlamellar cation, they have a swelling range in water between six and 20 mL/g, but they do not swell in organic liquids, and provide viscous aqueous dispersions at low clay concentrations (generally at concentrations from 2 to 6% by weight). Bentonites that do not swell in water do not have sodium as the predominant interlamellar cation, they exhibit water swelling between 2 and 3 mL/g and do not provide viscous aqueous dispersions at low clay concentration. Bentonites can be processed with quaternary ammonium salts to transform them into organophilic clays that swell in various organic liquids and provide with low concentration of clay, viscous dispersions in those organic liquids. Bentonites that swell in water, those that do not swell in water, organophilic and other types of

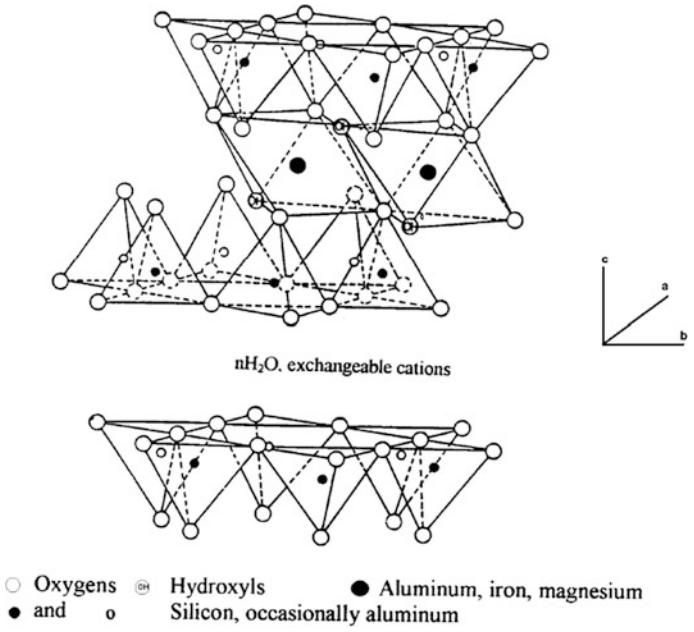

Fig. 1 Crystal structure of smectitic clays

modified bentonites have a myriad uses, being the main ones: thixotropic additives for water-based and oil-based drilling fluids [2], binders for sand molds for metals castings, binders for iron ore fines and pet litters. In the last decades, there has been an effort by the academy and the industry to study bentonites as nanometric fillers in bentonite/polymer nanocomposites and also their use in health and environment applications.

Brazil has a production of approximately 150,000 t/year, being in the top ten world producers of bentonite. In contrast with the United States and Argentina, Brazil does not have any known deposit of bentonites that can swell in water, this is the reason why bentonites are processed with sodium carbonate to turn them into bentonites that can swell in water [3].

The main deposits of bentonites explored in Brazil are in the county of Boa Vista (state of Paraíba) and in the county of Vitoria da Conquista (state of Bahia). Chocolate bentonites are one of the main types of bentonites in the Boa Vista county [4].

In this work a sample of chocolate color bentonite is characterized by XRD, XRF, BET specific surface area, sand content, and thermal analysis. The natural clay adsorption of oils capacity and its swellings in organic liquids after being organophilized are presented as well as data for their use as thixotropic additive for oil and gas drilling fluids.

Materials and Methods

The clay used in this study was a raw sample of Chocolate bentonite supplied by Bentonisa do Nordeste. It was dried at 60 °C, grounded, and sieved at 200 mesh. X-Ray Diffraction Analysis was carried out through the powder method, using a X-ray Philips XPERT-MPD diffractometer, CuK-α radiation, in steps of 0.02 at 1 s/step. DSC/TG analysis were performed in a Universal V4.1TA, with nitrogen atmosphere at 10 °C/min. X ray fluorescence was performed in a Shimadzu EDX 700. BET Specific surface area was measured via N_2 adsorption at −196 °C on a Micromeritics ASAP 2000 analyzer with the sample outgassed at 150 °C. Cation exchange capacity was measured using the ammonium acetate method. The sand content was measured using a Fann's Sand Content Kit, which uses a 200 mesh sieve.

The swelling capacity in liquids was measured by the Foster method [5], adding 1.0 g of clay in a cylinder containing 100 mL of water. Without stirring, the swelling of the clay was measured 24 h later in mL/g. The plasticity point and ability of absorption (g oil/g clay) were determined by adding oil to 5.00 g of clay, mixing and rubbing with spatula and repeating the operation until it was possible to conform an homogeneous ball of clay without crumble. With the quantity of oil added the plasticity point is calculated. The addition of oil with mixing and rubbing with spatula were continued until the formation of a brilliant film on the surface of the clay indicates the saturation of clay by oil. With the total quantity of oil added the capacity of the clay to incorporate oil was calculated. The method was based on

the ASTM D281-95 (reapproved 2007) "Standard Test Method for Oil Absorption of Pigments by Spatula Rub-out" used to measure the incorporation oils in pigments for use in paints.

The sodium activation procedure was made by the addition of 100 meq/100 g of Na_2CO_3, in concentrated aqueous solution, to a 50.0%, in weight, clay/water mixture. The mixture was homogenized with spatula and allowed to rest for one week in a humid chamber. The mixture was dried, grounded and passed in 200 mesh sieve (opening 0.074 mm). The ability of the sodium activated clay for use as thixotropic additive for oil and gas drilling fluids was made by measuring the Fann viscosities of a 6.0%, in weight, dispersion and Foster swelling of the sodium activated Chocolate bentonite. For comparison, a commercial sodium bentonite Volclay had also their 6% in water Fann viscosity and Foster swelling measured. For the organophilization of the clay, 100 meq/100 g of Na_2CO_3, in aqueous solution, was added to a 4.0%, in weight, clay/water dispersion. The dispersion was mechanical stirred for 20 min. and allowed to rest overnight. 100 meq/100 g clay of hexadecyltrimethylammonium chloride was added to the dispersion. The dispersion was mechanical stirred for 20 min. and vacuum filtered and washed with water. The cake was dried at 60 °C, grounded and passed in 200 mesh sieve. It was measured the swelling capacity of the organophilic Chocolate bentonite in querosene, toluene, ethanol, mineral oil and soy oil.

Results and Discussion

Figure 2 presents the bentonite diffractogram obtained by X-ray diffraction. The main peak at d_{001} = 1.5 nm corresponds to the montmorillonite group. The peak at $d_{(060)}$ = 0.15 nm corresponds to a dioctahedral smectite, as it is usual for the bentonites from Paraiba State. The main peak at 0.33 nm corresponds to quartz. The quartz content of the chocolate bentonites is approximately 1% and it can be easily removed for special uses like, for example, cosmetics [6]. No other major impurities minerals are observed by the XRD curve.

Table 1 presents the results of XRF. Chocolate sample has a chemical composition similar to Cebogelbentonite from Milos, Greece, with a low value of aluminum oxide and a high value of iron oxide [7]. In this case, the Brazilian bentonite has the most of its iron as impurities that do not appear in the XRD but are not important part of the structure of the clay mineral as mild acid attacks remove most of the chocolate color [8].

Figure 3 presents the thermal analysis curves. Between 30 and 200 °C, the sample loses its humidity and interlayer water, and has a little lose of possible organic matter near 250 °C. Between 400 and 580 °C the sample loses its dehydroxylation water. Such low temperature range is typical of high iron smectites, meaning that some structural iron is present in the sample. The DSC curve, as a bentonite, shows endo-exothermic peaks near 900 °C.

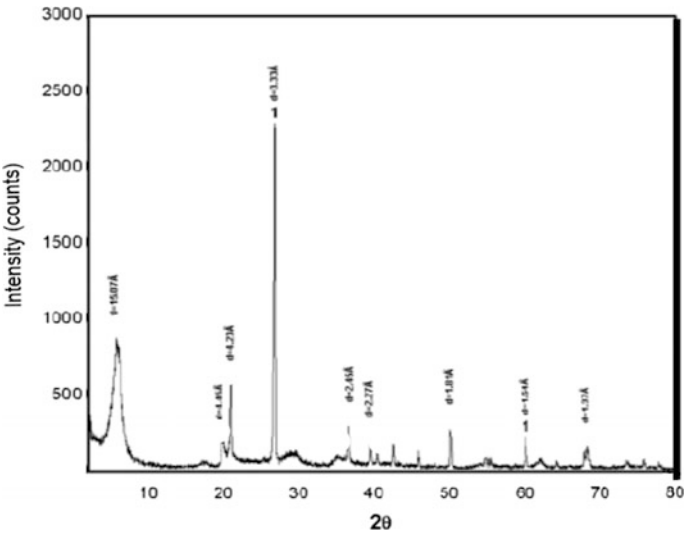

Fig. 2 XRD curve of Chocolate bentonite

Table 1 XRF results of bentonite submitted to treatment (quantitative analysis, values in percentage of oxides)

SiO_2	Al_2O_3	Fe_2O_3	MnO	MgO	CaO	Na_2O	K_2O	TiO_2	LoI
64.9	13.1	9.7	0.06	1.45	2.56	0.74	0.37	0.95	5.5

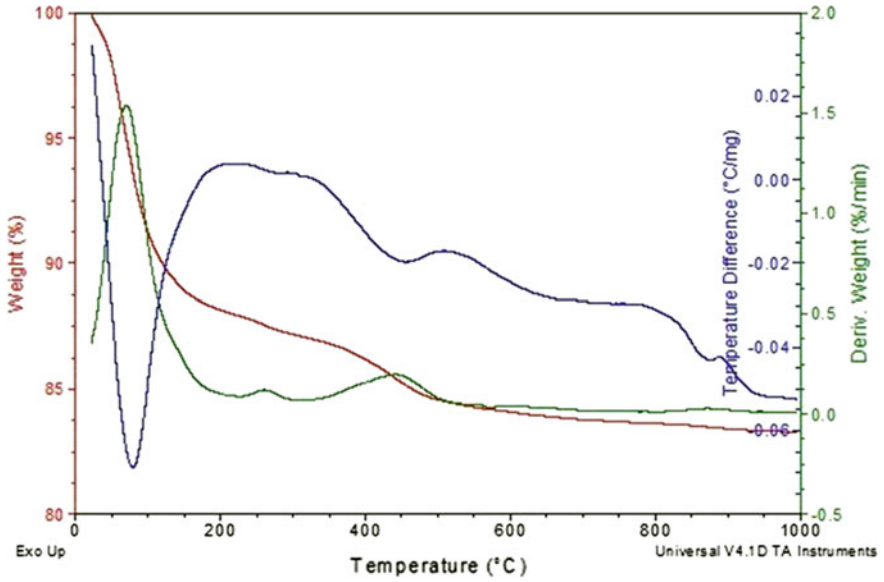

Fig. 3 DSC, TG and DTG curves of the Chocolate bentonite

Bentonites have a theoretical external surface area of approximately 800 m^2/g. The N_2 BET surface area of bentonites is mainly a consequence from the outer surface area of the bentonite agglomerates and not from the interlayer spaces, as the N_2 molecules cannot get into the interlayer spaces [9]. Here the BET surface area of the Chocolate bentonite is compared with the external area of an important industrial bentonite (Volclay) furnished by Diamond [9]: the BET specific surface area obtained for the chocolate bentonite was 80 m^2/g, which is higher than the external surface area of the Ca^{++} exchanged Volclay (49 m^2/g) and lower than the Na + exchanged Volclay (116 m^2/g).

The measured cation exchange capacity—CEC—of the Chocolate bentonite was 60 meq/100 g clay, which is similar to the CEC of some bentonites from Utah and 15% lower than the CEC of high swelling bentonites from Wyoming [10].

The plasticity point and saturation point of oils in natural Chocolate bentonite are present in Fig. 4. The bentonite can incorporate more than 20% of its weight in the studied oils, indicating its potential use in cosmetics [6].

A high sand content in bentonites is deleterious for its use in drilling fluids. The measured sand content of the Chocolate bentonite was 1% and the maximum value given by the American Petroleum Institute—API—for use in water based drilling fluids is 4% [11].

The swellen capacity on water of the sodium activated Chocolate bentonite was 12 mL/g and for the Volclay bentonite 15 mL/g. The apparent (AV) and plastic (PV) viscosities of the sodium Chocolate bentonite were AV = 19.0 cP and PV = 12 cP, and for Volclay Bentonite AV = 18.5 cP and PV = 15.0 cP. The swelling and viscosity values for the two clays are similar and indicate good rheological properties for use as additives for oil and gas drilling fluids.

After organophilization Chocolate bentonite did not present swelling capacity in soy oil (3 mL/g) and present swelling capacity in ethanol (7 mL/g), kerosene (7 mL/g)/mineral oil (7 mL/g), and toluene (19 mL/g). These values indicate that the Chocolate bentonite could be used in oil based drilling fluids additives, organic solvents paints, clay/polymer nanocomposites and other uses [12].

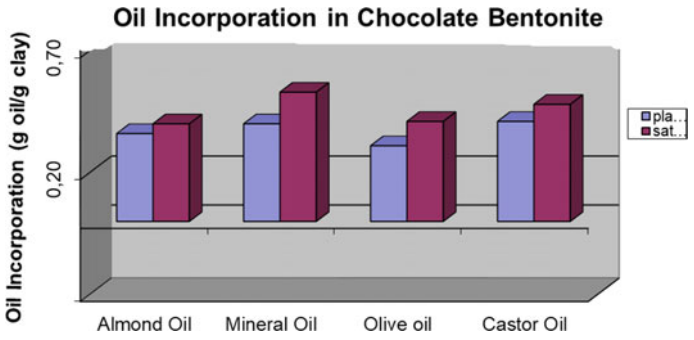

Fig. 4 Plastic and saturation values (g oil/g clay) of Chocolate natural clay in oils

Conclusion

By analyzing the data of XRD, XRF, thermal analysis, cation exchange capacity and BET surface area, it is observed that the chocolate clay is a pure bentonite with a small amount of quartz. This quartz can be easily removed and the clay has potential to be used in high value products. Natural chocolate bentonite has a capacity greater than 20% of its weight to absorb oils and therefore has potential for use in cosmetics. After being transformed into a sodium bentonite, it acquired the property of swell in water and with good rheological properties for use as an additive for water based drilling fluids. After being modified with a quaternary ammonium salt, it acquire a high swelling capacity in organic liquids, with potential use in additives for oil and gas oil drilling fluids, clay/polymer nanocomposites, paints, cosmetics and many other uses.

Acknowledgements Grants 11/50027-7 and 12/51871-9, São Paulo Research Foundation (FAPESP).

References

1. Grimm RE, Güven N (1978) Bentonites. Elsevier Scientific Publishing Company, Amsterdam, Oxford, New York, p 266
2. Chilingarian GV, Vorabutur P (1983) Drilling and drilling fluids. Elsevier Scientific Publishing Company, Amsterdam, p 788
3. Dematte CL (1980) Bentonitas: beneficiamento e uso no Brasil. Cerâmica 26(132):353
4. Cutrim A, Martin Cortes G, Valenzuela Diaz FR (2015) Bentonitas da Paraiba. Interciencia, Rio de Janeiro, p 200
5. Foster MD (1954) The relation between composition and swelling in clays. Clays Clay Miner 1(3):205–220
6. Silva-Valenzuela MG, Casarotte ARB, Silva AA, Valenzuela-Diaz FR, Characterization of functional clays for cosmetics. Cosmetique
7. POSIVA (2008) Quality assurance of the bentonite material, Working Report 2008-33
8. Bastos CG, Justo VF, Matos CM, Silva-Valenzuela MG, Valenzuela-Diaz FR (2015) Evaluation of acid treatment on brown bentonite. In: Characterization of minerals, metals and materials, TMS, Wiley, pp 735–742
9. Diamond S, Kinter EB (1956) Surface areas of clay minerals as derived from measurements of glycerol retention. Clays Clay Miner 5(1):334–347
10. Rollins MB, Pool DL (1968) Measuement of excheneable cations in bentonites. Clays Clay Miner 1(16):165–172
11. American Petroleum Institute (2010) Specification 13A. Specification for drilling fluids, Specification and testing. 18th edn., Aug 2010
12. de Paiva LB, Morales AR, Valenzuela Díaz FR (2008) Organoclays: properties, preparation and applications. Appl Clay Sci 42(1–2):8–24

Characterization of Tensile Properties of Epoxy Matrix Composites Reinforced with Fique Fabric Fiber

Maria Carolina Andrade Teles, Marcos Vinícius Fonseca Ferreira, Frederico Muylaert Margem, Felipe Perissé Duarte Lopes, Djalma Souza and Sergio Neves Monteiro

Abstract The development of composite materials is a combination of distinct materials, with applications in various areas, such as: aerospace, automobile, etc. Regarding mechanical resistance, composites reinforced with a dispersion phase in a fiber form is more relevant. The green idea is use composites with natural fibers instead of fiberglass, especially in non-structural applications. The Fique fiber has occupying an important place at Colombian agricultural and agribusiness sectors. Epoxy matrix composites reinforced with 1–6 Fique fabric layers were tested and the results indicated that the tensile properties improve with increasing the amount of Fique fabric layers. The fiber/matrix interaction was analyzed by scanning electron microscopy.

Keywords Composites · Epoxy · Fique fabric

Introduction

In the last decades, the use of composite materials has had a large increase in several industries such as construction, aerospace, and automotive. The great use of composite materials is due to their unique properties as for example the high specific strength, which is much higher than most monolithic materials such as metals, ceramics or polymers. The high specificity resistance makes the composite materials have a high resistance coupled to a low density [1].

However, the use of composites reinforced with synthetic fibers is very harmful to the environment since the production of these fibers generates a lot of CO_2 that

M. C. A. Teles (✉) · M. V. F. Ferreira · F. M. Margem · F. P. D. Lopes · D. Souza
Advanced Materials, Laboratory, LAMAV, State University of the Northern Rio de Janeiro, UENF, Av. Alberto Lamego, 2000, Campos dos Goytacazes 28013-602, Brazil
e-mail: mariacarolinateles@live.com

S. N. Monteiro
Instituto Militar de Engenharia, IME, Praça Gen. Tibúrcio n°80 Urca, Rio de Janeiro, RJ 22290-270, Brazil

B. Li et al. (eds.), *Characterization of Minerals, Metals, and Materials 2018*, The Minerals, Metals & Materials Series,
https://doi.org/10.1007/978-3-319-72484-3_49

contributes to the greenhouse effect. Another negative point of synthetic fibers is that they can neither be recycled nor incinerated [2, 3].

One solution to this problem is the use of natural fibers as composite reinforcement. Natural fibers are environmentally friendly since their production usually comes from disposal and does not emit CO_2 in their manufacture [4–11]. The use of natural fibers has been the target of a wide range of research and even is already applied in industries such as automotive [12, 13].

The fibers may be used as reinforcement in the form of individual cylinders aligned or in the form of fabric. The application in the form of fabric uses the interlaced fibers generating a greater adhesion between the fibers. A plant of Fique (Furcraea Andina) is native to the Andes of Ecuador—Colombia and Venezuela, but widespread in Colombian Andes. The fiber is resistant, fine, white and shiny. The normal annual production is 1 kg per plant, with exceptional yields of 3–6 kg per year [14].

The objective of this work is to analyze the tensile strength of epoxy polymer composites reinforced with woven interwoven Fique fabric.

Experimental Procedure

The materials used in this work were the fabric Fique fiber. The Fique fiber is extracted from the leaf of the Fique plant (Fig. 1), which was supplied by its producers in Colombia. The Fique plant has a trunk that can reach 30 cm in diameter with leaves ranging from 0.5 to 2 m in length and 8 to 14 cm in width. The dried fibers are average length of 63 cm. The Fique plant has a life ranging from 12 to 20 years and in some special cases from 60 to 70 years. The density of the fibrous varies widely. The average density is 0.68 g/cm^3, which is relatively low compared to other synthetic fibers such as fiber glass 2.4 g/cm^3 (ALTOÉ, 2016).No treatments were applied to the fibers surface.

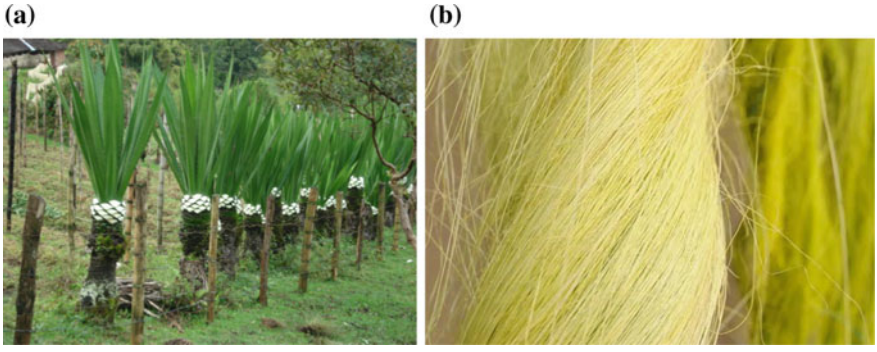

Fig. 1 Fique plant (**a**) and Fique fibers (**b**)

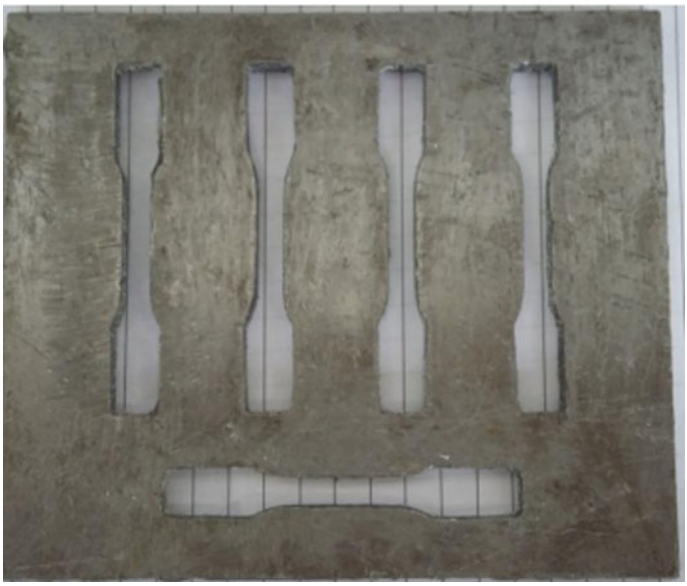

Fig. 2 Metal molds for preparation of test specimens composites epoxy reinforced with different volumetric fractions of Fique fibers

Composite specimens were individually prepared with 1 up 4 layers of Fique fabric fiber placed inside dog-bone shape metal molds, Fig. 2. Still fluid epoxy resin was poured with the layers of Fique fabric fiber, and cured for 24 h.

These specimens were subjected to tensile tests in a model 5582 Instron machine shown in Fig. 3 at room temperature and 0.5 mm/min. For each volume fraction of Fique fiber, from 0 to 30% in volume, nine samples were tested and the results statistically analyzed. The specimens were gold sputtered and observed by scanning electron microscopy (SEM) in a model SSX 550 Shimadzu microscope.

Results and Discussion

Figure 4 shows typical curves of the force versus elongation for composites of epoxy resin embedded with Fique fabric fiber. These curves were directly obtained from the data acquisition system of the machine and revealed that Fique fibers act not only as effective reinforcement, but also increase the plastic deformation of the composites. Polymeric matrices, for example, in fiber reinforced polymeric composites are used to protect, align and stabilize the fibers, as well as to ensure the transfer of tension from one fiber to another. In general, both the rigidity and the strength of the matrix are lower than those of the reinforcing fibers (LACH, 1998).

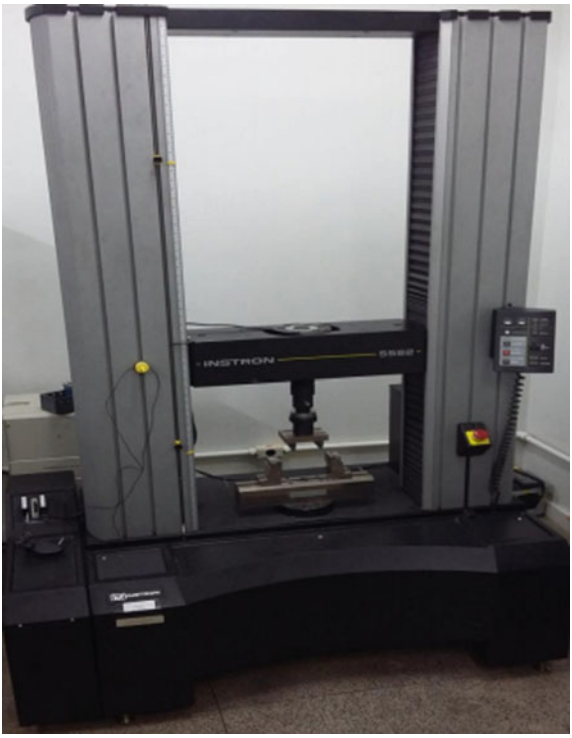

Fig. 3 Instron universal testing machine, model 5582

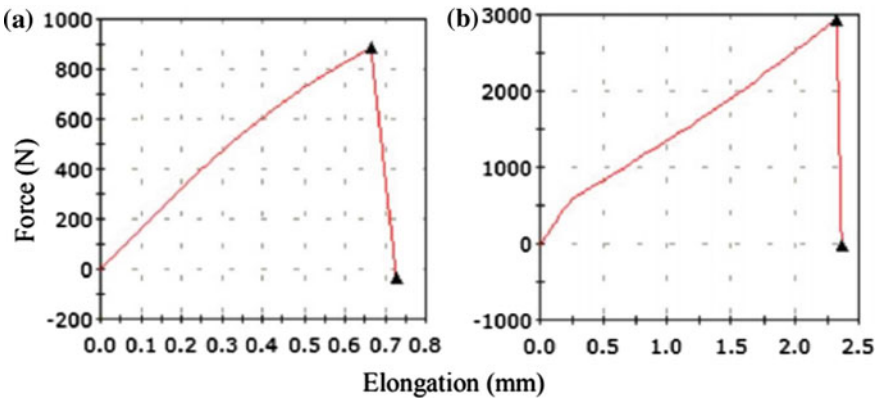

Fig. 4 Example of a force versus elongation curves for epoxy composites reinforced with: **a** 0 vol% and **b** 30 vol% of Fique fibers

Table 1 Tensile properties of epoxy composites reinforced with Fique fibers

Volume fraction of Fique fiber (%)	Tensile strength (MPa)	Elasticity modulus (GPa)
0	42.80 ± 19.02	1.23 ± 0.57
10	60.26 ± 7.88	1.61 ± 0.46
20	84.23 ± 13.90	1.72 ± 0.13
30	100.94 ± 15.20	1.86 ± 0.24

Based on the results in Fig. 4, it was plotted the curves of tensile stress versus strain and to calculate the values for the average tensile strength and elastic modulus for each amount of fiber, as shown in Table 1.

The values of the tensile stress and elasticity modulus, listed in Table 1 for the epoxy composites, are showed in Fig. 5 as a function of volume fraction of layer Fique fabric fiber. In this figure it is noteworthy that the introduction of layers fibers significantly increases both strength, Fig. 5a, and the stiffness, Fig. 5b, of the epoxy matrix composites. An important result to be mentioned in Fig. 5 is that, as the percentage of Fique fiber increases, the tensile strength and elastic modulus also increase following an almost linear relationship.

The fiber has a set of fibrils. These fibrils have different diameters that resist differently to the same tensile applied in the fiber. This is sufficient to know that each fibril breaks at different times of the test. Therefore, the fiber does not break in a totally fragile way, as soon as it supports a quantity of plastic deformation, this aspect is very important, because it enables the use of composite materials for a wide range of applications. Figure 6 shows the microstructural difference for Fique fibers of different diameters.

The analysis of the micrographs of the tensile fracture allowed a better understanding of the mechanism responsible for the hardness of epoxy reinforced with Fique fabric. Figure 7 shows the appearance of the surface of pure epoxy (0% fiber) specimen fracture and test specimens with 10, 20 and 30% of Fique fabric.

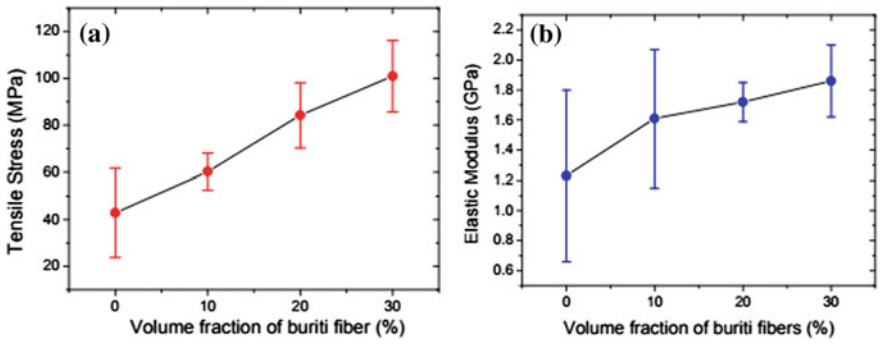

Fig. 5 Variation of the tensile strength (**a**) and elastic modulus (**b**) with the volume fraction of Fique fibers

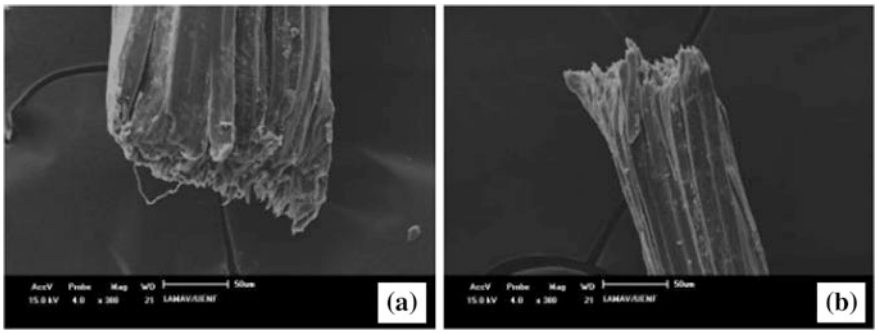

Fig. 6 Aspect of the fracture of the Fique fiber, ×300, 0.18 < d < 0.21 mm (**a**) 0.21 < d < 0.24 mm (**b**)

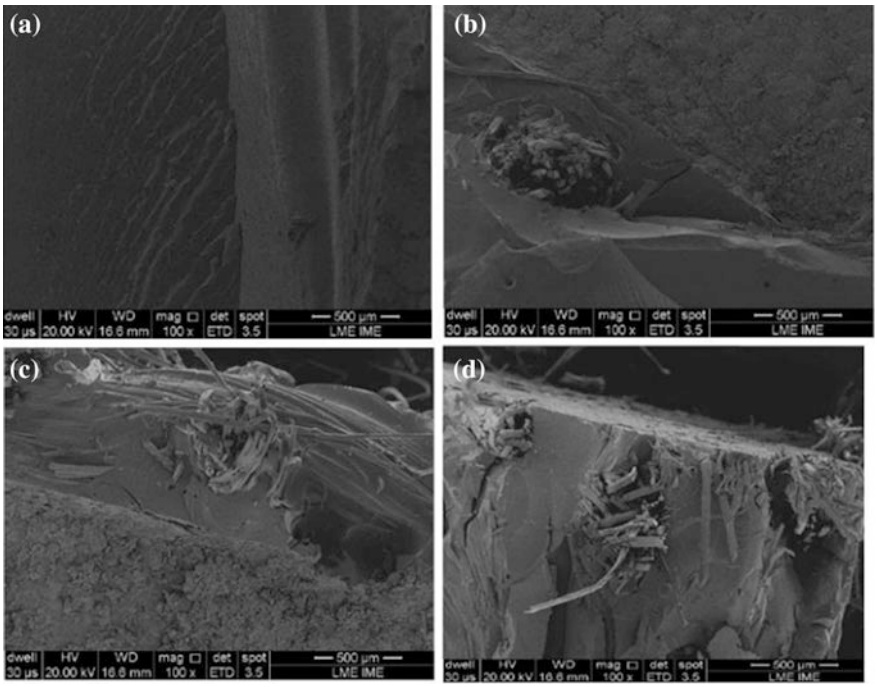

Fig. 7 Appearance of the surface of pure epoxy (0% fiber) specimen fracture and test specimens with 10, 20 and 30% of Fique fabric

The uniform fracture surface (Fig. 7b) indicates that the rupture is caused by the propagation of a single crack, with the propagation of the typical crack on the smooth and fragile surface. Figure 7d presents details of fracture surface of a epoxy

composite with 30% of Fique fiber. It is observed that some fibers were separated from the matrix and broken after the rupture, also the cracks propagate at the fiber/matrix interface.

The participation of Fique fibers shown in Fig. 7 indicates that their increasing amount tends to be associated with a heterogeneous macroscopic feature, owing to a change in the uniform, transversal rupture of the brittle epoxy matrix.

Conclusions

Incorporation of Fique fibers increases the tensile resistance of epoxy matrix composites when compared to pure resin, which shows that Fique fibers are a good reinforcement material to tensile loads. This increase can be attributed to Fique fibers with thinner diameter acting as a barrier for the crack propagation throughout the brittle epoxy matrix. Along with the retention of some whole Fique fibers upon tensile strength, low interfacial resistance results in greater energy absorbed due to the propagation of cracks in the fiber/matrix interface, allowing the formation of a higher longitudinal fracture area in relation to a transverse fracture, which should occur in the matrix for breaking the fibers.

References

1. Kalia S, Kaith BS, Kaurs I (2011) Cellulose fibers: bio- and nano-polymer composites. Springer, New York
2. Zah R, Hischier R, Leão AL, Brown IJ (2007) Cleaner production, vol 15, p 1032
3. Crocker J (2008) Materials technology, vols 2–3, p 174
4. Mohanty AK, Misra M, Drzal LT (2005) Natural fibers, biopolymers and biocomposites. Taylor & Francis, Boca Raton, FL
5. Neto FL, Pardini LC (2006) Compósitos estruturais. Edgard Blücher, São Paulo, SP
6. Monteiro SN, Lopes FPD, Ferreira AS, Nascimento DCO (2009) Natural fiber polymer matrix composites: cheaper, tougher and environmentally friendly. JOM 61(1):17–22
7. Satyanarayana KG, Sukumaran K, Kulkarni AG, Pillai SGK, Rohatgi PK (1999) Fabrication and properties of natural fiber-reinforced polyester composites. Composites 17:274–329
8. Crocker J (2008) Natural materials innovative natural composites. Mater Technol 2–3: 174–178
9. Callister WD (2007) Materials science and engineering—an introduction, 7th edn. Wiley, New York
10. Mallick CK (2007) Fiber-reinforced composites—materials, manufacturing and design. LLC, Boca Raton, FL
11. Lucas AA, Ambrósio JD, Bonse BC, Bettini SHC (2011) Natural fiber polymer composites technology applied to the recovery and protection of tropical forests allied to the recycling of industrial and urban residues. In: Advances in composite materials—analysis of natural and man-made materials, Intech, pp 165–194

12. AL-Oqla FM, Sapuan SM (2014) Natural fiber reinforced polymer composites in industrial applications: feasibility of date palm fibers for sustainable automotive industry. J Cleaner Prod 66:347–354
13. Giacomini NP (2003) Compósitos reforçados com fibras naturais para a indústria automobilística, Dissertação de Mestrado, USP—Universidade de São Paulo, São Carlos, SP, p 21
14. Castellanos F (2009) Definición de la Agenda prospectiva de investigación en la cadena productiva agroindustrial de Fique a partir de sistemas de inteligencia tecnológica. 1st edn. Ministerio de Agricultura y Desarrollo Rural. Bogotá, DC

Clay Smectite Synthetic: Characterization and Application in Nanocomposites

Thamyres C. Carvalho, Edemarino A. Hildebrando, Roberto F. Neves and Francisco R. Valenzuela-Diaz

Abstract Synthetic clays are an option of materials that can be modified to obtain better and specific properties when compared with natural clays. Although clays are found in nature, they have many disadvantages that limit the use of them, such as existence of impurities, and variations in composition. Therefore, the objective of this work was to obtain synthetic clay/polyester resin nanocomposites. To characterize the clay, we used X-ray Diffraction (XRD), Total Attenuated Reflection Spectroscopy in the Fourier Transform Infrared Region (ATR-FTIR) and Scanning Electron Microscope with Field Emission (FEG-SEM) methods and the nanocomposites were characterized by XRD and mechanical resistance to compression. The results show the purity of the clay and the time of synthesis is an important parameter for its crystallization process. The clay/polyester nanocomposites were obtained and showed an increase in the ductility.

Keywords Clay · Synthetic · Nanocomposites · Mechanical properties

T. C. Carvalho (✉) · R. F. Neves · F. R. Valenzuela-Diaz
ARGILAB, Applied Clays Laboratory, Polytechnic School
of the University of São Paulo, São Paulo, SP, Brazil
e-mail: thamyrescc@gmail.com

R. F. Neves
e-mail: rfn@ufpa.br

F. R. Valenzuela-Diaz
e-mail: frrvdiaz@usp.br

E. A. Hildebrando · R. F. Neves
Federal University of Pará, Belém, PA, Brazil
e-mail: edemarino@ufba.br

B. Li et al. (eds.), *Characterization of Minerals, Metals, and Materials 2018*, The Minerals, Metals & Materials Series,
https://doi.org/10.1007/978-3-319-72484-3_50

Introduction

Nanocomposites are a new class of polymeric materials that have the potential to increase the fields of use [1]. They have been largely used in recent years mainly because of their scientific-technological importance. The nanocomposites consist of a polymer matrix and dispersed inorganic particles at nanoscale [2].

In the commercial market it is possible to find different types of nanofillers that can be incorporated in the polymer matrix, depending on the application and the expected property. Among them, clays, silica, alumina, nanotubes and others [3]. Highlighting natural and synthetic clays, particularly smectite, which were used as nanomaterials in various innovative applications, especially because of their layered structure [4–6], to be a material with lower cost and readily available. Although there are numerous reports on the preparation of nanocomposites with natural smectite clay, their properties are very difficult to control, due to the presence of impurities and fluctuations in the composition that end up restricting their use [7]. The presence of these crystalline impurities and non-homogeneous morphology are probably the main obstacle in its use as nanomaterial and the removal of impurities is very difficult, so that the currently applied procedures can irreversibly and unpredictably alter the physicochemical properties of smectites [8]. With this emerges the interest in synthetic clays in their well-defined compositions and high purity [9, 10], mainly in their application as nanofiller for nanocomposites fabrication [11], demonstrating to be a promising alternative.

The objective of this study was to use a synthetic smectite clay (stevensite) to obtain the polymeric nanocomposites of polyester resins and evaluate their properties compared to the pure polymer.

Materials and Methods

Materials

Synthetic trioctahedral smectite clay, stevensite (supplied by the Laboratory of Applied Clays (ARGILAB) of the Polytechnic School of the University of São Paulo) was used as nanofiller. The procedure for preparing the samples is not shown due to patent issues. The clays were named according to the time they were synthesized: 24, 48 and 72 h, respectively, (S24, S48 and S72). For the preparation of the hybrids, the polymer matrix employed was a orthophthalic polyester resin and the curing agent used was a methylethylketone, provided by DU Latéx—Industrial Products Ltda.

Methods

Preparation of Nanocomposites

The orthophthalic polyester resin (75 ml) and the synthesized clay (3.75 g) in the form of a powder passing through ABNT nº 200 (D = 0.075 mm) sieve were mixed mechanically at 200 rpm for a period of 5 min at room temperature, forming an homogeneous mixture. After this time, the curing agent (20 mL) was added and mixed for 5 min at the same temperature. Finally, the dispersion obtained was placed into three molds for compression specimens (cylinders 25 mm high and 21 mm in diameter) and cured at room temperature for 24 h. For comparison purposes, the pure polyester resin was prepared under the same mixing conditions.

In order to evaluate the difference between clays (24, 48 and 72 h of synthesis), they were characterized by X-ray diffraction (XRD), Total Attenuated Reflection Spectroscopy in the Fourier Transform Infrared Region (ATR-FTIR) and Scanning Electron Microscope with Field Emission (FEG-SEM). The Hybrids were characterized by X-ray Diffraction (XRD) and mechanical resistance to compression, to evaluate the effect of the incorporation of the clay into the polymer.

Discussion Results

Characterization of Clays

X-ray Diffraction (XRD)

Figure 1 shows the XRD diffractograms of clays S24, S48 and S72. It is verified that the XRD patterns of the samples have a peak referring to basal distance d_{060}, 1.53 Å (2θ = 60.6°) typical of a trioctahedral smectite clay. It is observed that clays exhibit similar behavior and are consistent with the synthetic XRD patterns of synthetic stevensite clays reported in the literature [11–13] suggested by peaks at 2θ = 5.6° (15.78 Å), 19.8° (4.48 Å) and 34.6° (2.65 Å). This probably occurred due to an improvement in crystallinity and/or due to particle size and stacking.

Total Attenuated Reflection Spectroscopy in the Fourier Transform Infrared Region (ATR-FTIR)

The FTIR spectra (Fig. 2) of all clay samples contain vibration bands at about 3670, 1634, 1008, 795 and 663 cm^{-1} assigned respectively to the stretching of Zn–OH type bonds, OH stretch deformation, reaction products of urea and nitrate undissolved, indicative of trioctahedral clays (in this case characterized as Stevensite) and Si–O–Zn bonds. It is also possible to observe some differences in the spectra of

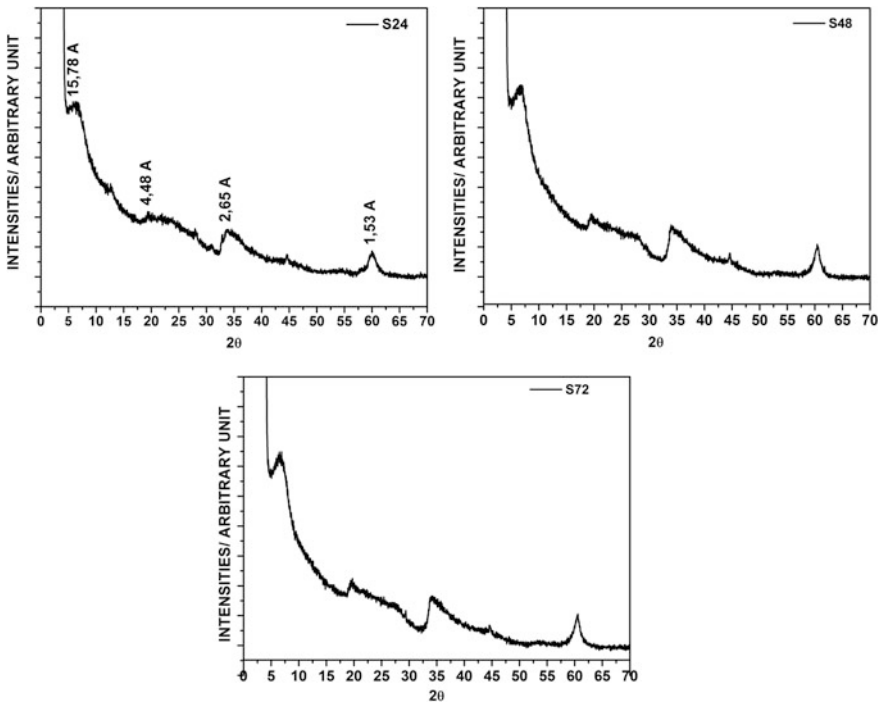

Fig. 1 Diffractograms of the clays: S24; S48 and S72

the samples: The intensity of the peaks that become more intense with the increase of the time of synthesis; the peak in the range of 1095–990 related to the NH_4 in the sample S24 tends to become more acute in the samples S48 and S72. That probably occurs due to a longer interaction between the reagents, improving crystallinity corroborating the XRD analysis [11].

Scanning Electron Microscope with Field Emission (FEG-SEM)

Figure 3a–c shows the FEG-MEV images of clays S24, S48 and S72 consecutively. By the photomicrographs it was possible to observe that the clays have a similar behavior, with small regular and uniform particles in the order of nanometers that tend to aggregate and coil on the edges of the thinner plates [14], a similar behavior was verified by other authors [11, 12]. As the synthesis time increases, the particle size of the agglomerates decreases and the typical lamellar structure of the smectites becomes more visible. Confirming that the synthesis time is an important parameter for the definition of its properties.

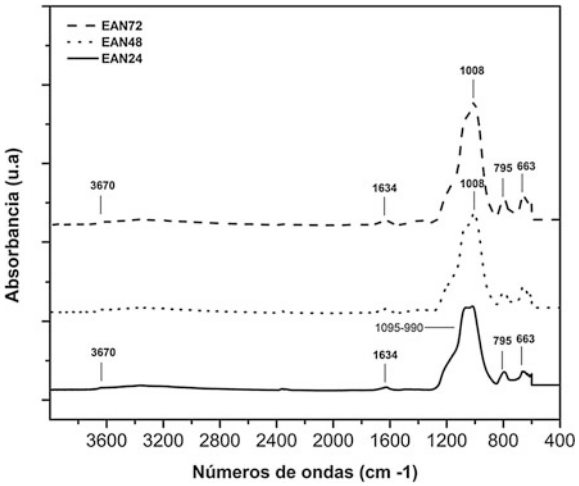

Fig. 2 FTIR spectra of the clays: S24, S48 and S72

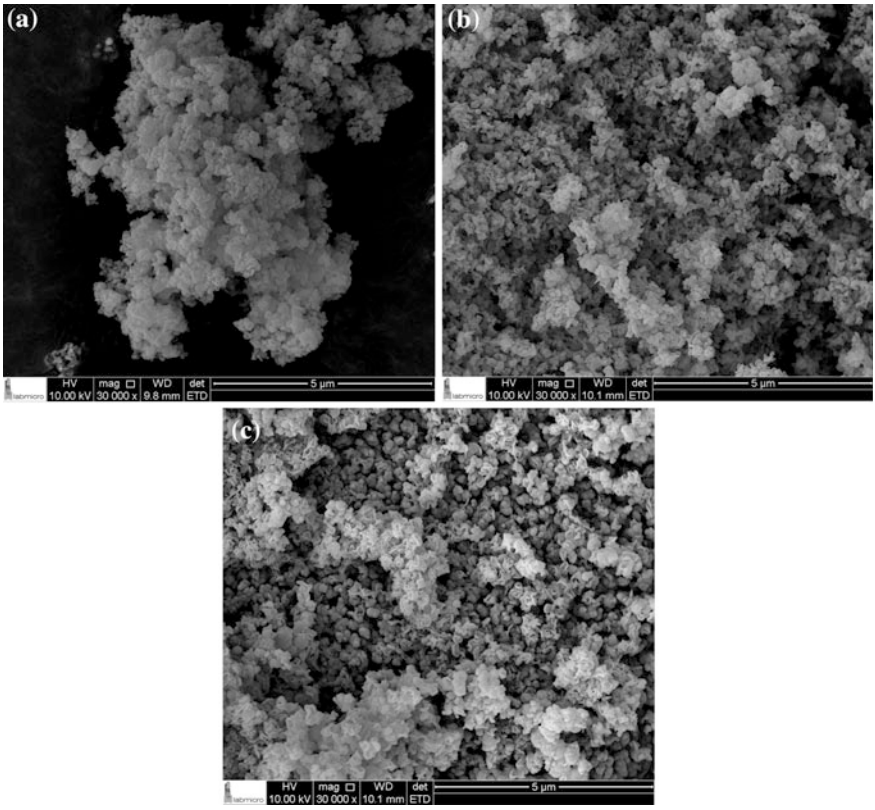

Fig. 3 FEG-SEM micrographs of the clays: **a** S24; **b** S48 and **c** S72

Stevensite Smectite Clay in Nanocomposites

For the production of the nanocomposites, the synthetic clay denominated of S72 that presented more crystallinity was chosen as nanofiller.

X-ray Diffraction Curve (XRD) of the Nanocomposite

Figure 4 shows the XRDs of the polyester resin, the synthetic clay (S72) and the polyester/synthetic hybrid (S72). In the resin diffractogram it is possible to observe the presence of a peak at approximately 20° relative to the defective crystalline phase and a shoulder at 42.5° corresponding to the amorphous portion of the pure matrix, probably due to a malformation of the polymer chain in the crystallization of the polymer [15]. The hybrid XRD curve (Polyester/clay S72) shows peaks related to interplanar distances of 1.53 and 3.33 Å, referring to characteristic peaks of stevensite smectite clay. The disappearance of peak d_{001} (15.78 Å) suggests the obtaining of an exfoliated nanocomposite, condition that usually provides better mechanical properties [2].

Compression Mechanical Resistance

The pure polyester resin showed a more brittle behavior than the clay sample. Modulus of elasticity was similar to 1.8 GPa for pure polyester samples and 1.7 GPa for samples without clay, with 9 and 42% rupture deformations respectively. The maximum resistance of the samples without clay is equal to their resistance at rupture and presents a value of 162 MPa. The sample with clay presented a maximum resistance of 123 MPa and in the rupture of 101.3 MPa.

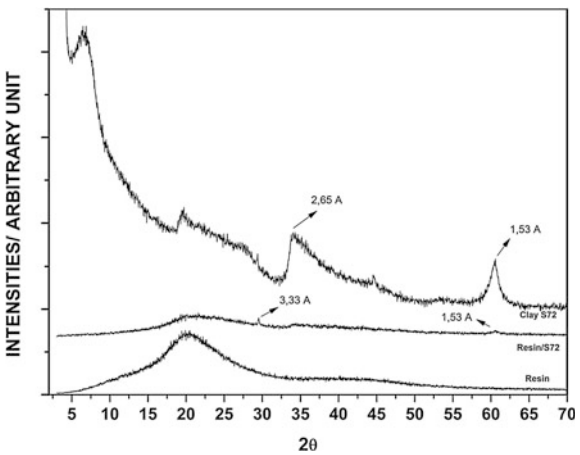

Fig. 4 Diffractograms of the hybrid polyester resin/argila S72

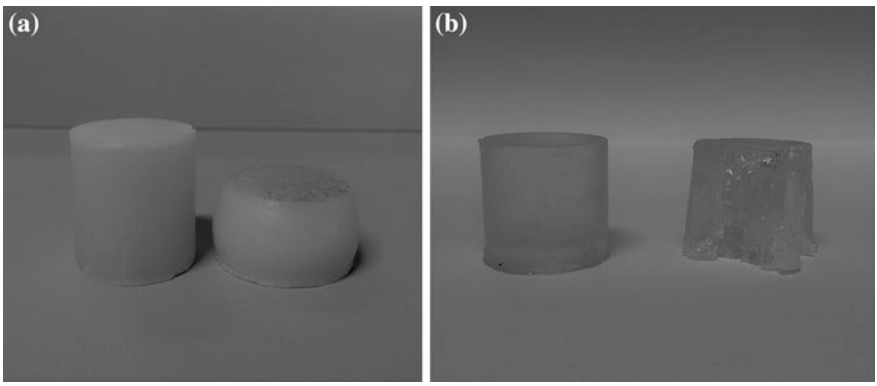

Fig. 5 Sample before and after the compression test: **a** polyester resin and **b** clay/polyester resin nanocomposites

The values of maximum strength, modulus of elasticity of deformation at the rupture of the samples without clay are similar to those obtained by the tensile stress curves for orthophthalic polyester resin by Davallos [16].

The nanocomposite showed a compression deformation five times higher than that presented by the pure resin. This behavior may be related to the polymer-clay bonds that partially compensate for the broken reticular chemical bonds, thus functioning as a plasticizer. Figure 5a, b shows the samples of the pure polyester resin and the polyester/clay nanocomposite before and after being subjected to the compression test, respectively.

Conclusion

According to the results, the clay used was a synthetic smectite clay of the stevensite type. In addition, it was evidenced that the time in which the clays were synthesized is an important parameter for the improvement of the properties of the samples. Nanocomposites of polyester resin/synthetic clay were produced and their mechanical properties by compression were evaluated. From XRD it was observed that the peak of the synthetic clay disappeared when incorporated into the polyester suggesting the formation of an exfoliated structure. The nanocomposites showed a high value of the deformation in the compression when compared to the pure polyester resin, indicating that the polymer-clay bonds are balancing, the broken reticular chemical bonds, thus functioning as a plasticizer.

Acknowledgements We acknowledge FAPESP projects 12/51871-9 and 11/50027-7.

References

1. Mallakpour S, Samira M (2012) Dispersion of chiral amino acid organomodified Cloisite Na+ in poly(vinyl alcohol) matrix for designing of novel bionanocomposite films. Prog Org Coat 74:8–13
2. Ray SS, Okamoto M (2003) Polymer/layered silicate nanocomposites: a review from preparation to processing. Prog Polym Sci 28:1539–1641
3. Almeida AS (2010) Preparation and characterization of poly (L-lactide) nanocomposites and nanoparticles of sodium clay, organophilic clays and silica oxides. M.Sc. dissertation, Federal University of Rio de Janeiro
4. Wang Z, Massam J, Pinnavaia TJ (2000) In: Pinnavaia TJ, Beal GW (eds) Polymer–clay nanocomposite. Wiley, Chichester, West Sussex, pp 127–149
5. Schoonheydt RA (2002) Smectite-type clay minerals as nanomaterials. Clays Clay Miner 50:411–420
6. Ogawa M (2004) Photoprocess in clay–organic complexes. In: Auerbach SM, Carrado KA, Dutta PK (eds) Handbook of layered materials. Marcel Dekker, New York, pp 191–259
7. Roelofs JCAA, Berben PH (2006) Preparation and performance of synthetic organoclays. Appl Clay Sci 33:13–20
8. Kimura H, Nakashima A, Takahashi S, Tsuchida A, Kurosaka K (2015) Changes of viscosity in stevensite aqueous dispersions with application of an electric field of the order of a few V/mm. Appl Clay Sci 114:120–123
9. Zhang D, Zhou CH, Lin CX, Tong DS, Yu WH (2010) Synthesis of clay minerals. Appl Clay Sci 50:1–11
10. Kloprogge JT (1998) Synthesis of smectites and porous pillared clay catalysts: a review. J Porous Mater 5:5–41
11. Hildebrando EA, Valenzuela MDGDS, Neves RF, Diaz FRV (2014) Síntese e caracterização de argila esmectita Zn-estevensita. Cerâmica 60:273–278
12. Pascua CS, Ohnuma M, Matsushita Y, Tamura K, Yamada H, Cuadros J, Ye J (2010) Synthesis of monodisperse Zn-smectite. Appl Clay Sci 48:55–59
13. Sychev M, Prihod'ko R, Koryabkina A, Hensen EJM, Van Veen JAR, Van Santen RA (2000) The application of non-hydrothermally prepared stevensites as support for hydrodesulfurization catalysts. Stud Surf Sci Catal 143:257–265
14. Souza Santos P (ed) (1992) Science and technology of clays. São Paulo
15. Weber GJ, Silva GG, Meira SLG, Vieira SLG (2017) Absorção de água e propriedades mecânicas de compósitos poliméricos utilizando resíduos de MDF. Polím Ciência Tecnol 27:48–55
16. Davallo M, Wilkinsona AN, Ziaratib P (2004) Mechanical properties of polyester resin formed by resin transfer moulding (RTM). Technology 23:4057–4063

Comparison of Performance Between Granite Waste Pigments Based Paints and Soils Pigments Based Paints

Márcia Maria Salgado Lopes, Rita de Cássia Silva Sant'Ana Alvarenga, Leonardo Gonçalves Pedroti, Beatryz Cardoso Mendes, Fernando de Paula Cardoso and Afonso Rangel Garcez de Azevedo

Abstract This work aims to produce paints using granite waste, as a pigment, and compare their performance to soil pigments based paints, in terms of hiding power and abrasion resistance. Initially, the residue and soils were physically, mineralogically and morphologically characterized. For the production of the paint samples, an experimental model was defined, based on the variation of the proportions of pigment and resin. The proportion of water varied in each sample, in order to maintain the viscosity within a range considered ideal for application. Sequentially, tests were done to determine the hiding power and abrasion resistance of inks. It was found that, in comparison to soil paints, the granite residue paints presented greater hiding power. This result can be explained by the characteristics of the granite residue, which allowed a high nonvolatile content in the mixtures. With respect to abrasion resistance, granite residue paints showed less resistance than soil paints, possibly due to the granulometry of the residue that resulted in a greater roughness of film. In addition, none ink sample satisfied the minimum specifications prescribed in the Brazilian standards for hiding power and abrasion resistance, at the same time. This means that these inks, when used, will require more repair and repainting over time than conventional paints.

Keywords Granite waste · Pigments · Paints · Soil pigments · Sustainable development

Introduction

The sustainability issue is one of the main challenges of current buildings. So, professionals from many knowledge areas are led to seek solutions to minimize the environmental impacts caused by the activities developed in this sector.

M. M. S. Lopes · R. C. S. S. Alvarenga · L. G. Pedroti · B. C. Mendes (✉)
F. P. Cardoso · A. R. G. de Azevedo
Viçosa, Brazil
e-mail: beacm03@gmail.com

B. Li et al. (eds.), *Characterization of Minerals, Metals, and Materials 2018*, The Minerals, Metals & Materials Series,
https://doi.org/10.1007/978-3-319-72484-3_51

When analyzing the energy life cycle of buildings, Oliveira [1] found that the negative impacts of conventional building inks exist from their production process in the industry to their final destination. According to Uemoto et al. [2], these paints are composed of potentially toxic substances that harm the environment, the salubrity of the indoor environments and, consequently, the human health, due to the release of VOCs (volatile organic compounds).

An ecological alternative able to minimize such impacts is the use of manufactured and low cost paints. Among the most commonly manufactured paints used throughout history, soil based paints are the most important. According to Genestar and Pons [3], natural earths have been used as artistic pigments since prehistoric times. They can be found in art works everywhere and in any historical period, due to their availabilities, high colouring capacities and stabilities under a variety of weather conditions.

In the past, soil based paints were empirically produced. Currently, there are works, such as Faria [4] and Cardoso et al. [5], which were developed to study technological solutions for the production of these paints and evaluation of their performance.

It is believed that, just like the soil is used, as pigment, for manufactured paints, industrial wastes can also be used to perform this function. Pigments are solid materials that have very fine granulometry and are dispersed in the ink, being insoluble in the environment. They provide color and opacity; improve the resistance to bad weather; increase solids content; among others [6].

Granite waste is a material consisting of very fine particles of rock, which has chemical, physical, mechanical, and mineralogical characteristics that encourage its use in paints. This waste is generated in large amounts during the sawing process and the polishing of rock blocks. Putting this material in inappropriate place may cause damages to human health and to the environment [7].

Many studies about the use of granite wastes in construction materials have already been developed, such as the production of ceramics [8, 9], concrete [10, 11], mortars [12, 13], and soil-cement bricks [14]. However, the amount of reused waste is still insignificant, which requires its application in other projects [10].

Considering this context, the purpose of this work is to produce manufactured paints based on granite waste and soils and compare their performance, in terms of hiding power and abrasion resistance. Therefore, there is an alternative to use the waste on a larger scale in order to contribute to the expected sustainable development, without compromising the quality of the final product.

Materials and Methods

This work selected two kinds of soil, commonly found in the city of Viçosa, Brazil. They were already being used by the local population for the production of paints, one of ocher yellow type and the other of red earth type. The granite residue was

collected in the Southern region of the state of Espírito Santo, Brazil. The selected solvent was water and the selected resin was vinyl polyacetate, due to its low cost.

The methodology used is based on a series of processes developed for a context of self-production, whose steps are detailed below.

Treatment of the Soils and the Granite Waste

The preparation of the pigments of soils and of granite residue was done based on the method developed by Cardoso et al. [5]. This method consists of the mechanical disaggregation and dispersion of the particles in water, using the Cowles disk coupled to a mechanical stirrer, at a speed of 1500 rpm. The process was completed when the vortex created by the material at full stirring stabilized. It indicates the situation in which there is no further absorption of water by the particles and the viscosity stabilization occurs. Finally, the sieving of the blends was carried out in ASTM 80 mesh sieve, with opening of 0.177 mm. This sieve was used because of the correspondence between its opening and that of nylon stockings, thus facilitating the reproduction of this social technology.

Characterization of Pigments

The characterization of the soils and the granite residue was carried out after the treatment described in item 2.1. For the physical characterization, the granulometric distribution curve was determined based on the requirements of ABNT NBR 7181 [15], the specific mass of grains, according to ABNT NBR 6508 [16], and the particle density, according to EMBRAPA [17]. For the mineralogical characterization, the X-ray diffraction was performed by the D8-Discover diffraction system. Finally, for the morphological characterization, scanning electron microscopy was performed with the Leo 1430VP equipment.

Experimental Model

In order to reach the objective proposed in this work, it was decided to use an experimental design of mixtures. It was defined that the water should vary in each mixture, so as to maintain the viscosity within a constant range, allowing the proper application of the paint. Thus, after a series of preliminaries, it was determined that the kinematic viscosity considered ideal for the application of the studied paints corresponds to the flow time of 12 ± 1 s, as measured by the Ford cup viscometer with orifice number 4, according to ABNT NBR 5849 [18].

Therefore, the independent variables of the mixing design are the proportions of soil or granite residue pigment and resin. The ink samples were produced by varying the resin content in 20, 30, 40, 50, and 60% of the pigment content of the blend. The proportion of the components of each formulation is shown in Table 1.

Preparation and Characterization of the Paint Samples

For the production of the paint samples, a quantity of the soil or granite residue pigments dispersed in water was blended with the vinyl polyacetate resin, so that the mass of the pigment and resin obeyed the proportions defined in Table 1. To carry out the mixtures, the Cowles disk coupled to the mechanical stirrer was used, producing stirring for 10 min, at a speed of 500 rpm.

The viscosity of the mixture was measured with the Ford cup viscometer with orifice number 4. When necessary, the viscosity, was corrected by adding more water to the mixture, followed by stirring and re-measurement of the viscosity, until the mixture showed the set flow time.

For the characterization of the samples, the non-volatile content of each mixture was determined, according to ASTM-D 3723 [19] and the pigment volume concentration (*PVC*) was calculated by Eq. (1), in which *Vp* is the pigment volume and *Vv* is the volume of solid resin.

$$PVC\,(\%) = \frac{V_p}{V_p + V_v} \cdot 100 \tag{1}$$

Determining Performance of the Paint Samples

To determine the performance of the paint samples, tests were carried out to measure the hiding power and abrasion resistance, according to ABNT NBR 14942 [20] and ABNT NBR 15078 [21], respectively. The hiding power is given by the maximum area applied (m^2) per unit volume (L), which has a contrast ratio of 98.5%. The abrasion resistance is given by the number of cycles that paint film is able to withstand up to at least 80% wear of the area traveled by the brush.

Table 1 Mixing experiments performed for each type of ink

Sample	Pigment (g)	Resin (g)
1	100	20
2	100	30
3	100	40
4	100	50
5	100	60

Results and Discussion

Characterization of Pigments

In Table 2, the results of the physical characterization for each of the pigments used in this research are presented.

It is observed that the red soil sample is very clayey, while the yellow soil is a clayey silt and the granite residue is very silty. It is verified, according to the medium diameter values presented in Table 2, that the granite residue presents particles with granulometry much larger than the soil particles. However, according to Legodi and Waal [22], to be used in the production of paints, the size of the pigment particles in the 10.0 μm range is still acceptable.

The mineralogical analysis of the granite residue, yellow soil and red soil, through the identification of crystalline phases, are presented in Figs. 1, 2 and 3, respectively. It is verified that the granite residue presents more intense peaks of quartz (SiO_2) and albite ($NaAlSi_3O_8$), and little intense peaks of muscovite ($KAl_2Si_3AlO_{10}$ (OH, F)$_2$) and microcline ($KAlSi_3O_8$). The yellow soil has more intense peaks of kaolinite ($Al_2Si_2O_5$ (OH)$_4$) and small peaks of quartz, gypsite ($CaSO_4 \cdot 2H_2O$), and goethite (FeO(OH)). The red soil has more intense peaks of kaolinite and some small peaks of quartz, gypsite, goethite, and hematite (Fe_2O_3).

As for the morphological characterization, the morphologies of the granite waste, yellow soil, and red soil particles are presented in Figs. 4, 5 and 6, respectively. According to Stoffer [23], the shape of the particles affects the packaging of the particles and, consequently, the hiding power of the paint film.

The granite waste (Fig. 4) is a material with a varied diameter distribution, composed of particles with irregular morphology and angled edges. This morphology is due to the sawing and polishing process of ornamental rock blocks [24].

The yellow soil (Fig. 5) consists of lamellar and granular particles of different sizes, such as kaolinite and iron oxides, respectively. However, the red soil (Fig. 6) has some larger particles, but most of this material is formed by particles of very small size (iron oxides), which naturally tend to flocculation.

Table 2 Physical characteristics of pigments

Pigment	Specific mass (g/cm^3)	Particle density (g/cm^3)	Granulometry (%)			Medium diameter (μm)
			Clay	Silt	Sand	
Granite waste	2.68	2.56	13.1	73.1	13.8	10
Yellow soil	2.82	2.46	37.5	48.4	14.2	5.5
Red soil	2.89	2.65	63.8	21.9	14.3	<1

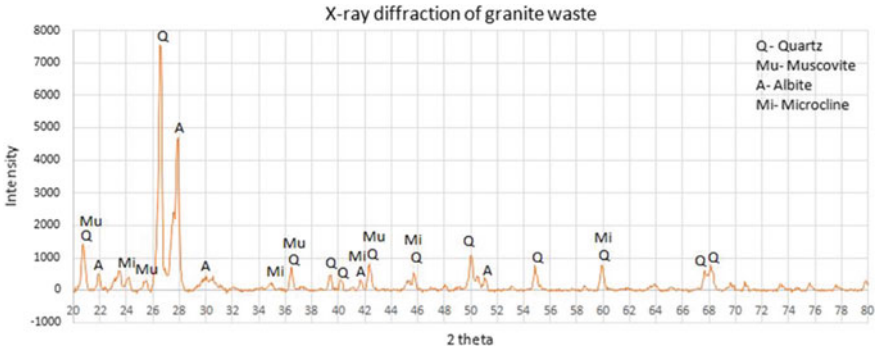

Fig. 1 Result of X-ray diffraction for granite waste

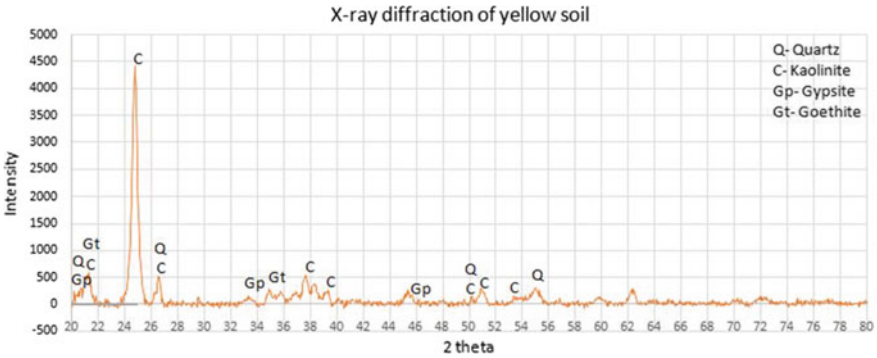

Fig. 2 Result of X-ray diffraction for yellow soil

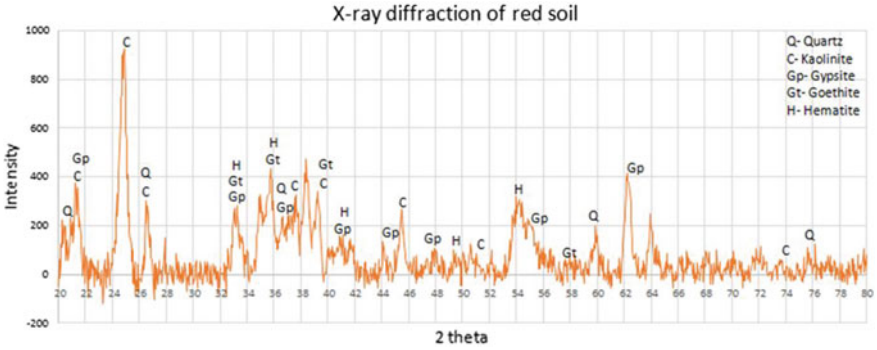

Fig. 3 Result of X-ray diffraction for red soil

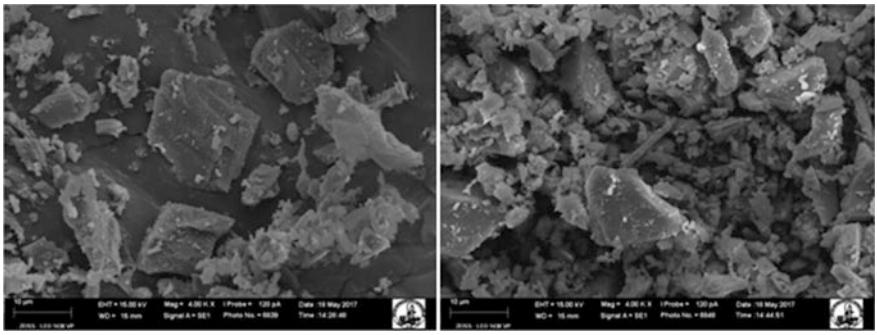

Fig. 4 Morphology of the granite waste pigment with increase of 4000 times

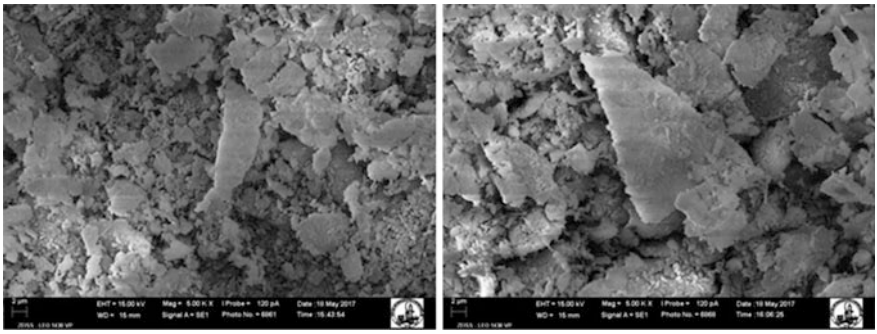

Fig. 5 Morphology of the yellow soil pigment with increase of 5000 times

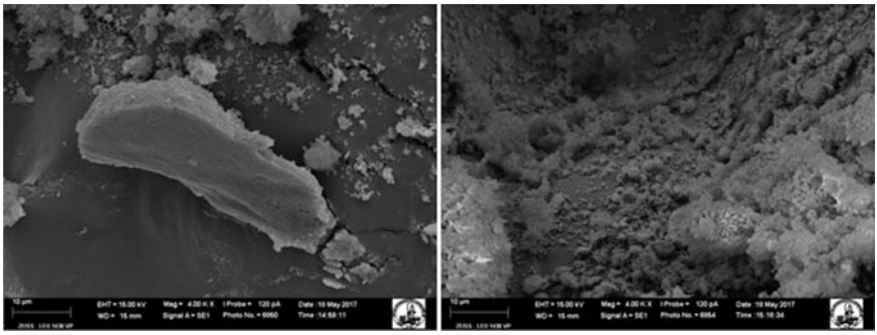

Fig. 6 Morphology of the red soil pigment with increase of 4000 times

Performance of the Paint Samples

Table 3 presents the results of nonvolatile content (NC), pigment volume concentration (PVC), hiding power (HP), and abrasion resistance (AR) of the produced inks. In addition, the results of hiding power and abrasion resistance of the paints in function of the PVC are graphically shown in Fig. 5. These graphs also present the minimum specifications of the performance properties, according to ABNT NBR 15079 [25].

According to Tiarks et al. [26], the smaller the particle diameter, the better the hiding power of paint film. However, through Table 3 and Fig. 7, it can be noted that granite residue pigments based paints exhibit much greater hiding power than soil pigments based paints, even the waste particles had larger diameter than the soil particles. This can be explained by the characteristics of the residue, which is considered an inert material. Therefore it is a material that has little solubility in the water and does not present agglomeration problem, that is, there is no electrostatic attraction between particles. This allows the production of paints with high nonvolatile content, maintaining a viscosity considered ideal for application of the product.

According to Silva and Uemoto [27], the nonvolatile content of latex paints found in the market presented values in the range of 35.6–52%. From Table 3, it is noted that residue pigments based paints exhibit solids content in the range of 51–57%, while yellow and red soils pigments based paints present nonvolatile content in the range of 21–23% and 17–20%, respectively. It happens because soil particles are highly soluble in water. Thus, in order to maintain an acceptable viscosity for application of the product, the amount of nonvolatile content has to be low.

It is also observed that the yellow soil pigments based paints have a greater hiding power than the red soil pigments based paints. This is due to the characteristics of the soils. The yellow soil presents particles with lamellar morphology, as in the case of the kaolinite, which provides greater hiding power. In contrast, the red soil also presents kaolinite, but it is constituted mainly by the clay fraction rich in iron oxide. These particles are very small, therefore have a high specific surface area, providing more interactions between the particles and the formation of agglomerates, which impairs the hiding power of the inks.

The existence of agglomerates in the blend may be the result of a low efficiency dispersion. This shows the need to improve the preparation of the pigments. According to Tiarks et al. [26], a good dispersion should not only be able to separate the agglomerates of pigments, but also to electrostatically stabilize the particles, in order to avoid their re-agglomeration.

According to ABNT NBR 15079 [25], the minimum hiding power for economical paints is 4 m^2/l. It is observed, as Fig. 7, that none of the soil pigment based paints met this specification. Unlike the waste pigments based paints, whose formulations with PVC higher than 67% had a hiding power bigger than that established by ABNT.

Table 3 Characteristics and performance properties of the ink samples

Paint sample	Granite waste pigments based paint				Yellow soil pigments based paint				Red soil pigments based paint			
	NC (%)	PVC (%)	HP (m^2/l)	AR (cycles)	NC (%)	PVC (%)	HP (m^2/l)	AR (cycles)	NC (%)	PVC (%)	HP (m^2/l)	AR (cycles)
1	56.8	80.40	6.69	30	21.44	81.02	2.72	21	17.77	79.85	2.47	24
2	55.8	73.22	5.78	47	22.17	74.00	2.68	33	18.3	72.54	2.35	31
3	54.09	67.22	4.01	67	22.72	68.09	2.45	83	18.81	66.46	2.32	54
4	53.16	62.13	3.05	77	23.24	63.06	2.21	117	19.31	61.31	2.26	88
5	51.62	57.76	1.86	101	23.04	58.72	2.06	141	19.79	56.91	2.1	300

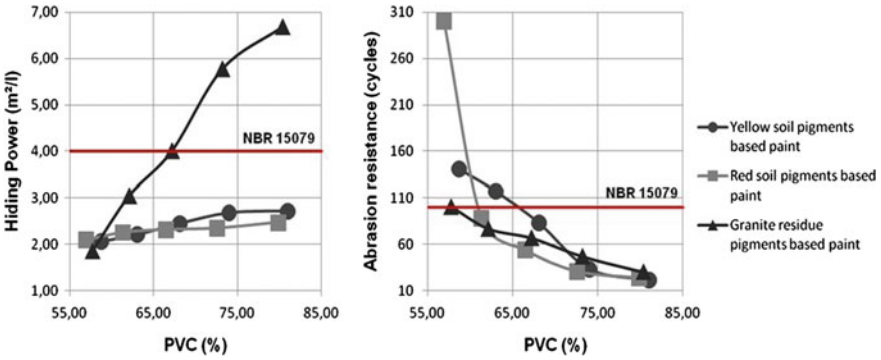

Fig. 7 Graphic of hiding power and abrasion resistance of the paints in function of PVC

In relation to abrasion resistance, granite residue pigments based paints exhibited a slightly higher resistance than soil pigments based paints in cases where PVC was larger than 70%. This result is possibly related to the composition of the residue, constituted of rock fragments. The presence of quartz in the granite waste is probably responsible for the abrasive properties of the material [28]. However, in comparison to soil pigments based paints, when PVC is less than 70%, residue pigments based paints exhibit less abrasion resistance. This is related to the granulometry of the waste, which is much larger than that of the soil. The higher pigment granulometry, the greater roughness, the higher friction and the lower abrasion resistance. This is also the explanation for the high abrasion resistance of red soil pigments based paints with low PVC, since the red soil consists mostly of very small particles, which reduces the roughness of the paints.

According to ABNT NBR 15079 [25], the minimum abrasion resistance for economical paints is 100 cycles. Figure 7 shows that only the low PVC ink samples were able to meet this specification.

Finally, it is observed that none of the ink samples met the minimum specifications prescribed in ABNT NBR 15079 [25] for hiding power and abrasion resistance, simultaneously. It happens because the hiding power and the abrasion resistance have an antagonistic effect. In order to improve the hiding power of the paint film, it is necessary to increase the PVC, as shown in Fig. 7. To improve the abrasion resistance, it is necessary to do the opposite.

It does not mean, however, that these inks cannot be used. It means that the studied inks require more repair and repainting over time, when compared to conventional paints. However, when considering issues such as the salubrity of indoor environments, environmental impact and human health, the use of manufactured paints is more recommended than conventional paints.

Conclusions

This study was carried out to explore the use of the granite residue, as a pigment, in paints for buildings and to compare the performance between granite waste pigments based paints and soils pigments based paints. On the basis of results of the experimental model, it can be concluded that:

- The use of granite waste, as a pigment, in paints has positively influenced the hiding power of the product. This is due to the characteristics of the granite residue and the high solids content obtained in the mixtures, keeping the viscosity within the range considered ideal for application of the product.
- The application of granite waste in inks has adversely affected the abrasion resistance. It happens due to the larger granulometry of the granite residue, which increases the roughness of the paint film and thus reduces the abrasion resistance.
- In comparison with soil paints, granite residue paints presented greater hiding power in almost every studied range of PVC. Regarding abrasion resistance, when PVC was higher than 70%, granite residue paints showed higher abrasion resistance than soil paints.
- None of the paint samples met the minimum specifications prescribed in the Brazilian standards for hiding power and abrasion resistance at the same time. However, it doesn't mean that inks can't be used. It means that the inks will need more repair and repainting over time, when compared to conventional paints.
- Considering issues such as the salubrity of indoor environments, environmental impact and human health, the use of the paints studied in this work is more recommended than conventional paints.

Acknowledgements The authors want to thank the CNPq for the support provided to this investigation.

References

1. Oliveira CN (2009) The paradigm of sustainability in the selection of building materials and components. Masters dissertation, Federal University of Santa Catarina
2. Uemoto KL, Ikematsu P, Agopyan V (2006) Environmental impact of building paints. In: Porto Alegre: Habitare. Construction and Environment, Porto Alegre, pp 58–95
3. Genestar C, Pons C (2005) Earth pigments in painting: characterisation and differentiation by means of FTIR spectroscopy and SEM-EDS microanalysis. Anal Bioanal Chem 382:269–274
4. Faria FC (2015) Production of natural paints for building: tests for preparation, application and evaluation of accelerated intemperismo. Masters dissertation, Federal University of Parana

5. Cardoso FP, Alvarenga RCSS, Carvalho AF, Fontes MPF (2016) Production process and evaluation of performance requirements of soil pigments based paint for buildings. Ambient Constr 16(4):167–183
6. Fazenda JMR (2009) Tintas e vernizes: ciência e tecnologia, 4th edn. Edgard Blücher, São Paulo
7. Torres P, Fernandes HR, Agathopoulos S, Tulyaganov DU, Ferreira JMF (2004) Incorporation of granite cutting sludge in industrial porcelain tile formulations. J Eur Ceram Soc 24:3177–3185
8. Aguiar MC, Gadioli MCB, Babisk MP, Candido VS, Monteiro SN, Vieira CMF (2014) Clay ceramic incorporated with granite waste obtained from diamond multi-wire sawing technology. Mater Sci Forum 775–776:648–652
9. Lima RCO, Lira HL, Neves GA, Silva MC, França KB (2014) Study of the influence of granite residue in different compositions to prepare ceramic membranes. Mater Sci Forum 798–799:542–547
10. Vijayalakshmi M, Sekar ASS, Ganesh Prabhu G (2013) Strength and durability properties of concrete made with granite industry waste. Constr Build Mater 46:1–7
11. Singh S, Nagar R, Agrawal V (2016) Performance of granite cutting waste concrete under adverse exposure conditions. J Clean Prod 127:172–182
12. Mármol I, Ballester P, Cerro S, Monrós G, Morales J, Sánchez L (2010) Use of granite sludge wastes for the production of coloured cement-based mortars. Cement Concr Compos 32:617–622
13. Ramos T, Matos AM, Schmidt B, Rio J, Coutinho JS (2013) Granitic quarry sludge waste in mortar: effect on strength and durability. Constr Build Mater 47:1001–1009
14. Ribeiro SV, Holanda JNF (2014) Soil-cement bricks incorporated with granite cutting sludge. Int J Eng Sci Innovative Technol 3(2):401–408
15. ABNT. NBR 7181(1984) Solo—análise granulométrica. ABNT, Rio de Janeiro
16. ABNT. NBR 6508 (1984) Grãos de solos que passam na peneira de 4,8 mm—Determinação da massa específica. ABNT, Rio de Janeiro
17. EMBRAPA (1997) Manual de métodos de análises de Solos. Embrapa Solos, Rio de Janeiro
18. ABNT. NBR 5849 (2015) Tintas—determinação de viscosidade pelo copo Ford. ABNT, Rio de Janeiro
19. ASTM D3723 (2011) Standard test method for pigment content of water-emulsion paints by low-temperature Ashing. ASTM International, West Conshohocken
20. ABNT. NBR 14942 (2012) Tintas para construção civil. Método para avaliação de desempenho de tintas para edificações não industriais. Determinação do poder de cobertura de tinta seca. ABNT, Rio de Janeiro
21. ABNT. NBR 15078 (2004) Tintas para construção civil. Método para avaliação de desempenho de tintas para edificações não industriais. Determinação da resistência à abrasão úmida sem pasta abrasiva. ABNT, Rio de Janeiro
22. Legodi MA, Waal D (2007) The preparation of magnetite, goethite, hematite and maghemite of pigment quality from mill scale iron waste. Dyes Pigm 74:161–168
23. Stoffer J (1997) Extender pigments. Am Paint Coat J, 19–23
24. Rodrigues GF, Alves JO, Tenório JAS, Espinosa DCR (2011) Estudo de resíduos de rochas ornamentais para a produção de materiais vítreos. Tecnol Metal Mater Miner 8(3):203–207
25. ABNT. NBR 15079 (2011) Tintas para construção civil. Especificação dos requisitos mínimos de desempenho de tintas para edificações não industriais. ABNT, Rio de Janeiro
26. Tiarks F, Frechen T, Kirsch S, Leuninger J, Melan M, Pfau A, Richter F, Schuler B, Zhao CL (2003) Formulation effects on the distribution of pigment particles in paints. Prog Org Coat 48:140–152
27. Silva J, Uemoto KL (2005) Caracterização de tintas látex para construção civil: diagnóstico do mercado do estado de São Paulo. Boletim Técnico. Escola Politécnica da Universidade de São Paulo, São Paulo
28. Ciullo PA, Robinson S (2002) Functional silicate fillers: basic principles. Paint Coat Ind Mag. http://www.pcimag.com/articles/84909-functional-silicate-fillers-basic-principles. Accessed 10 Aug 2017

Development and Characterization of Recycled-HDPE/EVA Foam Reinforced with Babassu Coconut Epicarp Fiber Residues

Mariana M. Arantes, Julyana Santana, F. R. Valenzuela-Díaz, Vijay K. Rangari, Olgun Guven and Esperidiana A. B. Moura

Abstract Nowadays, the development of polymeric materials reinforced with residues of vegetal fibers is becoming popular for application in different segments, from the automotive to the civil construction and furniture industry. Vegetal fiber residues may be used as reinforcement of the recycled polymer materials, for instance, to produce foams to packaging or to thermal and acoustic isolation for green building application. This work is focused on the development and characterization of recycled-HDPE/EVA foam reinforced with fiber residues from babassu coconut epicarp. Firstly, composites based on recycled-HDPE/EVA blend reinforced with babassu coconut fiber were obtained by melting extrusion process. The composites were then extruded in a special single screw for foaming. The foam samples were submitted to mechanical tests, density measurement, DSC, TG, and FE-SEM analysis.

Keywords Recycled HDPE/EVA blend · Babassu coconut fiber Foam · FE-SEM

M. M. Arantes (✉) · J. Santana · E. A. B. Moura
Center for Chemical and Environmental Technology, Nuclear and Energy Research Institute, 242 Prof. Lineu Prestes Av., São Paulo, SP 05508-000, Brazil
e-mail: mariana.arag@gmail.com

M. M. Arantes
ITPAC—Institute Tocantinense President Antonio Carlos S/A, Av. Filadelfia, 568, Araguaína, TO 77816-540, Brazil

F. R. Valenzuela-Díaz
Metallurgical and Materials Engineering Department, Polytechnic School, University of São Paulo, Av. Prof. Mello de Moraes, 2463, São Paulo, PA 05508-030, Brazil

V. K. Rangari
Department of Materials Science and Engineering, Tuskegee University, Tuskegee, AL, USA

O. Guven
Polymer Chemistry Division, Department of Chemistry, Hacettepe University, Beytepe, Ankara, Turkey

B. Li et al. (eds.), *Characterization of Minerals, Metals, and Materials 2018*, The Minerals, Metals & Materials Series,
https://doi.org/10.1007/978-3-319-72484-3_52

Introduction

The development of polymeric materials reinforced with residues of vegetal fibers is becoming popular for application in different industrial segments. These composite materials may be used to replace the conventional polymeric composite used in automotive industry, to produce particleboard, medium-density fiberboard (MDF) and hardboard for application in the development of low cost construction elements, furniture industry, and also, to produce foams to packaging or thermal and acoustic isolation for green building application. Recycled polymer materials reinforced with vegetal fiber residues may be a potential alternative material to the production of foams for thermal and acoustic isolation panels for application in low-cost constructions [1–3]. The application of vegetal fiber residues in development of polymer composite materials contributes to the production of more sustainability products, while promoting the reduction of the environmental impact caused by unutilized residues. The unutilized vegetal fiber residues many times are left in nature and can lead to accidental burned, quickly destroying kilometers of green area, increase the release carbon dioxide, and lead to soil erosion [4–6].

The production and consumption of plastic products made from conventional polymers (petroleum resources and non-biodegradable) have increased much during the last decades in the worldwide. Besides its wide use in packaging for preservation and distribution of food, they are extensively used in automotive industrial applications, medical delivery systems, artificial implants and other applications that are too many to mention here. Its low density, strength, user-friendly design and fabrication capabilities and low cost, are the drivers of such growth. As a result, a large amount of waste has been produced which has led to disposal problems in the worldwide and increased concerns about of final disposal of these residues [7–9]. Among the alternatives to minimize these problems are the reuse and recycling practices that are increasing over time [9, 10]. Therefore, the use of recycled polymer to produce new materials reinforced with vegetal fiber residues for application in the development of foams for application in packaging industry or thermal and acoustic isolation panels of the low-cost constructions, it can be an alternative to reduce the waste whose traditional disposal practice include incineration and discarding landfill.

The aim of this work was to development and characterization of recycled-HDPE/EVA foam reinforced with fiber residues from babassu coconut epicarp.

Experimental

Materials

Recycled-HDPE (high density polyethylene) (MFI = 0.13 g/10 min at 190 °C, 2.16 kg);
Recycled-EVA (ethylene vinyl acetate) (MFI = 20.14 g/10 min at 190 °C, 2.16 kg);
Babassu coconut epicarp fiber residues;
Foaming Agent "F.A." (Endex 2650 (Endex International)).

Preparation of Babassu Coconut Epicarp Residues

The babassu coconut epicarp fiber residues were dried at 80 °C ± 2 °C for 24 h in an air-circulating oven. The dry residues were reduced to fine powder, with particle sizes equal or smaller than 60 μm, by using ball mills and dried again at 80 °C ± 2 °C for 24 h in an air-circulating oven to reduce its moisture content to less than 2%.

Preparation of Blend and Composites

The recycled-HDPE/EVA blend (r-HDPE/EVA) (50/50 wt%) and its Composite were processed by melt extrusion using a twin-screw extruder Haake Rheomix with 16 mm and L/D = 25 rate from Thermo Scientific. The temperature profile was 140/155/175/185/195/200. Screw speed was 40 rpm. The extrudates coming out of the extruder were cooled down for a better dimensional stability, pelletized by a pelletizer.

Preparation of Foams

The foams were produce by addition blend and composite samples with 1.5 wt% of Endex 2650 Foaming Agent "F.A.", an endothermic foaming agent into a flat die single screw extruder (HAAKE Rheomex P332, Thermo Scientific). The temperature profile used during processing was 145/150/170/190/195/195 °C for and the screw' rotation was 50 rpm.

Characterization Methods

Density of foams: the specimens' densities were calculated by Eq. (1):

$$\rho = \frac{m}{V} \tag{1}$$

where ρ is the density; m is the mass, V is the volume of the samples [11].

Tensile Tests were performed on INSTRON 5567 testing machine at room temperature according to ASTM 882-91.

TG curves were obtained using TGA/SDTA851e (Mettler Toledo). The samples were heated from 30 to 580 °C under a nitrogen atmosphere (50 ml/min) at heating rate of 10 °C/min.

DSC analysis were performed using Mettler Toledo DSC 822e differential scanning calorimetry. Firstly, the thermal history of each sample was eliminated heating them from 25 to 250 °C at a scanning rate of 10 °C/min. Subsequently, the samples were cooled down to room temperature at rate of 10 °C/min. Finally, DSC curves were obtained heating them from 25 to 250 °C at a rate of 10 °C/min. The samples' melting temperature was determined as the temperature at which the endothermic peak occurred and the fusion enthalpy was obtained integrating the peaks at the melting temperature.

FE-SEM: The samples' cryofractured morphology was studied using a Quanta FEG 650 scanning electron microscope at 15 kV. The specimens were fractured in liquid nitrogen.

Results and Discussion

Density of Foams

The density of foams for each sample is shown in Table 1. The highest density of foams was obtained for HDPEr/EVAr blend compared with the composites. The foaming agent content reduced their density but as can be seen the wood fiber content increased 25% when compared with HDPEr/EVAr (F.A. 1.5%).

Table 1 Densities of HDPEr/EVAr blend and foams

Sample	Foam density (g/cm^3)
HDPEr/EVAr	0.92 ± 0.04
HDPEr/EVAr (F.A. 1.5%)	0.56 ± 0.04
HDPEr/EVAr/babassu composites (F.A. 1.5%)	0.70 ± 0.03

Differential Scanning Calorimetry (DSC) Analysis Results

Figure 1 shows DSC melting curves of HDPEr/EVAr Blend and foams from HDPEr/EVAr Blend and HDPEr/EVAr/Babassu composites. Figure 1 shows two distinct endothermic peaks corresponding to the melting of two different crystallites for HDPEr/EVAr Blend and its foam. This indicates that HDPE and EVA were incompatible in the crystalline region [12]. For HDPEr/EVAr/Babassu foam three distinct endothermic peaks were observed.

The DSC melting temperature and enthalpy results are presented in Table 2.

It can be seen in Table 2 an important decreasing in melting temperature and enthalpy of HDPEr/EVAr Blend and foams from HDPEr/EVAr Blend and HDPEr/EVAr/Babassu composites when compared with neat HDPEr. Based on these results and according to literature it is possible to conclude that if melting enthalpy of the composite is lower than 80% of the value for neat HDPE melting enthalpy, it means that the fiber residues interact with the polymer matrix decreasing its melting enthalpy and, consequently its crystallinity [13].

Thermogravimetric (TG) Analysis Results

Figure 2 shows the TG thermograms of HDPEr/EVAr Blend and foams from HDPEr/EVAr Blend and HDPEr/EVAr/Babassu composites.

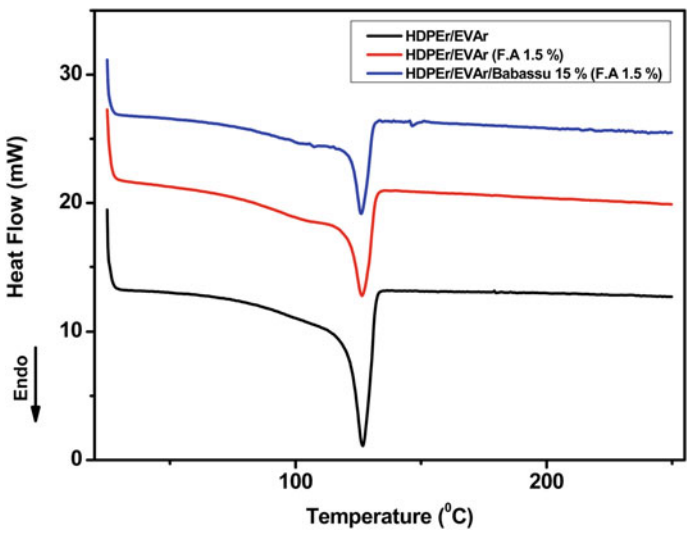

Fig. 1 DSC melting curves of HDPEr/EVAr blend and foams

Table 2 DSC analysis results of HDPEr, HDPEr/EVAr blend and foams

Materials	Melting temperature (T_m, °C)	Melting enthalpy (ΔH_m, J g^{-1})
HDPEr	132	189
HDPEr/EVAr blend	120	124.4
HDPEr/EVAr (F.A. 1.5%)	119	112
HDPEr/EVAr/babassu composites (F.A. 1.5%)	121	92

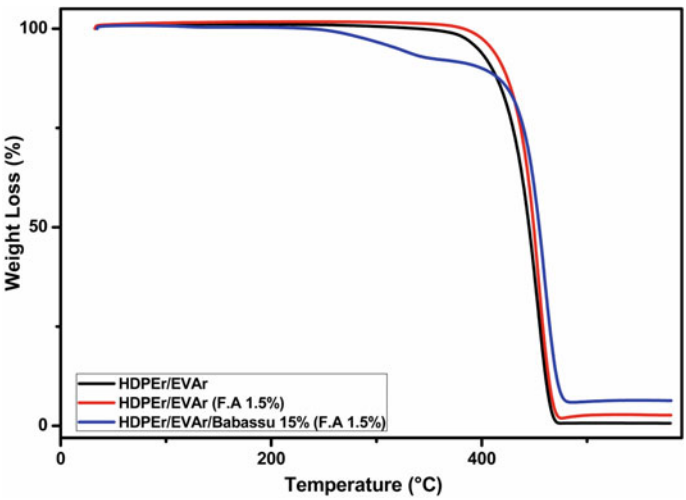

Fig. 2 TG thermograms of the HDPEr/EVAr blend and foams

Table 3 presents the decomposition temperatures and weight loss of HDPEr/EVAr Blend and foams from HDPEr/EVAr Blend and HDPEr/EVAr/Babassu composites.

As can be seen in Table 3, HDPEr/EVAr blend showed a single stage of degradation temperature at 390.3 °C. For HDPEr/EVAr foams was observed a higher degradation temperature at 403 °C compared to the blend. In the case of

Table 3 Decomposition temperatures and weight loss of HDPEr/EVAr blend and foams

Materials	T_{onset} (°C)	T_{max} (°C)	Weight loss (%)
HDPEr/EVAr blend	390.3	579	99.3
HDPEr/EVAr (F.A. 1.5%)	403	579	97.3
HDPEr/EVAr/babassu composites (F.A 1.5%)	230/358/416	580	93.7

composites, an initial peak between 91 and 131 °C, which corresponds to a mass loss of absorbed moisture was showed. After this, the TG curve showed three-stage loss of mass. The first, a decomposition shoulder peak of low intensity centered of around 230 °C, characteristic of low molecular weight fiber constituents, such as hemicelluloses and pectin [11, 14, 15]. The second one, appearing at higher temperatures with a small hump in the temperature range from 250 to 375 °C with centered peak at 358 °C corresponded to the thermal degradation of cellulose [15, 16], lignin content in these fiber residues and foaming agent contribution. The third stage of degradation temperature occurred at 416 and 580 °C corresponds to the thermal degradation of composites, foam agent contribution, and lignin content. According to the literature, lignin is thermally decomposed over a wide range as compared to hemicellulose and cellulose, due to its complexity. Lignin is completely decomposed at a high temperature as 900 °C [15].

Mechanical Tests

Tensile tests results: Fig. 3 shows the diagram stress (MPa) X strain (%) for the foams from of HDPEr/EVAr Blend and HDPEr/EVAr/Babassu. The results presented shows the average values calculated from the data obtained in tests for five test specimens. The results show a significant reduction at tensile strength, elongation and Young's modulus of blend due to babassu fiber residues addition and foaming agent.

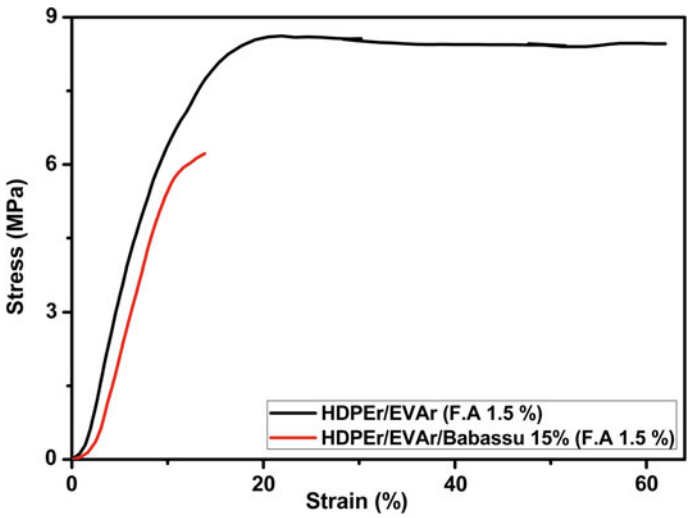

Fig. 3 Diagram stress (MPa) X strain (%) for the foams

Table 4 Tensile test results for HDPEr/EVAr blend and foams

Materials	Tensile strength at break (MPa)	Elongation at break (%)	Young's modulus (MPa)
HDPEr/EVAr blend	19.7 ± 1.7	852 ± 31	89.7 ± 4.0
HDPEr/EVAr (F.A. 1.5%)	8.3 ± 0.5	111 ± 8.6	66.5 ± 2.1
HDPEr/EVAr/babassu composites (F.A. 1.5%)	6.3 ± 0.5	16.6 ± 2.0	65.4 ± 4.2

Table 4 presents the results of tensile tests for the foams from of HDPEr/EVAr Blend and HDPEr/EVAr/Babassu. The results presented shows the average values calculated from the data obtained in tests for five test specimens.

Field Emission Scanning Electron Microscopy (FE-SEM) Analysis Results

FE-SEM micrographs of cryofractured surfaces of the foams from HDPEr/EVAr Blend and HDPEr/EVAr/Babassu composites are showed in Fig. 4. It can be seen in Fig. 4a, b a mixed morphology of open and closed-cell structures for

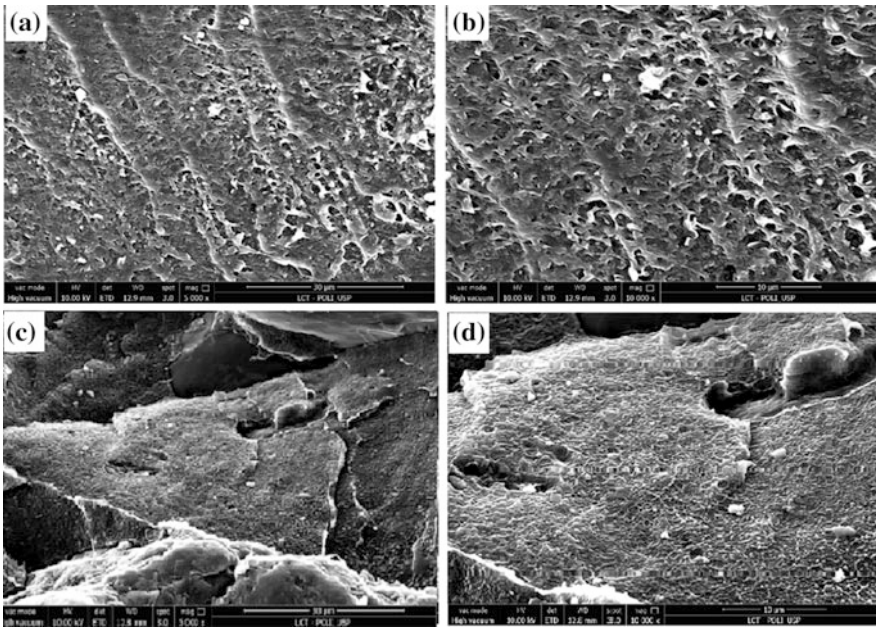

Fig. 4 FE-SEM micrographs of cryofractured surfaces for foams from HDPEr/EVAr Blend: **a** (5000×), **b** (10,000×); HDPEr/EVAr/Babassu composites: **c** (5000×), **d** (10000×)

HDPEr/EVAr Blend samples. HDPEr/EVAr/Babassu composites samples, Figs 4c, d shows a closed-cell structure with a relatively homogeneous cell size distribution and some babassu fiber residues particles agglomerated distributed on the micrographs surfaces.

Conclusion

This work presented the development and characterization of HDPEr/EVAr foams reinforced with fiber residues from babassu coconut epicarp. The results showed an increase of density of foam and a closed-cell structure with a relatively homogeneous cell size distribution due to babassu fiber residues addition. However, it can be seen some babassu fiber residues particles agglomerated distributed on the micrographs surfaces. On the other hand, the foams prepared from HDPEr/EVAr Blend presented a mixed morphology of open and closed-cell structures, but with superior tensile strength and elongation properties when compared with foam from HDPEr/EVAr/Babassu composites. The melting enthalpy of the HDPEr/EVAr/Babassu composite foams is lower than 80% of the value for neat HDPE melting enthalpy. Based on these results it is possible to conclude that the babassu fiber residues interacted with the HDPEr/EVAr Blend matrix decreasing its mechanical properties, melting enthalpy and, consequently, its crystallinity.

Acknowledgements The authors wish to thank CAPES to provide the support for this work.

References

1. Madurwar MV, Ralegaonkar RV, Mandavgane SA (2013) Application of agro-waste for sustainable construction materials: a review. Constr Build Mater 38:872–878
2. Panthapulakkal S, Sain M (2007) Agro-residue reinforced high-density polyethylene composites: fiber characterization and analysis of composite properties. Compos Part A 38:1445–1454
3. Faustino J et al (2012) Impact sound insulation technique using corn cob particleboard. Constr Build Mater 37:153–159
4. Ardanuy M, Antunes M, Velasco JI (2012) Vegetable fibres from agricultural residues as thermo-mechanical reinforcement in recycled polypropylene-based green foams. Waste Manag 32:256–263
5. Sahari J, Sapuan SM (2011) Natural fibre reinforced biodegradable polymer composites. Rev Adv Mater Sci 30:166–174
6. Yan L, Chouw N, Jayaraman K (2014) Flax fibre and its composites—a review. Compos B 56:296–317
7. Najafi SK (2013) Use of recycled plastics in wood plastic composites—a review. Waste Manag 33:1898–1905
8. Azwa ZN, Yousif BF, Manalo AC, Karunasena W (2013) A review on the degradability of polymeric composites based on natural fibres. Mater Des 47:424–442

9. Ammala A, Bateman S, Deana K, Petinakis E, Sangwan P, Wong S, Yuan Q, Yu L, Patrick C, Leong KH (2011) An overview of degradable and biodegradable polyolefins. Prog Polym Sci 36:1015–1049
10. Scott G (2000) Green' polymers. Polym Degrad Stab 68:1–7
11. Einhorn-Stolla U, Kunzek H, Dongowsk G (2007) Thermal analysis of chemically and mechanically modified pectins. Food Hydrocolloids 21:1101–1112
12. Dalai S, Wenxiu C (2002) Radiation effects on HDPE/EVA blends. J Appl Polym Sci 86:553–558
13. Araujo JR, Waldman WR, De Paoli MA (2008) Thermal properties of high density polyethylene composites with natural fibres: coupling agent effect. Polym Degrad Stab 93:1770–1775
14. Rachini A, Le Troedec M, Peyratout C, Smith A (2009) Comparison of the thermal degradation of natural, alkali-treated and silane-treated hemp fibers under air and an inert atmosphere. J Appl Polym Sci 112:226–234
15. Razali N, Salit MS, Jawaid M, Ishak MR, Lazim Y (2015) A study on chemical composition, physical, tensile, morphological, and thermal properties of roselle fibre: effect of fibre maturity. BioResources 10:1803–1824
16. Monteiro SN, Calado V, Rodriguez RJ, Margem FM (2012) Thermogravimetric stability of polymer composites reinforced with less common lignocellulosic fibers—an overview. J Mater Res Technol 1:117–126

Evaluation of Microcapsules of PBSL/MMT-K and PBSL/OMMT-K Nanocomposites

B. B. Michel, F. R. Valenzuela-Diaz, H. Wiebeck, W. S. Hui and M. G. Silva-Valenzuela

Abstract Biodegradable polymer microcapsules have been used as a control sustained release system with many applications. Studies reveal that the incorporation of nanoparticles improves matrix properties, even more so if the clay is modified. The objective of this work was to compare microcapsules of poly (succinate-co-butylene lactate) (PBSL) reinforced with Brazilian clay, composed of smectites and kaolinite, in its natural (MMT/K) and modified (O-MMT/K) forms. Nanocomposites and microcapsules were synthesized by emulsification-diffusion of solvent and solvent diffusion methods. Its characterization was then performed by scanning electron microscopy (SEM), stereomicroscopy and wide-angle X-ray diffraction (XRD). The results reported corroborate that PBSL/OMMT-K form an intercalated montmorillonite and kaolinite nanostructure, capable of generating uniform spherical microcapsules with diameter values smaller than that of PBSL/MMT-K, reaching 5–10 μm. DRX indicates that there was a real change in the clay structure. The incorporation of modified clay showed an improvement in surface quality and the strength of microcapsules, making it possible to produce smaller sizes.

Keywords Microcapsule · Nanocomposite · PBSL · Organoclay

B. B. Michel (✉) · F. R. Valenzuela-Diaz · H. Wiebeck · W. S. Hui
M. G. Silva-Valenzuela
Metallurgic and Materials Engineer Department, Polytechnic School of University of São Paulo, Avenida Prof. Mello Moraes, 2463, São Paulo, SP 05508-030, Brazil
e-mail: bianca.michel@usp.br

M. G. Silva-Valenzuela
Naturals and Humans Science Centers, Federal University of ABC, Avenida dos Estados, 5001, Santo André, SP 09210-580, Brazil

B. Li et al. (eds.), *Characterization of Minerals, Metals, and Materials 2018*, The Minerals, Metals & Materials Series,
https://doi.org/10.1007/978-3-319-72484-3_53

Introduction

According to BTC Research data published in 2016, the nanocomposites world market is set to reach $1.6 billion and should grow annual by 26.7% until 2021, meaning by this time it could hit the $5.3 billion mark. This trend is noticeable in the area of development.

Nanocomposites are synthesized by two elements, matrix and nanocharge and these compose a system of three components: particle, interfacial component (surfactant) and polymer matrix chains, their relationship determine the material properties [1]. Although complete exfoliation does not prevent charge action, such as making it fire retardant and enhancing mechanical properties, the more homogeneous the dispersion the more properties can be improved [2]. These can be obtained by maintaining the stirring throughout the process, controlling temperature and with the addition of a surfactant capable of improving the relationship of the polymer-surface [1], in other words, the key to nanocomposite production depends on the degree of dispersion of the clay sheets on the matrix.

Clays are a mineral of lamellar structure made of octahedral and tetrahedral sheets of aluminum and silicon oxides. Sheets are classified in two ways: smectites and kaolin of 2:1 and 1:1 structure proportion of tetrahedral and octahedral sheets, respectively. Smectites are the most used in nanocomposites applications. Water absorption and cation exchange capacity, characteristics of these materials, especially smectites, depend on ions presented in the interlamellar region. In this respect, smectites that have greater swelling properties are sodic bentonites [3]. Organophilization is a method of cation exchange by which interlayering of inorganic cations are swapped with organic ones, making the lamella surface hydrophobic, consequently there is an interlayer distance increase. That last factor facilitates lamella exfoliation, that is, this procedure can be used as a tool to increment nanocomposite dispersion [4].

Lamella exfoliation on a polymer matrix restricts the movement of chains and increases interfacial interaction strength. As consequence there are substancial improvement of heat resistance, higher Young modulus and biodegradability. And, also, a decrease of gas permeability [5].

Clays have been used as substitutes of charge in calcium carbonate and fiberglass, its application goes from automotive panels to controlled drug release systems in health treatments. On this last item, nanocomposites can be synthesized as microcapsules containing drug agents that, when inserted into an environment, their casing decomposes and release the active compound. Considering the degradation factor, the most indicated matrix is a biodegradable one. This present study intends to analyses if an organoclay-biodegradable polymer association favors microcapsules formation, improving properties and contribute to its application as controlled release system.

Objectives

Synthesis and characterization of nanocomposites microcapsules of poly (butylene succinate co-lactate) (PBSL) and Brazilian organoclay.

Materials

The clay used in this study was obtained by a purification process of a raw sample from Vitória da Conquista (Bahia/BR). As result of the procedure, three granular fractions were acquired, with different colors. The thinnest and most purple sample was chosen, its average particle size is 20.55 ± 7.09 μm and it is classified as polycationic bentonite that contains 50% of montmorillonite and 40% of kaolin [6], for which the abbreviation MMT-K is used.

The Polymer used is poly (butylene succinate co-lactate) was produced by Mitsubishi Chemical® (commercial name: GS-PLA and abbreviated as PBSL). It is a polyester synthesized of succinic acid, 1, 4-butanodiol and L-lactate acid monomers, all of them can be obtained from green sources.

Methods

Organophilization

First, a 20 g clay dispersion on 480 mL of distilled water was prepared in a 2 L beaker with mechanical stirring of 1500 rpm for 20 min, and then for 5 min at 14,000 rpm on a Hamilton Beach mixer, at 25 °C.

Second, 5.3 mL of Na_2CO_3 50% was added, stirred at 1500 rpm for 20 min. This promoted activation of the interlamellar region.

Still stirring, 42.6 mL of 50% solution of quaternary salt cetyl trimethyl ammonium chloride ($C_9H_{42}NCl$) was added, with a molecular weight of 320.02 g. After 30 min, the solution was removed from stirring and allowed to rest overnight.

The resultant dispersion was vacuum filtered using 2 L of distillated water, dried at 60 °C overnight and sifted through 200 mesh.

Nanocomposite Preparation

Initially, a 50 mL PBSL-5% solution and a 50 mL MMT-K-0.5% solution was prepared using CH_2Cl_2 as a solvent under 500 rpm magnetic agitation for 15 min, at 25 °C. Then, still stirring, a solution of PBSL was poured over MMT-K

dispersion, generating a nanocomposite solution that was left to stir for 3 h and, at last, at rest for 20 h. A 2 mL sample was deposited on a Petri plate to film production for additional analyses.

The exact same process was applied to the production of organoclay (OMMT-K) nanocomposite.

Microcapsule Preparation

The emulsification-diffusion method was used to produce the microcapsules. The solution of the PBSL/MMT-K nanocomposite was transferred to a 1% polyvinyl alcohol solution with the aid of a Pasteur micropipette under mechanical stirring (1500 rpm) in a beaker at 25 °C. The mixture was allowed to stand for one hour for complete deposition of the microcapsules at the bottom of the beaker, supernatant was then removed for carrying out three steps washing process of microcapsules with distilled water.

X-ray Diffraction Analysis (XRD)

The study was carried out through a powder method, using an X-ray diffractometer of the Rigaku brand, model MiniFlex600. The conditions of analysis were copper ray tube, angular range 3°–100°, angular pitch 0.02°, with speed of 0.02°/min.

Scanning Electron Microscope (SEM)

Morphological characterization and composition were performed using a Scanning Electron Microscope (FEI, INSPECT F50) in the Department of Metallurgical and Materials Engineer laboratory of the Polytechnic School of USP. Samples were coated with gold to prevent e-beam charging.

Results and Discussion

X-ray Diffraction (DRX)

Figure 1 presents the obtained curves through X-ray diffraction of purified and modified clay. The first analysis indicates the main peaks as d_{001} = 14.5 Å and d_{002} = 4.5 Å of the montmorillonite group and d_{001} = 7.1 Å and d_{002} = 3.5 Å of the

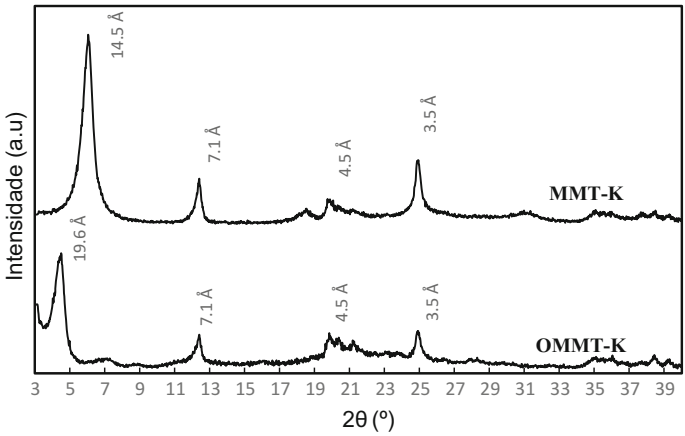

Fig. 1 Purified (MMT-K) and modified (OMMT-K) clay diffractograms

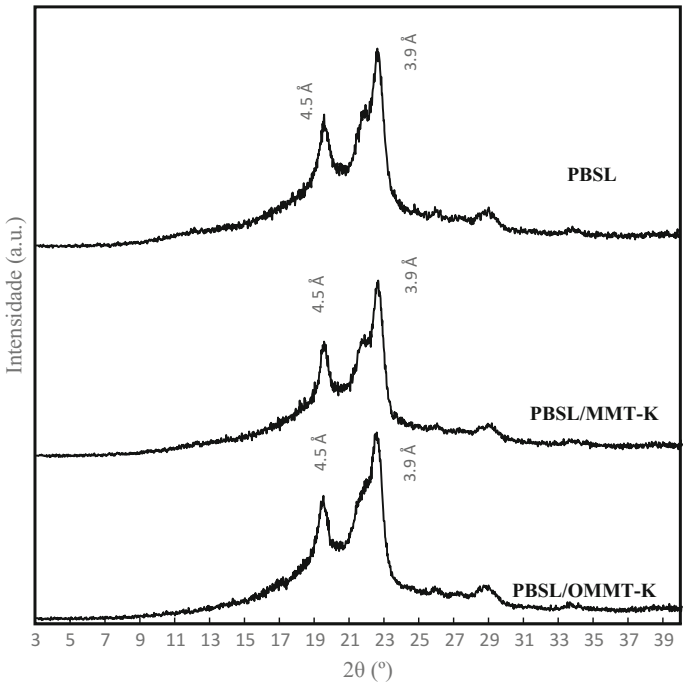

Fig. 2 Diffractograms of PBSL polymer, PBSL/MMT-K and PBSL/OMMT-K nanocomposite microcapsules

kaolin group. On the second curve, it is possible to notice that the initial peak is dislocated to left, suggesting the interlayer distance increased to d_{001} = 19.6 Å between MMT sheets. However this effect does not happen to kaolin peaks due to hydrogen bond that connects sheets, which does not permit cation exchange of quaternary salt, meaning the structure is preserved.

Diffractograms curves of nanocomposite (Fig. 3) and polymer matrix (Fig. 2) microcapsules are typical of the Poly (butylene succinate) copolyester, showing no peaks at low angles associated to peaks at d_{001} = 19.9 Å e d_{001} = 22.7 Å. When comparing three curves it is possible to say that there is no significant alteration of peaks, except that MMT and K peaks disappeared, implying that although the second group doesn't show structural modification through the organophilization process, polymer chains were capable of completely exfoliating both clay mineral due to the polar hydroxyl group presented by PBSL.

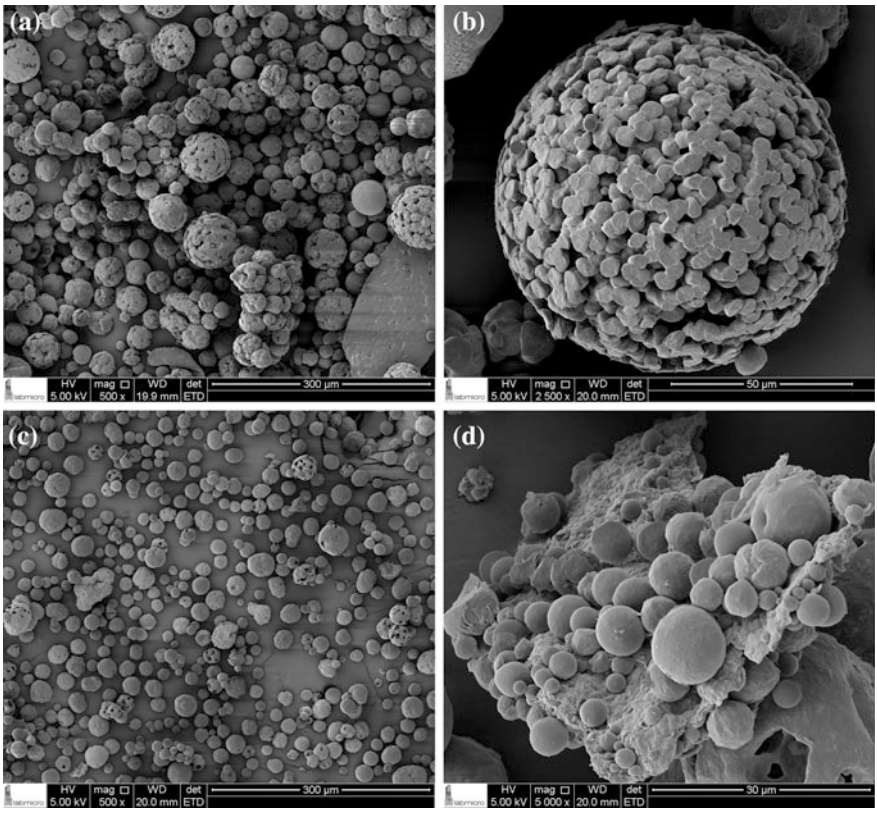

Fig. 3 SEM images of PBSL/MMT-K microcapsules 500× (**a**) and 2500× (**b**) and PBSL/OMMT-K microcapsules 500× (**c**) and 5000× (**d**)

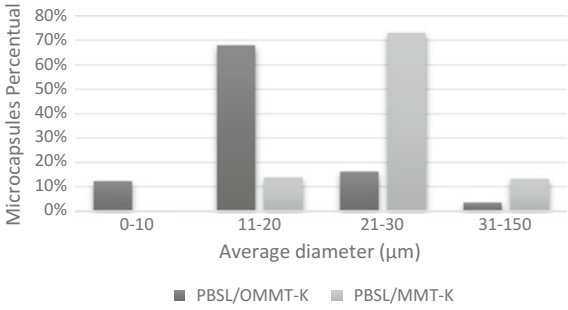

Fig. 4 Average diameter size distribution of PBSL/MMT-K and PBSL/OMMT-K nanocomposite microcapsules

Scanning Electron Microscope (SEM)

Microscopy investigation (Fig. 3) of PBSL/MMT-K nanocomposite microcapsules reveals preservation of spherical monolithic shape, rough surface and average diameter range of 10–150 μm. While results of PBSL/OMMT-K, shows hollow beads, with a smoother surface and average diameter range of 5–50 μm.

An structure analysis indicates a significantly reduction of average diameter size of organoclay nanocomposite in relation to purified clay nanocomposite. About 68% PBSL/MMT-K microcapsules diameter are in the range of 11–20 μm. In other hand, 73% of Pare in the range of 21–30 μm, this means a 30% size reduction (Fig. 4).

These results are in agreement with those described by de Paiva et al. [7]. Where it is observed that the insertion of the quaternary salt by the organophilization process increases the clay-polymer affinity, with consequent increase of energy between the bonds and the energy surface of the microcapsules, being able to produce particles of smaller size in relation to the system with purified clay.

Conclusion

Activities carried out by the present research concludes that the matrix-nanocharge microstructure of purified and modified MMT-K was able to intercalate, producing nanocomposite materials, as indicated by the results of the microcapsule XRD analysis. The presence of kaolinite on clay composition, showed by XRD analyzes, suggests that this clay, as well as montmorillonite, are present in the nanocomposite in the exfoliated form.

Clay organophilization process was efficient, leading to the production of smaller diameter spheres, with a predominance of structures from 11 to 20 μm, compared to 21–30 μm, obtained from those with crude clay. This occurs due to the increased affinity of the clay-polymer system resulted from the insertion of cetyl trimethyl ammonium chloride ($C_9H_{42}NCl$) quaternary salt ions. Another

consequence of this relationship was the reduction of surface roughness, producing smoother microcapsules.

The PBSL/OMMT-K nanocomposite has shown to be a potential candidate to produce microcapsules encapsulated with active ingredients and likely to be applied on pharmaceutical, cosmetic and wastewater treatment industries, for example, representing another important step on nanocomposites studies produced from organophilized clays. However, further studies are needed to determine its influence on structure and to improve method to avoid microcapsules agglomeration.

Acknowledgements We thank to Coordination for Improvement of Higher Education Personnel (CAPES) and São Paulo Research Foundation (FAPESP) for financial support.

References

1. Fischer H (2003) Polymer nanocomposites: from fundamental research to specific applications. Mater Sci Eng 23:763–772. https://doi.org/10.1016/j.msec.2003.09.148
2. Markarian J (2010) Automotive and packaging offer growth opportunities for nanocomposites. Plast Addit Compd 18–21
3. Brigatti MF, Galan E, Theng BKG (2006) Chapter 2 Structures and mineralogy of clay minerals. In: Handbook of clay science. Elsevier, Oxford, pp 19–86
4. He H, Ma L, Zhu J, Frost RL (2014) Synthesis of organoclays: a critical review and some unresolved issues. Appl Clay Sci 100:22–28. https://doi.org/10.1016/j.clay.2014.02.008
5. Sinha Ray S, Okamoto M (2003) Polymer/layered silicate nanocomposites: a review from preparation to processing. Prog Polym Sci 28:1539–1641. https://doi.org/10.1016/j.progpolymsci.2003.08.002
6. da Silva-Valenzuela MG, Carvalho FSM, Sayeg IJ, Sant'Anna LG (2012) Purification and characterization of a natural Brazilian clay blend. Mater Sci Forum 727–728:1439–1443. doi:10.4028/www.scientific.net/MSF.727–728.1439
7. de Paiva LB, Morales AR, Valenzuela Díaz FR (2008) Organoclays: properties, preparation and applications. Appl Clay Sci 42:8–24. https://doi.org/10.1016/j.clay.2008.02.006

Evaluation of the Quality of Concrete with Waste of Construction and Demolition

Niander Aguiar Cerqueira, Victor Barbosa de Souza, Afonso Garcez de Azevedo, Anna Carolina Lopes Rabello, Renan Tavares Vicente, Amanda Camerini and André Raeli Gomes

Abstract Civil construction is a sector of extreme impact in the Brazilian economy, with construction and demolition waste (RCD) having an extreme impact on the amount of urban solid waste. In this research it was proposed to propose a way of using these residues in the construction of concrete artifacts for structural use. Concrete specimens with sand substitution by RCD were produced in different percentages as a way to contribute to reduce, recycle and reuse this large amount of waste from the construction industry. The objective of this work was to study the mechanical properties of structural concrete with total and partial replacement (25, 50, 75 and 100%) in sand mass. The results of the compression test indicate good quality for concretes with mass substitution of up to 75% per RCD.

Keywords Concrete · RCD · Waste reuse · Civil buildings

Introduction

Civil construction has experienced great growth in recent years in Brazil, in particular due to the pent-up demand for housing and the scarcity of infrastructural investments.

This demand was also increased by large works carried out in Brazil during the last years for the world cup and the Olympic Games, etc.

N. A. Cerqueira (✉) · V. B. de Souza · A. G. de Azevedo · A. C. L. Rabello · R. T. Vicente · A. Camerini · A. R. Gomes
Redentor University Center (UNIREDENTOR), BR 356, KM 25, Itaperuna, Rio de Janeiro, Brazil
e-mail: coord.niander@gmail.com

N. A. Cerqueira · A. G. de Azevedo
State University of the Northern Darcy Ribeiro—UENF, Campos dos Goytacazes, Rio de Janeiro, Brazil

V. B. de Souza
Federal University Fluminense (UFF), Niterói, Rio de Janeiro, Brazil

B. Li et al. (eds.), *Characterization of Minerals, Metals, and Materials 2018*, The Minerals, Metals & Materials Series,
https://doi.org/10.1007/978-3-319-72484-3_54

Table 1 Estimated RCD generation in some countries

Region	In millions (kg/year)	In kg/resident/year
Sweden	1,200–6,000	136–680
Holland	12,800–20,200	820–1,300
U.S.	136,000–171,000	463–584
United Kingdom	50,000–70,000	880–1,120
Belgium	7,500–34,700	735–3,359
Denmark	2,300–10,700	440–2,010
Italy	35,000–40,000	600–690
Germany	79,000–300,000	963–3,658
Japan	99,000	785
Portugal	3,200–4,400	325–447
Brazil	31,000	230–760

Source IPEA [1]

Table 1 illustrates the amount of waste generated in some countries.

Several authors have dedicated themselves to researching the problems related to construction and demolition waste, proposing solutions ranging from reuse by crushing and using as powder stone and gravel, such as the use in the production of ceramic artifacts, mortars and concrete, among others [2–5].

In this work a study was carried out to produce concrete with sand substitution by RCD, in different percentages, in order to reduce, recycle and reuse this large amount of waste from the civil construction industry. This work aimed to study the mechanical properties of structural concrete with total and partial replacement (25, 50, 75 and 100% replacing sand).

A composite is a multiphase material that presents combined properties of the parts that constitute it in order to obtain a better combination of properties [6].

Concrete is a composite and can be classified as one of the most important elements in construction. It is the result of the bonding of binder, fine aggregate (sand), coarse aggregate (crushed stone) and water, and may still receive some additives or additions. Concrete can be used in the fabrication of structural elements (beams, slabs, pillars, shoes, etc.), such as flooring, plumbing, etc. [7].

The properties of the concrete are varied, however, its main advantage is the excellent compression behavior and one of its main disadvantages is the poor traction behavior [8].

The mechanical strength of the concrete is influenced by several factors such as: curing time and water/cement factor [9].

As for the age of the concrete i.e. its cure time, there is an increasing ratio of the same, so test standards indicate doing the same at ages as 7, 14 and 28 days, for example. Regarding the water/cement factor, there is a minimum of water that must be used because of the chemical reactions that must occur through the hydration of the cement, but the larger the amount of water, the lower the mechanical resistance of the concrete.

Table 2 Classification of RCD

Classification	Typology
Class A	Reusable or recyclable waste as aggregate, such as: (a) the construction, demolition, renovations and paving repairs and other works of infrastructure, including soil from excavation; (b) construction, demolition, renovations and building repairs: ceramic components (bricks, blocks, tiles, flooring boards, etc.), mortar and concrete; (c) the manufacturing process and/or demolition of precast concrete parts (blocks, pipes, curbs, etc.) produced at construction sites
Class B	Are recyclable waste to other destinations such as: plastics, paper/cardboard, metal, glass, wood and others
Class C	It is waste for which economically feasible technologies or applications are not designed to allow their recycling/recovery, such as products from the plaster
Class D	They are hazardous waste from the construction process, such as asbestos, paints, solvents, oils and other contaminated or those coming from demolitions, renovations and repairs of radiology clinics, industrial facilities and others

Source CONOMA [12, 13]

With regard to RCD, Levy [10] defined the construction waste as the general portion of the waste from the construction and demolition activities.

Zordan [11] adds that waste should be uncontaminated for reuse. It also considers RCD waste from construction and demolition of roads, including pipelines, asphalt pavements, among others.

According to National Council for the Environment (CONAMA) [12, 13] the waste can be divided into four classes, as shown in Table 2.

In this work only Class A waste was used.

Experimental Procedure

The test specimens were prepared according to Brazilian standards [14–17], using five different concrete traces, using the ratio 3:2:1 (three sand, two crushed stone zero and one of cement), varying with different percentages of RCD in substitution to the sand for its composition (Table 3).

Table 3 Mass ratio of the traces

Trace	Sand (kg)	Gravel (kg)	Cement (kg)	RCD (kg)
1st trace—0R	57.5	34.8	14.9	0.0
2nd trace—25R	43.2	34.8	14.9	14.4
3rd trace—50R	28.8	34.8	14.9	28.8
4th trace—75R	14.4	34.8	14.9	43.2
5th trace—100R	0.0	34.8	14.9	57.5

In the production of the specimens CP III—32 cement was used and the curing method was the wet curing with the use of tarpaulin to maintain humidity. The sand as the RCD used in the preparation of the specimens were sieved in the sieve 4 (4.76 mm).

All specimens were obtained from a mold 100 × 200 mm, according to the technical standards already mentioned. Some specimens are shown in Fig. 1.

The compression tests were performed at the ages of 7 and 28 days, in 10 specimens for each trace, all of which were performed in a Soloteste compression machine (Fig. 2), at the Construction Materials Laboratory of UniRedentor, Itaperuna-RJ, at a compression speed of 5 mm/min.

Fig. 1 Test specimens

Fig. 2 Machine used for the compression test

Results and Discussion

The results obtained were satisfactory, with the mean values of the mechanical resistance to compression presented in Table 4.

The results obtained for each trace and the lines are indicated in the graphs of Figs. 3 and 4, indicating the trend line of each curve and also the equation that best defines each model.

The results obtained point to an excellent performance regarding the partial replacement of sand by RCD in the concrete mass in the values of 25, 50 and 75%.

Table 4 Compressive strength

Trace	Age	Compressive strength—average (MPa)	Sample standard deviation
0R	7	19.3	0.151
	28	21.5	0.278
25R	7	15.6	0.122
	28	18.3	0.287
50R	7	14.6	0.186
	28	17.9	0.320
75R	7	12.5	0.263
	28	16.4	0.307
100R	7	10.3	0.193
	28	13.6	0.186

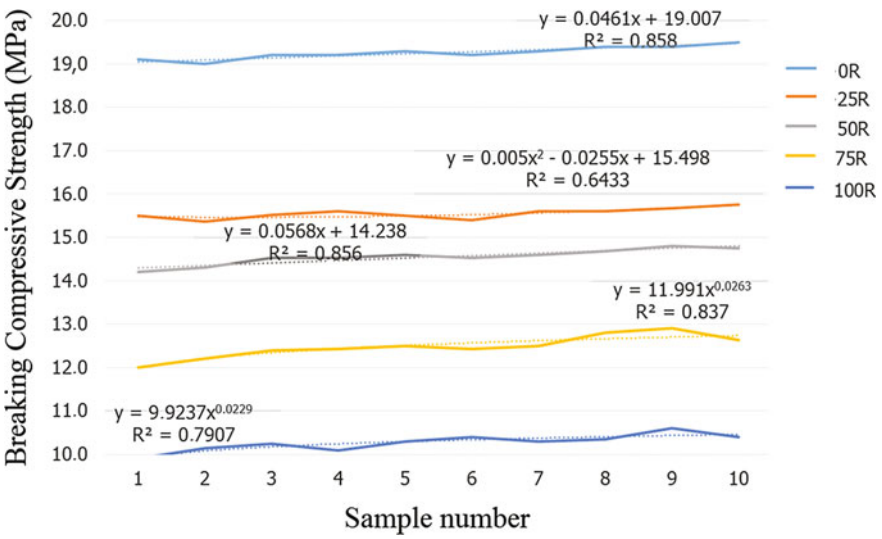

Fig. 3 Results at 7 days

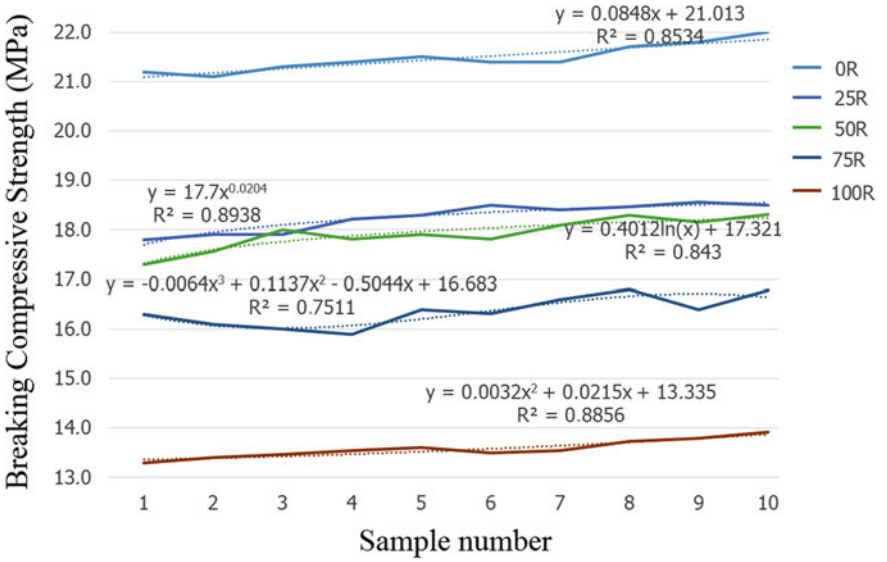

Fig. 4 Results at 28 days

The results for the total replacement of sand by RCD indicate a reasonable behavior and can be used for less demanding mechanical resistance to compression.

Conclusions

The large RCD production that comes each year being illegally deposited in the environment or even being used in less noble services is a serious problem that still needs more investment from the government and industry.

Mechanical compressive strengths above 15 MPa at 28 days were verified for all partial compositions with residues, and for the case of 100% RCD, average resistance was found around 13.5 MPa, which may have several utilities structures.

Therefore, the present work contributes to the search of the solution of this problem, presenting an excellent use of the RCD for the production of blocks of concrete masonry with RCD, for the production of blocks for pavements and sidewalks, among other utilities.

References

1. Fernandez JAB (2012) Diagnosis of solid residues of civil construction: research report. Instituto de Pesquisa Econômica Aplicada, IPEA, Brasília (In Portuguese)

2. McMahon V, Garg A, Aldred D, Hobbs G, Smith R, Tothill IE (2008) Composting and bioremediation process evaluation of wood waste materials generated from the construction and demolition industry. Chemosphere 71:1617–1628
3. Merino MR, Gracia PI, Azevedo ISW (2010) Sustainable construction: construction and demolition waste reconsidered. Waste Manage Res 28:118–129
4. Ponnada MR, Kameswar P (2015) Construction and demolition waste management—a review. Int J Adv Sci Technol 84:19–46
5. Zhao W, Leeftink RB, Rotter VS (2010) Evaluation of the economic feasibility for the recycling of construction and demolition waste in China: the case of Chongqing. Resour Conserv Recycl 54:377–389
6. Callister W (1999) Materials science and engineering, 5ª edn. LTC, Rio de Janeiro (In Portuguese)
7. Mehta PK, Monteiro PJM (1994) Concrete—structure, properties and materials. Ed. Pini, São Paulo (In Portuguese)
8. Falcão Bauer LA (1993) Construction materials, vol 2. Livros Técnicos e Científicos, Rio de Janeiro (In Portuguese)
9. Petrucci EGR (2005) Concrete portland cement, 14ª Edição. Ed. Globo, São Paulo (In Portuguese)
10. Levy SM (2000) Recycling of waste in construction: contribution to methodology and development. Habilitation Thesis, University of São Paulo (In Portuguese)
11. Zordan SE (2002) Rubble from the construction industry. PCC-EPUSP, São Paulo. Available in: http://www.reciclagem.pcc.usp.br (In Portuguese)
12. National Council for the Environment (CONAMA) (2002) Resolution No. 307. Brasília (In Portuguese)
13. National Council for the Environment (CONAMA) (2004) Resolution No. 308. Brasília (In Portuguese)
14. Brazilian Association of Technical Norms. NBR 5738 (2015) Molding and curing cylindrical bodies of the test piece or prismatic concrete. Rio de Janeiro (In Portuguese)
15. Brazilian Association of Technical Norms. NBR 5739 (2007) Concrete—compression test of cylindrical bodies of the test piece. Rio de Janeiro (In Portuguese)
16. Brazilian Association of Technical Norms. NBR 7680-1. Concrete—extraction, preparation, testing and analysis of concrete structures—part 1: resistance to axial compression. Rio de Janeiro (In Portuguese)
17. Brazilian Association of Technical Norms. NBR 7680-2. Concrete—extraction, preparation, testing and analysis of concrete structures—part 2: flexural tensile strength. Rio de Janeiro (In Portuguese)

Evaluation of Two Different Pulsed Plasma Nitriding Conditions on Steel Properties

Fabio Da Costa Garcia Filho, Gabriel Bartholazzi Lugão de Carvalho and Sergio Neves Monteiro

Abstract The thermochemical treatment of Pulsed Plasma Nitriding is employed as an alternative to improve the surface properties of metals, such as: increase surface hardness, improve wear resistance, extend fatigue life and also create a barrier to the diffusion of hydrogen into the steel to reduce the susceptibility to hydrogen embrittlement. In this study, the effect of such treatment on ASTM A36 steel is analyzed through two different nitriding conditions: 5 h and 660 Pa for the first condition and 15 h and 720 Pa for the second one. In both cases, the temperature was held at 300 °C. Thus, in order to verify the results, Vickers hardness analysis and metallographic observation were carried out under an optical microscope. Only the second condition was able to achieve what was proposed, the formation of a uniform nitriding layer and an expressive increase of hardening on the surface.

Keywords Pulsed plasma nitriding · Metallographic observation
Hydrogen embrittlement

Introduction

The development of technologies capable of promoting substantial improvements in material performance has been well researched in the last decades, which has leaded to the development of various surface treatment techniques. The interest in developing such technique is necessary to increase the useful life of materials under service conditions. This property is directly related to the quality of the material surface as deterioration processes of materials as mechanical wear and corrosion reactions occur in the surface region [1–4].

F. Da Costa Garcia Filho (✉) · G. B. L. de Carvalho · S. N. Monteiro
Department of Materials Science, Military Institute of Engineering—IME Praça General Tibúrcio, 80, Praia Vermelha Urca, RJ, CEP, Urca, Rio de Janeiro, RJ 22290-270, Brazil
e-mail: fabiogarciafilho@gmail.com

B. Li et al. (eds.), *Characterization of Minerals, Metals, and Materials 2018*, The Minerals, Metals & Materials Series,
https://doi.org/10.1007/978-3-319-72484-3_55

In this context, thermochemical treatment of nitriding is known as an efficient way to improve the surface properties of ferrous metals [5–7]. In this treatment the diffusion of nitrogen atoms is favoured on the surface of the materials, which results in the improvement of properties such as surface hardness, fatigue life, wear resistance, lower friction coefficient. Also, this creates a barrier to the diffusion of hydrogen, making the material less susceptible to hydrogen embrittlement [8–12].

Among the nitriding methods, the pulsed plasma nitriding technique is the most efficient [13–15]. Some advantages of this technique are:

- High reactivity of nitrogen when used as plasma at low pressures.
- Use of non-toxic gases, hydrogen and nitrogen. Also, low pressure contributes to avoid risks related to the environment and health.
- The use of a pulsed source instead of a typical DC source makes it possible to obtain a higher proportion of more reactive ionic species, accelerating the formation of the layer.

In the present research the treatment of pulsed plasma nitriding in ASTM A36 steel was carried out in order to obtain a uniform and thick surface layer. Two different treatment conditions were employed. Finally, it was measured the Vickers hardness and average layer thickness of the samples which the treatment was effective.

Materials and Methods

The first step in this process was to obtain the metal samples to be used at the Pulsed Plasma Nitriding treatment from ASTM A36 steel constituent parts. Figure 1 shows the samples that were cut from a tube section in the form of a parallelogram with dimensions 15 mm × 10 mm × 6 mm. Table 1 shows the typical composition of ASTM A36 steel.

After the samples were cut, a cleaning process is required to remove any kind of grease, oxidation and possible surface contamination. This step is very important to ensure that the treatment is as efficient as possible. The parameters of the two nitriding conditions are presented in Table 2.

In order to evaluate if the desired goal was achieved the samples were polished and chemically attacked with a 5% nitric acid solution to reveal the microstructure and the nitride layer. The samples were analysed in a Leica DMRM optical microscope. In the Vickers hardness investigation, an E. Leitz/Wetzlar equipment with a 50 g load during 30 s was employed. The average thickness of the formed layer was measured by the image processing software, Image Pro Plus©.

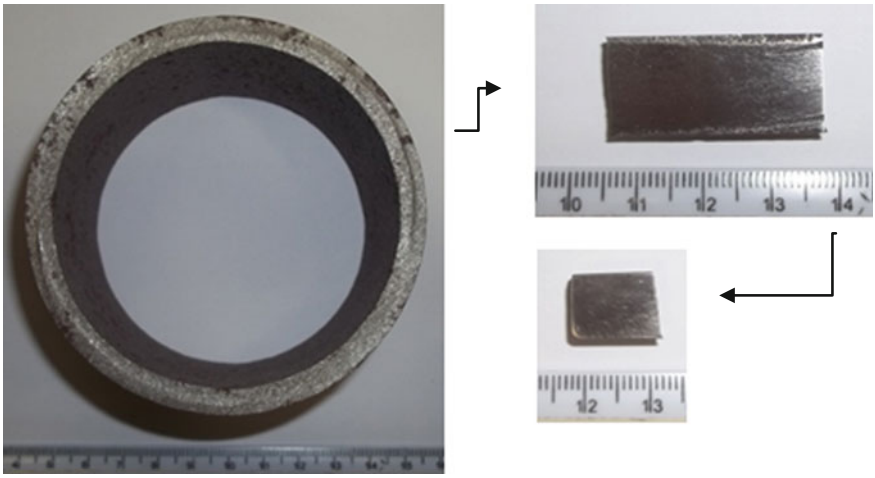

Fig. 1 Process to obtain the samples of ASTM A36 steel

Table 1 Typical composition of ASTM A36 steel

Element	C	Mn	P	S	Si	Cu
Weight %	To 0.28	0.6–0.9	To 0.04	To 0.05	To 0.04	Least 0.2

Table 2 Parameters of treatment

	Time (h)	Pressure (Pa)	Gas mixture (N_2/H_2 %)	Frequency (Hz)	Temperature (K)
C1	5	660	(70/30)	600	573
C2	15	720	(70/30)	600	573

Results and Discussion

Figure 2a, b present sample micrographs after the treatment with condition 1 (C1) and condition 2 (C2), respectively.

It is evident that the nitriding treatment carried out in the sample C2, with a longer treatment time and richer N_2 and H_2 environment, was more efficient, as the formed layer presents a homogeneous appearance throughout the specimen length. In sample C1, the layer formed is extremely thin and it does not show uniformity throughout the specimen. There are areas with formation of layer and spots without the visible layer therefore it did not reach the initial goal. The average thickness of the formed layers is shown in Table 3.

Therefore, the cross-sectional and longitudinal Vickers hardness test was performed only on the C2 sample since the C1 sample did not reach the expected layer thickness and uniformity.

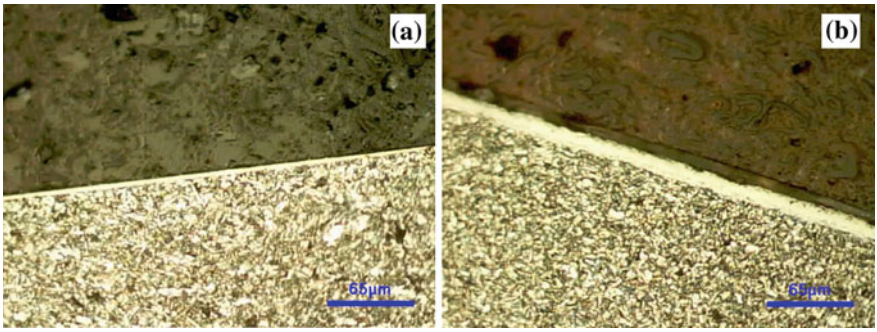

Fig. 2 Microstructure of the samples after the treatment under condition 1 (**a**) and condition 2 (**b**)

Table 3 Average thickness of the layers

Treatment condition	Average thickness (μm)	Standard deviation
C1	4.2	2.39
C2	19.3	0.93

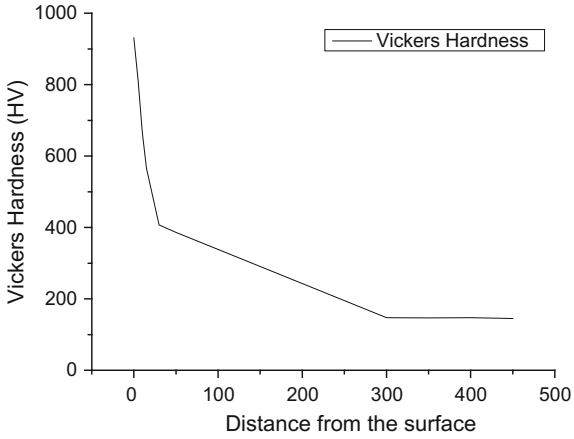

Fig. 3 Vickers hardness profile of the sample after treatment under condition 2

Figure 3 shows the Vickers hardness profile from the surface along the entire depth of the sample.

It is verified that the nitrites layer hardness is quite high, exceeding the hardness of the base metal by a factor of approximately six times and reaching a maximum hardness of 931 HV. It can also be noted that the influence of the treatment extends beyond the benefits of the nitride layer. This is evident at 50 μm where there is no

visible layer and the sample hardness is much higher than the base metal hardness, 386 HV against 147 HV.

Conclusions

- The nitriding process of ASTM A36 steel can be performed as a way of obtaining the aforementioned properties, such as higher hardness, longer fatigue life, lower surface friction and higher wear resistance, with the ultimate goal of increasing the material service life.
- The pulsed plasma ionic nitriding process (condition 2) proved to be efficient in the surface treatment of ASTM A36 steel, ensuring a significant improvement in surface hardness. Furthermore, a maximum value of 931 HV and thick and uniform layer was obtained.

Acknowledgements The authors thank the support of this investigation by the Brazilian agencies: CNPq, FAPERJ and CAPES.

References

1. Zhang ZL, Bell T (1985) Structure and corrosion resistance of plasma nitrided stainless steel. Surf Eng 1:131–136
2. Czerwiec T, Renevier N, Michel H (2000) Low-temperature plasma-assisted nitriding. Surf Coat Technol 131:267–277
3. Menthe E, Bulak A, Olfe J, Zimmermann A, Rie KT (2010) Improvement of the mechanical properties of austenitic stainless steel after plasma nitriding. Surf Coat Technol 133(134):259–263
4. Paschke H, Weber M, Kaestner P, Braeuer G (2010) Influence of different plasma nitriding treatments on the wear and crack behavior of forging tools evaluated by Rockwell indentation and scratch tests. Surf Coat Technol 205:1465–1469
5. Ibrahim MM, EI-Hossaq FM, Abed M, Ricker RE (1992) Effect of RF plasma nitriding time on microhardness and corrosion resistance of 304 stainless steel. Surf Sci 59:253–260
6. Basu A, Dutta Majumdar J, Alphonsa J, Mukherjee S, Manna I (2008) Corrosion resistance improvement of high carbon low alloy steel by plasma nitriding. Mater Lett 62(17–18):3117–3120
7. Wang S, Cai W, Li J, Wei W, Hun J (2013) A novel rapid D.C. plasma nitriding at low gas pressure for 304 austenitic stainless steel. Mater Lett 105:47–49
8. Zakroczymski T, Lukomski N, Flis J (1995) The effect of plasma nitriding-base treatments on the absorption of hydrogen by iron. Corros Sci 37(5):811–822
9. Æwiek J, Baczynska M (2010) Behaviour of nitrided layers subjected to influence of hydrogen. Sci Eng 43(1):30–41
10. Lepienski C, Kuromoto N, Souza J, Foerster C, Serbena F, Silva S (2006) Effect of hydrogen on mechanical properties of nitrided austenitic steels. Philos Mag 86(33–35):5407–5418

11. Bruzzoni P, Bruhl SP, Gomez BJ, Nosei L, Ma Ortiz, Feugeas JN (1998) Hydrogen permeation modification of 4140 steel by ion nitriding with pulsed plasmas. Surf Coat Tech 110(1):13–18
12. Asgari M, Barnoush A, Johnsen R, Hoel R (2011) Microstructural characterization of pulsed plasma nitrided 316L stainless steel. Mater Sci Eng A 529:425–434
13. Torkar M, Leskovsek V (1995) Pulsed-plasma nitriding of Fe-12,5 Al alloy. Intermetallics 3:427–430
14. Naches JL (2006) Surface modification of steels by ionic nitriding and circulation of currents at low frequencies. Ph.D. thesis, UNR, Rosario, Argentina
15. Alves C Jr, Rodrigues JA, Martinelli AE (1999) The effect of pulse width on the microstructure of d.c.-plasma-nitrided layers. Surf Coat Technol 122(2–3):112–117

Flexural Mechanical Characterization of Polyester Composites Reinforced with Jute Fabric

Foluke S. de Assis, Artur C. Pereira and Sergio N. Monteiro

Abstract Jute fibers are among the lignocellulosic with great potential for use in polymer composites. In this work, polyester matrix composites incorporated jute fabric were investigated for their flexural behavior. Specimens with up to 30% in volume of jute fabric were bend-tested until rupture. The results showed an increase in both the composite mechanical strength, principally to a polyester composite reinforced with 30% in volume of jute fabric. A fractograph analysis by SEM disclosed a moderate adhesion mechanism between the jute fabric and the polyester matrix. This mechanism is apparently responsible for the improved performance of the composites.

Keywords Jute fabric · Polyester composite · Flexural properties

Introduction

A significant change in the transportation sectors, for example the automotive, occurred last century with the introduction of stronger and lighter materials. The most relevant example was the polymer composite reinforced with synthetic fiber. They are nowadays replacing conventional materials such as the aluminum alloys in airplane body owing to superior specific strength. In recent years, however, environmental problems in a global scale are imposing a reversion in the use of synthetic fiber specially the glass fiber. In spite of its higher specific strength, this fiber and its polymer composites can neither be recycled nor incinerated in a thermal plant to generate electricity [1]. Moreover, the fabrication and processing of a glass fiber composite are associated with CO_2 emission, a major contributor to warming [2]. A possible substitute for glass fiber without the above-mentioned environmental problems could be lignocellulosic fibers that are obtained from

F. S. de Assis (✉) · A. C. Pereira · S. N. Monteiro
Military Institute of Engineering, IME, Praça Gen. Tibúrcio, nº 80 Urca, Rio de Janeiro, RJ 22290-270, Brazil
e-mail: Foluke.assis@hotmail.com

B. Li et al. (eds.), *Characterization of Minerals, Metals, and Materials 2018*, The Minerals, Metals & Materials Series,
https://doi.org/10.1007/978-3-319-72484-3_56

cellulose-lignin-rich plants. Moreover, they are already being used in several engineering fields, particularly the automobile industry [3–9]. In recent years a growing number of publications [10–13] have been dedicated to lignocellulosic fibers and their polymer composites. The results justify the current application as new engineering materials with advantages not only in terms of environmental issues but also economical, societal and even technical, the lignocellulosic fibers present some advantages as compared with synthetic fibers: renewable, recyclable, biodegradable and also they present a high strength and high elastic modulus, low density and principally low cost [10–15]. Recent studies show that the polymeric composites reinforced with lignocellulosic fibers can be applied in ballistic armor as intermediate layer in multilayered armor system [16–18].

The major challenge faced by the lignocellulosic fiber and their composites is to shorten the distance to the performance of the corresponding synthetic ones. Here, drawbacks such as non-uniform properties and limited dimension as well as weak adhesion to polymeric matrix, are still impeding technical factors to the expansion on the use of lignocellulosic fibers [15].

The jute fiber (*Corchorus capsularis*) present density 1.3–1.45 g/cm^3 and tensile strength, 593–800 MPa, that it may be a possible lignocellulosic fiber to replace synthetic fiber in polymer composites [15]. Then the jute fiber present very interesting potential improvement as seen before in literature. This work evaluated the flexural mechanical characterization of polyester composites reinforced with jute fabric with different volume fractions (0 up to 30 vol.%).

Experimental Procedure

The jute fabric (Fig. 1) investigated in this work was supplied by Companhia SISALSUL.

Fig. 1 Jute fabric

After cleaning at room temperature, the jute fabric was mixed in amounts of 0, 10, 20 and 30% in volume with unsaturated polyester resin to prepare the composites. Plates of the composites with 6 mm thickness were fabricated in a rectangular steel mold with dimensions of 152 × 125 mm.

The still liquid polyester resin, together with 0.5% catalyst based on methyl-ethyl- ketone, was poured into the jute fabric inside the mold. The composite was cured for 24 h at room temperature. The plate of each different composite was then cut in bars measuring 100 × 16 × 6 mm. These bars (24 samples) were used to prepare samples for flexural test, according to ASTM D790 [19]. These specimens were tested in a model 5582 Instron machine with 100 kN of capacity at a velocity of strain 0.5 mm/min. The fracture surface of specimens after flexural test was analyzed in a scanning electron microscopy (SEM) in a model Quanta FEG 250 FEG.

Results and Discussion

Table 1 presents the values of flexural strength for polyester resin and the composites with different volume fraction of jute fabric.

From the results in Table, Fig. 2 shows the variation of the flexural strength of the Polyester composites with the amount of jute fabric. In this Figure, one should note that only the polyester composite reinforced with 30 vol.% of jute fabric has presented a significantly increases (62.3 MPa) when it is compared with polyester resin (36.3 MPa).

Figure 3 shows the fracture specimens of polyester resin and the polyester jute composites after the flexural test. In this Figure, it can be observed the different types of fracture, fragile fracture of the polyester resin that has broken in different regions when the material reached the maximum value of flexural strength, and the polyester-jute composites have presented a type of fracture more concentrated in the point of action of the cleaver.

Figure 4 shows the SEM analysis of the microstructure of the fractured region resulting from flexural test of polyester resin and the polyester composites. Regarding the pure resin, Fig. 4a, the fracture appearance is typical of polyester rupture, in another words, it is possible observed the transversally fracture of polyester resin. Figure 4b shows the polyester composites reinforced with 30 vol.% of jute fabric. Jute fibers were pulled out (holes) from the polyester matrix by crack

Table 1 Flexural results for the polyester composites reinforced with jute fabric

Volume fraction of jute fabric (%)	Flexural strength (MPa)
0	36.28 ± 6.35
10	31.23 ± 5.91
20	32.92 ± 2.38
30	62.25 ± 1.73

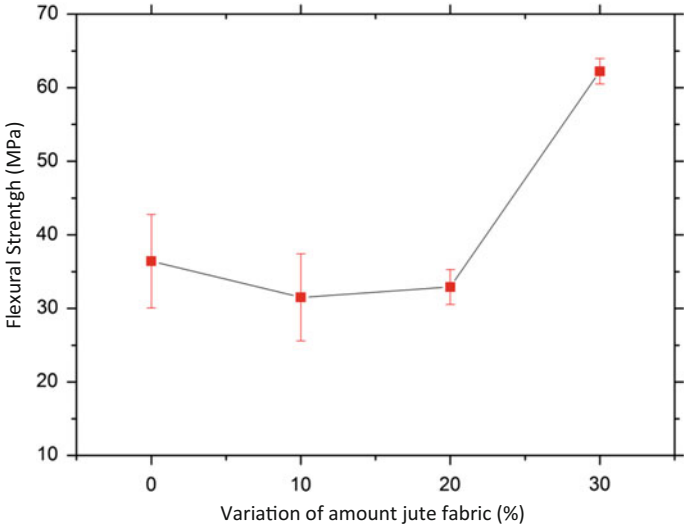

Fig. 2 Flexural strength as a function of amount of jute fabric

Fig. 3 Typical macrostructural aspects of flexural specimens of polyester composites reinforced with different volume fractions of jute fabric

propagation through the surfaces due to the relatively low interfacial tension between jute/polyester. The low adhesion between the jute/polyester changed the orientation of crack propagation to transversal to longitudinal, and it results in aspect favorable to increase the flexural strength. The longitudinally separated area is larger than the section through the matrix [20].

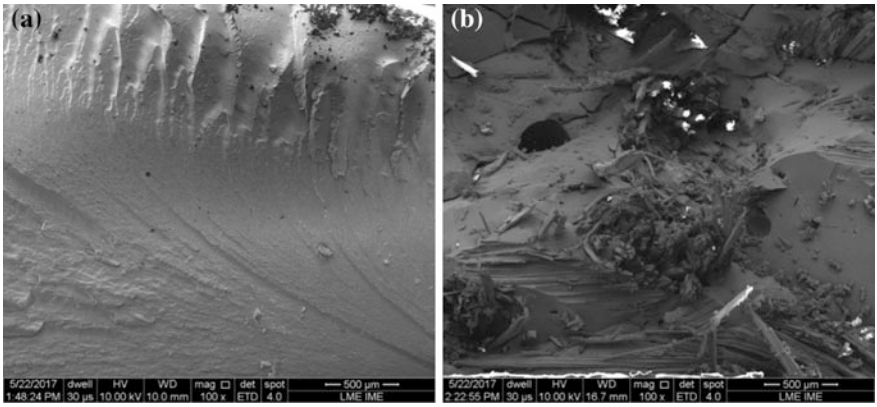

Fig. 4 SEM of pure resin (**a**) and polyester jute composites: **b** 30 vol.% of jute fabric

Conclusions

Polyester matrix composites reinforced with jute fabric show an fibers show an improvement in the flexural strength as compared to the pure polyester matrix.

The visual observation and SEM fractographs revealed that above 10%, transversal cracks are effectively arrested by the fibers. As a consequence, longitudinal propagation through the weak fiber/matrix interface causes delamination and results in an efficient contribution to the relatively stronger jute fiber to the final rupture of the composite, which then occurred at higher strength.

Acknowledgements The authors thank the support to this investigation by the Brazilian agencies: CNPq, CAPES, FAPERJ.

References

1. Wambua P, Ivens I, Verpoest I (2003) Natural fibres: can they replace glass in fibre reinforced plastics? Comp Sci Tech 63:1259
2. Gore A (2006) An inconvenient truth. Emmaus, Rodale Press, Pennsylvania
3. Hill S (1997) Cars that grow on trees. New Sci 153:36
4. Larbig H, Scherzer H, Dahlke B, Poltrock R (1998) Natural fibre reinforced foams based on renewable resources for automotive interior applications. J Cell Plast 34:361
5. Marsh G (2003) Mater. Today 6(4):36–43
6. Zah R, Hischier R, Leão AL, Brown I (2007) Curaua fibers in automobile industry—A sustainability assessment. J Clean Prod 15:1032
7. Bledzki AK, Gassan J (1999) Composites reinforced with cellulose-based fibers. Prog Polym Sci 4:221
8. Nabi Sahed D, Jog JP (1999) Natural fiber polymer composites: a review. Adv Polym Technol 18:221

9. Mohanty AK, Misra M, Drzal LT (2002) Sustainable bio-composites from renewable resources: opportunities and challenges in the green materials world. J Polym Environ 10:19
10. Satyanarayana KG, Guimarães JL, Wypych F (2007) Studies on lignocellulosic fibers of Brazil. Part I: Source, production, morphology, properties and applications. Comp A 38:1694
11. Satyanarayana KG, Arizaga GGC, Wypych F (2009) Biodegradable composites based on lignocellulosic fiber: an overview. Prog Polym Sci 34:982
12. Faruk O, Bledzki AK, Fink H, Sain M (2012) Biocomposites reinforced with natural fibers: 2000–2010. Prog Polym Sci 37:1552
13. Crocker J (2008) Natural materials innovative natural composites. Mat Tech 2–3:174
14. Monteiro SN, Lopes FPD, Ferreira AS, Nascimento DCO (2009) Natural fiber polymer matrix composites: cheaper, tougher and environmentally friendly. JOM 61:17
15. Monteiro SN, Lopes FPD, Barbosa AP, Bevitori AB, Silva ILA, Costa LL (2011) Natural Lignocellulosic Fibers as engineering materials: an overview. Met Mat Trans A 2011 (42):2963
16. Monteiro SN, Lima EP, Louro LHL, Silva LC, Drelich JW (2014) Unlocking function of aramida fibers in multilayered ballistic armor. Met Mat Trans A
17. Monteiro SN, Candido VS, Braga FO, Bolzan LT, Weber RP, Drelich JW (2016) Sugarcane bagasse waste in composites for multilayered armor. Eur Polym J 78:173
18. Luz FS, Lima EP, Louro LHL, Monteiro SN (2015) Ballistic test of multilayered armor with intermediate epoxy composite reinforced with jute fabric. Mater Res 18:170
19. ASTM Designation D790 (2015) Standard test methods for flexural properties of unreinforced and reinforced plastics and electrical insulation materials. West Conshohocken, PA
20. Yue CY, Looi HC, Quek MY (1995) Assessment of fibre-matrix adhesion and interfacial properties using the pullout test. Int J Adhes Adhes 15:73–80

Influence of Coupling Agent on the Modification Effects of Vanadium Tailing as a Polymer Filler

Tiejun Chen, Min Lu and Peiwei Hu

Abstract Based on the analysis of properties of vanadium tailing (VT), the surface modification study was carried out as a polymer filler. The modification effects of the three kinds of coupling agents on VT and the mechanical properties of polypropylene (PP) composites with a modified vanadium tailing (MVT) were compared to determine the suitable surface modification agent and modification processes for VT. The results show that the best one is aluminate coupling agent DL-411. When the content is 1.2 wt% and the temperature was 100 °C, the activity index of modified vanadium tailing (MVT) is 95.53%. FTIR analysis shows that DL-411 has the strongest binding ability on VT. XRD analysis shows that VT has a heterogeneous nucleation on PP to induced β form formation, and DL-411 could enhance this nucleation. So the composites has higher strength and better toughness. When the content of MVT is 10 phr, the tensile strength, impact strength, flexural strength and flexural modulus of the composites are 47.51 MPa, 38.43 kJ/m^2, 59.57 and 1654.36 MPa, respectively.

Keywords Vanadium tailing · Surface modification · Heterogeneous nucleation Mechanics performance

T. Chen (✉) · M. Lu · P. Hu
College of Resources and Environment Engineering,
Wuhan University of Science and Technology, Wuhan 430081, China
e-mail: ctj_56@163.com

T. Chen · M. Lu · P. Hu
Hubei Provincial Engineering Technology Research Center of High Efficient Cleaning Utilization for Shale Vanadium Resource,
Wuhan 430081, China

T. Chen · P. Hu
Hubei Collaborative Innovation Center for High Efficient Utilization of Vanadium Resources, Wuhan 430081, China

B. Li et al. (eds.), *Characterization of Minerals, Metals, and Materials 2018*, The Minerals, Metals & Materials Series,
https://doi.org/10.1007/978-3-319-72484-3_57

Introduction

The extraction of vanadium from vanadium shale is an important direction in the development of vanadium in China. With the rapid development of the shale vanadium industry, the annual output of vanadium tailings (hereinafter referred to as VT) is up to 580–770 million tons, which will not only occupy vast amounts of land, cause secondary environmental pollution, but will also create waste [1–4]. After grinding, roasting, and acid leaching vanadium, the VT particle size is fine and the mineral structure effectively destroyed. Due to its main components of quartz and gypsum, VT can act as a mineral filler for polymers as a replacement for natural inorganic minerals. However, research on the preparation of polymer fillers with shale vanadium tailings has been rarely reported. Furthermore, it is possible to learn from other solid waste comprehensive utilization techniques [5–7] to develop new ways of using VT.

Filler is an essential part of polymer products and has a content of about 15%. The function and the properties of polymer products are not only affected by the chemical composition of the filler, but also by the interfacial interaction between the filler and polymer matrix [8–10]. FTIR analysis shows that there is an abundance of hydroxyls on the surface of VT. The surface of VT has a strong polarity and is hydrophilic. It is necessary to modify VT given the weak compatibility between the hydrophilic VT and hydrophobic polymer matrix. As there is an abundance of hydroxyls, VT easily reacts with modifiers. Surface modification optimizes the properties of VT, which is an effective method of broadening its application field and utility value. The potential applications of VT as a polymer filler of VT cannot only reduce the cost of polymer production, but also provide a new effective utilization of VT to solve the problem of its large amount waste.

In this paper, the acid leaching slag from vanadium shale in Hubei, China was used as the VT. The surface modification and the preparation of PP composites with VT as filler were carried out. The effect of different coupling agents on the modification of VT was investigated.

Experiments

Materials

(1) Vanadium tailing

The VT utilized in this study was obtained from Hubei Province, China, which was washed to neutral-pH with water and then ground to fine powder (D_{90} = 17.95 μm). The mainly composed of VT are SiO_2 and CaO, accounting for more than 60 wt% of the total (in Table 1), which are thought to be quartz and gypsum (in Fig. 1). The surface of VT contains a large number of hydroxy

Table 1 Chemical composition of vanadium tailing (wt%)

Components	SiO_2	Al_2O_3	CaO	Fe_2O_3	BaO	K_2O
Weight (%)	53.98	2.47	7.60	2.71	1.15	0.61
Components	MgO	Na_2O	TiO_2	V_2O_5	SO_3	Loss
Weight (%)	0.17	0.27	0.35	0.17	16.51	13.61

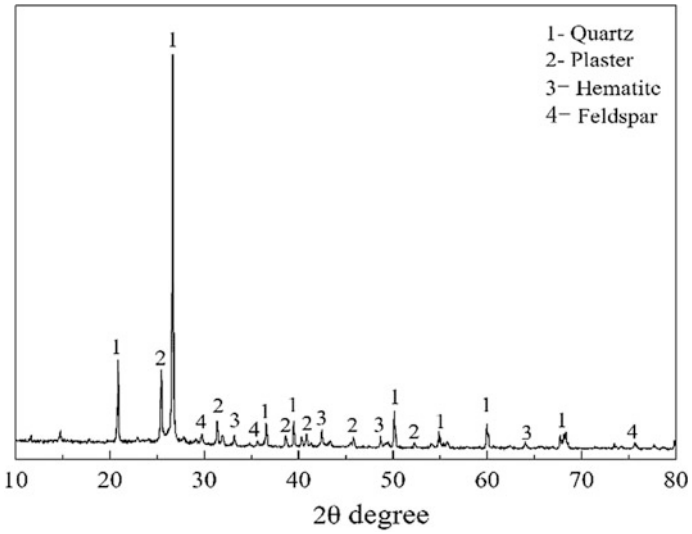

Fig. 1 X-ray diffraction pattern of VT

Fig. 2 FTIR spectra of raw VT

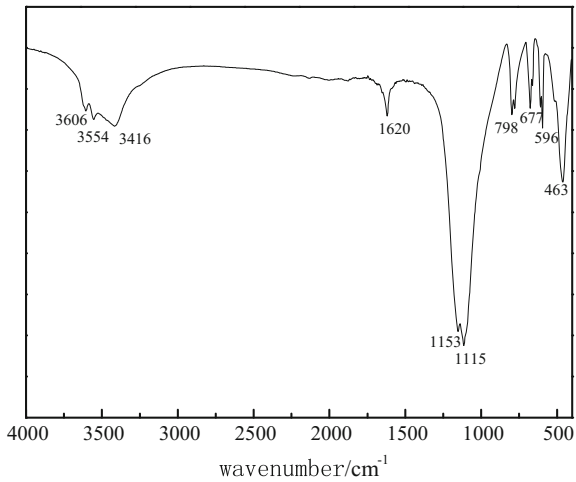

(in Fig. 2). The silanol group is active and easy to react with the external organic functional groups.

(2) Polymer matrix

The polymer matrix used in this study is PP (polypropylene, density 0.9 g/cm^3, melt flow index 10.0 g/10 min, China Petroleum and Chemical).

(3) Coupling agents

Since the main mineral chemical composition of VT is SiO_2 (53.98 wt%, in Fig. 1), three types of coupling agents were used for modification. Silane coupling agent KH-570, titanate coupling agent LK-105 and aluminate coupling agent DL-411 were purchased from Nanjing Pinning Chemical Co., Ltd. (China). All of the reagents were analytical-grade.

Methods

Modification of Vanadium Tailings

Prior to use, the VT was ground into ultrafine powder (<20 μm), and then modified by different coupling agents in a high-speed mixer (SHR-10A). For pretreating 200 g VT was used. First, VT was preheated in the high-speed mixer at the temperature of 80 °C for 5 min with a speed of 1100 rpm. And then the prepared coupling agent was put into high-speed mixer. The mixture was stirred at a higher speed of 1100 rpm for 30 min. Under the condition of optimum temperature of each coupling agent(KH-570 at 100 °C, LK-105 at 90 °C, DL-411 at 100 °C), the effect of three kinds of coupling agents and the content of them (0.4, 0.8, 1.2, 1.6, 2.0 wt%) in modification process were investigated. Finally, dried the modified VT (MVT) at 100 °C for 2 h.

Preparation of Composites

The VT (MVT) and PP resin were mixed in a high-speed mixer at a speed of 1000 rpm and a temperature of 80 °C for 20 min. Then the mixture was mixed melt extrusion in a miniature double-screw extruder (SJSZ-10B) at a screw speed of 30 rpm with barrel temperatures set at 170/175/180/185/180 °C. Finally, the test samples of VT/PP (MVT/PP) composites were injection molded by miniature injection molding machine (SJS-20). The mold temperature was maintained at 45 °C, while the injection pressure and the holding pressure were set at 0.6 and 0.2 MPa, respectively. The obtained samples were used for further measurements.

Characterization

The pre-evaluation of the modified vanadium tailing powder was characterized by the wettability (activity index) [11], while the binding states of different coupling agents on the surface of the VT were analyzed by FTIR. The tensile properties of composites were measured by electronic universal testing machine (DR-506) with a speed of 50 mm/min according to ISO 527-2:2012 standards and the impact properties were measured by pendulum impact tester according to ISO 179-1-2010. The effect of VT on the crystal structure of PP matrix was analyzed by XRD. The compatibility of VT and PP matrix in composites was analyzed by SEM. The effect of VT on thermal stability of composites was analyzed by TG-DTG. The effects of composites on the immobilization of heavy metal elements in VT were investigated by heavy metal leaching test.

Results and Discussion

Activity Index and Oil Absorption Value

Owing to its high density and hydrophilic surface, the VT powder will freely sink in water. After modification with coupling agents, the surface of the VT powder changes from hydrophilic to hydrophobic, thus enabling it to float on water. Based on this phenomenon, the effects of modification can be obviously judged by the active index.

The VT powder was modified by three types of coupling agents at the rotating speed of 1100 rpm and a temperature of 100 °C. Figure 3 shows that the activity index of the modified VT (MVT) powder increased with an increased dosage of KH-570 and DL-411. However, the value was only 20.72% when the dosage of KH-570 was 2.0 wt%, resulting in a negative modified effect. The activity index of the MVT powder modified by DL-411 increased quickly at first, and then

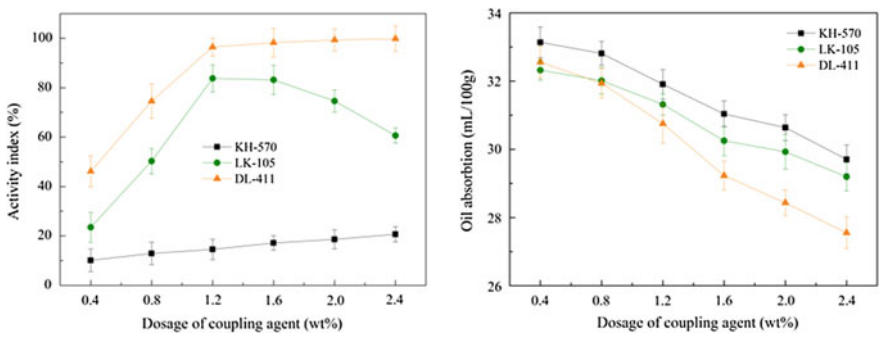

Fig. 3 Effect of dosage of the coupling agent on the activity index and oil absorption of VT

became slower. When the dosage of DL-411 was 1.2 wt%, the activity index reached 95.53%. The activity index of the MVT powder modified by LK-105 first increased to 83.96%, then decreased when the content was more than 1.2 wt%. The oil absorption value of the MVT powder showed a decreasing trend with an increase in the dose of the coupling agent. These results indicated that the coupling agent formed an organic film on the surface of the VT powder after modification, which reduced the agglomerate of VT powder and increased the gap between the VT particles.

Amounts of 2.0 wt% KH-570, 1.2 wt% LK-105, and 1.2 wt% DL-411 were used to modify 200 g VT powder at different temperatures. Figure 4 shows that the effects of temperature on the activity index of MVT powder modified by KH-570 and DL-411 were not significant. However, it was interesting that the value of the latter (modified by DL-411) was much larger than the former (modified by KH-570). The activity index of the MVT powder modified by DL-411 was 95.53% at 100 °C and then changed a little over this temperature. The active index of the MVT modified by LK-105 first increased to 87.52%, then decreased when the temperature was higher than 90 °C. The oil absorption values of the MVT modified by KH-570 or DL-411 decreased rapidly at first, then decreased slowly, while the oil absorption value of the MVT modified by LK-105 first decreased and then increased. The lowest oil absorption value of the VT powder modified by LK-105 was obtained at 90 °C, which was 31.19 mL/100 g. The oil absorption value of the MVT modified by DL-411 and KH-570 at 100 °C were 30.76 mL/100 g and 30.68 mL/100 g, respectively.

A monomolecular layer of the agent formed on the surface of the VT powder since the coupling agent was a single alkoxy type. The optimum content of agent used in the modification was to keep the surface of each particle covered with a uniform layer of the coupling agent molecules. With an increase in agent, the surface of powder changed from hydrophilic into hydrophilic gradually and the aggregate of the VT powder was opened. So, the activity index increased and the oil absorption values decreased sharply. When the surface of the particle was completely covered by the agent, the activity index changed little or decreased as the

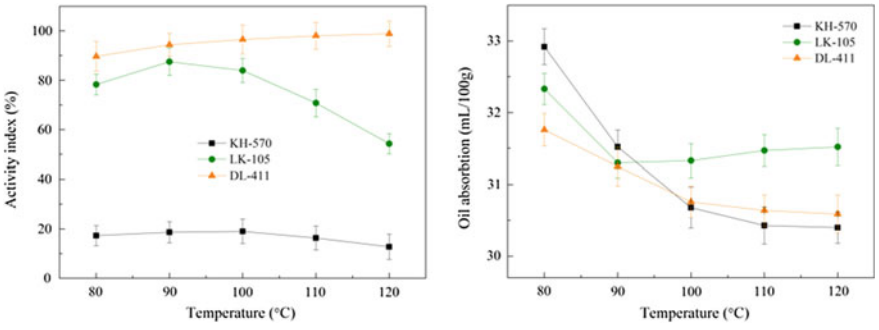

Fig. 4 Effect of reaction temperature on the activity index and oil absorption of VT

content continued to increase. Under the current experimental conditions, the optimum content of KH-570, LK-105 and DL-411 were 2.0, 1.2, and 1.2 wt%, and the optimal modified temperatures were 100, 90, and 100 °C, respectively.

FTIR Analysis

To confirm the formation of the molecular layer and the difference in adsorption of the three types of coupling agents, FTIR spectra of the surface features of the VT powder before and after modification (Fig. 5) were obtained. Figure 5a shows that the surface of the VT powder contained rich groups and a large number of hydroxyls. The peak at 463 cm^{-1} was assigned to the bending vibration of Si–O; peaks at 798, 677, and 596 cm^{-1} are all assigned to symmetric stretching vibration of Si–O, peaks at 1153, 1115 cm^{-1} were assigned to the asymmetric stretching vibration of Si–O; the peak at 1620 cm^{-1} was assigned to the peak of –OH in crystal water; and the peaks at 3545 and 3406 cm^{-1} were assigned to the stretching vibration of –OH in the VT powder. Furthermore, the infrared absorption peaks changed after modification. The peaks at approximately 2920, 2850, 1625, and 1580 cm^{-1} were assigned to the $–CH_3$, $–CH_2–$, and C=O absorption peaks, respectively, which were provided by the organic groups in the coupling agents. The reduction of peaks at 3545 and 3406 cm^{-1} and the appearance of peaks at 2920, 2851, 1625, and 1580 cm^{-1} indicated that the surface groups of VT powder changed from –OH to $–CH_3$, $–CH_2–$ or –C=O and the coupling agent molecules were absorbed on the surface of the VT powder, which increased the surface hydrophobicity of the VT powder. In addition, the vibration peaks of Si–O at 463–1153 cm^{-1} were strengthened by the combination of the coupling agents and the VT to generate Si–O on the surface.

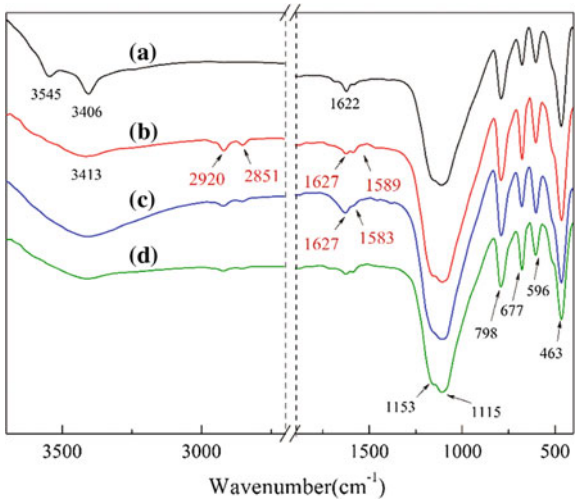

Fig. 5 FTIR spectral analysis: **a** untreated VT; **b** MVT treated by DL-411; **c** MVT treated by LK-105; **d** MVT treated by KH-570

It was obvious that the strength of the $–CH_3$ and $–CH_2–$ absorption peaks in Fig. 5b were stronger than that in Fig. 5c, d. This suggests that the binding capacity of DL-411 on the surface of VT was stronger than that of LK-105 and KH-570. The results were consistent with the variation trend of the activity index test. Therefore, the binding ability of DL-411 on the surface of the VT powder and the modification effect of VT were better than the other two.

Mechanical Properties

The purpose behind the surface modification of VT powder was to develop its potential application as a polymer filler. The composites were prepared by a PP matrix filled with MVT powder (modified under the optimal conditions), and the content of MVT was 10 phr (parts per hundred of resin matrix).

Figure 6a shows that the tensile strength of the MVT/PP composites first increased, then decreased with an increase in DL-411 and LK-105, but gradually increased with the increase of KH-570. The effects of the three types of coupling agents on the tensile properties of the composites were as follows: LK-105 > DL-411 > KH-570. Figure 6b shows that the tensile elongation of the composites at break increased with an increased dose of the coupling agent, and its value after modification by LK-105 and DL-411 was higher than that of KH-570. Figure 6c shows that the impact properties of the MVT/PP composites increased gradually with the increase in the dose of the coupling agents, but decreased slightly when LK-105 and Dl-411 was more than 1.2 wt%. The effects of the three types of coupling agents on the impact properties of the composites were as follows: DL-411 > LK-105 > KH-570. Figure 6d, e show that the flexural properties of the composites increased with the increase in dosage of the coupling agent. However, flexural strength decreased when the dosages of DL-411 and LK-105 were more than 1.2 wt%. Among them, the flexural strength of the composites modified by DL-411 was higher than the composites modified by LK-105 and KH-570, but the flexural modulus was lower than that of the other two, indicating that the composites had a higher strength and better toughness than the others.

The effect of the different types and content of the coupling agents on the mechanical properties of the composites were similar to the variation trends of the activity index. Moderate content of a coupling agent could improve the interface compatibility between the VT and PP matrix, and enhance its interface bonding. However, an excess of the coupling agent provided no further increase in the mechanical properties of the composites as they will bind to the combined molecules with van der Waals' forces to form a multilayer coating on the surface of the VT powder [12, 13], which reduces the active groups on the surface of the VT and make the interfacial compatibility between the VT and PP matrix worse.

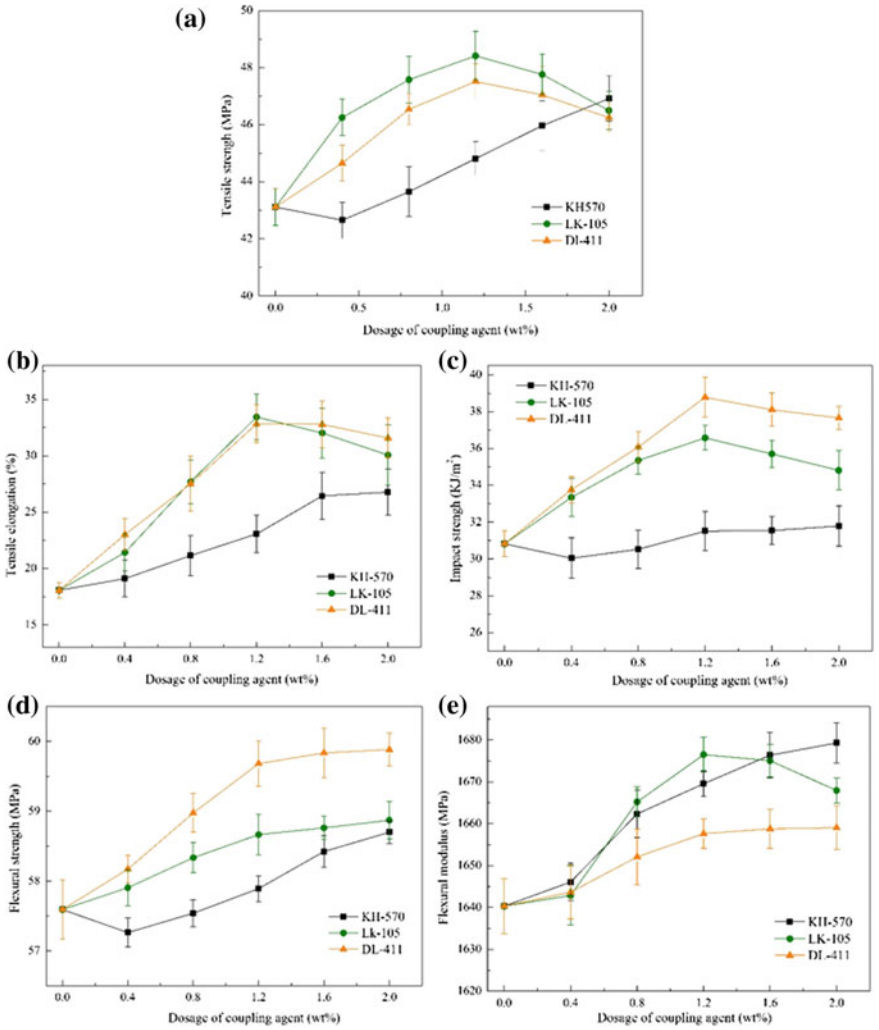

Fig. 6 Effect of dosage of coupling agent on the mechanical properties of composite: **a** tensile strength, **b** tensile elongation, **c** impact strength, **d** flexural strength, **e** flexural modulus

Thus, the mechanical properties of the composites do not increase. Under the current experimental conditions, the comprehensive mechanical properties of the MVT/PP composites modified by DL-411 were optimal. The dose of DL-411 was 1.2 wt%, the filling amount of the MVT powder was 10 phr, and the tensile, impact, flexural strength, and flexural modulus of the composites were 47.43 MPa, 38.78 kJ/m^2, 59.68, and 1660.06 MPa, respectively.

XRD Analysis

PP is a crystalline polymer, which mainly contains α and β crystal forms, with a large number of extended segments in the β-crystal form region relative to the α-crystal form [14]. When destroyed by external forces, the β-crystal form region can absorb more energy to improve the toughness of the material. The XRD patterns (Fig. 7) showed that the composites still had the characteristic diffraction peaks of PP, indicating no alteration in the arrangement of chains and a complete crystal structure of the PP matrix. The α-crystal diffraction peaks position on the (110), (040), (130), (111), and (131) planes did not change significantly, but the intensity was different. In the XRD patterns of the composites, some new diffraction peaks appeared in the vicinity of 16.5°, 25.4°, and 26.6°, which are the characteristic diffraction peaks of β-crystal in a PP matrix [15], and gypsum and quartz in the VT powder, respectively. These patterns confirmed the presence of β-crystal and VT powder.

The crystallization parameters of pure PP and the composites are listed in Table 2. The data indicate that the addition of VT (MVT) powder into PP resulted in an increase in degree of crystallinity and relative content of β-crystal by approximately 4–10, and 4–7%, respectively. This suggests that the mineral grain in

Table 2 The crystallization parameters of pure PP and the composites

Material	X_c/%	I_β/%	$\sum I_\alpha$/%	K_β/%
PP	58.04	–	138.3	–
VT/PP	62.01	7.3	155.9	4.7
MVT/PP-1 (KH-570)	64.53	9.7	181.3	5.08
MVT/PP-2 (LK-105)	68.15	15.3	209.8	6.80
MVT/PP-3 (DL-411)	68.87	15.6	205.6	7.05

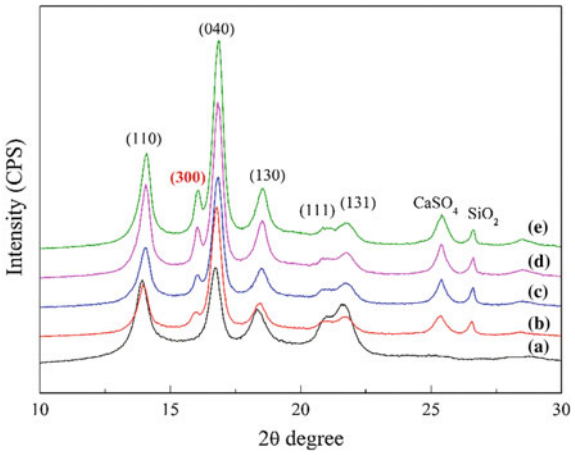

Fig. 7 X-ray diffraction pattern of composites: **a** neat PP; **b** MVT treated by DL-411; **c** MVT treated by LK-105; **d** MVT treated by KH-570

VT had a nucleation effect on PP and could induce the formation of β-crystal in the PP matrix [16, 17]. The coupling agent strengthened the nucleation effect and the induction of β-crystal. The data (Xc%, Iβ%, Kβ%) of MVT/PP-2 and MVT/PP-3 were bigger than the others, which indicated that the dispersion of the MVT powder in the matrix and the compatibility between MVT and the matrix were better. Thus, the MVT powders modified by LK-105 and DL-411 had a better heterogeneous nucleation effect on the PP matrix. In addition, the degree of crystallinity and relative content of β-crystal of MVT/PP-3 are slightly above that of MVT/PP-2, performance on a slightly higher toughness of the composites.

Conclusion

The effects of the three types of coupling agents on the modification of VT powder were as follows: LK-105 > DL-411 > KH-570. The mechanical properties of the MVT/PP composites modified by DL-411 were better than that of KH-570 and LK-105 due to a stronger hydrophobicity of the VT powder. DL-411 was superior to the others under the current experimental conditions where the optimum content was 1.2 wt% and the modification temperature was 100 °C. The activity index of the MVT powder was 95.53% and the oil absorption value was 30.76 mL/100 g. The tensile, impact, flexural strength, and flexural modulus of the composites prepared with 10 phr MVT powder (modified by DL-411) were 47.43 MPa, 38.78 kJ/m^2, 59.68, and 1660.06 MPa, respectively. Furthermore, the degree of crystallinity and relative content of β-crystal in the composites increased by approximately 10.83, and 7.05%, respectively, with the addition of MVT powder (modified by DL-411).

This study provides a technology for the potential application of VT as a filler in polymers. It is an advantageous way to beneficially recycle VT, which will solve the environmental problems caused by accumulation of a large amount of VT.

Acknowledgements This research was supported by the Key Science and Technology Support Program (No. 2011BAB05B04) from the Ministry of Science and Technology of China.

References

1. Zhang YM, Bao SX, Liu T et al (2011) The technology of extracting vanadium from stone coal in China: history, current status and future prospects. Hydrometallurgy 109(1–2):116–124
2. Zhang YM, Bao SX, Liu T et al (2015) Research status and prospect of vanadium extraction from stone coal in China. Nonferrous Metal 2:24–30 (In Chinese)
3. Liu JH, Tan AH (2010) Status review on technologies of extracting vanadium from stone coalvanadium ore. Hunan Nonferrous Metal 26(5):11–14 (In Chinese)

4. Jiao XK, Zhang YM, Chen TJ (2013) Thermal stability of a silica-rich vanadium tailing based geopolymer. Constr Build Mater 38:43–47
5. Arijit D, Satapathy BK (2011) Structural, thermal, mechanical and dynamic mechanical properties of cenosphere filled polypropylene composites. Mater Design 32:1477–1484
6. Gong G, Xie BH, Yang MB et al (2007) Mechanical properties and fracture behavior of injection and compression molded polypropylene/coal gangue powder composites with and without a polymeric coupling agent [J]. Compos A Appl Sci 38:1683–1693
7. Zhai WS, Wang Y, Deng Y et al (2014) Recycling of asbestos tailings used as reinforcing fillers in polypropylene based composites. J Hazard Mater 270:137–143
8. Yang FS, Qu JL, Yang ZY et al (2007) Thermal decomposition behavior and kinetics of composites from coal and polyethylene. J Chin Univ Min Technol 17:25–28 (In Chinese)
9. Li N, Xia Y, Mao ZW et al (2013) Synergistic effect of SiO_2 on intumescent flame-retardant polypropylene. Polym Polym Compos 21(7):439–447
10. Qazviniha1 MR, Abdouss M, Musavi M et al (2016) Physical and mechanical properties of SEBS/polypropylene nanocomposites reinforced by nano $CaCO_3$. Materialwiss. Werkst 47 (1):47–52
11. Qian HY, Ye XC, Zhang SM (2001) Technology of non-metallic mineral particle surface modification and its evaluation. Non-Metal Mines 24:10–12 (In Chinese)
12. Velichko H, Marina K, Georg M (2006) The influence of excess coupling agent on the microde formation processes and mechanical properties of poly (propylene)/wood-flour composites. Macromol Mater Eng 291(6):677–683
13. Hiroshi H, Joji K, Toshiyuki Y et al (2012) Treatment of inorganic filler surface by silane-coupling agent: investigation of treatment condition and analysis of bonding state of reacted agent. Int J Chem Mole Nucl Mater Metal 6(1):2–6
14. Jiang Q, Jia H, Wang J et al (2012) Effects of nucleating agents on crystallization behavior and mechanical properties of high-fluid polypropylene. Iranian Polym J 21(3):201–209
15. Wu H, Li X, Chen J et al (2013) Reinforcement and toughening of polypropylene/organic montmorillonite nanocomposite using-nucleating agent and annealing. Compos B Eng 44 (1):439–445
16. Liang JZ, Li B, Ruan JQ (2015) Crystallization properties and thermal stability of polypropylene composites filled with wollastonite. Polym Test 42:185–191
17. Iyer KA, Torkelson JM (2015) Importance of superior dispersion versus filler surface modification in producing robust polymer nanocomposites: the example of polypropylene/ nanosilica hybrids [J]. Polymer 68(26):147–157

Influence of Electron-Beam Irradiation on the Properties of LDPE/EDPM Blend Foams

Julyana Santana, Marcus Vinicius de S. Seixas, Vijay Rangari, Francisco Valenzuela-Díaz, Helio Wiebeck and Esperidiana Moura

Abstract Closed-cell polyethylene (PE) foams have been extensively used in many applications such as packaging, transportation, sports, construction, and agriculture because of their variety of properties including light weight, chemical resistance, thermal and electrical insulation. The objective of this study is to evaluate the influence of electron-beam irradiation on the properties of LDPE/EPDM blend foams. The LDPE/EPDM blend (80/20 wt%) were prepared by melt extrusion, using a twin-screw extruder machine. The foam structure of LDPE/EPDM blends was obtained by melt extrusion process, using a special single screw for foaming with 1.5 wt% of foaming agent as blowing agent. The foam samples were irradiated by electron-beam at radiation dose of 25, 50, 75 and 100 kGy and submitted to heating in an oven at 100 °C. The specimen tests samples of irradiated and non-irradiated foams were submitted to mechanical tests, DSC, TG analysis and density measurement.

Keywords LDPE/EPDM blend · DSC · Tensile tests · Irradiation

Introduction

Polymer blends are frequently challenged with by new applications desiring more advanced properties. It is an effective way to create a brand new polymeric material with balanced and better properties for various applications that can successfully be

J. Santana · M. V. de S. Seixas (✉) · E. Moura
Center for Chemical and Environmental Technology (CQMA), Nuclear and Energy Research Institute, Sao Paulo, SP, Brazil
e-mail: marcus.seixas@usp.br

M. V. de S. Seixas · F. Valenzuela-Díaz · H. Wiebeck
Metallurgical and Materials Engineering Department, Polytechnic School, University of Sao Paulo, Sao Paulo, SP, Brazil

V. Rangari
Department of Materials Science and Engineering, Tuskegee University, Tuskegee, AL, USA

B. Li et al. (eds.), *Characterization of Minerals, Metals, and Materials 2018*, The Minerals, Metals & Materials Series,
https://doi.org/10.1007/978-3-319-72484-3_58

employed in different areas. Polymer nanocomposites can be foamed by any of the existing foaming processes using either physical or chemical blowing agents [1]. To produce nanocomposite foams, it is possible to find different forms, like using injection molding, extrusion and compression molding processes. Foaming injection molding processes allows obtaining materials with well-defined shapes, allow obtaining very well shape-defined materials, by extrusion can be carried out in single or twin-screw extruders, and for compression molding a single or two-steps have been widely used, both for scientific and industrial purposes due to their intricacy [2–4]. In this work, the LDPE/EPDM foam was produced firstly using a twin-screw extruder followed by and after a single screw for foaming, to obtain homogeneity and a uniform surface. Polyolefins are plastics of great commercial and economic importance, especially, low-density polyethylene (LDPE). LDPE are one of the most widely used resins, it exhibits a wide range of properties such as light weight, good electrical and chemical resistance, easy processing, and high toughness at low temperature, flexibility, toughness, thermal stability, heat shrinkable properties, and relatively low cost compared with other plastics, which make it suitable for many applications [5, 6].

Ethylene propylene diene terpolymer (EPDM) are an elastomer, exhibits high crosslinking ability, radiation resistance, thermal resistance, impact strength, flexibility and dynamic damping properties [7]. Crosslinking of EPDM after irradiation is expected to generate different types of network, which could be reflected on the properties of the polymer. Thermoplastic and elastomeric materials based on blends of EPDM and polyolefins like polyethylene combine their technical advantages in processing of thermoplastics with better physical properties of elastomers, therefore gaining significant importance in a variety of applications, as automotive industry, extruded profiles for windows, electrical cables and wires, packaging materials, and that is why; LDPE/EPDM blends have got their attention for many applications [8, 9].

Nowadays many investigations have been studying and reported on application of ionizing radiation in polymers and its effects on chemical structure and their physical properties. The irradiations of polymers with high-energy radiation, like gamma and electron-beam, result in scission of the main chain, generally termed as “degradation” or cross-linking with the concomitant formation of covalent bonds among polymer chains. During the more than fifty years of research in polymer radiation chemistry, researchers have reported the occurrence of cross-linking and other useful effects [10–12]. Today, a substantial commercial industry is in place based on the processing of polymers with radiation. Therefore, the radiation technologies being applied to polymer processing comprise a diverse set, with many different radiation types and source used, many different types and combination of materials, and many different application objectives being addressed. In this work, the influence of electron-beam irradiation on the morphology, thermal and mechanical properties of LDPE/EDPM foams was studied.

Experimental

Material

- Low density polyethylene, LDPE, (manufactured by Braskem Co. Ltd.);
- Ethylene propylene diene monomer, EPDM;
- Endothermic chemical foaming agent (F.A) ENDEX 2650 TM (manufactured by Endex International Co. Ltd.).

Preparation of LPDE/EPDM/ENDEX Foams

The blend 80% LDPE and 20% EPDM were processed by twin-screw extrusion and extrusion blown film processing. The LDPE/EPDM/ENDEX flexible foams with addition of 1.5 wt% of foaming agent were prepared by melting extrusion process, using a twin-screw extruder Haake Rheomex P332 with 16 mm and L/D = 25 rate from Thermo Scientific. The temperature profile was of 115/125/130/135/140/145 °C and a screw speed of 30 rpm. The extrudates materials were cooled down for a better dimensional stability, pelletized by a pelletizer, dried again and fed into extrusion foam, single screw machine (Carnevalli) with 25 mm diameter and foam test samples were obtained. The temperature profile used in the blow extrusion process of LDPE/EPDM/ENDEX flexible foams were 125/130/135/145/150/155 °C and screw speed was 30 rpm.

Electron-Beam Irradiation

Part of LDPE/EPDM/ENDEX flexible films were submitted to electron-beam irradiation at 25, 50, 75 and 100 kGy, using a 1.5 meV electron beam accelerator, at room temperature in presence of air.

Characterization of LDPE/EPDM/ENDEX Irradiated Foams

Mechanical tests: Tensile tests were determined using an INSTRON Testing Machine model 5564, according to ASTM D 882-91 in order to evaluate the mechanical behavior of the materials studied. Each value obtained represented the average of five samples.

Differential scanning calorimetry (DSC): analyses were carried out using a Mettler Toledo DSC 822e from 25 to 250 °C at a heating rate of 10 °C/min under

nitrogen atmosphere (50 ml/min). DSC analyses of the materials were performed on four samples of the materials. DSC were carried out to obtain melt temperature (Tm) and melting enthalpy (ΔHm).

Thermogravimetric analysis (TG): In this study, the TG analyses were made in a Mettler Toledo TGA module "TGA/SDTA851e" from 25 to 500 °C at a heating rate of 10 °C/min under nitrogen atmosphere (50 ml/min).

Relative density of the foam: Determination of apparent density in flexible foam of irradiated and non-irradiated LDPE/EPDM/ENDEX samples as ABNT NBR 8537.

Density of foams: the specimens' densities were calculated by Eq. 1:

$$\rho = \frac{m}{V}; \tag{1}$$

where ρ is the density; m is the mass, V is the volume of the samples [13].

Results and Discussion

Tensile Tests Results

Figure 1 shows the diagram stress (MPa) X strain (%) for LDPE/EPDM Blend and LDPE/EPDM foams. The results presented shows the average values calculated from the data obtained in tests for five test specimens. The results show a significant

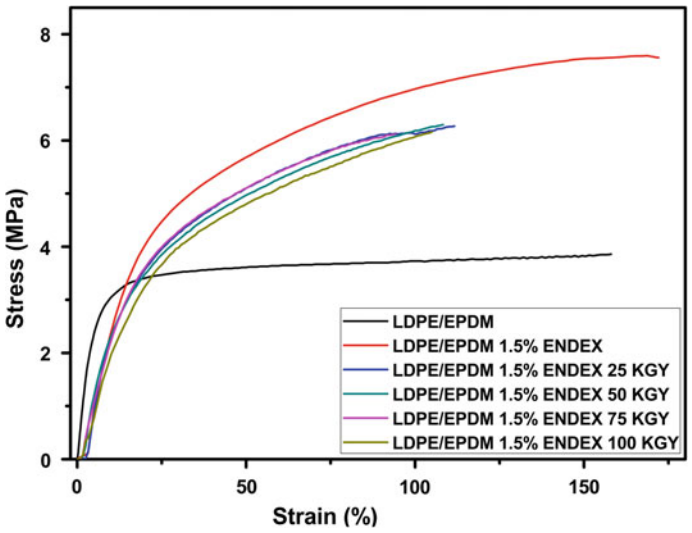

Fig. 1 Diagram stress (MPa) X strain (%) for LDPE/EPDM blend and foams

Table 1 Tensile test results for LDPE/EPDM blend and LDPE/EPDM foams

Materials	Tensile strength at break (MPa)	Elongation at break (%)	Young's modulus (MPa)
LDPE/EPDM	4.8 ± 0.2	490 ± 67	1.3
LDPE/EPDM 1.5% ENDEX	3.7 ± 0.3	178 ± 15	9.3
LDPE/EPDM 1.5% ENDEX 25 kGy	6.2 ± 0.2	126 ± 9	9.4
LDPE/EPDM 1.5% ENDEX 50 kGy	6.4 ± 0.2	127 ± 5	9.3
LDPE/EPDM 1.5% ENDEX 75 kGy	6.1 ± 0.6	107 ± 10	10
LDPE/EPDM 1.5% ENDEX 100 kGy	6.2 ± 0.2	128 ± 6	9

reduction on elongation at break of LDPE/EPDM 1.5% Endex irradiated blends when compared to the LDPE/EPDM and LDPE/EPDM 1.5% Endex.

Table 1 presents the results of tensile tests for LDPE/EPDM Blend and LDPE/EPDM foams. The Young's modulus presents an increase in LDPE/EPDM with addition of 1.5% of foaming agent Endex, and remains almost the same with increase of irradiation dose. It can be seen that increasing irradiation dose increases the tensile strength at break for all LDPE/EPDM 1.5% Endex foams, except for LDPE/EPDM 1.5% Endex 75 kGy that has a lower increase. However, it decrease elongation at break when compared to LDPE/EPDM blend and LDPE/EPDM 1.5% Endex. Which means a slight increase in tensile strength occurred with increasing irradiation dose, and higher decrease in elongation at break for the irradiated foams.

DSC Analysis Results of LDPE/EPDM Blend and LDPE/EPDM Foams

Figure 2 shows the melting temperature for all irradiated and no irradiated samples remains almost unchanged even after the different radiation dose.

However, as shown in Table 2, the irradiated foams showed a decrease in melting temperature according to the received dose, but the melting enthalpy remains the same in all foams, except for LDPE/EPDM 1.5% Endex 75 kGy that can be seen a small decrease. For all crosslinked blends, melting temperature is decreasing due to compact network formation crystallizing efficiencies of chains are reduced for LDPE and EPDM respectively. So after exposure to electron beam irradiation, the melting enthalpy and respectively crystallinity of all LDPE/EPDM foams presented slightly changes with increase of electron beam radiation dose.

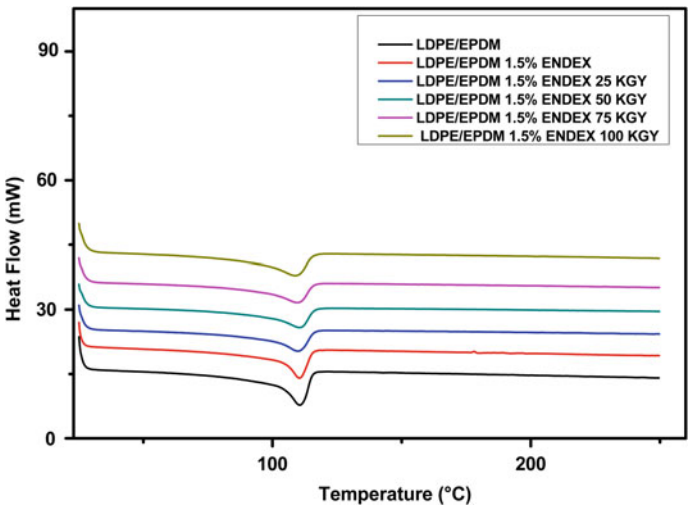

Fig. 2 DSC analysis results for LDPE/EPDM blend and LDPE/EPDM foams

Table 2 DSC analysis results of LDPE/EPDM blend and LDPE/EPDM foams

Composites	Melting temperature (T_{m1}, °C)	Melting enthalpy (ΔH_{m1}, J g^{-1})
LDPE/EPDM	100.48	77.6
LDPE/EPDM 1.5% ENDEX	102.12	71.6
LDPE/EPDM 1.5% ENDEX 25 kGy	95.5	77.8
LDPE/EPDM 1.5% ENDEX 50 kGy	93.9	77.4
LDPE/EPDM 1.5% ENDEX 75 kGy	92.2	78.7
LDPE/EPDM 1.5% ENDEX 100 kGy	90.5	79.0

Thermogravimetric Analysis (TG) Results

Figure 3 shows the TG of LDPE/EPDM blend and LDPE/EPDM foams. The LDPE/EPDM blend showed a single step of decomposition. If initial decomposition temperature at which 10% weight loss were considered were assumed to be a measurement of thermal stability, LDPE/EPDM decomposes at 410 °C, while, after foaming agent addition, decomposes at 430 °C.

The decomposition temperatures and weight loss for LDPE/EPDM/ENDEX flexible foams are presents in Table 3. The table shows that onset temperature of decomposition, increases for the irradiated samples, indicating higher thermal stability of the LDPE/EPDM 1,5% Endex after electron beam irradiation which may be due to cross-linking process. LDPE/EPDM blend decomposes at lower temperature and quicker when its compared to LDPE/EPDM with 1.5% foaming agent.

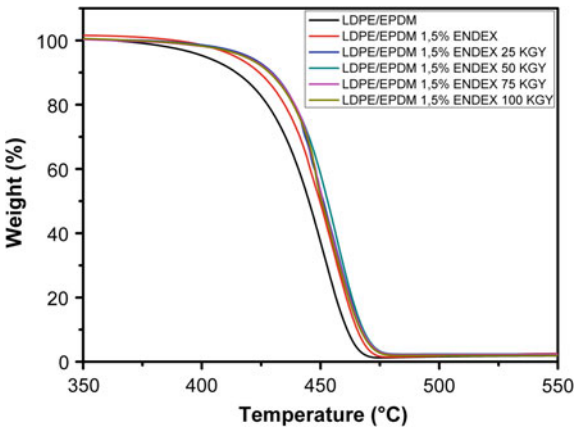

Fig. 3 TG analysis results for LDPE/EPDM blend and LDPE/EPDM foams

Table 3 Decomposition temperature and weight loss of LDPE/EPDM blend and LDPE/EPDM foams

Flexible films	T_{onset} (°C)	T_{max} (°C)	Weight loss (%)
LDPE/EPDM	401.9	578.6	98
LDPE/EPDM 1.5% ENDEX	406.0	580.0	97
LDPE/EPDM 1.5% ENDEX 25 kGy	419.4	580.0	98
LDPE/EPDM 1.5% ENDEX 50 kGy	416.5	580.1	99
LDPE/EPDM 1.5% ENDEX 75 kGy	417.4	580.2	99
LDPE/EPDM 1.5% ENDEX 100 kGy	416.5	580.2	98

The degradation temperature can be observed, as the same at higher and lower doses indicating the crosslinking were independent of the dose level.

Density of Foams

The density of foams for each sample is shown in Table 4. The highest degree of foaming was obtained for LDPE/EPDM 1.5% Endex 25 kGy and the samples irradiated with 50 and 75 kGy showed decreasing of foaming degree and therefore an increase in foam density.

Table 4 Densities of foams for each blend and composites

Samples	Foam density (g/cm^3)
LDPE/EPDM	0.65 ± 0.04
LDPE/EPDM 1.5% ENDEX	0.64 ± 0.04
LDPE/EPDM 1.5% ENDEX 25 kGy	0.59 ± 0.04
LDPE/EPDM 1.5% ENDEX 50 kGy	0.62 ± 0.04
LDPE/EPDM 1.5% ENDEX 75 kGy	0.62 ± 0.04
LDPE/EPDM 1.5% ENDEX 100 kGy	0.60 ± 0.04

Conclusion

This work presented the development and characterization of LDPE/EPDM Blend and LDPE/EPDM foams treated by electron-beam radiation. Analysis of the mechanical properties of the LDPE/EPDM blend showed that the addition of foaming agent increases the Young's modulus and decrease the elongation at break. Furthermore, the irradiated samples showed increase at tensile strength at break. Thermal analysis showed a decrease in melting temperature according to the received dose, but the melting enthalpy remains the same in all foams, except for LDPE/EPDM 1.5% Endex at radiation dose of 75 kGy that can be seen a small decrease. In addition, the density of irradiated foams presented a decrease in comparison with non-irradiated samples. The reduction of foam density was higher for samples irradiated with 25 and 100 kGy. The melting enthalpy and respectively crystallinity degree of irradiated LDPE/EPDM foams presented slightly changes with increase of electron beam radiation dose.

Acknowledgements The authors wish to thank CAPES and CNEN to provide the support for this work.

References

1. Mills NJ (2004) Polyolefin foams. Review report 167, vol 14, no 11, RAPRA Ltd, Shawbury, Shropshire
2. Guo MC, Heuzev MC, Carreau PJ (2007) Cell structure and dynamic properties of injection molded polypropylene foams. Polym Eng Sci 47:1070–1081
3. Abbasi M, Khorasani SN, Baheri R, Esfahani JM (2011) Microcellular foaming of low density polyethylene using nano-$CaCO_3$ as a nucleating agent. Polym Compos 32:1718–1725
4. Throne JL (2004) Thermoplastic foams extrusion. An introduction. Hanser Publishers, Munich
5. Lima JA, Felisberti MIJ (2008) Eur Polym 44:1140–1148
6. Aucejo S, Marco C, Gavara R (1999) J Appl Polym Sci 74:1201–1206
7. Airinei A (2013) Structural characteristics of some high density polyethylene/EPDM blends. Polym Test 32:187–196
8. Ehsani M, Zeynali ME, Abtahi M, Harati AA (2009) LDPE/EPDM blends as electrical insulators with unique surface, electrical and mechanical properties. Iran Polym J 18:37–47

9. Senna MM, Youssef HA, Eyssa HM (2007) Effect of electron beam irradiation, EPDM and azodicarbonamide on the foam properties of LDPE sheet. Polym Plast Technol Eng 46:1093–1101
10. Kitamaru R, Mandelkern L (1964) J Polym Sci B2(511):1019–1023
11. Saito O, Kang HY, Dole M (1967) J Chem Phys 46:3607–3616
12. Chawla AS, Pierre LE (1972) J Appl Polym Sci 16:1887–1891
13. Einhorn-Stolla U, Kunzek H, Dongowsk G (2007) Thermal analysis of chemically and mechanically modified pectins. Food Hydrocoll 21:1101–1112

Influence of the Areal Density of Layers in the Ballistic Response of a Multilayered Armor System Using Box-Behnken Statistical Design

Fábio de Oliveira Braga, Pedro Henrique L. M. Lopes, Fernanda Santos da Luz, Édio Pereira Lima Jr. and Sergio Neves Monteiro

Abstract Several works have been dedicated to study the ballistic response of multilayered armor systems (MAS), including those using natural fiber composites as second layer. These composites disclosed good ballistic performance, having economic and environmental advantages. In the present work, the objective was to investigate the effect of areal densities of each MAS layer, in the overall performance of a MAS with an alumina ceramic front, a curaua fabric reinforced composite filling, and an aluminum alloy backing the target. Ballistic "backface signature" tests were conducted, varying the areal densities of the MAS layers according to a Box-Behnken design. The results showed a similar influence of the ceramic and aluminum layers in the MAS "backface signatures", although deformation and failure mechanisms were significantly different. The composite also showed significant participation in the overall MAS performance. Since the composite is cheaper and lighter, a balance minimizing the other layers would be advantageous.

Keywords Ballistic test · Multilayered armor system · Natural fiber composite Box-Behnken design · Areal density

Introduction

Several works have been dedicated to study the ballistic response of multilayered armor systems (MAS) [1, 2], including those using natural fiber composites as second layer [3–5]. These composites disclosed good ballistic performance, having economic and environmental advantages [6, 7]. Among the natural fibers, stand out a highly resistant natural fiber found in the Amazon Forest, called *Ananas Erectifolius* or simply curaua [7].

F. de Oliveira Braga (✉) · P. H. L. M. Lopes · F. S. da Luz · É. P. Lima Jr. · S. N. Monteiro
Militar Institute of Engineering—IME, Rio de Janeiro, Brazil
e-mail: fabio_obraga@yahoo.com.br

B. Li et al. (eds.), *Characterization of Minerals, Metals, and Materials 2018*, The Minerals, Metals & Materials Series,
https://doi.org/10.1007/978-3-319-72484-3_59

An important method to examine the ballistic performance of materials and structures is the one found in the international standard NIJ-0101.06 (2008) [8]. In this method, the ballistic target to be examined is fixed in front of a Roma Plastilina type clay witness, and hit by a high speed projectile. The deformation left in the clay witness by target is measured and took as an indicator of the ballistic performance of the material. This deformation is often called "backface signature" or "trauma". To be considered efficient for a specific type of bullet, the deformation behind the target shall not pass a standard value. For the 7.62 mm type of bullet, which is known as level III of protection, the trauma cannot pass 44 mm (1.73 pol).

In a recent work, Braga et al. [9] studied a MAS using an alumina ceramic front, a curaua non-woven fabric reinforced composite filling, and an aluminum alloy backing. They found out that this MAS is promising for ballistic applications, presenting satisfactory performance using inexpensive materials. The trauma was measured as 28 mm, which is considered efficient for the level III, however, the areal density 60.26 kg/m^2 is still high for MAS applications. The present work is a development of Braga et al. [9] studies, since the same it is an attempt to optimize the MAS using those inexpensive materials. Therefore, the objective of the present work is to investigate the effect of areal densities of each MAS layer, in the overall performance of the three-layered MAS studied by Braga et al. [9], aiming to reach a high performance system with optimized properties such as low weight and low cost.

Materials and Methods

The MAS studied in the present work has three layers: a front ceramic tile (Al_2O_3-4%Nb_2O_5), a second layer using an epoxy composite reinforced with 30 vol.% of curaua non-woven fabrics, and a backing 5052 H34 aluminum alloy. The origin of the materials and the specimen preparation can be consulted elsewhere [9]. The MAS plates were produced by bonding the layers with polyurethane adhesive.

All materials were produced, in the case of the ceramic and the composite, or bought, in the case of the aluminum, with distinct thickness as follows: Ceramic (8.5, 10.5 and 12.5 mm), composite (8.5, 11.5 and 14.5 mm) and the aluminum (3, 5 and 7 mm).

Ballistic tests were performed following the methodology specified by the NIJ-0101.06 Standard, by positioning the target in front of a Roma Plastilina type clay witness, in the configuration shown in Fig. 1. The ballistic tests equipment is available in the Brazilian Army shooting range facility (CAEx, Rio de Janeiro) [8]. The MAS studied in the present work is intended to be used to protect against level III types of threats, so 7.62 × 51 mm (9.7 g) NATO commercial ammunition should be used. The shooting device was a model B290 High Pressure Instrumentation (HPI) equipment, and the projectile's velocity was measured by an optical barrier. The trauma in the clay witness was measured with a special Mitutoyo caliper with 0.01 mm of accuracy.

The statistical method was the Box-Behnken Design (BBD) in conjunction with the Response Surface Methodology (RSM), which are multivariate analysis

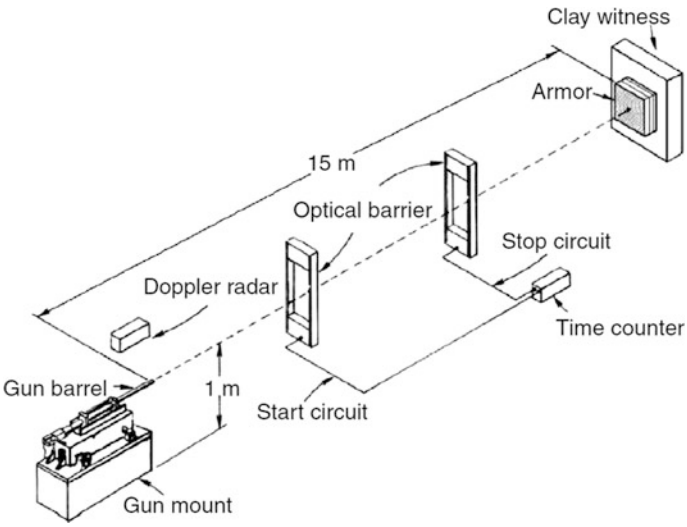

Fig. 1 Experimental arrangement of the ballistic tests

methods. The advantages of the BBD are the smaller number of experiments and the possibility to quantify the correlation of two variables. To apply the method, it is necessary to code the variables using the Eq. 1 [10]

$$c_i = \frac{x_i - x_m}{\delta} \tag{1}$$

where for Eq. 1, c_i is the coded factor value assumed by the variable x_i, x_i is the value assumed by the variable x, x_m is the average value of the x variable, and δ is the interval $|x_i - x_m|$. The adjusted model with the coded variables is shown in Eq. 2.

$$y(c_1, c_2, c_3) = a + b_1c_1 + b_2c_2 + b_3c_3 + (\cdots) + b_nc_n \tag{2}$$

where for Eq. 2, c_i is the coded factor value assumed by the variable x_i, a is the linear coefficient of the regression and b_i are the angular coefficients of the regression.

In the present work the thickness of each layer was considered as a single independent variable in the BBD, and responses of areal density (*Dsup*), trauma and cost were analyzed. The model with the original values is represented by Eq. 3.

$$y\,(t_1, t_2, t_3) = \alpha t_1 + \beta_1 t_2 + \beta_2 t_3 + (\cdots) + \beta_n t_n \tag{3}$$

where for Eq. 3, t_i is the value assumed for the thickness of the layer, α is the linear coefficient of the regression and β_i are the angular coefficients of the regression.

Three responses y were evaluated: the areal density (*Dsup*), the cost of the materials and the trauma measured in the ballistic tests. The objective was to study

the advantages of each layer configuration of the MAS. The values of *Dsup* were obtained by calculating the average value of the material densities. The costs were obtained in the literature [11], and through consultation of the market price. The experimental configurations followed the 3-factor/3-levels BBD matrix. All analyzes were done in duplicates, except the central point (000) of the BBD, which was done in triplicate.

Results and Discussions

Figure 2 show the influence of the layers thickness in the general areal density (*Dsup*) of the armor. In all response surfaces of the present work, it was chosen to fix the thickness of the aluminum in 5 mm, to summary the results.

As expected, in Fig. 2, the response surface is a plane, since the variable *Dsup* is linear as function of the coded thickness.

The multiple regression equation for the *Dsup* with coded factor is shown in Eq. 4, while the response of original value follows Eq. 5. As expected, the coefficients of the Eq. 4 are the average densities of each layer.

$$Dsup\,(kg/m^2) = 60.3 + 6.6c_1 + 3.2c_2 + 5.3c_3 \tag{4}$$

$$Dsup\,(kg/m^2) = 3.30t_1 + 1.07t_2 + 2.66t_3 \tag{5}$$

Figure 3 shows the influence of the layers thickness in the backface signature (trauma) in the clay witness. The multiple regression equation for the trauma with coded factor is shown in Eq. 5, and the response of the original value can be calculated by Eq. 6. The linear adjustment was $R^2 = 0.9535$, which means that 95% of the trauma variation can be explained by the variation of the thickness.

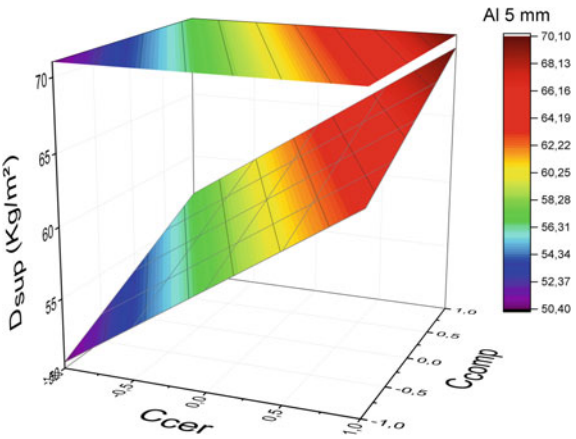

Fig. 2 Response surface for the areal density (*Dsup*) as a function of the coded thickness of the MAS

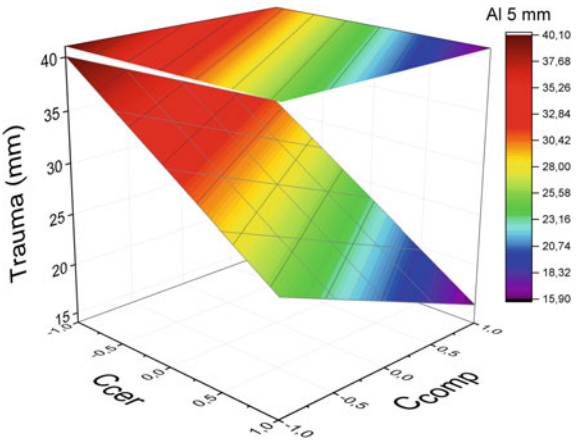

Fig. 3 Response surface for the trauma (*Dsup*) in the clay witness as a function of the coded thickness of the MAS

The standard error of the regression is 5.24. As can be seen in in Eq. 6, the coefficients b_5 and b_6 are not null, which means that some interaction between the layers were detected. It might be attributed to the synergy existing between these layers. It is known that the ceramic front erodes the projectile's tip, spreading the impact pressure in a larger area, and the other layers must collect the fragments and absorb the rest of the energy through different mechanisms [9]. The absorption mechanism in the aluminum alloy would be the plastic deformation, since the ballistic impact promotes a high pressure in the structure. This also contributes to the non-linearity of the response curve equation (Fig. 3).

$$\begin{aligned} Trauma(mm) = (28 \pm 3) - (7.5 \pm 1.3)c_1 - (4.6 \pm 1.3)c_2 - (9.3 \pm 1.3)c_3 \\ + (4.3 \pm 1.9)c_1c_3 + (5.8 \pm 1.8)c_2c_3 \end{aligned} \quad (6)$$

In all specimens, the ceramic layer was totally fragmented. The behavior of the other layers varied, depending on the material thickness. When the ceramic layer was thinner (Fig. 4), typically, the projectile would not totally fragment, and could

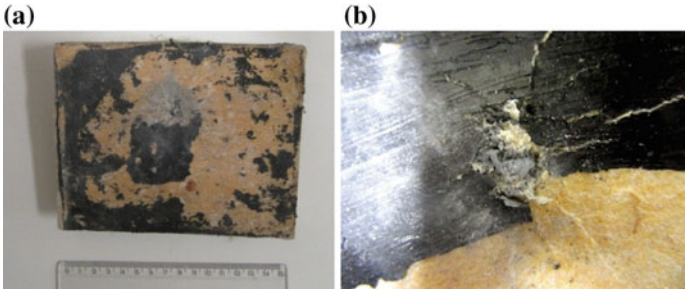

Fig. 4 Ballistic tested specimen type $\bar{I}10$: **a** general front aspect; **b** detail of the back of the composite

be recovered, as shown in Fig. 4b. In the $\bar{1}10$ configuration, since the composite was thick ($c_2 = +1$) and the aluminum was intermediate ($c_3 = 0$), the armor was efficient, and the trauma were 20 and 25 mm (two samples).

When the trauma was too high, approaching 40 mm, and the ceramic layer was thin, as in the $\bar{1}\bar{1}0$ configuration, the armor tend to fail, as seen in Fig. 5.

The best typical behavior of the armor is shown in the Fig. 6a and b, for the $1\bar{1}0$ and 110 configurations. The ceramic was fragmented, and the composite layer was not perforated. The other specimens followed one of the mentioned mechanisms.

The cost analysis is represented by the response surface in Fig. 7. Together with Fig. 2 and 7 shows that the composite almost does not influence the cost, since it is very cheap. Therefore, it can be an interesting advantage to maximize the composite thickness, and minimize the others, when respecting the minimum performance by the NIJ-0101.06 [8].

It is important to mention that there analyzes are not valid for the thickness (and areal densities) outside the studied interval. However, the results have a high amplitude, since the smaller trauma found was 9 mm, for the 110 configuration, and the highest trauma was 53 mm the $\bar{1}0\bar{1}$, resulting in the failure of the MAS.

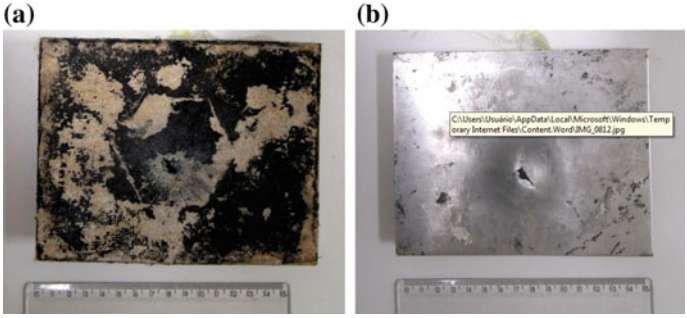

Fig. 5 Ballistic tested specimen type $\bar{1}\bar{1}0$: **a** general front aspect; **b** general back aspect of the MAS

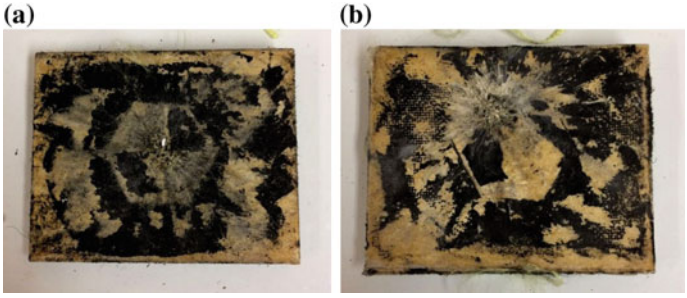

Fig. 6 Ballistic tested specimen type: **a** $1\bar{1}0$ and **b** 110

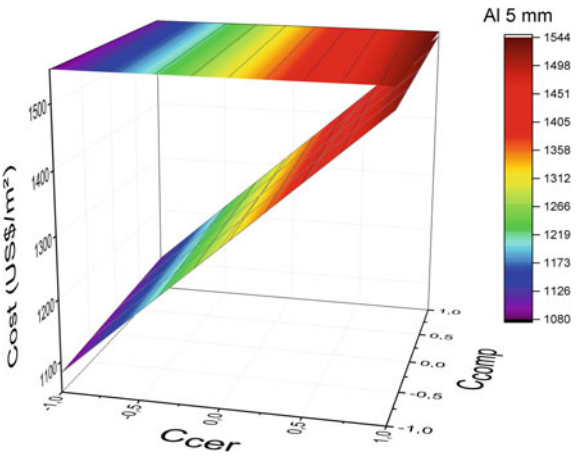

Fig. 7 Response surface for the armor cost as a function of the coded thickness of the MAS

Summary and Conclusions

Multilayered armor systems (MAS) composed of a front ceramic tile (Al_2O_3-4% Nb_2O_5), a second layer of an epoxy composite reinforced with 30 vol.% of curaua non-woven fabric, and a backing 5052 H34 aluminum alloy, were studied by means of the ballistic tests.

The Box-Behnken Design (BBD), in conjunction with the Response Surface Methodology (RSM), was used to evaluate the effect of the areal density of each MAS layer in the overall performance of the three-layered MAS. In the NIJ "backface signature" ballistic tests, the calculated coefficients of the BBD multiple regression for the trauma was 7 for the ceramic, 5 for the composite and 9 for the aluminum, indicating the importance of the aluminum for the energy absorption in the MAS.

The ceramic is important for the energy absorption, however, as shown by previous studies, another important feature is its fragmentation, redistributing the energy over a larger area.

Although the trauma coefficient for the composite is lower, sometimes it is advantageous to maximize the thickness of this layer, since it is lighter and less expensive. However, it is important to observe if the other layers are not too thin, resulting in too high trauma and/or fracture of the aluminum.

Acknowledgements The authors thank the Brazilian agencies CAPES and CNPq for the financial support, and CAEX for performing the ballistic tests.

References

1. Akella K, Naik NK (2015) Composite armour—A review. J Indian Inst Sci 95(3):297–312
2. Monteiro SN, Lima EP Jr, Louro LHL, Silva LC, Drelich JW (2014) Unlocking function of aramid fibers in multilayered ballistic armor. Metall Mater Trans A 46:37–40
3. Monteiro SN, Milanezi TL, Louro LHL, Lima EP Jr, Braga FO, Gomes AV, Drelich JW (2016) Novel ballistic ramie fabric composite competing with Kevlar™ fabric in multilayered armor. Mater Des 96:263–269
4. Monteiro SN, Candido VS, Braga FO, Bolzan LT, Weber RP, Drelich JW (2016) Sugarcane bagasse waste in composites for multilayered armor. Eur Polym J 78:173–185
5. Monteiro SN, Louro LHL, Trindade W, Elias CN, Ferreira CL, Lima ES, Weber RP, Suarez JCM, Figueiredo ABS, Pinheiro WA, Silva LC, Lima Jr. EP. Natural curaua fiber-reinforced composites in multilayered ballistic armor. Metall Mater Trans A 46 (10):4567–4577
6. Monteiro SN, Lopes FPD, Barbosa AP, Bevitori AB, Silva ILA, Costa LL (2011) Natural lignocellulosic fibers as engineering materials—An overview. Metall Mater Trans A 42A:2963–2974
7. Oliveira FH, Helfer AL, Amico SC (2012) Mechanical behavior of unidirectional curaua fiber and glass fiber composites. Macromol Symp 319:83–92
8. NIJ Standard 0101.06. (2008) Ballistic resistance of body armor. US Depart. of Justice
9. Braga FO, Bolzan LT, Luz FS, Lopes PHLM, Lima Jr. EP, Monteiro SN (2017) J Mater Res Technol Published online: http://doi.org/10.1016/j.jmrt.2017.08.001
10. Rodrigues MI, Iemma AF (2014) Design of experiments and process optimization (in Portuguese), 3rd edn. Casa do Espírito Amigo, Brazil
11. Callister WD, Rethwisch DG (2010) Materials science and engineering: an introduction, 8th edn. John Wiley & Sons

Influence of the Blocks and Mortar's Compressive Strength on the Flexural Bond Strength of Concrete Masonry

Gustavo H. Nalon, Rita de C. S. S. Alvarenga, Leonardo G. Pedroti, Marcelo A. Alves, Roseli O. G. Martins, Carol F. R. Santos, Igor K. R. Andrade and Beatryz C. Mendes

Abstract This work presents an experimental investigation of the influence of concrete blocks and mortar's compressive strength on the flexural bond strength, normal to the bed joints, of concrete structural masonry. Third-point beam tests were performed on concrete prisms, considering two different kinds of concrete blocks (compressive strength of 5.9 and 8.2 MPa) and six different cement-lime mortar compositions (compressive strength around 30, 70, and 120% of the blocks' net area compressive strength). Units' absorption and mortar's initial flow and water retentivity were not varied, but remained within the suitable range for use in structural masonry. For both types of concrete blocks, it was observed an increase on the prism's flexural bond strength with the increase of the mortars' compressive strength. A lower mortar's water-cement ratio led to higher bond strength. When fixing the ratio between mortar's and concrete block's compressive strength, it was

G. H. Nalon (✉) · R. de C. S. S. Alvarenga · L. G. Pedroti · M. A. Alves · R. O. G. Martins · I. K. R. Andrade · B. C. Mendes
DEC—Civil Engineering Department, UFV—Federal University of Vicosa, Av. PH Rolfs, S/N, Vicosa, Minas Gerais 36570-900, Brazil
e-mail: gustavohnalon@gmail.com

R. de C. S. S. Alvarenga
e-mail: rcassia.alvarenga@gmail.com

L. G. Pedroti
e-mail: lpedroti@gmail.com

M. A. Alves
e-mail: marcelo.a.arruda@ufv.br

R. O. G. Martins
e-mail: roseli.ogm@gmail.com

I. K. R. Andrade
e-mail: igor.klaus@ufv.br

C. F. R. Santos
EESC—Sao Carlos School of Engineering, USP—University of Sao Paulo, Av. Trabalhador São-Carlense, 400, Parque Arnold Schimidt, São Carlos, São Paulo 13566-590, Brazil
e-mail: carolfrezendes@gmail.com

B. Li et al. (eds.), *Characterization of Minerals, Metals, and Materials 2018*, The Minerals, Metals & Materials Series,
https://doi.org/10.1007/978-3-319-72484-3_60

noticed that the increase on the blocks' strength contributed to a slight increase on the masonry's flexural bond strength, except when using high strength mortar, in which the increase was significantly greater.

Keywords Masonry structures · Mortar properties · Concrete blocks properties Flexural bond strength

Introduction

Structural masonry is a construction system in which blocks, mortar, and, eventually, grout, are responsible for supporting the acting loads and transferring them to the foundation elements. Then, this kind of structure is constructed with different components, each one with its own mechanical and elastic properties. Therefore, the masonry's strength, deformability, and failure mode are directly related to the properties of its basic components. Moreover, all of the masonry's components are considerably heterogeneous, so that their mechanical behavior also depends on the properties of the cement, lime, and aggregates used in their production.

At this point, it is possible to understand the difficulties of correctly predicting the overall behavior of structural masonry from simplified analytical and numerical models. Laboratory experimentation is also necessary in order to verify the influence of the properties of each component on the behavior of the whole structure.

Concrete blocks have a primordial function in the behavior of the structural masonry. According to Ramalho and Correa [1], the units are the main responsible for the strength of masonry elements. On the other hand, the main functions of the mortar are the union of the units, the uniform transmission of loads, and the accommodation of small deformations, as the same authors point out. The Brazilian Standard NBR 15961-1:2011 [2] requires that the mortar compressive strength should be at most 70% of the concrete blocks' net area compressive strength. ASTM C 1329 [3] and C 270 [4] classify mortars in various types (M, S, N, and O), which have different kinds of application.

Masonry elements are not subject only to vertical actions, but also to the lateral pressure of the wind and earthquakes, or to the effect of eccentric loads. These types of actions mobilize the elements' bending and shear strength. Many authors already studied the occurrence of masonry's bending due to horizontal actions, which are responsible for the development of tensile stresses in different directions. According to Brown and Melander [5], the direction of the stresses (parallel or normal to the bed joints) determine the failure mechanism of masonry walls. Testing solid clay masonry walls, the authors found that the flexural strength parallel to bed joints depends mainly on the shear strength of the bed joints. On the other hand, the flexural strength normal to the bed joints is very dependent of the bond between blocks and mortar.

In this respect, Parsekian, Hamid, and Drysdale (2012) [6] state that the flexural bond strength is related to the block/mortar adhesion mechanism, which depends on

the chemical adhesion and mechanical interlocking between these components. Lumantarna et al. [7] tested unreinforced clay brick masonry of existing buildings in New Zealand, and also concluded that almost all of the field samples presented bond failures on the mortar joints.

Different properties of blocks and mortar can affect the masonry's flexural bond strength. According to Rao et al. [8], increases in the cement mortar's compressive strength contribute to increases in the masonry's flexural bond strength, irrespective of the kind of block. Low cement content leads to lower values of flexural bond strength. The same authors also verified that units with higher roughness and greater wall thickness led to greater masonry's flexural bond strength. Yuen and Lissel [9] investigated how the bond strength depends on the bricks' absorption, construction methods, and curing methods, and stablished correlations between these factors. Ajith et al. [10] investigated the flexural bond strength of concrete masonry with 2 mm polymer glue mortar. They concluded that the flexural bond strength depends on the type of mortar, the techniques of dispersion, and the roughness of the blocks. They found that thin bed masonry presents better flexural bond strength than the conventional masonry.

Flexural tests with simply supported beams or vertical walls can be performed in order to determine the masonry's flexural bond strength, normal to the bed joints. This work aims to experimentally evaluate elements of concrete structural masonry submitted to flexural stresses. Using different types of concrete blocks and cement-lime mortar compositions, an experimental program was developed in order to verify the influence of the concrete blocks and mortar's mechanical properties on the masonry's flexural bond strength.

Materials and Methods

Two different concrete block strength levels were selected for this study. All of the blocks were produced in Contagem, Minas Gerais, Brazil, and had a nominal size of (140 × 190 × 390) mm. Experimental tests were conducted in order to determine concrete blocks' actual dimensions, water absorption, initial rate of absorption, net area and compressive strength, as prescribed by NBR 12118: 2013 [11]. The splitting tensile strength was determined as recommended by the ASTM C1006—07 [12]. To determine the static modulus of elasticity of the blocks, the Brazilian standard NBR 8522: 2008 [13] was used. The longitudinal deformation of the blocks was measured by electrical strain gauges positioned at two points of the block's longitudinal walls. The load was applied by an EMIC hydraulic press, PCE200PLUS model, and recorded by the machine's load cells. The modulus of elasticity was calculated between the points of compressive stress of 0.5 MPa and 30% of the estimated blocks' compressive strength. Images of some of these tests are presented in Fig. 1.

Different cement-lime mortar compositions were produced, which had compressive strength close to 30, 70, and 120% of the concrete blocks' net area

Fig. 1 Characterization of the concrete blocks

compressive strength. Thus, one of them would have compressive strength close to the maximum limit stipulated by the Brazilian standard for structural masonry, another below and the other above this limit. To produce the mortar, the following construction materials were used: natural sand from Porto Firme, Minas Gerais, Brazil; Portland cement CP II E-32, produced by Tupi; and hydrated lime CHIII Supercal, produced by Ical.

The preparation of each mortar composition started by mixing sand, lime, and water in the appropriate proportions. The mixture was then weighed and allowed to mature for approximately 24 h. After this time, the cement and the amount of water lost by evaporation were added, following a new mechanical mixing. The temperature and humidity of the environment at the time of mixing were recorded. After preparation, the mortar was submitted to experimental tests to determine the consistency index, according to NBR 13276:2016 [14], and water retentivity, according to NBR 13277:2005 [15]. The goal was to maintain the mortar's flow in the range of (230 ± 10) mm, which is recommended for structural masonry, according to Parsekian and Soares [16]. As the same authors state that high water retentivity is desirable, this parameter was maintained in the range of (90 ± 5)%.

Four-block prisms were produced with each kind of block and mortar, according to the recommendations of NBR 15961-2: 2011 [17], and using full mortar bedding and joint thickness of (10 ± 3) mm. The production steps of these specimens are presented in Fig. 2. Before placing the mortar, the concrete blocks were moistened, since the water retentivity of the mortars was high. For each batch of prisms, six (40 × 40 × 160) mm mortar prisms and four (50 × 100) mm cylindrical specimens were cast to be tested after 28 days of cure. Table 1 summarizes a couple of specific characteristics of the batches of prisms. Each batch had three specimens.

The prisms were kept immobile for 28 days, and protected from heat and wind. The mortar specimens were left inside the environmental room for the same period. After this time, mortar flexure and compression tests were conducted, according to NBR 15961-2: 2011 [17]. Mortars` modulus of elasticity was determined with the cylinder specimens, which was calculated between the points of compressive stress of 0.5 MPa and 30% of the mortar's estimated compressive strength. Mortar characterization tests are shown in Fig. 3.

Fig. 2 Four-block prisms production

Table 1 Characteristics of the batches of prisms

Name of the prisms batch	Block's net area compressive strength	Mortar's compressive strength
B1 M < 40	f_{bk}^{B1}	$f_a \leq 0.40 f_{bk}^{B1}$
B1 M70		$f_a \approx 0.70 f_{bk}^{B1}$
B1 M > 100		$f_a \geq 1.00 f_{bk}^{B1}$
B2 M < 40	f_{bk}^{B2}	$f_a \leq 0.40 f_{bk}^{B2}$
B2 M70		$f_a \approx 0.70 f_{bk}^{B2}$
B2 M > 100		$f_a \geq 1.00 f_{bk}^{B2}$

Fig. 3 Characterization of cement-lime mortars

In order to determine the flexural bond strength, normal to the bed joints, third-point beam tests were performed on the concrete prisms. The prisms were horizontally placed under the movable plate of an EMIC universal testing machine, model 23-600, supported on steel rollers in the positions shown in the diagram if the Fig. 4. The diagram also shows the position of two other rollers on the central

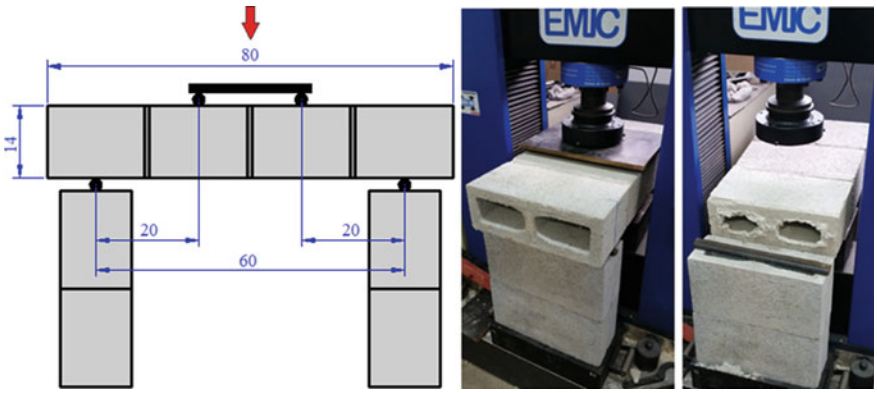

Fig. 4 Third-point beam tests

blocks of the prism. These rollers work as a support for a plate centralized in the load axis of the testing machine. The load was applied by displacement control, at a speed of 0.01 mm/s, until the rupture of the prism.

Results and Discussion

Table 2 shows the properties obtained from the characterization tests of the concrete blocks. The net area compressive strength of B2 blocks was 36.7% greater than that of the B1 blocks. Both types of blocks had a water absorption lower than the maximum value suggested by the Brazilian standard, 10%. The strongest block showed a lower water absorption and initial rate of absorption. Splitting tensile strength was around 15% of the compressive strength of the blocks.

Table 3 summarizes, for each mortar composition, the proportions between cement, lime, sand, and water; its consistency index and water retentivity. Flow and water retentivity were within the ranges recommended by Parsekian and Soares [16].

The flexural bond strength f_t of the masonry, normal to the bed joints, was determined based on the results of the third-point beam tests, with the following equation:

$$f_t = \frac{6}{l \times t^2}\left[\frac{(W/H) \times L^2}{8} + \frac{P \times b}{2}\right]$$

In this equation, W and H are the prism's weight and height, respectively; l and t are the concrete block's length and width, respectively; P is the failure load; and L is the distance between the support rollers.

Table 2 Characterization of the concrete blocks

Property	B1 blocks	B2 blocks
Average width (mm)	138	140
Average length (mm)	390	390
Average height (mm)	190	190
Water absorption (%)	6.2	5.5
Initial rate of absorption (IRA) [(g/193.55 cm^2)/min]	8.27	7.09
Ratio of A_n/A_g (%)	0.54	0.55
Gross area average compressive strength (MPa)	7.6	9.4
Gross area characteristic compressive strength (MPa)	5.9	8.2
Net area characteristic compressive strength (MPa)	10.9	14.8
Splitting tensile strength (MPa)	0.83	1.28
Modulus of elasticity (MPa)	7,310	15,769

Table 3 Mortar compositions, flow and water retentivity

Mortar	Used in the prisms	Mix proportions (by mass)				Flow (mm)	Water retentivity (%)
		Cement	Lime	Sand	Water		
M1	B1 M < 40	1.00	2.20	8.50	2.25	232	94
M2	B1 M70	1.00	0.39	6.44	1.32	230	91
M3	B1 M > 100	1.00	0.25	4.22	0.90	226	89
M4	B2 M < 40	1.00	0.45	7.48	1.49	218	85
M5	B2 M70	1.00	0.32	5.25	1.07	212	92
M6	B2 M > 100	1.00	0.20	3.39	0.74	231	86

Table 4 presents the properties obtained from third-point beam and mortar tests. The third-point beam tests presented a large dispersion of results, so the use a greater number of specimens is a suggestion for these types of tests. Despite this, it was still possible to verify interesting trends in the masonry behavior, which will be discussed below. All of the batches of prisms presented the desired values for the ratio between mortar's compressive strength and block's net area compressive strength. The modulus of elasticity of the mortar increased with the increase of its compressive strength, in proportions similar to those reported by some of the works cited by Brooks [18].

For any kind of prism, the rupture occurred in a brittle and sudden manner, due to the loss of adhesion between the face of the block and the mortar joint, most often in just one of the prism joints. Figure 4 represents this failure mode. It was noted that the blocks were practically intact at the end of the tests. The factors that interfere in the adhesion between block and mortar deserve, therefore, more attention. Comparing all of the prism batches, mortar's flow and water retentivity did not change significantly. The AAI of B1 blocks was slightly smaller than the AAI of B2 blocks. Labor and type of cure also did not vary between the batches.

Table 4 Results of the third-point beam and mortar tests

Prisms	Average flexural bond strength f_t (MPa)	Mortar strength f_m (MPa)	f_m / f_{bk} Net Area (%)	f_m / f_{bk} Gross Area (%)	Modulus of elasticity of the mortar E_m (MPa)
B1 M < 40	0.147	3.9	35.8	62.7	5,506
B1 M70	0.210	7.5	68.8	118.6	13,575
B1 M > 100	0.279	14.3	131.2	208.5	17,649
B2 M < 40	0.149	4.3	29.0	52.4	8,145
B2 M70	0.218	10.2	68.9	124.4	14,745
B2 M > 100	0.408	18.4	124.3	224.4	19,769

Then, the main parameters varied were the compressive strength of mortar and concrete blocks.

The prisms' flexural bond strength, normal to the bed joints, increased significantly when the mortar's compressive strength increased, either when using the weakest blocks (B1 blocks) or the strongest blocks (B2 blocks). The use of mortar compositions with greater amount of cement, in comparison to the other components, provided a better mechanical interlocking of the suctioned paste into the pores of the concrete. When the mortar compressive strength increased by about four times, the average flexural bond strength increased by 90% when using B1 blocks and 174% when using B2 blocks.

In general, prisms with high strength mortar presented the best performance in the third-point beam tests. However, it is worth remembering that mortars with very high compressive strength do not give the masonry a good structural performance in compression. The experimental results of Alvarenga et al. (2017) [19] showed that the use of low-strength mortars prevents an excessively brittle rupture of the masonry under compression, and does not compromise the masonry's compressive strength and stiffness. Therefore, it is desirable to choose a mortar that provides a good structural performance of the masonry under both vertical and lateral actions.

The increase of the blocks' compressive strength did not increase the flexural bond strength of the masonry in the prisms whose mortar's compressive strength complies with the maximum limit stated by the Brazilian standard (70% of the block's net area compressive strength), that is, the batches B1 M < 40, B1 M70, B2 M < 40, and B2 M70. When the maximum limit is extrapolated (B1 M > 100 and B2 M > 100), a significant increase of the flexural bond strength is verified when stronger concrete blocks are used. In fact, when using mortars with compressive strength greater than the blocks' net area compressive strength, there was a nearly 50% gain in the flexural bond strength of the masonry by increasing the blocks' compressive strength by about 40%.

Conclusions

In conclusion, the masonry's flexural bond strength, normal to the bed joints, is directly related to both the characteristics of its basic components, and the complex interaction between them. Third-point beam tests were satisfactory to evaluate the influence of blocks and mortar's compressive strength on the structural behavior of masonry subjected to lateral actions. The failure mode typically verified in these tests was the breaking of adhesion between block and mortar. The use of stronger mortars ensured better bonding of the mortar's binder components in the masonry units. Then, the masonry's flexural bond strength increased with the increase of the compressive strength of the mortar, regardless of the block's compressive strength. Since the low strength mortars presented a lower flexural bond strength, they should not be used for structural masonry. The Brazilian standard stablishes a minimum compressive strength of 1.5 MPa for mortar's structural masonry. Despite the gains of flexural bond strength with the increase of the mortar's compressive strength, it is not advisable to use very high strength mortars, as they can cause a very brittle failure of the masonry when it is subjected to compressive stresses. Therefore, the prisms whose mortar had a compressive strength close to 70% of the concrete blocks' net area compressive strength (B1 M70 and B2 M70), presented the structural behavior that seems to be the most suitable for the concrete structural masonry subjected to flexure or compression. When the mortar's compressive strength is lower than 70% of the block's net area compressive strength, the experimental results showed that the use of stronger blocks did not significantly contribute to the increase of the masonry's flexural bond strength

Acknowledgements The authors would like to express gratitude to the agencies: National Counsel of Technological and Scientific Development (CNPq), Research Support Foundation of Minas Gerais (FAPEMIG), and Coordination for the Improvement of Higher Education Personnel (CAPES), for the great support to this research.

References

1. Ramalho MA, Correa MRS (2003) Projeto de edifícios de alvenaria estrutural. Pini, São Paulo, p 169
2. Brazilian Association of Technical Norms. NBR 15961-1 (2011) Structural masonry—Concrete blocks Part 1: Design. Rio de Janeiro, p 42 www.abntcatalogo.com.br
3. ASTM C1329/C1329 M-16 (2016) Standard specification for mortar cement. ASTM International, West Conshohocken, PA. www.astm.org
4. ASTM C270-14a (2014) Standard specification for mortar for unit masonry. ASTM International, West Conshohocken, PA. www.astm.org
5. Brown RR, Melander J (2015) Flexural bond strength of mansory parallel to the bed joints. 9th Canadian mansory symposium, p 12
6. Parsekian GA, Hamid AA, Drysdale RG (2012) Comportamento e dimensionamento de alvenaria estrutural. EdUFSCar, São Carlos, p 625

7. Lumantarna R, Biggs DT, Ingham JM (2014) Compressive, flexural bond, and shear bond strengths of in situ New Zealand unreinforced clay brick mansory constructed using lime mortar between the 1880s and 1940s. J Mater Civ Eng 26(4)
8. Rao KVM, Reddy BVV, Jagadish KS (1996) Flexural bond strength of mansory using various blocks and mortars. Mater Struct 29:119–124
9. Yuen CG, Lissel SL (2007) Flexural bond strength of clay brick masonry. WIT Trans Eng Sci 57. doi:10.2495/MC070251
10. Ajith TJ, Dhanasekar M, Cheng Y (2012) Characterization of flexural bond strength in thin bed concrete masonry. 15th international brick and block masonry conference, florianopolis
11. Brazilian Association of Technical Norms (2013) NBR 12118: Hollow concrete blocks for concrete masonry—Test methods. Rio de Janeiro, p 14 www.abntcatalogo.com.br
12. ASTM C1006-07 (2013) Standard test method for splitting tensile strength of masonry units. ASTM International, West Conshohocken, PA. www.astm.org
13. Brazilian Association of Technical Norms (2008) NBR 8522: Concrete—Determination of the elasticity modulus by compression. Rio de Janeiro, p 16 www.abntcatalogo.com.br
14. Brazilian Association of Technical Norms (2016) NBR 13276: Mortars applied on walls and ceilings—Determination of the consistence index. Rio de Janeiro, p 2 www.abntcatalogo.com.br
15. Brazilian Association of Technical Norms (2005) NBR 13277: Mortars applied on walls and ceilings—Determination of the water retentivity. Rio de Janeiro, p 3 www.abntcatalogo.com.br
16. Parsekian GA, Soares MM (2010) Alvenaria estrutural em blocos cerâmicos—projeto, execução e controle. Telo Melo, São Carlos, p 234
17. Brazilian Association of Technical Norms (2011) NBR 15961-2: Structural masonry—Concrete blocks Part 2: Execution and site control. Rio de Janeiro, p 35 www.abntcatalogo.com.br
18. Brooks JJ (2015) Concrete and masonry movements. Elsevier, Waltham, p 599
19. Alvarenga RCSS, Nalon GH, Fioresi LAF, Pinto MC, Pedroti LG, Ribeiro JCL (2017) Experimental evaluation of the influence of mortar's mechanical properties on the behavior of clay masonry. Charact Miner Met Mater 2017:671–679. https://doi.org/10.1007/978-3-319-51382-9_74

Influence of Two Solubilization Conditions at 718 Superalloy Hardness and Microstructure

Fabio da Costa Garcia Filho, Dian Souza de Oliveira and Sergio Neves Monteiro

Abstract The properties of the nickel based superalloys, in particular 718 nickel-based alloy, are mainly improved by the hardening mechanism, which is based on precipitation of second phases. This work aimed to compare the evolution of precipitation hardening in a 718 alloy microstructure for two different solubilization conditions: 1050 °C for 2 h and 970 °C for 2 h, followed by a period up to 120 h of aging at 800 °C and correlated to the values of hardness. The microstructure was analyzed by optical microscopy. Vickers hardness test was performed and the grain size was measured. It was verified an increase on the hardeness of this material up to 15 h of aging, after that the value decreased to a level that is maintained until 120 h for both solubilization conditions.

Keywords Precipitation hardening · 718 alloy · Optical microscopy

Introduction

The continuous research for materials capable of being put into extreme conditions of temperature, load and corrosive environments, without significant losses of properties, resulted in the development of so-called super alloys during the 1950s [1].

Among nickel superalloys, 718 alloy are especially noteworthy once they are the most manufactured nickel alloy, finding applicability in several industries, such as aerospace, nuclear or petroleum. The great applicability of this alloy is based on the combination of excellent mechanical properties, fatigue and creep resistance, as well as ductility and stiffness, corrosion resistance, good formability and welding properties [1–4].

The properties of the 718 alloys are due the hardening mechanism which is the precipitation of the second phases or aging. In the 718 superalloy, the matrix shows

F. da Costa Garcia Filho (✉) · D. S. de Oliveira · S. N. Monteiro
Department of Materials Science, Military Institute of Engineering - IME, Praça General Tibúrcio, 80, Praia Vermelha, Urca, Rio de Janeiro, RJ CEP 22290-270, Brazil
e-mail: fabiogarciafilho@gmail.com

B. Li et al. (eds.), *Characterization of Minerals, Metals, and Materials 2018*, The Minerals, Metals & Materials Series,
https://doi.org/10.1007/978-3-319-72484-3_61

a face centered cubic (FCC) crystalline structure. The γ± phase (Ni_3Nb—tetragonal) has a prominent role in the mechanical properties of the alloy, as the main hardening phase, while the γ′ phase (Ni_3 (Al, Ti)—FCC) is coherent and ordered with the matrix and less effective in the hardening of this alloy. On the other hand, the γ″ and γ′ phases are metastable and under certain conditions can present transformations for stable phases, such transformation in the case of γ″ results in the appearance of the δ phase, of the same composition (Ni_3Nb), with orthorhombic crystal structure, which may have deleterious effects on the alloy, decreasing the mechanical properties of the alloy [5–12].

The superalloy is hardened by the precipitate γ″ and the degree of hardening is a function of the amount, size and distribution of γ″ in the matrix. In this context, this paper aimed to verify the hardness of the alloy and to correlate with the microstructure of the material. So, two different thermal treatments of solubilization were performed, the first at 1050 °C while the second at 970 °C, both for 2 h, followed by aging at 800 °C for a period up to 120 h. The difference of this treatment can lead to a difference in the microstructure and, in this way, results on the properties of the alloy.

Materials and Methods

The 718 nickel-based alloy used was obtained from the company Multialloy, and was received in the form of a hot rolled round bar. This bar was cut into several 1.5 cm samples to allow different tests and heat treatment conditions to be analyzed. The chemical composition of the sample received is shown in Table 1 and it is in agreement with the percent values of the 718 alloys [1]. Figure 1 shows the sample as received (in bar form) as well as samples already cut.

After the samples were cut, they were submitted to different aging conditions. Carbolite CWF 13/23 was used for this purpose. Table 2 presents the summary of thermal treatments performed.

To perform the Vickers hardness measurement, INDENTEC digital equipment was used. The equipment Olympus, model GX71 was used for the optical microscopy observation. The chemical attack used in order to reveal the microstructure is described in Table 3. The average grain size was measure by the software AnaliSIS Auto.

Table 1 Composition (wt%) of 718 superalloy samples

Ni	Cr	Fe	Nb	Mo	Ti	Al	Co	V	Zr
54.1	17.28	18.65	4.78	3.02	0.87	0.57	0.322	0.022	0.015
C	Mn	Si	P	S	B	Cu	W	Mg	Sn
0.046	0.101	0.09	0.0064	0.0082	0.0049	0.028	0.088	0.024	0.0082

Fig. 1 Received bar form (**a**) and cut samples (**b**)

Table 2 Summary of thermal treatments

	Solubilization			Aging		
Condition #01	T = 1050 °C	t = 2 h	Water quenching	T = 800 °C	t = 30 min. 1 h. 2 h. 4 h. 8 h. 15 h. 30 h. 60 h e 120 h	Water quenching
Condition #02	T = 970 °C	t = 2 h	Water quenching	T = 800 °C	t = 30 min. 1 h. 2 h. 4 h. 8 h. 15 h. 30 h. 60 h e 120 h	Water quenching

Table 3 Chemical attack used to reveal the microstructure and the procedure

Compounds	Volume (ml)	Procedure
Acetic acid	10	Immerse the sample into the solution for about 30 s, remove the sample, clean with alcohol and blow-dry
Nitric acid	10	
Hydrochloric acid	15	
Glycerin	5	

Results and Discussion

Figure 2 shows the Vickers hardness versus aging time curve for the two solubilization conditions. This result represents an indicator of the microstructural evolution of each of the conditions.

Condition 1 of solubilization presents the minimum value of hardness, approximately 175 HV. which represents the sample in supersaturated solid solution condition. In this condition neither γ'' nor γ' should be observed as well as the δ

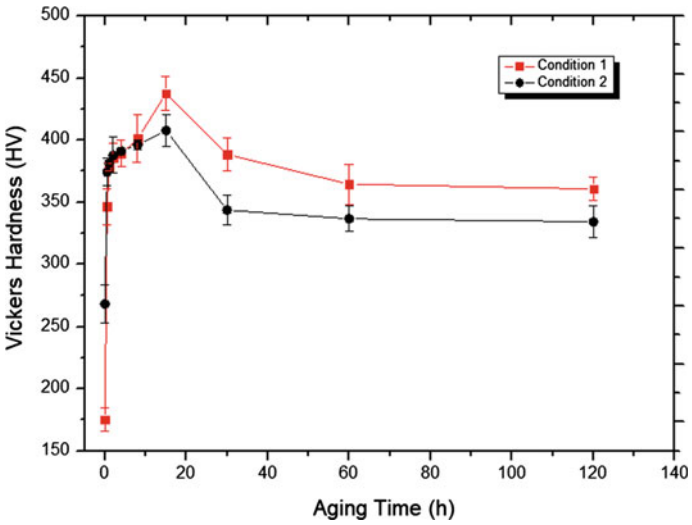

Fig. 2 Vickers hardness versus aging time curve for the two solubilization conditions performed

phase. It is possible to see a continuous increase in the hardening of the material until between 8 and 15 h of the aging treatment where the higher hardness of the alloy were obtained, approximately 440 HV. This represents two and a half times the average hardness for the solubilized condition. It was also verified a third stage in the hardness versus aging curve, in which after the maximum of properties were obtained, a drop to a plateau of approximately 375 HV is observed, where the properties remain approximately constant even for long periods of exhibition. The decline of the properties may be associated with the coalescence of γ'' precipitates as well as their dissolution in favor of δ precipitation.

Condition 2 of solubilization, it is observed that under the condition of a supersaturated solid solution the alloy has an average hardness of about 275 HV. From then there is a hardness increase up to the maximum value that occurs with 15 h of aging treatment. 400 HV. after this maximum there is a decrease in the properties until the plateau of approximately 330 HV that remains until the end of exposure, 120 h.

It is noteworthy that both curves present similar behavior. It is clear the existence of three distinct stages in the hardness curve of this alloy. The first is the minimum hardness point, which occurs in the condition of supersaturated solid solution, from that point there is a continuous increase of hardness until the maximum value of hardness is obtained in both cases with 15 h of aging. After the maximum, there is a decline in properties until it reaches a plateau that remains approximately constant until long periods of exposure 120 h. On the other hand, some differences are observed and the following discussion tries to explain them.

The hardness of the solubilized condition presents a higher value for condition 2, approximately 270 HV against 175 HV in condition 1. This difference may

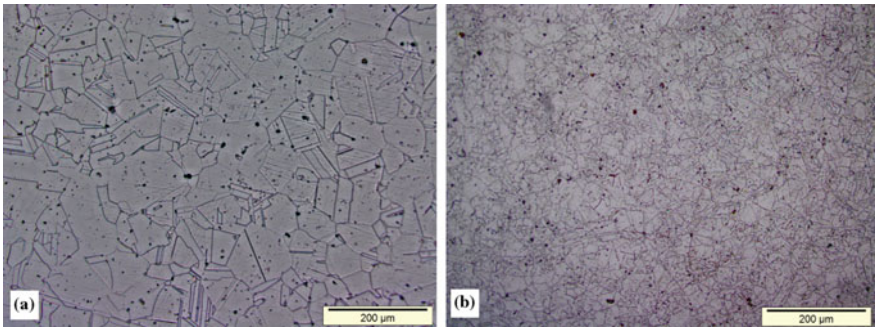

Fig. 3 Microstructure of the solubilized samples for conditions 1 (**a**) and 2 (**b**). 200×

be associated with grain size, since in the solubilized condition we do not have the precipitation of hardening phases (γ'' and γ'). Figure 3 shows the microstructure of the solubilized samples for conditions 1 and 2.

The average grain size measurement was performed and the results are summarized in Table 4. It is clear that the higher solubilization temperature of condition 1 allowed a higher grain growth and consequently lower hardness when compared to condition 2.

The maximum hardness value found in condition 2 is about 10% lower than that found in condition 1, which may be related to the fact that the solubilization temperature of condition 2 is below the solubilization temperature of δ (around 1000 °C), and thus the existence of this phase in the condition of "as received" (previous to the heat treatments performed) would imply the lowest amount of Nb in solid solution for the precipitation of the hardening phase γ''. Cai et al. [13], presents a study on the kinetics of dissolution of the δ phase in 718 alloy, the authors show that for temperature of 1020 °C there is the total dissolution of δ in the matrix γ after 2 h. On the other hand, by maintaining the alloy at 980 °C for up to 6 h a certain amount of δ can still be detected. Thus, solubilization condition 1 (1050 °C for 2 h) would allow the total dissolution of δ. but condition 2 (970 °C for 2 h) would not be able to do so. Figure 4 shows the microstructure of the solubilization condition 2, and the presence of δ phase in the grain boundaries is observed, which was not observed for the solubilization condition 1, in this way, agreeing to what was discussed.

The decrease in mechanical properties that occurs after the maximum hardness is more pronounced in condition 2 than in condition 1, reaching a plateau of 330 and 375 HV. This represents a drop of about 18% for condition 2 and 15% for condition 1. The difference may also be associated with the presence of δ in the "as received" condition and growing of this phase.

Table 4 Grain size measure

	Grain size (μm)	Standard deviation
Condition #01	31.025	3.685
Condition #02	10.225	0.403

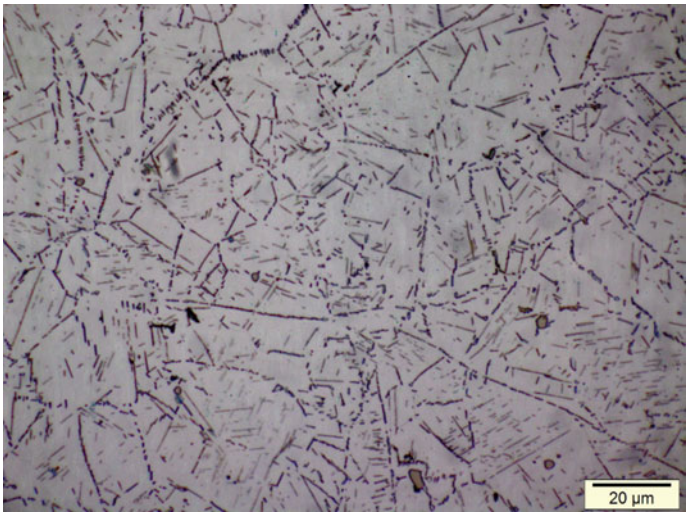

Fig. 4 Microstructure of the solubilization condition 2, and the presence of δ phase in the grain boundaries. 1000×

Conclusions

- Precipitation of the second phases, such as γ″ and γ′, is the main hardening mechanism in the 718 nickel-based super alloy. At both studied condition the higher value of hardness was achieved after 15 h of treatment, 440 and 400 HV for each condition.
- The grain size also represents an important hardening mechanism, when there is the absence of second phases. It was showed that when the material was in the condition of supersaturated solid solution, the decrease of the grain size increased the hardness of the material. In this case, an average grain size of 31.025 μm obtained 175 HV while an average grain size of 10.225 μm obtained 270 HV.
- The presence and growth of δ phase presents a decrease in the hardness of the material which could be well observed at hardness versus aging time curve. The differences between the curve of both solubilized condition was also discussed, and it was verified that the temperature of solubilization of one of the conditions

was not able to dissolute all δ phase of "as received" condition while the other was able promote the total dissolution of the δ phase.

Acknowledgements The authors thank the support to this investigation by the Brazilian agencies: CNPq. FAPERJ and CAPES.

References

1. ASM Speciality Handbook (2000) Nickel, Cobalt and their alloys, ASM International, Materials Park
2. Reed RC (2006) The superallys: fundamentals and applications. Cambridge University Press, Cambridge
3. Bhadeshia HKDH Nickel Based Superalloys, disponível em: http://www.ctia.com.cn/Marketing/Print.asp?ArticleID=14319, acessado em 07/04/2015
4. Donachie MJ, Donachie SJ (2002) Superalloys: A technical guide, 2ª Ed., ASM International, Materials Park
5. Thomas A, El-Wahabi M, Cabrera JM, Prado JM (2006) High temperature deformation of Inconel 718. J Mater Process Technol 177:469–472
6. Ping DH, Gu YF, Cui CY, Harada H (2007) Grain boundary segregation in a Ni-Fe bases (Alloy 718) superalloy. Mater Sci Eng A 456:99–102
7. Hsu CY, Lin YY, Lee WS, Lo SP (2008) Machining characteristics of Inconel 718 using ultrasonic high temperature-aided cutting. J Mater Process Technol 198:359–365
8. Kuo CM, Yang YT, Bor HY, Wei CN, Tai CC (2009) Aging effects on the microstructure and creep behavior of Inconel 718 superalloy. Mater Sci Eng A 510–511:289–294
9. Azadian S, Wei LY, Warren R (2004) Delta phase precipitation in Inconel 718. Mater Charact 53:7–16
10. Slama C, Abdellaoui M (2000) Structural characterization of the aged Inconel 718. J Alloy Compd 306:277–284
11. Ghosh S, Yadav S, Das G (2008) Study of standard heat treatment on mechanical properties of Inconel 718 using Ball indentation technique. Mater Lett 62:2619–2622
12. Chaturvedi MC, Han Y (1983) Strenghtening Mechanisms in Inconel 718 Superalloy. Metal Sci 17:145–149
13. Cai D, Zhang W, Nie P, Liu W, Yao M (2007) Dissolution kinetics of delta phase and its influence on the notch sensitivity of Inconel 718. Charact 58:220–225

Irradiation Influence on the Properties of HMS-Polypropylene Clay/AgNPs Nanocomposites

Washington Luiz Oliani, Duclerc Fernandes Parra, Vijaya Kumar Rangari, Nilton Lincopan and Ademar Benevolo Lugao

Abstract Due to its versatility and low cost, polypropylene (PP) is one of the most widely used polymers in the world, consequently in research and development of new products. The polypropylene modified was prepared by gamma irradiation in acetylene at 12.5 kGy dose, technical polymer also known as high-melt-strength-polypropylene (HMSPP). It was mixed with montmorillonite (MMT) clay and silver nanoparticles (AgNPs) for bactericide activity. HMS-Polypropylene-clay-silver nanocomposites were manufactured using twin-screw extruders. Those materials were prepared by a melt mixing process via twin screw extrusion with a wide range of processing conditions. The polypropylene nanocomposites (PPNC) surfaces were exposed to gamma-radiation (^{60}Co) source in presence of nitrogen as inert atmosphere at 1; 3; 5; 10; 20 and 50 kGy doses for modified the surfaces in order to enhance biocide activity. The samples surfaces were characterized by Differential Scanning Calorimetry (DSC), X-ray Diffraction (XRD), Thermogravimetric Analysis (TGA), Scanning Electron Microscopy (SEM), Energy Dispersive Spectroscopy (EDX) and evaluated by determination of bactericide effects. The results indicate the formation of structures predominantly intercalated of HMSPP nanocomposite. Contact tests for antibacterial activity of the hybrid polymer were applied against *Escherichia coli*

W. L. Oliani (✉) · D. F. Parra · A. B. Lugao
Nuclear and Energy Research Institute, IPEN, CNEN/SP, Av. Prof. Lineu Prestes, 2242, Pinheiros, CEP, 05508-000 São Paulo SP, Brazil
e-mail: washoliani@usp.br

V. K. Rangari
Department of Materials Science and Engineering, Tuskegee University, Tuskegee, AL, USA

N. Lincopan
Department of Microbiology, Institute of Biomedical Sciences, University of Sao Paulo, Sao Paulo, Brazil

N. Lincopan
Department of Clinical Analysis, School of Pharmacy, University of Sao Paulo, Sao Paulo, Brazil

B. Li et al. (eds.), *Characterization of Minerals, Metals, and Materials 2018*, The Minerals, Metals & Materials Series,
https://doi.org/10.1007/978-3-319-72484-3_62

(Gram-negative) and *Staphylococcus aureus* (Gram-positive) bacteria. The irradiations on the samples surfaces were insufficient to promote activity on contact biocide tests.

Keywords Polypropylene · AgNPs · Clay · Gamma irradiation
HMSPP

Introduction

Linear polypropylene (PP) has very attractive properties such as high modulus and tensile strength rigidity and excellent heat resistance. However, its linear structure leads to poor processability in processes involving melt stretching, such as extrusion coating, foam extrusion and film blowing. Branches are introduced into linear PP to produce "high-melt-strength polypropylene" having enhanced processability [1–3].

The radiation induces reactions in polymers and is thus named: crosslinking and/or scission, and grafting and/or curing. The addition of oxygen with the polymeric free radical forms the peroxy and hydroperoxides species, which on decomposition forms smaller molecules and polymer degradation [4].

PP is known to be little resistant to energy gamma-irradiation due to a tendency to orientation and oxidation embrittlement. The effect of gamma-rays induces chain scission and degradation effects resulting in a reduced melt viscosity and severe embrittlement. Phenolic antioxidant application is recommended to avoid degradation in processing [5].

Otaguro et al. [6] studied the degradation of high molecular weight iPP subjected to gamma radiation in nitrogen atmosphere. They reported that at low irradiation doses (below 12.5 kGy) the chain scission was the preferential process. As the dose level was increased above 12.5 kGy, the crosslinking predominated. Recent study [7] investigated the influence of gamma-irradiation doses from zero up to 50 kGy on the polypropylene foams, and reported the mainly impact of radiation on their structural and physical properties. The irradiation was performed under air environment and the results were crosslinking when exposed to low doses, 1 and 5 kGy, while scission occurred at higher doses.

Long-Chain-Branching (LCB) polypropylene obtained by IPEN process [8] adds specific properties, such as: visbreaking, high extensional viscosity, etc. In this sense is also desirable to develop polypropylene nanocomposite with the addition of inorganics for obtain the called HMSPP nanocomposites with typical properties [9].

Polymer nanocomposites (PCNs) are polymer based materials that incorporate filler elements at least one dimension in the nanometer range. Products are increasingly developed for commercial applications ranging from building infra-structure of food packaging to biomedical devices among others products [10].

Silver incorporation in MMT plays an important role due to the possibilities of creating an antibacterial material with slow release of silver species in order to obtain a prolonged antibacterial activity [11].

The dispersion of particle clusters is important in productive processes, whose purpose is to improve properties in products [12]. Sonochemistry offers a simple route to nanomaterials synthesis with the application of ultrasound [13]. In addition ultrasound proved to be an important tool for the promotion of inorganic clusters dispersion, including clay and silver [14].

In recent paper the polypropylene nanocomposite materials were prepared with 5 and 10 wt% Cloisite C20A clay, jointly with 0.6 and 1.2 wt% of maleic anhydride (MA) for the simultaneous polymer functionalization and clay dispersion in a twin screw extruder. The greater level of clay dispersion was verified by the displacement of the XRD diffraction peak to lower angles, indicating an intercalated-exfoliated structure [15].

Polyethylene fibers containing AgNPs were prepared through the chemical reduction under ultrasound irradiation. The effect of reducing reagent, power of ultrasound source, reaction time and temperature in growth of the nanometric silver were studied. Particle sizes and morphology of nanoparticles are depending on power of ultrasound irradiation [16]. The processing by extrusion of polyolefins (polyethylene and polypropylene) nanocomposites with acquisition of properties and biocide activity should be an economically viable method and is has been intensely researched [17–19].

The aim of this research is to study the influence of surface radiation and changes in the morphology of HMS-polypropylene nanocomposite with clay/nanosilver, as well as dispersion of inorganic clusters. It would be desirable if surface radiation of HMSPP could promote silver exposition for detect biocide activity in polypropylene films.

Experimental

Materials

The isotactic Polypropylene (iPP) was supplied by Braskem—Brazil in pellets with MFI = 2.1 dg min^{-1}, M*w* = 470,000 g mol^{-1} and density = 0.905 g cm^{-3}. The acetylene 99.8% supplied by White Martins S/A, of Brazil, was used to synthesis of modified polypropylene. The AgNPs were purchased from Sigma Aldrich, and PVP (average molecular weight = 1,300,000 g mol^{-1}), which acted as a surfactant for the AgNPs, was Plasdone. Silver nanoparticles (AgNPs) were purchased from Sigma Aldrich. The commercial nanoclay Cloisite 20 was provided by BYK Additives Company and antioxidant (BASF Irganox B225ED) was added in small amount 2.0 wt%, to prevent the polypropylene from oxidizing.

Radiation Process

The irradiation of the PP pellets was performed under acetylene atmosphere and used ^{60}Co gamma source at dose rate of 5 kGy h^{-1}. The polypropylene irradiation was performed at 12.5 kGy dose, monitored by a Harwell Red Perspex 4034 dosimeter. After irradiation, the PP pellets were subjected to heat treatment in order to eliminate recombination and residual radicals [20, 21].

Preparations of Clay@AgNPs-PP Nanocomposites

The PP0 (HMSPP 12.5 kGy) in pellet was mixed with Irganox B 215 ED in a rotary mixer and maintained under this condition for 2 h. The mixing Clay@AgNPs was prepared by sonochemical method. For the preparation the solution of PVP with ethanol and AgNPs was in first step, sonificated by 3 h and added with clay, in second step, by one of hour. It was used a Unique ultrasound equipment model DES 500, with a working frequency of 20 kHz and maximum intensity output of 500 W.

Then the mixture was processed with the addition of silver nanoparticles (AgNPs 0.5% by weight) with Clay in a twin-screw extruder Haake co-rotating, model Rheomex PTW 16/25, with the following processing conditions: the temperature profile (feed to die) was 180–210 °C, with a speed of 100 rpm and torque of 37–40 Nm. After processed, the nanocomposites were granulated in a granulator Primotécnica W702-3. These masterbatches (PP0 with AgNPs and clay) were irradiated at doses of (1; 3; 5; 10; 20 and 50 kGy) under an inert atmosphere of nitrogen. The samples were pressed at 190 °C for 15 min in the mold and then cooled to 23 °C. Samples of films in the square dimension of 4 × 4 cm^2 were tested. In this work, the samples are presented according Table I and the PPNC films obtained by extrusion are reported in Scheme 1.

Table 1 Polypropylene nanocomposites (wt%) description

Samples	Dose (kGy)	Irganox	Clay	AgNPs
PP0	0	2	0	0
PPNC0	0	2	1	0.5
PPNC1	1	2	1	0.5
PPNC3	3	2	1	0.5
PPNC5	5	2	1	0.5
PPNC10	10	2	1	0.5
PPNC20	20	2	1	0.5
PPNC50	50	2	1	0.5

Obs.: *PP0* HMSPP 12.5 kGy; *PPNC* Polypropylene nanocomposite

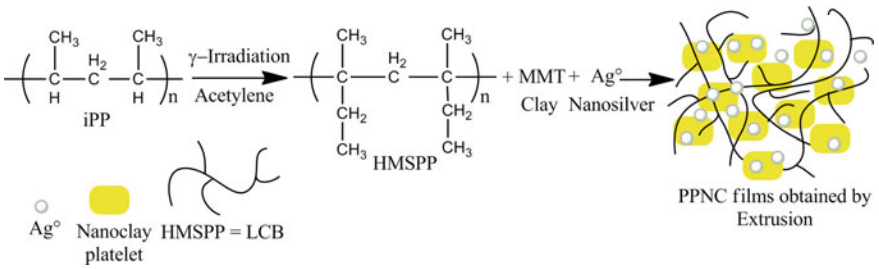

Scheme 1 Model illustrates stabilization and distribution of AgNPs and nanoclay-platelet in film of polypropylene (PPNC)

Simplified Scheme 1 of the preparation process of HMS-polypropylene nanocomposite represents the polymer matrix the iPP being irradiated with gamma rays in the presence of acetylene gas. Consequent formation of long chains branched (LCB) is favorable to homogeneous dispersion of nanosilver. The distribution of the clay is preferably exfoliated and the AgNPs are anchored in PP matrix favorable by LCB chains.

Characterization

Differential Scanning Calorimetry

DSC 822e (Mettler Toledo) was carried out to investigate the crystallization and melting temperature. The samples about 10 mg were melted at 280 °C for 5 min, followed by cooling at a rate of 10 °C min^{-1}. Non-isothermal crystallization were carried out by cooling samples program of −50 to 280 °C at heating rate 10 °C min^{-1} under nitrogen atmosphere with two cycles of heating and cooling.

The crystallinity was calculated according to the Eq. (1):

$$X_C(\%) = Px\frac{\Delta H_f \times 100}{\Delta H_0}. \quad (1)$$

Where: ΔH_f is melting enthalpy of the sample, ΔH_0 is melting enthalpy of the 100% crystalline PP which is assumed to be 209 kJ kg^{-1} [22], and P was the fraction content of PP in the sample.

X-ray Diffraction

X-ray diffraction measurements were carried out in the reflection mode on a PANalytical, model X'Pert PRO, operated at 40 kV voltage and current of 45 mA equipped with an X′ Celerator solid-state linear detector. The diffractometer CuKα radiation (λ = 1.541841 Å) and the spectra were recorded in the 2θ range of 1.0°–80°.

Thermogravimetric Analysis

The thermogravimetric (TG) measurements were performed using Mettler-Toledo, SDTA 851, at temperature range from 25 to 600 °C at heating rate 10 °C min^{-1} under nitrogen atmosphere.

Scanning Electron Microscopy and Energy Dispersive Spectroscopy

Specimens were examined with a Hitachi TM3000 Table-top SEM coupled with a Bruker QUANTAX 70 for the collection of EDX data. SEM coupled with backscattered electron detector (BSE) and energy dispersive X-ray spectroscopy (EDX). Sample sections for the EDX analysis were taken at Analy Mode, and the acquisition period was 120 s.

Determination of Antibacterial Activity

An aliquot (400 μL) of a cell suspension of either *Staphylococcus aureus* ATCC 27853 (10^6 cells mL^{-1}) or *Escherichia coli* ATCC 25922 (10^6 cells mL^{-1}) prepared using the method described in JIS Z 2801 [23]. were held in intimate contact with each of the 2 replicates of the test surfaces supplied using a 45 × 45 mm^2 polypropylene film for 24 h at 37 °C under humid conditions. The viable cells in the suspension were enumerated by viable cell counts on MacConkey Agar after incubation at 37 °C for 24 h using a 100 μL sample taken from the test surfaces.

Results and Discussion

Differential Scanning Calorimetry

The radiation induces changes in the crystallinity of polypropylene and combination of two opposing effects: (1) increase caused by chain scission, therefore degradation and (2) decrease induced by crosslinking of the polymer [24].

The DSC results are summarized in Table 2 and Fig. 1 shows the DSC event of melting in the second heating run of the PP0, as well as the polypropylene nanocomposite PPNC.

According to the results showed in Fig. 1 and Table 2, polypropylene nanocomposite crystallinity is clearly affected by radiation dose. The lower

Table 2 Effects of γ irradiation dose on thermal properties of polypropylene nanocomposite

Samples	Melting peak temperature T_{m2}/°C (±0.1%)	Degree of crystallinity, X_C /% (±0.5%)
PP0	161.1	47.6
PPNC0	161.4	47.3
PPNC1	160.2	44.6
PPNC3	159.7	44.3
PPNC5	158.9	44.4
PPNC10	158.8	45.9
PPNC20	158.8	43.0
PPNC50	157.0	37.6

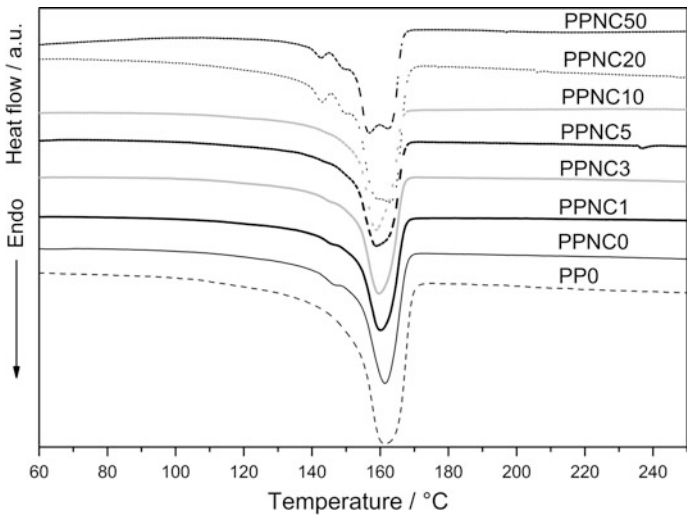

Fig. 1 DSC curves in the melting of the second heating run of PP with different doses radiation (kGy)

crystalline phase percentage was verified mainly in 20 kGy and 50 kGy samples, therefore the reduction in crystallinity was accompanied by formation of crosslinking. The occurrence of double endotherms during DSC in samples PPNC 20 kGy and 50 kGy is attributed to the presence of different crystal transformation during heating, reorganization during heating and segregation of molecules with irregularities that form crystals with lower T*m* [25]. The rise in crystallinity of polypropylene is attributed to the scission of tie molecules located in amorphous phase followed by chemicrystallization forming new perfect lamellae of alfa-crystal chains. However, the reduction in crystallinity at 25 kGy doses was accompanied by formation of crosslinking, β and gamma-phases [26], corroborating with results reported in Table 2 and Fig. 1, for PPNC20 and PPNC50 samples.

X-ray Diffraction

The X-ray diffraction patterns of typical PP@AgNPs@Clay films are illustrated in Fig. 2.

The crystal structure and nature of AgNPs formed were analyzed by XRD. The XRD profiles show, in Fig. 2, characteristics peaks of scattering angles (2θ) of 38.1 and 44.3, 64.4 and 77.3 corresponding respectively to the (111), (200),

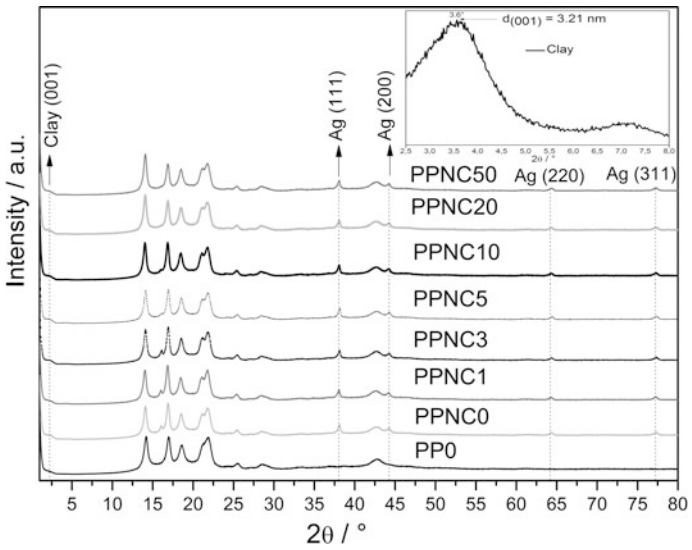

Fig. 2 XRD diffraction patterns of the PP0 and PPNC, polypropylene nanocomposites samples. Highlighted, inset is a framework structure graphic of a Cloisite clay

(220) and (311) crystallographic planes. Diffraction peaks corresponded to interplanar distance of the silver: $d_{(111)}$ = 0.23 nm; $d_{(200)}$ = 0.20 nm; $d_{(220)}$ = 0.14 nm; $d_{(311)}$ = 0.12 nm. Those diffraction peaks represent the face centered cubic crystalline structure of metallic silver [27], respectively (JCPDS file nº 00-004-0783) [28]. Considering the diffraction peaks related to Cloisite 20, the nanocomposites showed a value in the range 3.5–4.4 nm. Nanoclay interlayer diffraction peak $d_{(001)}$ indicated intercalation and exfoliation of the nanoclay platelets owing to displacement of original value from $d_{(001)}$ = 3.2 nm.

Thermogravimetric Analysis

The TG patterns of irradiated PP0 and PPNC films are illustrated in Figs. 3 and 4.

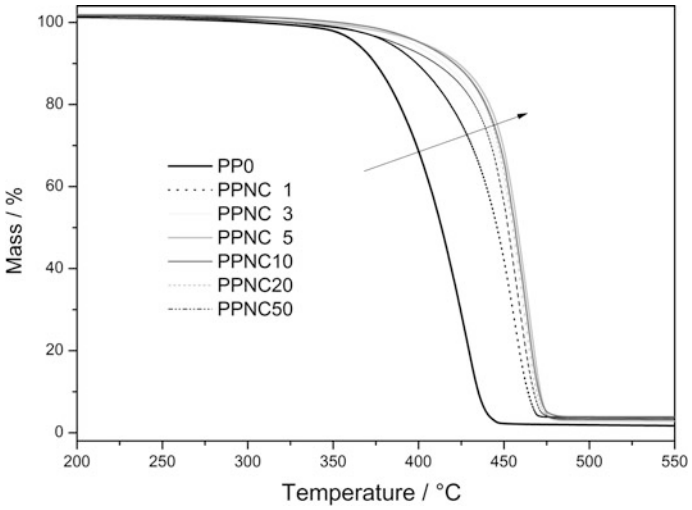

Fig. 3 TG curves of the irradiated samples with different doses radiation

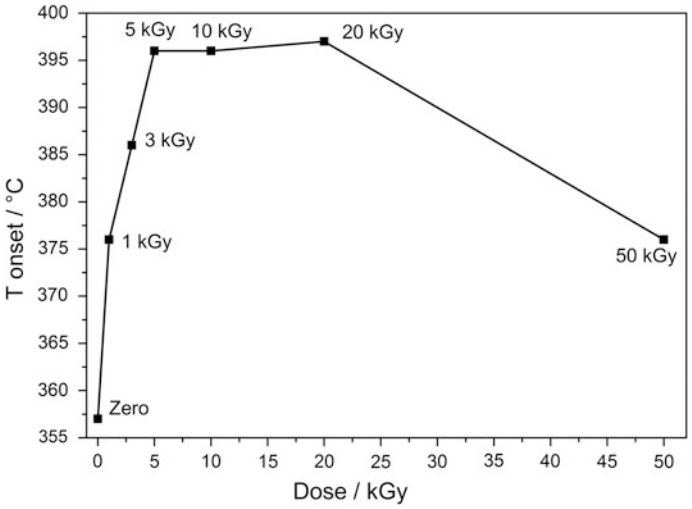

Fig. 4 Onset temperature values of the decomposition step

The influence of ultrasound treatment reflected in better clay dispersion. In consequence a higher decomposition temperature was observed for PPNC. This behavior is related with the clay dispersion and this thermal stability is associated with degree of intercalation/exfoliation, promoting a barrier to the diffusion of oxygen, similar to the result [27]. The ultrasound improved the dispersion of the clay and in consequence the thermal stability. It was evident that improved thermal stability of the material also is associated with gamma radiation to 20 kGy corroborating with the work [29].

Scanning Electron Microscopy and Energy Dispersive Spectroscopy

The Fig. 5 shows the SEM image and EDX data for film PP with silver nanoparticles and silicon and distribution of the particles.

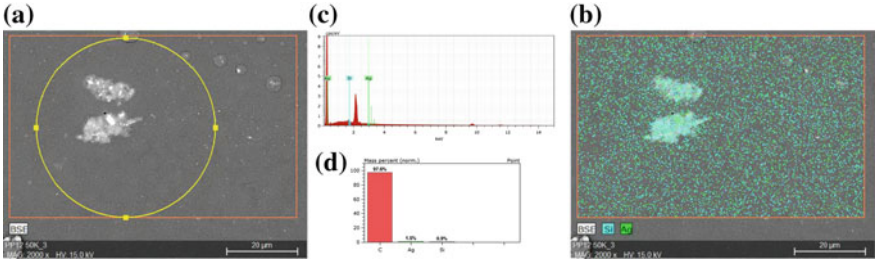

Fig. 5 SEM images and EDX mapping of AgNPs dispersed in the film of polypropylene **a** SEM film PPNC20, scale = 7 μm; **b** mapping of the film with Silicon and silver; **c** EDX data showed silver and silicon; **d** semi-quantitative analysis of silver and silicon

In Fig. 5a, b the evidence of the elemental analysis suggests that the nanofiller are well dispersed within and throughout the bulk PP matrix, supporting the observation that the composite processing was effective. SEM/EDX microscopy showed the one homogeneous distribution of nanoclay and AgNPs in the reposition of regions. The EDX elemental analysis confirmed the presence of silver, Fig. 5c by presence of the peak at around 3.40 keV, energy bands of AgL state, and presence of high concentration of silicon at around 1.75 keV, energy band of SiKα [30–32].

Antibacterial Activity

The antibacterial activity test was performed for all PPNC samples, but the results were not favorable in direct contact of bacteria with the films, and not expressed activity against bacteria *Escherichia coli* and *Staphylococcus aureus.*

Conclusion

The PPNC crystallinity is affected by radiation dose and the lower crystalline phase percentage was verified mainly 20 kGy and 50 kGy samples. The reduction in crystallinity was accompanied by crosslinking and formation of β phase. XRD showed crystal structure of AgNPs in characteristics peaks of scattering angles at 2θ = of 38.1°, 44.3°, 64.4° and 77.3°. The DRX diffraction peak d_{001} displacement values for nanocomposites in 2θ = 2.2° showed the range 3.5–4.4 nm, in comparison to the pure clay indicated intercalation and concomitant exfoliation. Ultrasonic treatment provided better dispersion and in consequence, higher thermal stability was obtained for nanocomposite materials (PPNCs). The tendency of crosslinking of the polypropylene increased with radiation dose of the nanocomposite until 20 kGy. After that dose tendency to degrade was observed by scission

effect. The SEM/EDX showed homogeneous distribution of clay and silver in the film of polypropylene nanocomposite. The antibacterial activity test with the films was not favorable in direct contact test of bacteria and no revealed activity against *Escherichia coli* and *Staphylococcus aureus* bacteria. The irradiations of the surfaces were insufficient to promote silver activity on contact biocide test.

Acknowledgements The authors acknowledge financial support for this work from CAPES-Process: CSF-PVE's-88887.115684/2016-00, CCTM/IPEN, for microscopy analysis (SEM) and multipurpose gamma irradiation facilities at the CTR/IPEN.

References

1. He C, Costeux S, Wood-Adams P, Dealy JM (2003) Molecular structure of high melt strength polypropylene and its application to polymer design. Polymer 44:7181–7188
2. Oliani WL, Parra DF, Lima LFCP, Lugao AB (2012) Morphological characterization of branched PP under stretching. Polym Bull 68:2121–2130
3. Yoshiga A, Otaguro H, Parra DF, Lima LFCP, Lugao AB (2009) Controlled degradation and crosslinking of polypropylene induced by gamma radiation and acetylene. Polym Bull 63:397–409
4. Bhattacharya Amit (2000) Radiation and industrial polymers. Prog Polym Sci 25:371–401
5. Parparita E, Zaharescu T, Darie RN, Vasile C (2015) Biomass effect on γ-irradiation behavior of some polypropylene biocomposites. Ind Eng Chem Res 54:2404–2413
6. Otaguro H, Lima LFCP, Parra DF, Lugao AB, Chinelatto MA, Canevarolo SV (2010) High-energy radiation forming chain scission and branching in polypropylene. Radiat Phys Chem 79:318–324
7. Mrlik M, Maadeed MAAA (2016) Tailoring of the thermal, mechanical and dielectric properties of the polypropylene foams using gamma-irradiation. Polym Degrad Stab 133:234–242
8. Ojeda M, Tokumoto S, Bracanca ALD, Cassinelli LF, Lugao AB, Hutzler BW (2004) Patent application publication Pub. No.: US 2004/0171712 A1
9. Komatsu LGH, Oliani WL, Lugao AB, Parra DF (2016) Nanocomposites of irradiated polypropylene with clay are degradable? Radiat Phys Chem 118:11–15
10. Duncan TT, Pillai K (2015) Release of engineered nanomaterials from polymer nanocomposites: diffusion, dissolution, and desorption. ACS Appl Mater Interfaces 7:2–19
11. Giraldo LF, Camilo P, Kyu T (2016) Incorporation of silver in montmorillonite-type phyllosilicates as potential antibacterial material. Curr Opin Chem Eng 11:7–13
12. Fanelli M, Feke DL, Zloczower IM (2006) Prediction of the dispersion of particle clusters in the nanoscale. Part II—unsteady shearing responses. Chem Eng Sci 61:4944–4956
13. Pokhrel N, Vabbina PK, Pala N (2016) Sonochemistry: science and engineering. Ultrason Sonochem 29:104–128
14. Berenguer IO, Oliani WL, Parra DF, Komatsu LGH, Lincopan N, Lugao AB, Rangari VK (2016) TMS2016—annual meeting supplemental proceedings. Wiley, Hoboken, New Jersey-EUA, 143, Doi:https://doi.org/10.1002/9781119274896.ch18
15. Martínez-Colunga JG, Sánchez-Valdés S, Ramos-de-Valle LF, Muñoz-Jiménez L, Ramírez-Vargas E, Ibarra-Alonso MC, Lozano-Ramirez T, Lafleur PG (2014) Simultaneous polypropylene functionalization and nanoclay dispersion in PP/Clay nanocomposites using ultrasound. J Appl Polym Sci 131(16):1–8

16. Abbasi AR, Kalantary H, Yousefi M, Ramazani A, Morsali A (2012) Synthesis and characterization of silver nanoparticles @polyethylene fibers under ultrasound irradiation. Ultrason Sonochem 19:853–857
17. Oliani WL, Parra DF, Lima LFCP, Lincopan N, Lugao AB (2015) Development of a nanocomposite of polypropylene with biocide action from silver nanoparticles. J Appl Polym Sci 132(42218):1–7
18. Fages E, Fenollar O, Sanoguera DF, Balart R (2010) Study of antimicrobial properties of polypropylene filled with surfactant coated silver nanoparticles. Polym Eng Sci 51:804–811
19. Sahoo RK, Mohanty S, Nayak SK (2016) Effect of silver nanoparticles on the morphology, crystallization, and melting behavior of polypropylene: a study on non-isothermal crystallization kinetics. Polymer Science A 58:443–453
20. Oliani WL, Parra DF, Lugao AB (2010) UV stability of HMS-PP (high melt strength polypropylene) obtained by radiation process. Radiat Phys Chem 79:383–387
21. Oliani WL, Lima LFCP, Parra DF, Dias DB, Lugao AB (2010) Study of the morphology, thermal and mechanical properties of irradiated isotactic polypropylene films. Radiat Phys Chem 79:325–328
22. Mark JE (2007) Physical properties of polymers handbook, 2nd edn. Springer, New York
23. JIS Z2801 (2010) Industrial standard—antibacterial products—test for antibacterial activity and efficacy
24. Suljovrujic E (2009) The influence of molecular orientation on the crosslinking/oxidative behaviour of iPP exposed to gamma radiation. Eur Polymer J 45:2068–2078
25. Rabello MS, White JR (1997) Crystallization and melting behaviour of photodegraded polypropylene—II. Re-crystallization of degraded molecules. Polymer 38(6):6389–6399
26. Alariqi SAS, Kumar AP, Rao BSM, Singh RP (2009) Effect of γ-dose rate on crystallinity and morphological changes of γ-sterilized biomedical polypropylene. Polym Degrad Stab 94:272–277
27. Kakkar R, Sherly ED, Madgula K, Devi DK, Sreedhar B (2012) Synergetic effect of sodium citrate and starch in the synthesis of silver nanoparticles. J Appl Polym Sci 126:E154–E161
28. Zhanga A, Tian Y, Xiao Y, Sun Y, Li F (2015) Large scale synthesis and formation mechanism of silver nanoparticles in solid-state reactions at ambient temperature. Mater Sci Eng, B 197:5–9
29. Hassan MM, El-Kelesh NA, Dessouki AM (2008) The effect of gamma and electron beam irradiation on the thermal and mechanical properties of injection-moulded high crystallinity poly(propylene). Polym Compos 29:883–889
30. Quang DV, Sarawade PB, Hilonga A, Kim JK, Chai YG, Kim SH, Ryu JY, Kim HT (2011) Preparation of silver nanoparticle containing silica micro beads and investigation of their antibacterial activity. Appl Surf Sci 257:6963–6970
31. Xu G, Qiao X, Qiu X, Chen J (2011) Preparation and characterization of nano-silver loaded montmorillonite with strong antibacterial activity and slow release property. J Mater Sci Technol 27(8):685–690
32. Hegde RR, Bhat GS, Spruiell JE, Benson R (2013) Structure and properties of polypropylene-nanoclay composites. J Polym Res 20(12):320–323

Limit Speed Analysis and Absorbed Energy in Multilayer Armor with Epoxy Composite Reinforced with Mallow Fibers and Mallow and Jute Hybrid Fabric

Lucio Fabio Cassiano Nascimento, Luis Henrique Leme Louro, Sérgio Neves Monteiro, Fábio Oliveira Braga, Fernanda Santos da Luz, Jheison Lopes dos Santos, Rubens Lincoln Santana Blazutti Marçal, Hugo Concolato de Oliveira Freitas and Édio Pereira Lima Júnior

Abstract Epoxy matrix composites reinforced with up to 10, 20 and 30 vol% of continuous and aligned natural mallow fibers and 30 vol% of mallow and jute hybrid fabric were for the first time ballistic tested as personal armor against class III 7.62 mm FMJ ammunition. The ballistic efficiency of these composites was assessed by measuring the dissipated energy and residual velocity after the bullet perforation. The results were compared with that in similar tests of aramid fabric (Kevlar™) commonly used in vests for personal protections. Visual inspection and scanning electron microscopy analysis of impact-fractured samples revealed failure mechanisms associated with fiber pullout, rupture and layers delamination. When compared to Kevlar™, the mallow fiber and hybrid fabric composite displayed practically the same ballistic efficiency. However, there is a reduction in both weight and cost, which makes both, mallow fiber and hybrid fabric composites, a promising material for personal ballistic protection.

Keywords Ballistic test · Mallow fibers · Composites

Introduction

The development of ballistic armor systems, increasing efficiency, appears as a fundamental element to guarantee personal and vehicle security for military applications.

L. F. C. Nascimento (✉) · L. H. L. Louro · S. N. Monteiro · F. O. Braga · F. S. da Luz
J. L. dos Santos · R. L. S. B. Marçal · H. C. de Oliveira Freitas · É. P. Lima Júnior
Militar Institute of Engineering—IME, Rio de Janeiro, Brazil
e-mail: lucio_coppe@yahoo.com.br

B. Li et al. (eds.), *Characterization of Minerals, Metals, and Materials 2018*, The Minerals, Metals & Materials Series,
https://doi.org/10.1007/978-3-319-72484-3_63

Therefore, a tripod formed by mobility, resistance to penetration and impact absorption is the main factor that make ballistic armouring efficient. However, the improvement in one of these factors often negatively influences another. For example, an increase in penetration resistance may cause a reduction in mobility, due to the necessary increase of thickness and, consequently, weight in monolithic steel armours [1]. With this, it becomes necessary to seek new engineering solutions to improve the targets protection. In this context, armours constituted by ceramic components associated with other materials, such as polymer composites, are employed to favor a good ratio between ballistic protection and weight [2]. These are called multilayer armouring systems (MAS).

However, synthetic materials, such as Kevlar™, present in the composite as the intermediate layer, have drawbacks, such as high acquisition and processing costs, as well as environmental damages, due to their degradation time after the service life. As a result, constant research efforts are looking for new alternative materials that can efficiently replace synthetic ones and are environmentally friendly. In this context, natural lignocellulosic fibers (NLFs) can play an important role because of its advantages, such as: good specific properties (low specific mass), low toxicity, biodegradability, low cost, etc. In addition, they make it possible to foster the economic and technological development of Brazil's less favored regions, such as the northern and northeastern regions, which are major producers of natural fibers. Other properties can be found in Table 1.

The goal of this study is to analyze the ballistic efficiency of epoxy matrix composites with different percentage of mallow fibers (0, 10, 20 and 30 vol%.) and 30 vol% of hybrid fabric mallow and jute (70 wt% mallow/30 wt% jute). The ballistic test consists in determining the residual bullet velocity after its impact on the target (specimen). This velocity is related to the energy that the composite absorbs during the impact—the greater that energy, the more efficient the composite will be. After, a scanning electron microscopy (SEM) is performed to observe fracture mechanisms in the composites.

Table 1 Properties of aramid fiber, mallow fiber, jute fiber and epoxy resin [2–6]

Materials	Density (g/cm^3)	Tensile resistance (MPa)	Young's modules (GPa)	Specific resistance (MPa)	Specific modules (GPa)
Aramid	1.4	3000–3150	63–67	2143–2250	45–48
Mallow	1.4	160	17.4	116	13
Jute	1.3–1.4	393–800	13–27	271–615	9.3–21
Epoxy	1.1–1.3	60–80	2–4	46–73	1.5–3.6

Materials and Methods

The mallow fiber and mallow and jute hybrid fabric has been used as reinforcement in the composite. The fibers were provided by State University of Northern Rio de Janeiro (UENF) and hybrid fabric commercially supplied by the Brazilian firm Castanhal Textile Company. Firstly, the fibers were cleaned, aligned and cut in length of 150 mm. After, they were maintained in an oven for 24 h to reduce the absorbed moisture. The hybrid fabric was cut in the dimensions of 150 × 120 mm and kept in an oven for 24 h. The as received bundle of fibers and the mallow and jute hybrid fabric are showed in Fig. 1.

The composite matrix was diglycidyl ether of the bisphenol A (DGEBA), which is a commercial epoxy resin, mixed with trietylene tetramine (TETA) hardener in a proportion of 13 parts of hardener per 100 parts of resin in weight. Both components are fabricated by the Brazilian firm Dow Chemical and commercially supplied by the distributor RESINPOXY Ltda.

Composites with 0, 10, 20 and 30% in volume of mallow fibers and composites with 30 vol% of mallow and jute hybrid fabric (Fig. 2) were manufactured, in a

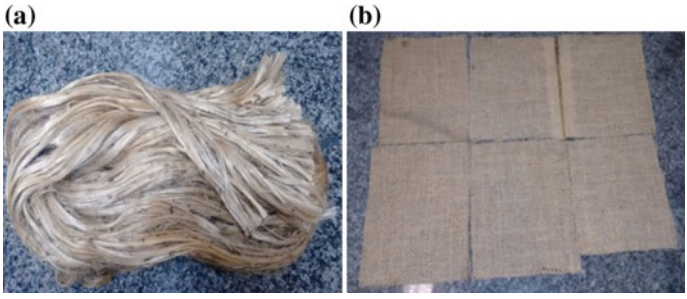

Fig. 1 Mallow fibers: **a** as received bundle of fibers; **b** mallow and jute hybrid fabric (70 wt% mallow/30 wt% jute)

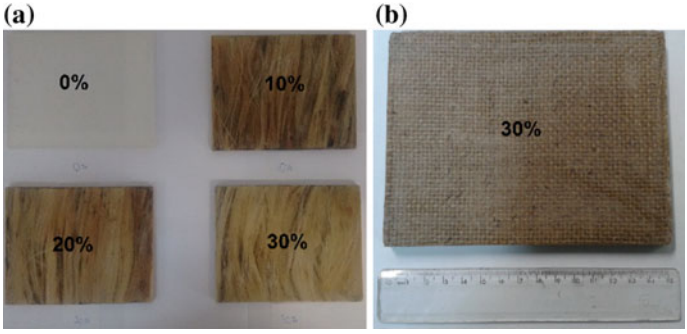

Fig. 2 Composite plates of epoxy reinforced with: **a** 0, 10, 20 and 30 vol% of mallow fibers. **b** 30 vol% of mallow and jute hybrid fabric

total of 8 unites for each concentration. A pressure of 5 MPa was applied and the composite plate, cured for 24 h [2, 7]. It was used, to mallow fibers and hybrid fabric an initial density reference of 1.40 g/cm^3 [8] and for the epoxy resin (DGEBA-TETA) a value of 1.11 g/cm^3 [7].

The ballistic tests were conducted at the Brazilian Army shooting facility, CAEX, Rio de Janeiro. The tests were carried out according to the NIJ 0101.04 standard, using 7.62 mm FMJ military ammunition (m = 9.7 g—Armor level III). Figure 3 shows, schematically, the exploded view of the ballistic test setup. A dashed straight line indicates the projectile trajectory. A steel frame was used to position the target, which was held in place by spring clips (Fig. 4a). The gun, located 15 m from the target, was aligned by laser beam. The projectile velocity was measured at three moments: leaving the gun; immediately before impacting (V_i); and, after the impact, the residual velocity (V_r) was measured by an optical barrier and a SL-52 OP Weibel fixed-head Doppler radar system (Fig. 4b). The Kinetic energy (ΔE_d) dissipated inside the target, could then be estimated by the Eq. (1):

$$\Delta E_d = \frac{1}{2} m\left(V_i^2 - V_r^2\right) \tag{1}$$

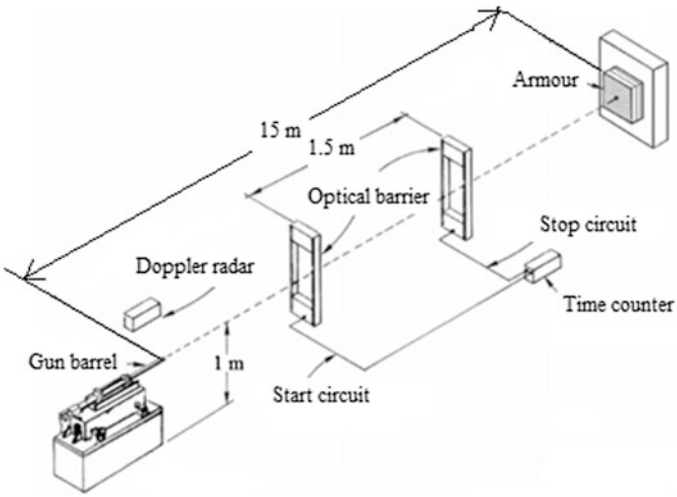

Fig. 3 Schematic exploded view of the ballistic experimental setup [2]

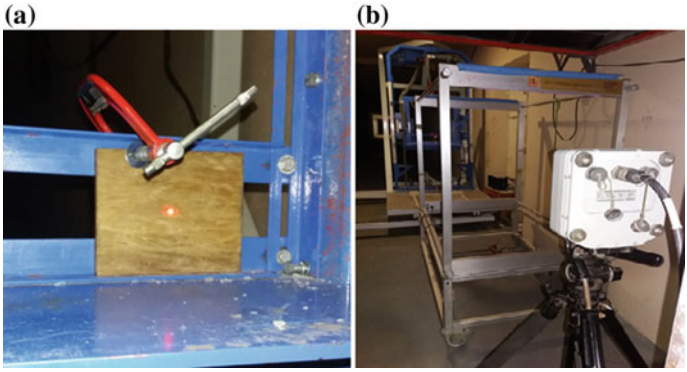

Fig. 4 **a** Specimen of composite plate fixed in the metal bracket with spring clips. **b** Apparatus of CAEX for ballistic testing with ammunition and doppler radar

Results and Discussions

In order to verify the individual ballistic resistance of each component of the MAS, the residual velocity test was performed, and it was possible to estimate the absorbed energy (E_{abs}) and the limit velocity (V_L) of each sample with the aid of a radar (Fig. 4b) and using Eq. (1). In the tests, all the samples were perforated and crossed by the projectile, fact that allowed the measurement of the energy absorbed by each component present in the armour. Figure 5 exemplifies the experimental

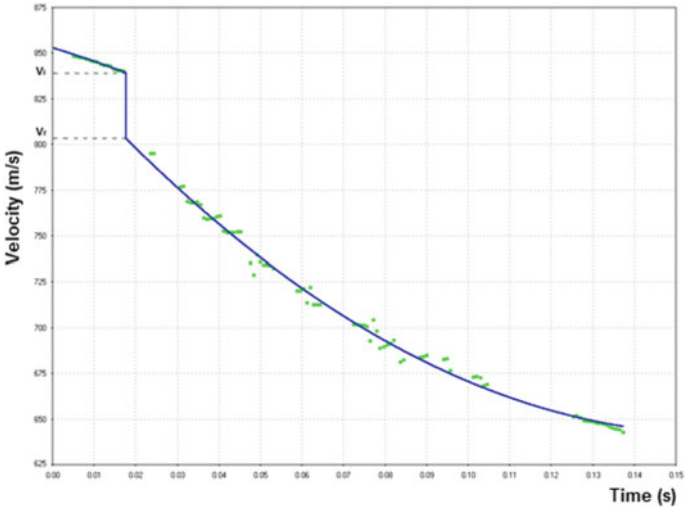

Fig. 5 Graph of experimental points of the reinforced epoxy composite with 30% vol. of mallow fibers

Table 2 Impact, residual velocities and internally dissipated energy data in ballistic tested in composites reinforced with mallow fibers [2, 7, 9, 10]

Armour components	V_i (m/s)	V_r (m/s)	E_{abs} (J)	% E_{abs}	V_L (m/s)	References
Aramid fabric (16 layers)	862 ± 7.00	835 ± 10.00	221.00	6.10	212 ± 23	[10]
Composite 100% epoxy	848.08 ± 6.20	817.01 ± 8.87	250.73	7.20	227.02 ± 12.52	*PW
Composite hybrid 70 wt% mallow/30 wt% jute (30 vol%) —fabric	845.62 ± 4.67	815.13 ± 4.86	245.59	7.08	224.40 ± 16.83	*PW
Composite 100% mallow (30 vol%)– fibers	840.00 ± 11.19	807.96 ± 11.52	256.02	7.48	229.54 ± 10.06	*PW
Composite 100% mallow (20 vol%)— fibers	843.39 ± 5.33	807.07 ± 8.57	290.53	8.42	243.81 ± 21.42	*PW
Composite 100% mallow (10 vol%)— fibers	845.02 ± 6.78	815.09 ± 9.78	240.72	6.95	220.92 ± 28.77	*PW
Composite epoxy–jute (30 vol%)—fabric	841.45 ± 6.50	822.81 ± 6.41	150.50	4.40	176.16	[2]
Composite epoxy–sisal (30 vol%)—fabric	844.91 ± 6.04	817.46 ± 4.82	221.33	6.40	213.62	[9]
Composite epoxy–curauá (30 vol%)— fibers	848.30 ± 6.36	835.29 ± 6.17	106.16	3.00	147.95	[7]

* PW - Present Work.

points obtained from the Doppler radar spectrum of a test specimen of the epoxy composite mallow fibers (30 vol%) and the adjusted continuous polynomial curve.

It can be seen, that at approximately 840 m/s there was an abrupt drop in velocity, characterizing the moment of impact on the target. This velocity was defined as the velocity of impact (V_i) and the minimum velocity reached at that fall defined as the residual velocity (V_r). Similar graphs were obtained for other components of the MAS and based on the results extracted from these graphs both the limit velocity (V_L) and the absorbed energy (E_{abs}) were determined. The results of the average impact velocity (V_i), mean residual velocity (V_r), absorbed energy (E_{abs}) and their percentage in relation to total energy (% E_{abs}) are shown in Table 2, as well as the estimated limit velocity (V_L). For comparative purposes, data from other authors who also studied MAS based on natural fibers were also presented in Table 2 [2, 7, 9, 10].

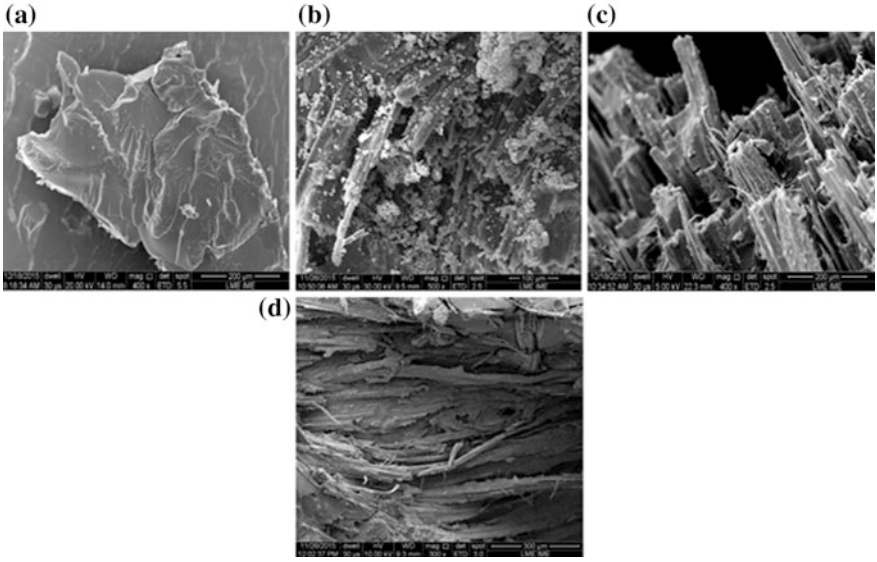

Fig. 6 **a** Composite 100% epoxy (400x); **b** composite epoxy reinforced with mallow fabric 30 vol% (500x); **c** composite epoxy reinforced with mallow fibers 30 vol% (400x); **d** composite epoxy reinforced with 30 vol% of mallow and jute hybrid fabric (70 wt%/30 wt%) (300x)

The values of the limit velocity (V_L) and absorbed energy (E_{abs}) for epoxy matrix composites reinforced with hybrid mallow /jute (70/30) or mallow fibers presented values higher than those found by other authors for aramid [10], epoxy reinforced with sisal [9], epoxy reinforced with curauá fibers [7], epoxy-jute fabric [2]. This fact can be explained by the good mechanical properties of mallow and jute, as shown in Table 1. Besides, the fragile fracture mechanisms of the epoxy matrix, together with ductile mechanisms such as delamination between layers, elastic deformation of the composite, shear of the layers and stress at fiber rupture are responsible for the dissipation of a greater amount of kinetic energy [2].

Regardless of the type of composite tested, SEM images (Fig. 6b, c and d) clearly demonstrates the similarity in the main fracture mechanisms: layer delamination, fiber fracture and fiber pull-out. As an exception, the image of Fig. 6a shows a fracture surface of the 100% epoxy plate, which presented complete fracture after ballistic impact, justifying the high-energy absorption, compatible with the other groups tested. However, the main working mechanisms were those corresponding to fragile and catastrophic fracture, typified by the cleavage of planes and river marks.

Conclusions

Scanning electron microscopy analysis of the fractured surfaces showed the mallow, as fibers or fabrics with jute, contributed in an effective way to increase the resistance of the epoxy matrix through mechanisms of energy absorption, such as delamination of layers, detachment and disruption of fibers.

The values of limit velocity (V_L) and absorbed energy (E_{abs}), for epoxy matrix composites reinforced with mallow fibers or hybrid mallow/jute fabrics (70 wt%/30 wt%) presented higher values than those found by other authors for aramid [10], epoxy reinforced with jute fabric [2], epoxy reinforced with sisal fabric [9], epoxy reinforced with curauá fibers [7]. In all cases analyzed by this work, the parameters obtained for limit velocity and absorbed energy were higher than those found for aramid fabric, which shows the viability of natural lignocellulosic fibers for use in ballistic applications as a component of a multilayered armour system.

Acknowledgements The authors acknowledge the support to this investigation by the Brazilian agencies CNPq, CAPES, FAPERJ and UENF for supplying the mallow fibers.

References

1. Borvik T, Langseth M, Hopperstad OS, Malo KA (1999) Ballistic penetration of steel plates. Int J Impact Eng 22:885–886
2. Luz FS (2014) Ballistic behavior evaluation multilayered armour with epoxy composite reinforced with jute fiber (dissertation). Military Engineering Institute, Rio de Janeiro (in Portuguese)
3. Medvedovski E (2010) Ballistic performance of armour ceramics: influence of design and structure. Part 1. Ceram Int 36:2103–2115
4. Lee YS, Wetzel ED, Wagner NJ (2003) The ballistic impact characteristic of Kevlar woven fabrics impregnated with a colloidal shear thickening fluid. J Mater Sci 38:2825–2833
5. Nascimento LFC (2017) Characterization of the epoxy-mallow fiber composite for use in multilayer ballistic armouring (thesis). Military Engineering Institute, Rio de Janeiro (in Portuguese)
6. Margem JI (2013) Analysis of structural characteristics and properties of polymer composites reinforced with mallow fibers (thesis). State University of Norte Fluminense, Rio de Janeiro (in Portuguese)
7. da Silva LC (2014) Ballistic behavior of natural fiber epoxy composite multi-layer armour (thesis). Military Engineering Institute, Rio de Janeiro (in Portuguese)
8. Oliveira JTS (1998) Characterization of eucalyptus wood for construction (thesis). Polytechnic School of the University of São Paulo, São Paulo (in Portuguese)
9. de Araújo BM (2015) Evaluation of ballistic behavior of multi-layered armouring with epoxy composite reinforced with sisal fiber (dissertation). Military Engineering Institute, Rio de Janeiro (in Portuguese)
10. Braga FO (2015) Ballistic behavior of a multi-layered armouring using polyester-Curauá composite as intermediate layer (dissertation). Military Engineering Institute, Rio de Janeiro (in Portuguese)

Mechanical, Thermal and Electrical Properties of Polymer (Ethylene Terephthalate—PET) Filled with Carbon Black

Anderson dos Santos Mesquita, Leonardo G. de Andrade e Silva and Leila Figueiredo de Miranda

Abstract This work seeks to understand if PET compounds with carbon black can be uses to replace polypropylene and polystyrene for anti-static packaging materials. PET compounds were fabricated containing 10.0; 11.0; 12.0 and 15.0 weight % of carbon black with a particle size 325 mesh. We determined the thermomechanical properties (Dynamic Mechanical Analysis—DMA, Tensile Properties, Fracture Toughness, and Hardness) and Electrical properties of the compounds. In conclusion the results show the compound based on PET filled with 15.0% carbon black might be used in the handling, transportation and storage of electronic components because their mechanical properties, thermal and resistivity are satisfactory for this purpose.

Keywords Carbon black · Conductivity · Ethylene terephthalate

Introduction

Some polymers present electric conductivity decrease being this conductivity low in the organic polymers.

The organic conductive polymers have been widely used due to their properties and capacity to conduct electricity. Moreover, they allow the addition of doping agents, which increase the conductivity of these materials [1].

The conductive polymers have a common characteristic, a variance of simple bonds (σ) and double (π) along the chain.

Anderson dos S. Mesquita (✉) · L. G. de Andrade e Silva
Instituto de Pesquisas Energéticas e Nucleares (IPEN-CNEN/SP),
Av. Prof. Lineu Prestes, 2242, São Paulo, SP 05508-000, Brazil
e-mail: anderson.mesquita@usp.br

L. F. de Miranda
Universidade Presbiteriana Mackenzie, Rua da Consolação 930,
São Paulo, SP 01302-907, Brazil

B. Li et al. (eds.), *Characterization of Minerals, Metals, and Materials 2018*, The Minerals, Metals & Materials Series,
https://doi.org/10.1007/978-3-319-72484-3_64

From the decade of 1960 it is known that the variance of double bonds can show semi conductive properties in the polymers. The first conductive polymers had little technological value, since they were infusible and insoluble due to having rigid chains to be rigid with a conjugated structure [2].

Since their discovery in the middle of the decade of 1970, the conductive polymers have been developed by several research institutions. These researches have helped the industry in the development of conductive polymers and have provided the understanding of the physics, chemistry and of the science of the materials. The recognition of the importance of these polymers started in the year of 2000 year when the Chemistry Nobel Prize was awarded for three researchers of conductive polymers: Alan MacDiarmid, Alan Heeger and Hideki Shirakawa [3].

The great economical interest is to mix the properties of a semiconductor with the characteristics of a polymer.

The carbon black (CB) is a widely used additive as anti-static agent in polymers such as polypropylene (PP) and also in polystyrene (PS) in the manufacture of packings in order to increase the conductivity of these packings avoiding electric unloading and, consequently, damage.

Brady et al. [4] report that usually polymers are conductors of electricity with the addition of carbon black, fiber of carbon, conductive ceramic, nickel, silver, or other metal. The resistance of plastics and rubbers, which normally are between 2.5×10^8 V/in (10^8 Ω/cm) can be reduced between 0.25 V/in (1021 V/cm) and 2.53106 V/in (106 Ω/cm) in addition of conducting materials. The CB is the most used load. The relation added to the material and the resistance in volume is not proportional. With up to 25% of conductive load, it increases significantly, but it falls drastically after that. Generally, the addition of CB reduces the mechanical properties of the polymers. However, the use of fibers of carbon to improve conductivity improves the mechanical properties.

Nowadays due to the economic growth and the consumption of goods and services there has been an increased consumption of packings.

Materials with mechanical properties and good conductive properties have been interest of several sectors of industry, especially the automotive and electronic components.

Despite the use of the anti-static additive in ethylene terephthalate—PET [5], there are not many studies regarding the usage of this polymer filled with CB and its features for using in the transport and storage of electronic products.

The standards ASTM-D-257 and the ASTM-D-991 were given out in 1925 and 1948 respectively by the American Society For Testing and Materials (ASTM). These tests were designed to define and measure the anti-static material [6].

The classification of resistance [7] is shown in Fig. 1.

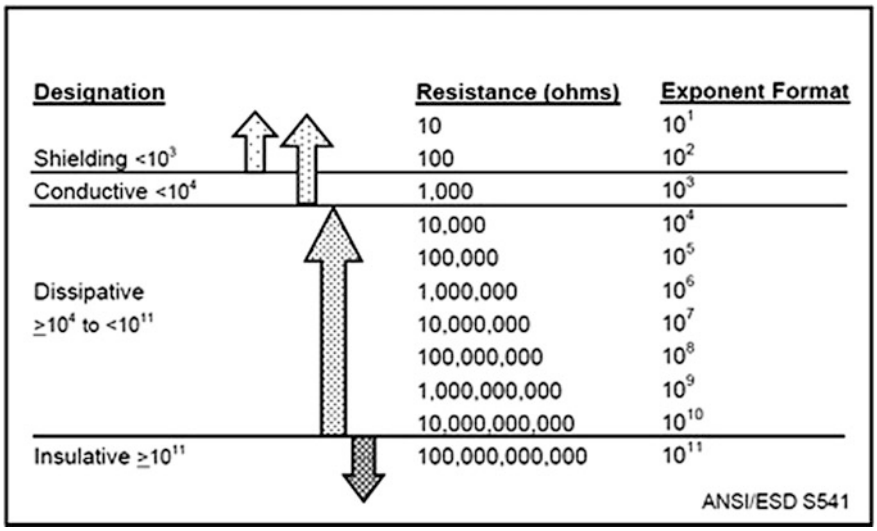

Fig. 1 Resistance classifications

Experimental

Materials and Compounds

Table 1 shows the quantity of PET filled with carbon black.

PET compounds were fabricated containing 10.0; 11.0; 12.0 and 15.0 weight % of CB.

The CB reduces the superficial resistance of polymers such as polyamide and polypropylene. The reduction of the superficial resistance is observed in concentrations up to 10% of the mass of the formed compound [8].

After the separation of the materials, the mixtures were put in a closed mixer, where the temperature had been taken close to 230 °C, resulting in a black polymer mass.

The polymer compounds obtained after the cooling were broken up in a cutting mill manufactured by SEIBT and were used in the subsequent process of injection. To obtain the samples, the materials were dried out in dehumidifier with circulation of air at the temperature of 100 °C, for 2 h and subsequently they were injected.

The materials and samples are shown in Table 1. The samples can be seen in Fig. 2.

Table 1 Basic information of the raw materials used in this study

Samples	Materials
Compound 1—C1	PET + 10% CB
Compound 2—C2	PET + 11% CB
Compound 3—C3	PET + 12% CB
Compound 4—C4	PET + 15% CB

Fig. 2 Images of the samples after the injection process

Characterization

4 types of samples for characterization were obtained (Table 1).

The samples were characterized according to:

Mechanical Properties: Tensile strength, fracture toughness and hardness;
Thermal Properties: Dynamic mechanical analysis (DMA);
Electric Properties: Resistance.

The tensile strength was carried out according to the ASTM D-638 standards. The equipment used was the Universal Machine of Tests Q-Test, model 65 J. The samples were kept at a temperature of (23 ± 2) °C, with relative moisture of (50 ± 5)%, during 72 h before the beginning of the tests. The tests were carried out at the standard atmosphere, always obeying to the same conditions. In the tests of tension 10 samples of each composite were used. The speed of dislocation of the crossbeam for the composites was of 5.00 mm/min.

Elongation at break (%) and tensile strength (MPa) of the samples were analyzed. The tension (σ) corresponds to strength (F) divided by the area of the section (A) of the sample.

The fracture toughness was carried out in the equipment of the Tinius Olsen, model 892 and carved in a mountain range model Tinius Olsen 899, following the ASTM D-256 standards. In the preparation of the samples were used 10 pieces, for each type of compound of PET filled with CB.

By using a digital caliper rule measurements of thickness of each one of the pieces were taken. The samples of this test presented thickness from 3.19 to 3.45 mm.

The hardness was measured by using a digital hardness test Shore D, according to the ASTM D-2240 standards.

The dynamic mechanical analyses were carried in equipment by the Perkin Elmer Instruments, model DMA 8000 of the ASTM D-4092 standards.

The electric resistance tests were carried by using the surface resistance meter by POWER, model 386, according to the ASTM D-257 standards.

The samples were kept at a temperature of (23 ± 2) °C, with relative moisture of (50 ± 5)%, during 72 h before the beginning of the tests. The tests were carried out at atmosphere standard, following the same conditions.

Results and Discussion

Tensile Properties and Glass Transition Temperature

The basic mechanical properties of the compounds filled with carbon black are shown in Fig. 3 and summarized in Table 2. It can be observed from Fig. 2 that the bigger concentration of CB in the compound PET/CB to the great tensile strength of the compound. Comparing the values of tensile strength of the compounds of PET containing CB, it verified that in the compound PET/11% CB there was an increase of the order of 15.46% of the tension regarding the compound PET/10% CB. In the compound PET/12% CB the increase was of the order of 58.41% regarding the compound PET/10% CB and in the compound PET/15% CB this increase was 157.39% regarding the compound PET/10% CB, showing that the CB acts like a load of reinforcement in the compound. The bigger the concentration of CB in the compound the PET/CB is the biggest very deformation in the break of the compound.

Comparing the values of elongation at break of the compounds of PET containing CB, it verified that in the compound PET/11% CB there was an increase of the deformation of the order of 25% regarding the compound PET/10% CB. In the compound PET/12% CB the increase was of the order of 100% regarding the compound PET/10% CB. In the compound PET/15% CB this increase was of the order of 225% regarding the compound PET/10% CB. The bigger the concentration of CB in the compound the PET/CB least is the module of elasticity of the compound, indicating that the presence of the CB reduces the rigidity of the compound. Probably, the presence of the CB reduces the crystallinity of the PET. Comparing

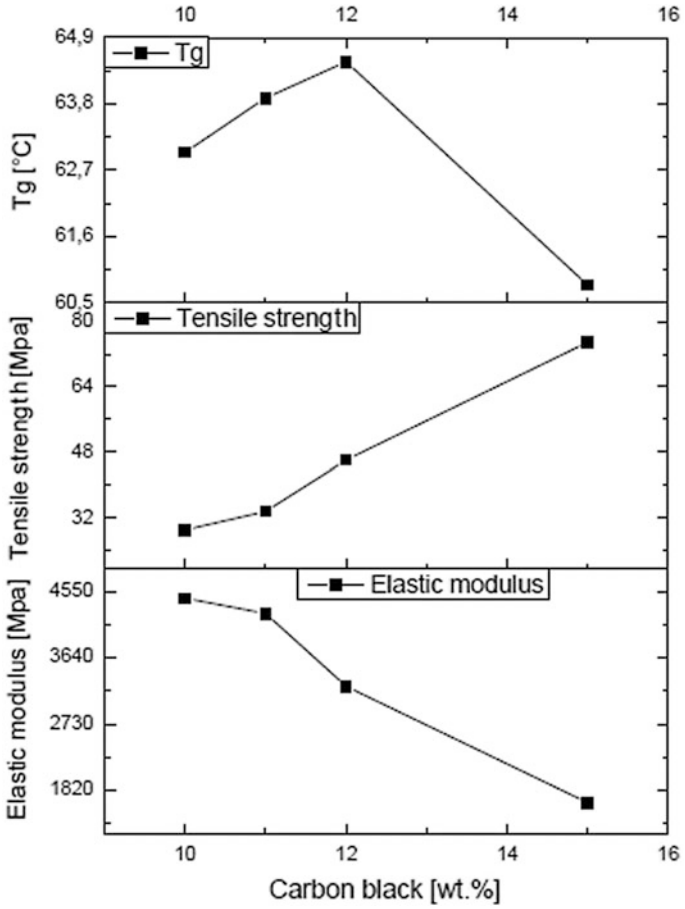

Fig. 3 Tensile properties and glass transition temperature of the PET filled with carbon black compounds

the values of the elasticity module of the compounds of PET containing CB, it verified that in the compound PET/11% CB there was a decrease in the order of 4.92% in the values obtained for the compound PET/10% CB. In the compound PET/12% CB the decrease was of the order of 37.24% regarding the compound PET/10% CB.

In the compound PET/15% CB the decrease was of the order of 170.16%, showing that the increase in the concentration CB probably causes a decrease in the crystallinity of the compounds.

The glass transition temperature (Tg) of the compounds is summarized in Table 2. The mobility of the atoms in the molecules is straightly proportional to the temperature, so, the chemical-physical knowledge of the characteristics of a polymer is basic for the understanding of his thermomechanical performance [9].

Table 2 Mechanical properties, glass transition temperature and resistance of PET+CB compounds

Compound	Modulus (MPa)	Tensile strength (MPa)	Elongation at break (%)	Fracture toughness (J/m)	Tg(°C)	Hardness (Shore-D)	Resistance (Ω)
PET + 10% CB	4459 ± 611	29.1 ± 5.6	0.8 ± 0.2	15.09 ± 1.60	63.0	83.8 ± 0.6	$10^{10} \pm 10^{2}$
PET + 11% CB	4250 ± 605	33.6 ± 4.0	1.0 ± 0.1	15.56 ± 2.36	63.9	83.8 ± 2.0	$10^{9} \pm 10^{1}$
PET + 12% CB	3249 ± 115	46.1 ± 5.0	1.6 ± 0.2	15.92 ± 2.21	64.5	86.0 ± 0.7	$10^{8} \pm 10^{1}$
PET + 15% CB	1649 ± 550	74.9 ± 6.0	2.6 ± 0.5	17.12 ± 1.68	60.8	86.4 ± 0.5	$10^{6} \pm 10^{1}$

The % weight of CB increased the temperature of glass transition (Tg) presented in the compounds of PET/CB, except in the compound PET/15% CB, where the considered result (60.8 °C) is lower than PET/12% CB (64.5 °C) the major value. The presence of the CB increases the interaction between the chains of PET and reduces his elastic properties. Probably, for concentrations bigger than 12% the CB reduces the interaction between the polymeric chains.

Fracture Toughness and Hardness

The fracture toughness of the PET filled with carbon black compound is presented in Table 2. The variation in the energy absorbed under impact was less, except in the PET/15% CB that increased 13.45% regarding the PET/10% CB, 10.02% regarding the PET/11% CB and 7.54% regarding the PET/12% CB (Fig. 4).

The % weight of CB increased the resistance to the impact of the compounds to the base of PET.

The hardness is summarized in Table 2. The % weight of CB increased the hardness Shore D of the compounds, except for the compounds filled with 10 and 11% CB, where there was no variation in the considered values.

The major hardness value was PET/15% CB (86.4 D) that regarding the compounds PET/10 and 11% CB had a value 3.10 bigger % and only 0.47% regarding the compound PET/12% CB.

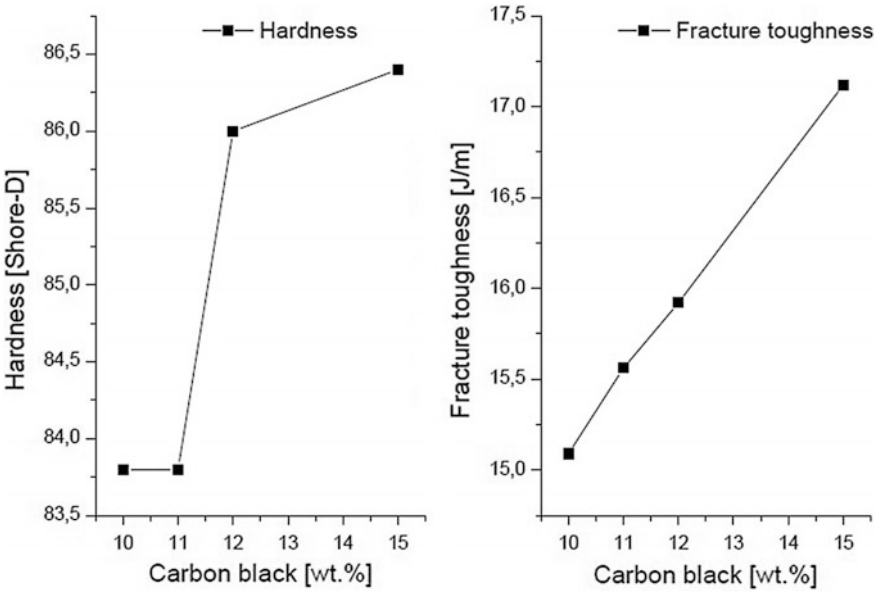

Fig. 4 Fracture toughness and hardness of the PET filled with carbon black compounds

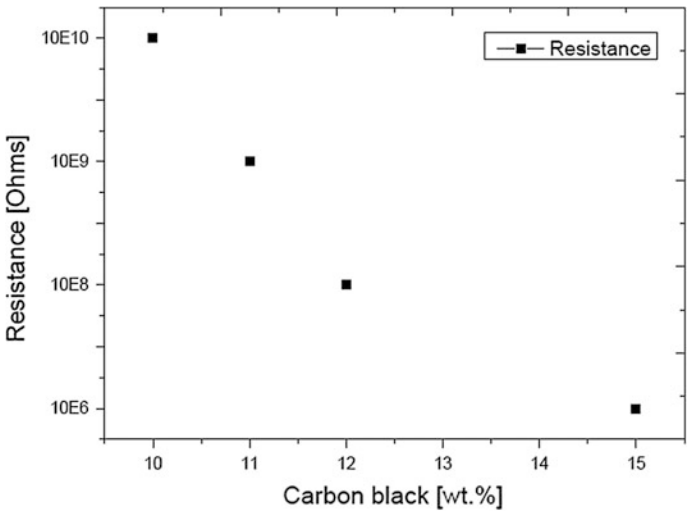

Fig. 5 Resistance of the PET filled with carbon black compounds

Resistance

The resistances of the compounds are shown in Table 2 and are plotted in Fig. 5. The presence of the CB increased the conductivity of the compounds to the PET/CB and decreased linearly the resistance. Its ability to conduct electricity is based on the alignment of the polymeric chains [simple (σ) and double bonds (π)] due to presence of CB. The compound 4 filled with 15% of carbon black showed resistance equal to $10^6 \pm 10^1$ Ω that according to the resistance classifications, it would fit as dissipative, if it was used for electronic transport components.

Conclusions

This work allowed us a better understanding about the PET compounds filled with carbon black.

In conclusion the results showed the compound based on PET filled with 15.0% carbon black might be used in the handling, transportation and storage of electronic components because their mechanical properties, thermal and resistivity are satisfactory for this purpose. The carbon black besides reducing the resistance of the compound, acts like filled of reinforcement.

The analysis of the thermal properties showed coherent results.

Acknowledgements The authors thank Universidade Presbiteriana Mackenzie for supporting this project. The authors also thank both the professionals of the "Grupo M&G", Edson Oliveira and

Fabio Xavier for providing samples of PET, and the technicians Luiz Henry Silveira, Abner Cabral Neto and Maria Lioba Crespo, of the Laboratory of Tests and Characterization of Materials of the Universidade Presbiteriana Mackenzie for the support to obtain and characterize the samples of this work.

References

1. Fried JR (1995) Polymer science and technology. Prentice Hall, New Jersey
2. Maia D, De Paoli M, Alves O, Zarbin A, Neves S (2000) Síntese de polímeros condutores em matrizes sólidas hospedeiras. Quim Nova 23(2):204–215
3. Wallace GG, Spinks GM, Kane-Maguire LAP, Teasdale PR (2003) Conductive electroactive polymers: intelligent materials systems. CRC Press, Florida
4. Brady GS, Clauser HR, Vaccari JA (2004) Materials handbook. McGraw-Hill, Nova York
5. Fabris S, Freire MTA, Reyes FG (2006) Embalagens Plásticas: tipos de materiais, contaminação de alimentos e aspectos de legislação. Revista Brasileira de Toxicologia 19 (2):59–70
6. Weitz S (2013) Electro-Tech System. Trends in ESD test methods
7. ESD Association Standard—ANSI/ESD S541-2008 (2008) For the protection of electrostatic discharge susceptible items—packaging materials for ESD sensitive items. New York
8. Dahman SJ (2003) All polymeric compounds: conductive and dissipative polymers in ESD control materials. RTP Company, East Front St, Winona
9. Canevarolo Junior SV (2002) Ciência dos polímeros: um texto básico para tecnólogos e engenheiros. Artliber, São Paulo

Mineralogical Analysis of a Chrome Ore from South Africa

Ming-Feng Ye and Guang-Liang Wu

Abstract The investigations on chemical composition, mineral composition, embedded figures, texture and microstructure of chrome ores were conducted systematically by various analysis methods such as chemical analysis, XRF, SEM, and MLA 650 system. The results showed that there are 92.66% chromite and a small amount of chlorite and forsterite as the main mineral compositions, the content of quartz is very low. Elements as Cr and Fe are almost all present in chromite. The content of Cr_2O_3 is 41.84% and Cr_2O_3/FeO is 2.1. The main elements in the chromite are Cr, Fe, Mg, Al, O; the main elements in the chlorite are Mg, Al, Si, O and a small amount of Fe; the main elements in the forsterite are Mg, Si and O. On the basis of clarifying the mineralogical characteristics, to produce high-grade alloy, this ore should not be separately put into the submerged arc furnace without pretreating. However, it also seems to be difficult to separate the gangue compositions by the conventional physical upgrading methods, such as magnetic separation and gravity separation. So, chemical mineral processing should be taken into account.

Keywords Chrome ore · Mineralogy · Mineral composition · Embedded characteristics

Introduction

Chrome ore is mainly used in metallurgy, refractory and chemical industries, the proportion consumption of chrome ore in the metallurgy industry accounts for more than 80% [1, 2], and With the rapid development of stainless steel industry, this proportion will further increase [3]. In China, the chrome ore is mainly imported from South Africa, Turkey, Iran and other countries. In recent years, the proportions

M.-F. Ye (✉) · G.-L. Wu
School of Minerals Processing and Bioengineering,
Central South University, Changsha 410083, China
e-mail: csuymf@163.com

B. Li et al. (eds.), *Characterization of Minerals, Metals, and Materials 2018*, The Minerals, Metals & Materials Series,
https://doi.org/10.1007/978-3-319-72484-3_65

of chromite ore imported from South Africa have reached above 70% comparing with the total imports [4]. As one of the most important strategic resources, chromite ore is in a short supply in China, therefore, It is of great significance to strengthen the efficient utilization of chrome resources imported, before which, detailed process mineralogy research plays a very critical role in the determination of the characteristics of ore resources and the formulation of mineral processing conditions [5]. Chrome ore is the basic raw material for the production of chromium alloy, such as high carbon ferrochrome, medium carbon ferrochrome and low or micro carbon ferrochrome. In the ore, the higher Cr grade and Cr_2O_3/FeO are, the better [6, 7]. Latest researches of chrome ore are usually focused on the formation of chromite and other gangue minerals in the geology of mining areas [8, 9], the pretreatment such as mineral processing [10] and agglomeration [11], researches about process mineralogy of chrome ore are rarely reported. So, to produce high grade chromium alloy, the mineralogical studies, including the chemical compositions, the mineral compositions, and the embedded relationships between minerals of a South African chrome ore were studied by a series of detecting means, such as optical microscopy, scanning electron microscopy and MLA 650 process mineral automatic detection system and so on. The identified chrome ore is provided by a ferroalloy plant in Hunan province, and the samples are well representative.

Macroscopic Characteristics

The macroscopic morphology of the chrome ore is shown in Fig. 1. The block size of the lump ore ranges in 10–50 mm. The texture is very compact, the specific gravity is 4.6, the surface is grayish black, mingling with some sporadic light white, yellow and green materials. There are no specific cleavages appear after breaking the ore. And the ore has a certain magnetic. After crushing and grinding to almost 100% 150 mesh below, the color of fines become slightly yellowish brown.

Fig. 1 Macroscopic morphology of block chrome ore and grinding fines

Main Minerals and Their Embedded Characteristics

MLA is currently the world's most advanced mineral automatic analysis instrument. Samples of fines were tested through MLA 650 mineral automatic detection system, results in Figs. 2 and 3 showed that the main mineral compositions are chromite, chlorite and forsterite. Table 1 shows that a total of 13,011 particles in the sample were analyzed, and the total area of mineral particles is 3,545,364.68 μm^2, according to the counted area ratios, chromite, chlorite, forsterite account for 91.45, 5.66, 1.71% respectively, the rest minerals accounted for 1% or less totally.

Table 2 and Fig. 2 show that chromite particles are in the crystal form, whose the monomer dissociation is 92.66%, the remaining part of chromite particles are associated with other minerals. Figure 3 shows that particle shapes are very angular after grinding. Some chromite particles are wrapped by chlorite, part of the chlorite exists along the edge of the chromite particles as filling cementation. Although the origins and deposits of chromite are different according to previous research reports, but the origins of chromite minerals are similar, it is generally believed that

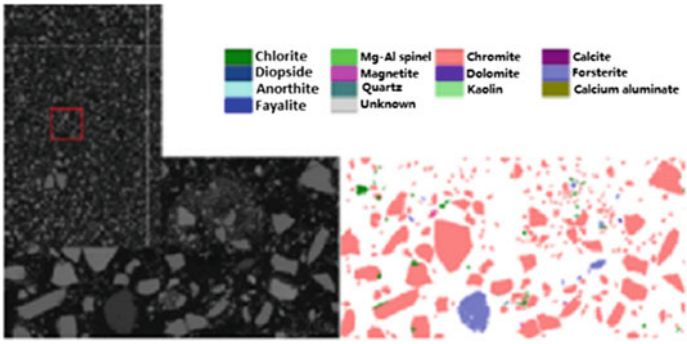

Fig. 2 Morphology and phase identification of particles before and after grinding

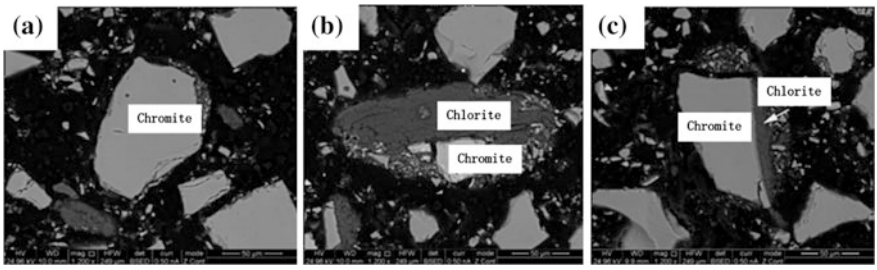

Fig. 3 Phase and structure of chromite particles in chrome fines. **a** Mono particles of chromite; **b** some chromite particles are coated by chlorite; **c** chromite and chlorite particles are adjacent to each other

Table 1 Mineral percentages in chrome fines

Minerals	Ratio of area (%)	Area (μm^2)	Particle number	Grain number
Chlorite	5.66	200,813.70	2948	4795
Chromite	91.45	3,242,365.18	11,179	18,351
Calcite	0.05	1702.36	37	39
Diopside	0.70	24,977.27	253	330
Magnetite	0.12	4252.49	243	270
Dolomite	0.18	6340.70	81	86
Forsterite	1.71	60,655.40	412	565
Anorthite	0.04	1282.88	27	28
Quartz	0.04	1271.67	37	38
Kaolin	0.01	192.25	5	5
Fayalite	0.01	496.24	40	41
Total	100.00	3,545,364.68	13,011	24,562

Table 2 Quantitative determination of embedded features of chromite among other minerals (%)

Mineral	Chlorite	Calcite	Diopside	Forsterite	Magnetite	Others
Growing with chromite	6.11	0.05	0.04	0.66	0.08	0.14
Coated by chromite	0.12	0.00	0.02	0.08	0.01	0.03
Degree of chromite' liberation	92.66					

chromite as a kind of magmatic minerals, often exists in ultra-basic type rocks [12, 13].

Table 3 and Fig. 4 show that most of the chlorite particles are in the form of monomer dissociation, the monomer dissociation degree of 56.59, and 39.83% of the chlorite particles are co-symbiotic and adjacent to chromite in the harbor-like and strip-like states; 1.01% chlorite and forsterite are in the form of metathesis dissolution and disseminated conjunctive bodies.

Table 4 and Fig. 5 show that after crushing and grinding the ore, forsterite particles are mainly in the form of monomer dissociation, and the monomer dissociation degree of 73.65%. Most forsterite particles are in the presence of independent particles under the scanning electron microscope. There are many cracks on the surface of the forsterite particles. A small part of forsterite is symbiotic with chlorite, and there are some regular shape of chromite and forsterite presenting in symbiosis, there are a small part of forsterite whose edge erosed into chlorite, some chromite is embedded into the forsterite. Forsterite appears in the form of adjacent to and wrapping with chromite and chlorite.

Table 3 Quantitative determination of embedded features of chlorite between other minerals (%)

Minerals	Chromite	Dolomite	Magnetite	Forsterite	Quartz	Others
Growing with chlorite	39.83	0.34	0.07	1.01	0.05	0.08
Coated by chlorite	1.03	0.14	0.02	0.76	0.00	0.08
Degree of chlorite' liberation	56.59					

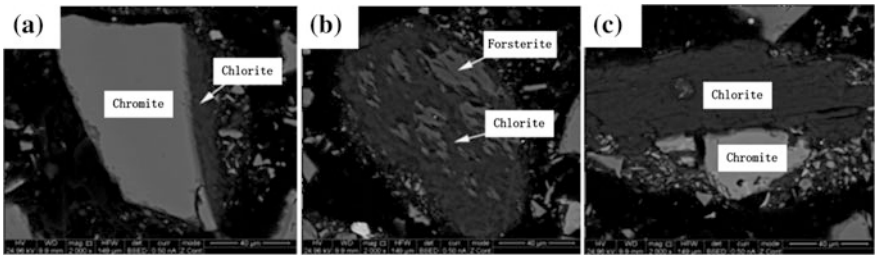

Fig. 4 Phase and structure of chlorite in chrome fines. **a** Chlorite adjacent to chromite; **b** metasomatic chlorite eroded by forsterite; **c** chlorite coating Small particles of chromite

Table 4 Quantitative determination of embedded features of forsterite between other minerals/%

Minerals	Chlorite	Chromite	Diopside	Dolomite	Others	Total
Growing with forsterite	4.54	8.10	6.21	0.00	0.00	18.85
Coated by forsterite	3.32	3.74	0.41	0.03	0.00	7.50
Degree of chlorite' liberation	73.65					

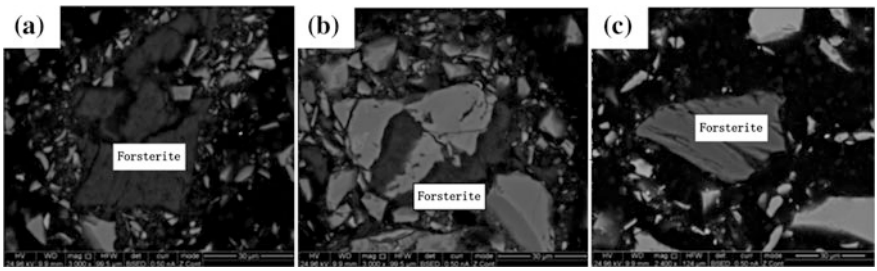

Fig. 5 Phase and structure of forsterite in chrome fines. **a** Forsterite transformed to chlorite marginally; **b** forsterite wrapping chromite particles; **c** mono particles of chromite

The Chemical Composition and Main Elements

The chemical compositions of chrome ore are obtained by chemical analysis and XRF analysis. It can be seen from Table 4 that the content of Cr_2O_3 is 41.84%, but the content of element Fe is high, which makes the Cr_2O_3/FeO smaller than 2.5, which the minimum requirement of the furnace load's. If there are no enrichment, it must charge with other high-grade metallurgical grade chrome ores. The contents of MgO and Al_2O_3 in chromite are as high as 15.84 and 16.47% respectively in Table 5, which means that the content of impurity in ore is high.

The main elements present in different minerals are showed in Fig. 7. Divalent elements as Ca, Mg and trivalent elements as Al, Cr and both divalent and trivalent Fe are mainly concentrated in the chromite. In the ore, 97.87% Cr and 97.13% Fe are rich in chromite. There are a small amount of Mg, Al, Si existing in the chlorite, Mg and Si are main composing elements in the forsterite in Table 6.

The existing forms of elements in minerals are usually divided into three [14]: micro inclusion, isomorphism and ion adsorption. Scanning images can show the distribution of elements in minerals directly. When elements in the mineral presenting a decentralized state and distributing uniformly, they can be initially identified as isomorphism. Elements that exist in the form of micro-inclusions are usually distributing very unevenly, which are always enriched in scattered small areas or points. The distributions of the main elements in the single minerals of chromite, chlorite and forsterite are shown in Figs. 6, 7 and 8. It can be seen that Fe,

Table 5 Chemical composition analysis of chrome fines wt%

Material	Cr_2O_3	Fe_2O_3	FeO	CaO	SiO_2	Al_2O_3	MgO	TiO_2	V_2O_5	LOI
Chrome ore	41.84	–	20.09	0.86	2.02	18.47	17.84	0.22	0.31	1.12

Table 6 Distribution of major elements in different minerals (wt/%)

Minerals	Ca (%)	Cr (%)	Fe (%)	K (%)	Mg (%)	Na (%)	Si (%)	Al (%)
Chlorite	4.96	2.01	1.61	0.00	10.23	0.00	55.82	12.54
Chromite	80.67	97.87	97.13	0.00	84.49	0.00	6.45	87.31
Calcite	0.49	0.00	0.01	0.00	0.01	0.00	0.02	0.01
Diopside	8.10	0.04	0.04	0.00	0.95	72.16	8.93	0.00
Magnetite	0.16	0.01	0.73	0.00	0.02	0.00	0.09	0.00
Dolomite	3.26	0.00	0.00	0.00	0.32	0.00	0.00	0.00
Forsterite	1.59	0.06	0.44	0.00	3.97	0.00	27.25	0.01
Anorthite	0.64	0.01	0.00	0.00	0.00	0.00	0.42	0.01
Quarz	0.00	0.00	0.00	0.00	0.00	0.00	0.79	0.00
Kaolin	0.00	0.00	0.00	0.00	0.00	0.00	0.14	0.12
Fayalite	0.09	0.00	0.05	100.00	0.00	27.84	0.08	0.00
Total	100.00	100.00	100.00	100.00	100.00	100.00	100.00	100.00

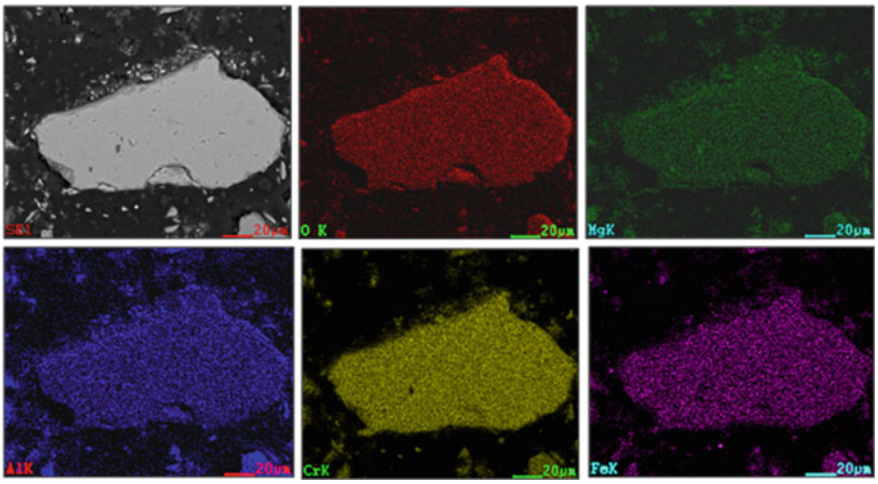

Fig. 6 Distribution of main elements on a single chromite particle

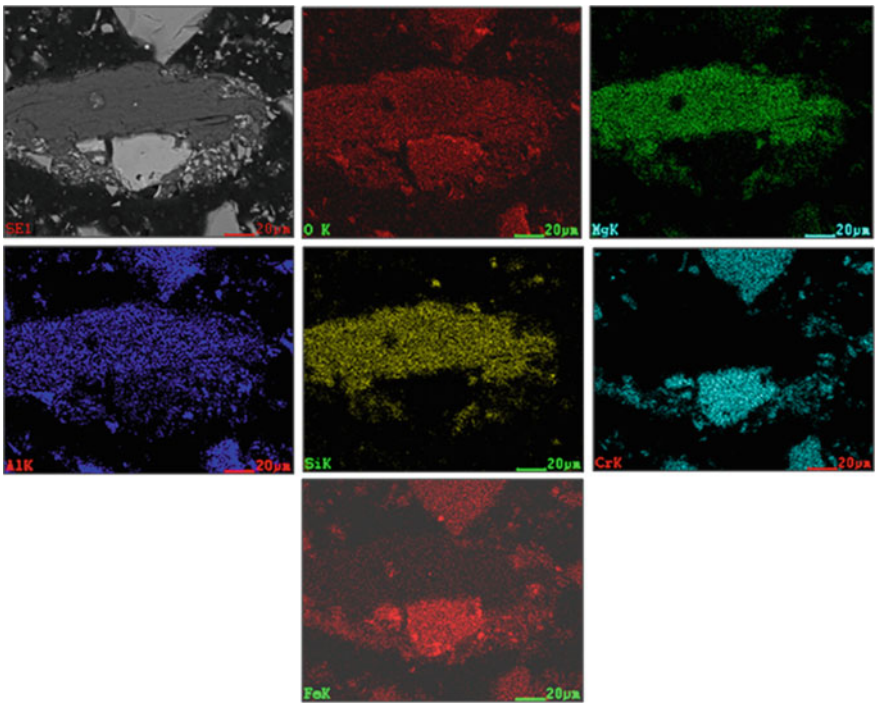

Fig. 7 Distribution of main elements on a single chlorite particle

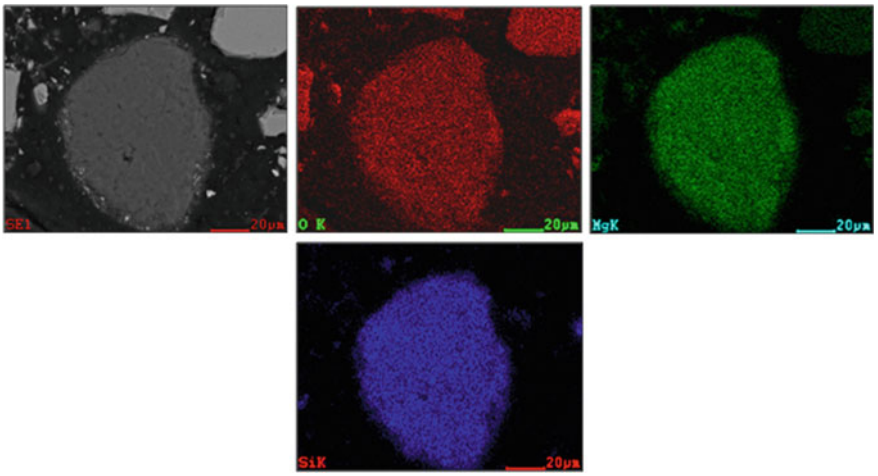

Fig. 8 Distribution of main elements on a single forsterite particle

Cr, Al, Mg, O elements are almost uniformly distributed in chromite, and there are almost no Si element in chromite.

Chlorite is composed of Mg, Fe, Al, as an aluminosilicate mineral with structural water, which is mainly the product of medium and low temperature hydrothermal, shallow metamorphism and sedimentation. The main constituent elements are O, Mg, Al, Si with a small amount of Fe, and the distribution of elements is relatively uniform. The color of the distribution image shows that the iron content in the chromite is higher than that in the adjacent chlorite.

Forsterite is a magnesium-rich member of the same category as the composition of the fayalite. Figure 8 shows the distribution of elements in a forsterite mono layer. The results show that forsterite has a higher content of Mg and Si than surrounding chromite. And elements O, Mg, Si are evenly distributing in single mineral particles.

Conclusion

1. The compositions of the South African chrome ore are relatively simple, chromite is the main mineral, and accounts for more than 91%; chlorite and forsterite are the main gangue minerals. The main elements in the pyrite are Mg, Al, Si, O and a small amount of Fe; the main elements in the forsterite are Mg, Si and O;
2. After grinding to almost 100% 150 mesh below, the dissociation degree of chromite was 92.66%, the dissociation degree of chlorite was 56.59%, the dissociation degree of forsterite was 73.65%, which indicating that chromite can

be separated from most of the forsterite, but the chlorite is closely interconnected with chromite;

3. The Cr_2O_3/FeO of the chrome ore is only 2.1, less than 2.5, which is one of important standards on the compositions of chrome ore used in submerged arc furnace. However, it can be mixed with other higher Cr grade and Cr_2O_3/FeO chrome ores as furnace burden, or be pretreated at first to improve its Cr grade and Cr_2O_3/FeO, to meet the production of higher grade chromium alloy (medium carbon ferrochrome, micro carbon Ferrochromium, etc.). Since more than 97% of elements Fe and Cr are basically enriched in chromite, it is difficult to achieve the purpose of improving Cr grade and Cr_2O_3/FeO in this chrome ore by using traditional selection and magnetic separation methods. But, the chemical dressing methods aiming to remove iron should be a choice.

References

1. Zheng MG, Lai LG (2011) Scenario analysis of China's demand for chrome ore. Res Ind 13 (4):43–49
2. Chen J, Wang SB, Lin WM et al (2005) Development and resource status of Chinese chrome industry in 21th century. Ferro-alloy 36(2):39–41
3. Li YJ, Zhang JT (2011) Current situation of chromite ore in China and recommendation on its sustainable supply. Metal Mine 10:27–30
4. Hu DW, Ma CY, Chen JB (2004) Supply and demand of chromite ore in China and counter measures of its sustainable supply. Conserv Util Miner Res 3:9–11
5. Zhou MG (2012) Application of technological mineralogy in ore prospecting and comprehensive utilization of mineral resources. Multipurp Util Miner Res 3:7–9
6. Ringdalen E, Olsen SE(1998) The effect of chromite ore mineralogy on reduction mechanism and reducibility. In: Paper presented at 8th Int. Ferroalloy Cong., Beijing, China, Jul 1998. pp 124–130
7. Murthya YR, Tripathya SK, Kumar CR (2011) Chrome ore beneficiation challenges and opportunities—a review. Miner Eng 24:375–380
8. Liu JG, Wang JA (2016) Formation of Al-rich type podiform chromitites in the Kudi ophiotite. Acta Geol Sinca 90(3):1182–1194
9. Huang Z, Yang JS, Zhu YW et al (2015) The discovery of diamonds and deep mantle minerals in chromitites of Hegenshan Ophiolite Inner Mongolia. Geol China 42(3): 1493–1514
10. Hu YM, Huangfu MZ, Zhang Y et al (2016) Experimental research on beneficiation for a chromite ore in South Africa. Multipurp Util Miner Res 4:81–84
11. Zhu DQ, Li J, Fan XH et al (2004) Literature review of the agglomeration of chromite fines. Sinter Pelletizing 29(2):27–30
12. Xiong FH, Yang JS, Ba DZ et al (2014) Different type of chromitite and genetic model from Luobusha ophiolite. Acta Petrol Sin 30(8):2137–2163
13. Haslam HW (1976) Chromite-chlorite intergrowth in periodotite at Chimwadzulu Hill, Malawi. Mineral Mag 40:695–701
14. Zhou LG (2006) Process mineralogy. Metallurgical industry press, Beijing

Pilot Trial of Detoxification of Chromium Slag in Cyclone Furnace and Preparation of Glass-Ceramics with the Water-Quenched Melt

Guizhou Zhao, Lingling Zhang and Daqiang Cang

Abstract Pilot trial of the detoxification of chromium slag in cyclone furnace and the preparation of glass-ceramics were investigated in a power plant in China. 10 wt.% chromium slag were mixed with pulverized bituminous coal and limestone as the raw materials of the cyclone furnace. Cr(VI) in chromium slag was reduced to Cr_2O_3 inside the cyclone furnace. The melt was water-quenched into frit and then fired into glass-ceramics with a laboratory ceramic roller kiln. The preparation and crystallization behavior of glass-ceramics were investigated with differential thermal analysis (DTA), physical and mechanical properties testing, X-ray diffraction (XRD) and scanning electron microscopy (SEM). The optimal flexural strength exceeding 90 MPa were achieved in firing temperature zone of 1170–1200 °C. Anorthite ($CaAl_2Si_2O_8$) and diopside [$Ca(Mg, Fe)Si_2O_6$] can be identified in the glass-ceramics and $CaAl_2Si_2O_8$ is the predominant crystal phase. Fine particles with average diameter of 200 nm distributed uniformly in the glass-ceramics. Granular crystals are intensively interconnected and constituted a crystal skeleton soaked in the glass matrix. Leaching toxicity test detected Cr(VI) of 0.016 and 0.010 mg/L of the water-quenched frit and glass-ceramics, respectively. This method provides an effective and comprehensive technique for the detoxification and utilization of chromium slag at low cost and large-scale.

Keywords Chromium slag · Cyclone furnace · Detoxification
Glass-ceramics

G. Zhao · D. Cang
School of Metallurgy and Ecological Engineering, University of Science and Technology Beijing, Beijing 100083, China
e-mail: zhaowow2008@outlook.com

G. Zhao · D. Cang
State Key Laboratory of Advanced Metallurgy, University of Science and Technology Beijing, Beijing 100083, China

L. Zhang (✉)
School of Energy and Environmental Engineering, University of Science and Technology Beijing, Beijing 100083, China

B. Li et al. (eds.), *Characterization of Minerals, Metals, and Materials 2018*, The Minerals, Metals & Materials Series,
https://doi.org/10.1007/978-3-319-72484-3_66

Introduction

Chromium slag discharged from chromate or metallic chromium manufacturing industries is one of the most hazardous solid wastes due to its high content of dissolvable Cr(VI) [1]. Over 6 million tons chromium-containing slag discharged from chemical industries were accumulated over a span of more than 30 years and 0.2–0.3 million tons are being discharged annually [2]. Hexavalent chromium [Cr(VI)] is considered as hazardous pollutant due to its severely toxic and carcinogenic.

The majority techniques of the detoxification of chromium slag are reducing Cr (VI) into less toxic and easily immobilized Cr(III) [3]. Several physical, chemical and biochemical methods were proposed to detoxify, solidify or stabilize Cr(VI) in chromium slag [4–12]. However, high cost, low efficiency and incomplete removal restricted the application of these techniques. The chromium slag was buried underground after treatment in many techniques [13], resulting in waste of slag resources and potential threat of Cr(VI). Therefore, it is pretty urgent to explore an effective technique for the detoxification and utilization of chromium slag.

In this article, pilot trial of detoxification of chromium in cyclone furnace and preparation of glass-ceramics from water-quenched melt were investigated. Chromium slag was mixed with pulverized coal and limestone as the raw materials of cyclone furnace. The water-quenched melt was prepared into glass-ceramics with a laboratory ceramic roller kiln. The specific processes and characteristics of the glass-ceramics were investigated.

Materials and Methods

Materials

Raw materials used in this pilot trial were chromium slag, pre-mixed bituminous coal and limestone. The chemical compositions of the raw materials and parent glass were determined by X-ray fluorescence spectrometer (XRF-1800, SHIMADZU, Japan). Table 1 shows the chemical compositions of chromium slag and coal ash. Chromium slag and coal ash are mainly constituted of CaO, SiO_2, MgO, Fe_2O_3 and Al_2O_3. Chromium slag and limestone (CaO > 50 wt.%) can be

Table 1 Main chemical compositions of chromium slag and coal ash (mass ratio, %)

	SiO_2	Al_2O_3	CaO	MgO	Fe_2O_3	Cr_2O_3
Chromium slag	12.36	8.64	35.86	23.24	10.12	5.68
Coal ash	54.30	21.54	2.21	1.86	5.68	–

applied as additives to reduce the melting temperature and improve the fluidity of the melt due to the high content of CaO. Coals were burned into coal ash after combustion and then formed the melt with additives.

Pilot Trial

Mixture of pre-mixed pulverized bituminous coals with 10 wt.% chromium slag and 0–10 wt.% limestone was belt transported and then blown into the cyclone furnace. Chromium slag and limestone were melted at high temperature inside cyclone furnace due to coal combustion. Cr(VI) in chromium slag was reduced to Cr_2O_3 inside the cyclone furnace with reducing atmosphere and high temperature. The melt (normally 1600–1700 °C) formed by chromium slag and coal ash was discharged and water-quenched into glass frit by circulating water.

In the pilot trial the processed glass frit was fired to glass-ceramics since the utilization of chromium slag in cement have been forbidden in China (whether detoxified or not). The frit was grounded, sieved with 100 mesh sieve and dried at 105 °C for 12 h to prepare parent glass. Table 2 shows the main chemical compositions of parent glass. Samples of 500 × 500 × 5 mm were hydraulically compacted at 15 MPa and then fired to glass-ceramics at different temperature for 45–60 min in a laboratory ceramic roller kiln.

Leaching Toxicity Test

Leaching toxicity test was conducted according to Chinese Environmental Protection Standard HJ/T 299-2007. Extraction fluid with pH value of 3.20 ± 0.05 was prepared by dissolving sulphuric acid and nitric acid (mass ratio of 2:1) in distilled water. Extraction fluid mixed with the pulverized sample (liquid to solid ratio of 10:1) was then rolling-over at 30 ± 2 rpm for 18 ± 2 h on oscillator. Cr(VI) content of the filtered leachate was detected by 1,5-diphenylcarbohydrazide spectrophotometric method according to Chinese National Standard GB/T 15,555.4-1995. Hazardous standard of Cr(VI) leaching concentration was determined according to Chinese National Standard GB 5085.3-2007.

Table 2 Main chemical composition of parent glass (mass ratio, %)

	SiO_2	Al_2O_3	CaO	MgO	Fe_2O_3	Cr_2O_3
Parent glass	50.78	14.98	15.20	3.25	3.21	0.96

Results and Discussion

Detoxification Mechanism of Chromium Slag

Cr(VI) in the filtered leachate of chromium slag is 281 mg/L, which highly exceeded the Chinese national standard. Cr(VI) in chromium slag mainly existed in the form of Na_2CrO_4 or $CaCrO_4$. Na_2CrO_4 or $CaCrO_4$ can be considered as $Na_2O{\cdot}CrO_3$ or $CaO{\cdot}CrO_3$ and decomposed into Na_2O/CaO and CrO_3 at high temperature. The instability of CrO_3 resulted in the reduction of CrO_3 to Cr_2O_3 by CO or [C] in the melt with high temperature and reducing atmosphere [14]. The average residence time of $\sim$300 s of the melt inside the cyclone furnace could ensure the complete reduction of Cr(VI). Cr(VI) in the filtered leachate of the water-quenched frit is 0.016 mg/L. Fly ashes contained 150 $\sim$ 200 mg/kg Cr(VI) were collected by electrostatic precipitator and then sent back into the cyclone furnace after re-melting. The overall reduction rate of Cr(VI) to Cr(III) exceeds 99.9%.

The detoxification of chromium slag was completely attached to the operation system of the cyclone furnace. Chromium slag partially replaced the limestone as additives due to its high CaO and MgO content. The heat balance and power generation efficiency of the cyclone furnace were not significantly affected and 2–3 t/h chromium slags can be detoxified in the cyclone furnace.

DTA Analysis

DTA curve of the parent glass at heating rate of 10 °C/min is shown in Fig. 1. A tiny exothermic peak near 945 °C and a large broad exothermic peak near 1170 °C can be seen from the DTA curve, respectively. It can be deduced from the DTA curve that the proper crystallization temperature is 1170 °C. An endothermic dip near 1280 °C indicating the melting of the samples.

The firing schedule of the glass-ceramics was determined according to the DTA curve and the operation system of the ceramic roller kiln. In the pilot trial, the samples were quickly heated to firing temperature at a varying heating rate of 120–300 °C/min and the total heating time was 8–15 min. The firing temperature was initially selected as 1170 $\pm$ 100 °C based on the DTA curve and finally obtained according to the testing results.

XRD Analysis

Phase identification of the parent glass and glass-ceramics were determined by X-ray diffraction (XRD, M21X apparatus, Cu Kα radiation, MAC Science Co. Ltd.,

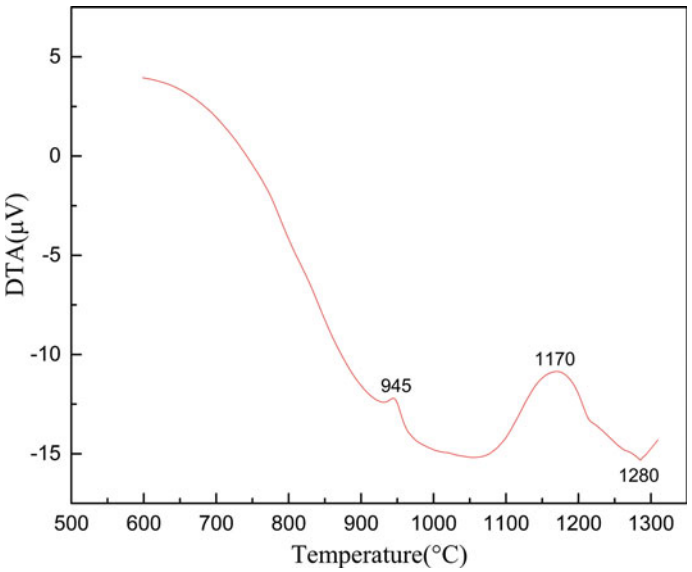

Fig. 1 DTA curve of parent glass

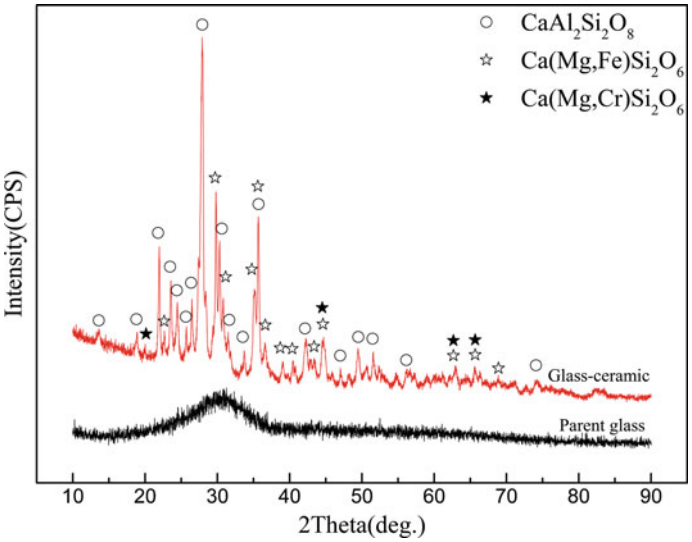

Fig. 2 XRD spectra of parent glass and glass-ceramics fired at 1170 °C

Japan). The XRD spectra of the parent glass and glass-ceramics fired at 1170 °C is shown in Fig. 2. The XRD spectra of the parent glass depicted typical scattering spectra of amorphous glass. The amorphous spectra without crystalline peak

illustrates the vitreous structure of the parent glass. The melt was fast cooled to frit during the water-quenching process and thus the vitreous phase was obtained.

Parent glass with binary basicity (CaO/SiO_2 mass ratio) of 0.3 were then fired to prepare glass-ceramics and crystallization occurred during the firing process. Anorthite ($CaAl_2Si_2O_8$) and diopside [$Ca(Mg, Fe)Si_2O_6$] can be identified in the glass-ceramic samples and $CaAl_2Si_2O_8$ is the predominant crystal phase. Silica forms the main Si-O tetrahedron structure of the glass-ceramics and Al_2O_3 enhances the glass network structure by forming Al-O tetrahedron as a glass forming oxide like silica. Trace chrome diopside [$Ca(Mg, Cr)Si_2O_6$] detected in the glass-ceramics indicated that the glass network can immobilize chromium.

SEM Analysis

The glass-ceramics exhibited dark black color and smooth surface without crackles and deformations. SEM images of the glass-ceramics fired at 1170 °C are depicted in Fig. 3. It can be seen from Fig. 2a that crystals were precipitated from the glass phase and then adhered to the glass basis before complete crystallization. Figure 2b depicted extremely fine particles with average diameter of 200 nm distributed uniformly in the glass-ceramics. Granular crystals are intensively interconnected and constituted a crystal skeleton soaked in the glass matrix, which improves the mechanical properties of the glass-ceramics.

Physical and Mechanical Properties

The samples were kept at the firing temperature for 3–5 min and then cooled down to room temperature at 30–100 °C/min. The samples were poorly densified below 1500 °C. The flexural strength of the samples fired at 1150 °C reaches Chinese national standard for building materials (35 MPa). Increasing in firing temperature

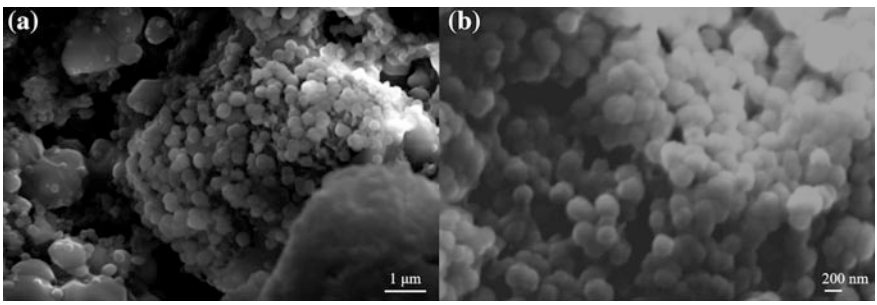

Fig. 3 SEM images of glass-ceramics fired at 1170 °C

increases the flexural strength of the samples. Flexural strength of the glass-ceramics exceeded 90 MPa in the firing temperature zone of 1170–1200 °C. Surface swelling, deformation, decrease in flexural strength and even smelting of the samples occurred with firing temperature exceeding 1200 °C due to the grain overgrowth and re-crystallization resulted by over firing. This is consistent with the DTA curve of the parent glass. Liquid phase generated at high temperature (normally over 1100 °C) promoted the rapid densification and crystallization of the green samples. The samples can be fired to glass-ceramics with flexural strength exceeding 90 MPa at firing temperature zone of 1170–1200 °C with short firing period of 30–60 min.

2–3 t/h chromium slag can be detoxified by the cyclone furnace. The detoxification of chromium slag was attached to the regular operation of the cyclone furnace and the power generation efficiency of the cyclone furnace were not significantly affected. China have forbidden the utilization of chromium slag in cement production and the water-quenched slag were stockpiled or deposited, which occupied large amount of land and wasted the slag resources. In the pilot trial, the water-quenched slag was fired into glass-ceramics which can be applied as building and construction materials. This technique provides an effective and comprehensive technique for the detoxification and utilization of chromium slag at low cost and large-scale, which has great significance and prospects.

Conclusions

In the pilot trial, 10 wt.% chromium slag were mixed with pre-mixed bituminous coal and limestone for the detoxification of Cr(VI) inside cyclone furnace. Cr(VI) in chromium slag was reduced to Cr_2O_3 inside the cyclone and the overall reduction rate of Cr(VI) exceeded 99.9%. Leaching toxicity test detected Cr(VI) of 0.016 and 0.010 mg/L of the frit and glass-ceramics, which is far below Chinese national standard. The optimal flexural strength exceeding 90 MPa were achieved in the firing temperature zone of 1170–1200 °C with short firing period of 30–60 min. Anorthite ($CaAl_2Si_2O_8$) and diopside [$Ca(Mg, Fe)Si_2O_6$] can be identified in the glass-ceramics and $CaAl_2Si_2O_8$ is the predominant crystal phase. Fine particles with average diameter of 200 nm distributed uniformly in the glass-ceramics. Granular crystals are intensively interconnected and constituted a crystal skeleton soaked in the glass matrix, which improves the physical and mechanical properties of the glass-ceramics. This technique provides an effective and comprehensive technique for the detoxification and utilization of chromium slag at low cost and large-scale, which has great significance and prospects.

References

1. Wu C, Zhang H, He P et al (2010) Thermal stabilization of chromium slag by sewage sludge: effects of sludge quantity and temperature. J Environ Sci 22(7):1110–1115
2. Li H, Wang Z, Yang Z et al (2012) Static and dynamic leaching of chromium (VI) from chromium-containing slag. Environ Eng Sci 29(6):426–431
3. Pillay K, Von Botnets H, Petersen J (2003) Ageing of chromium (III)-bearing slag and its relation to the atmospheric oxidation of solid chromium (III)-oxide in the presence of calcium oxide. Chemosphere 52(10):1771–1779
4. Wang Y, Yang Z, Chai L et al (2009) Diffusion of hexavalent chromium in chromium-containing slag as affected by microbial detoxification. J Hazard Mater 169 (1):1173–1178
5. Chai L, Huang S, Yang Z et al (2009) Cr (VI) remediation by indigenous bacteria in soils contaminated by chromium-containing slag. J Hazard Mater 167(1):516–522
6. Quan X, Tan H, Zhao Y et al (2006) Detoxification of chromium slag by chromate resistant bacteria. J Hazard Mater 137(2):836–841
7. Duchesne J, Laforest G (2004) Evaluation of the degree of Cr ions immobilization by different binders. Cem Concr Res 34(7):1173–1177
8. Hu J, Lo IMC, Chen G (2005) Fast removal and recovery of Cr (VI) using surface-modified jacobsite ($MnFe_2O_4$) nanoparticles. Langmuir 21(24):11173–11179
9. García-Ramos E, Romero-Serrano A, Zeifert B et al (2008) Immobilization of chromium in slags using MgO and Al_2O_3. Steel Res Int 79(5):332–339
10. Deja J (2002) Immobilization of Cr^{6+}, Cd^{2+}, Zn^{2+} and Pb^{2+} in alkali-activated slag binders. Cem Concr Res 32(12):1971–1979
11. Zhang M, Yang C, Zhao M et al (2017) Immobilization potential of Cr (VI) in sodium hydroxide activated slag pastes. J Hazard Mater 321:281–289
12. Cheung KH, Gu JD (2007) Mechanism of hexavalent chromium detoxification by microorganisms and bioremediation application potential: a review. Int Biodeterior Biodegradation 59(1):8–15
13. Hori M, Shozugawa K, Matsuo M (2015) Hexavalent chromium pollution caused by dumped chromium slag at the urban park in Tokyo. J Mater Cycles Waste Manage 17(1):201–205
14. Huan B (1995) Internal process of burning chromium slag in cyclone furnace. Power Eng 15 (02):5–14 (In Chinese)

Preparation of Refractory Materials from Ferronickel Slag

Foquan Gu, Zhiwei Peng, Huimin Tang, Lei Ye, Weiguang Tian, Guoshen Liang, Mingjun Rao, Yuanbo Zhang, Guanghui Li and Tao Jiang

Abstract The amount of slag produced from a typical ferronickel smelting process is 4 to 6 times that of the metal product, and handling this slag is a huge challenge to the ferronickel industry. The feasibility of a technological route for preparing refractory materials from a ferronickel slag was verified in this study. Based on the thermodynamics analysis, the effect of the sintering temperature on the properties of refractory material from the slag was studied in the presence of magnesia. The results of thermodynamics calculation showed that the reaction of MgO with SiO_2 generated forsterite and enstatite, whereas the reaction between MgO and Fe_2O_3/Al_2O_3 produced corresponding magnesia spinels. The experimental results showed that a refractory material with refractoriness of 1580 °C, bulk density of 2.88 g/cm^3, compressive strength of 106.9 MPa, and apparent porosity of 5.8% was obtained under the conditions of magnesia addition of 15 wt %, sintering temperature of 1350 °C and sintering time of 3 h. With increasing sintering temperature, the bulk density and the compressive strength of refractory material increased but the apparent porosity decreased, mainly attributed to the formation of the liquid phase which promoted the densification of the refractory material.

Keywords Ferronickel slag · Refractory material · Sintering · Forsterite

F. Gu · Z. Peng (✉) · H. Tang · L. Ye · M. Rao · Y. Zhang · G. Li · T. Jiang
School of Minerals Processing and Bioengineering, Central South University, Changsha 410083, Hunan, China
e-mail: zwpeng@csu.edu.cn

W. Tian · G. Liang
Guangdong Guangqing Metal Technology Co. Ltd., Yangjiang 529500, Guangdong, China

B. Li et al. (eds.), *Characterization of Minerals, Metals, and Materials 2018*, The Minerals, Metals & Materials Series,
https://doi.org/10.1007/978-3-319-72484-3_67

Introduction

Ferronickel slag is a waste of ferronickel smelting process with amount of almost 4–6 times that of the metal product [1, 2]. Compared with other metallurgical slags, the ferronickel slag is characterized by low activity, low recovery value and large quantity. Thus handling this slag is a huge challenge to the ferronickel industry.

At present, a majority of ferronickel slag is discarded and sent for landfilling or dumping [3]. Disposing such a huge quantity of ferronickel production waste occupies a lot of land resources, leading to potential soil and water contamination. It is essential to seek feasible and viable applications of the ferronickel slag that ensure its maximal utilization. Efforts have been carried out in laboratory and pilot-scale trials for its utilization, among which (i) production of cement and concrete, as additive in the cement or substitute of aggregates [4–8], (ii) production of construction materials, as additive in ceramic tiles and bricks, in high strength concrete, in fre-resistant bricks and in anti-slippery pavement tiles [9, 10], (iii) synthesis of inorganic polymers [11, 12] are the most commonly used methods. Although the above applications of the ferronickel slag are technically feasible, the low activity of ferronickel slag, large contents of hazardous elements (e.g., Cr) and high operation cost restrain their development. Therefore, more effective technologies should be built to improve the value of ferronickel slag with low overall processing cost.

The main mineral phase components of the ferronickel slag are magnesia and silica, which exhibit similar composition to forsterite refractory materials, characterized by low dielectric permittivity, low thermal expansion, good chemical stability and excellent insulation properties even at high temperatures, with wide applications in steel-making as drainage sand, continuous casting tundish, non-ferrous metal smelting, glassmaking, rotary cement kiln and so on [13, 14]. Developing refractory material from ferronickel slag not only can improve the value of ferronickel slag, but also avoid potential soil and water contamination. A large quantity of refractory materials have been produced from high-magnesia and silica waste, including ferrochromium slag [15] and iron ore tailing [16] by altering their chemical composition. Hence it is may be possible to prepare a forsterite refractory material by a similar approach.

In this study, the feasibility of a technological route for preparing refractory materials from a ferronickel slag was verified by altering its chemical and phase composition in the presence of sintered magnesia. The effect of sintering temperature on the properties of refractory material was explored based on a detailed thermodynamic analysis.

Experimental

Materials

Ferronickel slag

The ferronickel slag sample was obtained by the Rotary Kiln-Electric Furnace (RKEF) process of ferronickel smelting. Its chemical composition is shown in Table 1. The sample was characterized by high contents of silica and magnesia, and the ratio of magnesia to silica was 0.64. The X-ray diffraction (XRD) pattern (Fig. 1) shows that the ferronickel slag mainly consisted of olivine. The ferronickel slag sample was ground to about 89 wt% passing 74 μm.

Sintered Magnesia

Sintered magnesia was used as a source of MgO material in this study. The chemical composition of the magnesite is given in Table 2.

Methods

Experimental procedure

The suitable molar ratio of magnesia to silica in forsterite refractory material is 0.94–1.33 [17]. According to the chemical compositions of ferronickel slag and sintered magnesia, the theoretical dosage of sintered magnesia should be in the range of 14.1–26.31% to ensure the forsterite as the main phase of the refractory material. In this study, the dosage of sintered magnesia was 15 wt%.

Initially, the mixture of ferronickel slag and sintered magnesia was carefully mixed in a planetary ball mill for 20 min. Briquettes of 20 mm in diameter and 20 mm in height were produced by manual hydraulic pressing at 100 MPa using 5 wt% of 1.3 g/cm^3 magnesium chloride solution as the binder. The briquettes were then dried in a vacuum drying oven at 105 °C for 4 h. After drying, the briquettes were placed in a muffle furnace (furnace size: 150 mm × 150 mm × 150 mm) for sintering. After sintering at a designated temperature for a given period of time, the briquettes were cooled to room temperature and then taken out for the subsequent characterization tests.

Table 1 Main chemical composition of ferronickel slag (wt%)

Component	FeO	NiO	SiO_2	CaO	MgO	Al_2O_3	Cr_2O_3
Content	7.39	0.06	48.29	2.40	30.95	4.04	2.11

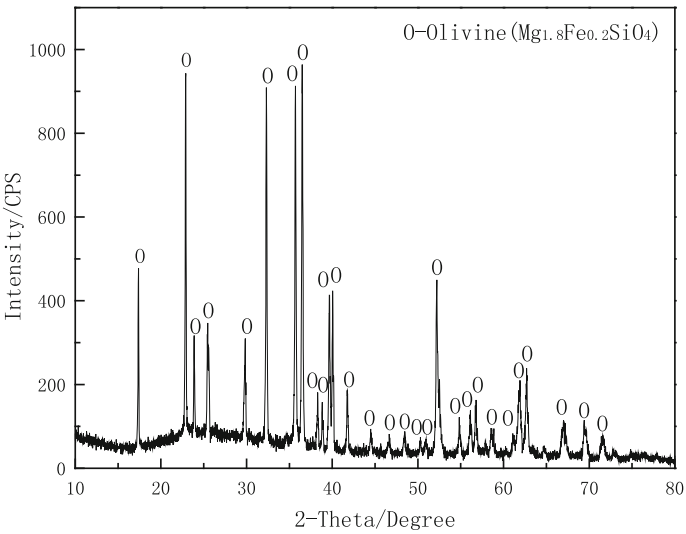

Fig. 1 XRD pattern of ferronickel slag

Table 2 Main chemical composition of sintered magnesia (wt%)

Component	MgO	CaO	SiO_2	Al_2O_3	Fe_2O_3
Content	94.51	1.53	0.98	1.13	0.65

Instrumental Analyses

The chemical compositions of the sintered samples were examined using an X-ray fluorescence spectrometer (XRF, PANalytical, Axios mAX, Almelo, The Netherlands). Their mineral phase compositions were determined by an X-ray diffraction spectrometer (XRD, Rigaku, D/Max 2500, Tokyo, Japan), using a Cu-anode target with the wavelength of 1.54056 Å, scan mode for the step scan, and step length of 0.02°.

Testing Standards

The refractorinesses of the samples were determined by the pyrometric cone equivalent method according to the Chinese National Standard Test Method (GBT 7322-2007). The bulk density and the apparent porosity of the refractory materials were measured according to the Chinese National Standard Test Method (GBT 2997-2000). The compressive strength of the refractory materials were method according to the Chinese National Standard Test Method (GBT 5072-2008).

Results and Discussion

Properties of Refractory Materials

The software Factsage 7.0 was used for calculation of thermodynamics associated with the liquid phase induced by the addition of 15 wt% sintered magnesia to ferronickel slag (Fig. 2). The results showed that at the sintering temperature of 1200 °C, there was no liquid phase in the refractory material. As the sintering temperature increased, the liquid phase content gradually increased. At 1500 °C, the theoretical liquid phase content of the refractory material reached 27.34%. The appearance of liquid phase could accelerate the reaction, with more complete reaction and denser material. Hence, the sintering temperature could be reduced. However, excessive liquid phase will deteriorate the high-temperature performance of the sintered material. According to Fig. 2 the suitable sintering temperature of ferronickel slag in the presence of 15 wt% sintered magnesia was 1200–1500 °C.

The effect of sintering temperature on the refractoriness of the refractory material was studied by fixing the sintered magnesia addition of 15 wt%, the magnesium chloride solution addition of 5 wt% and the sintering time of 3 h. According to Fig. 3, when the sintering temperature increased from 1200 to 1500 °C, the refractoriness of refractory material increased from 1510 to 1600 °C. It demonstrated that sintered magnesia can react with ferronickel slag more completely and faster.

The effect of sintering temperature on the bulk density, apparent porosity and compressive strength of the refractory material was studied by fixing the sintered

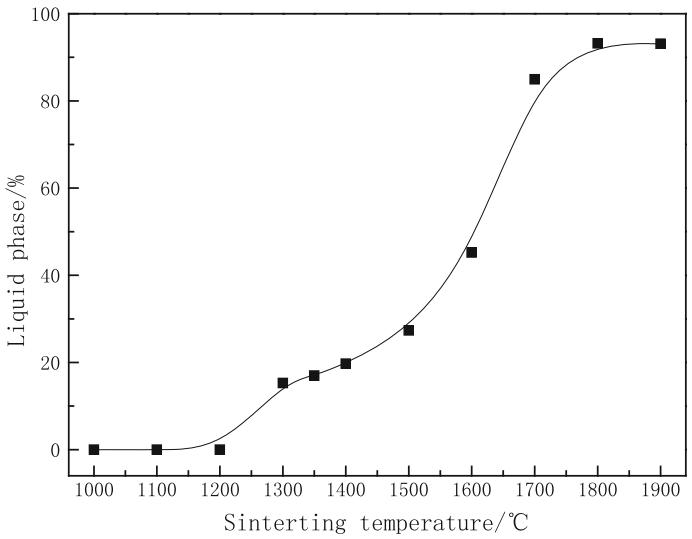

Fig. 2 Calculated liquid phase content of refractory material at different sintering temperatures

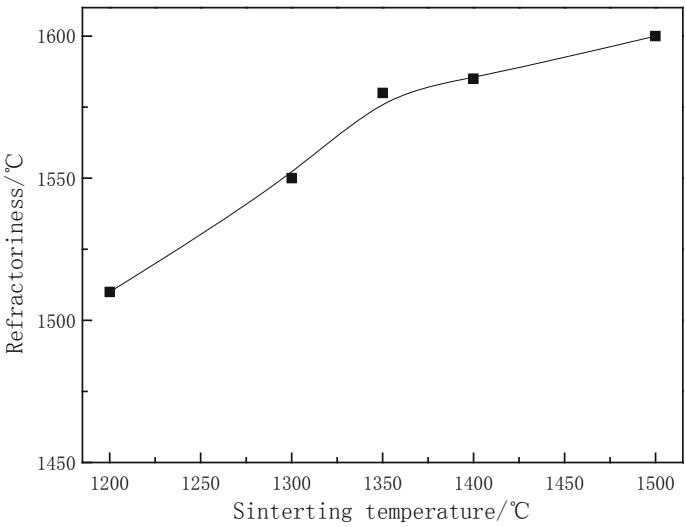

Fig. 3 Effect of sintering temperature on the refractoriness of refractory material

magnesia addition of 15 wt%, the magnesium chloride solution addition of 5 wt% and the sintering time of 3 h. Figure 4 shows that the bulk density of refractory material increased rapidly with the sintering temperature from 1200 to 1350 °C. At 1350 °C, the bulk density reached 2.88 g/cm^3. As the sintering temperature increased continuously, the bulk density gradually increased. This is because there was little liquid phase formed at the low sintering temperature. When the sintering temperature increased, the liquid phase content of the sintered material increased, contributing to the densification of the material. Increasing the sintering temperature reduced the apparent porosity. As the sintering temperature increased from 1200–1500 °C, the apparent porosity of the refractory material decreased considerably from 26.66 to 1.25%. The compressive strength of refractory material gradually increased with sintering temperature, similar to the variation of bulk density. Correspondingly, the porosity of refractory material declined.

According to the above results, a refractory material with refractoriness of 1580 °C, bulk density of 2.88 g/cm^3, compressive strength of 106.9 MPa, and apparent porosity of 5.8% could be obtained under the conditions of sintered magnesia addition of 15 wt%, sintering temperature of 1350 °C and sintering time of 3 h.

Sintering Mechanism

The reactions between olivine and the magnesia under sintering conditions are given by:

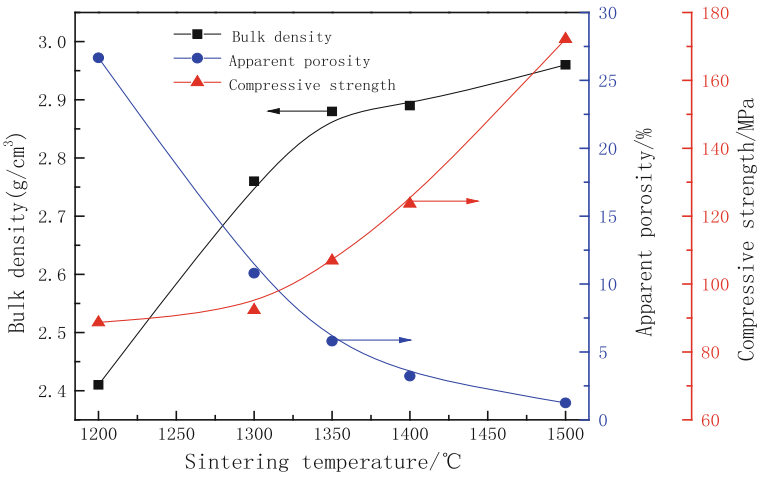

Fig. 4 Effects of sintering temperature on the bulk density, apparent porosity and compressive strength of refractory material

$$2(\mathrm{Mg}\cdot\mathrm{Fe})\mathrm{O}\cdot\mathrm{SiO_2} \xrightarrow[800^{\circ}\mathrm{C}]{\text{Oxidizing atmosphere}} 2\mathrm{MgO}\cdot\mathrm{SiO_2}+\mathrm{SiO_2}+\mathrm{Fe_2O_3}. \quad (1)$$

$$2\mathrm{MgO}\cdot\mathrm{SiO_2}+\mathrm{Fe_2O_3}\rightarrow \mathrm{MgO}\cdot\mathrm{SiO_2}+\mathrm{MgO}\cdot\mathrm{Fe_2O_3} \quad (2)$$

$$\mathrm{MgO}\cdot\mathrm{SiO_2}+\mathrm{MgO}\rightarrow 2\mathrm{MgO}\cdot\mathrm{SiO_2} \quad (3)$$

$$\mathrm{SiO_2}+2\mathrm{MgO}\rightarrow 2\mathrm{MgO}\cdot\mathrm{SiO_2} \quad (4)$$

At first, the FeO in olivine will be oxidized to Fe_2O_3, as given by Reaction (1). Fe_2O_3 will react with $2MgO{\cdot}SiO_2$ to generate $MgO{\cdot}SiO_2$ and $MgO{\cdot}Fe_2O_3$. The $MgO{\cdot}SiO_2$ may further react with MgO to form $2MgO{\cdot}SiO_2$. According to reaction (4), the SiO_2 generated by olivine decomposition reaction can also react with MgO to form $2MgO{\cdot}SiO_2$. As shown in Fig. 5, the melting point of $2MgO{\cdot}SiO_2$ is 1890 °C, and the eutectic temperature of $2MgO{\cdot}SiO_2$ and MgO is 1850 °C. Conversely, the eutectic temperature of $2MgO{\cdot}SiO_2$ and $MgO{\cdot}SiO_2$ is only 1557 °C. Also, the presence of $2FeO{\cdot}SiO_2$ can form an infinite solid solution with $2MgO{\cdot}SiO_2$, which will reduce the liquid phase formation temperature of the system. In other words, the presence of $MgO{\cdot}SiO_2$ and $2FeO{\cdot}SiO_2$ will decrease the refractoriness of the refractory material. The addition of sintered magnesia not only converts $MgO{\cdot}SiO_2$ to $2MgO{\cdot}SiO_2$ to improve the refractoriness of the refractory material, but also decreases the adverse effect of FeO on the refractoriness. This claim can be confirmed by the XRD patterns in Fig. 6. In the presence of 15 wt% sintered magnesia, the peaks of olivine and fayalite in the refractory material obtained at different

sintering temperatures were not observed. As the sintering temperature increased, the peak intensity of forsterite gradually increased and the intensity of enstatite diminished. At the sintering temperature above 1400 °C, the enstatite peaks disappeared.

Conclusions

The feasibility of a technological route for preparing refractory materials from a ferronickel slag was verified. A refractory material with refractoriness of 1580 °C, bulk density of 2.88 g/cm^3, compressive strength of 106.9 MPa, and apparent porosity of 5.8% was obtained under the conditions of sintered magnesia addition of 15 wt%, sintering temperature of 1350 °C and sintering time of 3 h. With increasing sintering temperature, the bulk density and the compressive strength of the refractory material increased but its apparent porosity decreased, due to the densification-promoting effect of liquid phase formed in the refractory material. The olivine phase in the ferronickel slag would decompose under the oxidizing sintering conditions, and the decomposition products could react with the additive to generate high-melting-point phases, such as $2MgO{\cdot}SiO_2$ and $MgO{\cdot}Fe_2O_3$, which restrained the adverse effect of FeO on the refractoriness of the refractory material.

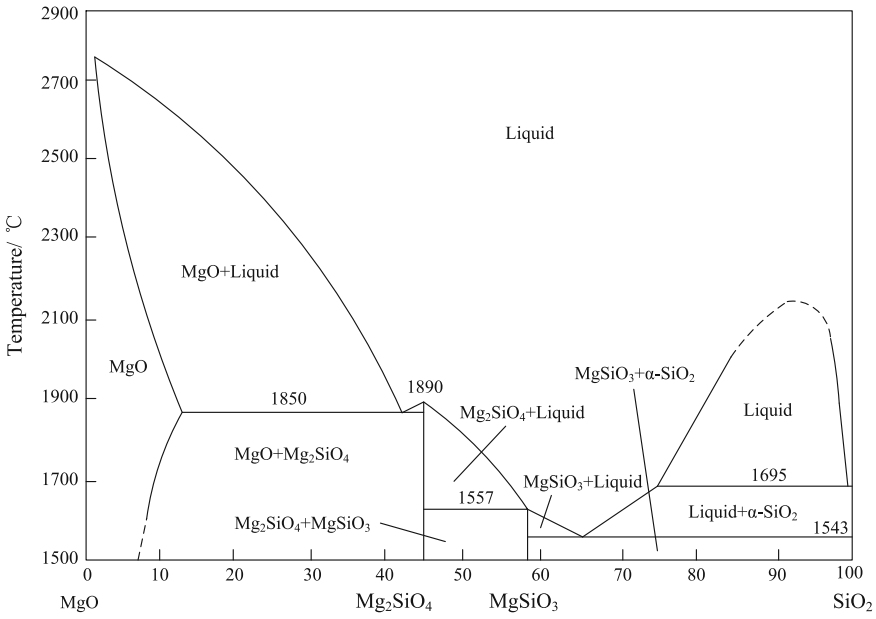

Fig. 5 Phase diagram of $MgO–SiO_2$ system

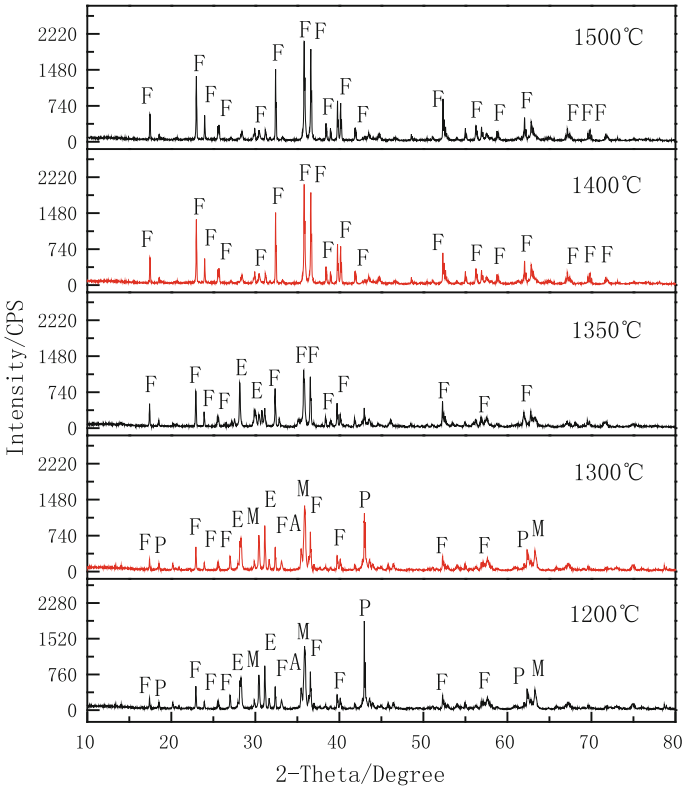

Fig. 6 XRD patterns of the refractory materials sintered at different temperatures (F—forsterite, P—periclase, E—enstatite, M—magnesite-chrome spinel, A—magnesia spinel)

Acknowledgements This work was partially supported by the Guangdong Guangqing Metal Technology Co. Ltd., the Open Fund of Key Laboratory for Solid Waste Management and Environment Safety (Tsinghua University) under Grant SWMES2017-04, the Innovation-Driven Program of Central South University under Grant 2016CXS021, and the Shenghua Lieying Program of Central South University under Grant 502035001.

References

1. Dourdounis E, Stivanakis V, Angelopoulos GN, Chaniotakis E, Frogoudakis E, Papanastasiou D, Papamantellos DC (2004) High-alumina cement production from FeNi-ERF slag, limestone and diasporic bauxite. Cem Concr Res 34(6):941–947
2. Balomenos E, Panias D (2013) Iron recovery and production of high added value products from the metallurgical by-products of primary aluminum and ferronickel industries. In: Proceedings of the 3rd International Slag Valorisation Symposium. Belgium, Leuven. pp 161–72

3. Lemonis N, Tsakiridis PE, Katsiotis NS, Antiohos S, Papageorgiou D, Katsiotis MS, Beazi-Katsioti M (2015) Hydration study of ternary blended cements containing ferronickel slag and natural pozzolan. Constr Build Mater 81:130–139
4. Kirillidi Y, Frogoudakis E (2005) Electricarc furnace slag utilization. In: Proceedings of the 9th international conference on environmental science and technology, Rhodes, Greece, pp 768–772
5. Saha AK, Sarker PK (2016) Expansion due to alkali-silica reaction of ferronickel slag fine aggregate in OPC and blended cement mortars. Constr Build Mater 123:135–142
6. SahaA K, Sarker PK (2017) Sustainable use of ferronickel slag fine aggregate and fly ash in structural concrete: mechanical properties and leaching study. J Clean Prod 162:438–448
7. Rahman MA, Sarker PK, Shaikh FUA, Saha AK (2017) Soundness and compressive strength of Portland Cement blended with ground granulated ferronickel slag. Constr Build Mater 140:194–202
8. Katsiotis NS, Tsakiridis PE, Velissariou D, Katsiotis MS, Alhassan SM, Beazi M (2015) Utilization of Ferronickel slag as additive in Portland Cement: a hydration leaching study. Waste Biomass Valoriz 6(2):177–189
9. Fidancevska E, Vassilev V, Milosevski M, Parvanov S, Milosevski D, Aljihmani L (2007) Composites based on industrial wastes III. Production of composites from Fe-Ni slag and waste glass. Journal of the University of Chemical Technology and Metallurgy 42(3):285–290
10. Vassilev V, Fidancevska E, Milosevski M, Parvanov S, Milosevski D, Aljihmani L (2007) Composites based on industrial wastes IV. Production of porous composites from Fe–Ni slag and waste glass. J Univ Chem Technol Metall 42(4):369–376
11. Maragkos I, Giannopoulou IP, Panias D (2009) Synthesis of ferronickel slag-based geopolymers. Miner Eng 22(2):196–203
12. Komnitsas K, Zaharaki D, Perdikatsis V (2009) Effect of synthesis parameters on the compressive strength of low-calcium ferronickel slag inorganic polymers. J Hazard Mater 161 (2–3):760–768
13. Othman AG, Khalil NM (2005) Sintering of magnesia refractories through the formation of periclase-forsterite-spinel phases. Ceram Int 31(8):1117–1121
14. Hossain S, Mathur L, Singh P, Majhi M R (2017) Preparation of forsterite refractory using highly abundant amorphous rice husk silica for thermal insulation. J Asian Ceram Soc 5 (2):82–87
15. Sahu N, Biswas A, Kapure GU (2016) Development of Refractory Material from Water Quenched Granulated Ferrochromium Slag. Miner Process Extr Metall Rev 37(4):255–263
16. Li J, Qi W, Liu J, Li P (2009) Synthesis process of forsterite refractory by iron ore tailings. J Environ Sci Suppl 21(S1):S92–S95
17. Xue Q, Xu W (2013) Refractory materials. Metallurgical Industry Press, Beijing

Process Improvement on the Gradation Uniformity of Steel Slag Asphalt Concrete Aggregate

Can-hua Li, Ming-sheng He, Huo-guo Pang, Xiao-dong Xiang and Hong-bo Jin

Abstract The specification of the steel slag aggregate will be mutated if the aggregate is prepared by a single type crusher. The specification stability of the steel slag improved significantly when the jaw crusher and the cone-crusher are combined in the crushing process. The combination of the crusher and screen is applied to produce steel slag aggregate while the roller washing process for removing the dust from the surface of aggregate. A pilot production line has been established by this technology. The specification stability and the road performance indicators of the steel slag aggregates have been greatly improved by this pilot production line as compared with the traditional production line. The particulate of the steel slag aggregate is decreased by 81% compared to the traditional line.

Keywords Steel slag · Gradation variability · Crushing process Aggregate

C. Li (✉) · X. Xiang
Technical Research Center of Green Manufacturing and Energy-Saving and Emission Reduction, Wuhan University of Science and Technology, Wuhan 430080, China
e-mail: licanhua1979@163.com

M. He
Frontier Technology Institute of Wuhan Branch of Bao-Steel Central Research Institute, Wuhan Iron and Steel Co., Ltd., Wuhan 430082, China

H. Pang · X. Xiang
School of Resources and Environmental Engineering, Wuhan University of Science and Technology, Wuhan 430080, China

H. Jin
Anhui Transport Consulting & Design Institute Co., Ltd., Hefei 230091, China

B. Li et al. (eds.), *Characterization of Minerals, Metals, and Materials 2018*, The Minerals, Metals & Materials Series,
https://doi.org/10.1007/978-3-319-72484-3_68

Introduction

Overseas scholars had done much earlier research on the use of steel slag paving materials, and made many important conclusions [1–5]. The steel slags were applied as coarse aggregate to asphalt concrete by Ahmedzade P, and it was showed that steel slag asphalt concrete had excellent mechanical properties and water damage resistance [6]. At present, the steel slag has a very high utilization rate, almost 100%, in Europe and the United States, and Japan, and 40–60% of them used in road paving. China has also carried out a lot of research on the steel slag used as a road aggregate [7–9]. The studies have also shown that steel slag asphalt concrete had excellent road performances [10, 11]. However, there are a few systematic researches on the production of steel slag aggregate. There is no mature control technology of the performance index of steel slag in china, so the enterprise has not formed the technology or experience to produce steel slag aggregate of stable uniformity. How to control the variability of steel slag aggregate becomes the key to ensure the use of the steel slag asphalt concrete.

Variation of Steel Slag Aggregate Gradation and Its Causes

The process has a direct effect on steel slag specifications and performance. At present, steel slags are broken only by jaw crusher in most iron and steel enterprises. The process is shown in Fig. 1. The steel slags are transported by the feeder to the jaw crusher for crushing. They are taken into magnetic separation after broken, to remove the slag blocks containing more iron. Then they are graded into different size directly through the vibrating screen.

The poor specification stability of steel slag aggregate is mainly caused by the process of a single crushing and screening equipment. The steel slags are a

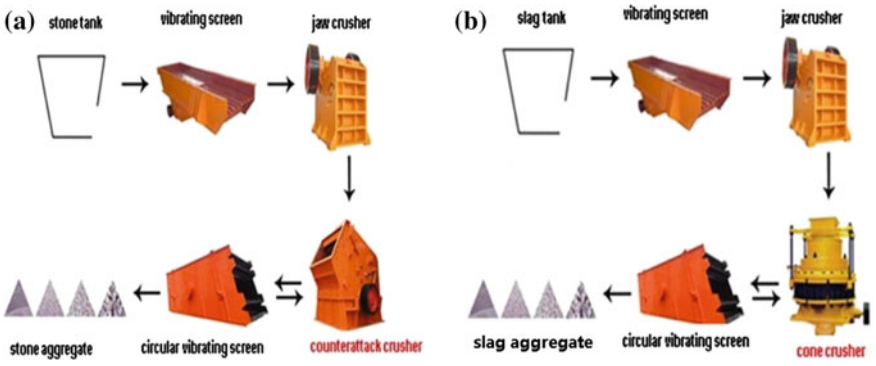

Fig. 1 Substitution of counterattack crusher to cone crusher in aggregate preparation: **a** Traditional aggregate preparation system, **b** New aggregate preparation system

byproduct in the process of steel making and have complex and changeable composition, which result that the steel slags in different batches and different parts have different damage resistance capacity. When with a single crusher, it is difficult to obtain a variety of steel slag aggregates, but easy to bring out interrupted grading phenomenon. In the other hand, specification instability of the broken steel slag aggregate will be caused by the changing hardening capacity of the steel slag. The steel slag blocks are broken easily and sometimes difficultly. Some steel slag blocks contain much of parts easy to be broken. However, some steel slag blocks contain relatively little. This result the output of steel slag aggregate are very unstable, and change in a wide range, which caused that the workload of the shaker are heavy and sometimes light, and the steel slag aggregates of different specification are unable to separate quickly and mix with each other. The unstable specifications of steel slag aggregates are related to the mechanical properties of them. The slag crushing specifications are related to the ability of impact resistance. The mechanical properties of the different aggregates are different. Its agglomeration caused unstable mechanical properties. The crushing values of different broken steel slags broken by jaw crusher in a steel slag pile of a steel mill are tested. The results are shown in Fig. 2. It can be seen from Fig. 2 that the crushing values of different parts of the same steel slag aggregate pile are very different, so the performance of them are not stable.

The surface of the steel slag coarse particles produced by the traditional steel slag crushing line due to the lack of coarse aggregate separation of equipment, are wrapped with a thick fine particles (fine steel slag, sludge, etc.) layer. In the wet environment, it is difficult to remove this fine particles layer because of its cementation with steel slag surface. As a result, the steel slag aggregates turned into ellipse, and the angularity of them has changed significantly (Fig. 3). It is not conducive to the formation of intercalation between coarse aggregate particles, when they are used as coarse aggregates of asphalt concrete.

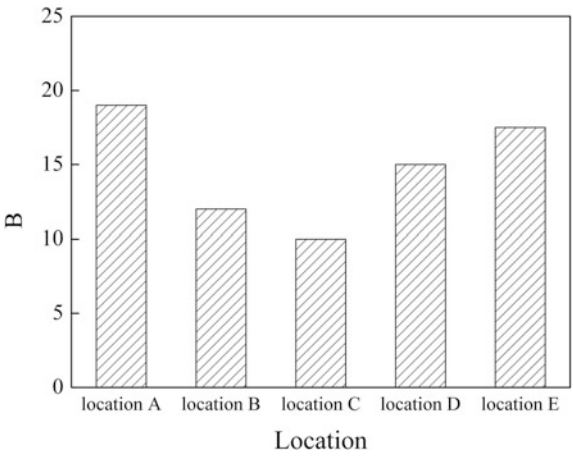

Fig. 2 Crushing value of steel slag based traditional line

Fig. 3 Appearance topography of the steel slag coarse aggregate

Study on the Crushing Equipment and Combination Configuration

Study on Variability of Different Single Crushing Equipment

The road aggregate are mainly produced with jaw crusher, impact crusher, cone crusher and other crusher at present. In order to ensure good specification and grain of the aggregates, road aggregate are produced by multi-stage crushing process in most of the aggregate processing enterprises. In this paper, the variabilities of steel slag aggregates are studied when the steel slag crushed with single crusher. The steel slag coarse aggregates are processed with jaw crusher, impact crusher, cone crusher respectively, and the steel slag coarse aggregates (particle size greater than 10 mm) are screened for samples. The results are shown in Fig. 4.

From the large sample screening results, it can be seen that the steel slags crushed with a single device and multiple screens had poor consistency, especially when using jaw crusher and counterattack crusher. However, the steel slags crushed with single cone crusher have better consistency than the single jaw crusher and the single impact crusher. It can not achieve the purpose of producing stable specifications of steel slag, when using single jaw crusher, or single impact crusher or single cone crusher.

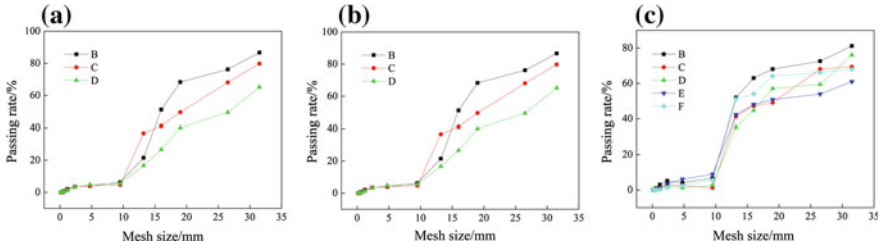

Fig. 4 Steel slag prepared by different single crushing equipment: **a** by jaw crusher, **b** by impact crusher, **c** by cone crusher

Study on Variability of the Combination of the Jaw Crusher and the Cone Crusher

The jaw crusher is selected for crushing large-size slag block in most enterprises. The choice of jaw crusher for its early break has a significant advantage. So the jaw crusher can be used as the first piece of steel slag equipment. Cone crusher is currently more advocate for crushing steel slag. Cone crusher can crush steel slag selectively. In this study, cone crusher is used as a fine crusher.

In this study, the jaw crusher is used to crush steel slag firstly, and the cone crusher is used to fine crush. The specification stability of the coarse steel slags is analyzed, after being screened out the particle size less than 10 mm. Three batches of steel slag are analyzed and compared with the steel slag coarse aggregate (diameter greater than 10 mm) produced in the traditional production line. The test results were shown in Figs. 5 and 6, respectively. The results show that the stability of the coarse particles has been improved significantly when the steel slag crushed by the combination of the jaw crusher and the cone crusher.

Study on the Screening Process of Steel Slag

Usually the aggregates are crushed firstly, and then screened. Steel slag contains many fine particles when it is crushed. The proportion of diameter less than 10 mm is about from 40 to 50% of the total steel slags, which are produced by the jaw crusher production line. In this study, the steel slags are processed in combinations of the crusher and screen, as shown in Fig. 7. The steel slags first pass through the vibrating screen. The fine particles of diameter less than 10 mm are removed. They are primary milled by the jaw crusher, and then fine-broken by the cone crusher. The steel slag aggregates, which fine-broken by the cone crusher, again passed

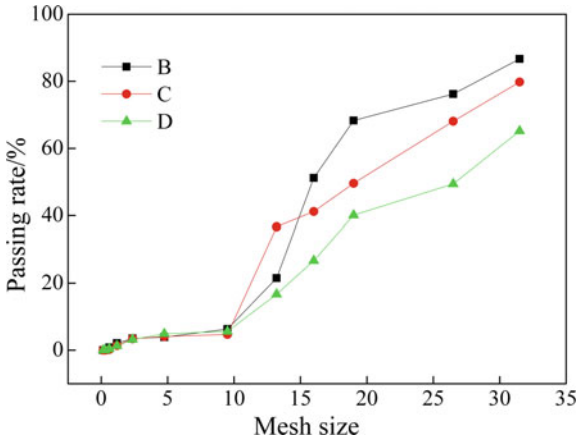

Fig. 5 Sieving of steel slag based on production line of WISCO

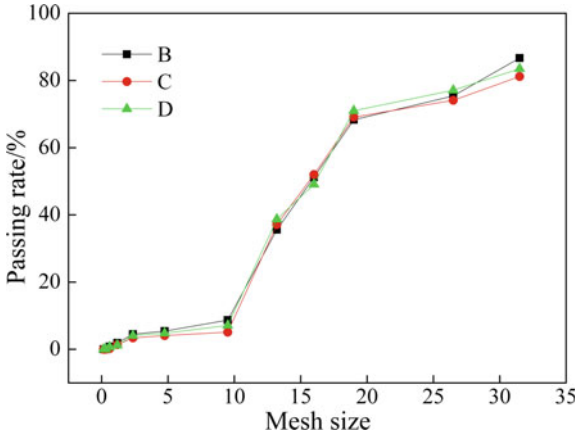

Fig. 6 Sieving of steel slag based on jaw crusher and cone crusher

through the vibrating screen to remove the fine particles of diameter less than 10 mm. Finally the steel slag aggregates are graded into different specifications by different-sized vibrating screens.

Study on the Cleaning Process of Steel Slag

It is difficult to remove the fine steel slag particles coating on the surface of the slag aggregate when they had been stored for a long time. The fine steel slags particles will changes the surface morphology of the slag aggregate. The XRD analysis is shown in Fig. 8. It is shown that the steel slag contain tri-calcium silicate (C_3S) and dicalcium silicate (C_2S) [12, 13]. The silicate minerals can hydrate in humid conditions [14]. The cementation of the fine particles on the surface of the steel slag is mainly due to the hydration of silicate minerals. Silicate minerals are hydrated to produce $Ca(OH)_2$ and C-S-H gels. The C-S-H gels have gelling properties and make the hydrated product to bind to the surface of the steel slag aggregates. The degree of cementation increases with time. Therefore, it should be promptly removed the fine steel slag particles coating on the surface of the slag aggregate, and make to ensure the steel slag aggregates a good angularity.

In this study, water is used to clean the steel slag aggregates, and take away with the dusts at the same time. The sewage goes into the sedimentation tank for filter

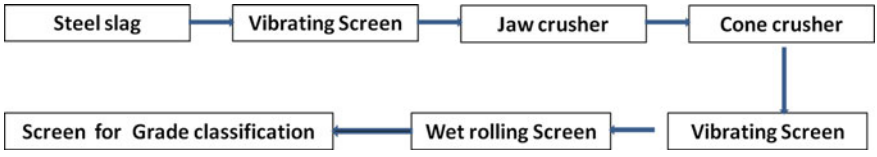

Fig. 7 Multi-stage process of slag aggregate preparation

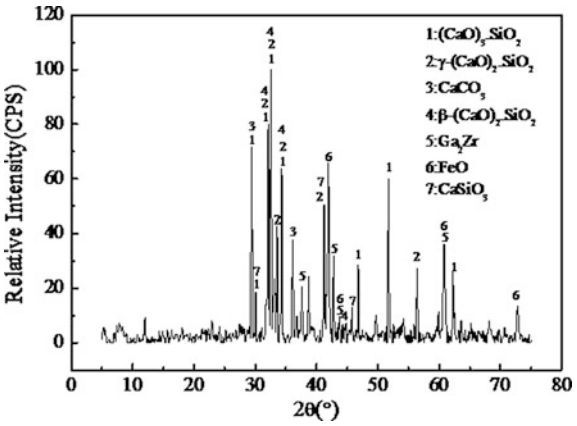

Fig. 8 XRD result of steel slag

dust. The water can be recycled. It indicates that there is a unique advantage for cleaning steel slag with a drum sieve. The steel slag aggregates are conveyed by the belt to the tail of the drum sieve. The drum sieve has a certain inclination angle. The steel slag aggregates move to the head of the drum screen while the high pressure water is injected from the head of the drum screen. The effluent containing fine powder and mud are discharged from the holes in the side wall of the drum screen and collected into the sedimentation tank (Fig. 9).

Study on The Steel Slag Pilot Plant

Process Introduction

The process flow of the pilot production line is as follows. The steel blocks are sent into the feeder with a truck. The iron of the steel slag is pick out with the drum magnetic. In order to improve the efficiency of jaw crusher, the steel slags are

Fig. 9 Cleaning technology of BOF slag aggregate

sieved with a vibrating screen to remove the small particles (particle size less than 10 mm) before they are sent into the jaw crusher. The steel slags are fine-broken by the cone crusher after being primary milled by the jaw crusher. After being fine-broken, recovering iron has done again. Because the broken steel slag contained more fine particles, the fine particles are removed from it again using a circular vibrating screen. Finally the steel slag aggregates cleaned by water are graded into different specifications by different-sized vibrating screens.

Performance Test of Steel Slag

The specification variation and the road performance of the slag aggregate produced by the pilot production line are tested. The screening results for the slag aggregate samples of different batches are shown in Fig. 10. It can be seen from the results that the screening results of each material are consistent with each other, which indicate that the stability of steel slag has a significant improvement as compared with the traditional line. It Indicate that the improved technology can achieve to produce particle size controllable steel slag aggregate.

The road performance tests of the steel slag aggregate include apparent relative density, Los Angeles abrasion, water absorption, ruggedness, needle-like content, crushing value, dust (mud) content. The tests are carried out in accordance with *Highway Engineering Aggregate Test Code* and *Highway Engineering Asphalt and Asphalt Mixture Test Code*. The road performance indicators of the steel slag asphalt concrete should meet *Highway asphalt pavement construction technical specifications*, JTG F40-2004. The test results are shown in Table 1.

It can be seen from Table 1, all road performance indicators of steel slag aggregate in the production process meet the requirements, and the crushing value and Los Angeles wear value are much smaller than the code limits. This indicates that steel slags have good wear resistance and good performance.

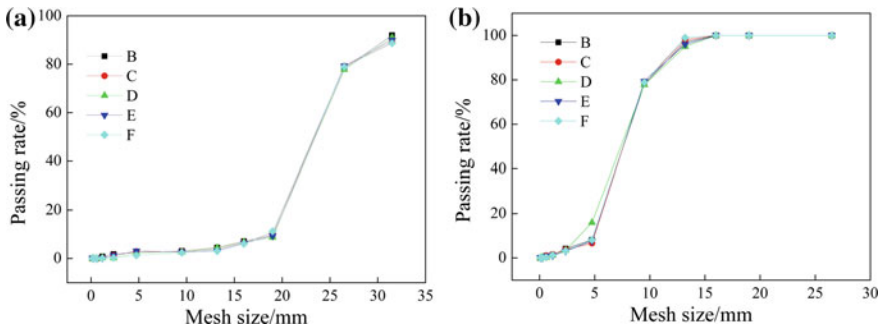

Fig. 10 Screening result of slag aggregate with size variation: **a** 25–16 mm, **b** 16–10 mm

Table 1 Property test of steel slag in the pilot line

Item			Result	Requirement
Density test	>25 mm	Apparent relative density	3.396	>2.6
		Adsorption rate (by mass)/%	1.15	<3
		Dust content (by mass)/%	0.8	<1
	16–25 mm	Apparent relative density	3.354	>2.6
		Adsorption rate (by mass)/%	1.353	<3
		Dust content (by mass)/%	0.8	<1
	10–16 mm	Apparent relative density	3.261	>2.6
		Adsorption rate (by mass)/%	1.958	<3
		Dust content (by mass)/%	0.9	<1
Crushing value (by mass)/%			13.6	≤ 26
Los Angeles abrasion (by mass)/%			13.2	≤ 28
Flakiness content (by mass)/%		4.75–9.5 mm	5.1	≤ 18
		>9.5 mm	4.3	≤ 12
Adhesion level			5	≥ 4

Table 2 Indexes comparison between old slags and new ones

Index	Traditional line	Pilot line
Iron content (by mass)/%	12.2–22.6	9.6–15.5
Apparent relative density	3.386–3.505	3.261–3.396
Dust content (by mass)/%	2.5–4.6	0.8–0.9

Compared with the traditional production line, the new production line had done a lot of changes. Multi-stage magnetic separation device and washing process with drum screen have an effect on iron content, density, dust content of the steel slag aggregate. We have made a comparison with the new line and the traditional line in these indicators. The results are shown in Table 2. The results show that the multi-stage magnetic separation device reduced the iron content in the steel slag to a certain extent. The decrease of the iron content also reduced the density of the slag aggregate. The dust content of the steel slag reduced significantly by 81% due to the washing process as compared to the traditional line.

Conclusion

(1) Multiple screening results for steel slags crushed by a single crushing device are very bad consistency, and specification variation of steel slag aggregate is great. However, the stability of the steel slag coarse aggregate is improved significantly, when the steel slag is crushed by the combination of the jaw crusher and the conical crusher.

(2) The steel slag aggregates can efficiently be produced with good variability when using the combination of crusher and screen. The drum washing process can improve the performance of the steel slag aggregate by removing the dusts from their surface.
(3) Compared to the traditional production line, the new pilot production line adopts combination of the jaw crusher and the cone-crusher, screen and washing process. The steel slag aggregate produced by the new pilot production line have better specifications stability and road performance indicators, compared with the traditional process.

References

1. Geiseler J (1996) Use of steelworks slag in Europe. Waste Manag 16(1):59–63
2. Motz H, Geiseler J (2001) Products of steel slags an opportunity to save natural resources. Waste Manag 21(3):285–293
3. Kehagia F (2009) Skid resistance performance of asphalt wearing courses with electric arc furnace slag aggregates. Waste Manage Res 27(3):288–294
4. Kök BV, Kuloğlu N (2010) Effects of steel slag usage as aggregate on indirect tensile and creep modulus of hot mix asphalt. Gazi Univ J Sci 21(3):97–103
5. Haga N, Konno M, Mizoguchi I et al (1981) Utilization of blast furnace and steel slags in road construction. Nippon Steel Tech Rep Overseas (17):52
6. Ahmedzade P, Sengoz B (2009) Evaluation of steel slag coarse aggregate in hot mix asphalt concrete. J Hazard Mater 165(1–3):300–305
7. Ding QJ, Li C, Peng B et al (2001) Study of the practicability of asphalt concrete confected by steel slag. J Wuhan Univ Technol 23(6):9–13
8. Li CH, Zhou XY, Sun D (2003) Study on the high temperature stability of steel slag asphalt mixtures. Multipurp Utilization Miner Resour 3:71–74
9. Chen F, Wu SP, Chen MZ et al (2010) Manufacture and application of steel slag asphalt concrete. Road Mach Constr Mech 27(009):20–23
10. Wu SP, Yang WF, Xue YJ et al (2003) Research and application of steel slag asphalt concrete. In: Chinese society of ceramics 2003 annual conference on cement-based materials proceedings
11. Lu FL, Li J (2013) Study on gradation characteristics of steel slag asphalt mixture. Highway (07):222–227
12. Wang YJ, Ye GX (1981) A study of the mineral phases of oxygen converter slag and their cementious properties. J Chin Ceram Soc 9(3):302–308
13. Hou GH, Li WF, Guo W et al (2008) Micro-structure and mineral phase of converter slag. J Chin Ceram Soc 36(4):436–443
14. Wang Q, Yan P (2010) Hydration properties of basic oxygen furnace steel slag. Constr Build Mater 24(7):1134–1140

Research on the Interaction of Humic Acid with Iron Minerals

Guihong Han, Shengpeng Su, Yijun Cao, Yanfang Huang and Xiangyu Song

Abstract Binder is indispensable in the production of iron ore pellets and the quality of pellets seems to be related to the interactions between binders and iron minerals. Humic acid is proved a suitable binder for iron ore pelletizing. In this paper, the interactions between humic acid and iron minerals were investigated by adsorption experiments and molecular dynamic simulations. Adsorption experimental results show that the adsorption of humic acid on hematite is easier than that on magnetite, and the maximum adsorption capacities of humic acid on hematite and magnetite reach 17.1, 7.39 mg/g, respectively. The results of adsorption isotherms indicate that the Langmuir model provides the best correlation of the experimental data, while the thermodynamics results demonstrate that the adsorption process is a spontaneous exothermic process. Molecular dynamic simulations reveal that the interaction between hematite and humic acid is stronger than that between humic acid and magnetite.

Keywords Humic acid · Iron minerals · Adsorption · Molecular dynamics simulation

Introduction

Iron ore pellets, with advantages of high Fe content and good metallurgical performance, are considered to be suitable for blast furnace. Simultaneously, the production of iron ore pellets also complies with the desire of energy conservation

G. Han · S. Su · Y. Huang (✉) · X. Song
School of Chemical Engineering and Energy, Zhengzhou University, Zhengzhou 450001, People's Republic of China
e-mail: hlele114@163.com

G. Han
e-mail: guihong-han@hotmail.com

G. Han · Y. Cao
Henan Province Industrial Technology Research Institute of Resources and Materials, Zhengzhou University, Zhengzhou 450001, People's Republic of China

B. Li et al. (eds.), *Characterization of Minerals, Metals, and Materials 2018*, The Minerals, Metals & Materials Series,
https://doi.org/10.1007/978-3-319-72484-3_69

and environmental protection in iron and steel industry [1, 2]. Binder is indispensable in the production of iron ore pellets, which can significantly influence the quality of finished products.

A large number of binders have been developed in recent decades, such as, lime, bentonite, asphalt, papermill sludges and so on [3, 4]. So far, bentonite is still the most commonly used binder in pellet production. However, because of the poor bonding properties of bentonite in China, the usage amount of bentonite is much higher than that in foreign pellet plan [5].

Humic acid, extracted from poor lignite, is a kind of organic macromolecule polymer consisted of carboxyl groups and hydroxyl groups [6]. Theoretically, humic acid should be a better alternative because of their ideal adhesive molecular conformation. A few of researches have been carried on humic acid used as binders for pelletizing. The detailed adsorption characteristics of humic acid onto iron ore particles has been investigated by Han guihong et al. [7] and adsorption of humic acid onto natural magnetite, hematite and quartz surfaces as a function of initial humic acid concentration has been comparatively investigated by Zhou youlian et al. [8]. It was found that humic acid has a good adsorption property with iron ore.

In this paper, hematite and magnetite were used as raw materials while humic acid was used as iron mineral binder. Adsorption experiments and molecular dynamic simulations were conducted to research the interaction between humic acid and iron minerals

Experimental

Materials

In this paper, two typical iron ore minerals (hematite and magnetite) were used as raw materials. Single crystal hematite and magnetite samples obtained from Tianjin province, China, and the XRD patterns of hematite and magnetite were shown in Fig. 1. These samples were kept in a dryer to prevent further surface oxidation and ensure reproducibility of the tests. Humic substances based binders are extracted from lignite coals. All the other reagents used in this study were analytical grade and were used without further purification.

Adsorption Experiments

Adsorption experiments were conducted by adding a certain amount of adsorbent to a series of 100 mL conical flasks filled with 25 mL diluted solutions (0–100 mmol/L). The conical flasks were then sealed and placed in a shaker and shaken at 150 rpm with a required adsorbent time at 25 °C and natural pH. After equilibrium, the solution was centrifuged for 3 min at 3500 rpm. All the concentrations were

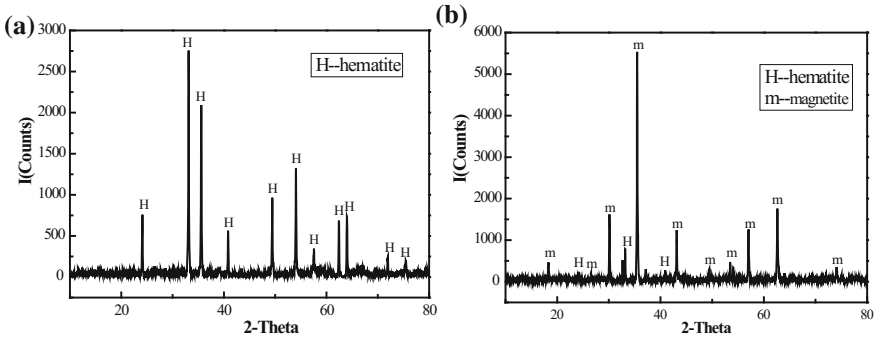

Fig. 1 XRD patterns of hematite (**a**) and magnetite (**b**)

measured at the wavelength corresponding to max absorbance, λmax = 254 nm, using a UV/vis spectrophotometer (PUXI, TU-1901). The amount of humics at equilibrium q_e (mmol/g) on hematite and magnetite was calculated from the following equation:

$$q_e = \frac{(C_0 - C_e)V}{m} \tag{1}$$

where C_0 and Ce (mmol/L) are the liquid phase concentrations of humics at initial and equilibrium, respectively. V is the volume of the solution (L) and m is the mass of adsorbent used (g).

Molecular Dynamics Simulations

All simulations were performed with the commercial Materials Studio software package [9]. The process of humic acid adsorption on hematite (010) and magnetite (111) surface was investigated by performing molecular dynamics (MD) using the Forcite module. MD was conducted in a simulation box with periodic boundary conditions (PBC) using the universal force field, which is a full periodic table force field for molecular mechanics and molecular dynamics simulations [10]. The minimization was performed using the Smart algorithm that automatically combines appropriate features of the other available methods in a cascade. Simulations were carried out in the NVT ensemble using the Nose algorithm for a run time of 4 ns with a 1 fs time step at 298 K. The simulations were initialized with the minimum energy structures and random initial velocities. The non-bonded interactions were calculated using the Ewald [11] method.

Results and Discussion

Adsorption Isotherms

In order to determination of equilibrium adsorption isotherm, the equilibrium experimental data for adsorbed data humic acid on hematite and magnetite were analyzed using the Langmuir, Freundlich isotherms in this study. Figure 2 shows that the equilibrium adsorption of humic acid (q_e vs. C_e) onto hematite and magnetite. The results show that adsorption capacities of humic acid on hematite and magnetite reach 17.1, 7.39 mg/g, respectively.

The Langmuir isotherm is most widely used for the adsorption process [12]. The Langmuir isotherm is represented as follows:

$$q_e = \frac{K_L C_e}{1 + a_L C_e} \tag{2}$$

where q_e (mg/g) and C_e (mg/L) are the amount of adsorbed humic acid per unit weight of adsorbent and humic acid concentration in solution at equilibrium, respectively. The K_L (L/g) and α_L (L/mg) are the Langmuir isotherm constants.

Equation (2) can be rearranged to obtain a linear form:

$$\frac{C_e}{q_e} = \frac{1}{K_L} + \frac{a_L}{K_L} C_e \tag{3}$$

The Freundlich isotherm is expressed by the following equation [13]

$$q_e = K_F C_e^{1/n} \tag{4}$$

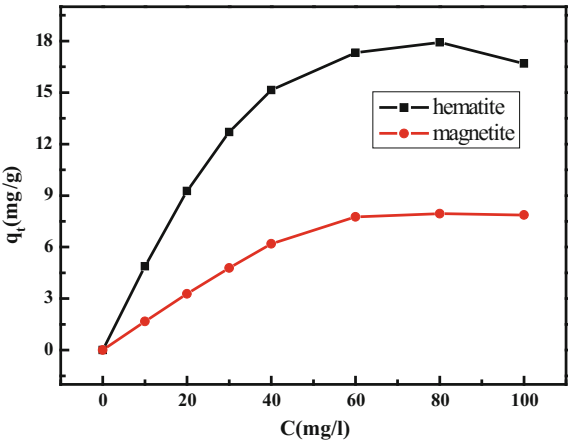

Fig. 2 Equilibrium adsorption of humic acid on hematite and magnetite

Table 1 Langmuir, Freundlich isotherm constants for humic acid adsorption

	Langmuir			Freundlich		
	K_L (L/g)	α_L (L/mg)	R^2	K_F ($mg^{1-1/n}$ $L^{1/n}$ g^{-1})	n (g/L)	R^2
Hematite	26.1	1.51	0.997	9.10	5.13	0.957
Magnetite	16.1	2.01	0.999	4.42	5.03	0.930

where K_F ($mg^{1-1/n}$ $L^{1/n}$ g^{-1}) is the Freundlich constant related to the bonding energy, and n (g/L) is the heterogeneity factor. A linear form of the Freundlich isotherm can be obtained by taking logarithms of Eq. (4):

$$\log q_e = \log K_F + \frac{1}{n}\log C_e \tag{5}$$

The Langmuir, Freundlich isotherm constants for humic acid adsorption are summarized in Table 1, and the adsorption isotherms were found to be linear over the entire concentration range studies with a good linear correlation coefficient ($R^2 > 0.995$), which indicate that data correctly fit the Langmuir isotherm.

Adsorption Thermodynamics

The thermodynamic parameters such as change in standard free energy (ΔG), enthalpy (ΔH) and entropy (ΔS) were determined by using the following equations [14]:

$$\Delta G = \Delta H - \Delta S \bullet T \tag{6}$$

$$lnk = \frac{\Delta S}{R} - \frac{\Delta H}{RT} \tag{7}$$

where R (8.314 J/mol K) is the gas constant, T (K) the absolute temperature and k (L/g) is the standard thermodynamic equilibrium constant defined by q_e/C_e. The values ΔH and ΔS can be estimated from the slopes and intercepts in the graph of lnk versus 1/T.

Table 2 Thermodynamic parameters of humic acid adsorption on hematite and magnetite

Temperature (K)	Hematite			Magnetite		
	ΔG (kJ/mol)	ΔH (kJ/mol)	ΔS (J/mol·K)	ΔG (kJ/mol)	ΔH (kJ/mol)	ΔS (J/mol·K)
298	−6.11	−25.42	0.059	−6.11	−55.50	−0.17
308	−2.24			−2.41		
318	−2.84			−2.84		

Thermodynamic parameters of humic acid adsorption on hematite and magnetite are reported in Table 2, and the negative values of ΔG and ΔH obtained demonstrate that the adsorption is a spontaneous exothermic process. The positive value of ΔS suggests increased randomness at the solid/solution interface occur in the structure of the adsorption of humic acid onto hematite surface.

Molecular Dynamic Simulations

The structure of humic acid adsorbed on hematite (010) or magnetite (111) surface were constructed using MD simulation in an attempt to understand the interactions between humic acid and hematite or magnetite surface. Figure 3a, b show the initial and equilibrium configuration of humic acid molecule on hematite surface, and Fig. 4a, b show the initial and equilibrium configuration of humic acid molecule on magnetite surface. According to the initial and equilibrium configuration of the humic acid molecule adsorbed on hematite (010) or magnetite (111) surface, A conclusion can be drawn that that the humic acid molecule can be parallelly absorbed on the hematite (010) or magnetite (111) surface.

The interaction energies between the hematite or magnetite surface and humic acid were calculated according to the following equation [15]:

$$\Delta E = E_{total} - E_{surface} - E_{humic} \tag{8}$$

where E_{total} was the total energy of the iron minerals crystal together with the adsorbed humic acid molecule; and $E_{surface}, E_{humic}$ was the total energy of the hematite or magnetite crystal and free humic acid molecule, respectively.

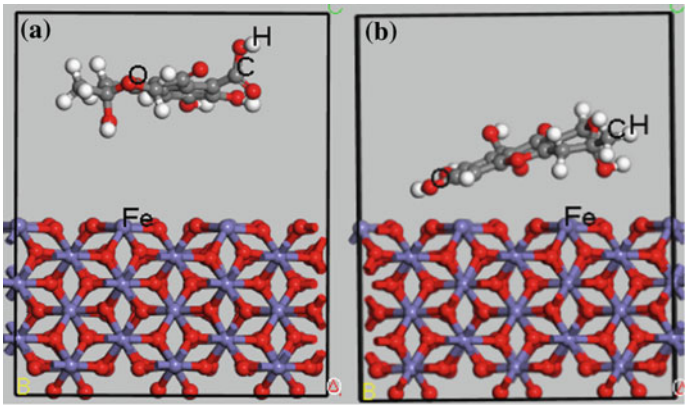

Fig. 3 Configurations of humic acid molecule adsorbed on hematite (010) surface, **a** initial, **b** equilibrium

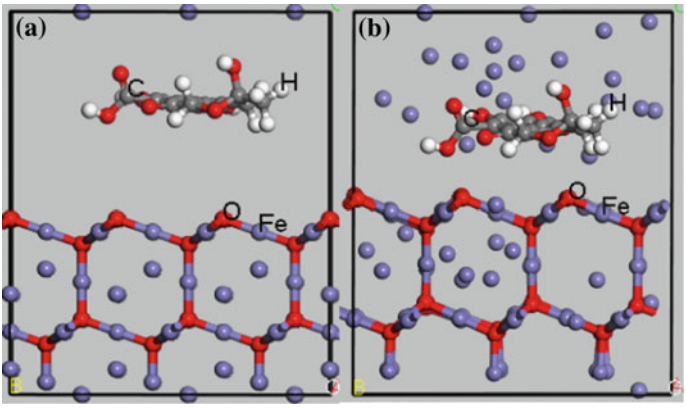

Fig. 4 Configurations of humic acid molecule adsorbed on magnetite (111) surface, **a** initial, **b** equilibrium

Table 3 Adsorption energies of humic acid acid on the surface of iron ore

Mineral	Humic acid			
	E_{total} (kJ/mol)	$E_{surface}$ (kJ/mol)	E_{humic} (kJ/mol)	ΔE (kJ/mol)
Hematite	−330.54	859.53	11.79	−1201.86
Magnetite	−59,438.65	−59,191.86	−45.83	−200.96

The adsorption energies of the humic molecule on hematite (010) and magnetite (111) surface are shown in Table 3. The high absolute value of the adsorption energies show that strong adsorption of these humics occurs on the iron ore surface. It can be seen that the adsorption energies of humic acid with hematite and magnetite were −1201.86, −200.96 kJ/mol, respectively, which demonstrate that the adsorption of humic acid on the hematite surface is easier, which is consistent with experiments results that we observed.

Conclusions

The interactions between humic acid and iron minerals were investigated by adsorption experiments and molecular dynamics simulations in this paper. The results indicate that the adsorption of humic acid on the hematite surface is easier than that of magnetite, and adsorption capacities of humic acid on hematite and magnetite reach 17.1 and 7.39 mg/g, respectively. The results of isotherms show that the Langmuir model provides the best correlation of the experimental data, whereas the thermodynamics results demonstrate that the adsorption is a spontaneous exothermic process. Molecular dynamic simulations reveal that the

interaction between hematite and humic acid is stronger than that between humic acid and magnetite, which is consistent with results of the performed adsorption experiments.

Acknowledgements The authors acknowledge the financial supports of the National Science Fund of China (No.51404213, No. 51404214, No. 51674225 and No. 51774252), Educational Commission of Henan Province of China (No. 17A450001, No. 18HASTIT011 and No. 18A450001) and the Development Fund for Outstanding Young Teachers of Zhengzhou University (No.1421324065).

References

1. Chun T, Long H, Di Z, Wang P, Meng Q (2017) Influence of microwave heating on the microstructures of iron ore pellets with coal during reduction. Ironmak Steelmak 44(7): 486–491
2. Savel'ev SG, Gubin GV, Stoikova YaA (2013) Prospects for the production of iron-ore pellets. Steel Transl 43(8):499–502
3. Bentonite RJS (1964) A challenge for Canadian industry. CIM Bull 57:648–652
4. Haas LA, Aldinger JA, Nigro JC (1989) Utilization of papermill sludges as binders for iron ore concentrate. Report of Investigations, United States Bureau of Mines, No. 9257
5. Huang YF, Zhang YB, Han GH et al (2010) Sodium-modification of ca-based bentonite via semidry process. J Cent South Univ T 17(6):1201–1206
6. Qiu G, Jiang T, Li H, Wang D (2003) Functions and molecular structure of organic binders for iron ore pelletization. Colloids Surf A 224(1–3):11–22
7. Inc. AS (2016) Materials studio release notes, release 8.0. Accelrys Software Inc., San Diego, CA
8. Han GH, Huang YF, Li G, Zhang YB, Jiang T (2014) Detailed adsorption studies of active humic acid fraction of a new binder on iron ore particles. Miner Process Extr Metall Rev 35 (1):1–14
9. Zhou Y, Zhang Y, Li P, Li G, Jiang T (2014) Comparative study on the adsorption interactions of humic acid onto natural magnetite, hematite and quartz: effect of initial ha concentration. Powder Technol 251(1):1–8
10. Rappe AK, Casewit CJ, Colwell KS, Iii WAG, Skiff WM (1992) Uff, a full periodic table force field for molecular mechanics and molecular dynamics simulations. J Am Chem Soc 114(25):10024–10035
11. Hohenberg P, Kohn W (1964) Inhomogeneous electron gas. Phys Rev 136(3):B864
12. Ozacar M, Sengil IA (2005) Adsorption of metal complex dyes from aqueous solutions by pine sawdust. Bioresour Technol 96(7):791–795
13. Ozacar M, Sengil IA (2003) Adsorption of reactive dyes on calcined alunite from aqueous solutions. J Hazard Mater 98(1–3):211–224
14. Hameed BH, Ahmad AA, Aziz N (2007) Isotherms, kinetics and thermodynamics of acid dye adsorption on activated palm ash. Chem Eng Sci 133(1–3):195–203
15. Xia S, Qiu M, Yu L, Liu F, Zhao H (2008) Molecular dynamics and density functional theory study on relationship between structure of imidazoline derivatives and inhibition performance. Corros Sci 50(7):2021–2029

Study of Different Process Additives Applied to Polypropylene

Patricia N. S. Poveda, Juliana Augusto Molari, Deborah Dibbern Brunelli and Leonardo G. A e Silva

Abstract There are several additives aimed on improving the processing characteristics as well as mechanical properties of the plastic materials. Being polypropylene is one of the main polymers used in the plastic processing industry due to its easy processability and application versatility, was chosen as the base resin for this study. Additives can aid the processing of polypropylene, either by promoting a better slip between the chains (lubricants), or by contributing to nucleation and crystallinity (nucleating). In this study, the raw materials copolymer polypropylene, lubricant (internal and external action), organic nucleating agent (metallic salt) and inorganic nucleating agent (metallic oxide) were considered. Mechanical tensile tests, Charpy impact and spiral flow to verify melt index were performed to characterize the samples with additives and standard (copolymer polypropylene). The interference of these additives with polymeric matrix was observed.

Keywords Polypropylene · Lubricant · Nucleating · Characterization

P. N. S. Poveda (✉) · L. G. A e Silva
Instituto de Pesquisas Energéticas E Nucleares (IPEN-CNEN/SP), São Paulo, Brazil
e-mail: patricianegrini@usp.br

L. G. A e Silva
e-mail: lgasilva@ipen.br

J. A. Molari · D. D. Brunelli
Instituto Tecnológico de Aeronáutica (ITA), São José dos Campos, Brazil
e-mail: Juliana_augusto89@yahoo.com.br

D. D. Brunelli
e-mail: deborah@ita.br

B. Li et al. (eds.), *Characterization of Minerals, Metals, and Materials 2018*, The Minerals, Metals & Materials Series,
https://doi.org/10.1007/978-3-319-72484-3_70

Introduction

Nowadays, polymers available on the market have a wide variety of properties. There are polymers capable of replacing metals, ceramics, and even glasses for certain applications [1].

The purpose of add an additive in a polymer is to obtain synergy between the constituents and to produce a material with superior properties when compared to original polymer. Additivation may also provide other results such as cost reduction of the final polymer and achievement of stability during processing and final product life cycle [2].

Polymers have high molar mass, thus, become viscous when melted. The higher the molar mass, the greater the viscosity. The high viscosity makes it difficult to process, especially in injection process, since the plastic must often pass through injection channels with narrow diameters. Therefore, it is necessary to reduce the viscosity of the polymer mass to ensure less wear of the machines and molds, higher productivity (faster cycles) and, consequently, electrical energy savings [3].

There are two different ways to achieve lower viscosity in a molten mass:

- By increasing processing temperature (which is not recommended, as the rate of degradation of the molecules will be higher, as well as the cooling time of the product and, consequently, the cycle time);
- By introducing auxiliary processing additives.

Lubricants facilitate the processing of polymers by increasing flow properties and decreasing the interaction of the melting with the walls of the machine [2].

When the polymer is processed, the melting temperature is higher than the temperature of the lubricant; thus, it fuses before than the polymer. The lubricant penetrates the plastic, and the level of penetration will depend on its solubility [3].

The nucleating agents may not significantly affect the rate of crystallization of all polymers. In order to a polymer be sensitive to nucleation during its crystallization process, the growth rate of the crystal must not be extreme (too high or too low). In case of polypropylene (PP), the rate of crystalline growth is intermediate, being one of the easiest polymers to form nuclei [4].

The physical or chemical nature of the nucleating agents may be quite diverse. A nucleating agent may be:

- an impurity, for example, a catalyst residue;
- an organic compound, such as benzoic acid;
- an inorganic compound, such as talc or a pigment.

For this study, a lubricant based on fatty acid ester, an organic nucleating of the metallic salt type and an inorganic metal oxide nucleating were used.

Experimental

The following raw materials were used:

- polypropylene Copolymer (PPC) with flow index of 40.0 g/10 min;
- internal and external lubricant;
- organic nucleating agent of the metal salt type;
- inorganic nucleating agent of the metal oxide type.

The proposed formulations are presented in Table 1.

In order to obtain test samples, an injection standardized test Type I tool was used according to ASTM D-638-10 [5], obtaining 20 test samples without additive (A—standard sample) and 20 test samples with each additive, characterizing samples B, C and D.

Tensile test provides information on the mechanical properties of the materials, such as tensile strength, elongation at break and modulus of elasticity. ISO 527-1 [6] specifies the general principles for determining the tensile properties of plastics and plastic composites under defined conditions.

Results and Discussion

Figures 1, 2, 3 and 4 show the behavior of the samples for the mechanical assays. Table 2 presents the results of the tests.

Charpy impact strength test may be used to investigate the behavior of certain sample types under defined impact conditions and to estimate the fragility or hardness of samples within the limitations inherent to the test condition. The results of this test are shown in Table 3.

In order to identify how much the fluidity index of the polymer is changed with the addition of the additives, this material characteristic was measured according to the method described in Table 4.

In this method, the molding flow of the thermoplastic material was evaluated. It was injected into a constant trapezoidal section spiral with subdivisions in centimeters or inches. The mold was filled from the center of the spiral and the pressure was maintained until the flow stops, indicating the flow distance. The results for the spiral flow test can be seen in Fig. 5.

Table 1 Formulations with different process auxiliary additives (%, by mass)

Components	A	B	C	D
PPC	100.0	99.5	99.5	99.5
Lubricant	–	0.5	–	–
Metal salt	–	–	0.5	–
Metal oxide	–	–	–	0.5

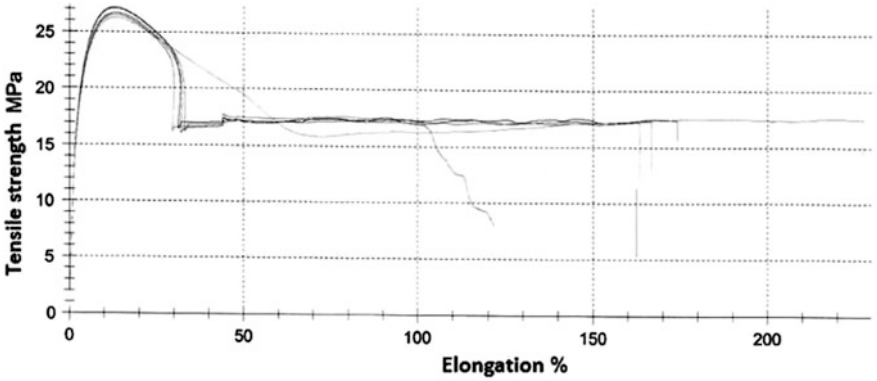

Fig. 1 Tensile properties of sample A (PPC)

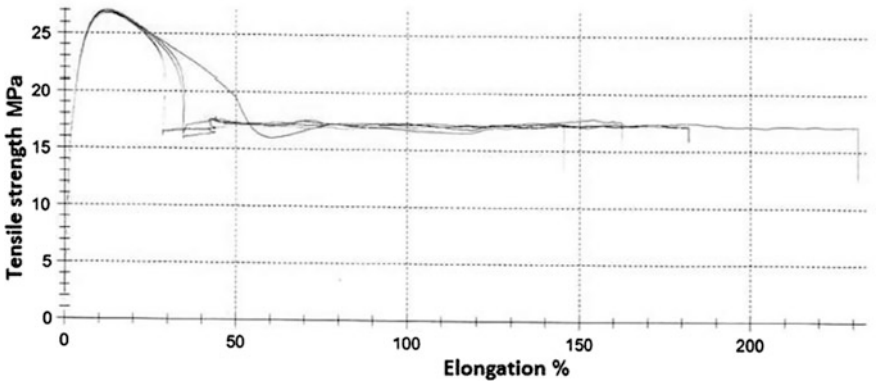

Fig. 2 Tensile properties of sample B (lubricant)

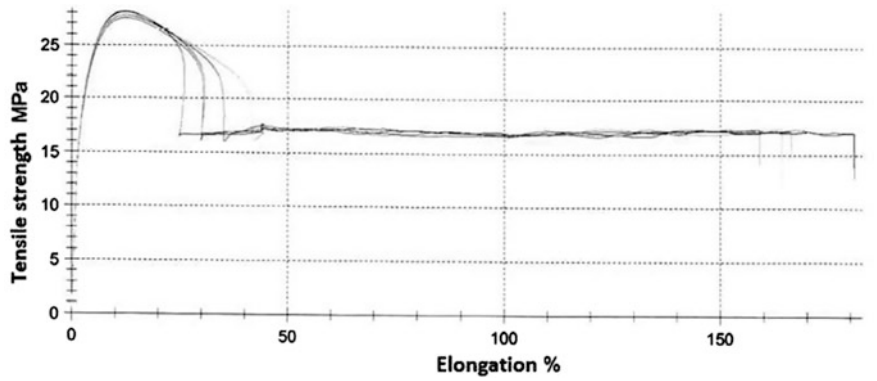

Fig. 3 Tensile properties of sample C (metal salt)

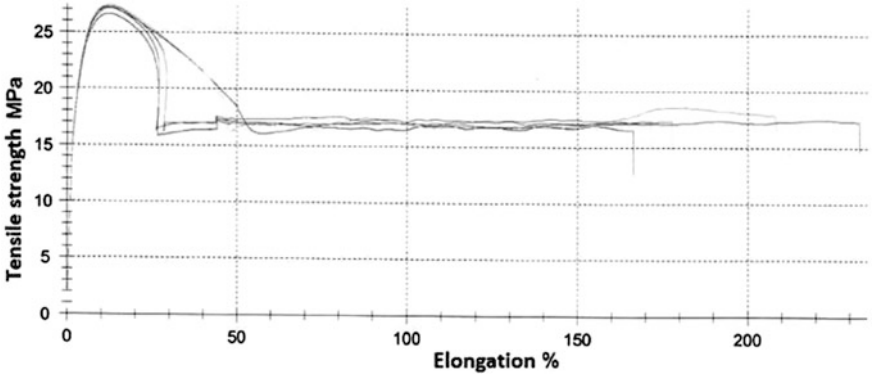

Fig. 4 Tensile properties of sample D (oxide)

Table 2 Results of the tensile strength test

Tensile properties	A $\bar{x}$	A s	B $\bar{x}$	B s	C $\bar{x}$	C s	D $\bar{x}$	D s
Modulus of elasticity E (MPa)	889.00	31.80	1020.00	34.90	982.00	25.90	933.00	35.70
Maximum tensile strength δ (MPa)	26.70	0.38	26.90	0.11	27.80	0.24	27.10	0.29
Tensile elongation ε (%)	13.00	0.15	12.40	0.15	12.50	0.19	12.30	0.18

Table 3 Results of the charpy impact strength test (kJ/m^2)

Charpy impact	A $\bar{x}$	A s	B $\bar{x}$	B s	C $\bar{x}$	C s	D $\bar{x}$	D s
Without notch (kJ/m^2)	99.81	0.00	99.80	0.00	87.68	20.02	99.81	0.00
Notched (kJ/m^2)	7.09	0.72	6.62	0.46	6.32	0.55	4.64	0.54

Table 4 Spiral flow method

Parameter	Unit	Value
Toll temperature	°C	50
Dosing	cm^2	20
Injection pressure	bar	700
Pack and hold pressure	bar	700
Pack and hold time	s	10
Cool time	s	10
Molding temperature	°C	200
Injection speed	cm^2/s	20

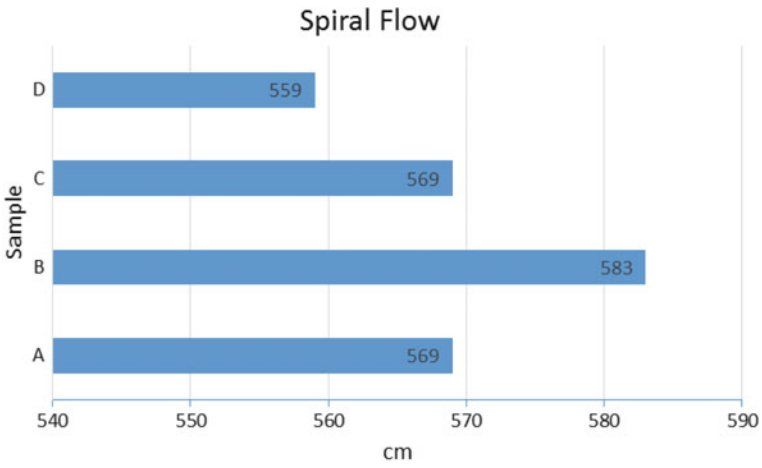

Fig. 5 Spiral flow test results

Conclusions

In general, samples B (lubricant) and D (metal oxide) presented different performance when compared to standard sample A (PPC).

Concerning the results of the tensile properties, it was observed that the sample B (lubricant) showed higher elastic modulus result when compared to the other samples, it had similar results in maximum tensile stress and elongation at maximum force.

For the Charpy impact test, sample D (metal oxide) presented the most outstanding result in relation to the notched test, being 30.43% lower than the other samples, on average. This can be explained by the greater fragility caused by the increase of the degree of crystallinity in this sample.

In relation to possible interferences with the melt index of the base polymer and / or standard A (PPC), it was observed that sample B (lubricant) showed a spiral flow

result about 3% higher than the average of the other samples. Thus, it is concluded that sample C (metal salt) was interfered less with the base polymer, keeping the results very close to the standard sample. Sample D (metal oxide) presented a more interfering character, since it increased the crystallinity and made the sample more fragile. Sample B (lubricant) was considered an interesting alternative for the processing facilitation of the studied polymer due to the promotion of higher flow, without presenting losses in the mechanical properties evaluated.

Acknowledgements The authors thank IPEN-CNEN/SP and ITA for their support and encouragement in carrying out this work.

References

1. Pitt FD, Boing D, Barros AAC (2011) Desenvolvimento histórico, científico e tecnológico de polímeros sintéticos e de fontes renováveis. Unifebe, Santa Catarina
2. Murphy J (2001) Additives for plastics handbook. Elsevier Advanced Technology, Oxford
3. Rabello M (2000) Aditivação de polímeros. Artliber Editora Ltda, São Paulo
4. Zweifel H, Maier RD, Schiller M (2009) Plastics additives handbook. Hanser Publisher, Munich
5. American Society for Testing and Materials (2010) Standard test method for tensile properties of thin plastic sheeting. ASTM (ASTM D882—10)
6. International Organization for Standardization (2012) Plastics—determination of tensile properties—part 1: general principles. ISO (ISO 527-1)

Study of Durability of Mortars with Effluent Sludge from Paper Industry Exposed to Salt Spray

A. R. G. Azevedo, J. Alexandre, G. C. Xavier, E. B. Zanelato, M. T. Marvila, N. A. Cerqueira, B. C. Mendes and S. N. Monteiro

Abstract Mortar is a widely used building material and has its application in buildings in extremely vulnerable environments and susceptible to degradation, such as facades. The objective of this work was to evaluate the loss of mechanical resistance to compression and flexure and the loss of mass of the mortars with effluent sludge from paper industry, when exposed to saline environments. The specimens were done with 0, 5, 10 and 15% of incorporation in lime paste and subjected to saline mist equipment that sprays salt solution in cycles simulating natural degradation conditions using literature data. It can be concluded that mortars with a 15% incorporation obtained a significant loss of mass and a decrease in their mechanical resistance, which impairs their use in civil construction and influence in other properties of the material, with a level of incorporation of 10% the results within Brazilian standards.

Keywords Mortar · Paper waste · Salt spray

A. R. G. Azevedo (✉) · J. Alexandre · G. C. Xavier · E. B. Zanelato · M. T. Marvila · N. A. Cerqueira
LECIV—Civil Engineering Laboratory, UENF—State University of the Northern Rio de Janeiro, Av. Alberto Lamego, 2000, Campos dos Goytacazes, Rio de Janeiro 28013-602, Brazil
e-mail: afonso.garcez91@gmail.com

A. R. G. Azevedo
IFF—Federal Institute Fluminese, DIRINF—Directorate of Infrastructure Rectory, St. Cel. Valter Kramer, 357—Parque Vera Cruz, Campos dos Goytacazes, Rio de Janeiro 28080-565, Brazil

B. C. Mendes
Federal University of Viçosa, UFV, Av. Peter Henry Rolfs, s/n—Campus Universty, Viçosa, Minas Gerais 36570-000, Brazil

S. N. Monteiro
Department of Materials Science, IME—Military Institute of Engineering, Square General Tibúrcio, 80, Rio de Janeiro 22290-270, Brazil

B. Li et al. (eds.), *Characterization of Minerals, Metals, and Materials 2018*, The Minerals, Metals & Materials Series,
https://doi.org/10.1007/978-3-319-72484-3_71

Introduction

The civil construction sector has shown considerable growth in the last decades, having great influence in social and economic terms, proof of this are the sector's employability indicators. This sector is the activity with the greatest consumption of natural resources of the planet [1], both in the manufacturing of applied materials, as in the construction processes (water, sand, clay, limestone and energy are highly consumed in different stages). Thus, cement is the second most consumed product in the world today, second only to water [2]. In addition, it is important to highlight the environmental pollution caused by the construction sector. The cement industry itself is highly polluting because of the high levels of carbon dioxide released in the production of cements and other binders.

With the aim of reducing the use of Portland cement and the natural materials used in the manufacture of mortar, the civil construction industry has been incorporating industrial waste into the building materials. These residues, previously presented as a material to be discarded and an environmental problem to be solved, must be incorporated in a way that does not harm the properties of the materials, for this, it is essential the characterization of the material and verification of its influence when incorporated to its destination, since the durability of the mortar coverings is essential for a reduction in the consumption of the materials in the long term.

Among the residues available for use is the waste from the paper industry. The pulp and paper industry has great economic and social importance in generating income and resources. It is estimated that the papermaking industry has grown steadily in recent years, however, this increase has traditionally been linked to a myriad of problems. It can exemplify as serious environmental problems the great consumption of natural resources such as wood, generation of a considerable amount of solid waste, in the case of effluents and pollution of the atmosphere with the emission of gases.

Checking the durability of a mortar with addition of a new residue is important because even if it achieves suitable properties, the mortar must be durable. A coating with little life beyond financial losses, will also consume more natural resources in its replacement. Among the environments where the durability is most affected are environments exposed to high salinity, which justifies the verification of this work regarding the behavior of mortar with effluent of the papermaking sludge in contact with salt spray [3]. The contact with saline environment promotes the penetration of chlorine in saline environment and promotes multiple interactions of deterioration depending on the property of the cement material, w/c ratio [4], age [5] and addition of alternative materials such as minerals [6] and fly ash [7].

The objective of this work is to evaluate the durability of mortars with incorporation of effluent sludge from the paper industry instead of lime. Replacements of 5, 10, 15% were made in addition to the reference with 0% of sludge. The evaluation of durability was carried out in saline exposure through the salt spray performed and the weight loss test, the compressive strength and tensile strength.

Materials and Methods

Effluent Sludge from Paper Industry

During the production of paper are generated several residues, among the various wastes generated was chosen the sludge for study, however, it can be divided into three classes, primary, secondary or tertiary. Primary sludge is the material that sediments in the primary decanters in the effluent treatment system, consisting of sand, cellulose, fibers and other minerals. Secondary sludge is composed of soluble organic material, with a large amount of nutrients such as phosphorus and potassium. However, the tertiary sludge is composed of chemical precipitation, usually with aluminum sulphate and polyelectrolyte.

Figure 1 is illustrates the location of waste collection in the paper industry.

Mortars

The mortars were measured in Trace 1: 1: 6 (cement, lime and sand). Table 1 indicates the quantity of materials for each replacement. The amount of water was changed to maintain consistency according to NBR 13276 [7]. The test is performed in order to measure the spreading of the mortar on a table of consistency with application of strokes by height of fall, where the spreading is potentiated.

In addition to the sludge from the paper industry, the following materials were used in the manufacture of mortar:

- Cement (CPII—E—32)
- Lime (CH III)
- Small aggregate (Sand removal of river)
- Water (Provided by the distributor).

Fig. 1 View of an effluent treatment plant from a pulp paper industry. *Source* own author

Table 1 Traits developed in the work

Residue (%)	Cement (g)	Lime (g)	Sand (g)	Residue (g)	Water (g)
0	150	150.0	900	0	240.00
5	150	142.5	900	7.5	245.00
10	150	135.0	900	15.0	250.00
15	150	127.5	900	22.5	255.00

Salt Spray

The salt spray test will be performed using Equilam brand equipment (Fig. 2), which meets the specifications of NBR 8094 [8] for the exposure of coated and uncoated metal material to salt fog corrosion. A 5% NaCl solution will be used for the salt spray test by spraying the plates tested. The specimens were arranged in the apparatus so that the entire surface is exposed to the mist. Within the chamber the saline solution is sprayed as a thin mist over the samples where the internal temperature remains constant. The test should last 300 h.

After exposure of the test specimen in the saline fog chamber, they will be submitted to two types of tests: mass loss and mechanical resistance. The mass loss consisted of placing the test body in a balance with adequate precision and comparing the mass found before the exposure with the measurement after, thus being able to find how much was lost.

In order to perform the flexural strength test, the prepared specimens were placed in the support devices of the test equipment so that the shallow face is not in contact with the supporting devices or with the devices of load. Subsequently, a load of

Fig. 2 Salt spray equipment. *Source* own author

(50 ± 10) N/s was applied until the specimen was ruptured. For the compression resistivity test, the two halves of ruptured specimens were used. The specimens shall be positioned so that the shallow face does not come into contact with the support device or the loading device. A load of (500 ± 50) N/s was applied until the specimen was ruptured.

Results

For the preparation of the specimens, the consistency test was first carried out to verify the amount of water to be added. After successive attempts with different amounts of water added for each trait, the values presented in Table 2 were obtained.

After the preparation of the mortar specimens and exposure to the saline mist, tests of mass loss, compressive strength and tensile strength were performed, as described in the methodology described above.

The mass loss test, as shown in Fig. 3, indicates a decrease in the amount of mass lost due to exposure to the saline mist with increasing amount of sludge,

Table 2 Consistency test

Trait (% residue)	Amount of water (g)	Mortar spreading (mm)
0	240	258
5	245	261
10	250	260
15	255	258

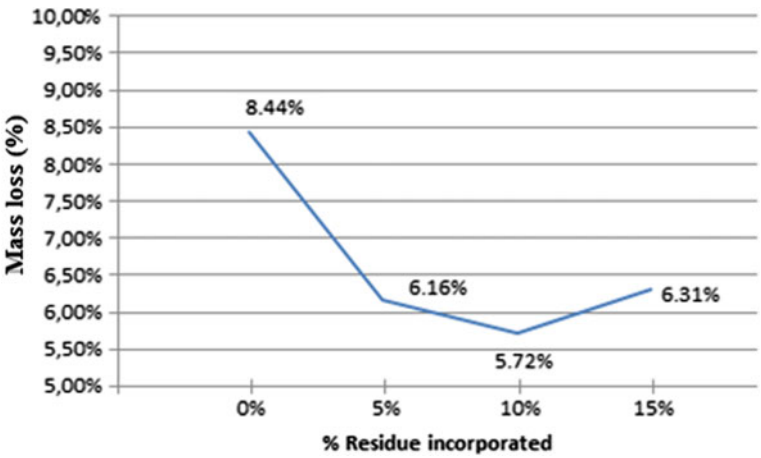

Fig. 3 Result of mass loss after exposure to saline mist

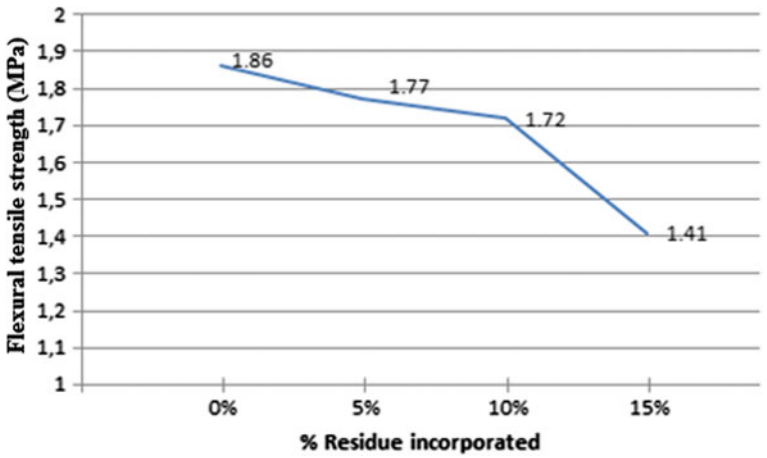

Fig. 4 Results of tensile strength in flexion

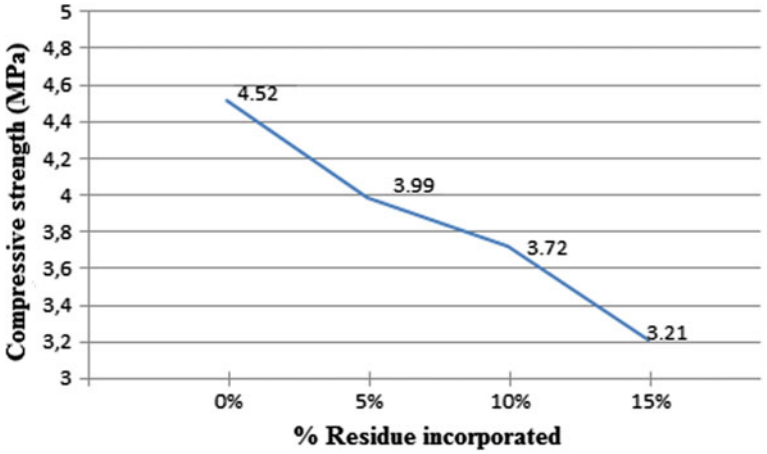

Fig. 5 Results of compressive strength

however, with 15% incorporation the results indicate a growth, therefore, it is verified that 10% of incorporation achieved the lowest mass loss.

The results obtained in the flexural tensile strength test, as indicated in Fig. 4, showed a tendency to decrease the resistance with increasing amount of residue. The loss of strength 15% corporate residue was significant, whereas incorporation of 5 and 10% showed no significant reduction compared to the reference.

Similar to that obtained in the flexural tensile strength test, the results of the compression test, according to Fig. 5, indicate a decrease in the compressive strength with increased residue incorporation. However, the decrease in strength was significant for all residue incorporations [9].

Conclusion

It can be concluded from this work that the incorporation of paper waste presented a reduction in the mass loss when exposed to the salt mist, which is generally beneficial to the mortar. However, in relation to the resistance, there was decrease when incorporating the paper residue.

Among verified embodiments, embodiments with values above 10% have marked loss trend important properties for mortar, therefore, incorporation of 5 and 10% despite the loss less pronounced resistance can be used as a target for these rejects, provided that they meet the minimum requirements of the final application.

Durability is an important parameter to be analyzed in building materials, especially those exposed to the environment, as the mortar. The loss of mass influence on mechanical resistance and compactness of the mass in the hardened state, working for example on penetration of CO_2 that can be harmful to cementitious matrix due to formation of portlandite, because it reacts with the substrate that can trigger damage to the buildings. In addition, excess portlandite can cause damage to the existing reinforcement, in some cases, causing the formation of oxides and their deterioration.

Acknowledgements The authors thank the Brazilian agencies: CNPq, CAPES and FAPERJ for the support provided to this investigation.

References

1. Vladimir GH, Graça V, Paulo BL (2011) Influence of aggregates grading and water/cement ratio in workability and hardened properties of mortars. Constr Build Mater 156(3):2980–2987
2. Zhang L, Gustavsen A, Jele BP, Yang L, Gao T, Wang Y (2017) Thermal conductivity of cement stabilized earth blocks. Constr Build Mater 151(1):504–511
3. Sugiyama T, Bremner T, Tsuji Y (1996) Determination of chloride diffusion coefficient and gas permeability of concrete and their relationship. Cem Concr Res 26(5):781–790
4. Güneyisi E, Gesoğlu M, Özturan T, Özbay E (2009) Estimation of chloride permeability of concretes by empirical modeling: considering effects of cement type, curing condition and age. Constr Build Mater 23(1):469–481
5. Wee T, Suryavanshi AK, Tin S (2000) Evaluation of rapid chloride permeability test (RCPT) results for concrete containing mineral admixtures. Mater J 97(2):221–232

6. Simcic T, Pejovnik S, Schutter G, Bosiljkov VB (2015) Chloride ion penetration into fly ash modified concrete during wetting–drying cycles. Constr Build Mater 93:1216–1223
7. Brazilian Association of Technical Standards. (2016) NBR 13276 Mortars applied on walls and ceilings—Determination of the consistence index. Rio de Janeiro, 2016
8. Brazilian Association of Technical Standards. (1983) NBR 8094 Coated and uncoated metallic material—corrosion by exposure to salt spray—test method. Rio de Janeiro, 1983
9. Azevedo ARG, Alexandre J, Zanelato EB, Marvila MT (2017) Influence of incorporation of glass waste on the rheological properties of adhesive mortar. Constr Build Mater 148(8): 359–368

Study of the Incorporation of Residue of Ornamental Rocks in Ceramic Tiles

M. T. Marvila, J. Alexandre, A. R. G. Azevedo, E. B. Zanelato, S. N. Monteiro, G. C. Xavier, M. Goulart and B. Mendes

Abstract The incorporation of industrial waste into ceramic tiles is a major trend in the search for alternative raw materials, and also in the search for environmentally correct disposal of waste. In order to evaluate the effect of the incorporation of residues from the ornamental stone industries, in the properties of ceramic tiles, incorporations of up to 40% by weight of the residue in ceramic mass were studied. It is noteworthy that this residue is constituted basically by limestone and its characterization was performed by grain size analysis, Atterberg boundaries, grain density and chemical analysis by X-ray fluorescence. The specimens were burned at 800 °C and the following properties were evaluated: linear retraction, water absorption and bending rupture stress. The results indicated that the residue of ornamental rocks is a material with potential to be used as a component in the mass of red ceramic tiles.

Keywords Ceramic tiles · Ornamental stone waste and red ceramic

M. T. Marvila (✉) · J. Alexandre · A. R. G. Azevedo · E. B. Zanelato · G. C. Xavier · M. Goulart
UENF—State University of the Northern Rio de Janeiro LECIV—Civil Engineering Laboratory; Av. Alberto Lamego, 2000, Campos Dos Goytacazes, 28013-602 Rio de Janeiro, Brazil
e-mail: markssuel@hotmail.com

A. R. G. Azevedo
DIRINF—Directorate of Infrastructure Rectory, IFF—Federal Institute Fluminese, St. Cel. Valter Kramer, 357—Parque Vera Cruz, Campos Dos Goytacazes, Rio de Janeiro 28080-565, Brazil

S. N. Monteiro
Department of Materials Science, IME—Military Institute of Engineering Square General Tibúrcio, 80, Rio de Janeiro, Glória, Rio de Janeiro 22290-270, Brazil

B. Mendes
Federal University of Viçosa, UFV. Av. Peter Henry Rolfs, S/N—Campus Universty, Viçosa, Minas Gerais 36570-000, Brazil

B. Li et al. (eds.), *Characterization of Minerals, Metals, and Materials 2018*, The Minerals, Metals & Materials Series,
https://doi.org/10.1007/978-3-319-72484-3_72

Introduction

The large clay reserve of the municipality of Campos dos Goytacazes motivated the advance of the red ceramics market in the region. However, even though it is a sector of great reach, the technological advances of the sector are still stationed and consequently the processes used since the beginning of the activities continue being used in great part of the ceramics.

It can also be verified a predominance of the exclusive manufacture of ceramic blocks, being the manufacture of tiles restricted to some ceramics of the region. The lower availability of tiles is justified by the inferior quality of the region [1], which provide ceramic pieces with a not so high quality and therefore, due to the high quality requirements of the tiles [2], these clays are not indicated for manufacture thereof.

In order to improve the quality of the ceramic pieces manufactured, in order to be able to produce tiles with the clay of the region, the incorporation of non-conventional materials becomes an alternative. Among the available materials in the region is the ornamental rock residue from Cachoeiro de Itapemirim, Espirito Santo.

The municipality of Cachoeiro de Itapemirim in the state of Espirito Santo, has one of the largest poles of ornamental stone production in Brazil and stands out by the beneficiation. The beneficiation is carried out by the cutting and polishing of the rock, however, these processes generate a residue of great potential pollutant and with great environmental impact, as Fig. 1.

In order to improve the properties of the ceramic pieces produced in the city of Campos dos Goytacazes, in addition to providing a suitable destination for the ornamental rock industry residue, this work aims to evaluate the properties of the ceramic pieces with substitution of clay by the residue in the incorporations of 0, 10, 20, 30 and 40%. With the addition of the residue it is expected that suitable properties for the production of ceramic tiles are obtained.

Fig. 1 The residue cutting rock ready for use

Materials and Methods

The materials to be used in the work are clay and the ornamental rock residue.

The clay used in the work was collected in one of the ceramics where tiles are already made with the clay in question. To characterize the clay, the granulometry, chemical analysis, Atterberg limits and actual grain density tests were performed.

The ornamental rock residue used in the work was collected in one of the industries responsible for the ornamental rock processing and where the residue is generated. The residue is composed of a slurry of high humidity, therefore, for use of the material at work, the material was dried at room temperature exposed to the sun and subsequently in an oven. To characterize the residue, the granulometry, chemical analysis and actual grain density tests were performed.

After the characterization of the materials was carried out, the ceramic specimens were prepared with 10, 20, 30 and 40% in addition to the reference with 0% substitution of the clay for the residue. The specimens were prepared by extrusion. Burning of the specimens was done in an oven at 800 °C.

Ceramic specimens were analyzed by linear variation, water absorption and flexural strength tests as recommended by NBR15310 [3].

Results and Discussion

The granulometric distribution has similarities between the materials, the sum of the silt + clay fraction for the soil used corresponds to 93.7%, whereas for the residue it corresponds to 98%. However, the residue presents bigger grain size since its main composition is of silt whereas the one of the soil is of clay (Table 1).

Table 2 indicates the results obtained in the chemical analysis of the clay and the residue. There can be great disparity between the materials in relation to the chemical elements.

Table 3 shows the results obtained by the Atterberg limits for clay and the actual density of the grains for the clay and the residue.

After the characterization of the materials and preparation of the test specimens, the tests were carried out on them. Figure 1 shows the results obtained for linear variation. It can be observed that the increase of the incorporation causes the decrease of the linear variation, however, the 40% content presented values significantly higher compared to the reference with 0% of incorporation (Fig. 2).

Table 1 Granulometric distribution

Samples	Boulder			Sand			Silte	Clay
	Thick	Medium	Fine	Thick	Medium	Fine		
Clay	–	–	–	0.5	0.8	5.0	35.1	58.6
Residue	–	–	–	–	1.1	0.9	58.9	39.1

Table 2 Chemical characterization

	SiO_2	Al_2O_3	Fe_2O_3	CaO	K_2O	MgO	TiO_2	SO_3	Na_2O	Others
Clay	60.02	11.94	8.65	3.57	2.26	5.12	0.89	0.27	3.14	4.14
Residue	7.21	9.23	0.75	80.26	–	1.08	0.33	0.97	–	0.17

Table 3 Atterberg boundaries and actual grain density

	CLAY	RESIDUE
LL	72.6	–
LP	28.7	–
IP	43.9	–
Yg	2.62	2.09
USCS	CH	SC

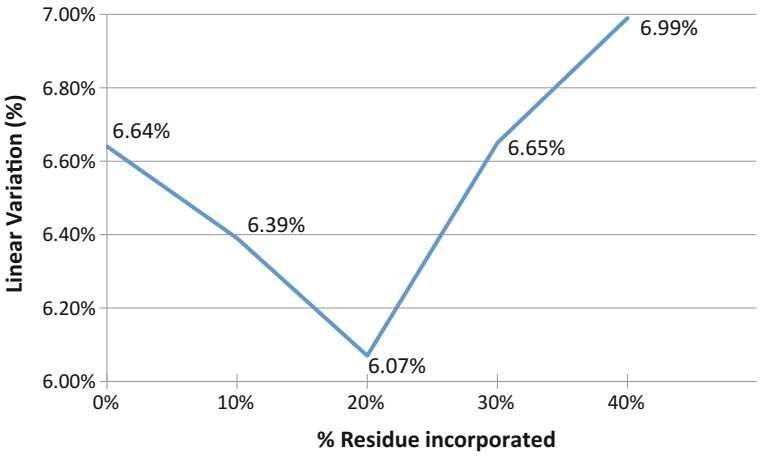

Fig. 2 Linear variation

The substitution of clay by residue also showed a decrease in water absorption, as well as in linear variation, the substitution of 20% of the clay by residue obtained the best results, besides, the incorporation of 40% also presented water absorption results expressively higher to reference (Fig. 3).

The flexural strength test also indicates the behavior of the other tests, where the incorporation of 20% obtained the highest strength and the incorporation of 40% resistance lower than the reference (Fig. 4).

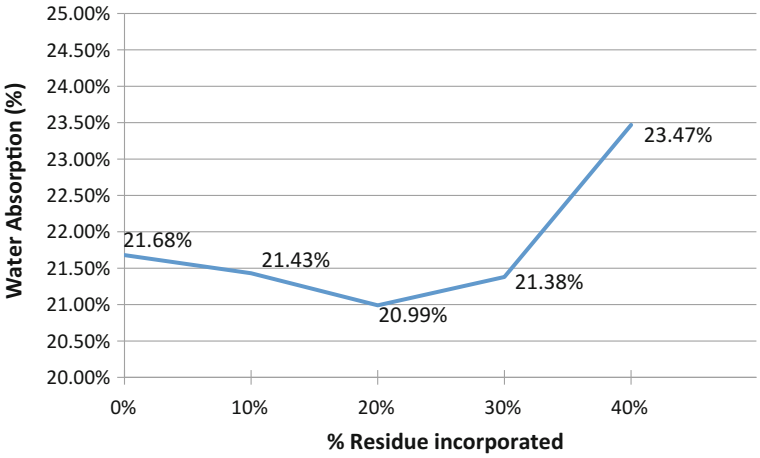

Fig. 3 Water absorption

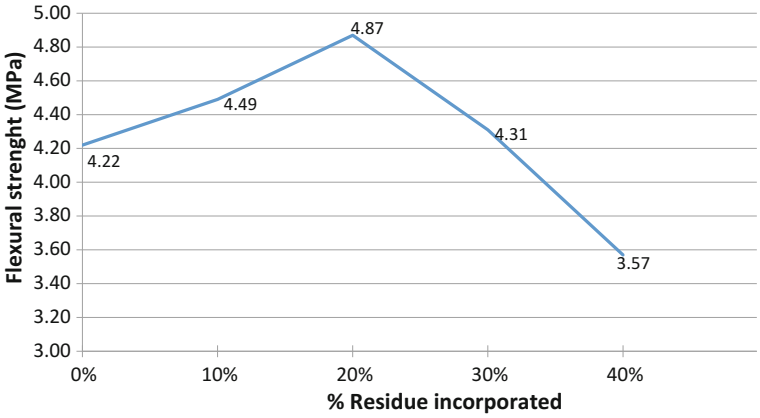

Fig. 4 Flexural strength

Conclusion

The use of ornamental rock residue in the production of ceramics is feasible, however, the amount of residue should be limited by up to 30% so that the properties of the tiles are not precarious.

Among the incorporations tested for use, the incorporation of 20% of residue presented the best results and is the most indicated to potentiate the properties of the tiles, however, all the results obtained by the water absorption test were higher than the NBR 15270-1 [4] requires, where the maximum value that a tile can have of water absorption is 20%.

It can thus be concluded that even with the improvement of tile properties due to incorporation of the residue, an increase is still necessary in order to further reduce the water absorption of the tiles so that they can be made in the standards required by the standard.

References

1. Vieira CMF, Soares TM, Sánchez R, Monteiro SN (2004) Incorporation of granite waste in red ceramics. Mater Sci Eng A V 373:115–121
2. Menezes RR, Ferreira HS, Neves GA, Lira HL, Ferreira HC (2005) Use of granite sawing wastes in the production of ceramic bricks and tiles. J Eur Ceram Soc 25:P1149–P1158
3. Brazilian Association of Technical Standards NBR 15310 (2009) Ceramic components—Tiles—Terminology, requirements and test methods. Rio de Janeiro
4. Brazilian Association of Technical Standards NBR 15270-1 (2005) Ceramic components Part 1: Hollow ceramic blocks for non load-bearing masonry—Terminology and requirements. Rio de Janeiro

Study of the Incorporation of Smectite in Powder Coating

Simeão Lopes Ferreira, Mathilde Julienne Gisele Champeau Ferreira, Francisco Rolando Valenzuela-Díaz and Maria das Graças da Silva-Valenzuela

Abstract The use of clays to formulate powder coating can improve physical properties, besides a final product with more sustainable characteristics due to the elimination of some additives, which may be substituted for the clay. We investigate the use of a modified smectite clay to formulate powder coating based on polyester resin. Four compositions of incorporated clay were evaluated (0, 4, 7, and 10 wt%). Powder coating were prepared in a twin-screw extruder at 105 °C, and characterized by XRD, FTIR and SEM. Tests of flexibility, adhesion and impact strength in accordance to ASTM standards were performed. Diffractograms of the samples showed the characteristic peak of the modified smectite in d(001) ∼ 37°(2θ), indicating exfoliation of the clay. Micrographs by SEM showed the presence of lamellar structure for the clay-based powder coating. Mechanical assays were found for all analyzed coatings, indicating that sample containing 7% of clay presents the best performance.

Keywords Powder coating · Nanocomposite · Smectite · Organoclay

Introduction

Bentonites are important industrial clays with a high number of applications [1]. There are two main types of industrial bentonites. Those that swell in water and those that do not swell in water. Those that swell in water have sodium as the preponderant interlamellar cation, may exhibit water swellings greater than 20 mL/g and may provide viscous and thixotropic aqueous dispersions at low clay concentrations. Those that do not swell in water exhibit water swells in the order of 2 mL/g and do not provide

S. L. Ferreira · M. J. G. C. Ferreira · M. d. G. da Silva-Valenzuela (✉)
Naturals and Humans Science Center of Federal, University of ABC, Avenida dos Estados, 5001, 09210-580 Santo André, SP, Brazil
e-mail: gracavalenzuela@gmail.com

F. R. Valenzuela-Díaz · M. d. G. da Silva-Valenzuela
Metalurgic and Materials Engineer Department, Polytechnic School of University of São Paulo, Avenida Prof. Mello Moraes, 2463, 05508-030 Sao Paulo, SP, Brazil

B. Li et al. (eds.), *Characterization of Minerals, Metals, and Materials 2018*, The Minerals, Metals & Materials Series,
https://doi.org/10.1007/978-3-319-72484-3_73

viscous and thixotropic aqueous dispersions even at high concentrations of clay. The main uses of water-swelling bentonites are as rheological additives of water-based drilling fluids such as sand binders in metal casting molds, mineral fines binders, binder component of animal feed, active material or rheological additive for cosmetics and pharmaceuticals, and as gelling, thixotropic and suspending agents in water-based paints [2]. The organophilic bentonites, obtained from the treatment of crude bentonite with quaternary salt, for example, show swelling (delamination, with formation of thixotropic dispersions at low concentrations of clay) in specific organic liquids [3]. Organophilic bentonites are obtained by the ionic exchange of cations present in sodium smectite clays with organic cations mainly from quaternary ammonium salts [4]. The main uses of organophilic bentonites are as thixotropic additives in oil-based oil drilling fluids, adsorbents of toxic substances, components of cosmetics, and components of inks and enamels based on organic solvents [3]. Nanocomposite materials based on polymers and clays have, generally, some improved properties, in relation to the original polymer, due to the reinforcement of the clay acting as nanometric charge. Smectites are widely used to form nanocomposite systems. These clays have a lamellar structure which favors the dispersion of the polymer between their lamellae while they intercalate or exfoliate to form the structure of a polymer/clay nanocomposite. The montmorillonite clay (MMT) is the most used smectite in the formation of these nanocomposites. Powder coating is obtained without the use of solvents from basic formulation which may include polyester resin as the main raw material, besides to other chemical agents having the function of catalysts, accelerators and fillers. Modifications in the formulation of such polymer coating by the addition of clay, substituting some components of the formulation, may result in a powder coating presenting improved properties due to the formation of a polyester resin/clay nanocomposite. Such improvement generally is described through barrier, mechanical, and thermal properties. Moreover, anticorrosive properties for powder coating has been observed by incorporating 2 and 4 wt% of montmorillonite to the formulation of a polyester-based powder coating [5]. In the present work, we investigate the synthesis and characterization of a polyester-based powder coating, and the influence of a organophilic clay (OMMT) on its mechanical properties.

Experimental

Materials

The materials utilized to obtain the powder coating were polyester resin, kindly provided by Clean Coat Chemical, from São Paulo, Brazil, a commercial organophilic montmorillonite of trade name HP-PLUS®, triglicidilisocyanurate (TGIC), 2-hydroxy 1,2-diphenylethanone (Benzoin), and polysiloxanes/polyacrylates special mix.

Methods

Powder Coating Preparation

The powder coating was prepared in five basic formulations containing different quantities of OMMT. Four formulations, F1, F2, F3, and F4, were prepared with 0, 4, 7, and 10 wt% of the organophilic clay, respectively, and other materials were not used as charge; one formulation, F5, was prepared with calcium carbonate 10 (wt%) substituting the clay as charge material. Table 1 list the composition of the five formulations, where it is observed that the amount of resin decreases as the amount of clay increases.

The components of each formulation suggested in Table 1 were placed in a plastic bag and sealed with excess of compressed air. The mixture was then homogenized for 60 min on a seesaw shaker at 300 rpm. After the time under stirring, the material was transferred to a twin-screw extruder, where it was melted at 105 °C, and after compressed through cooled calenders to obtain slides which were first processed into chips and then milled and sieved through a 170 mesh to produce a powder material with an average particle diameter of approximately 90 μm, the powder coatings.

X Ray Diffraction (XRD)

X ray diffraction was used to determine the structures of the clay, polyester resin and powder coatings (F1–F5). XRD patterns were recorded by a Rigaku X-ray diffractometer, model MiniFlex 600, for angular range 3°–90° (2θ), and counting time 10 s per step of 0.02°.

Table 1 Formulations used to obtain the powder coatings

Components	Formulations (wt%)				
	F1	F2	F3	F4	F5
Polyester resin	91.2	87.6	84.8	82.0	82.0
TGIC	6.9	6.6	6.4	6.2	6.2
Benzoin	1.2	1.2	1.2	1.2	1.2
Polysiloxanes/ polyacrylates	0.6	0.6	0.6	0.6	0.6
OMMT	0	4	7	10	0
Calcium carbonate	0	0	0	0	10

Scanning Electron Microscopy (SEM)

Morphology of samples of the clay, polyester resin and powder coatings (F1–F5), were analyzed by a SEM (FEI INSPECT F50).

Fourier-Transform Infrared Spectroscopy (FTIR)

Absorption spectra by FTIR were recorded for the clay, polyester resin and powder coatings (F1–F5) samples by using an apparatus from Thermo Nicolet, model iS5, in the wavenumber range 4000–400 cm^{-1}.

Mechanical Strength Analysis

Mechanical strength analysis was performed for all powder coating samples. A thin layer of each powder coating was applied onto small steel panels measuring $12 \times 9 \times 0.1$ (cm), using a corona electrostatic gun, forming a film, then the panels were taken to the oven for drying at 200 °C for 10 min. After cooling to room temperature, the mechanical strength tests were performed for each panel to observe the behavior of the films, which presented average thickness of 77 μm.

Adhesion

Adhesion tests were performed as described in ASTM D3359:2017 standard, for F1–F5 samples. Cuttings were made in grid shapes with the aid of a stylet. Thereafter, fibrous adhesive tape was placed over the cuts and then removed, verifying if parts of the applied powder coating were withdrawn.

Flexibility

Flexibility was observed for F1–F5 samples following the ASTM D522 M-13 standard. In this test, the panel was folded into a conical mandrel and the presence or absence of cracks in the film was analyzed.

Impact Resistance

Impact resistance tests were realized as described in ASTM D2794: 2010, where a ball-point with 1.0 kg was inserted into a dropped column and launched on the panel of a given height, generating a rapid deformation on the panel, what can cause alteration in the applied film.

Results and Discussion

Figure 1 shows the XRD patterns for the clay and the F1–F5 samples. The clay diffractogram presents two main peaks, one attributed to the organophilic smectite in the intercalated form in d(001) = 23.5 Å, and another peak in d(001) = 12.08 Å attributed to the crude smectite. The XRD curves of the powder coating samples F2, F3 and F4 have a peak in d(001) $\sim$ 37 Å attributed to the organophilic smectite in the intercalated form and the peak in d(001) $\sim$ 18.00 Å attributed to the crude smectite. These results indicated the formation of the polyester resin/smectite nanocomposites where the clay was exfoliated.

The FTIR spectra of the clay, polyester resin, and F1–F5 samples, shown in Fig. 2, reveals changes in the spectra of F2, F3, and F4 samples in the region between 1100 and 1000 cm^{-1}, presenting a little peak around 1040 cm^{-1}, indicating interaction of the resin with the clay and complementing the results of XRD [6].

Differences in the surface structure among analyzed sample were observed by scanning electron microscopy (Fig. 3), which showed that the F2, F3, and F4 samples, in comparison with F1 and F5 samples, presented lamellar surface structure, what were acquired by incorporation of the clay in the polyester resin. This characteristic is more visible in Fig. 3d that shows the distribution of the clay minerals lamellae in the polymer matrix in higher magnification (10,000×), where it is possible to observe a rough surface structure, while the Fig. 1b shows a predominantly smooth surface structure.

Tests of mechanical resistance were carried out based on international standards. They are important to observe deformations caused after application of the material on the panel and consequent manipulation, as well as the exposure to the weather.

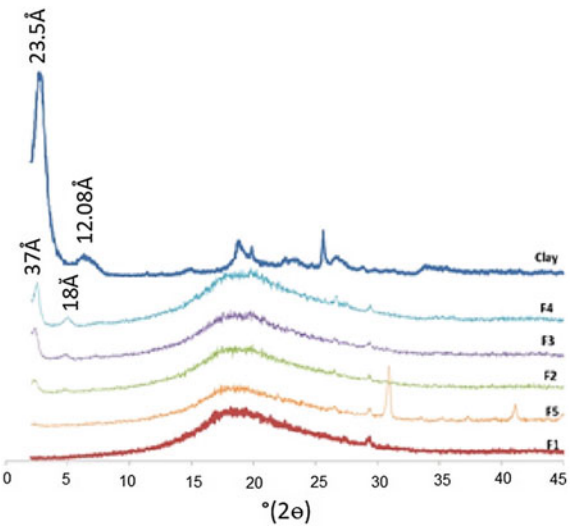

Fig. 1 XRD patterns for clay and polyester resin/clay samples

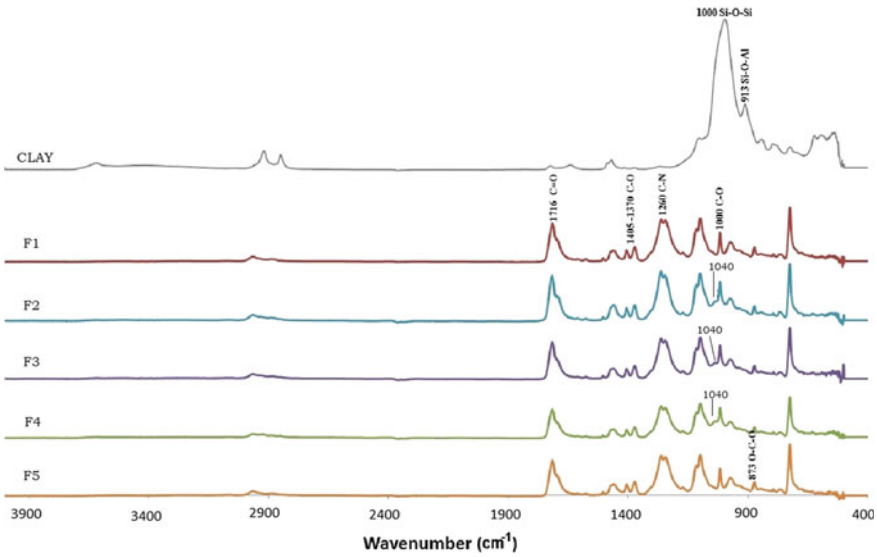

Fig. 2 FTIR spectra of the clay and F1–F5 samples

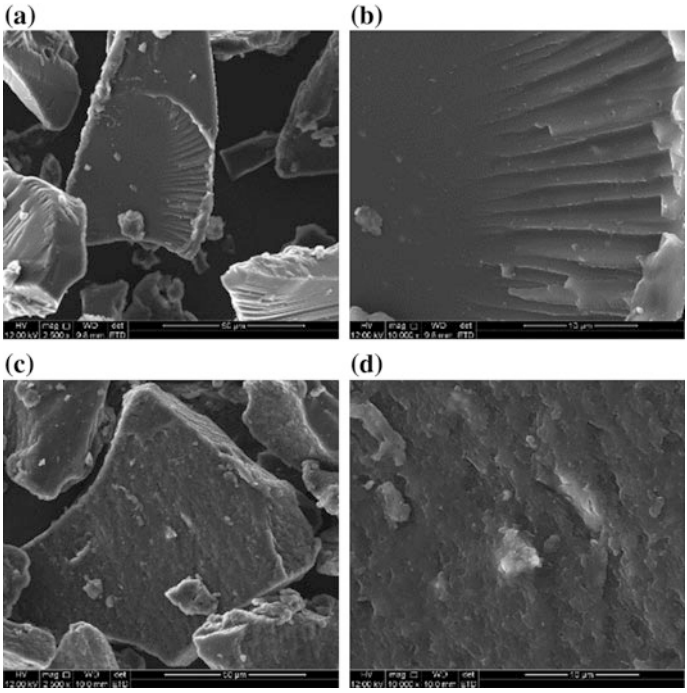

Fig. 3 Micrographs by SEM for F1 (**a**, **b**) and F4 (**c**, **d**)

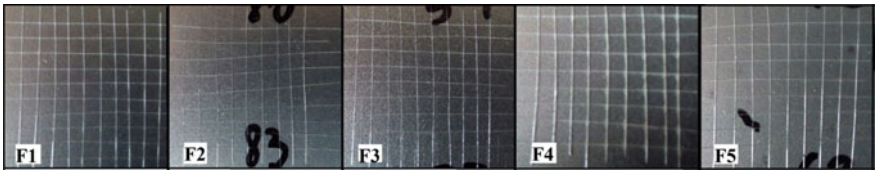

Fig. 4 Images of the adhesion tests for F1–F5 samples

In general, the purpose of these tests is to observe and evaluate the appearance of cracks causing peeling of the powder coating on the applied surface.

Adhesion tests were performed to evaluate the surface adhesiveness among powder coating samples on the panels. The results of these tests showed that the five formulations analyzed showed adequate adherence, that is, the applied powder coating did not detach from the panels, as shown in Fig. 4.

Flexibility and impact resistance assays were realized for all samples. Samples of the formulations F1–F3 and F5 presented good results, showing that homogeneity of the films on the panels was conserved after the tests, which is an indication that the reticulation process was complete. However, for F4, changes related to cracks suffered by the powder coating film on the panel were observed for both tests, flexion and impact tests, indicating that this formulation, which uses 10% of clay, presents less mechanical resistance compared to the other formulations analyzed. Figures 5 and 6 shows illustrative images of that tests.

A special characteristic observed for the powder coatings containing clays (F2, F3, and F4), analyzed in this present work, is texture appearance in comparison to the samples containing no clay, as can be observed in the Figs. 5 and 6.

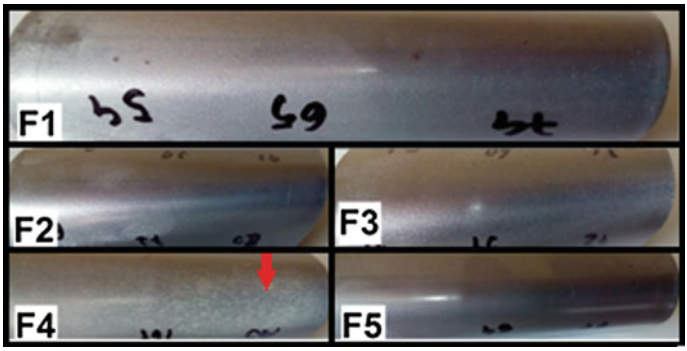

Fig. 5 Images of flexibility tests for analyzed samples, showing cracks for the F4 sample (red arrow) (Color figure online)

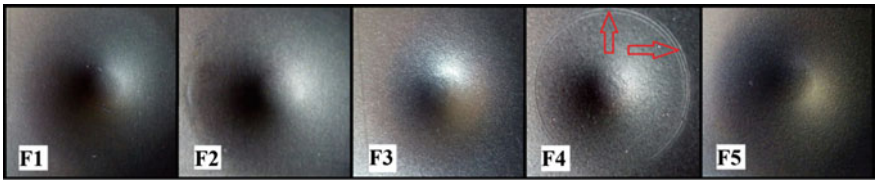

Fig. 6 Images of impact resistance tests for F1–F5 samples, showing cracks for the F4 sample. F4 (red arrow) (Color figure online)

Conclusion

In the present work, the synthesis and characterization of polyester resin/clay nanocomposites as powder coating were evaluated from formulations containing different concentrations of clay, which were compared to formulations without clay. It was observed that the clay-based powder coatings presented texture aspect, and tests indicated that 4 and 7% concentration appear more suitable for the formulation of powder coating because showed more mechanical strength. In these materials clay replaces charges generally used in the formulations, such as barium sulfate, dolomite and calcium carbonate, besides others, forming a nanocomposite with the polyester resin. We conclude that 7% concentration it is the most viable analyzed formulation, and can contribute to obtain a lower cost and environmentally friendly material. However, further studies should be performed to evaluate structures, processes for obtaining, and quantifying the mechanical strength.

Acknowledgements We are grateful to São Paulo Research Foundation (FAPESP) for financial support. One of us (SLF) would like to thank ABC Federal University for research scholarship.

References

1. Murray HH. (2007) Applied clay mineralogy: Occurrences, processing and application of kaolins, bentonites, palygorskite sepiolite, and common clays, 1st edn. Elsevier Science, Amsterdam
2. Bergaya F, Lagaly G, Vayer M (2006) Cation and anion exchange. In: Bergaya F, Theng BKG, Lagaly G (eds) Handbook of clay science, 1st edn. Elsevier Science, Amsterdam, pp 79–100
3. Paiva LB, Morales AR, Valenzuela-Díaz FR (2008) Organoclays: properties, preparation and applications. Appl Clay Sci 42:8–24
4. Valenzuela-Díaz FR (2001) Preparation of organophilic clays from a Brazilian Smectite Clay. Key Eng Mater 189–191:203–207

5. Piazza D, Silveira DS, Lorandi NP, Birriel EJ, Scienza LC, Zattera AJ (2012) Polyester-based powder coatings with montmorillonite nanoparticles applied on carbon steel. Prog Org Coat 73 (1):42–46. https://doi.org/10.1590/1516-1439.312714
6. Silva-Valenzuela MG, Fabozzi GA, Cebukin F, Wiebeck H, Valenzuela-Díaz FR, Wang SH. (2016) Preparation and characterization of microcapsules from PBSL/VMF2 nanocomposite. In: Ikhmayies SJ, Li B, Carpenter JS, Hwang J-Y, Monteiro SN, Li J, Firrao D, Zhang M, Peng Z, Escobedo-Diaz JP, Bai C (eds) Characterization of minerals, metals, and materials 2016. Wiley, Hoboken. doi:https://doi.org/10.1002/9781119263722.ch28

Study of the Mineralogical Composition of the Tailings of Coscotitlán, Hidalgo, México

R. Aislinn Michelle Teja, T. Julio Cesar Juárez, P. Martín Reyes, C. Leticia Hernández, G. Mizraim Uriel Flores, D. Iván Alejandrox Reyes, L. Miguel Pérez and T. Raúl Moreno

Abstract This study shows the characterization of tailings from the mining district of Coscotitlán, State of Hidalgo, Mexico. Chemical analysis by Spectroscopy of atomic absorption (AAS) allowed to quantify the concentration of Fe, Mn, Zn, and Pb as the most abundant elements in the mineral sample; in addition to the presence of Sn, Te, Bi, Ni, Co, and Cd. The presence of precious metals as the Ag (64 g ton^{-1}) and Au (0.65 g ton^{-1}) were identified. The greater distribution of Ag was detected in particles with diameter of 74 μm. Species as pyrite (FeS_2), galena (PbS) and hematite (Fe_2O_3) were observed in a matrix of quartz (SiO_2) by Polarized

R. Aislinn Michelle Teja (✉) · T. Julio Cesar Juárez · P. Martín Reyes · C. Leticia Hernández
L. Miguel Pérez · T. Raúl Moreno
Área Académica de Ciencias de la Tierra y Materiales, Universidad Autónoma
Del Estado de Hidalgo, Carretera Pachuca-Tulancingo Kilómetro 4.5,
42184 Pachuca, HGO, Mexico
e-mail: ice9791@gmail.com

T. Julio Cesar Juárez
e-mail: jcjuarez@uaeh.edu

P. Martín Reyes
e-mail: mreyes@uaeh.edu.mx

C. Leticia Hernández
e-mail: lesperanza.hernandez@gmail.com

L. Miguel Pérez
e-mail: MIGUELABRA@hotmail.com

T. Raúl Moreno
e-mail: morenot@uaeh.edu.mx

G. Mizraim Uriel Flores
Área de Electromecánica Industrial, Universidad Tecnológica de Tulancingo,
Camino a Ahuehuetitla 301 Col. Las Presas, 43642 Tulancingo, HGO, Mexico
e-mail: uri_fg@hotmail.com

D. Iván Alejandrox Reyes
Catedrático CONACYT-Instituto de Metalurgia, Universidad Autónoma de San Luis Potosí,
Av. Sierra Leona no. 550, Lomas 2da Sección 78210, 78210 Potosí, SLP, Mexico
e-mail: ivanalejandro2001@hotmail.com

B. Li et al. (eds.), *Characterization of Minerals, Metals, and Materials 2018*, The Minerals, Metals & Materials Series,
https://doi.org/10.1007/978-3-319-72484-3_74

Optical Microscopy (POM), these species were also identified by X-ray Diffraction (XRD). Both the elemental and mineralogical composition of tailings was corroborated by the technique Scanning Electron Microscopy - Energy Dispersive Microanalysis (SEM-EDS).

Keywords Tailings · Silver · Thiosulfate · Characterization

Introduction

In Mexico, mining is one of the most traditional economic activities, which has been developed for nearly five centuries. Due to this, the mining industry faces environmental problems such as the accumulation of tens of millions of tonnes of mining waste known as tailings. In the State of Hidalgo, the tailings produced by the Pachuca-Real del Monte mining district Were generated like wastes from three technologically different periods: milling-amalgamation, milling-cyaniding and milling-flotation-cyaniding [1, 2]. The state of Hidalgo has been a major producer of lead, zinc, copper, gold and silver. Most of the metals of economic interest of this region are associated to a complex and variable mineralogy constituted by calcosilicates, sulfosales, oxides and sulfides like pyrite, chalcopyrite, galena and blenda. Some refractory gold and silver minerals are also part of the regional mineralogy, this characteristic makes them difficult to extract by conventional hydrometallurgical processes [3, 4].

Currently, the benefit of metals from mining waste represents an important secondary source of recovery, which is considerably profitable due to the tonnage and concentration of various elements such as Cu, Pb, Zn, Fe, Mn, Mg, Sb, As and Ni, as well as the content of precious metals and rare earths. The process of cyanidation has been used for more than a hundred years for the extraction of metallic values of gold and silver from its minerals; however, one of the disadvantages of this process is its high degree of toxicity and its inefficiency to the dissolution of refractory minerals. For the treatment of this type of complex minerals or the use of secondary sources, leaching alternatives have been studied. The leaching with thiosulphates ($S_2O_3^{2-}$) is currently considered as a non-toxic alternative to the cyanidation process [5, 6]. This system has been developed as means for dissolving precious metals immersed in quartz matrices since one of the advantages of the process with respect to the cyanide is the selectivity in the silver extraction.

The addition of metallic ions to the system like copper and zinc [7] has favored the process, reaching higher percentages of dissolution of precious metals and reducing the times of leaching to different temperatures [8–10].

In the present study, the chemical and mineralogical characterization of the Coscotitlán tailings was developed, with the purpose of identifying the metallic values and the species that contain them, paying special attention to the concentration of silver, due to the intention to generate a proposal of recovery of this metal,

through the leaching with thiosulphate in the presence of oxygen and adding Ni^{2+} ions as oxidizing agent of the precious metal, trying to improve the percentages of dissolution with respect to the conventional process.

Experimentation—Experimental Methods

The sample of the jales comes from the Ex-hacienda of Coscotitlán and was provided by the Real del Monte and Pachuca Company, the state's most important mining and productive company located in the cities of Pachuca de Soto and Real del Monte, in Hidalgo, Mexico.

The mineral sample was totally dried, homogenized and repeatedly chopped up to obtain a representative 200 g sample. The mineral tailing were mounted in epoxy to know their morphology and to identify the mineral species present in the ore by using Scanning electron microscopy-Energy-dispersive X-ray spectroscopy (SEM-EDS). The dust in the sample was also mineralogicaly analyzed through the X-ray diffraction technique (XRD). The chemical analysis was performed in triplicate using 1 g of mineral digested with aqua regia (3 parts HCl for 1 part HNO_3) and heated until dry. A smaller volume of aqua regia was then added, the insoluble was filtered and the remaining solution was gauged at 0.1 L. The identification and quantification of the elements present in the mineral sample was conducted by Atomic Absorption Spectrophotometry (AAS), using a spectrophotometer Perkin Elmer-Analyst 200.

The equipment used for the mineralogical study was the following: INEL EQUINOX 2000 X-ray diffractometer, with a Cu-Ka1 radiation of 1.540598 Å, operation at 30 mA and 20 kV, 220 V and a resolution of 0.095 FWHM. JEOL JSM 6701F scanning electron microscope, with a voltage of 25 kV and a depth of field of 16.5 mm at different magnifications with secondary electrons. In order to determine the viability of dissolution of the silver in the $S_2O_3^{2-}-O_2-Ni^{2+}$ system, two preliminary experiments were performed under the following experimental conditions: Particle diameter = 53–74 μm, mineral sample amount = 40 gL^{-1}, pH = 9, volume of solution = 0.5 L, stirring speed = 670 min^{-1}, $[S_2O_3^{2-}]$ = 40 gL^{-1}, oxygen partial pressure = 1 atm, $[NiSO_4]$ = 2 gL^{-1}, temperature = 298 K and leaching time = 300 min

Results and Discussion

In accordance to the conditions described in the experimental method, the samples of tailings were chemically and mineralogicly characterized using the following techniques.

Chemical Analysis by Chemical Analysis by Atomic Absorption Spectrometry (AAS)

In the Pachuca-Real del Monte Mining District, a large volume of mining waste (tailings or dumps) has been generated, produced by the exploitation and benefit of the most common deposits in the country. These deposits are of the epithermal type, which contain precious metals related to sulfides of Ag–Au paragenesis (Pb–Zn). Table 1 shows the elemental content of the Coscotitlan tailings, where a significant concentration of Ag (64 g ton^{-1}) is observed. The Teluro is an element that is related to the gold content in the Mexican deposits, which sustains the presence of 0.65 g of Au per ton. In Fig. 1, Fe, Mn, Zn, Cu and Pb are observed as the most abundant elements in these samples, in addition to the minority content of As Cr, Sb, Se, Hg, Sn, Bi, Ni, Ce, Co and Cd. The elemental chemical analysis focused on the metallic content of the tailings, the remaining percentage of the reading of the samples corresponds to gangue species.

Table 1 Chemical analysis of Coscotitlán tailings

Element	Cu	Pb	Zn	Fe	Cd	Mn	Ni	Co	Cr	As
Weight (%)	0.156	0.132	0.227	2.685	0.001	0.675	0.002	0.001	0.018	0.042
Element	Sb	Te	Bi	Se	Hg	Sn	Cu	Ce	Au	Ag
Weight (%)	0.017	0.006	0.006	0.010	0.030	0.008	0.156	0.001	64 g ton^{-1}	0.65 g ton^{-1}

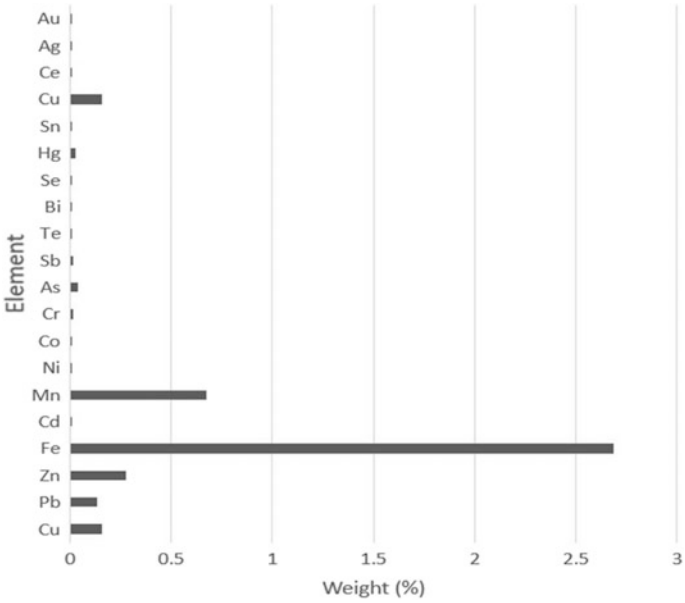

Fig. 1 Elemental content of Coscotitlán tailings

Polarizing Light Microscopy (PLM)

The quartz (SiO_2) is the most abundant mineral in the gangue of typical minerals of the mining district of Pachuca-Real del Monte, followed by calcite ($CaCO_3$) and albite ($NaAlSi_3O_8$). Rodonite ($MnSiO_3$) and bustamite [$CaMn_5(SiO_3)_6$] are found in small amounts and usually associated with silver-rich ores. After careful observation in the optical polarization microscope, it was identified that part of the metal mineralization of the tailings consists of sulphides and oxides. Figure 2a shows the pyrite (FeS_2) which is present as metallic inclusions in the quartz matrix (SiO_2) [JCPDS No. 99-101-1684], while in the micrographs of Fig. 2b, c, metal particles corresponding to iron oxides in form of hematite (Fe_2O_3) [JCPDS No. 99-200-4059] and lead sulfide in form of galena (PbS) [11, 12] are observed. Quartz (SiO_2) was identifed like the most abundant non-metallic mineral phase was corroborated by XRD, in addition to the presence of silicates such as orthoclase ($KAl_{1.02}Si_{2.98}O_8$) [JCPDS No. 99-101-0311], which is considered part of the gangue. The elemetal composition of the species identified by MOP was corroborated by the results obtained using XRD and the elemental chemical analysis.

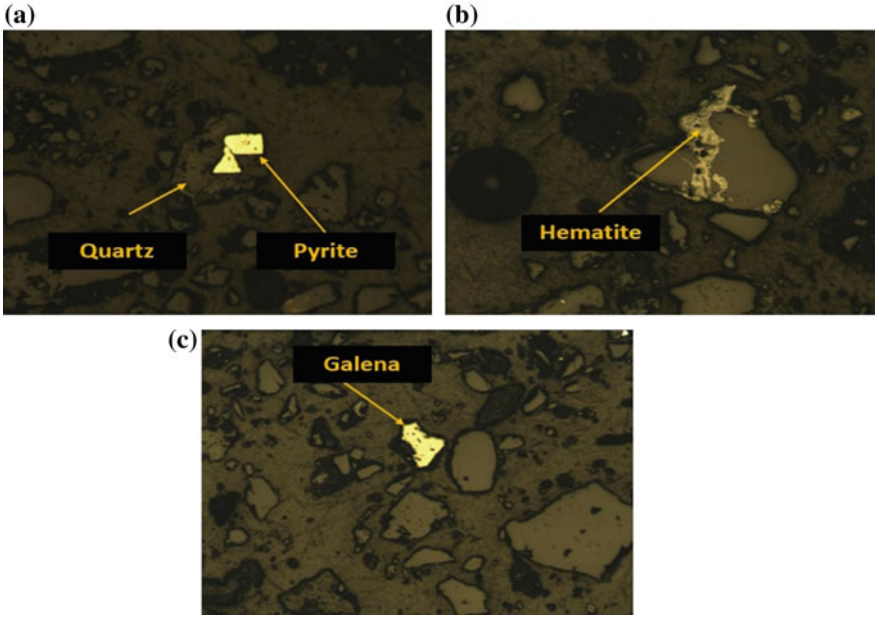

Fig. 2 Optical micrograph of the tailings de Coscotitlán where the presence of metallic particles is observed in a majority phase of quartz. Image obtained at 10×. **a** Inclusion of pyrite in quartz matrix; **b** hematite; **c** galena

Scanning Electron Microscopy with Energy Dispersion X-Ray Spectroscopy (MEB-EDS)

The obtained results show that the mineral has an irregular morphology where quartz particles predominate, being observed also other nonmetallic species less abundant in the form of silicates. Figure 3 shows a micrograph obtained with backscattered electrons, in which the presence of quartz is observed as a non-metallic mineral phase more abundant with metallic inclusions (bright white particles) corresponding to oxides of titanium and potassium silicoaluminates [13, 14] as confirmed by the X-ray dispersive energy microanalysis of Fig. 4.

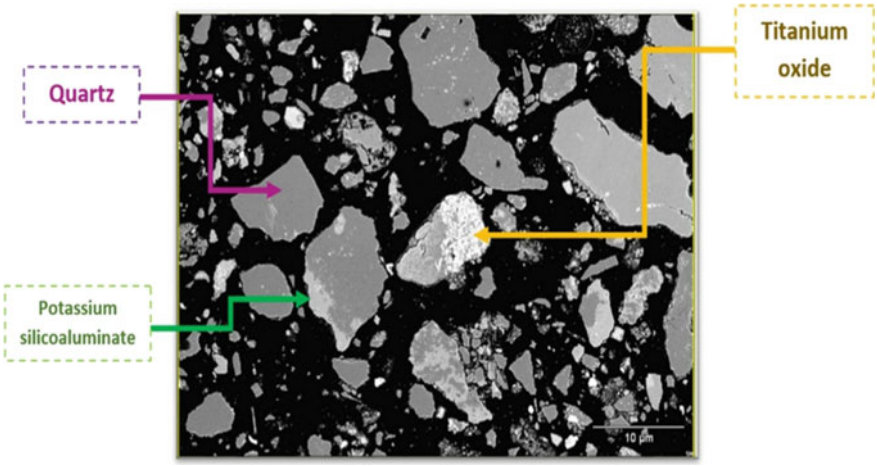

Fig. 3 Identification of metallic particles contained in the sample of the Coscotitlán

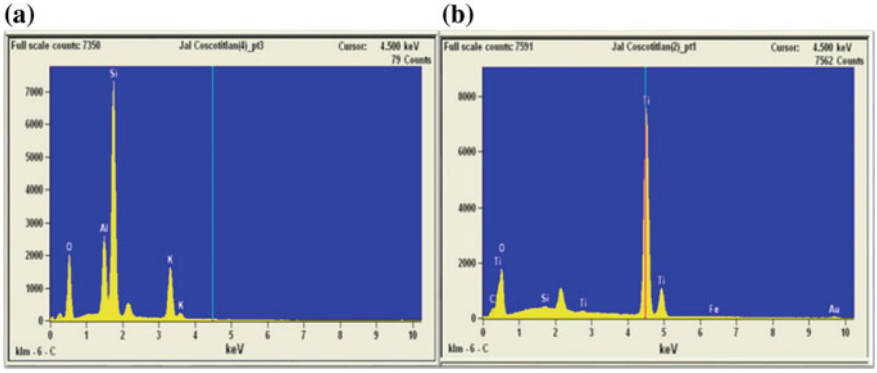

Fig. 4 Energy-dspersive X-ray Spectrum obtained by spot analysis. **a** Elemental content corresponding to potassium silicoaluminates. **b** Elemental content corresponding to titanium oxide

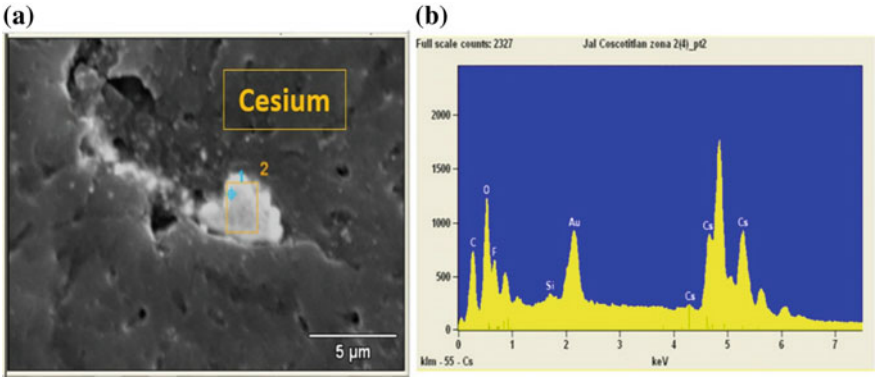

Fig. 5 **a** Micrograph with backscattered electrons showing the presence of rare earths. **b** Energy-dispersive X-ray spectrum showing characteristic peaks of cesium

However, although several meticulous sweeps were performed, the species or species containing silver were not identified. Part of the mineralization of these specimens, that was also identified in the chemical analysis, is the presence of rare earths detected by means of spot microanalysis made to several particles of irregular morphology of the order of 5 µm as shown in Fig. 5a. Finding that these bright particles correspond to Cesium as demonstrated by the spectrum obtained by X-ray energy dispersion of Fig. 5b.

Granulometric Analysis

To determine if the silver content is present at a specific particle diameter, the ratio between the silver law and the retained weight of the tailings at different particle size ranges with respect to the series of Tyler sieves was calculated as presented in Table 2. The results of the granulometric distribution of silver in the tailings of

Table 2 Granulometric analysis of the tailings of Coscotitlán

Número de malla	Apertura (micras)	Peso retenido (g)	Porcentaje retenido (%)	Ley de Ag (g ton^{-1})	% distribución Ag	Plata (g) por malla
80	177	24.88	21.14	66	31.64	13.95
100	149	9.77	8.30	33.1	6.23	2.75
140	106	21.18	18.00	37.2	15.18	6.70
200	75	28.78	24.46	36.9	20.46	9.03
270	53	18.24	15.50	40.7	14.31	6.31
325	45	6.36	5.40	44	5.39	2.38
400	38	8.46	7.19	41.6	6.78	2.99

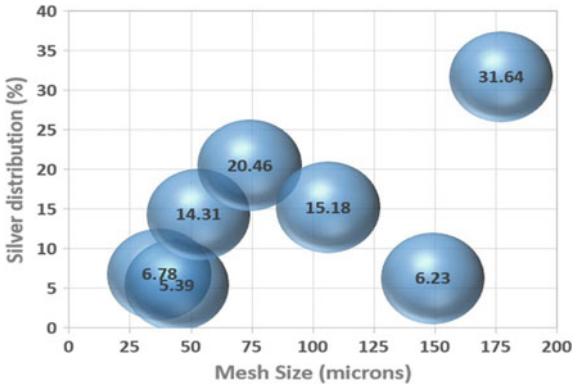

Fig. 6 Distribution of silver to different particle sizes

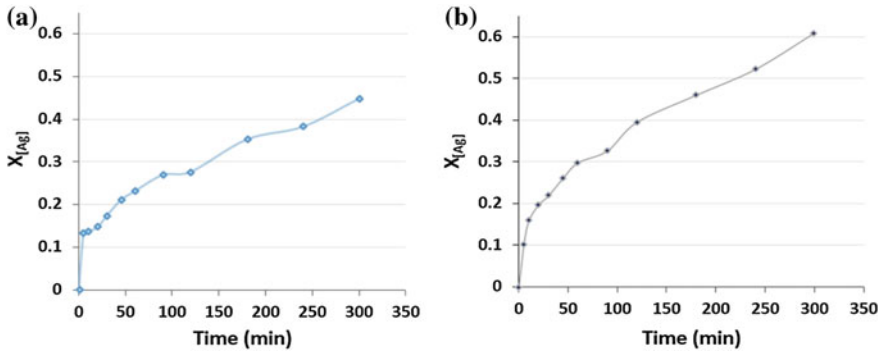

Fig. 7 Graphical representation of the silver solution in the system $S_2O_3^{2-}$–O_2 –Ni^{2+}. **a** Delimited mineral sample at 149 μm. **b** Delimited mineral sample at 74 μm

Coscotitlán are presented graphically in Fig. 6. The graph shows a distribution of monomodal form, where the largest distribution of silver is found in the particles corresponding to 177 μm (31.64% Ag), after which the graph shows a drop to the diameter of 149 μm (6.23%). However, from 105 μm, the silver distribution increases until reaching a 46.6% present in the 74 μm, particle size that was selected for the study of the silver solution in the system $S_2O_3^{2-}-O_2-Ni^{2+}$. The coarser particle sizes were discarded because they require a pre-leaching grinding process, in order to increase the contact area of the mineral sample with the leaching solution, however, this process would increase considerably the costs of the process.

The results obtained from the fraction of silver diluted in relation to the time are shown in Fig. 7, where it is observed that for particles to 149 μm maximum recovery values of 44.8% of Ag in the loaded solution are reached (Fig. 7a), while

74 μm was obtained 60.7% of silver diluted (Fig. 7b). Although both experiments were performed at room temperature and under the same conditions of additive concentration, the solution made with particles delimited to 149 μm shows a solution of silver 16% smaller than the solution where particles with 74 μm of diameter were used. This behavior is attributed to the fact that the silver distribution is lower in the 149 μm particles, in addition to that the surface area in contact with the leaching solution decreases as the particle size increases.

In both disolutions is observed that, as the time advances, the reaction increase. So it is suggested to increase the reaction times, in order to obtain better recoveries and to determine the time at which the reaction ends.

Conclusions

The chemical composition of the mineral studied revealed the presence of silver in economically profitable quantities reporting 64 g ton^{-1} of the precious metal. The majority mineral phase determined by MOP, MEB-EDS and XRD was quartz (SiO_2), which demonstrates the metallogenic nature of the deposit (quartz matrix veins), in addition minor minority species such as silicoaluminates. We suggest the exhaustive search for silver particles by means of SEM analyzes, to identify the elemental content of the silver-containing species.

It was observed the presence of pyrite and hematite, the latter confirmed by the MOP; technique in addition to the presence of galena, a mineralogical species commonly related to the presence of Ag. The punctual analyzes performed on the metal particles identified by MEB-EDS allowed us to confirm the presence of titanium oxides and rare earths in these mining residues. By means of the granulometric analysis and the preliminary tests it has been determined that the ideal particle size for the study of the silver solution is 74 μm, besides confirming the viability of the system as an alternative treatment for these mineral residues.

References

1. Nava C (2016) Enciclopedia de los municipios del Estado de Hidalgo, Mineral del Monte. In: Sistema integral de información del Estado de Hidalgo. http://www.hidalgo.gob.mx. Accessed 14 Mar 2017
2. Ortega J (1998) Aproximación a la Historia de la Minería en el Estado de Hidalgo. Secretaría de Educación Pública-FOMES, Colección Raíces, Hidalgo
3. González-Partida E, Carrillo-Chávez A, Levresse G, Tritlla J, Camprubı A (2003) Genetic implications of fluid inclusions in skarn chimney ore, Las Animas Zn–Pb–Ag(–F) deposit, Zimapa´n, Mexico. Ore Geology Reviews. doi:10.1016/S0169-1368(03)00015-5
4. Hernandez J, Patino F, Rivera I, Reyes IA, Flores MU, Juárez JC, Reyes M (2014) Leaching kinetics in cyanide media of Ag contained in the industrial mining-metallurgical wastes in the state of Hidalgo, Mexico. Int J Mining Sci Technol. http://dx.doi.org/10.1016/j.ijmst.2014.07.003

5. Rivera I, Patino A, Roca A, Cruells M (2015) Kinetics of metallic silver leaching in the O_2–thiosulfate system. Hydrometallurgy. https://doi.org/10.1016/j.hydromet.2015.05.009G
6. Alvarado-Macías G, Fuentes-Aceituno JC, Nava-Alonso F (2016) Study of silver leaching with the thiosulfate–nitrite–copper alternative system: effect of thiosulfate concentration and leaching temperature. Miner Eng. https://doi.org/10.1016/j,mineng.2015.12.011
7. Juárez JC, Rivera I, Patino F, Reyes MI (2012) Efecto de la Temperatura y Concentración de Tiosulfatos sobre la Velocidad de Disolución de Plata contenida en Desechos Mineros usando Soluciones S2O32–O2-Zn^{2+}. Información Tecnológica. https://doi.org/10.4067/S0718-07642012000400015
8. Hernández J, Rivera R, Patiño F, Juárez JC (2012) Estudio Cinético de la Lixiviación de Plata en el Sistema $S_2O_3^{2-}$-O_2-Cu^{2+} contenido en Residuos Minero-Metalúrgicos. Información Tecnológica. https://doi.org/10.4067/S0718-07642013000100007
9. Grosse AC, Dicinoski GW, Shaw MJ, Haddad PR (2003) Leaching and recovery of gold using ammoniacal thiosulfate leach liquors (a review). Hydrometallurgy. https://doi.org/10.1016/S0304-386X(02)00169-X
10. Hernández J, Rivera I, Patiño F, Juárez JC (2012) Estudio Cinético de la Lixiviación de Plata en el Sistema $S_2O_3^{2-}$-O_2-Cu^{2+} Contenido en Residuos Minero-Metalúrgicos. Información Tecnológica. https://doi.org/10.4067/S0718-07642013000100007
11. Moreno RT, Monroy MG, Castañeda EP (2009) Evaluación Geoquímica de residuos mineros (Jales o colas) de mineralización de tipo epitermal. Revista Geológica de América Central, Hidalgo, México. https://doi.org/10.15517/rgac.v0i41.4180
12. Hernandez J, Patino F, Rivera I, Reyes IA, Flores MI, Juarez JC, Reyes, M (2014) Leaching kinetics in cyanide media of Ag contained in the industrial mining-metallurgical wastes in the state of Hidalgo, Mexico. Int J Mining Sci Technol. doi:http://dx.doi.org/10.1016/j.ijmst.2014.07.003
13. Moreno RT, Tellez J T, Monroy FM (2012) Influencia de los minerales de los jales en la bioaccesibilidad de arsénico, plomo, zinc y cadmio en el distrito minero Zimapán, México. Revista internacional de contaminación ambiental. ISSN: 0188-4999
14. Geyne AR, Fries C, Segerstrom K, Black, RF, Wilson IF (1963) Geology and mineral deposits of the Pachuca-Real del Monte District, Stated of Hidalgo, Mexico, Consejo de Recursos Naturales no Removables, Hidalgo

The Influence of Clay Reinforcement on the Properties of Recycled Polymer Foams

Mariane Y. T. Oide, Julyana Satana, Renate Wellen, Francisco Valenzuela-Díaz, Olgun Guven and Esperidiana Moura

Abstract Poly [(ethylene)-co-(vinyl acetate)] (EVA) is a thermoplastic copolymer composed of randomly distributed polyethylene and polyvinyl acetate sequences within the molecular chain. EVA combines toughness with excellent flexibility, impact and puncture resistance. Because of these properties, this material is largely used for foam production as padding in equipment for various sports and as a shock absorber in sport's shoes. This work aims to study the influence of clay reinforcement on the performance of recycled polymer foams. The blend containing recycled HDPE (high density polyethylene) and recycled EVA (70/30 wt%, respectively) reinforced with 2 wt% of clays were prepared by melt extrusion, using a twin-screw extruder to obtain the composites. The composites and foaming agent were fed into a special single screw extruder for foaming. The samples of HDPE/EVA/Clay foams were characterized by tensile test, Field Emission Scanning Electron Microscopy (FE-SEM), Thermogravimetric Analysis (TG), Differential Scanning Calorimetry (DSC), X-ray Diffraction (XRD), density measurement and the correlation between the results was evaluated.

Keywords HDPE · EVA · Blend · Foam · Clay · Nanocomposite

M. Y. T. Oide (✉) · F. Valenzuela-Díaz
Polytechnic School of USP, Metallurgical and Materials Engineering Department, University of São Paulo (USP), Av. Prof. Mello Moraes 5643, Sao Paulo, SP 05508-010, Brazil
e-mail: mariane.oide@usp.br

J. Satana · E. Moura
Nuclear and Energy Research Institute (IPEN), Center of Chemical and Environmental Technology, Av. Prof. Lineu Prestes 2242, Sao Paulo, SP 05508-000, Brazil

R. Wellen
Materials Engineering Department, Federal University of Paraíba (UFPB), Cidade Universitária, João Pessoa, PB 058051-900, Brazil

O. Guven
Department of Chemistry, Polymer Chemistry Division, Hacettepe University, Beytepe, Ankara, Turkey

B. Li et al. (eds.), *Characterization of Minerals, Metals, and Materials 2018*, The Minerals, Metals & Materials Series,
https://doi.org/10.1007/978-3-319-72484-3_75

Introduction

Polymer composites have commercially attracted a lot of attention, principally in automotive and aerospace industries due to their improved mechanical and physical properties over pristine polymers. Nanocomposite is a new class of material that basically consists on composite in which the filler has one of its dimensions smaller than 100 nm (graphene, clay, e.g.). Studies have found that a small ratio of clay (3–5 wt%) like montmorillonite in a polymeric matrix is sufficient to raise their mechanical properties due to the enhancement of the tension transference from the polymeric matrix to the mineral [1]. In addition, nanocomposites have a great advantage over conventional composites. They can save weight because it is necessary smaller quantity of filler to reach the same modulus reinforcement than a conventional composite (glass fiber, e.g.) [2]. Montmorillonite is one of the widest used natural clay as nano-fillers from smectite group and it is basically formed by stacking plane of "SiO_2" (tetrahedron) and "AlO_6" (octahedron) units in ratios 2:1, respectively covalently bonded, forming platelets [3]. In this mineral some aluminum atoms are replaced by magnesium and the difference between the valences of these elements creates negative charges through the plane of the platelets which attract positive counter ions, typically sodium ions which are located in the gallery (interlayer) [2].

Clay also has been used for polymeric foams' production and their properties depend on bubble size and its distribution, the fillers' size, morphology and their distribution as well. Polymer foaming is a strategic technique used to create materials with low density, high shock absorbing, thermal and acoustic insulating properties [4]. These nanoparticles can modify the cellular structure and contribute for its improvement due to their capacity to act as a center of bubble nucleation and modify the rheological behavior favoring gas retention [5]. Cellular structure is very important for determining the foam's properties and it strongly depends on nucleation of embryos cells. Adding clay induces heterogeneous nucleation which has lower free energy barrier, as consequence, it is preferred over homogenous nucleation as the classical nucleation theory states [6, 7]. Wang and co-workers have showed that increasing the amount of montmorillonite (MMT) into a MMT/carbon foam the pore walls became thicker and the pore size decreased.

Although these advantages, it is difficult to disperse clays into a polymeric matrix because they are formed by layers of hydrous aluminum phyllosilicates with strong interlayer covalent bound within the sheet and each platelet is attracted by secondary bonds. Therefore it is necessary to modify them by a process called organophilization to produce nanocomposites. This process consists basically on changing the interlayer spacing by adding long chains or by grafting with a proper functional group by exchanging the interlayer cations with a cationic surfactant as primary, secondary, tertiary and quaternary alkylammonium which has a good interaction with the polymeric matrix, changing the hydrophilic property of the clay to hydrophobic character. Thus polymer will be able to be interleaved between clays' sheets or exfoliated and raise the polymers' properties [3]. In the current

work, recycled HDPE (high density polyethylene) and EVA were used for blend production. Two types of organophilized bentonite clays were used to produce nanocomposites and their respective foams. The samples were characterized by tensile test, FE-SEM, TG, DSC, XRD, density measurement and their morphology, mechanical and thermal properties were compared.

Experimental

Materials

Recycled HDPE (MFI = 0.13 g/10 min at 190 °C and a preload of 2.16 kg, Braskem), recycled EVA (MFI = 20.14 g/10 min at 190 °C and a preload of 2.16 kg, Braskem) and two thermal antioxidants, Irganox 1010 (Basf) and Songnox 1680 (Songwon), were used for blend production. An organophilized Brazilian bentonite clay from Cubati and commercially available organophilic bentonite clay (Rheotix VP provided by Rheotix) were utilized as nano-fillers. For foam production, Endex 2650 (Endex), an endothermic foaming agent was used. All nanocomposites and HDPE/EVA blend were produced by melting process using a flat die single screw extruder (HAAKE Rheomex P332, Thermo Scientific) and a co-rotating twin screw extruder (HAAKE Rheomex P332, Thermo Scientific), L/D = 25. The temperature profile used during processing was 145/150/170/190/195/195 °C for single screw extruder and 140/155/175/185/195/200 °C for twin screw extruder and the screws' rotation were 50 rpm.

Clay Preparation

Brazilian bentonite clay from Cubati was firstly modified with sodium carbonate (Na_2CO_3). In this process, calcium (Ca^{2+}) counter ions were exchanged by sodium (Na^+). Secondly, quaternary ammonium salt was added into the resulting product and mixed. Finally, the dispersed organophilized clay mixture was filtered, washed with deionized water and dried at 60 °C.

HDPE/EVA Blend, Nanocomposite and Foam Preparation

Recycled HDPE and EVA in 70/30 wt% proportion and the thermal antioxidants (0.1 wt%) were fed into a twin screw extruder for homogenization and blend production. The product was cooled down with air jet at room temperature and cut for pellets' production. For sheet production, the blend was added into a flat die

single extruder. Nanocomposites were prepared adding 2 wt% of clay and HDPE/EVA blend into a twin screw extruder for homogenization. The resulting material was cooled down by air jet at room temperature and it was cut for pellets' production. Then the material produced was fed into a flat die single extruder for sheet production. Foam was produced adding the nanocomposite/blend pellets with the endothermic foaming agent (1.5 wt%) into a flat die single screw extruder.

Characterization Methods

The specimens' densities and their degree of foaming were calculated by Eqs. 1 and 2, respectively:

$$\rho = \frac{m}{V} \tag{1}$$

$$\text{Degree of foaming}\,(\%) = \left(1 - \frac{\rho_f}{\rho_m}\right) \times 100 \tag{2}$$

where ρ is the density (ρ_f is the foams' density and ρ_m is the solid sheet's density); m is the mass, V is the volume of the samples [8].

Tensile tests were performed on INSTRON 5567 testing machine at room temperature. For tensile tests the samples were produced according to ASTM 882-91 and the moving rates used were 200 mm/min (foam) and 500 mm/min (solid).

XRD patterns were obtained for each nanocomposite sample produced and for the clays using Siemens—D5000 diffractometer operated at 40 kV and 40 mA, with copper Kα radiation (λ = 15.4 Å). The interlayer spacing (d) was calculated through Bragg's equation:

$$d = \frac{\lambda}{2\text{sen}\theta} \tag{3}$$

where λ = 1.514 Å is the incident radiation's wavelength and 2θ is the diffraction angle [9].

TG curves were obtained using TGA/SDTA851e (Mettler Toledo). The samples were heated from 30 to 580 °C under a nitrogen atmosphere (50 ml/min) at heating rate of 10 °C/min.

DSC analysis for each sample was performed using Mettler Toledo DSC 822e differential scanning calorimetry. Firstly, the thermal history of each sample was eliminated heating them from 25 to 250 °C at a scanning rate of 10 °C/min. Subsequently, the samples were cooled down to room temperature at rate of 10 °C/min. Finally, DSC curves were obtained heating them from 25 to 250 °C at a rate of 10 °C/min. The samples' melting temperature was determined as the temperature at which the endothermic peak occurred and the fusion enthalpy was obtained

integrating the peaks at the melting temperature. The crystallinity degree of the samples was calculated using Eq. 3:

$$\chi(\%\,\text{crystallinity}) = \frac{\Delta H_m}{\Delta H_0} \times \frac{100}{\omega} \quad (4)$$

where ΔH_m is the enthalpy of fusion which is acquired by integrating the area of DSC curve; ΔH_0 is the enthalpy of fusion for 100% crystalline HDPE at equilibrium temperature which corresponds to 293 J/g; ω is the weight fraction of HDPE in the sample [10].

FE-SEM: The samples' fracture morphology was studied using a Quanta FE 650 scanning electron microscope at 15 kV. The specimens were fractured in liquid nitrogen.

Results and Discussion

XRD

Figure 1 shows XRD patterns. As it can be observed in Fig. 1, all nanocomposite samples exhibited reminiscent basal peak of the organoclay but shifted which indicates the formation of intercalated structure. Adding Cubati's clay into the blend decreased the interlayer spacing from 1.8 to 1.4 nm for solid sample. This behavior was also observed for HDPE/EVA/Rheotix foam. The Rheotix clay interlayer spacing reduced from 2.3 to 1.5 nm when added into the blend as nano-fillers. Thus in these samples, despite the high processing temperature (reaching 200 °C) the quaternary ammonium salt was efficient to stabilize the clay avoiding the layers to collapse with each other. On the other hand, for solid HDPE/EVA/Rheotix and HDPE/EVA/Cubati foam the clays' basal peak shifted to $2\theta < 3°$ (3 degree) which is equivalent to interlayer spacing above 3 nm. This expansion may be caused by the polymer chains with low molecular weight that have interleaved into the gallery [2]. In addition, the basal peak intensity of solid and foam Cubati's clay nanocomposites decreased in relation to pristine Cubati's clay. However, the solid Brazilian nanocomposite basal peak intensity was significantly lower than observed in its respective foam. Therefore, it suggests that the exfoliation degree in the solid sample was higher than in the foam. It's known that when clays are added into a polymeric matrix besides the clays' XRD basal peaks shift for intercalated structure, their intensity decrease in relation to pristine clay either because the platelets become dispersed into the polymer, forming a low intensity and wide basal peak. This behavior might be evidence that exfoliation also occurred.

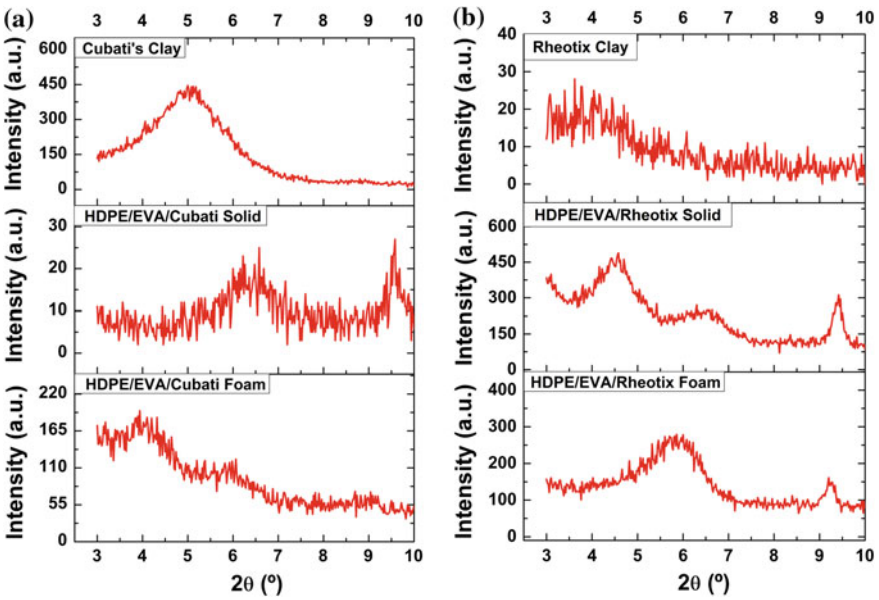

Fig. 1 XRD patterns of all nanocomposites and clays

Degree of Foaming

The degree of foaming for neat blend, HDPE/EVA/Cubati and HDPE/EVA/Rheotix were 36.3, 46.5 and 32.6%, respectively. The highest degree of foaming was obtained for HDPE/EVA/Cubati and enhancement of 28% was reached compared to neat blend. However, addition of Rheotix clay decreased the degree of foaming in 10% compared to neat blend and 30% compared to Brazilian clay nanocomposite foam. As observed in Fig. 1, Rheotix nanocomposite foam showed intercalated structure with interlayer spacing of 1.5 nm. On the other hand, HDPE/EVA/Cubati foam showed an intercalated/exfoliated structure with interlayer spacing above 3 nm. Therefore, the Brazilian clay's dispersion was more effective than Rheotix's one, enabling higher number of available bubble nucleation sites and reaching higher foaming degree than Rheotix clay nanocomposite.

DSC and TG

As it is seen in Table 1, the melting temperature for both foam and solid samples remains almost unchanged. However, the foams' and solid sheets' enthalpy of fusion increased with addition of clay, as consequence, the crystallinity as well. The solid samples showed lower crystallinity than the foams for all compositions. For

Table 1 Melting characteristics of foams and solids samples

HDPE/EVA	Foam			Solid		
	T_m (°C)	ΔH_m (J/g)	χ (%)	T_m (°C)	ΔH_m (J/g)	χ (%)
Neat	127.4	171.1	40.9	126.8	131.5	31.4
Cubati	126.9	173.5	41.4	127.4	135.8	32.4
Rheotix	126.4	180.8	43.2	126.9	178.7	42.7

neat HDPE/EVA solid sample, the crystallinity was 31.4%. Adding 2 wt% of Brazilian clay it raised to 32.4% but adding 2 wt% of Rheotix clay, the increase was more significant and it was 42.7%. For neat HDPE/EVA, HDPE/EVA/Cubati and HDPE/EVA/Rheotix foams, the crystallinities were 40.9, 41.4 and 43.2%, respectively.

Figure 2 shows the thermograms obtained for foam and solid samples by TG. All samples showed one-step thermal degradation. Meanwhile, in the literature, besides the degradation of ethylene at 460 °C, there are reports that between 350 and 400 °C occurs the decomposition of vinyl acetate to acetic acid and polyacetylene in HDPE/EVA blends which wasn't observed in these samples [9, 11]. Moreover, addition of clay into a HDPE/EVA blend catalyses the deacylation of EVA due to the presence of acidic sites in the organoclay structure, decreasing the thermal stability of the polymer [9]. However, for all samples, the thermal degradation of the nanocomposites were higher than pristine blends and using Rheotix clay as nano-filler showed to be more efficient than using Cubati's one because, probably, Rheotix clay was more effectively incorporated into the polymeric matrix, increasing the barrier effect which hinders the diffusion of harmful molecules and retards the blend degradation [9]. It can be also observed that for solid specimens, Rheotix clay showed to be more efficient either than Cubati's clay between 400 and 440 °C but in higher temperatures its thermal degradation became more expressive than Cubati's one.

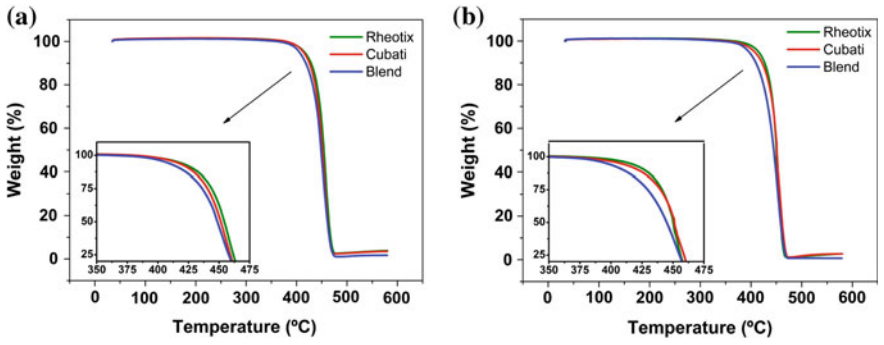

Fig. 2 TG thermograms of all samples **a** foams and **b** solid

Table 2 Young's modulus, tensile stress at break and tensile strain at break for all samples

HDPE/EVA	Foam			Solid		
	E (MPa)	σ_{break} (MPa)	ε_{break} (%)	E (MPa)	σ_{break} (MPa)	ε_{break} (%)
Neat	38.4 ± 0.8	7.6 ± 0.2	250 ± 24	58.4 ± 2.0	18.5 ± 0.6	818 ± 279
Cubati	30.1 ± 2.9	5.8 ± 0.2	104 ± 9	59.7 ± 3.4	19.7 ± 1.4	877 ± 62
Rheotix	41.1 ± 2.5	7.4 ± 0.3	66.5 ± 5.2	62.0 ± 2.7	18.3 ± 0.9	845 ± 51

Tensile Test

Mechanical behavior in tensile of HDPE/EVA blends and nanocomposites for both foam and solid samples are shown in Table 2. HDPE/EVA/Rheotix obtained the highest Young's modulus (E) for both foam and solid samples. These results are coherent with DSC analysis. The crystallinity degrees of these samples were the highest observed and their values were 43.2 and 42.7%, respectively. It's known that the crystalline region, where molecular chains are closely packaged, the secondary bounds are more relevant than in amorphous region. Then it's more difficult to move the chains, enhancing the polymers' mechanical properties and also decreasing their total elongation. Thus, for solid specimen due to the higher crystallinity degree of Rheotix nanocomposite than Cubati's one, its strain at break (845%) was lower than observed for the Brazilian clay nanocomposite (877%). However, the tensile strain at break (ε_{break}) for foams decreased with addition of clay, probably, due to low incorporation of clay into the polymeric matrix, and also due to the existence of areas with higher concentration of tension. Moreover, the tensile stress at break (σ_{break}) for HDPE/EVA/Cubati foam was smaller than observed in the others foam samples which the values were close due to its higher degree of foaming that decreased the transversal area during mechanical tests.

FE-SEM

Figure 3 shows the FE-SEM micrographs obtained for foam samples. As it is observed, all specimens showed heterogeneous macrocellular foam structure and clay aggregation for both nanocomposite foams. In addition, the Brazilian and Rheotix clay nanocomposites obtained microcellular structure. However, HDPE/EVA/Cubati foam obtained more defined cells than HDPE/EVA/Rheotix foam. Thus, Cubati's clay showed to be more efficient as bubble nucleating agent than Rheotix clay, as discussed above.

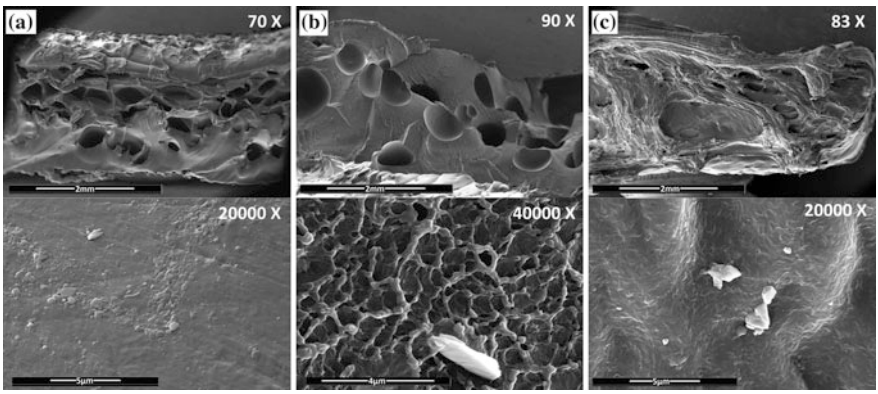

Fig. 3 FE-SEM micrographs for all foam samples **a** neat blend; **b** HDPE/EVA/Cubati and **c** HDPE/EVA/Rheotix

Conclusions

Addition of clay into HDPE/EVA blend produced with recycled raw materials enhanced the thermal properties and the degree of crystallinity for all samples. Adding Rheotix clay showed the best thermal stability for foams and solid specimens. This stability was observed at temperatures between 400 and 440 °C but in higher temperatures its thermal degradation became more expressive than Brazilian's one. Moreover, HDPE/EVA/Rheotix nanocomposite for both foam and solid samples presented the highest crystallinity degree, as a consequence, their mechanical properties were superior than foam and solid neat blend and HDPE/EVA/Cubati nanocomposites. In addition, Brazilian clay facilitated the bubble formation in the polymeric matrix more than Rheotix clay. All nanocomposite samples obtained intercalated morphology and for solid HDPE/EVA/Cubati specimen, high exfoliation degree was observed. Furthermore, despite the high processing temperature, the quaternary ammonium salt demonstrated to be efficient to stabilize the clays avoiding the layers to collapse with each other.

Acknowledgements The authors wish to thank CAPES to provide the support for this work.

References

1. Bhattacharya M (2016) Polymer nanocomposites—a comparison between carbon nanotubes, graphene, and clay as nano-fillers. Materials 9:1–35
2. Paul DR, Robeson LM (2008) Polymer nanotechnology: nanocomposites. Polymer 49:3187–3204
3. Kotal M, Bhowmick AK (2015) Polymer nanocomposites from modified clays: recent advances and challenges. Prog Polym Sci 51:127–187

4. Spina R (2015) Technological characterization of PE/EVA blends for foam injection molding. Mater Des 84:64–71
5. Laguna-Gutierrez E et al (2016) Low density polyethylene/silica nanocomposite foams. Relationship between chemical composition, particle dispersion, cellular structure and physical properties. Eur Polymer J 81:173–185
6. Yu J et al (2016) Preparation of polymer foams with a gradient of cell size: further exploring the nucleation effect of porous inorganic materials in polymer foaming. Mater Today Commun 9:1–6
7. Liu S et al (2016) Nanocellular polymer foams nucleated by core-shell nanoparticles. Polymer 104:22–30
8. Senna MM, Yossef HA, Eyssa HM (2007) Effect of electron beam irradiation, EPDM and azodicarbonamide on the foam properties of LDPE sheet. Polym Plast Technol Eng 46:1093–1101
9. Akhlaghi S et al (2012) Effect of stabilizer on the mechanical, morphological and thermal properties of compatibilized high density polyethylene/ethylene vinyl acetate copolymer/organoclay nanocomposites. Mater Des 33:273–283
10. Zarandi MB, Bioki HA (2013) Thermal and mechanical properties of blends of LDPE and EVA crosslinked by electron beam radiation. Eur Phys J Appl Phys 63:21101
11. Jofre-Reche JA, Martín-Martínez JM (2013) Selective surface modification of ethylene-vinyl acetate and ethylene polymer blend by UV-ozone treatment. Int J Adhes Adhes 43:42–53

The Quality of Tiles in Red Ceramic in Northwest of Rio De Janeiro and Southeast of Minas Gerais

Niander Aguiar Cerqueira, Victor Barbosa de Souza, Afonso Garcez de Azevedo, Priscila Oliveira Campos de Celebrini, Dienifer Daiana Konzen, Victor Tomazinho Bartolazzi, Mairyanne S. S. Souza and Sergio Neves Monteiro

Abstract Clay is used in the production and manufacture of materials for the construction of buildings from remote periods. Advances and improvements of its properties have allowed several applications to this raw material. In this work the quality of four types of ceramic tiles manufactured or used in the northwest of the state of Rio de Janeiro and in the southeastern state of Minas Gerais was evaluated. Geometric, physical and mechanical aspects were evaluated according to the Brazilian standard NBR 15310:2009. The results indicate numerous nonconformities with highlights for geometric parameters, surface flatness and yield tests. The nonconformities found in the samples indicate that there was a failure in the production control of the product and in the approval of the control of the lots.

Keywords Ceramic roof tiles · Quality testing · Civil construction Inspection

N. A. Cerqueira (✉) · V. B. de Souza · A. G. de Azevedo · D. D. Konzen
V. T. Bartolazzi · M. S. S. Souza
Redentor University Center (UNIREDENTOR), BR 356, KM 25, Itaperuna, Rio de Janeiro, Brazil
e-mail: coord.niander@gmail.com

N. A. Cerqueira · A. G. de Azevedo · M. S. S. Souza
State University of the Northern Darcy Ribeiro—UENF, Campos Dos Goytacazes, Rio de Janeiro, Brazil

V. B. de Souza
Federal University Fluminense (UFF), Niterói, Rio de Janeiro, Brazil

P. O. C. de Celebrini · S. N. Monteiro
Military Engineering Institute, Rio de Janeiro, Rio de Janeiro, Brazil

B. Li et al. (eds.), *Characterization of Minerals, Metals, and Materials 2018*, The Minerals, Metals & Materials Series,
https://doi.org/10.1007/978-3-319-72484-3_76

Introduction

According to data from the IBGE [1], the region studied in this research have as main sources of income agriculture and livestock, and mining activity can be considered as the third level. Among the exploited mineral assets are those that are applied as building materials, mainly decorative rock, mahogany and granite, and components for the cement industry that serves the states of Rio de Janeiro, Minas Gerais and Espírito Santo Holy. In the municipality of Itaperuna there is only one mine along the river Muriaé [2]. In the municipality of Bom Jesus do Itabapoana there is a terrace-alluvial deposit on the Itabapoana river. In the record of the DNPM [3], there is a mine in activity in quaternary sediments of the river Muriaé in Italva. In this region there is a group of companies that exploit the marble to manufacture cement. These clays can be derived from the change in ball wear.

The local ceramic industry has low-productivity, high-cost and non-standard products. Thus, the mining activity and the production of red ceramics were increasingly withdrawn in the state of Rio de Janeiro, putting pressure on the market for imports from other regions.

This study had as objective to evaluate the results of the characterization of several types of tiles commercialized regionally according to the current technical standard NBR 15310 [4].

Materials and Methods

In the present research, four models of tiles commercialized in the northwest of the state of Rio de Janeiro and southwest of the state of Minas Gerais, as defined in the scope of the work, were evaluated. Six specimens were tested for each model and the following properties were evaluated: audible and visual; geometric; impermeability; and water absorption.

The determined properties were compared to the quality parameters of ABNT's Brazilian standards [4, 5].

Among the tiles used in the market, the four models found were:

(a) Paulista ceramic tile: it is characterized by having the cover slightly less than the channel width. It provides a differentiated plastic movement to the rooftops;
(b) Plan tile: it is a variation of cover and canal, which has straight way;
(c) Roman tile: it presents low cost and it's one of the most popular models. A characteristic shape that fits lengthwise and crosswise. This type of tile has recently been standardized in 1996;
(d) Portuguese tile: not yet normalized by the standard, "has become a classic in the building world thanks to its attractive design and easy dispose of rainwater. Ensures a very short in the implementation, even for very large extensions, in perfect alignment and, consequently, high economy in the laying" [5].

The tiles were purchased in specific regional stores and analyzed in the laboratory of Redentor University Center, Campus Itaperuna/RJ.

The tests were performed following the specifications of the standard NBR 15310 [4].

These aspects were analyzed:

(a) Audible and visual;
(b) Geometric: manufacturing length (L), width (W), pin position (Lp), pin height (Hp), yield (Ym) and surface flatness.
(c) Functional and technological: impermeability and water absorption.

Visual Analysis and Sound

The ABNT [5] defines that the ceramic must present some aspects perceivable to the naked eye from a distance one meter, such as fine and smooth edges, brightness, uniformity of color, proper and uniform burning, texture and absence of burrs, cracks, breakages and body scrubs.

In the sound test, the samples were suspended and held at its widest end as a metal object beats on its opposite side. The sound of the beat must have a metallic character, otherwise it is not in compliance.

Geometric Analysis

According to ABNT [4], the samples were placed on flat surface and supported at its ends. With the help of caliper and squares each side of the tile must be measured. The average length and width of an oblong tile consists in the average of the measurements of two opposite sides.

The flatness is determined by the largest deviation in function of the obtained measure of the three point of the tile surface.

For the yield test, five samples of tiles are arranged, one set in the center and the other set around. The central tile must be replaced four times. With average values for width and lengths, calculate the useful area (A^u) tile, obtaining the average yield (Y^a).

$$Y^a = \frac{1}{A^u} \tag{1}$$

Functional and Technological Aspects

Impermeability

The specimens were placed in a horizontal position, elevated by their extremes. It was placed in its surface a sealed frame occupying 65% of the tile surface along with a constant column of water in its interior.

The samples remained for a day in this state. Finally, we checked the appearance of droplets in the lower face. The emergences of moisture spots are tolerated.

Water absorption

To perform the test, the ceramic tiles were placed in a 100 °C oven temperature for 24 h and removed after they had a dry weight measured. Continuing the procedure, they were submerged in a water tank for one day. The Percentage of water absorption is obtained by increasing the mass of the specimens after submerged, in accordance with the formula:

$$W\% = \frac{M_2 - M_1}{M_1} \times 100 \tag{2}$$

where:

M_2 wt. of the specimen after 24 h immersion in clean water;
M_1 wt. of the dry specimen.

Results

Visual Analysis and Sound

The NBR 15310 [4] appoints that "tile can display events such as scrubs, breakage, chipped and burrs that do not harm your performance."

Table 1 shows the results for *visual analysis and sound.*

Only the Roman type models were disapproved by the visual test. In the sound test, every specimen has the sound of the beat as metallic character, so they were approved.

Table 1 Surface quality

Specimen	Conforming	Non-conforming	% of tiles in the lot
Plan	40	0	100.0
Paulista	38	2	95.0
Roman	37	3	92.5
Portuguese	38	2	95.0
% of acceptable tiles in the lot	95 minimum		

Geometric Analysis

The dimensional tolerance permitted is ±2.0% for the manufacture dimensions. For the tiles pressed the pin must have a minimum height (Hp) of 7 mm.

For extruded tiles pin must have a minimum height (Hp) 3 mm. The accepted tolerance for the value of the yield (Y^a) is ±1% [4].

Table 2 shows the results for geometric aspects of extruded ceramic tiles.

Only one specimen of "Plan ceramic tile" was non-confirming in accord to the standards specifications, therefore, the type approved.

The ceramic tiles of Paulista type presents four samples exceeding the stipulated deviation. The average of size of specimens also was non-conforming. So, the geometric aspects of this type were reproved.

Table 3 shows the results for geometric aspects of extruded ceramic tiles.

The dry-pressed samples showed the measurements of length and width as the existing standard. However, the pin height found is lower, reproaching them.

Flatness

The values found in the measurement of flatness must not exceed 5 mm, regardless of the type of ceramic tile [4].

Table 4 shows the results for *surface flatness verification*.

Only the roman ceramic tiles were approved by this test.

Table 2 Geometric aspects of extruded ceramic tiles

Tiles		Plan				Paulista			
		L	W	Lp	Hp	L	W	Lp	Hp
Specimen	1	465.0	130.0	434.0	5.0	450.0	160.0	416.0	6.0
	2	463.0	124.0	434.0	5.0	450.0	161.0	415.0	7.0
	3	464.0	128.0	433.0	5.0	445.0	162.0	413.0	6.0
	4	464.0	128.0	434.0	5.0	450.0	160.0	418.0	6.0
	5	465.0	130.0	435.0	5.0	446.0	152.0	412.0	6.0
	6	466.0	128.0	435.0	5.0	450.0	161.0	418.0	7.0
Average of specimens (mm)		464.5	128.0	434.2	5.0	448.5	161.0	415.3	6.3
Average of size (mm)		460.0	130.0	434.0	8.0	450.0	160.0	424.0	8.0
Allowable deviation of the average size		2%			≥3 mm	2%			≥3 mm

Table 3 Geometric aspects of dry-pressed ceramic tiles

Tiles		Portuguese				Roman			
		L	W	Lp	Hp	L	W	Lp	Hp
Specimen	1	400.0	230.0	370.0	5.0	403.0	232.9	380.0	5.0
	2	405.0	235.0	374.0	6.0	402.0	232.0	380.0	5.0
	3	404.0	232.0	374.0	5.0	403.0	232.0	380.0	5.0
	4	400.0	233.0	370.0	6.0	401.0	232.1	381.0	5.0
	5	400.0	230.0	370.0	6.0	402.0	231.0	381.0	5.0
	6	400.0	230.0	370.0	6.0	400.0	232.0	376.0	5.0
Average of specimens (mm)		401.5	231.7	371.3	5.7	401.8	232.0	379.7	5.0
Average of size (mm)		400.0	232.0	377.0	8.0	400.0	230.0	365.0	8.0
Allowable deviation of the average size		2%		≥ 7 mm		2%		≥ 7 mm	

Table 4 Surface flatness

Specimen (6 units)	Average (mm)	Non-conforming tiles in the lot (units)
Plan	4.83	3
Paulista	6.17	3
Roman	3.,00	–
Portuguese	7.00	5
% of acceptable tiles in the lot	95 minimum	

Yield

The yield is expressed in roof tile unit per m^2. It allows a 1% coefficient of variation from the standard [5]. The extruded ceramic tiles were not examined for this test.

Table 5 shows the yield results of dry-pressed ceramic tiles.

All samples showed the yield higher than the specified.

Functional and Technological Aspects

Impermeability

All the ceramic roof tiles were accepted by the impermeability test.

Table 5 Yield of dry-pressed ceramic tiles

Specimen in the center	Portugues				Roman			
	Average useful length (mm)	Average useful width (mm)	Average useful area (mm^2)	Yield (t/m^2)	Average useful length (mm)	Average useful width (mm)	Average useful area (mm^2)	Yield (t/m^2)
1	350.00	150.50	52675.00	18.5	335.50	166.50	55861.00	17.9
2	345.00	152.50	52613.00	18.8	340.00	158.50	53890.00	18.6
3	344.00	152,00	52288.00	19.1	337.50	156.50	52819.00	18.8
4	347.50	153,00	53168.00	18.8	339.50	155.50	52793.00	19.2
5	346.63	152.00	52686.00	19.4	338.13	159.30	53840.00	18.6
Average yield				18.92	–			18.62
Allowable deviation of the average yield				1%				

Table 6 Water absorption

Specimen (6 units)		Dry mass M_1 (g)	Wet mass M_2 (g)	Absoption W%
Average	Plan	2.029,87	2.477,27	18.06
	Paulista	1.875,03	2.295,97	18.33
	Roman	2.407,10	2.954,53	18.53
	Portuguese	2.540,70	3.050,87	16.72

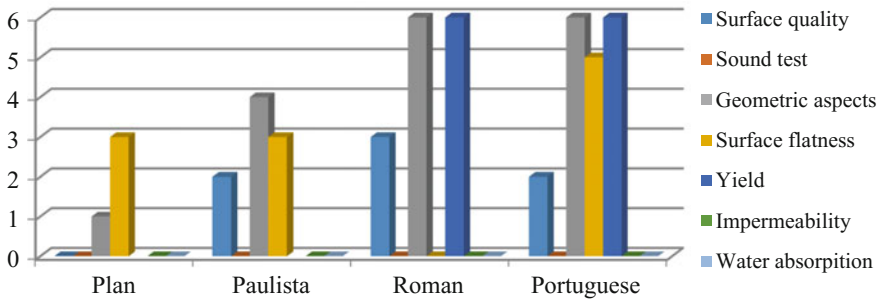

Fig. 1 Number of non-compliances detected in each of the tests

Water absorption

In temperate or tropical climates (as the study area), the water absorption limit of 20%.

Table 6 shows the water absorption results.

All specimens are approved.

The following chart (Fig. 1) describes the number of non-compliances detected in each of the tests.

Conclusion

The results indicate that there is a large number of nonconformities, thus there is a low quality trend of ceramic tiles in the market that does not meet the current parameters by the Brazilian standard.

As can be seen the geometric tests indicated the highest number of nonconformities, with only the flat tiles having the results approved, indicating the tendency of the existing ceramic tiles not to conform to this geometry requirement.

As for surface flatness and yield, many deviations were also observed in relation to the standard acceptable by Brazilian standards [4, 5].

The results indicate failures in the manufacturing control of the tiles and the release of lots from the different factories responsible for producing these products. Therefore, it is concluded that consumers find products on the market without standardization, which leads to the future appearance of pathologies in buildings.

References

1. IBGE—Instituto Brasileiro de Geografia e Estatística (2010) Gross National Product—2004–2008, Rio de Janeiro
2. CPRM—Serviço Geológico do Brasil (2012) Geology and mineral resources of "Folha Itaperuna". Programa Geologia do Brasil, Belo Horizonte
3. DNPM—Departamento Nacional de Produção Mineral (2011) Brazilian Mineral Yearbook 2008, Brasília
4. ABNT—Associação Brasileira de Normas Técnicas (2009), NBR 15310—Ceramic components—ceramic roof tiles—Termilogy, requirements and testing methods
5. ABNT—Associação Brasileira de Normas Técnicas (1997) NBR 13818—Specification and methods of test

Author Index

B. Li et al. (eds.), *Characterization of Minerals, Metals, and Materials 2018*, The Minerals, Metals & Materials Series,
https://doi.org/10.1007/978-3-319-72484-3

Subject Index

B. Li et al. (eds.), *Characterization of Minerals, Metals, and Materials 2018*, The Minerals, Metals & Materials Series,
https://doi.org/10.1007/978-3-319-72484-3